Targeted Nano-systems for Improving the Selectivity of Photodynamic Therapy

Melissa Jayne Bovis

A thesis submitted in fulfilment of the degree of

Doctor of Philosophy (Ph.D.)

May 2014

National Medical Laser Centre

Division of Surgery & Interventional Science

University College London

Statement of Originality

I, Melissa Jayne Bovis, certify that the work presented in this thesis is my own. Where information has been derived from other sources, I confirm that this has been indicated in the thesis.

Abstract

Introduction: Photodynamic therapy (PDT) is a minimally invasive treatment that requires a light-activated drug, known as a photosensitiser (PS), light of a specific wavelength and oxygen. 5,10,15,20-meta-tetra(hydroxyphenyl)chlorin (m-THPC) is one of the most potent PS's currently available for use in PDT, however, its undesirable accumulation in healthy tissues has prompted research to improve its uptake and selectivity into tumour tissue for the treatment of certain malignant diseases, whilst reducing adverse skin photosensitivity. In this investigation, a range of nanocarriers, eliciting a host of different properties, were developed to achieve more efficient delivery of m-THPC *in vivo*. These included liposomes, organically modified silica (ORMOSIL) nanoparticles (NPs) and polymeric NPs, which were additionally surface modified with a biocompatible polymer (PEG) coating to improve blood circulation times and the bioavailability of m-THPC. Further to this, studies investigating the conjugation of ligands, over-expressed on many cancers, to the NP surface aimed to increase active m-THPC-delivery via targeted nanocarriers. The overall objective of this study was to compare the pharmacokinetics of m-THPC delivery between the nanocarrier formulations and standard Foscan®, in normal rat and tumour-bearing animal models, to ultimately improve the efficacy of PDT.

Materials & Methods: The biodistribution of m-THPC in its standard formulation (Foscan) compared to its incorporation in untargeted and targeted pegylated NPs was assessed through quantitative chemical extraction methods and pharmacokinetic analysis. A range of tissue samples were collected over different time periods following *i.v.* administration of NPs (m-THPC dose equivalent) in both healthy and tumour-bearing murine models. Confocal and fluorescence microscopy techniques were employed for *in vitro* uptake studies and to examine *ex vivo* tissue localisation of encapsulated m-THPC. Finally PDT and skin photosensitivity studies were carried out *in vivo* to assess the efficacy of treatment to tumours and skin through histological analysis.

Results & Conclusion: Pharmacokinetic data typically indicated an increase in blood plasma $t_{1/2}$ of pegylated NPs in comparison to non-pegylated NPs or Foscan alone, indicative of the stealth properties conferred by the PEG corona. Peak accumulation of m-THPC in tumour tissue occurred between 6-24 h via passive uptake with untargeted NPs, attributed to the enhanced permeability and retention (EPR) effect. A significant improvement in tumour uptake, by a factor of three, was observed using pegylated liposomes compared to Foscan alone. Active targeting of NPs demonstrated a positive uptake into cells, unfortunately this did not translate to an improvement in m-THPC biodistribution or PDT results using *in vivo* models. Encouragingly anti-tumour PDT effects were observed with all NPs compared to Foscan, but treatment was most effective with untargeted pegylated liposomes.

Table of Contents

List of Figures

List of Tables

List of Symbols

Acronym	*Description*
PDT	Photodynamic Therapy
PS	Photosensitiser
ROS	Reactive Oxygen Species
m-THPC	*meta*-tetra(hydroxyphenyl)chlorin
FS	Foscan®, m-THPC in PEG 400 (3): EtOH (2): H_20 (5)
FP2%	FosPEG 2%, m-THPC in liposome, 100 nm, 2% mol PEG
FP8%	FosPEG 8%, m-THPC in liposome, 100 nm, 8% mol PEG
PEG	Polyethylene Glycol
PLGA	Poly(lactide-co-glycolic acid)
LA	Lactic Acid
GA	Glycolic Acid
ORMOSIL	Organically Modified Silica
NP	Nanoparticle
MDR	Multi-drug Resistance
PCI	Photochemical Internalisation
IR194	ORMOSIL NP: 2.34 % m-THPC, 19 nm
SF142UF	ORMOSIL NP: 1.5 % m-THPC, 95 nm
GG91UF	ORMOSIL NP: 2 % m-THPC, 100 nm
ER	Endoplasmic Reticulum
RES	Reticuloendothelial System
MPS	Mononuclear Phagocyte System
EPR	Enhanced Permeation and Retention
DMEM	Dulbecco's Modified Eagles Medium
RPMI-1640	Roswell Park Memorial Institute Medium
EDTA	Ethylene diamine tetra-acetic acid
FCS	Foetal Calf Serum
CAM	Chorioallantoic Membrane
PBS	Phosphate Buffer Solution
CCD	Charged-Coupled Device
FITC	Fluorescein Isothiocyanate
DAPI	4', 6-diamidino-2-phenylindole
FA	Folic Acid
FR	Folate Receptor
EGF	Epidermal Growth Factor
EGFR	Epidermal Growth Factor Receptor
VEGF	Vascular Endothelial Growth Factor
LDL	Low Density Lipoproteins
D_o	Initial Dosage
V_d	Volume of Distribution
C_o	Initial Concentration
C_l	Plasma Clearance
MRT	Mean Residence Time
AUC	Area Under the Curve
AUCM	Area Under the Moments Curve

$t_{1/2}$	Half-Life
RGD	Arg-Gly-Asp peptide
RAD	Arg-Ala-Asp peptide
EtOH	Mean Residence Time
MeOD	Deuterated Methanol
MeOH	Methanol
DMSO	Dimethyl Sulfoxide
SD	Standard Deviation
RCF	Relative Centrifugal Force
TEM	Transmission Electron Microscopy
SWCNTs	Single Walled Carbon Nanotubes

Cell lines

MC28	Methylcholanthrene-induced Rat Fibrosarcoma Cells
KB	HeLa Derived Human Nasopharyngeal Carcinoma Cells
MCF-7	Human Breast Carcinoma Cells
HCPC-1	Hamster Cheek Pouch Carcinoma Cells
CT26	Rat Colon Carcinoma Cells
A431	Human Epidermoid Carcinoma Cells
A549	Human Adenocarcinoma Alveolar Basal Epithelial Cells
HN5	Human Head And Neck Carcinoma Cells
CDD-34Lu	Human Fibroblast Cells
U937	Human Leukemic Monocyte Lymphoma Cells
HT29	Human Colorectal Adenocarcinoma Cells
MCF10A neoT	Human Breast Epithelial Cells
KYSE 510	Human Oesophageal Squamous Carcinoma Cells
HUVEC	Human Umbilical Vein Endothelial Cells
UCI-107	Human Epithelial Ovarian Carcinoma Cells

Acknowledgments

I would initially like to thank the EU's Seventh Framework Programme (Grant 201031 NANOPHOTO) for funding this project, without which this research would not have been possible.

I would like to acknowledge all my colleagues in the Department of Surgery & Interventional Science at the National Medical Laser Centre (NMLC), UCL, who have contributed to the progression of my project. I would like to give special thanks to; Prof Alexander MacRobert, Prof Stephen Bown and Dr Marilena Loizidou for their supervision, advice and invaluable experience in the field of PDT and Dr Josephine Woodhams for her endless help, understanding and guidance in a vast number of areas, in addition to allowing me the use of her PDT data in this report. I am also grateful to Dr Elnaz Yaghini, Dr Derick Adigbli and Ms Sandra Martinez de Pinillos for teaching me, providing much needed support during my PhD and for their great friendship.

Outside UCL I would like to thank; Biolitec (Jena, Germany), specifically Dr Dietrich Scheglmann for the preparation and provision of the liposomal nanocarriers, Dr Elena Reddi and Dr Fabrizio Mancin (University of Padova, Italy) for developing the ORMOSIL nanoparticles and supplying TEM images, Prof Janko Kos, Dr Matija Rojnik and Dr Petra Kocbek (University of Ljubljana, Slovenia) for the synthesis of the PLGA nanoparticles and Dr Wijnand Helfrich, Dr Marco Colombatti and Dr Marco de Bruijn (University Medical Centre Groningen, NL) for supplying the FITC-EDA-Folate conjugate.

Finally, I would like to dedicate this thesis to my wonderful parents, Alan and Lynn, my fantastic sisters, Laura and Katy, my life-long confidant, Ruth Brooker, and each of my amazing friends (you know who you are), for their endless love and support during the past five years, without any of whom this would not have been possible.

1. Photodynamic Therapy

1.1 Introduction

Cancer is a leading cause of death worldwide; accountable for 7.6 million deaths in 2008 (Ferlay J et al. 2008). With 12.7 million new cases reported in the same year, global statistics predict over 20 million people will be diagnosed with cancer by 2030 due to the increase in life expectancy and population growth (Boyle, P. &. L. B. 2008). The demand for effective cancer treatments that address the current issues of systemic, conventional therapies is ever-increasing. Photodynamic therapy (PDT) is a minimally invasive, powerful tool that can be harnessed to treat a variety of cancers (De Rosa, F. S. et al. 2000;Veenhuizen, R. et al. 1997;Wang, J. B. et al. 2007;Wang, K. K. et al. 2008;Wang, X. H. et al. 2009). It requires the administration of a non-toxic drug, known as a photosensitiser (PS), which only becomes activated when illuminated by a light source at a specific wavelength (Kübler, A. C. 2005;Robertson, C. A. et al. 2009). In oxygenated tissues, this leads to the generation of cytotoxic species which consequently induce cell death and tissue degradation (Castano, A. P. et al. 2005;Schuitmaker, J. J. et al. 1996). The fundamental specificity of PDT is highly attractive in its application in oncology; however, the limited selectivity of the photosensitiser into malignant tissues is a crucial inadequacy, which results in adverse prolonged cutaneous photosensitivity. Additionally, light and dosage parameters need to be optimised to enhance its efficacy. This study aims to reduce inter-patient variability of PDT by improving the delivery of a potent PS, *meta*-tetra(hydroxyphenyl)chlorin (*m*-THPC), into 'target' tumour tissues in comparison to normal tissues by its encapsulation into pegylated nanoparticles (NP).

1.2 History of PDT

Phototherapy has been known for over 3000 years (Spikes, J. D. 1985) and the use of light to treat diseases has been investigated since the beginning of the last century when Niels

Rydberg Finsen won the Nobel Prize in 1903 for Physiology-Medicine after treating 800 patients suffering from skin tuberculosis with phototherapy (Szeimies, R. M. et al. 2001). Around the same time, Oscar Raab was investigating the concept of inducing cell death through the interaction of light and chemicals under Dr Hermann Von Tappeiner (Raab, O. 1900). Using dyes such as acridine and eosin in the presence of light, and crucially oxygen (Ledoux-Lebards 1902), it was discovered that paramecia were rapidly killed and the term 'photodynamic action' was introduced (Tappeiner, H. v. et al. 1904). Porphyrins were the first photosensitisers to be identified (Dolmans, D. E. et al. 2003) and tested in humans (skin) by Friedrich Meyer-Betz, who observed pain and inflammation (extreme photosensitisation) for over 2 months when exposed to light after injecting himself with 200 mg haematoporphyrin (Meyer-Betz, F. 1913). Although retention and accumulation of haematoporphyrin was observed in neoplastic tissues in 1942 (Auler, H. et al. 1942), PDT, was not used to kill cancer cells until 1972 by Diamond *et al*., (Diamond, I. et al. 1972) in rats. It was soon discovered that deeper regions of the tumour tissue remained viable after treatment, which indicated that activation of the photosensitiser was only superficial and longer wavelengths of light were required to penetrate tissue further to kill remaining cancerous cells. This was achieved when Dougherty (Dougherty, T. J. et al. 1975) and Kelly (Kelly, J. F. et al. 1975) used red light (+ 630 nm) to successfully eradicate tumours in mice and humans with the a haematoporphyrin derivative (HPD). It was found numerous PDT treatments could be given to reoccurring malignancies due to its `minimal invasiveness in comparison to other available conventional therapies (e.g. surgical resection, radiotherapy and chemotherapy), which had previously failed. Since then, the development of new photosensitisers has enhanced the field of PDT, as different sensitisers require activation at different wavelengths of light, therefore therapy can be tailored to treat a whole range of cancerous tissues, where any damage to surrounding normal tissue is within an acceptable or tolerable level from which it can recover; gynaecological (Soergel, P. et al. 2008), pancreatic (Bown, S. G. et al. 2002), brain (Popovic, E. A. et al. 1996), head and neck (Hopper, C. et al. 2000).

1.3 Photochemistry

At room temperature almost all molecules are found in their lowest energy (ground) state (S_0) and electrons are orbitally paired in configuration. These electronic energy levels are dictated by electronic potential energy and are subdivided into (i) vibrational levels,

reflecting energy due to oscillations, and (ii) rotational levels (electron spin). When a photon of light is absorbed by the system (chromophore), electrons are excited from low energy orbitals (S_0) to unoccupied higher energy orbitals (S_1). These excited states are more short-lived due to differences in electronic distribution and a lower energetic stability; and as a result must release this surplus energy. This can occur via a number of mechanisms, illustrated in the Jablonski diagram (Jablonski, A. 1933) (Fig 1.1).

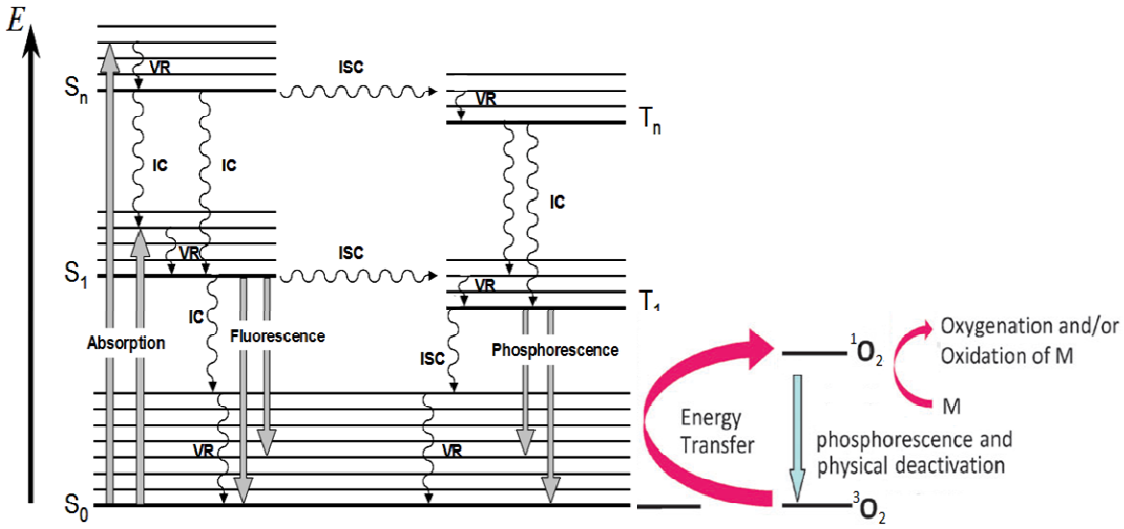

Figure 1.1. Jablonski diagram illustrating the electronic states of a photosensitiser (S^0, S^1, S^n, T^n, T^1) following absorption of a photon, energy transitions between them (IC, VR, ISC) and the production of singlet oxygen ($^1O_2$). The states are arranged vertically by energy and horizontally by spin multiplicity *(Ogilby, P. R. 2010)*; vibrational ground states are indicated by thick lines, higher rotational states by thinner lines, straight arrows show absorption and radiative transitions and curly arrows show non-radiative transitions.

Although photochemical reactions may be initiated from higher energy states (S_n), short lifetimes (10^{-9}-10^{-6} s) mean that these processes have low yields, therefore excited electrons are quickly converted to their lowest vibrational level (S_0 or S_1), through both non-radiative and radiative transitions (Yaghini, E. 2011) (Fig 1.1).

Non-radiative transitions

- *Vibrational Relaxation* (VR), a molecule in a high vibrational level of an excited state (S_n) will quickly fall to the lowest vibrational level of this state.
- *Internal Conversion* (IC), a molecule can fall from an excited singlet state (S_1) to ground state (S_0) by losing energy in small increments to the environment, cascading down through the vibrational levels to S_0.

- *Intersystem Crossing* (ISC), ground state (S_0) excitation through absorption directly to the triplet state (T_1) is strictly forbidden in quantum mechanics due to prohibited changes in electron spin, from antiparallel ↑↓ (S_0) to parallel spin ↑↑ (T_1). This also applies for transitions through emission of radiation, from an excited singlet state (S_1) ↑↓ to an excited triplet state (T_1) ↑↑ of lower energy. However, if an electron requires a spin inversion to relax and the energy gap between S_1 and T_1 is small (their wave functions have some overlap, Franck-Condon Principle), this leads to favourable spin-orbit interactions but prolongs radiative decay of the electron. The probability of this process is greater for aromatic compounds.

Radiative transitions

- *Fluorescence*, a molecule in its lowest excited singlet state (S_1) may fall to a low vibrational level of the S_0 state (S→S) by giving off energy in the form of light (radiative transition, ~10^{-9} secs). As emitted photons have a lower energy to that which were absorbed, fluorescence emits a longer wavelength of light (λ) than was used to excite and consequently emission maxima is red-shifted compared to the absorption maxima (Stokes-Lommel's Law). This also provides a signal which can be used for imaging and dosimetry in PDT.
- *Phosphorescence*; a molecule may return to S_0 from its lowest excited triplet state (T_1) by emitting light (or by emitting heat) through ISC (S→T). As this process is spin forbidden it has a slower radiative decay (radiative transition, ~10^{-3} secs) and the signal is weak.

T_1 states tend to have longer half-lives than S_1 states, as a result of forbidden spin processes.

1.4 Mechanism of Action

Photodynamic therapy consists of two competing oxidative pathways; Type I and Type II reactions (Sharman, W. M. et al. 2000). The process requires three key components in order to function, without any one of which, a reaction does not occur; these are light, photosensitiser and oxygen. As with all photochemical reactions, light is initially absorbed by a chromophore, however, in photosensitisation reactions, this light activation induces chemical changes in additional molecules other than the chromophore itself.

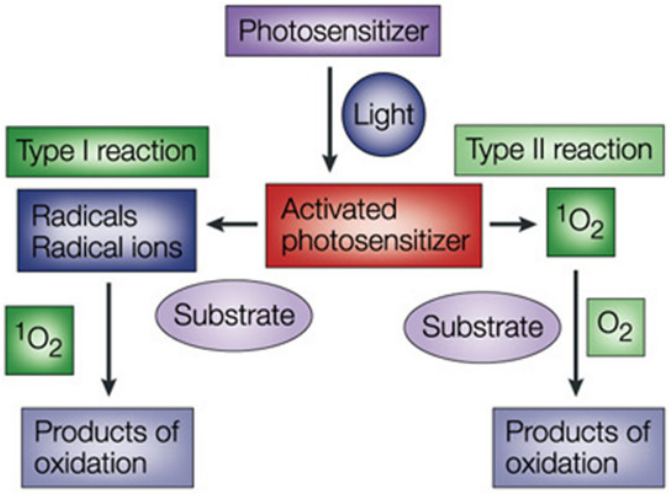

Figure 1.2. A schematic diagram of the two oxidation reaction pathways of PDT; Type I and Type II, following absorption of photons by a photosensitiser. *Diagram taken from (Dolmans, D. E. et al. 2003).*

Once activated, the chromophore promotes electronic excitation to higher energy states. In the case of PDT, when the photosensitiser (P) is exposed to light at a specific wavelength it becomes activated from a ground state (^{0}P) to an excited state (^{n}P*). In the presence of oxygen, the photosensitiser can undergo two types of reactions, transferring its energy as it returns to ground state (^{0}P). Intersystem crossing (ISC) from ^{1}P* to the excited triplet state (^{3}P*), typically a spin forbidden process, is a therapeutically important relaxation mechanism (Yaghini, E. 2011). Photosensitisers are able to undergo this transition with high efficiency due to a shift in energy levels from favourable electron spin-orbit interactions. For example, π bonds in the aromatic structure of the photosensitiser molecule create electron wavefunction overlap, allowing electrons to move from one orbital to another more easily (Plaetzer et al., 2009). In a biological environment the excited photosensitiser constantly collides with other molecules, and this provides ^{3}P* with alternative relaxation pathways (Hatz, S. et al. 2007). The first involves transfer of the electron to an acceptor molecule (Type I) and the second involves transfer of energy to oxygen molecules (Type II) (Foote, C. S. 1991).

In a *Type I* reaction; ^{3}P* reacts directly with the substrate (S) *i.e.* components of the cell, changing the charge on the photosensitiser molecule to form pairs of neutral radicals (e.g. $P^{\cdot-} + S^{\cdot+}$ or $P^{\cdot+} + S^{\cdot-}$) or radical ions ($O_2^{\cdot-}$, superoxide, or $^{\cdot}$OH. hydroxyl) following hydrogen or electron transfer (Calzavara-Pinton, P. G. et al. 2007). Both the excited photosensitiser (^{3}P*) and ground state substrate (S) can act as a hydrogen donor (undergo oxidation) and resulting radical species can react with O_2 to form peroxyl radicals ($SOO^{\cdot}$). Alternatively,

semi-reduced forms of photosensitiser ($P^{\cdot-}$) and substrate ($S^{\cdot-}$) can also react with O_2 to generate superoxide radical anions ($O_2^{\cdot-}$). These, in turn, can both produce and react with hydrogen peroxide (H_2O_2), the latter creating reactive hydroxyl radicals ($^{\cdot}OH$). These species are toxic and H_2O_2 is likely more mobile than singlet oxygen ($^1O_2$), passing easily through intracellular membranes (Bienert, G. P. et al. 2006), creating a greater potential for far reaching cellular damage.

Type II reactions are the predominant mechanism for which PDT is thought to occur and exert phototoxic effects (Dougherty, T. J. et al. 1976). In this instance, the photosensitiser in its excited triplet state ($^3P^*$) is able to transfer energy directly to ground state molecular oxygen present in living tissue, as it is naturally found in a triplet state configuration ($^3O_2$). An electron in $^3O_2$ may be promoted to the singlet excited state (Fig 1.1) upon receipt of energy from longer lived $^3P^*$ to generate singlet oxygen ($^1O_2$) and other reactive oxygen species (ROS):

$$P \rightarrow {}^1P^* \rightarrow {}^3P^* + O_2 \rightarrow P + {}^1O_2 \qquad (1.1)$$

The vast majority of photosensitisers are able to mediate $^1O_2$ production as they possess an energy gap exceeding that required to excite $^3O_2$ into its singlet state (>94 kJ mol^{-1}) as they absorb light at wavelengths $\lambda < 1260$ nm (Plaetzer, K. et al. 2009). As in its excited electronic state (excess energy), singlet oxygen is a potent oxidising agent, reacting aggressively with cell components to induce cellular toxicity (Levy, J. G. 1994). It has an extremely short life-time (< 0.04 µs) and a low diffusion constant in biological systems due to the presence of various quenchers, which consequently produces a short radius of action (< 0.02 µm) (Moan, J. et al. 1991) and compartmentalises photodamage. However, $^1O_2$ is not site-specific and is able to cause a cascade of destruction including lipid peroxidation (Rapozzi, V. et al. 2009), photo-oxidation of DNA guanine and damage to membranes and the cytoskeleton (Moan, J. et al. 1992) mediating cell death through necrosis and apoptosis pathways (Oleinick, N. L. et al. 1998). Is not site-specific In PDT, this singlet oxygen yield (Φ_Δ) is typically a good indicator of phototoxicity (Chen, W. et al. 2006), however, is dependent on a number factors that may limit therapeutic effects clinically, including, the diffusion of light and singlet oxygen through different biological tissues and photosensitiser aggregation *in vivo*.

1.5 Clinical PDT

In practice, achieving maximal destruction of tumour tissue can be challenging as the processes involved are complex. The availability of oxygen in the tissues is an essential PDT parameter. Vascular damage plays a vital role in PDT efficacy and contributes to long-term tumour control (Dougherty, T. J. et al. 1998); however a functional blood supply is critical in the delivery of oxygen to tissues, which is required to carry out treatment. If microvascular collapse occurs during the procedure, a photochemical reaction cannot take place and the treatment no longer becomes effective due to insufficient oxygen concentrations. It has been found that hypoxic tumour cells in murine RIF-1 tumours have been protected from PDT damage *in vivo* (Henderson, B. W. et al. 1989b) and decreasing cell death has been recorded with increasing distance from the vasculature supply (Korbelik, M. et al. 1994a). Therefore it is not preferential to restrict the blood flow to the tumour until after completion of PDT treatment which also prevents tumour regrowth. This can be achieved by delivering light sequentially over fractionated doses. A second destruction mechanism of PDT involves direct cell kill (Juarranz, A. et al. 2008), whereby tumour cells are targeted over the vasculature. The diffusion of photosensitiser out of the vasculature specifically into intracellular compartments of the tumour cells provides a killing mechanism, as ROS can only act close to the site of generation (Robertson, C. A. et al. 2009) due to the short diffusion distance of singlet oxygen. It is important to identify an optimal subcellular target (Dougherty, T. J. et al. 1998;Kessel, D. 1993) as complete tumour eradication by this mechanism is limited by the non-homogenous distribution of photosensitisers within the tumour tissue (Dolmans, D. E. et al. 2003). This will additionally prevent unwanted high volumes of photosensitiser distributing into normal tissues and is the focus of this investigation.

1.6 Why PDT?

PDT can be used in a number of applications, ranging from psoriasis, rheumatoid arthritis, and microbial infections. It has been successfully implemented in the treatment of diseases, both non-malignant and malignant, including age-related macular degeneration and a host of cancers. Common cancer treatments, currently employed, each have their own set of limitations and disadvantages; surgical resections can cause aesthetic implications, are costly in time and expense (prolonged hospitalisation) and have long recovery/healing periods. Systemic treatments, such as radiotherapy and chemotherapy,

have many unpleasant side-effects including; nausea, exhaustion, digestive problems, physical changes (skin, hair) and higher susceptibility to infection during/post-treatment due to non-selective uptake in other high-profilerating cells (Cancer Research UK 2014).

PDT is a minimally invasive technique (Allison, R. R. et al. 2009) due to a lack of culmulative toxicity and can therefore be applied repeatedly unlike most conventional methods where an administrative threshold is reached due to systemic application. PDT treatment periods are short (Mlkvy, P. et al. 1995) resulting in reduced hospital admission times (Bown, S. G. et al. 2002) and cost. The treatment is specific, selective (Alexiades-Armenakas, M. 2006) and safe, as each of the three components (photosensitiser, light and oxygen) have to be present in order for a reaction to occur. The administration of photosensitiser is non-toxic and will only become active once light is introduced to the tissue, therefore light can be directed to the exact tumour site. Although the rapid proliferation of tumours is known to result in hypoxic areas within the tissue (Brown, J. M. et al. 2004), repeatable PDT treatments mean efficient debulking of the tumour can still occur in oxygenated regions (Souza, C. S. et al. 2007). Furthermore, lymphocytes and macrophages may become sensitised as part of an immune response potentiated by PDT, which then seek to eliminate small foci of any remaining viable cancer cells under a reduced tumour burden (Dougherty, T. J. et al. 1998;Korbelik, M. et al. 1999). This has been reported by multiple studies *in vitro* documenting macrophage activation factors (TNF-β, DBPMAF) and *in vivo* through immune cell infiltration in murine SCCVII tumours (Korbelik, M. et al. 1994b). Additionally, PDT does not exhibit a thermal effect, as the fluence rate of light does not reach sufficient levels to induce heating of the tissue (Bown, S. G. 1990), therefore the integrity of underlying structures and connective tissues, such as collagen and elastin, are largely preserved (Hopper, C. et al. 2000). This produces very pleasing aesthetic outcomes, as healing is rapid, leading to huge cosmetic advantages (Nyst, H. J. et al. 2009). PDT itself has some remarkable benefits but can be particularly effective when used in combination with conventional and novel therapies, especially if the patient is already in a weakened state or these treatments have previously failed (Nathan, T. R. et al. 2002). Photochemical Internalisation (PCI) is a new technique, which exploits the mechanisms of PDT at a subcellular level to augment the intracellular delivery of endocytosed, biologically active macromolecules, such as cytotoxic chemotherapeutic agents to potentiate cell death. Its success *in vivo* has led to its progression into Phase II clinical trials and offers exciting potential.

1.7 Photosensitisers

Photosensitisers are archetypally planar, aromatic compounds with a core macrocycle composed of pyrrole rings. These rings are linked by either azone bridges (phthalocyanine) or methine bridges (porphin, chlorin, bacteriochlorin), which are all fully conjugated with double bonds (Fig 1.3).

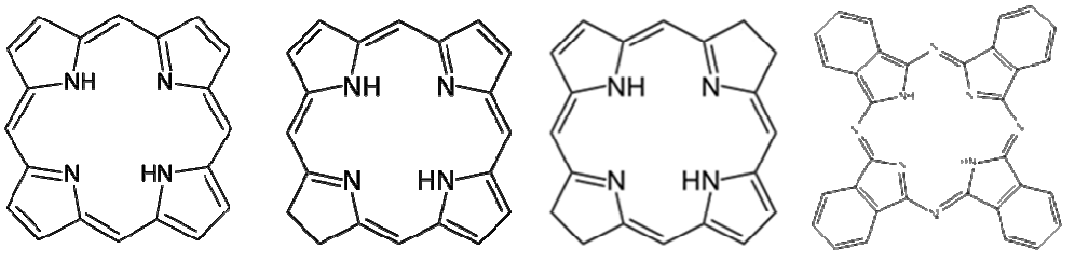

Porphin	Chlorin	Bacteriochlorin	Phthalocyanine
22 π-electrons	20 π-electrons	18 π-electrons	18 π-electrons
λ ~630 nm	λ ~650 nm	λ ~670 nm	λ ~670 nm

Figure 1.3. Basic structures of porphyrin, chlorin, bacteriocholrin and phthalocyanine with their corresponding π-electrons and emission wavelengths (λ) *(Bonnett, R. et al. 1999).*

The extensive π-conjugation system within these aromatic structures allows these photomolecules to absorb light in the visible region of the spectrum (λ = 350-750 nm), producing similar absorption spectra. Characteristically, porphyrins exhibit a strong absorption peak in the near-ultraviolet region ~400 nm (Soret Band) as a result of a strong transition from the ground state to higher excited states ($S^0 \rightarrow S^n$) and a weaker absorption peak between ~600-800 nm (Q band) from a weak transition to the first excited state ($S^0 \rightarrow S^1$). Despite the reduction in absorption, this secondary weaker peak is more preferable in clinical applications due to the greater penetration depth of red light (longer λ) into biological tissues in comparison to blue light (shorter λ), which is strongly absorbed or scattered by haemoglobins in the blood and other proteins (Bechet, D. et al. 2008). This π-conjugation system also potentiates a reduction in the transition energy (ΔE) between molecular excitation states, resulting in absorption of longer wavelengths of light (lower energy). Porphyrins have a greater number of π-electrons (22) due to the greater number of saturated double bonds in their structure (Fig 1.3) in comparison to chlorins (1 reduced

double bond, 20 π-e) and bacteriochlorin/phthalocyanine (2 reduced double bonds, 18 π-e). As a result, the absorption maxima of the Q band progressively increases in wavelength (λ) between each compound due to the loss of symmetry in the molecule and the lower level of energy required to induce transitional changes (Fig 1.3).

The disadvantages associated with PDT are largely attributed to the localisation and uptake of the photosensitiser. For example, prolonged photosensitivity of the skin and eyes is a result of undesirable accumulation in these tissues, which can lead to swelling, sunburn and blistering if exposed to bright light (Chatterjee, D. K. et al. 2008a) for several days or even weeks after treatment (depending on the PS). In both the clinic and animal models, hydrophilic photosensitisers (*e.g.* haematoporphyrin, tetrasulphonated porphyrins and phthalocyanines) are largely transported by albumin and globulins, whereas hydrophobic photosensitisers (porphyrin esters and chlorins) are preferentially incorporated into the lipid interior of lipoproteins (Jori, G. 1989). The systemic administration of more hydrophobic photosensitisers (non-polar molecules) through intravenous injection can create preliminary problems, due to the formation of aggregates in physiological aqueous conditions (Chen, B. et al. 2005). Their hydrophobicity may also lead to interactions with other circulating PS molecules, which can affect the photophysical properties of the PS, such as the production of singlet oxygen (Φ_Δ) (Bechet, D. et al. 2008). Furthermore, the stimulated binding of plasma proteins to hydrophobic aggregate-complexes can lead to rapid PS elimination from circulation and preferential uptake by cells of the reticuloendothelial system (RES), such as the Kupffer cells of liver, followed by the spleen and the lungs (Brannon-Peppas, L. et al. 2004).

FDA approved photosensitisers absorb in visible regions of the spectrum (< 700 nm), which can be restrictive clinically, as light penetration is limited (mm) and therefore only superficial lesions can be treated (without the use of fibre-optic scopes). In addition, technical difficulties in the application of PDT to a wide range of oncological diseases, can lead to high inter-patient variability with many photosensitisers in terms of PDT treatment response. However, tissues irradiated at wavelengths exceeding this (>700 nm) may not generate adequate levels of energy to produce ROS. Finally, and perhaps more importantly, selectivity of the photosensitiser to diseased tissue may not sufficiently outweigh that of normal tissue.

Ideal photosensitisers should fulfil several requirements (Bonnett, R. et al. 1989a) for use in clinical applications, established by Bonnett *et al*.,:

- Chemically pure with stable composition
- Strong absorption in the red region of the visible spectrum (> 650 nm)
- High quantum yield in triplet formation ($^3P^*$) (energy > 94 kJ mol^{-1}) for high production of singlet oxygen and greater phototoxicity
- Minimal dark toxicity
- High tumour selectivity over normal host tissue
- Good pharmacokinetic clearance profile

In 1993 PDT was first approved for the treatment of bladder cancer in Canada (Dolmans, D. E. et al. 2003), which was carried out using the PS, Photofrin® (PII). PII is partially purified haematoporphyrin derivate (HpD), that contains the porphyrin moiety. Porphyrins are comprised of four pyrrole rings interconnected by methine bridges to form a heterocyclic structure. Upon the introduction of light, these alternating single and double bonds in the ring chains of the molecule, allow activated electrons to circulate around them, retaining and transferring energy from one molecule to another non-energised molecule (Wald, G. 1959). Porphyrins were named the first generation photosensitisers. They have been approved for a range of cancer treatments over the last 20 years (Brown, S. B. et al. 2004) having never produced any serious side-effects indicating good long-term safety and repeatability. However, PII is not a pure compound and is synthesised in a complex mixture of porphyrin dimers and oligomers (Fadel, M. et al. 2010;Verma, S. et al. 2007). Its maximal absorption wavelength is 630 nm, at the lower end of the therapeutic window, producing limited penetration depth of light. It also possesses poor tumour selectivity, which can lead to skin photosensitivity lasting for several weeks (Moriwaki, S. I. et al. 2001).

Second generation photosensitisers including; phthalocynanines, napthalocyanine and chlorins, are porphyrin derivatives developed to try and overcome some of the limitations and unfavourable properties of porphyrins (Chatterjee, D. K. et al. 2008a). Temoporfin, also known as 5,10,15,20-*meta*-tetra(hydroxyphenyl)chlorin (m-THPC) (Fig 1.4) or trade name formulation, Foscan®, is a second generation photosensitiser (Bonnett, R. et al. 2002) and was approved in the European Union and Japan for the treatment of head and

neck cancers in 2001 (Brown, S. B. et al. 2004). Since this time, it has been used to treat early squamous cell carcinomas (Copper, M. P. et al. 2003), basal cell carcinomas (Baas, P. et al. 2001), prostate (Moore, C. M. et al. 2006) and pancreatic cancer (Bown, S. G. et al. 2002). m-THPC was synthesised as a stable 'm' isomer, based on the '*meta'* position of the hydroxy group on the benzene ring (Fig 1.4), and was found to be the most active isomer in *in vivo* assays (Bonnett, R. et al. 1989b). It was derived from porphyrin (Bonnett, R. et al. 1989b) and as a result is ≥98% chemically pure (Glanzmann, T. et al. 1998). It is a potent photosensitiser and has an exceptionally strong phototoxcity, as it produces high quantum yields of singlet oxygen (0.87) (Hopper, C. et al. 2000) due to its longer half-life in the excited triplet state and its effectiveness in PDT has been reported as being ~200-fold higher than that of PII (Ball, D. J. et al. 1999;Sharman, W. M. et al. 1999;Vangeel, I. P. J. et al. 1995). This implies lower PDT light exposures (10 j cm^{-2}) (Ris, H. B. et al. 1991) and lower photosensitiser drug doses can be administered in order to elicit a similar PDT response; typically 0.15-0.3 mg kg^{-1} compared to 10 mg kg^{-1} for PII (Dougherty, T. J. et al. 1998;Jones, H. J. et al. 2003), even for large surface treatment. m-THPC also has a strong absorption peak in the far red region of the visible spectrum (λ = 652 nm) and a molar extinction coefficient of 29,600 M^{-1} cm^{-1} at this wavelength (PII = 1170 M^{-1} cm^{-1}). This longer wavelength of light can penetrate biological tissues at a depth greater than PII of approximately 7 mm (Dougherty, T. J. et al. 1998;Palumbo, G. 2007) at relatively low light fluencies.

1. Photodynamic Therapy

Active Drug	Product name	Application	Approved
Haematoporphyrin derivative (HpD), porfimer sodium	Photofrin® (Axcan Pharm)	Lung, oesophageal adenocarcinoma, cervical, gastric, bladder cancer	Selected countries worldwide, 1993
meta-tetra(hydroxyphenyl)chlorin (*m*-THPC)	Foscan® (Biolitec Pharma)	Head and neck cancer	EU, Norway, Iceland, Japan, 2001
5-aminolevulinate (ALA) *precursor to* Protoporphyrin (Pp) IX	Levulan® (DUSA Pharma)	Topical; actinic keratosis	US, 1999
Methyl aminolevulinate	Metvixia® (Photocure)	Topical; actinic keratosis, basal-cell carcinoma	EU, Australia, 2001
mono-L-aspartyl chlorin e6 (Talaporfin)	Laserphyrin® (Meiji Seika Pharma)	Lung cancer	Japan, 2004
Aluminium sulfonated phthalocyanine (AlPcS)	Photosense® (NIOPIK)	Head and neck cancer	Russia, 1995
Hexyl aminoevulinate	Hexvix	Diagnosis	Sweden, EU, 2005
Benzoporphyrin derivative (BPD), Verteporfin	Visudyne® (Novartis)	Age-related macular degeneration	≥70 countries worldwide, 2001
2-(1-Hexyloxyethyl)-2-devinyl pyropheophorbide-a (HPPH)	Photochlor	Lung cancer	Phase II clinical trials, 2011
Motexafin lutetium	Antrin	Topical, prostate cancer, photoangioplasty	Phase I clinical trials, 2009
Hexylaminolevulinate (HAL)	Cevira	Precancerous cervical lesions (HPV)	Phase II clinical trials, 2012

Table 1.1. Drugs approved for PDT in oncology, diagnosis and non-malignant disease and drugs in clinical trials.

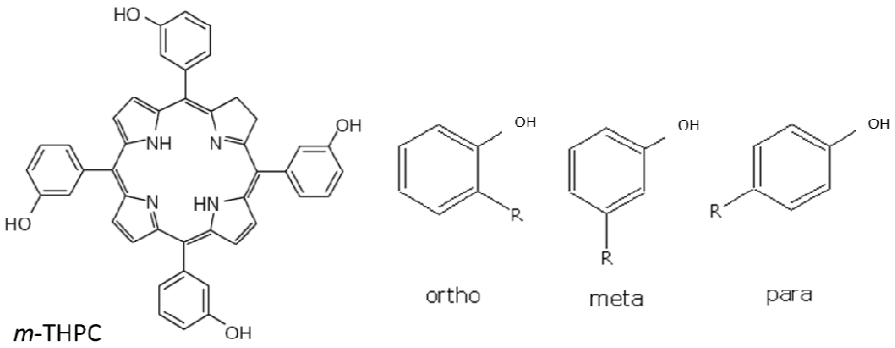

Figure 1.4. Structure of 5,10,15,20-*meta*-tetra(hydroxyphenyl)chlorin (m-THPC) and the *meta* (m), *para* (p) and *ortho* (o) isomers of the hydroxyphenyl substituent.

When administered systemically through intravenous injection in its standard Foscan® formulation (m-THPC in buffer; 30% PEG 400: 20% ethanol: 50% H_2O), the biodistribution of m-THPC *in vivo* has been shown to change over time in murine models, which also differ to clinical data, due to the binding of various available serum proteins that exist in different concentrations, *i.e.* low density lipoproteins (LDL) (Jori, G. et al. 1993;Triesscheijn, M. et al. 2007) and albumins (Verma, S. et al. 2007). *In vitro* studies carried out with HT29 human colon adenocarcinoma cells using m-THPC show a good uptake and distribution of the photosensitiser intracellularly after short incubation periods of 3 h (Melnikova, V. O. et al. 1999b). Marchal *et al*., also demonstrated m-THPC localisation in the nuclear envelope in human MCF-7 breast cancer cells, however, it was suggested m-THPC predominantly localised in the ER and Golgi apparatus (Marchal, S. et al. 2007;Melnikova, V. O. et al. 1999b) as these were the primary sites of PDT-induced damage. ER localisation supports apoptotic cell death as it improves the photoactivation of the caspase-7 pathway but both apoptotic and necrotic pathways are implicated in PDT cell death (Marchal, S. et al. 2007). Binding of serum proteins in foetal calf serum (FCS) *in vitro* has shown to monomerise hydrophobic aggregates of m-THPC in myeloid leukaemia cells (Chen, J. Y. et al. 2000) and facilitate its cellular uptake *via* receptor mediated endocytosis (Palumbo, G. 2007;Verma, S. et al. 2007). m-THPC has been found to be a moderately photolabile compound, susceptible to changes under the influence of radiant energy. Kinetic analysis shows two types of aggregated species, dimers and higher aggregates, each with distinct disaggregation rate constants that significantly increase with higher temperatures (Hopkinson, H. J. et al. 1999). Further *in vivo* studies show unusual pharmacokinetics with human plasma, as following intravenous injection, m-THPC initially binds to an unknown protein in large quantities before being redistributed to

lipoproteins (Hopkinson, H. J. et al. 1999). Secondary m-THPC concentration peaks in the plasma are produced at 6 and 10 h, indicating very slow m-THPC release kinetics (Glanzmann, T. et al. 1998). LDL is up-regulated on the surface of cancers due to their increased cell proliferation (Misawa, J. et al. 2005), which is thought to aid in the accumulation of m-THPC in tumour tissues over normal tissues (Lin, C. W. et al. 1991), as hydrophobic PSs are preferentially bound by lipoproteins (Jori, G. 1989). Although similar findings of m-THPC binding to various protein fractions in rat models have been observed *in vivo*, the identification of hydrophobic molecules in the plasma by the host immune system, result in opsonisation of m-THPC, where major loss of the photosensitiser from circulation is observed, as it is directly distributed to the cells of the RES for clearance *i.e.* residing macrophages in the liver, spleen, kidneys (Kudinova, N. V. et al. 2009;Peng, Q. et al. 1995).

During PDT treatment, the production of reactive oxygen species (ROS) and intermediates react not only with biological substrates but the photosensitiser itself, causing transformation changes or destruction of the photosensitiser molecule, known as photobleaching. Comparisons *in vivo* using a Balb/c mouse model show the rate of photobleaching for m-THPC was ~20 less than a similar porphyrin derivative, m-THPBC, 5,10,15,20-*meta*-tetra(hydroxyphenyl)bacteriochlorin (Rovers, J. P. et al. 2000). This photobleaching rate was increased further to ~90 fold when in solution (methanol-water, 3:2) compared to m-THPC. However, at high m-THPC concentrations, self-quenching of the triplet states is believed to result in a loss of photosensitising efficiency (Sasnouski, S. et al. 2007).

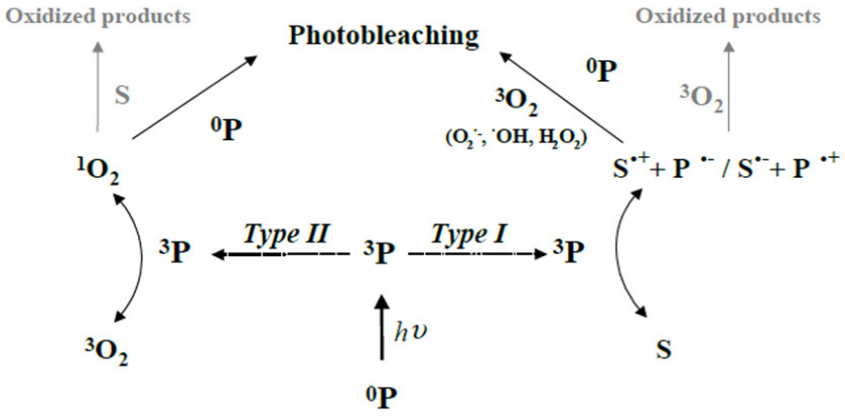

Figure 1.5. A schematic diagram of the mechanisms involved in photobleaching during Type I and Type II reactions following absorption of photons by a photosensitiser (P).

Although m-THPC creates great promise in enhancing PDT, issues associated with its hydrophobic nature generate several drawbacks. For example, its residual photosensitivity is unfortunately not much lower than some first generation photosensitisers (Moriwaki, S. I. et al. 2001), showing little selectivity between normal and malignant tissues *in vivo* (Braichotte, D. et al. 1996;Brown, S. B. et al. 2004), resulting in a large range of tissue responses in patients despite identical treatment parameters. This poor selectivity also leads to long drug-light treatment intervals, where patients must be protected from light for up to 3 days before PDT treatment due to its unusual pharmacokinetic profile in human plasma (Triesscheijn, M. et al. 2007). Therefore third generation photosensitisers have been developed, whereby encapsulation of the photosensitiser into novel 'nano vehicles' have been to designed to improve photosensitiser delivery and uptake into malignant tissues. A range of materials and different techniques can be used to incorporate photosensitisers into nano-sized particles, in order to obtain highly desirable properties (Tallury, P. et al. 2008). The size, composition and surface characteristics have been well documented in determining the biodistribution profile and stability of the nanoparticles in the body (Alexis, F. et al. 2008) and they can be multifunctionalised, integrating several modalities within a single particle, *i.e.* imaging agent, targeting molecule and photoactive drug (Tallury, P. et al. 2008). Ultimately, improving devliery of the photosensitiser should increase its accumulation in target tumourous tissue and with this higher tissue uptake, a greater intracellular localisation of PS within the tumour cells is expected. These factors are believed to positively contribute towards the destruction of tumour cells and efficacy of PDT treatment, which we wish to established through this investigation.

2. Nanotechnology

2.1 Introduction

Nanotechnology incorporates the design, characterisation, synthesis and application of materials which have nanoscale structural properties, *i.e.* one billionth of a metre (Birrenbach, G. et al. 1976). A fast evolving area of science and engineering, nanotechnology has become integrated into the design and manufacture of functional systems in a vast range of applications. Due to their size, nanoparticles exhibit a range of unique properties, not observed with macro or micro-particles, offering multiple advantageous characteristics and prompting extensive research into the assembly and fabrication of nanometre-sized colloid structures.

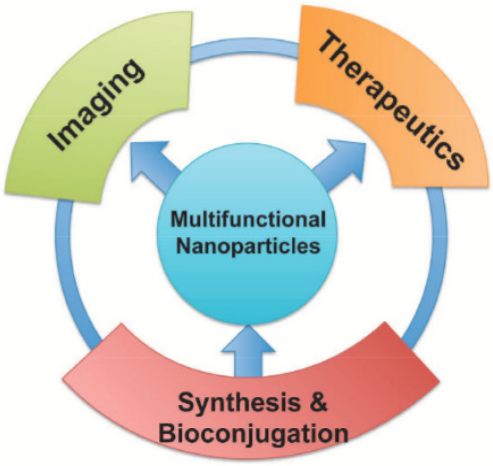

Figure 2.1. The *in vivo* applications of nanotechnology in the field of biomedicine *(Choi J et al. 2011).*

Among other areas of research, the use of nanoparticles have been widely implemented in medicine (Fig 2.1), referred to as 'nanomedicine' (Liu, Y. Y. et al. 2007;Zhang, L. et al. 2008). Their use extends to drug delivery (Farokhzad, O. C. 2008), targeted cancer

therapy (Gu, F. et al. 2009), cell biomanipulation (Desai, J. P. et al. 2007) and as novel analytical devices (biosensors) (Luz R et al. 2013) and diagnostic tools (Fan, Z. et al. 2013). The popularity of their utilisation in biomedicine has been heavily reflected in the literature in the past decade (Doane, T. L. et al. 2012;Kawasaki, E. S. et al. 2005;Zhang, L. et al. 2008). In 2006, it was reported that over 150 companies were developing nanoscale therapeutics in Europe and currently more than 20 nanoparticle-based products are available on the pharmaceutical market (Wagner V et al. 2006). Although some pioneering nanotherapeutics have been approved for clinical use and have shown success, the long-term safety associated with nanotechnology, particularly in *in vivo* applications, has yet to be clearly defined (Choi J et al. 2011).

Nanoparticles can be tailored to their purpose and designed to obtain highly desirable properties, such as; high sensitivity, stability, imageability, biocompatibility and targetability (Tallury, P. et al. 2008). As a result they have been applied to almost every branch of medicine, from oncology to dentistry (Farokhzad, O. C. et al. 2006;Farokhzad, O. C. et al. 2009). Due to the broad spectrum of applications encompassed in this ever-expanding field, this chapter will predominantly focus on the utilisation of nanotechnology in PDT.

2.2 The Role of Nanotechnology in PDT

When designing nanoparticles for use in PDT, several key considerations must be taken into account in order to obtain effective treatment outcomes (Box 2.1).

Box 2.1. Key properties of nanoscale drug delivery systems for PDT

i. Material must allow for transmission of light to activate photosensitiser (PS) and release of reactive oxygen species (ROS)

ii. Encapsulation of photosensitiser should improve its solubility, maintain high ROS yield and prevent its premature release

iii. Nanoparticle (NP) incorporation should promote high PS uptake at desired site and reduce systemic levels of PS in healthy tissues

iv. Ability to conjugate biocompatible polymers and targeting ligands to nanoparticle surface for directed passive or active uptake

v. Potential for NP to serve as multifunctioning platform for combinational therapies (i.e. imaging, diagnostic tools, drug-delivery agent)

Nanoparticles have been developed in the field of PDT to improve the bioavailability and selective delivery of photosensitisers *in vivo* to malignant tissues. Issues associated with systemic photosensitiser administration and a lack of selectivity at tumour sites has proved problematic, as successful PDT to solid tumours requires specific delivery of light-sensitive agents to establish dosimetric parameters and ensure local drug activation by irradiation (Master, A. et al. 2013). Undesirable PS accumulation in healthy tissues can cause irritation to areas easily exposed to ambient light, such as the eyes and skin, resulting in prolonged phototoxicity and photosensitivity in patients, which has to be continually managed, particularly following multiple PS doses (Hopper, C. 2000). Presently, clinical PDT is predominantly used to treat malignant and pre-malignant topical lesions that are easily accessible owing to the delivery of the PS (Master, A. et al. 2013). While advancements in the design of laser technologies have improved selective activation of photosensitive drugs through the delivery of light via novel image-guided pathways and fibre-optics interstitially and intra-tumourally, nanomedicine can further enhance selectivity by providing an effective way to resolve challenges associated with both the systemic intravenous administration of PS and its accumulation in deep tissue tumours.

Nanoparticles synthesised from an array of materials and via various manufacturing techniques have been used to incorporate hydrophobic, insoluble photosensitisers in order to improve drug delivery. This encapsulation increases PS solubility and prolongs its half-life in systemic circulation by reducing protein binding and rapid uptake via the reticuloendothelial system (RES), which may occur before the PS has had time to elicit a therapeutic effect. By reducing unfavourable accumulation in healthy tissues, adverse side-effects associated with non-specific localisation can be minimised. Despite these improvements through nanoparticle encapsulation, modifications at the particle surface can be made via the conjugation of biocompatible polymers, such as polyethylene glycol (PEG), to combat further delivery issues such as fast PS drug release rates, immunogenicity, non-specific biodistribution and fast clearance of nanoparticles. These highly hydrated flexible PEG polymer chains have been used to enhance the pharmacokinetic parameters of many nanoparticle formulations and positive results have prompted the fabrication of PEG-coated drugs for use in the clinic both within the field of PDT (Table 4.1 **Chpt 4**; Table 5.1 **Chpt 5**; Table 6.2 **Chpt 6**, Table 7.3 **Chpt 7**) and outside (*e.g.* Adagen, Macugen, Pegasys and Oncaspar). Furthermore, the extremely small size (nm) of nanoparticles provides a unique high surface-area-to-volume ratio (Bechet, D.

et al. 2008;Peer, D. et al. 2007), facilitating the attachment of specific targeting ligands at high surface densities to direct PS uptake into cancer cells. Finally, particles can be multifunctional, possessing more than one modality. Imaging agents, targeting molecules and photoactive drugs can be integrated within a single particle for combinational therapies (Tallury, P. et al. 2008).

The efficacy of PDT is primarily related to the production of the reactive oxygen species (ROS), largely singlet oxygen, generated from the activation of accumulated PS in tissue. Therefore in designing nanocarrier systems the synthesis and release of these ROS is crucial. Photosensitisers are highly planar molecules, which can be physically entrapped through strong hydrophobic interactions or chemically linked (*i.e.* covalent bonding) within nanoparticles. Unlike other therapeutic agents (*i.e.* chemotherapeutics) it is not essential that the active drug molecule be released from the nanoparticle to elicit a therapeutic effect only that ROS are able to escape into surrounding tissue. The two most commonly adopted approaches used to achieve this are incorporation of PS inside biodegradable and non-biodegradable nanoparticles. Each system has its own advantage; biodegradable nanoparticles are able to release the PS once the matrix has broken down, which can then be irradiated to generate singlet oxygen. This is attractive in ensuring the case material does not cause any long-term toxicity itself, but leaching and premature loss of the PS through degradation can occur (Jain, R. K. et al. 2010). Simple physical entrapment of the PS within non-biodegradable nanoparticle can also result in PS transfer to serum proteins and significant leakage (Compagnin, C. et al. 2009). Conversely, its chemical linkage inside non-biodegradable particles can help to overcome these problems. Whilst excited singlet oxygen molecules can diffuse in and out of porous nanoparticle matrices freely to exert phototoxic effects, the consequence of adopting non-biodegradable materials may lead to potential *in vivo* toxicity from sustained accumulation (Bechet, D. et al. 2008). In either nanocarrier example, the intrinsic PS concentration must also be considered in order to calculate sufficient PS loading within the nanoparticle to produce maximal ROS but simultaneously reduce aggregation and self-quenching of the PS for efficacious PDT.

i. Micelles/Liposomes

Micelles and liposomes are examples of biodegradable nanocarrier drug-delivery systems formed by phospholipids molecules, similar to biological membranes, generating closed, spherical structures (Hofheinz, R. D. et al. 2005). The former, micelles, are detergent-like molecules comprised of a fatty acid core due to the arrangement of phospholipid monolayers, in comparison to liposomes which contain an internal aqueous hydrophilic compartment and a hydrophobic shell as a result of their closed spherical phospholipid bilayer structure (Fig 2.2). Although micelles have shown application in drug delivery (Kato, K. et al. 2012;Matsumura, Y. et al. 2004), liposomes are typically favoured, as greater concentrations of hydrophobic drug molecules, such as photosensitisers, can be 'packaged' into their larger shell (Torchilin, V. P. 2005) and amphiphilic molecules can partially reside in lipo- or hydrophilic regions (Frederiksen, L. et al. 1997). As a result, liposomes account for more than 80% of the nanoscale therapeutic products currently available on the market (along with polymer-drug conjugates) and can be synthesised from various lipidic compositions in a range of sizes and lamellarity (number of bilayers) (Zhang, L. et al. 2008). They are typically classified into three categories; (i) small unilamellar vesicles or oligo-lamellar, (ii) large unilamellar vesicles and (iii) multilamellar vesicles.

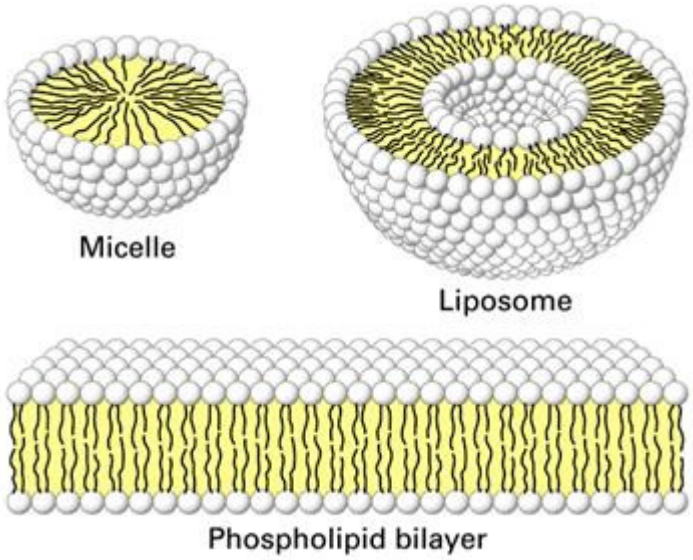

Figure 2.2. The structure of liposomes contain an internal aqueous compartment as a result of their closed spherical phospholipid *bi*layer structure. Micelles lack an aqueous core due to their formation through closed phospholipid *mono*layers therefore contain a fatty acid core. *Taken from (Pharmainfo.net 2014).*

Conventional liposomes (unmodified) carrying photosensitisers, however, are not able to enhance tumour-to-normal tissue ratios alone, as they are swiftly degraded (mins) upon entering the blood circulation (Derycke, A. S. et al. 2004). Long-circulating or 'Stealth'® liposomes have been developed, through PEG modification at the liposome surface (Allen, T. M. et al. 1995;Klibanov, A. L. et al. 1990;Oku, N. et al. 1994) to minimising protein binding when in systemic circulation and increase the probability of accumulation in tumour tissues (Li, S. D. et al. 2008). The use of these nanocarriers in drug delivery and PDT is investigated and discussed at greater depth in **Chapter 4**: Liposomes.

ii. Polymeric nanoparticles

Alternatively, polymeric nanoparticles are the most commonly investigated materials for use as biodegradable nanocarrier systems due to the comprehensive catalogue of polymers available and numerous combinations for nanoparticle fabrication (Fig 2.3). Their use as anticancer drug carriers was originally reported in 1979 by Couvrer *et al*., and doxorubicin-loaded nanoparticles entered clinical trials in the mid-1980s (Couvreur, P. et al. 1982). In recent years they have been the focus of many studies due to the multitude of positive characteristics they elicit. These include high drug loading, unique designs in chemical composition, architecture and surface properties, biocompatibility of a large variety of materials, and the controlled release of drugs through targeting components and polymer degradation (Chatterjee, D. K. et al. 2008a). Polymeric nanoparticles can be constructed from synthetic and natural polymers. In the former instance, two of the most commonly utilised polymers are poly(lactic acid) (PLA) and the co-polymer poly(lactide-co-glycolide) (PLGA), both of which are FDA approved (Hrkach, J. S. et al. 1997). In the latter, examples include chitosan (Agnihotri, S. A. et al. 2004;Calvo, P. et al. 1997) albumin (Kratz, F. 2008) and collagen (El-Samaligy, M. S. et al. 1983), which can be used to encapsulate drug molecules without the need for chemical modification. Controlled degradation for the release of therapeutics can occur in response to the local environment via surface or bulk erosion, diffusion of the drug through the polymer matrix or swelling followed by diffusion (see **Chapter 6**: Polymeric Nanoparticles) (Peer, D. et al. 2007).

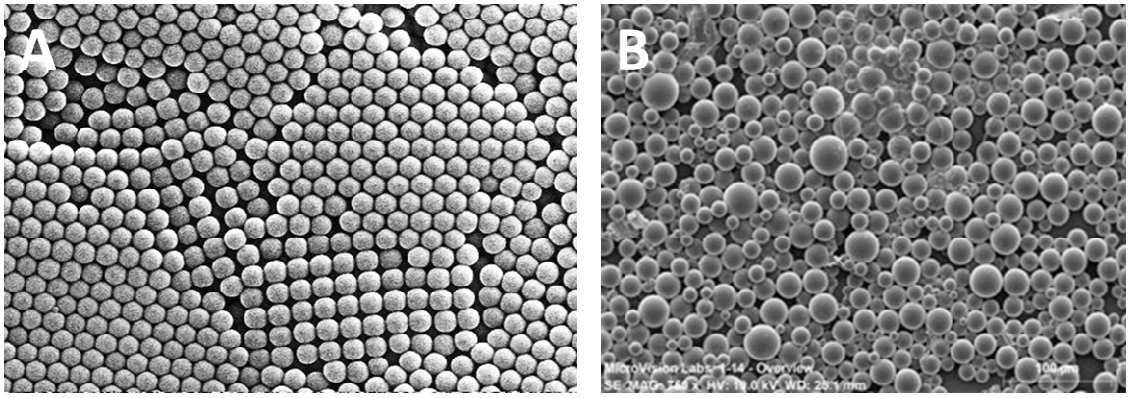

Figure 2.3. 200 nm nanoparticles (**A**) polystyrene and (**B**) poly(lactic-co-glycolic acid) PLGA. *Taken from (Fraikin, J. L. et al. 2011;Tang, K. S. et al. 2013).*

These attractive characteristics have prompted much interest and research into polymeric nanoparticle utilisation. In PDT, the different ratios of polymers from which the nanoparticles are composed, have been suggested to strongly affect the photodynamic activity through differences in degradation, carrier uptake and intracellular localisation, which is dependent on their hydrophilic nature (Chatterjee, D. K. et al. 2008a). Increasing the percentage of more hydrophilic glycolic acid polymers (PLGA) in 200 nm PLGA: PLA has been shown to increase the biodegradation rate and phototoxicity of encapsulated meso-tetra(*p*-hydroxyphenyl) porphyrin (*p*-THPP) *in vitro* in EMT-6 mouse tumour cells (Konan, Y. N. et al. 2003). A significant photodynamic activity was demonstrated again *in vitro* in P388-D1 cells with zinc phthalocyanine (ZnPc)-loaded PLGA NPs, which showed encapsulated PS was able to retain its photophysical properties (Ricci-Junior, E. et al. 2006). More recent studies with the same ZnPC-loaded NPs (374 nm and 200 nm) carried out *in vivo* in tumour-bearing mice showed a significant increase in tumour growth delay studies and smaller mean tumour size (Fadel, M. et al. 2010). Additionally, smaller PLGA NPs (~167 nm) loaded with verteporfin have demonstrated a rapid diminishment in cutaneous photosensitivity from early to longer light exposure time points (Konan-Kouakou, Y. N. et al. 2005) and temoporfin delivered to mice via pegylated PLGA nanoparticles have exhibited therapeutically favourable tissue distribution (Rojnik, M. et al. 2012). These promising results are encouraging for PLGA nanoparticle applications in PDT but concerns have arisen involving the structural heterogeneity of polymers (high polydispersity indices), internal drug distribution and homogenous size distribution of nanoparticles. These issues and a more extensive literature review into the use of other polymeric nanoparticles for applications in PDT are discussed at greater depth in **Chapter**

6: Polymeric Nanoparticles, along with *in vivo* investigations into the use of pegylated poly($_D$, $_L$-lactide-co-glycolide) (PLGA) nanoparticles (~250 nm).

iii. Dendrimers

Dendrimers are comprised of synthetic, highly branched, repetitive polymer molecules that can be further divided into sub branches along a carbon atom backbone (Fig 2.4). Unlike classic polymeric nanoparticles, their structure has a high degree of molecular uniformity and they represent a relatively new field in polymer chemistry (Peer, D. et al. 2007). Their well-defined structure enables nanoparticles of a narrow size distribution, shape and size to be produced.

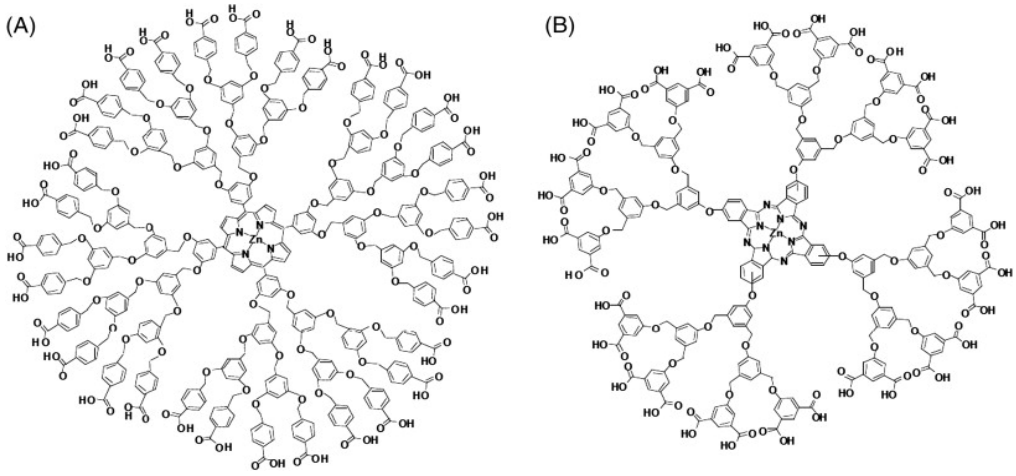

Figure 2.4. Chemical structures of (A) dendrimer porphyrin (DP) and (B) dendrimer phthalocyanine (DPc). *Taken from (Nishiyama, N. et al. 2009b).*

Dendrimers have been used to deliver various photosensitisers increasing their solubility to improve drug selectivity and phototoxic effects in tumours (Huang YY et al. 2012). The spatial alignment between branches of the dendrimer ensures the PS at the central core is less likely to form aggregates, as it is more sterically stable. Nishiyama *et al*., demonstrated a great improvement in tumour PDT efficacy both *in vitro* (A549) and in corresponding *in vivo* models (A549 tumours in nude mice) with dendrimer phthalocyanine-loaded micelles (Fig 2.4), whilst a simultaneous reduction in skin phototoxicity was observed (Nishiyama, N. et al. 2009a). The addition of a poly-$_L$-lysine PEG (PEG-PLL) complex on the dendrimer surface formed 50 nm micelles and was found to positively correlate to PDT tumour necrosis. Furthermore, *in vitro* studies using ALA-dendrimers have shown these nanocarriers helped to enhance cell uptake of ALA in A431

cells and murine keratinocytes. The precursor (ALA) to the natural synthesis of porphyrin (via the haem pathway) was able to produce porphyrin more efficiently when incorporated in dendrimers compared to free ALA (Battah, S. et al. 2007). The simple conjugation of targeting molecules, imaging agents and drugs has led to their further pre-clinical development (Gillies, E. R. et al. 2005), however, their costly and multi-step synthesis, in comparison to other nanoparticles, has posed challenges in large-scale commercial production (Peer, D. et al. 2007).

iv. Ceramic nanoparticles

Non-biodegradable nanocarrier systems have shown to be equally successful in their application in PDT (Bechet, D. et al. 2008;Chatterjee, D. K. et al. 2008a) through the encapsulation or chemical linkage of photosensitisers in organic or inorganic materials. Ceramic-based, mesoporous particles are inorganic systems that include silica (Fig 2.5), titania and alumina. They have recently emerged as suitable drug vehicles as they offer multiple benefits over biodegradable nanoparticles (Cherian, A. K. et al. 2000) and their properties have led to the development of mesoporous silica nanoparticles entering the preclinical stage in targeted cancer therapy (Rosenholm, J. M. et al. 2012). In PDT, their optically transparent matrices, porosity (ROS diffusion), protective casing, water dispersity, general inertness, resistance to microbial attack, or extreme pH/temperatures and reported increase in PS photostability from encapsulation are particularly attractive (Tallury, P. et al. 2008). However, one of the main concerns is their inability to break down into biologically inert components, facilitating their accumulation in the body and thus potentially causing undesirable effects (Gupta, A. K. et al. 2005). Ideally particle size needs to be controlled to ensure as small a size as possible in order to avoid RES uptake and encourage clearance from the body via renal filtration (≤ 5.5 nm) (Choi, H. S. et al. 2007).

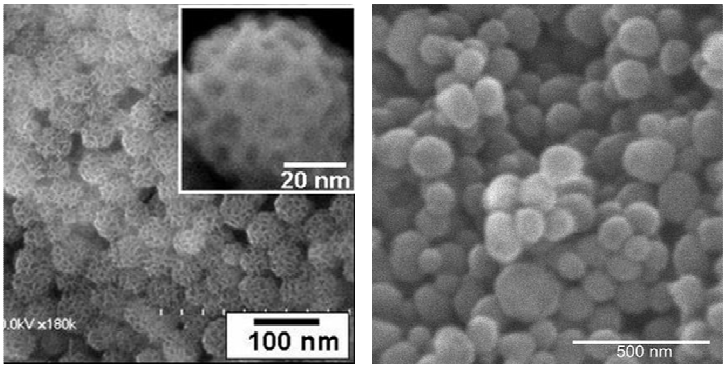

Figure 2.5. Examples of mesoporous silica nanoparticles. *Taken from (Nandiyanto, A. B. D. et al. 2009).*

Various studies have shown photosensitisers physically entrapped (non-covalently bound) within nanoparticles have photocytotoxic effects, as singlet oxygen generation and its diffusion through porous particles is maintained, eliciting oxidative damage to cells (Roy, I. et al. 2003). However, the method of incorporation of PS into these porous particles is inadequate, as serum proteins *in vivo* can cause PS leakage into the plasma, which consequently results in a loss of the PDT agent, non-specific accumulation and uptake into macrophages before particles reach target tissues (Compagnin, C. et al. 2009). Organically modified silica (ORMOSIL) nanoparticles (NP) have been developed which form self-assembling micelles during the oil-in-water microemulsion preparation process through the presence of both hydrophilic and hydrophobic groups whilst helping to improve biocompatibility and reduce RES uptake of particles. Additionally the PS can be immobilised within particles through covalent binding (Ohulchanskyy, T. Y. et al. 2007). Despite chemical linkage to anchor the PS to the internal silica matrix, covalently incorporated photosensitisers have been shown to retain their spectroscopic and functional properties, producing high quantum yields of singlet oxygen upon illumination (Roy 2003). These nanoparticles are also stable in aqueous environments and can be synthesised at small sizes (~20 nm). *In vitro* studies of ORMOSIL NPs incorporating 2-Devinyl-2-(1-hexyloxyethyl) pyropheophorbide (HPPH) demonstrated a high uptake into the cytosol of tumour cells, which enhanced cytotoxic effects with PDT treatment (Ohulchanskyy, T. Y. et al. 2007;Roy, I. et al. 2003). Studies with MB (Tang, W. et al. 2005), PpIX (Qian, J. et al. 2009;Simon, V. et al. 2010), m-THPC (Compagnin, C. et al. 2009;Yan, F. et al. 2003); and HA (Zhou, L. et al. 2010) have also been carried out *in vitro* and showed effective singlet oxygen generation compared to free PS in the latter cases. Primary biodistribution studies *in vivo* with ORMOSIL NPs showed greater accumulation of these particles in the liver, spleen and stomach, indicating they are cleared by the hepatobiliary excretion pathway but no toxicity or abnormalities in tissues were observed after 15 days (Kumar, R. et al. 2010). Chen *et al*., also demonstrated their potential as multifunctional platforms, incorporating MB and an Fe^{2+}/Fe^{3+} magnetic core within the silica matrix to enhance anti-tumour effects through targeted PDT (Chen, Z. L. et al. 2009). The use of these nanocarriers in PDT is investigated and discussed at greater depth in **Chapter 5**: ORMOSIL nanoparticles.

v. Metallic nanoparticles

Metallic particles possess highly favourable optical and chemical properties for biomedical imaging (diagnostic) and therapeutic applications (Hirsch, L. R. et al. 2006). Metallic nanoparticles have versatile surfaces, distinguishing photo-properties and are easily tuneable in size. Those that incorporate metallic ions within their cores (*i.e.* iron oxide) are classed as superparamagnetic agents and are particularly valuable in MRI imaging. Their surfaces can be coated with biological molecules such as dextran, phospholipids or polymers (PEG) to inhibit aggregation and enhance stability. The adopted use of different metallic nanoparticles is largely dependent on the application, for example, silver nanoparticles (AgNPs) are used for their antibacterial and fungicidal capabilities whereas gold nanoparticles are exploited for their catalytic, conductive and colouring properties (Fig 2.6).

Figure 2.6. Different metallic nanoparticles in solution; Silver (Ag), Gold (Au), Ruthenium (Ru) and Platinum (Pt). *Right,* gold nanoparticle functionalised with carboxyl groups on the surface. *Taken from (Kim, B. et al. 2010).*

Gold nanoparticles (AuNPs) can induce changes in their optical properties due to the confinement/arrangement of surface electrons (plasmon resonance effect) on account of their small size, producing quantum effects which can be exploited for use in diagnostic tools, such as novel nano-optic biosensors *e.g.* where a conjugate might be cleaved to provoke a colour change (Huang YY et al. 2012). When dispersed, they are red in solution, however, upon aggregation the electrons delocalise over two nanoparticles, causing a colour shift to blue (Kim, T. et al. 2008). AuNPs have also been studied extensively for applications in PDT based on their distinctive characteristics. They can be used as effective PS-delivery vehicles through surface conjugation of molecules (covalent or non-covalent), similar to other inorganic nanoparticles. PEG-coated AuNPs have been

used *in vivo* to successfully penetrate tumour tissue to deliver non-covalent Pc4 (Cheng, Y. et al. 2011b). Similarly, effective results have also been obtained with AuNP-modified porphyrin-brucine conjugates *in vivo* with complete tumour regression observed in comparison to free PS (Zaruba, K. et al. 2010), whilst *in vitro* studies with hematoporphyrin-nanogold showed more effective PDT with larger AuNPs (45 versus 15 nm) due to the increase in porphyrin transported to tumour cells (Gamaleia, N. F. et al. 2010). AuNPs have been used in photo-thermal tumour ablation, which involves laser irradiation, taking advantage of the strong near infrared (NIR) absorption of gold nanoshells to destroy tissues through heat. Although proven effective in the destruction of tumour tissue *in vivo*, with mice appearing tumour free >90 days, unlike PDT, the thermal activity means loss of structural integrity in normal tissues, leading to functionality and aesthetic complications.

vi. Quantum Dots

Quantum dots (QDs) are semiconductor crystals that have become popular in recent years on account of their small size (<10 nm), which dictates their unique fluorescence properties, making them powerful diagnostic imaging tools. Their tuneable size regulates the band-gap (energy level between the highest valence band and lowest conduction band) and their fluorescence spectra, producing narrow emission peaks (Fig 2.7). Upon absorption of light, QDs can transfer energy to surrounding O_2, forming ROS and causing toxicity to cells.

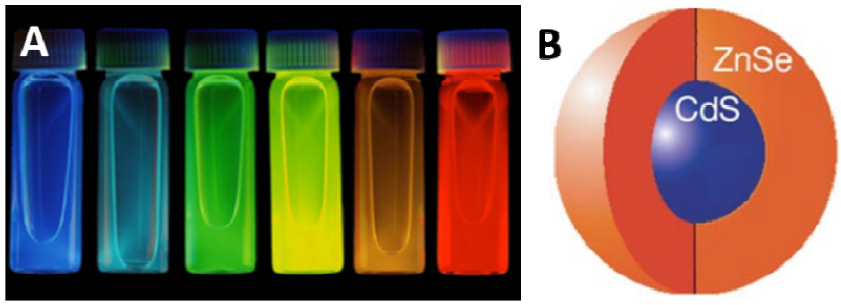

Figure 2.7. (A) Quantum dots in solutions fine-tuned to various sizes to absorb light across the colour spectrum and (B) structure of a quantum dot with a heavy metal CdS core and ZnSe coating. *Taken from (Pietryga, J. M. et al. 2004).*

As such, QDs can act as photosensitisers on their own; however, inefficient generation of ROS *e.g.* $^1O_2$ for effective PDT has promoted the covalent attachment of photosensitisers on to the QD surface. This improves the excitation properties of the PS by acting as a

primary energy donor via Forster resonance energy transfer (FRET), yielding higher ROS production. QDs have been developed in this capacity to activate the PS, Pc4, chemically linked to the particle surface, using shorter wavelengths of light. Unfortunately, this produced ineffective results as singlet oxygen generation was low (He, J. et al. 1997). *In vitro* studies have shown QD fluorescence in cells is quenched due to accumulation in acidic endocytic vesicles (Generalov, R. et al. 2011). Conversely, i*n vivo* studies have found their small size (≥5 nm) is beneficial in promoting renal clearance and in attempting to overcome long-term accumulation but their heavy metal ion cores (*i.e.* cadmium selenide (CdSe), cadmium sulphide (CdS) and indium phosphide (InP)) (Fig 2.7) pose potential toxicity problems due to risks associated with heavy metal leaching *in vivo* (Weng, J. et al. 2006). This, combined with low water solubility, means for use in biological applications it is crucial quantum dots be coated with other organic materials to allow for dispersion and prevent such leakage (Medina, C. et al. 2007). Moreover, efforts to synthesis Cadmium- or heavy metal-free QDs are currently under way to address some of these issues.

vii. Carbon Nanotubes

Working with materials on a nanoscopic level results in the production of a hugely diverse range of products. This is perhaps best demonstrated by the various arrangements of identical single carbon atoms which form a variety of naturally occurring structures; diamond (cubic), graphite (planar) or soot (amorphous). Combined with technological advancements, carbon atom alignment can be manipulated further to manufacture artificial structures, such as fullerenes and carbon nanotubes (Fig 2.8), which have been reviewed extensively for use in PDT (Huang YY et al. 2012). Fullerenes are novel carbon allotropes with a polygonal structure made up exclusively by 60 carbon atoms. These nanoparticles are characterized by having numerous points of attachment and whose surfaces can also be functionalized for tissue binding (Bosi, S. et al. 2003). Remarkably, fullerenes act as pro-oxidants under illumination and antioxidants in the absence of light. Their application in PDT is limited by their extreme hydrophobicity and absorption in the blue/green regions of the visible spectrum, where penetration of light into biological tissue is poor (Huang YY et al. 2012). Carbon nanotubes have been extensively studied due their ability to produce light-weight materials with high electrical conductivity and great strength. Carbon nanotubes can be formed from a single sheet of graphite rolled to form a seamless cylinder

and exist in two classes, single-walled (SWCNT) and multi-walled (MWCNT). MWCNTs are larger and consist of many single-walled tubes stacked one inside the other. Functionalised carbon nanotubes have emerged as novel components in nanoformulations for the delivery of therapeutic molecules (Pagona, G. et al. 2006) and their large surface area allows for greater packaging of hydrophobic drugs, such as doxorubicin (Zhang, L. et al. 2010) and photosensitisers.

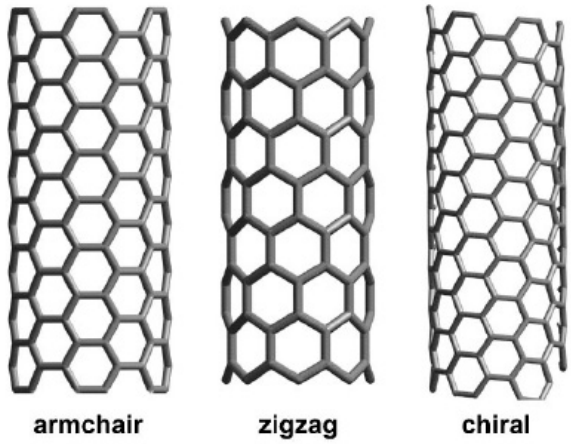

Figure 2.8. Single walled carbon nanotubes (SWCNTs) from *left to right;* armchair, zigzag and chiral structures forming concentric cylinders. *Taken from(Chemical, B. &. M. E. C. 2008).*

In PDT, sophisticated techniques have been used to selectively deliver the PS and enhance local singlet oxygen production using aptamers (Han, D. et al. 2013;Zhu, Z. et al. 2008), coating polymers (Erbas, S. et al. 2009) and polysaccharides (Shiraki, T. et al. 2011). *In vitro*, PDT kill has been significant (Huang, P. et al. 2011a;Tian, B. et al. 2011), however, there has been much confusion regarding the safety of CNTs *in vivo* in recent years due to conflicting evidence on their reported toxicity. It is thought that their biodistribution and pharmacokinetic behaviour is predominantly associated with their surface coating, route of administration and shape and/or size rather than the base material (Yang, K. et al. 2012).

viii. Size and shape

Unlike larger molecules (macro or micro), nanoparticles exhibit a greater total surface area to volume ratio therefore surface atoms dominate the properties of the material. Compounds deemed previously inert in bulk, may become catalysts on at the nanoscale level. The size, composition and surface characteristics have been well documented in determining the biodistribution profile and stability of the nanoparticles in the body (Alexis, F. et al. 2008).

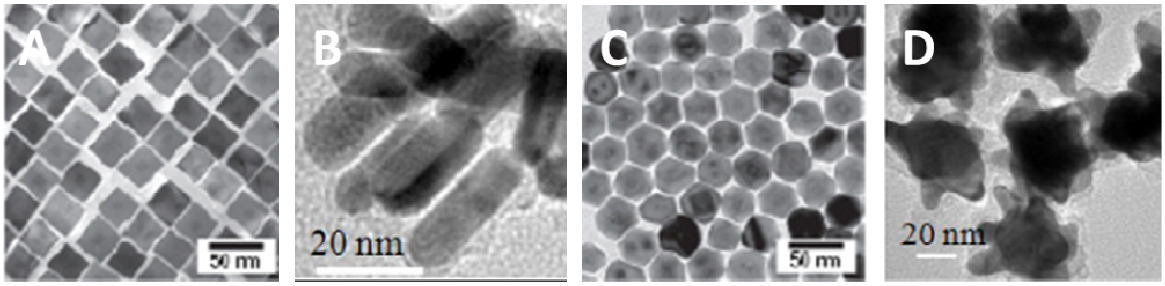

Figure 2.9. Nanoparticles of varying shapes and size (**A**) square (**B**) cylindrical (**C**) hexagonal and (**D**) star-shaped. *Taken from (Peng, Z. et al. 2009).*

Naturally occurring biological molecules in the nanometre-size range follow design rules and have evolved into well-defined structures of specific shapes, sizes and chemistry for optimal functionality. For example, virus particles (virions) occur as icosahedrals, rods or spheres and their geometries dictate their infection efficacy (Albanese, A. et al. 2012). The size and shape of the nanocarrier plays a particularly important role regarding its intracellular uptake and penetration into tissues (Chatterjee, D. K. et al. 2008a;Decuzzi, P. et al. 2010). Rod shaped particles have demonstrated the highest uptake rate, followed by spheres, cylinders and cubes (Fig 2.9) potentially due to their larger surface area and presentation to the cell in two different orientations (short or long axis), increasing uptake (Gratton, S. E. et al. 2008). However below 100 nm, spherical nanoparticles have proved more advantageous than rods, which is likely due to their unique surface area to volume ratio and subsequent properties at smaller sizes. Star-shaped nanoparticles create potential for controlling ligand presentation and increase the surface area of particles, but may also increase exposure to circulating blood proteins and inflammatory factors (Albanese, A. et al. 2010).

Smaller particle sizes are considered superior for delivery of photosensitisers on account of enhanced endocytosis and have been shown to improve a number of critical factors associated with PDT, including reduced toxicity, improved drug clearance, reduced skin sensitivity and improved PDT efficacy from greater singlet oxygen diffusion and phototoxic capability (Jori, G. et al. 1993). The benefits of adopting smaller particles *in vivo* are largely due to achieving optimal size thresholds for clearance pathways *i.e.* renal filtration, and deeper penetration into the unique structure of tumour tissue (Choi, H. S. et al. 2007). However, the effect of small nanoparticles on the permeability and integrity of the blood-brain barrier (BBB) are of toxicological concern, as despite an upper pore size

limit of <1 nm; particles with a diameter of several nanometres can cross the BBB by carrier-mediated transport (Sharma, H. S. et al. 2010). It should also be considered, much of this nanoparticle size-efficacy work has been carried out in cancerous (HeLa) cell lines, as opposed to primary cell lines. As each cell line expresses different levels of receptors and unique phenotypes, optimal nanoparticle uptake may be dependent on the cell line being investigated and internalisation mechanisms are likely to vary between cell types.

In the literature, Chatterjee *et al*., (Chatterjee, D. K. et al. 2008a) have reported preferable sub-50 nm silica NP size (maximum diameters ≤ 100 nm) for effective phototoxic treatment albeit only *in vitro*, which was supported by studies using 30 nm silica-based particles by Roy *et al*., (Roy, I. et al. 2003). Liu et al investigated the biodistribution of liposomes (30-400 nm in size) in mice and found 60% of the injected dose of 100-200 nm particles were found in the blood compared to liposomes smaller or greater than this size. This correlated closely to tumour uptake, which demonstrated a four-fold increase in accumulation of these 100 nm liposomes, compared to >300 nm and <50 nm liposomes (Liu, D. et al. 1992). In the delivery of therapeutic agents to solid tumours, nanoparticles between 30-200 nm are deemed more desirable due their longer circulation half-life and the related probability of passively accumulating in tumour tissue (Jain, R. K. et al. 2010). Smaller nanoparticles (20 nm) are also believed to penetrate tumours more effectively, as they are able to navigate between the tumour interstitium following extravasation from leaky tumour vessels but are not retained beyond 24 h (Albanese, A. et al. 2012). Conversely, larger nanoparticles (100 nm) are unable to permeate far beyond the blood vessels but remain trapped in the extracellular matrix (ECM) between cells (Albanese, A. et al. 2012;Jain, R. K. 1994;Stylianopoulos, T. et al. 2010), thus creating a caveat in optimising particle size.

ix. Charge

The surface charge of nanoparticles (zeta-potential, ζ) has proved equally important in establishing their fate. In systemic circulation, surface charge plays a pivotal role in nanoparticle distribution, metabolism, clearance, immunogenicity and uptake due to interactions with blood serum proteins, such as, immunoglobulins, lipoproteins, coagulation factors, metal- or sugar-binding proteins (Cedervall, T. et al. 2007). Nanoparticles with a neutral surface charge have been established as having a reduced

plasma absorption and uptake into macrophages, demonstrating a high blood half-life (Gbadamosi, J. K. et al. 2002). In comparison to both neutral and negatively charged nanoparticles, positively charged nanoparticles have shown a much faster clearance from the blood and an increase in the rate of non-specific tissue uptake, with higher accumulation in organs of the reticuloendothelial *i.e.* lungs (Arvizo, R. R. et al. 2010;Thorek, D. L. et al. 2008). This is thought to be due to cellular membranes having a slightly negative charge, which drives ionic/electrostatic interactions (Foged, C. et al. 2005;Jin, H. et al. 2009). As a result negatively charged nanoparticles are believed to promote local gelation at the lipid membrane, whereas positively charged nanoparticles augment fluidity (Albanese, A. et al. 2012). In biological environments the surface of nanoparticles is quickly coated in multiple proteins layers, known as a 'corona'. The corona is affected by surface charge and consists of two layers; a hard layer of strongly adsorbed proteins lies in direct contact with the particle surface and an exterior soft layer of serum proteins that weakly interact with the hard layer. The soft layer is much more dynamic as a result and can change over time, ultimately determining the nanoparticles fate (Lynch, I. et al. 2009). Positively charged nanoparticles experience this phenomenon more intensely, with rapid adsorption of serum proteins that identify them for removal by the RES (Albanese, A. et al. 2012). The addition of PEG groups can significantly reduce opsonisation by creating a more neutral particle surface charge.

x. Miscellaneous nanoparticles

In recent years, novel classes of nanoparticles have emerged for direct application in PDT. Upconversion (UC) nanoparticles represent a class of particles that can be efficiently excited at low excitation densities to improve the penetration depth of light into tissues (Haase, M. et al. 2011). This occurs through the emission of shorter wavelengths of light (higher energy) than those used to excite the particles (anti-Stokes-type emission), following the absorption of two or more photons (Huang YY et al. 2012). The UCNs achieve this through one of three quantum processes; energy transfer upconversion (ETU), excited-state absorption (ESA) and photon avalanche (PA). In the clinic this translates into a 'nanotransducer' converting deeply penetrating near-infrared (NIR) light of low energy into visible light of shorter wavelengths and higher energy to activate PS deep within tumour tissue, generating singlet oxygen for PDT (Chatterjee, D. K. et al. 2008b). This mechanism also has applications in biomedical imaging as greater penetration of tissue,

free from auto-fluorescence background, creates high sensitivity and better images (Cheng, L. et al. 2013). Some of the first PDT studies *in vivo* using mesoporous-silica–coated upconversion fluorescent nanoparticles (UCNs) with dual-photosensitisers conjugated to their surface (ZnPc and MC540) have shown successful tumour growth inhibition (Idris, N. M. et al. 2012).

In direct contrast to UCNs, simultaneous two-photon excitation nanoparticles require extremely high energy densities to induce excitation facilitated by a laser. As excitation with NIR light (λ>780 nm) of longer wavelengths is able to penetrate biological tissue but is of too low photon energy to activate most photosensitisers by one-photon excitation, two-photon absorption (TPA) is able to combine the energies of two identical photons arriving at the PS at the same time. Alternatively, the energy of one photon is provided at half the wavelength producing enough energy to activate the PS (Bhawalkar, J. D. et al. 1997). TPA-PDT has been demonstrated *in vivo* with mesoporous silica nanoparticles encapsulating porphyrin to treat tumours in mice with effect. Results showed a tumour growth delay thirty days after treatment compared to controls (Gary-Bobo, M. et al. 2011).

Finally, self-illuminating nanoparticles combine radiation therapy and PDT to induce Self Lighting Photodynamic Therapy (SLPDT) (Chen, W. et al. 2006). Here, scintillating or luminescent (light-emitting) particles are able to activate photosensitisers whose absorption spectrum matches that of the light emitted *i.e.* porphyrins, following exposure to ionising radiation. This produces singlet oxygen to enhance the killing of cancer cells. As X-rays can easily penetrate through tissues (X-ray photons), unlike visible light, they can activate photo-sensitive agents deep in tumour tissue through the use of these self-illuminating particles. Furthermore, combined with a PDT effect, lower doses of systemic radiation can be applied to stimulate tumour regression. In this capacity, quantum dots and other nanoparticles have been explored for their employment in treating internal tumours with this type of combination therapy (Juzenas, P. et al. 2008).

xi. Targeted nanocarriers

The nanomedicine approach provides a promising step towards enhanced control of photosensitiser biodistribution and tumour-selective delivery in PDT. The future of nanotechnology in clinical oncology is moving in the direction of creating multifunctional

particles, adapting nanoparticles for use as drug carriers, imaging agents and diagnostic tools for targeted cancer therapy (Liu, Y. Y. et al. 2007). This has been achieved through the fabrication of targeted nanoparticles, whereby ligands are attached to the surface of the particle, which are highly selective and bind with great affinity to complementary receptors over expressed or up regulated on cancer cells, in order to exploit active mechanisms of uptake into malignant cells (Fig 2.10) (Peer, D. et al. 2007).

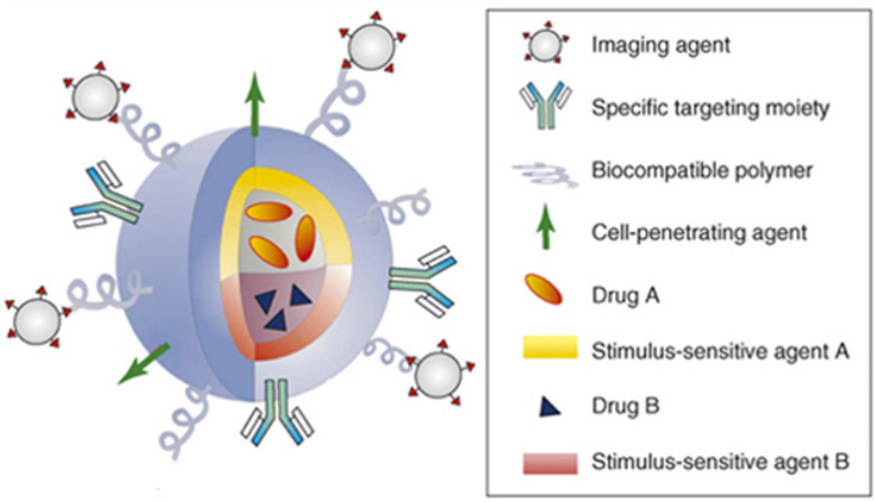

Figure 2.10. Multifunctional targeted nanoparticle. *Taken from (Aalto University 2012).*

Pegylation of nanoparticles to improve stability and circulation half-life has been shown to simultaneously weaken interactions between particles and cells due to steric hindrance, which may cause inefficient intracellular delivery (Li, S. D. et al. 2008). To solve this problem, polymer conjugation has been combined with functionalisation of nanoparticles through the further addition of specific targeting agents to help prevent immune system recognition and increase the efficiency of drug delivery. Surface modifications to particles include the conjugation of ligands, antibodies, vitamins, hormones and growth factors. Tumours, for example, display a variety of receptors that are unregulated on their surface, largely due to the rate at which they proliferate, but are found at much low numbers on normal cell surfaces. This has been exploited in cancer therapy as the ligand and the receptor have a high specificity and affinity for one another and bind tightly as a result. This, in turn, triggers signal transduction cascades and loaded nanoparticles may be internalised through target-mediated endocytosis. The utilisation of targeted nanoparticles in medical applications and PDT will be explored at greater depth in **Chapter 7**: Targeted Nanoparticles.

2.3 Tumour Biology

i. Enhanced Permeability and Retention (EPR) Effect

In PDT, common *in vivo* challenges include site-selectivity of drugs, light delivery and additional variability in tumour heterogeneity, including vascular perfusion, antigen expression and oxygen levels (hypoxia). These factors not only influence the delivery of therapeutics but also dictate PDT efficacy.

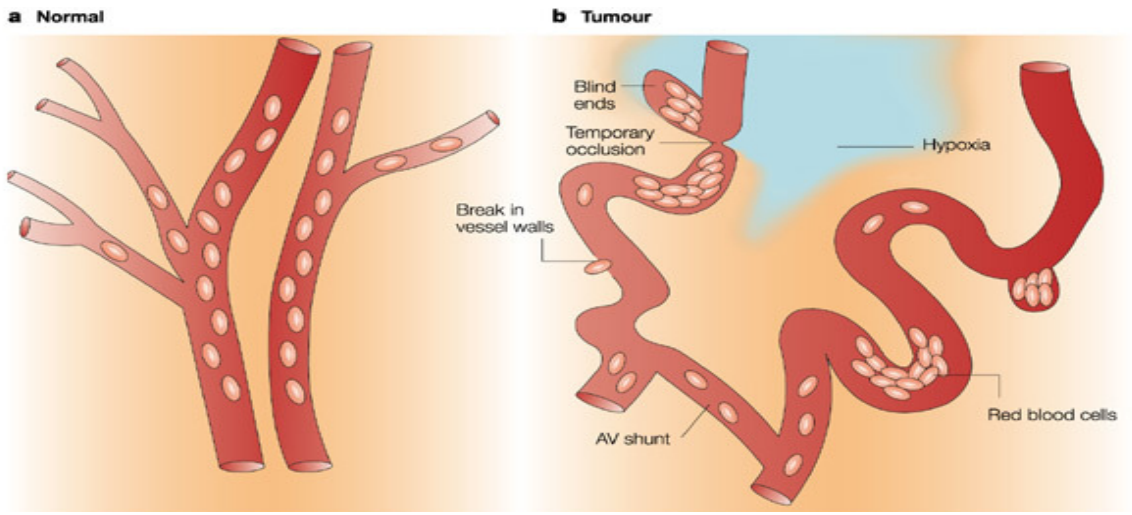

Figure 2.11. Vasculature in normal healthy tissue and tumour tissue. *Diagram taken from (Brown, J. M. et al. 2004).*

The biology, physiology and composition of tumour tissue is fundamentally different to that of normal tissue (Fig 2.11) (Wong, C. et al. 2011). These differences can be exploited when designing and implementing nanocarriers for passive targeting of anti-cancer therapeutics (Jori, G. 1996). In comparison to surrounding normal tissue, tumour tissue typically possess tortuous, abnormal vasculature (Brown, J. M. et al. 2004), acidic microenvironments (higher pH) and up regulated expression of specific cell surface receptors, including, glycoproteins *i.e.* folic acid (FA) (Leamon, C. P. 2008), growth factors (GFs) *i.e.* epidermal (EGF) or vascular epidermal growth factor (VEGF) (Yotsumoto, F. et al. 2009);(Kuwai, T. et al. 2008), signalling peptides and low density lipoproteins (LDLs) (Jori, G. et al. 1993). In the latter example, circulating hydrophobic PS-complexes, preferentially bound by lipoproteins, may be endocytosed by tumour cells through specific LDL receptor-mediated pathways, increasing the passive accumulation of the PS in neoplastic tissues (Jori, G. 1989).

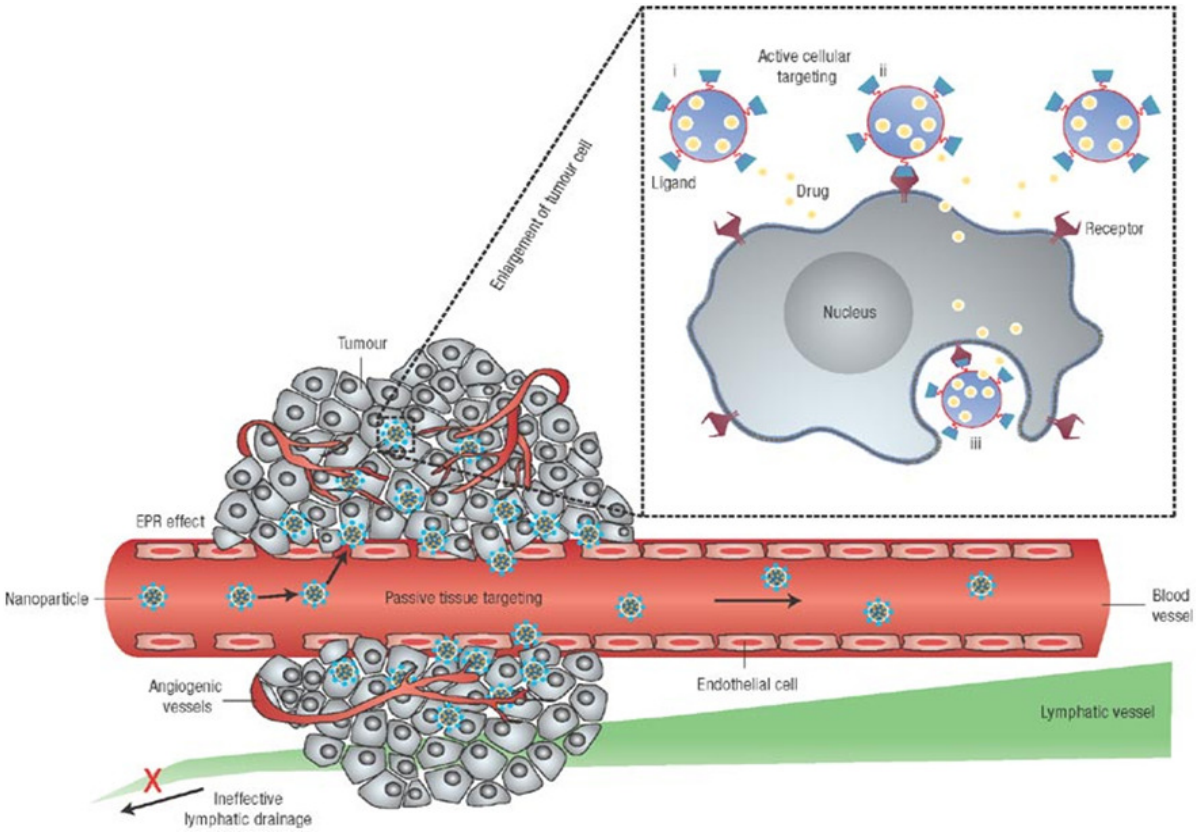

Figure 2.12. The Enhanced Permeability and Retention (EPR) effect in tumour tissue. *Diagram taken from (Peer, D. et al. 2007).*

The architecture of tumour vasculature is characteristic of rapid angiogenesis to serve fast-growing cancers compared to more hierarchically organised healthy blood vessels (Fig 2.11) (Brown, J. M. et al. 2004). Leaky tumour vessels allow nanoparticles to extravasate into tumour tissue through hyperpermeable, discontinuous endothelial walls (larger fenestrae), which combined with poor clearance mechanisms from a dysfunctional lymphatic drainage system, facilitates their accumulation in tumour tissue (Peer, D. et al. 2007). This is known as the 'enhanced permeability and retention' (EPR) effect (Maeda, H. et al. 2000;Yokoyama, M. et al. 1998) (Fig 2.12). Furthermore, the density of collagen fibres within the tumour may cause the compression of intratumoral blood vessels, affecting hydrostatic pressure, preventing the delivery of NPs within the tumour interior and reducing NP penetration through the collagen matrix (Tong, R. et al. 2013).

Data from numerous studies indicate the EPR effect favours the passive accumulation of sub-500 nm particles for optimum penetration through the tumour interstitium following delivery via blood vessels and retention in the parenchyma from poor lymphatic clearance (Couvreur, P. et al. 2006;Roy, I. et al. 2003;Torchilin, V. P. 2005;Yuan, F. et al.

1994;Yuan, F. et al. 1995). The size of the tumour fenestrae (100 – 1200 nm) (Moreira, J. N. et al. 2001) enhances vascular permeability and passive accumulation; creating high tumour-to-normal tissue ratios, providing the particles circulate for sufficient periods of time in the blood (Takeuchi, H. et al. 2001). However, Jain *et al*., have found that not all solid tumours exhibit the EPR effect and the permeability of vessels may differ throughout a single tumour (Jain, R. K. 1994).

ii. Tumour hypoxia and PDT

Hypoxia in tumours is a result of an inadequate supply of oxygen (O_2) reaching tissues on account of malignant propagation, which compromises biological functions. The disorder in the structure and function of the tumour microcirculation leads to pathophysiological deterioration causing hypoxic areas in tissue, with oxygen partial pressure up to two orders of magnitude lower than healthy tissues (Freitas, I. 1985). This in turn results in a signalling increase for hypoxia inducible transcription factor (HIF-1α) in order to restore oxygen homeostasis (Kunz, M. et al. 2003). Oxygen deficient regions are strongly resistance to therapies and, as such, have become a central issue in cancer treatment. This causes fundamental problems for the treatment of solid tumours with PDT, as sufficient tissue oxygenation is required to generate ROS via interaction with the PS. Without the presence of oxygen, the PDT effect is abolished. It is thought hypoxic tumour cells are resistant to PDT and a site for possible tumour recurrence post-irradiation (Master, A. et al. 2013). Strategies to reoxygenate heterogeneous tissues during or pre-treatment have been investigated, including molecular inhibition of HIF, hyperbaric oxygen therapy, ozone therapy and other combinational therapies (Muzykantov, V. R. et al. 2012), as well as destruction of hypoxic cells through hyperthermia (Sun, X. et al. 2010). Research into improving the penetration, uniformity and distribution of nanocarriers within tumour tissue aims to compound these results.

2.4 Future of Nanotechnology

Nanotechnology is playing an increasingly important role in the development of many areas of biomedicine, especially drug delivery. First generation nanoparticles were synthesised to demonstrate the capabilities of these novel materials for applications in biomedical research, using non-stealth particles as proof of concept for cellular uptake and safety *in vivo*. Since then, second generation nanoparticles have been developed to create

long-circulating particles that can be actively targeted to increase selective uptake. Currently, third generation multifunctional nanoparticles are being generated for use in combinational therapies. Alongside 'intelligent' particles that are able to respond to surrounding environments to exert their therapeutic effect, particles that enhance the photophysical properties of photosensitisers for PDT are being investigated in an attempt to overcome previous limitations. With continued research into this field and a growing number of nanoparticle-based therapeutics entering clinical trials, the impact of this technology in the clinic is only set to rise. This investigation seeks to explore the use of nanoparticles for application in PDT to treat solid tumours.

3. Aims of Thesis

The aim of this investigation was to determine whether encapsulation of the photosensitiser, m-THPC, into different nanocarriers altered its delivery to target tissues and improved photodynamic therapeutic efficacy. This was predominantly achieved through normal (healthy) and cancerous *in vivo* rodent models.

The first objective of this work was to investigate the *in vivo* biodistribution and accumulation of m-THPC when incorporated into pegylated nanoparticles. These nanocarrier delivery vehicles were composed of different materials and varied in size, degradability and surface ligands. Each was directly compared to the uptake of standard micellular clinical m-THPC formulation, Foscan®, following intravenously administered;

- liposomes (~ 100-120 nm)
- polymeric (PLGA) nanoparticles (~ 150-250 nm)
- organically modified silica (ORMOSIL) nanoparticles (~ 20-100 nm)
  + cRGD peptide

The major methodology employed to obtain pharmacokinetic data was chemical extraction of m-THPC from tissues, followed by spectrofluorimetric analysis. The resultant pharmacokinetic data were analysed through both compartmental and non-compartmental models.

The second objective was to determine whether specific nano-formulations of m-THPC and corresponding tumour uptake resulted in improved efficacy of PDT to tumours, and simultaneously, whether this reduced adverse effects in normal tissues using similar *in vivo*

models. Effects on efficacy of dose and light parameters were included. The central methodology employed was post mortem histological analysis to determine the extent of tumour PDT necrosis. Normal tissue damage was assessed through selected skin photosensitivity studies with biodegradable liposomal nanocarriers and toxicology studies in organs involved in major clearance pathways with non-biodegradable silica nanoparticles.

4. Liposomes

4.1 Introduction

The application of nanoparticles in medicine has become an attractive avenue in recent years due to their potential benefits in clinical practice. They offer solutions to some of the current limitations faced in the diagnosis and treatment of disease, such as improved pharmacokinetic properties, selective accumulation, controlled release of drugs and reduced systemic toxicity. In 2008, liposomal drugs and polymer-drug conjugates accounted for more than 80% of the total nanotechnology-based therapeutic products approved for clinical use (Farokhzad, O. C. 2008).

Liposomes, first discovered by Bangham in 1965, are inert, biodegradable nanocarrier systems. They are closed, spherical phospholipid bilayer structures composed of natural or synthetic amphiphilic lipid molecules, producing a hydrophilic aqueous core and a hydrophobic lipid shell. The suitability of their biological properties has made them a popular choice as pharmaceutical carries during the past decade, aiming to increase the therapeutic index whilst minimising adverse side-affects (Box 4.1).

Box 4.1. Desirable characteristics of liposomes for use in drug delivery

i. Ability to efficiently encapsulate both hydrophobic and hydrophilic therapeutics at high capacity

ii. Biologically inert and possess low intrinsic toxicity

iii. Protect therapeutics from hostile in vivo environment

iv. Biofunctionalisation with specific ligands to aid in targeted cellular uptake

v. Surface modification with biocompatible polymers to increase circulation on half-life and therapeutic bioavailability

Liposomal membranes consist of parallel components, such as phospholipids and cholesterol; the net properties of which determine their physical and chemical characteristics, including size, stability, fluidity, hydrophobicity, charge density and steric hindrance (Bawarski, W. E. et al. 2008). Liposome formation is spontaneous due to naturally occurring interactions between water molecules and the amphiphilic phospholipids, self-assembling into bilayers.

Liposomes, used as nanoparticles, typically measure 1-100 nm in diameter (Malam, Y. et al. 2009). In recent years, different manufacturing processes have been used to successfully incorporate a variety of drugs and dyes into their structure. Depending on their hydro- or lipophilic properties, different molecules occupy different liposome regions due to the hydrophilic head groups and hydrophobic chains of the phospholipids (Kozlowska, M. K. et al. 2009), determining drug distribution. Hydrophobic drugs penetrate the lipidic bilayer, whilst hydrophilic drugs usually localise to the surface or aqueous compartment of liposomes near the polar heads (Angeli, N. G. et al. 2000).

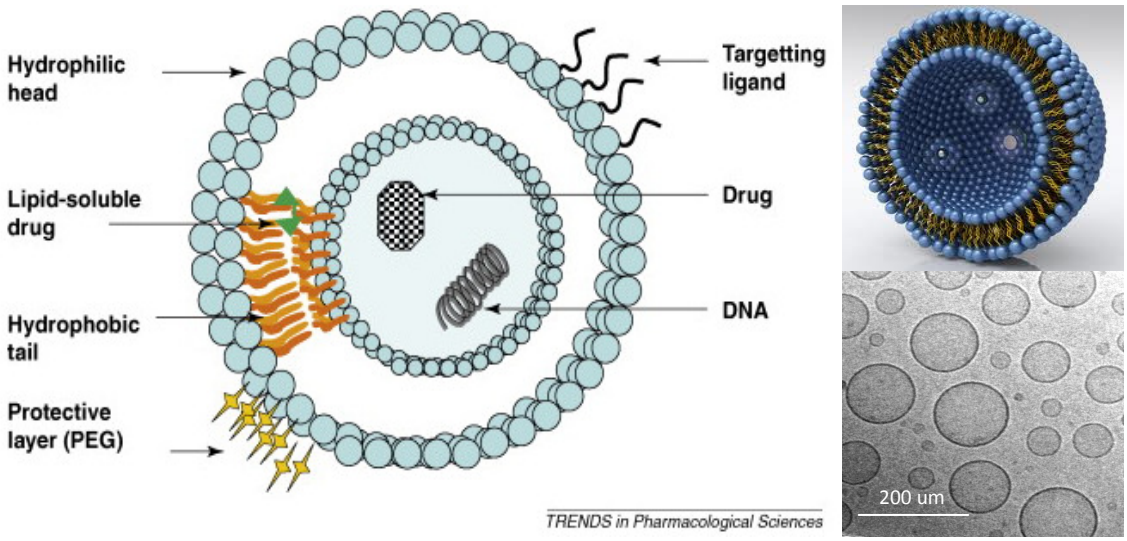

Figure 4.1. (Left) Schematic diagram of bilaminar liposome (Malam, Y. et al. 2009). Left: Drugs are either trapped in aqueous core or packaged into hydrophobic shell. Outer surface can be functionalised with active targeting ligands and/or pegylated. Top right: 3D model cross-section of liposome. Bottom right: Cryo-TEM image of liposomes (*courtesy of Dr Scheglmann, Biolitec, Germany*).

Packaging therapeutics into liposomes can protect molecules from degradation and the physical-chemical properties of liposomes can determine uptake and localisation *in vivo*, emphasising the importance of particle design. Lipid membrane components can be

manipulated to improve their stability *in vivo* through modification of the bilayer fluidity (Damen, J. et al. 1981). Cholesterol is renowned for its effect on membrane fluidity and has repeatedly been shown to increase liposome stability and reduce the permeability of the encapsulated drug molecules from the liposomal membrane (Vemuri, S. et al. 1995). Particle size can have a significant influence on uptake, with larger particles more likely to be eliminated from the blood circulation than smaller ones, due to the increase in cellular/tissue uptake of sterically favoured smaller particles (Senior, J. et al. 1982). This has been confirmed *in vitro* using EMT-6 mammary tumour cells, which showed a higher intracellular uptake of smaller nanoparticles via cellular endocytosis, along with a higher drug release rate once internalised, due to a corresponding increase in the total particle surface area exposed to the leaching medium (Konan-Kouakou, Y. N. et al. 2005). Liposome size can be used to passively target organs that have fenestrae (GI tract, kidneys) or a discontinuous endothelium (liver, spleen, bone marrow). The pores or gaps in the endothelial cells lining capillaries allow the passage of bulkier molecules, such as large proteins and liposomes, to pass through from the blood due to a lack (sinusoidal capillaries) or loosening in tight junctions between cells. These anatomical features can be beneficial or deleterious depending on the application. For example, it may be advantageous to passively target anti-parasitic or microbial drugs to organs of the reticuloendothelial system (liver, spleen) to treat infections (Basu, M. K. et al. 2004), however, for toxic chemotherapeutic or anti-cancer drugs, accumulation in the liver is undesirable. Often, a compromise exists between decreasing particle size and increasing the drug load to deliver sufficient quantities of drug to target tissues. Recently, Zheng *et al*., demonstrated that porphyrin molecules may be directly substituted into the lipid bilayer during formation of self-assembling lipid structures in order to conserve low particle size without compromising on drug loading (Lovell, J. F. et al. 2011).

Surface charge can affect liposome distribution and efficacy *in vivo*. Major problems associated with cationic liposomes, designed for gene delivery, have been observed as a result of their strong interactions with blood components and subsequent swift removal from circulation, dramatically lowering their transfection efficiency in an SK-1 mouse liver model (Senior, J. H. 1987;Zelphati, O. et al. 1998). Anionic (negatively charged) liposomes face similar problems, with a shorter half-life in circulation than those with a neutral net surface charge (Funato, K. et al. 1992). A linear relationship between the particle zeta potential and phagocytosis was recognised following surface modifications to

polystyrene microspheres. Upon neutralising their surface charge, a reduction in both plasma absorption and uptake into J774 A1 macrophage-like cells was observed (Gbadamosi, J. K. et al. 2002).

Liposomes can enter cells through a number of different mechanisms (Fig 4.2). This occurs through either; non-targeted (A) or targeted (B) delivery and leads to liposomal degradation and intracellular drug release. With non-targeted delivery, liposomes can be absorbed on to the cell surface or fuse to the plasma membrane, as they are formed of similar phospholipid constituents, to release their drug-load by micropinocytosis. Alternatively, they can undergo endocytosis through non-targeted or targeted delivery. Here, the whole liposome enters the cell via endosomes where they are either chemically degraded through hydrolytic enzymatic digestion following delivery to lysosomes, or they induce endosome destabilisation en route to lysosomes; both resulting in the release of encapsulated drugs into the cellular cytoplasm.

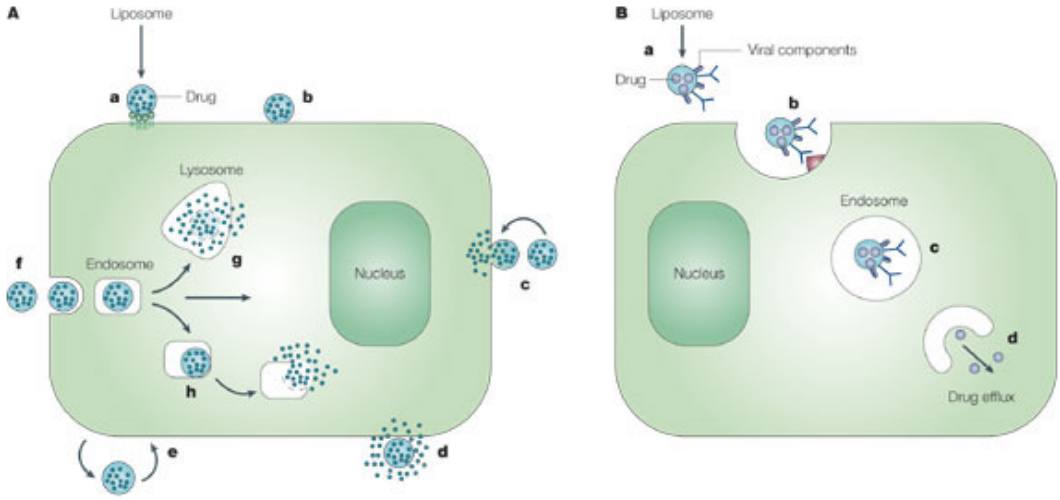

Figure 4.2. Entrance pathways of (**A**) untargeted liposomes and (**B**) targeted liposomes into a cell. *Diagram taken from Nature Reviews (Torchilin, V. P. 2005).*

It appears conventional liposomes (unmodified), are not able to enhance tumour-to-normal tissue drug ratios alone, as they are swiftly degraded (mins) upon entering the blood circulation (Derycke, A. S. et al. 2004). This can occur through a number of mechanisms (Fig 4.3). The first relates to the instability of the liposomes in plasma and their interaction with high (HDL) and low density (LDL) lipoproteins (Allison, B. A. et al. 1997). Irreversible disintegration through lipid exchange between the liposomes and lipoproteins

causes rapid release of the encapsulated drug. Although there is evidence to suggest LDL lipoproteins may help to enhance the tumoural uptake of liposome-released drugs (as discussed in **Chpt 1** & **2**). As the expression of LDL receptors is elevated on the surface of rapidly proliferating tumour cells due to the increased demand for cholesterol, required for membrane synthesis, this may dually facilitate the uptake of liposome-released hydrophobic drugs, bound to the lipid core of LDL lipoproteins, into tumour cells via LDL-receptor-mediated endocytosis (Renno, R. Z. et al. 2001). However, the localisation of drug-loaded liposomes within tumour tissue is thought to be more favourable in terms of therapeutic efficacy. The second method is through opsonisation of the liposomes from blood serum proteins, resulting in their removal from circulation and uptake into cells of the mononuclear phagocytic system (MPS), also known as the RES (Hoedemakers, R. M. et al. 1993). In this instance, the liposomes themselves are not recognised by the MPS but upon exposure to blood they become coated with plasma proteins (opsonins), which can take the form of immunoglobulins, fibronectin and glycoproteins (Patel, H. M. 1992), and determine the recognition and subsequent fate of the liposome by the MPS. Lastly, the host's immune system uses 'complement components' as a natural defence mechanism against invading pathogens. Membrane attack complexes (MAC) initiate cell membrane lysis by producing lytic pores. In the case of liposomes, this causes instability and release of their content, enhancing uptake by the MPS.

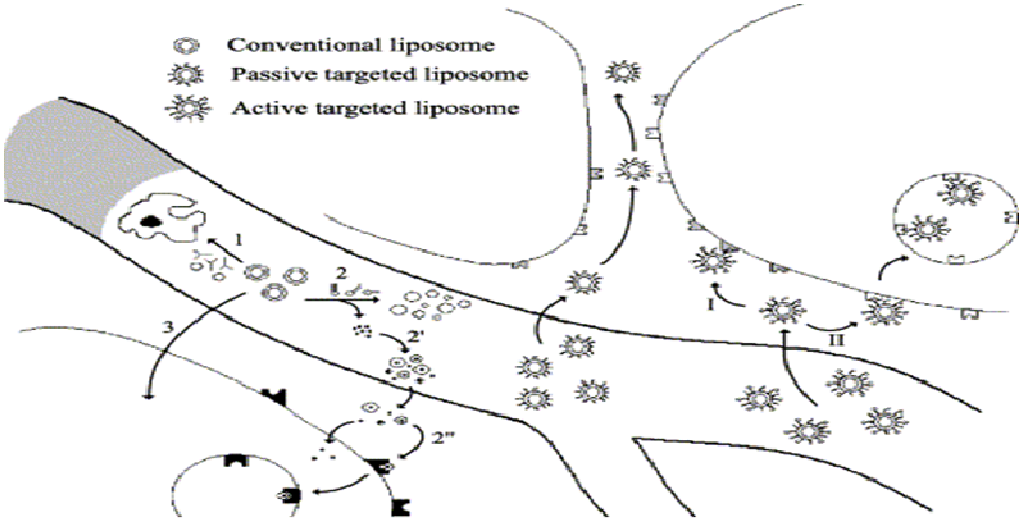

Figure 4.3. *In vivo* behaviour of different liposomes; (1) macrophage uptake, (2) lipid exchange between plasma proteins, (2) release of PS, (2') plasma protein association or (2") entry of free PS ino tumour cells via LDL-receptor mediate endocytosis, (3) direct internalisation of liposomes into tumour cells. Passive targeting into tumour interstitium or active targeting (I) non-internalising target or (II) endocytosis. *Diagram taken from Advanced Drug Delivery Reviews (Derycke, A.S. and De Witte, P.A., 2004).*

Long-circulating or Stealth® liposomes have been synthesised through modification of the liposome surface (Allen, T. M. et al. 1995;Klibanov, A. L. et al. 1990;Oku, N. et al. 1994), however, this cannot be achieved through the substitution of saturated phospholipids and cholesterol alone. For many nanoparticles, minimising protein binding is vital for developing long-circulating nanoparticles (Li, S. D. et al. 2008). This typically involves attaching a biocompatible polymer to the surface of the liposome to increase its hydrophilicity and discourage opsonisation. This can be achieved in several ways: (i) physically adsorbing the polymer on to the external shell surface, (ii) incorporating the pre-fabricated polymer-lipid conjugates during preparation or (iii) covalently attaching reactive groups to the surface of the liposome (Immordino, M. L. et al. 2006). The evidence for the effect of such polymers on increasing particle longevity is apparent, irrespective of their surface charge or addition of stabilising agents such as cholesterol (Immordino, M. L. et al. 2003).

Polyethylene glycol (PEG) is an uncharged, biocompatible polymer with low immunogenicity and toxicity which is readily incorporated onto the liposomal surface (pegylation) via a number of mechanisms (Dreborg, S. et al. 1990). In the current investigation, PEG is anchored to the liposomal surface via a cross-linker lipid, distearoylphosphatidylethanolamine (DSPE), to which it can be conjugated (DSPE-PEG). Typically in commercially PEG-modified liposomes, a more stable carbamate bond is used to conjugate PEG to DSPE, as used here, as esters are more prone to cleavage at certain pHs. As a linear polyether diol, soluble in aqueous and organic solutions (Powell GM et al. 1980), PEG helps to increase the hydrophilicity of the liposomes, whilst simultaneously providing good steric hindrance for the prevention of serum protein binding (opsonisation) (Blume, G. et al. 1993). This consequently enables particles to avoid recognition by scavenger receptors present on the macrophage cell surface (MPS/RES) and subsequent internalisation, degradation and removal from circulation, aiding in increasing their longevity and bioavailability to target tissues (Opanasopit, P. et al. 2002) (Zamboni, W. C. 2005). The chain length (or molecular weight) and surface graft density of PEG can be freely modulated and determine the degree of surface coverage, having a significant effect on particle biodistribution. Although shown to improve vesicle stability and prevent aggregation through promoting strong interbilayer repulsion (Needham, D. et al. 1992), higher concentrations of PEG attached to the surface of a liposome can jeopardise the stability of the lipid-based nanocarrier as the dense polymer chains can disrupt the integrity

of the phospholipid membrane (Dos, S. N. et al. 2007). Moreover, high pegylation can also weaken interactions between particles and cells, which can cause inefficient intracellular delivery (Li, S. D. et al. 2008).

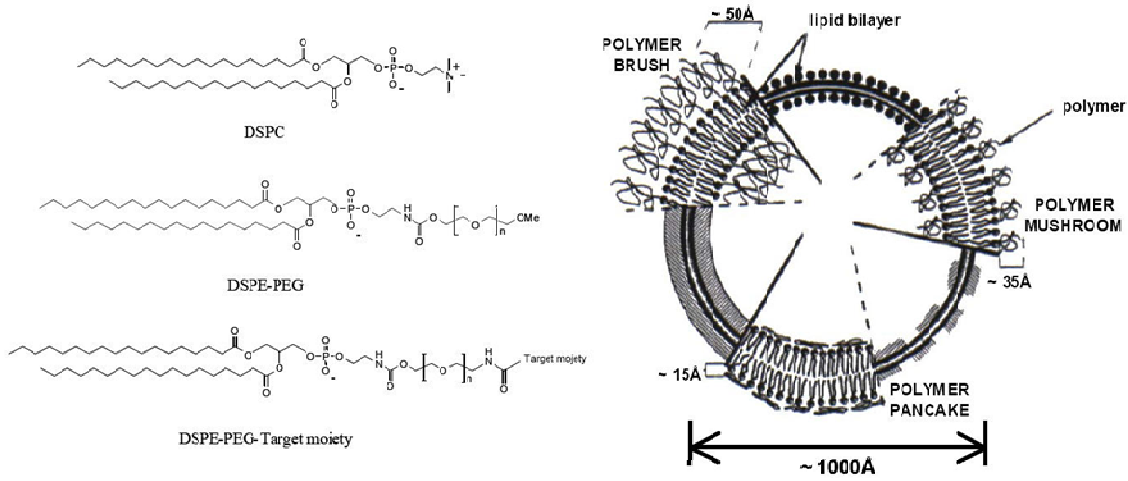

Figure 4.4. Left: Chemical structures of distearoylphophatidylcholine (DSPC), distearoylphophatidylethanolamine after conjugation with poly-(ethylene glycol) (PEG) (DSPE-PEG) and DSPE-PEG linked with a targeting moiety. Right: The behaviour of PEG when attached to the liposome surface, dependent on the graft density and molecular mass of the polymer which in turn determines surface coverage, distance between graft sites and polymer chain interaction creating (i) brush mode <8 mol% (ii) mushroom conformation <4 mol% & (iii) pancake, with DSPE-PEG 2000, *as proposed by DeGennes, 1980.*

PEG chains are highly flexible and water-soluble and can extend to give a hydrodynamic radius ~5–10 times greater than that of a globular protein of equivalent molecular weight. Owing to its high degree of hydration, the polymer chain helps to mask the surface to which it is bound by effectively forming a 'water shell' (Duncan, R. 2006). When polymer-coated surfaces come into contact with one another they experience repulsive forces (Helm, C. A. et al. 1992). At low surface polymer coverage, polymer chains can interact with the opposite surface independently of one another. As surface coverage increases, so does the probability of the polymer chains coming into contact with one another, forcing them to adopt extended configurations (see Fig 4.4). These interactions increase the thickness of the polymer layer and are believed to simultaneously increase steric stabilisation efficiency within this extended region (Helm, C. A. et al. 1992). Although there has been much evidence to suggest a reduction in particle aggregation and an increase in circulation times as a result of these properties, PEG has also been shown to interfere with cell interaction and intracellular trafficking (Xu, L. et al. 2011).

Numerous studies demonstrate the positive impact of pegylation on delivering cancer targeted drugs (Dadashzadeh, S. et al. 2008;Ichikawa, K. et al. 2004;Konan-Kouakou, Y. N. et al. 2005;Oku, N. et al. 1997;Park, J. W. 2002;Pegaz, B. et al. 2006;Symon, Z. et al. 1999;Zamboni, W. C. 2005) as a reduction in MPS uptake allows for passive accumulation in other tissues. In contrast to normal tissue vasculature, with tight junctions between capillary endothelial cells, malignant tumour vasculature is characterised by rapid angiogenesis, producing leaky vessels with large fenestrae. This facilitates the extravasation of liposomes into the interstitial space where they are allowed to passively accumulate due to a dysfunctional lymphatic drainage system via the enhanced permeability and retention (EPR) effect (Maeda, H. et al. 2000). However, the degree to which the active drug molecule is taken up and released into the interior of the tumour cell is unknown and the two mechanisms are not mutually exclusively. It has also been suggested that intracellular uptake and subsequent subcellular distribution of drugs within tumour cells has a great therapeutic effect than extravasation into the tumour interstitium alone (Richter, A. M. et al. 1993).

New generations of liposomes for passive targeting to tumour tissue have been created using intelligent design to improve selectivity. In addition to modifications at the liposome surface, the carriers incorporate specific trigger release mechanisms tailored to their target tissue environment in order to release their drug content and allow liberated molecules to interact with their surroundings. Examples include;

i. *Thermo-sensitive liposomes*; when the target tissue is heated above the phase-transition temperature of the liposomal membrane, the drug molecules are released as a result of membrane lipid disorder and an increase in the permeability of the membrane. Ideal candidates are liposomes composed of lipids that have a phase-transition temperature just above normal body temperature (37°C) that are triggered by local heating of tumour tissue. This treatment, however, may affect the integrity of surrounding normal tissue as heating causes destruction of structural collagen fibres (Gaber, M. H. et al. 1995) therefore may only be suitable for topical cancers.
ii. *Fusogenic liposomes*; viral proteins with fusogenic properties (e.g. Sendai virus coat-proteins) have been coupled to the surface of liposomes to create virosomes. These are used to deliver the contents of liposomes into the cytosol upon fusing with the cell membrane via non-internalising receptors. Drawbacks to this system

include the lack of tumour selectivity, as viral proteins dictate which cells are targeted (Metselaar, J. M. et al. 2002).

iii. *pH sensitive liposomes*; the microenvironment of tumour tissue (interstitial space) and tumour cells (endosomes/lysosomes) has a lower pH compared to the physiological pH of normal tissue, making it slightly acidic. This can be exploited by designing liposomes that incorporate acid-sensitive molecules which are charged at neutral pH but uncharged at acidic pH. This would cause liposomes to collapse in a low pH environment as protonation results in a reduction in interbilayer repulsion, releasing drug molecules into tumour tissue (Aicher, A. et al. 1994). Studies *in vivo* have shown that additional incorporation of modifying molecules, such as PEG, used to increase blood circulation times in rats, can reduce the pH sensitivity of these liposomes (Slepushkin, V. A. et al. 1997). In order to combat this, other studies have encouraged the detachment of PEG in local pathological conditions, *i.e.* low pH of tumours, to release their therapeutic load (Torchilin, V. P. 2005).

As previously discussed, the clinical utility of many therapeutics has been limited by their inability to localise in target tissues at sufficient concentrations or impairment by severe/harmful side-effects to normal tissues. Liposomes were first employed as drug delivery vectors in 1995 when Doxil® (Table 4.1) was the first liposomal pharmaceutical product to be approved for use the treatment of Kaposi's sarcoma (AIDS-related). It contains the chemotherapeutic drug Doxorubicin, which causes major cardiotoxicity (e.g. strongly binds to cardiolipin) when administered freely. Liposomes were developed to enhance the therapeutic index by reducing doxorubicin-related toxicity (Myocet®) and it was discovered the addition of PEG groups (Doxil®) and alterations in liposomal composition (LipoDox®) increased blood circulation times (stability) and improved the safety profile; as evidence suggests Doxil is metabolised by a different mechanism to doxorubicin from patient studies (Malam, Y. et al. 2009). Despite a reduction in severe cardiac events, new symptoms such as stomatitis (inflammation of mucosal lining) became the dose-limiting side-effect and the number of incidences increased with pegylated formulations, paradoxically, as a result of their longer half-life (Hong RL 2004;O'Brien, M. E. et al. 2004) . Since then, liposomes have been used in other applications including, but not limited to, ophthalmology, pain management, infections, vaccinations and further expansion into the effectiveness of anti-cancer drugs (Table 4.1) of which many have been either clinically approved or entered into Phase III clinical trials.

4. Liposomes

Active drug	Product name	Modified	Lipid composition (molar ratio)	Treatment
Amikacin*	Arikace	pegylated	DPPC, cholesterol	Lung infections
Amphoteracin B	Ambisome	Non- pegylated	HSPC, DSPG, cholesterol, Amp B (2:0.8:1:0.4)	Fungal infection
Cisplatin	LipoPlatin	pegylated	SPC, DPPG, cholesterol, mPEG 2000-DSPE	Epithelial malignancies
Cytarabine	DepoCyt	Non- pegylated	Cholesterol, triolein, DOPC, DPPG (11:1:7:1)	Lymphomatous meningitis
Daunorubicin	DaunoXome	Non- pegylated	DSPC, cholesterol (2:1)	Kaposi's sarcoma
Doxorubicin	Myocet	Non- pegylated	EPC, cholesterol (55: 45)	Recurrent breast cancer
Doxorubicin	Doxil/Caelyx	pegylated	HSPC, cholesterol, PEG 2000-DSPE (56:39:5)	Kaposi's sarcoma, breast, ovarian
Doxorubicin	LipoDox	pegylated	DSPC, cholesterol, PEG 2000-DSPE (56:39:5)	Kaposi's sarcoma, breast, ovarian
Doxorubicin*	Thermodox	pegylated	DPPC, MSPC, PEG 2000-DSPE (90:10:4)	Primary liver cancer
Inactivated virus	Epaxal	Non- pegylated	DOPC, DOPE	Hepatitis A vaccine
Inactivated virus	Inflexal V	Non- pegylated	DOPC, DOPE	Influenza vaccine
Verteporfin	Visudyne	Non- pegylated	EPG, DMPC (3:5)	Wet- macular degeneration
Vincristine	Marqibo	Non- pegylated	Cholesterol, egg sphingomyelin (45:55)	Non-Hodgkin's lymphoma

Table 4.1. Liposomal drugs approved for clinical application (market) or undergoing clinical evaluation (Phase III clinical trials*) *(Chang, H. I. et al. 2012).*

Applications in PDT

Drug delivery systems for photosensitising agents ideally should be soluble in aqueous solutions, in order to ensure suitability for administration via intravenous injection. In addition, they should be able to demonstrate increased selectivity towards tumours. Although many photosensitisers possess hydrophobic properties, which enable them to penetrate through the cell membrane, their hydrophobicity also causes delivery problems due to the strong aggregation of molecules in aqueous environments. Aggregated forms of photosensitisers are much less photoactive and bind strongly to certain serum proteins (Triesscheijn, M. et al. 2007). It has been shown, particularly for porphyrins, that their photophysical properties are dramatically altered upon aggregation, causing a decrease in the absorption coefficient and a reduction in the fluorescence yield and lifetime (Boyle, R. W. et al. 1996), largely in the triplet state, reducing singlet oxygen formation (Ricchelli, F. et al. 1998). Porphyrins, for example, exist in two aggregation formations; face-to-face aggregates (H-aggregate) (Hunter, C. A. et al. 1990) and edge-to-edge aggregates (J-aggregate) (Ribo, J. M. et al. 1994). Although liposomes do not completely prevent dimerisation of photosensitiser molecules they help to promote monomerisation along with the formation of possible planar aggregates, capable of photosensitising ability, thereby significantly increasing photoactivity and oxygen consumption (Derycke, A. S. et al. 2004;Ricchelli, F. 1995). This is known as the '*monomerisation effect'* and occurs as a result of the localisation of the photosensitiser molecules within hydrophobic bilayers (Angeli, N. G. et al. 2000). A second contributing factor is the '*concentration effect'*, as liposomes are able to incorporate large quantities of drugs, the local concentration of photosensitiser inside a vesicle is several orders of magnitude greater than that in the solvent solution. This can lead to a structurally controlled aggregation process in the liposomal bilayer (Borovkov, V. V. et al. 1996). Finally, the photosensitiser is located in a structured microenvironment within the liposome. An increase in microviscosity slows down internal movements of the embedded molecule, restricting their diffusion motion and as a result reducing collisional quenching of fluorophores in excited states (Gottfried, V. et al. 1988), known as the *'viscosity effect'*. Other contributing factors that may influence the photophysical properties of the liposomal encapsulated photosensitiser include the degree of rotational freedom of embedded molecules in the membrane, affecting quantum yields and singlet oxygen formation, and photobleaching inside the lipid bilayer (Gottfried, V. et al. 1988).

In PDT, problems associated with the biodistribution of PS to normal tissues and its clearance can result in residual cutaneous photosensitivity which must be managed until the drug is eliminated (Hopper, C. 2000). The selectivity of tumour uptake with PDT photosensitisers is also marginal. Liposomes have been used in recent years due to their suitability for packaging large quantities of hydrophobic photosensitisers into their lipid shells (Buchholz, J. et al. 2005;Lassalle, H. P. et al. 2009) and their ability to accumulate in tumour tissue through the enhanced permeability and retention (EPR) effect as a result of their size, as demonstrated numerous *in vivo* models (Maeda, H. et al. 2000). This selectivity, however, is also largely dictated by the plasma half-life and pharmacokinetics of the liposomes, therefore PEG can be used to coat the outer surface of the liposome to reduce susceptibility to the host's immune system and rapid uptake into the RES (Torchilin, V. P. 2005), hindering the loss of the liposome from circulation (Dos, S. N. et al. 2007). It is also essential that the photosensitiser be released from the liposome prior to irradiation with light, due to the short diffusion distance and half-life of singlet oxygen. Although excited photosensitiser may be able to oxidatively break down the liposomal carrier itself to release molecules, it may simultaneously prevent migration of reactive oxygen species into the local environment, limiting therapeutic effect (Derycke, A. S. et al. 2004).

Currently, Photofrin® (porfimer sodium), Visudyne® (verteporfin), Levulan® (5-aminolevulinic acid, 5-ALA) and Metvixia® (methyl aminolevulinic acid) have been approved for use as PDT drugs by the Food and Drug Administration in the US. Foscan® (m-THPC) has also been approved to treat head and neck cancers in the European Union and Japan (Hopper, C. et al. 2000). All other clinically approved PDT drugs are porphyrin-based molecules, with the exception of 5-ALA, and are hydrophobic with intrinsically low water solubilities, therefore excipient molecules, such as lipid mixtures (e.g. in Visudyne) and ethanol/poly(propylene glycol) (e.g. in Foscan), are used to solubilise these agents for systemic intravenous injections (Ding, H. et al. 2011).

Visudyne® is a successful, commercially available liposomal photosensitiser (non-pegylated) approved for clinical PDT since 2004 (Table 4.1). The active compound is the hydrophobic photosensitiser verteporfin, which is a benzoporphyrin derivative with a chlorin-like structure, activated upon illumination with 693 nm light (Bressler, N. M. et al. 2000). It was shown to be highly effective as a PDT agent *in vivo* from primate to murine

models, however, its low solubility in aqueous environments, means it typically undergoes self-aggregation, limiting its bioavailability. Liposomes were used as a means to inject verteporfin intravenously in its monomeric form (Visudyne). Visudyne was able to prevent the growth of destructive blood vessels (angiogenesis) without injury to surrounding tissues in patients due to its apparent selectivity to the vasculature and as such was used to treat wet age-related macular degeneration (AMD) with PDT, for which it is currently the only drug approved by the FDA (Chang, H. I. et al. 2012). 12 months post treatment patients had statistically better visual activity (67%) due to a reduction in the growth of abnormal blood vessels in the back of the eye (macular region) (Study Group 1999).

The photosensitiser, m-THPC, is similar to that of verteporfin. It is a highly potent, second generation PS that exhibits several favourable characteristics for PDT (Bonnett, R. et al. 1999). Being a chlorin it exhibits stronger absorption than porphyrins at longer wavelengths (652 nm); however, it is hydrophobic and prone to aggregation, which presents problems in optimising its formulation (Redmond, R. W. et al. 1985). The aggregated form of m-THPC is less photoactive and binds strongly to serum proteins (Triesscheijn, M. et al. 2007). High inter-patient variability of the current micellular m-THPC formulation, Foscan (Glanzmann, T. et al. 1998) is attributed to rapid uptake of PS-aggregates into cells of the reticuloendothelial system (RES) and poorer accumulation in tumour tissue. The unique microenvironment of solid tumours also limits PS delivery and distribution within cancerous tissue (Minchinton, A. I. et al. 2006), further contributing to differences in PDT response (Blant, S. A. et al. 2002).

The aim of the present study was to investigate the *in vivo* biodistribution and accumulation of two pegylated liposomal m-THPC formulations (FosPEG 2% and FosPEG 8%), in comparison to standard Foscan (m-THPC alone) (Table 4.2 & Fig 4.5). Linear clearance patterns of therapeutics are rarely observed in biological systems therefore theoretical mathematical compartmental and non-compartmental approaches were applied to obtain a host of pharmacokinetic parameters. Pharmacokinetic analysis was carried out in both normal Wistar rats and Hooded Lister rat models. The latter model having been subcutaneously implanted with a syngeneic fibrosarcoma cell line (MC28), which has been successfully used in previous m-THPC (Foscan) studies (Tsutsui, H. et al. 2002).

m-THPC	Foscan®		FosPEG	
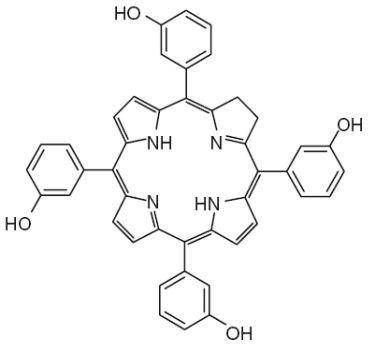	m-THPC	4.0 mg/mL	m-THPC	1.5 mg/mL
	DPPC	-	DPPC	18.0 mg/mL
	DPPG	-	DPPG	2.0 mg/mL
	DSPE-PEG 2000	-	DSPE-PEG 2000 (2 or 8 mol%)	2.0 or 8.0 mg/mL
	Ethanol	20%	Glucose in 10 mM histidine buffer pH 6.5	50 mg/mL
	PEG 400	30%		
	dH_20	50%		

Table 4.2. Foscan and FosPEG constituents and the molecular structure of m-THPC. FosPEG is composed of two phospholipids DPPC (Dipalmitoylphosphatidylcholine) and DPPG (dipalmitoylphosphatidylglycerol) in a liposome structure with varying degrees of PEG 2000-DSPE (distearoylphosphatidyl ethanolamine). *Information courtesy of Biolitec, Jena, Germany.*

Pharmacokinetic parameters obtained helped to deduce the *in vivo* behaviour of m-THPC in terms of its uptake and retention in different tissues over a selected time series. The uptake of m-THPC when incorporated in pegylated liposomes was then correlated with measurements of tumour PDT efficacy and skin photosensitivity in comparison to Foscan.

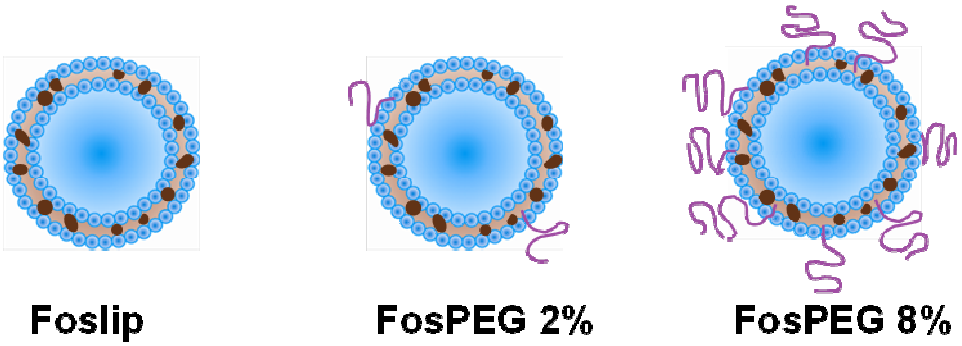

Figure 4.5. Schematic diagram illustrating the different liposomal nanocarrier formulations loaded with m-THPC. Liposome structure is formed with two phospholipids DPPC and DPPG. The diameter of the unilamellar liposomes are ~105 - 125 nm, loaded with ~20 000 m-THPC molecules per liposome. Foslip lacks a PEG coating and was not used in this study. FosPEG formulations are coated with either 2% mol (FosPEG 2%) or 8% mol (FosPEG 8%) PEG (polyethylene glycol). *Diagram courtesy of Biolitec, Jena, Germany.*

4.2 Materials & Methods

4.2.1 Chemicals and Photosensitisers

Biolitec AG (Jena, Germany) kindly provided all m-THPC formulations (Dr Dietrich Scheglmann). Foscan® was supplied in its standard formulation (m-THPC in ethanol/propylene glycol) at a stock concentration of 4 mg mL^{-1}. Liposomal formulations of m-THPC, FosPEG 2% and FosPEG 8%, were prepared as a 9:1 mixture of dipalmitoylphosphatidylcholine (DPPC) and dipalmitoylphosphatidylglycerol (DPPG) using a conventional film method (Compagnin, C. et al. 2011). The degree of pegylation was 2% and 8% (molar equivalent ratio) using 1,2-distearoyl-sn-glycero-3-phosphoethanolamine-N-[amino (polyethylene glycol)-2000] (DSPE-PEG2000) (Table 4,2). These were provided as stock solutions containing a molar equivalent concentration of 2.21 mM (or 1.5 mg mL^{-1}) m-THPC in 10 mM histidine buffer, containing 50 mg mL^{-1} glucose at pH 6.5. The mean number of m-THPC molecules in the hydrophobic phospholipid shell was estimated at 2×10^4 per liposome, based on the 9:1 molar ratio of lipid to m-THPC determined after extrusion (~10 % m-THPC). Mean particle size distribution and particle characterisation measurements were assessed using photon correlation spectroscopy, differential scanning calorimetry and cryo-TEM following extrusion and after storage. The mean particle diameter of liposomal formulations was between 105-125 nm (z-average) and polydispersity indices (PCI) were between 0.04 and 0.15, indicating narrow size distributions. All formulations remained stable in size for up to 12 months in storage buffer and upon dilution (slight decrease in size ~5%), with no changes in optical appearance and no drug precipitates or aggregates observed. Solvable™ (Perkin-Elmer, UK), which is a commercially available aqueous-based alkaline solvent, was used to dissolve animal tissues and release m-THPC in its monomeric form for spectrofluorimetric analysis, as aggregated photosensitisers cause dramatic changes in their absorption and fluorescence properties (Bonnett, R. et al. 1999).

4.2.2 Absorbance spectra

The absorbance spectra of m-THPC was measured for Foscan and each liposomal formulation in their equivalent buffers at 1 μM concentrations using a Lambda 25-UV/Vis spectrophotometer (Perkin-Elmer, UK). Absorbance spectra were recorded between 300 – 700 nm light wavelengths at 1 nm intervals. Spectra were obtained at a scanning speed of 480 nm min^{-1} and recorded through UV Winlab software®. Pure m-THPC powder (Scotia

Pharmaceuticals, UK) was additionally dissolved in ethanol and diluted into working stock solutions of 1 µM as a reference. In a separate group, absorbance of m-THPC was measured for all formulations at 1 µM concentrations when diluted in Solvable™ following incubation in Solvable™ at 50°C for 2 h, in order to replicate tissue chemical extraction conditions. This was to assess potential shifts in maximum absorbance peaks (λ_{max}) following extraction and ensure absorbance of m-THPC was not altered for spectrofluorimetric analysis. Optimal wavelengths at the highest sensitivity (minimise deviations from Beer's Law, $A = \varepsilon\ l\ c$) were set to obtain measurements (m-THPC λ_{exc} = 423 nm, λ_{em} = 652 nm). Absorbance measurements of each solution were taken in quartz cuvettes with a light path-length of 1 cm (Pye Unicam, UK). Cuvettes were rinsed with ethanol (Sigma, UK) before each reading. Spectra were normalised with background absorbance values of Solvable™, ethanol and formulation buffers.

4.2.3 Fluorescence spectra

The fluorescence emission spectra of m-THPC in liposomal formulations, FosPEG 2% and FosPEG 8%, were measured in histidine loading buffer or DMSO (dissolution) at m-THPC concentrations of approximately 0.5 µM in 96 well plates (averaged). Fluorescence emission spectra of known concentrations of m-THPC formulations in Solvable were measured to construct calibration curves for pharmacokinetic studies. Control solutions of m-THPC in DMSO/Solvable only were run simultaneously (as m-THPC is insoluble in aqueous buffer). An LS50B Perkin-Elmer spectrofluorimeter (Perkin-Elmer, UK) was used to obtain fluorescence spectra. Spectra were acquired using a multimode bifurcated fibre-optic probe to provide front surface excitation/detection geometry, which is unaffected by polarisation effects, unlike the conventional orthogonal excitation/detection configuration. The intensity of the fluorescence emission spectrum of m-THPC formulations was recorded between the 600 – 700 nm range after excitation (m-THPC λ_{exc} = 423 nm) using FL Winlab software. Fluorescence spectra were normalised with control readings from background wells.

4.2.4 Confocal microscopy in vitro

The intracellular localisation of m-THPC in MC28 (rat fibrosarcoma) cells was determined through confocal fluorescence microscopy taking advantage of its red fluorescence. 1 x 10^4 MC28 cells were seeded in 35 mm diameter glass-bottomed fluorodishes (WPI, UK). These were incubated over night to encourage adherence and optimal subconfluent cell

spreading for imaging. After 24 h, MC28 cells were incubated with fresh Dulbecco's modified Eagles Medium (DMEM) containing $_{L}$-glutamine, 4.5 g/L glucose (BioWhittaker, Lonza, Verviers Belgium), supplemented with 10% (v/v) foetal calf serum (FCS) (Sigma-Aldrich), 100 U/mL penicillin and 100 µg/mL streptomycin at 37ºC in a humidified, 6% CO_2 incubator under dark conditions for either 1 h or 6 h with 1 µM m-THPC (Foscan) or m-THPC liposomal formulation (FosPEG 2%). Following incubation, cells were washed twice with PBS before fresh media (minus serum and phenol red) was added. This is because FCS is known to interfere with cellular drug uptake (Jori, G. et al. 1984;Siboni, G. et al. 2002) and m-THPC emission is detected in the red region of the spectrum (Zguris, J. et al. 2006) (*see* ***Appendix I – A.3 Preparation of Fluorodishes: Foscan® and FosPEG2%***). Cells were observed using an inverted Olympus Fluoview 1000 confocal laser scanning microscope to determine intracellular localisation of m-THPC. Fluorescence confocal images obtained with 60x 1.4 NA oil immersion objective (Olympus) were analysed with Fluoview FV1000 (Olympus) and Image J software. m-THPC fluorescence was detected using a 405 nm laser and a set of detection filters with 400 nm excitation and 640-80 nm emission. Laser voltage, Gain and Offset were kept consistent throughout imaging.

4.2.5 Animals and tumour model

All animal experiments were carried out under the authority of project and personal licences granted by the UK Home Office and with reference to NCRI (National Cancer Research Institute) guidelines for the Welfare of Animals in Experimental Neoplasia (2010). All procedures were performed under general anaesthesia with inhaled isofluorane (Abbott Laboratories Ltd, Kent, UK). Buprenorphine hydrochloride (Reckitt & Colman Products Ltd, Hull, UK) was given subcutaneously for postoperative analgesia where necessary.

Female Wistar rats (180–220 g) were used for *in vivo* normal tissue pharmacokinetic studies and skin photosensitivity studies, since skin pigmentation is minimal. The same model was used previously by Weersink *et al*., in studies with a different photosensitiser (Weersink, R. A. et al. 2005). Each formulation was administered intravenously via a tail vein injection at a dose of 0.3 mg kg^{-1} m-THPC ***(see Appendix I –A.1 Dosage Calculations)***. At a specified time point between 2 and 168 h, animals were killed by

cervical dislocation. For plasma readings, animals were killed immediately after injection at an estimated time of ≤ 5 min.

The Wistar rat model was additionally chosen due to the large volume of literature published on PDT to normal tissues in these animals (*i.e.* liver and colon); therefore comparisons could be drawn with other available photosensitisers e.g. Palladium bateriopheophorbide (Tookad) (Woodhams, J. H. et al. 2006), Phthalocyanine (Pc) (Woodhams, J. H. et al. 2003), aminolevulinic acid (ALA) (Messmann, H. et al. 1995) and ATX-S10Na(II) (Harada, M. et al. 2005).

A methylcholanthrene-induced fibrosarcoma cell line (MC28), syngeneic and transplantable to Hooded Lister (HL) rats (Ashraf, S. et al. 1997;Tsutsui, H. et al. 2002) was cultured in Dulbecco's modified Eagles Medium (DMEM) containing $_{L}$-glutamine, 4.5 g/L glucose and phenol red (BioWhittaker, Lonza, Verviers Belgium). Media was supplemented with 10% (v/v) foetal calf serum (FCS) (Sigma-Aldrich), 100 U/mL penicillin and 100 µg/mL streptomycin (Sigma-Aldrich). Cells were cultured under aseptic conditions in monolayers and maintained at 37ºC in a humidified, 6% CO_2 incubator (LEEC Research CO_2 Incubator). At 80-90% confluence (~ 1-2 x 10^6 cells/T-150 flask),ells were passaged routinely; washing twice with phosphate buffered saline (PBS) (BioWhittaker, Lonza) before trypsinisation (0.05% Trypsin in 0.02% PBS/ EDTA) with 3 mL Trypsin-EDTA (ethylene diamine tetra-acetic acid, EDTA, calcium chelator) for 0.5 - 1 mins, to ensure cell detachment. Trypsin was neutralised with serum enriched culture medium and the cell suspension was centrifuged (5 mins, 17600 g RCF). Cells were resuspended in fresh media and re-plated at an optimal growth seeding density of 5000 cells/cm² ***(see Appendix I –A.2 Cell Counts and Calculations)***.

Female HL rats (150–220 g) were inoculated subcutaneously in the lower flank, where influence of respiratory movement is minimal, with approximately 1–2 × 10^6 MC28 cells in 0.1 mL injection volume (Ashraf, S. et al. 1997;Murphy, P. et al. 1986). Tumours were monitored continuously and reached an optimal size of approximately 10 mm^3 after 7–10 days at which point they were selected for studies. For longer time points (≥72 h) animals were recruited earlier to studies to account for continual tumour growth. This size was chosen based on previous publications which showed no evidence of spontaneous necrosis in tumours ≤10 mm in diameter in this model (Tsutsui, H. et al. 2002).

4.2.6 Pharmacokinetic study

Tissue samples selected for pharmacokinetic analysis included muscle, skin (right abdominal wall), liver, spleen, kidneys, lung, blood serum and tumour, taken from three animals at each time point. Immediately post-mortem tissues were removed under subdued lighting at 2, 4, 6, 18, 24, 72, 96 and 168 h from normal Wistar rats after intravenous administration of each m-THPC formulation at 0.3 mg kg^{-1}. For HL tumour rats, time points of 2, 4, 6, 24 and 72 h were chosen for intravenous administration of each m-THPC formulation at the same dose (0.3 mg kg^{-1}) due to maximal tumour growth threshold being attained by 72 h. Blood samples (~3 mL) were also taken immediately after injection at an additional ≤5 min interval and left to stand for 20 mins before centrifuging to separate the serum at 2000 rpm (~300 g RCF) for 10 min for pharmacokinetic analysis. Negative control animals at 0 h were run simultaneously. Samples were stored in the dark at −80 °C.

m-THPC accumulation in tissues was measured through a chemical extraction method combined with spectrofluorimetric analysis of m-THPC in the extract, adapted from Kascakova *et al*., (Kascakova, S. et al. 2008). Tissue samples of approximately 0.1 g wet weight were run in triplicate. These were incubated in 2 mL of 100% Solvable™, an aqueous-based alkaline solvent containing a mixture of dodecyldimethylamine oxide (2.5–10%), secondary alcohol ethoxylate (2.5–10%) and sodium hydroxide (≤2.5%) in water (Perkin-Elmer, UK). Samples were incubated for approximately 2 h at 50 °C in a shaking water bath, until completely dissolved without any visible tissue residue to ensure complete monomerisation of m-THPC (no binding of m-THPC to residual tissue). Fluorescence detection was used to construct a linear standard curve of known m-THPC concentrations (0–5 μM) from control tissues for each organ, prepared under identical conditions and diluted in the same solvent (Solvable™) as test samples (Table 4.3). The solubilised tissues were aliquoted (300 μL) into a 96 well plate. The fluorescence signal from each well was detected using a Perkin-Elmer LS 50B fluorescence spectrometer (Perkin-Elmer, UK) linked to a plate reader. Front surface excitation/detection was employed using a fibre-optic probe which minimises reabsorption and polarisation artefacts. Excitation and emission wavelengths for m-THPC fluorescence measurements were set at 423 nm and ~652 nm respectively, as determined by m-THPC absorbance spectra maxima. Slit widths, that select the band of incident light, were set at 10 nm for excitation/emission entry/exit with an additional internal 515 nm long-pass filter for

emission. Fluorescence was measured and recorded through Win lab® software. Fluorescence readings were used to calculate the mean tissue concentration of m-THPC. Readings from negative control samples (without m-THPC) were deducted to correct for the autofluorescence (endogenous fluorophores) of each organ. The mean and the standard deviation (SD) for all three animals at each time point were calculated (± s.d., n = 3). The blood pharmacokinetics were analysed by compartmental and non-compartmental mathematical methods (Clark B et al. 1981) (Yamaoka, K. et al. 1978).

	Rat 1			**Rat 2**			**Rat 3**			**Control Rat**		
	3 samples			**3 samples**			**3 samples**			**3 samples**		
	1	**2**	**3**	**4**	**5**	**6**	**7**	**8**	**9**	**10**	**11**	**12**
A												
B												
C												
D												
E												
F												
G												
H												
Std C	0	0.001	0.005	0.01	0.02	0.05	0.1	0.2	0.5	1	2	5**(µM)**

Table 4.3. Illustration of the well plate loading of tissue samples for spectrofluorimetric analysis. *e.g.* Tissue sample = liver, at time point = 2 h, drug = Foscan. Tissue removed from 3 separate animals (Rat 1 – 3) + negative control animal (Control Rat: m-THPC free) and extraction carried out in triplicate (Rows A-D: Columns 1-3 ■ , 4-6 ■, 7-9 ■, 10-12 □). A standard curve of known m-THPC concentrations (µM) was additionally constructed using control tissue (Rows E – H: Columns 1 – 12).

Raw data were collected in micro molar units of concentration (µM) and subsequently converted into micrograms per gram (µg g^{-1}) (*see* ***Appendix I – A.4 Chemical Extraction: Raw Data Calculations***). All data were represented as mean±SD. Statistical analysis was carried out using a Student's t –test, where $P \leq 0.05$ was considered statistically significant.

This method is based on previously published work on alkaline hydrolysis of *ex vivo* tissue for photosensitiser quantification (Wilson, B. C. et al. 1997). It has since been refined,

removing/adding steps to establish optimal solvent concentrations, pH and incubation periods specifically for m-THPC quantification (Kascakova, S. et al. 2008), which have been adopted here.

4.2.7 Photodynamic therapy on MC28 tumours

Treatment with each m-THPC formulation was initiated when tumours had reached an optimal diameter of 10 mm. Clinical m-THPC doses of 0.3 mg kg^{-1} (high), 0.1 mg kg^{-1} and 0.05 mg kg^{-1} (low) (Betz, C. S. et al. 2008) were administered to two groups of animals prior to light delivery. A DLI of 24 h was chosen for PDT studies based on chemical extraction data of tumour tissue. Tumours were irradiated with red laser light interstitially from a 652 nm diode laser (Diomed, Cambridge, UK) using a 400 μm bare cleaved tip optical fibre inserted approximately 1 mm into the tumour capsule via a small incision in the overlying skin and in the MC28 tumour capsule. This irradiation method has been used in previous studies with m-THPC in the same tumour model (Tsutsui, H. et al. 2002) within our laboratories and mimics interstitial clinical PDT with Foscan, predominantly carried out on head and neck tumours whereby the laser fibre is inserted into the tumour. A total energy of either 2 J or 10 J of light at 100 mW (20 or 100 s) was delivered to each tumour. Each treatment group consisted of five animals. Animals were killed 24 h after treatment by cervical dislocation and whole tumours resected for histological analysis.

4.2.8 Skin photosensitivity studies

Skin photosensitivity studies required shaving, depilating (Neet™) and cleaning an area on the lower flank in a separate group of female Wistar rats (180–220 g). Following m-THPC *i.v.* administration of either 0.3 mg kg^{-1} or 0.1 mg kg^{-1}, 4 circular areas of skin measuring 0.5 cm in diameter and 1 cm apart (grid design) were exposed sequentially to either 0 (0 J), 5 (30 J), 15 (90 J) or 30 min (180 J) of 100 mW cm^{-2} of light (1 sun=solar equivalent spectrum) from a solar simulator source (Olympus CLV-S30, Cambridge, UK) at drug-light intervals (DLI) of either 96 and 168 h (Fig 4.6).

This system incorporated a 300W (Olympus Endoscopic) xenon lamp, providing a uniform 2 cm diameter beam at the skin surface. Surrounding skin tissue was protected from light using a light impenetrable fabric. Illuminated areas were marked adjacently. Light power was measured using a laser power metre (Gentec, UK) and was calibrated before and after

each treatment. A spectra of the solar simulator light was also taken to ensure it correlated to the observed spectra of sunlight (*see* ***Appendix I – A.10 Skin Photosensitivity Studies: Solar Simulator Spectra***). Although this does not result in a perfect reproduction of the true solar spectrum, due to a lack of UV (< 400 nm) and infra-red (> 750 nm) regions of the spectrum, it should be sufficient for quantitative assessment of skin response for guiding clinical use of m-THPC.

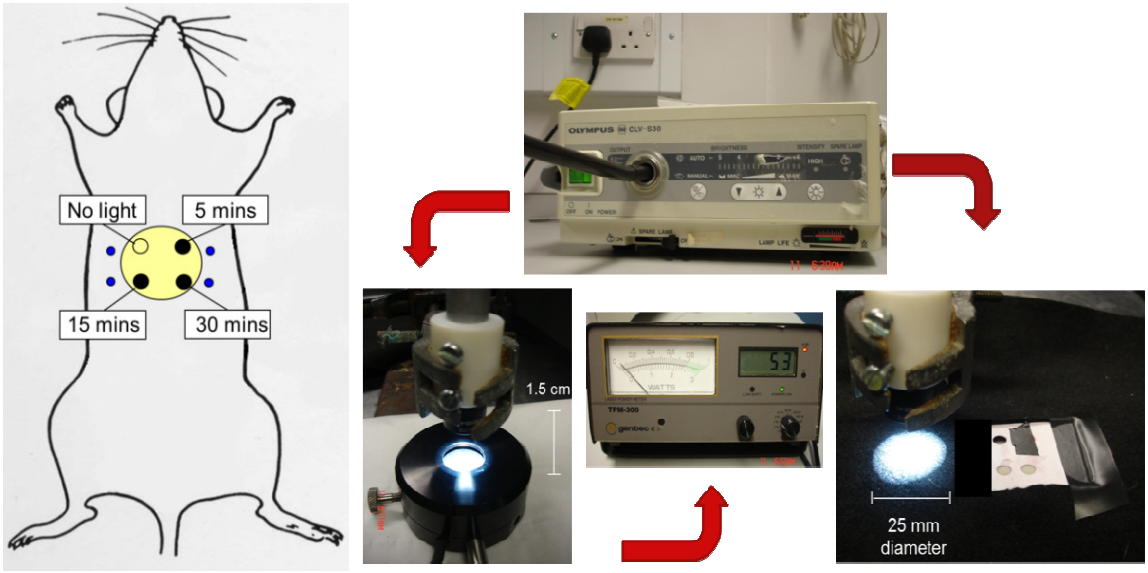

Fig.4.6. Experimental set-up for skin photosensitivity studies using female Wistar rats. Bare skin was irradiated with artificial sunlight from a solar simulator source (Olympus CLV-S30) for up to 30 mins. (Controls received either no PS or no light). The light source was calibrated before each treatment to ensure the power (100 mW) was constant and energy of light administered was accurate. The total diameter of the light beam was 25 mm, which was positioned 1.5 cm above the skin surface.

Treatments were carried out in a climate controlled room to prevent overheating of the skin. Visual assessment of skin reactions were carried out 24 h post-treatment and digital images taken. Imaged areas were then assessed by two independent scorers using a blinded grading model, previously established by Weersink *et al*., (Weersink, R. A. et al. 2005) (*see* ***Appendix I – A.11 Skin Photosensitivity Studies: Skin scoring model***). Grading was carried out on all images at one time to ensure subjective analysis across the data set was relative between animals. Each m-THPC formulation was allocated an ordinal value (0–8) and scores were averaged over each exposure time. Areas of skin treated at 0 min (no light control) and 30 min were removed for histological analysis. A separate group of animals that received no PS was also treated with 30 min of light to ensure skin effects were a result of the presence of PS, not light exposure.

4.2.9 Histology and measuring necrosis (Hamamatsu nanozoomer)

Whole tumours and skin tissue samples removed post-mortem were immersed in 4% neutral formalin buffer (4% w/v formaldehyde in phosphate buffered saline) for a minimum of 24 h at 20 °C. Samples were processed by routine histological methods. The tumours were cut in half (parallel to the laser fibre) and skin samples were cut through the centre of the treatment area, and adjacent halves of the tissue were embedded face down in paraffin wax blocks. Four-micrometre sections were cut and mounted on Vectabond (Vecta laboratories, UK) treated glass slides. Three sections were taken from each of the tissue halves. Slides were stained with Harris haematoxylin and eosin. Whole slides were scanned with the Hamamatsu Nanozoomer (Hamamatsu Photonics UK Ltd). Hamamatsu virtual microscopy imaging software was used to observe markers indicative of skin photosensitivity *i.e.* erythema and oedema. PDT damage in tumour tissue was assessed by measuring the surface area of necrosis from each section, as used previously in m-THPC PDT (Garrier, J. et al. 2010). The damage was calculated from each tumour as a percentage of the whole tumour surface area due to variability in tumour size and heterogeneity of tissue *(see* ***Appendix I –A.15 PDT: Hamamatsu Nanozoomer: Calculating the Area of Necrosis)***. Six sections were averaged per tumour (3 from each tumour half). The mean percentage surface area of tumour necrosis was calculated through blind analysis per group of five identically treated animals and all data were represented as mean±SD.

4.2.10 Statistical analysis

Mean and standard deviation was calculated for each animal group (±SD, n=3–5). All data were represented as mean±SD. Statistical analysis was carried out using a two-tailed Student's t-test and a Mann–Whitney U test for PDT data. $p \leq 0.05$ was considered statistically significant, unless stated otherwise.

4.3 Results

i. Absorption spectra

An absorbance spectrum of Foscan and each pegylated liposomal m-THPC nanocarrier formulation, FosPEG 2% and 8%, was taken in its corresponding buffer, as when administered in animals, to deduce peak absorbance wavelengths.

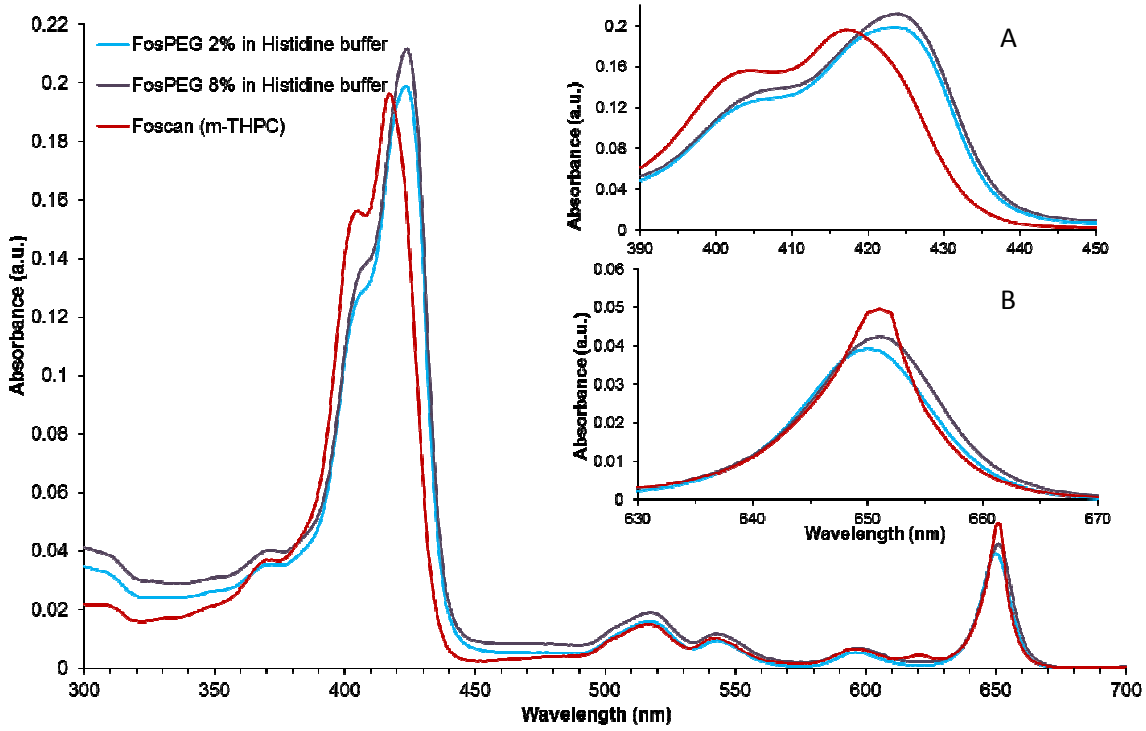

Figure 4.7. Absorbance spectra of Foscan (m-THPC in buffer: PEG 400 (3): EtOH (2): dH_2O (5)) and pegylated liposomal m-THPC, FosPEG 2% and FosPEG 8% in corresponding histidine loading buffer prepared at ~1 µM concentrations (A) inset: Soret band, (B) inset: Q band.

The absorbance spectra of Foscan (m-THPC in PEG buffer solvent system, PEG 400: EtOH: dH_2O) demonstrated two strong absorbance peaks (Fig 4.7), which showed absorption maxima at ~ 419 nm (Soret band) and ~651 nm (Q band). This is characteristic of the absorption peaks observed for chlorin-type compounds and corresponds to the literature (Kascakova, S. et al. 2008) (Bonnett, R. et al. 1999). Over a concentration range (c = 0–5 µM m-THPC) there was no evidence of spectral broadening or shifts in absorbance maxima with Foscan (data not shown) and solutions accurately followed Beer-Lambert's law. This suggests that the same photoactive species of m-THPC were present. The shoulder observed on the Soret band of Foscan is indicative of highly conjugated systems and is common for these chromophores, often solvent dependent. Absorbance

spectra of FosPEG formulations (liposomal m-THPC) demonstrates a bathochromatic shift (red shift) in the Soret band to longer wavelengths (λ = 423 nm), compared to Foscan, characteristic of J-aggregate formations. These changes in spectra are less pronounced in the Q band (~650 nm) for each m-THPC formulation.

Absorbance spectra of all m-THPC formulations were additionally taken following a 2 h incubation period in 100% Solvable (aqueous-based alkaline solvent) to mimic chemical extraction conditions when dissolving tissues and to ensure the spectrofluorimetric properties of m-THPC were not changed. Foscan and FosPEG formulations exhibited identical absorbance spectra in Solvable (c = 1 µM) with no detectable differences in the Soret or Q absorption bands (Fig 4.8).

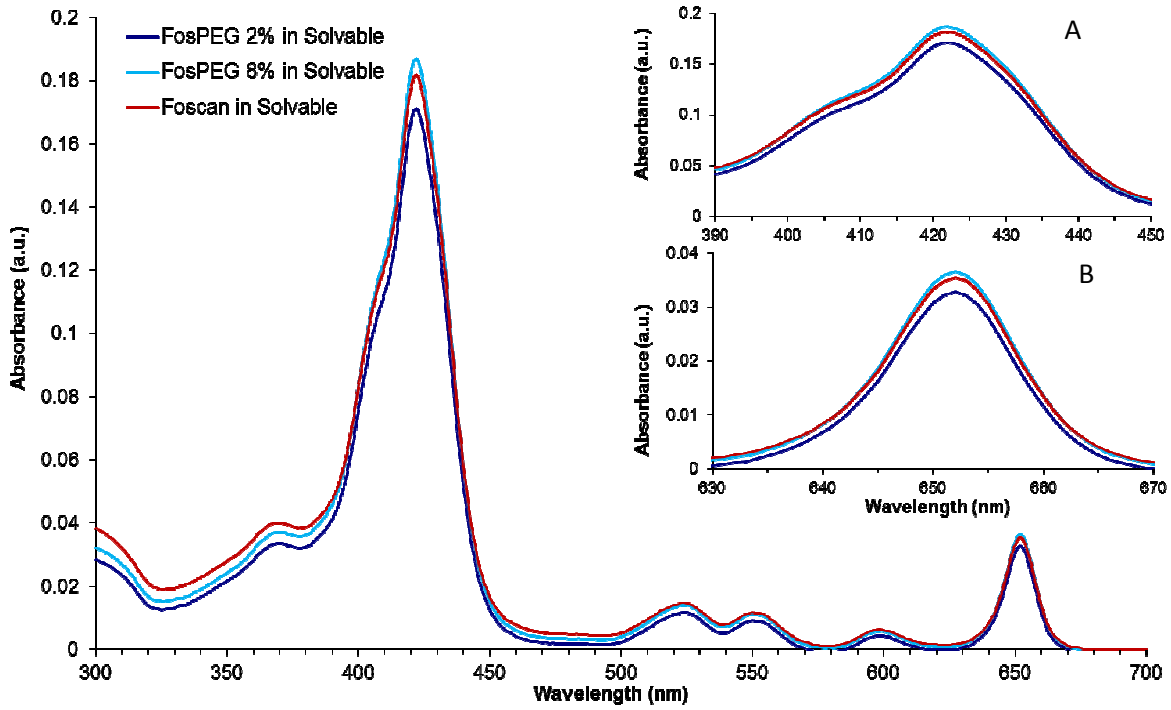

Figure 4.8. Absorbance spectra of Foscan (m-THPC in buffer: PEG 400 (3): EtOH (2): dH_2O (5)) and pegylated liposomal m-THPC, FosPEG 2% and FosPEG 8% in corresponding histidine loading buffer diluted to ~1 µM concentrations in Solvable™. (A) inset: Soret band, (B) inset: Q band.

When comparing the m-THPC spectra acquired in aqueous buffered solutions (Fig 4.7) to those of Solvable (Fig 4.8), there appear to be only small bathochromic shifts in the Soret and Q band with FosPEG solutions. Foscan also undergoes a red shift in the presence of Solvable, however, the most significant change in spectra observed is the loss of the shoulder on the Soret peak between solutions. These results correspond to the literature for

the spectroscopic properties of m-THPC (Foscan) in Solvable (Kascakova, S. et al. 2008). Slight differences in absorbance maxima at 423 and 652 nm may be due to experimental error in preparing m-THPC solutions.

ii. Fluorescence spectra

Fluorescence spectra were carried out in 100% Solvable with m-THPC (c = 0-0.5 µM) and FosPEG formulations (data not shown) to construct corresponding calibration curves of known m-THPC concentrations for pharmacokinetic studies.

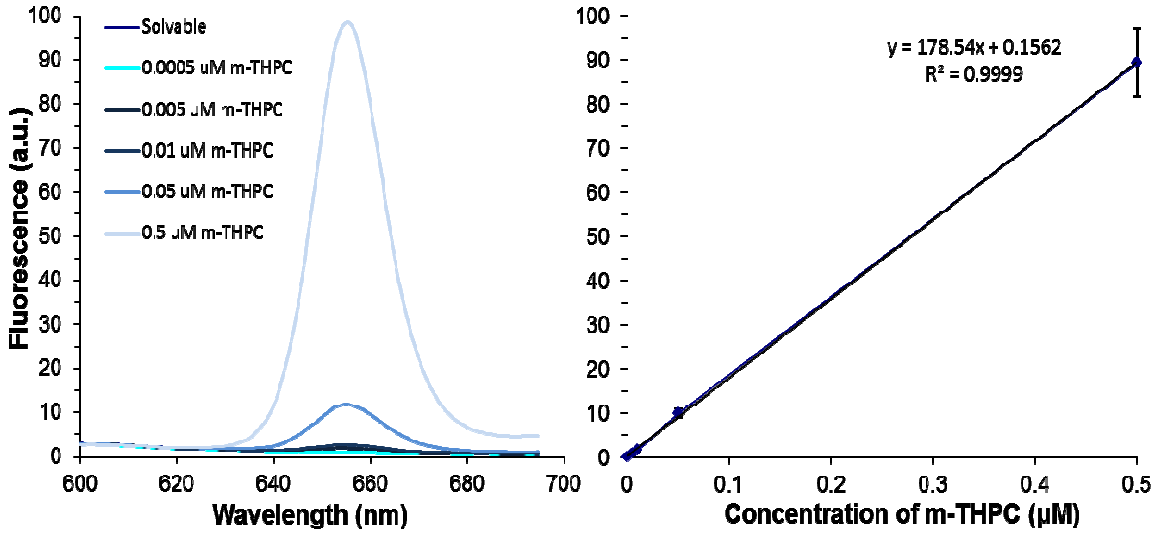

Figure 4.9. Fluorescence emission spectra (m-THPC λ_{exc} = 423 nm) of m-THPC diluted in Solvable and corresponding calibration curve (0-0.5 µM concentration range).

The fluorescence spectrum of m-THPC (Fig 4.9) in 100% Solvable was the same for all m-THPC formulations with increasing concentration. A slight shift from ~652 nm, when diluted in loading buffer (data not shown), to ~655 nm in Solvable was observed. This is in accordance with the literature (Kascakova, S. et al. 2008).

The fluorescence emission spectra of m-THPC were recorded for liposomes, FosPEG 2% and FosPEG 8%, in DMSO and in their loading (histidine) buffer. The peak emission, using 423 nm excitation, was recorded at 652 nm in each case but interestingly a higher peak intensity was observed with FosPEG 8% in its loading buffer (Fig 4.10) compared to FosPEG 2% (ratio of 1.25). Following complete dissolution of liposomes in DMSO, the fluorescence intensity almost doubled for both pegylated m-THPC liposomes, with little

difference in peak intensities between formulations. m-THPC is known to emit a negligible fluorescence in aqueous buffer (Kascakova, S. et al. 2008), therefore a control solution of m-THPC in DMSO, run in parallel, gave an identical fluorescence peak at 652 nm (data not shown).

Corresponding lifetime fluorescence data of these pegylated liposomes (histidine buffer) showed multi-exponential decays with significantly shorter lifetimes, in comparison to m-THPC in DMSO (9.6 ns) (Compagnin, C. et al. 2011): FosPEG 2%; 7.3, 2.5 & 0.9 ns and FosPEG 8%; 9.8, 1.1 & 3.0 ns (see **Chpt 6**: Fluorescence lifetime equations).

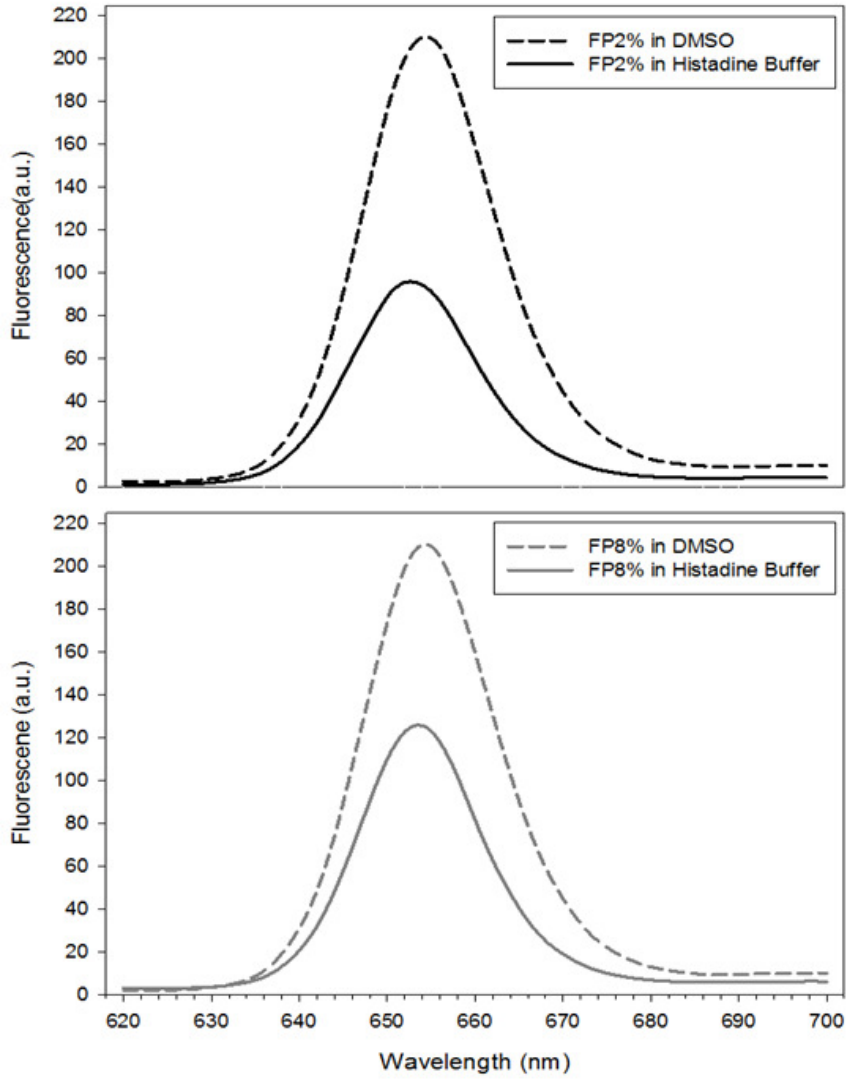

Figure 4.10. Fluorescence emission spectra of m-THPC in pegylated liposomes, FosPEG 2% and FosPEG 8%, either in their loading buffer or when dissolved in DMSO using an excitation wavelength of 423 nm. Peak emission was recorded at 652 nm.

iii. Confocal microscopy in vitro

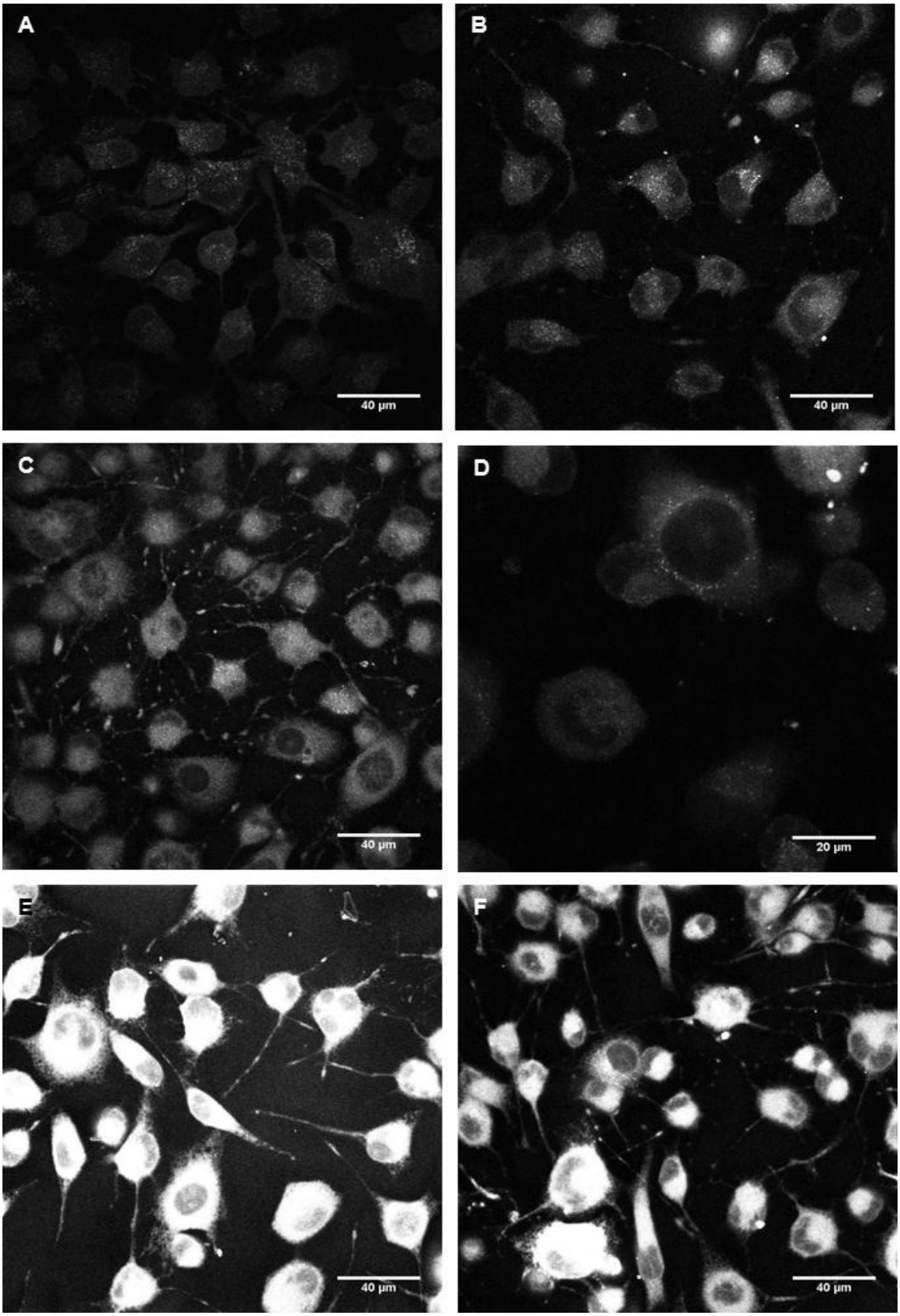

Figure 4.11. Confocal microscopy images of MC28 tumour cells following incubation with 1 µM m-THPC (Foscan) or m-THPC liposomal formulation (FosPEG2%) at different time intervals to determine cellular localisation. (A) Negative control MC28 cells no drug, (B) Foscan 1 h, (C) FosPEG 2% 1 h, (D) FosPEG 2% 1h (magnified), (E) Foscan 6 h and (F) FosPEG 2% 6 h.

Qualitative confocal microscopy results *in vitro* (Fig 4.11) show a greater uptake of m-THPC into MC28 tumour cells when delivered by both Foscan and FosPEG 2% after 6 h incubation time at 37°C in comparison to 1 h with m-THPC concentrations of 1 µM (FosPEG 8% solutions were not used in these studies). This is indicated by an increase in fluorescence of MC28 cells at 652 nm (Fig 4.11 E & F) in comparison to negative control cells (Fig 4.11 A), which received no drug. Although m-THPC fluorescence appears to be much lower following shorter incubation periods, at 1 h the images suggest there is a slight increase in the uptake of m-THPC when delivered by pegylated liposomal nanocarriers (FosPEG 2%) in comparison to Foscan (Fig 4.11 B & C) by a corresponding increase in fluorescence intensity. After 6 h incubation, m-THPC fluorescence reveals a more intense and uniform localisation pattern in cells, compared to 1 h incubation whereby m-THPC fluorescence is diffuse but sequestered to intracytoplasmic vesicles, illustrated by bright spots. Uptake of m-THPC appears to be localised to the cytoplasm and the perinuclear area of tumour cells with both m-THPC formulations, sparing the nucleotic centre, which remains dark and clearly visible at both times points (Fig 4.11 D). It is also important to note, although these cells were imaged in serum-free media, they were subjected to prior incubation with 10 % FCS supplemented media in the presence of each m-THPC formulations (1 or 6 h).

iv. Pharmacokinetics of m-THPC (Foscan versus FosPEG 2% and 8%)

Pharmacokinetic studies with m-THPC in untargeted pegylated liposomal nanocarrier formulations, FosPEG 2% and FosPEG 8%, were carried out in reference to standard Foscan formulation. Doses of 0.3 mg kg^{-1} (m-THPC drug equivalent) were employed in rats for a time series analysis to quantify m-THPC distribution *in vivo* (µg g^{-1}) by measuring uptake in different tissues through a chemical extraction method (*also see* ***Appendix I - A.21 %ID/g of liposomal m-THPC in different tissues in vivo***).

For the investigation in normal tissues, a range of organs were selected for pharmacokinetic analysis to compare relative uptake of m-THPC to that of tumour tissue. These tissues were selected for their primary role and participation in therapeutic circulation (blood), evasion or recognition by the host's immune system (RES; liver, spleen, lungs) and subsequent clearance or retention in the body (kidneys, colon, skin).

m-THPC was administered via a bolus intravenous injection into the tail vein and therefore introduced directly into the blood (central compartment). In order to study the distribution and elimination of m-THPC, blood serum was taken over a time course of 96 h.

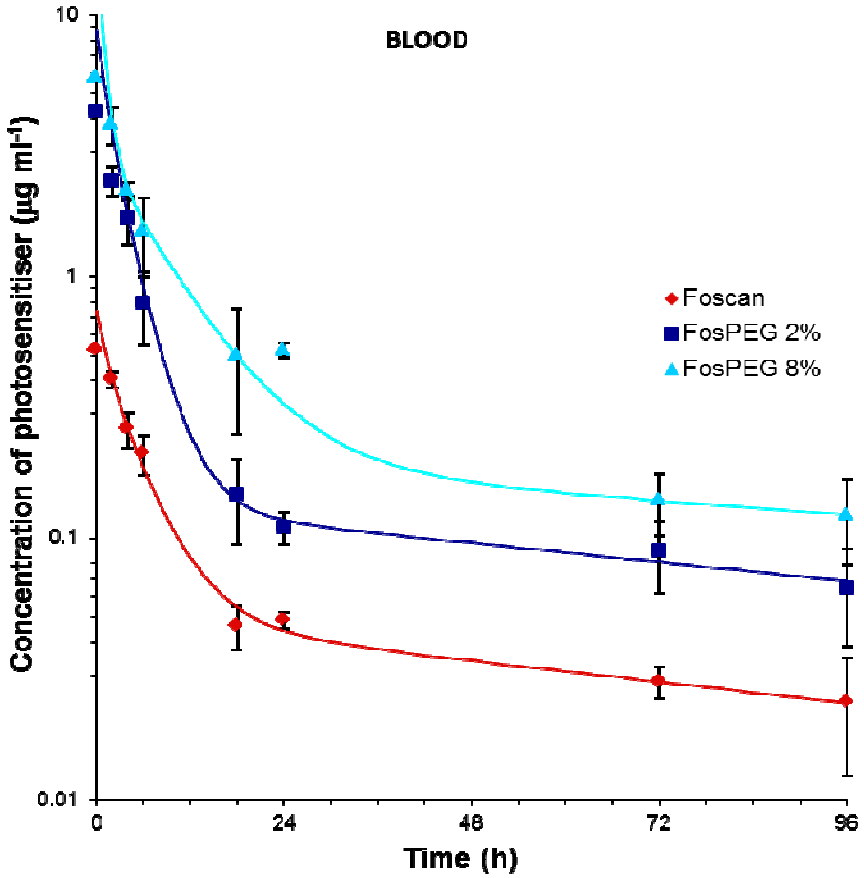

Figure 4.12. Semi-log plot of mean m-THPC concentration in blood serum after intravenous administration of 0.3 mg kg^{-1} m-THPC in Foscan, FosPEG2% or FosPEG8% liposomal formulation into female Wistar rats. This plot is fitted according to a three compartmental model. Data points show the mean ± SD, n = 3.

Figure 4.12 shows the blood clearance after a single *i.v.* injection of 0.3 mg kg^{-1} m-THPC in Foscan, FosPEG 2% and 8% formulations into the normal Wistar rat model between ≤5 min and 96 h. m-THPC delivery through Foscan was observed at the lowest concentration and was cleared most rapidly from the blood serum (Fig 4.12) in comparison to both untargeted liposomal nanocarriers. Serum concentrations peaked at approximately 0.5 µg mL^{-1} ≤ 5 mins and fell to ≤ 0.01 µg mL^{-1} by 96 h (Foscan). FosPEG 2% and FosPEG 8% m-THPC was observed at concentrations approximately 11-fold higher than Foscan at t=0 and remained significantly higher up to 96 h. This demonstrates a positive correlation between increased pegylation of the nanocarrier and increased blood circulation time of the m-THPC.

Pharmacokinetic parameter	**Foscan**	**FosPEG 2%**	**FosPEG 8%**
Three compartmental model			
Initial dosage (D_o, mg kg^{-1})	0.3	0.3	0.3
Initial concentration (C_o, µg mL^{-1}, t=0)	0.7	8.7	16.9
Initial volume of distribution (V_d, mL kg^{-1})	407.4	34.6	17.7
V_d of first compartment (mL kg^{-1})	1373.9	71.1	21.8
V_d of second compartment (mL kg^{-1})	640.1	69.5	100.9
V_d of third compartment (mL kg^{-1})	6086.2	2231.8	1505.8
$t_{1/2}$ of first compartment (h^{-1})	0.9	1.0	0.6
$t_{1/2}$ of second compartment (h^{-1})	3.3	2.3	5.5
$t_{1/2}$ of third compartment (h^{-1})	90.0	99.0	138.6
Non-compartmental model			
Blood clearance (C_l, mg kg^{-1} h^{-1})	30.0	6.41	3.21
Mean residence time (MRT, h^{-1})	61.9	72.5	90.3
Volume of distribution (V_d, mL kg^{-1})	1875.7	464.2	289.5
Half-life ($t_{1/2}$, h^{-1})	42.9	50.2	62.6
Elimination rate constant (K_{el}, h^{-1})	0.016	0.014	0.011

Table 4.4. Blood pharmacokinetic parameters of m-THPC after *i.v.* injected dose of 0.3 m kg^{-1} m-THPC in Foscan and each liposomal formulation in Wistar rats, calculated using the exponential equations of the three compartment model ($A e^{-\alpha t}+Be^{-\beta t}+Ce^{-\gamma t}$), and the non-compartmental method.

Following intravenous injection, m-THPC serum concentrations peaked at the earliest time point for each formulation and appeared to decline exponentially. Since m-THPC clearance from serum fitted multiple exponential decays; therefore data were analysed using both a compartmental (Clark B et al. 1981) and non-compartmental approach (Yamaoka, K. et al. 1978).

Using a compartmental approach (Table 4.4), the data best fit a tri-exponential decay curve, described by the equation $C = A e^{-\alpha t} + Be^{-\beta t} + Ce^{-\gamma t}$ (whereby C = concentration, A,

B, C = y-intercepts (at t = 0), and α, β, γ = elimination rate constants), which describes the rate of drug flow into and out of the central compartment and gave three compartmental half-lives ($t_{1/2}$) and elimination rate constants for Foscan, FosPEG 2% and 8% (Table 4.4) (*see* ***Appendix I – A.5 Pharmacokinetic Analysis: Compartmental Approach***).

$$\text{Foscan®, } C = 0.22e^{-0.78t} + 0.47e^{-0.21t} + 0.05e^{-0.008t},\ t_{1/2} = 0.9,\ 3.3\ \&\ 90\ \text{h.} \quad (4.1)$$

$$\text{FosPEG 2\%, } C = 4.22e^{-0.72t} + 4.32e^{-0.30t} + 0.13e^{-0.007t},\ t_{1/2} = 1.0,\ 2.3\ \&\ 99\ \text{h.} \quad (4.2)$$

$$\text{FosPEG 8\%, } C = 13.7e^{-1.18t} + 2.97e^{-0.13t} + 0.20e^{-0.005t},\ t_{1/2} = 0.6,\ 5.5\ \&\ 138.6\ \text{h.} \quad (4.3)$$

The biological half-live ($t_{1/2}$) of the third compartments (log/linear phase) show a 1.5-fold increase between Foscan and FosPEG 8%, 90 h vs. 138.6 h, which is confirmed by figures obtained through non-compartmental analysis (42.9 h vs. 62.6 h, Table 4.4) and suggests increased longevity of circulating m-THPC through liposomal encapsulation and increasing pegylation.

The non-compartmental model was also used to additionally calculate other pharmacokinetic parameters such as clearance and bioavailability, which can be directly determined from the area under the curve (AUC) of the serum-time concentration curve (Shargel, L. et al. 2005) (*see* ***Appendix I – A.6 Pharmacokinetic Analysis: Non-Compartmental Approach***).

The non-compartment model (Table 4.4) gives half-lives of 42.9 h for Foscan, 50.2 h for FosPEG 2% and 62.6 h for FosPEG 8%, with elimination rate constants of 0.016 h^{-1}, 0.014 h^{-1} and 0.011 h^{-1}, respectively. The compartmental model estimates the initial volume of distribution (V_d) from the central compartment as 407 mL kg^{-1} for Foscan®, 34.6 mL kg^{-1} for FosPEG 2% and 17.7 mL kg^{-1} for FosPEG 8%. However, the volume of distribution (V_d) for each formulation in each of the three compartments is much lower for FosPEG 2% and 8% than Foscan.

Bio-distribution of m-THPC (Foscan®, FosPEG 2% and 8%)

In normal tissues of the Wistar rat, the highest m-THPC concentrations were observed in the highly perfused tissues, such as the liver, spleen and lungs (Fig. 4.13-4.15) and show exponential decays. Concentrations of m-THPC for all drug formulations peak at the

earliest time points between 2 and 4 h, following *i.v.* injection. This ranges from approximately 2.5±3.5 µg g^{-1} in the liver (Fig 4.13) and 1.0±2.5 µg g^{-1} in the spleen (Fig 4.14) (*see* ***Appendix I – A.7 Time and Concentration of Maximal m-THPC Levels***). Concentrations of Foscan are significantly reduced in the spleen by 168 h, however, remain at approximately 0.5 µg g^{-1} in the liver after 72 h. FosPEG 2% displays favorably low accumulation in the liver (Fig 4.13), nearly half that of Foscan at the concentration maxima, and less than 1 µg g^{-1} in the spleen after 40 h, with complete clearance from both organs by ~96 h. FosPEG 8% encouragingly accumulates at low concentrations in the spleen, not exceeding 1 µg g^{-1}, and is almost absent after 168 h. However, unlike FosPEG 2%, remain at elevated concentrations in the liver (~ 3.5 µg g^{-1}), along with Foscan.

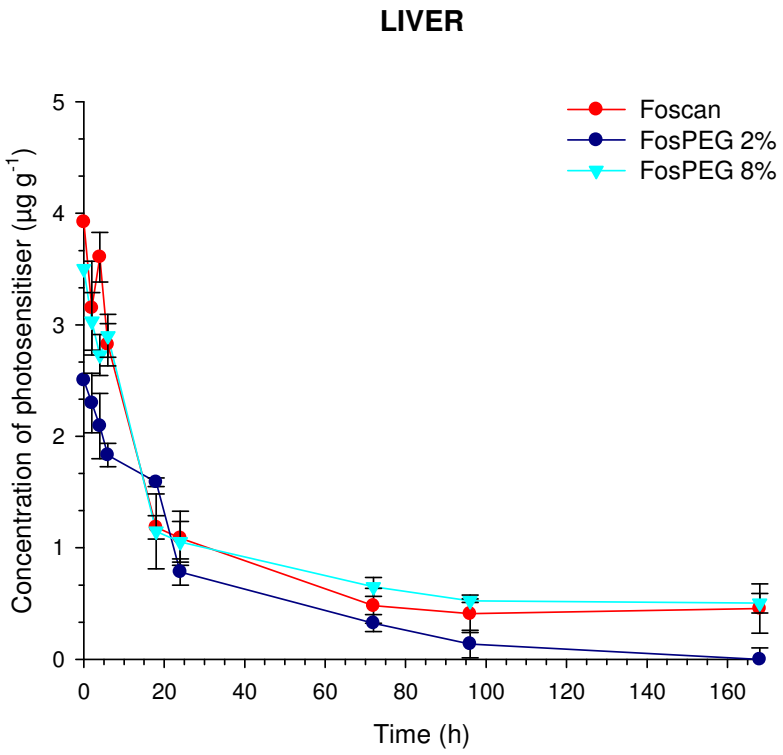

Figure 4.13. Concentration of m-THPC (µg g^{-1}) in the liver of the Wistar rat as a function of time following an intravenous injection of 0.3 mg kg^{-1} m-THPC in standard Foscan, FosPEG2% and FosPEG8% formulations. Data corrected for negative control tissue. Data points show the mean ± SD, $3 \leq n \leq 4$.

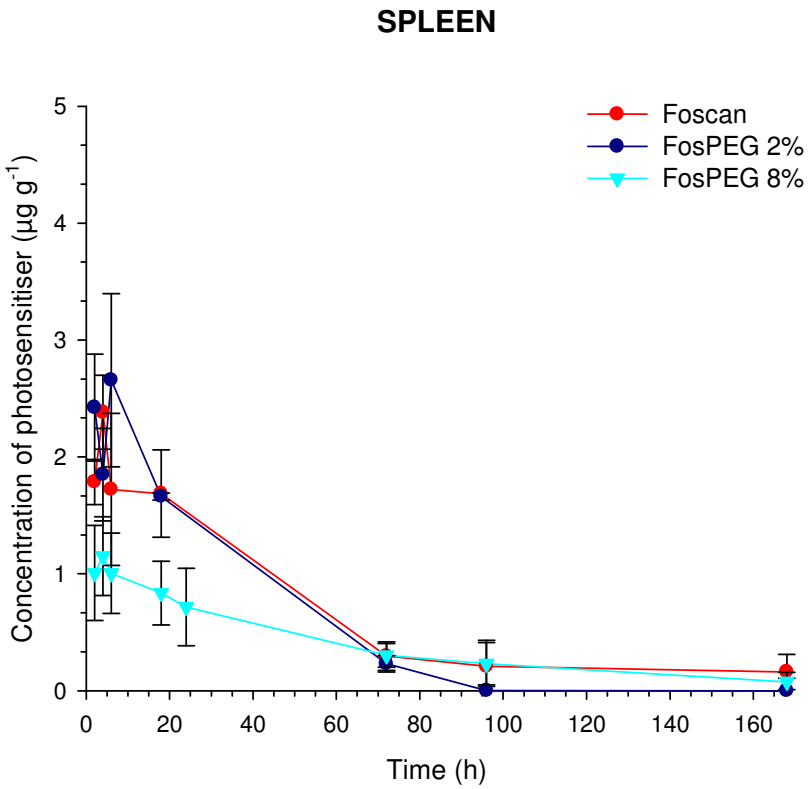

Figure 4.14. Concentration of m-THPC (µg g^{-1}) in the spleen of the Wistar rat as a function of time following an intravenous injection of 0.3 mg kg^{-1} m-THPC in standard Foscan, FosPEG2% and FosPEG8% formulations. Data corrected for negative control tissue. Data points show the mean ± SD, $3 \leq n \leq 4$.

FosPEG 8% also displays slower distribution kinetics, with a lower V_d and a higher mean residence time (MRT) and half-life ($t_{1/2}$) in the serum compared to FosPEG 2% and Foscan. In the spleen FosPEG 8% accumulates at the lowest concentrations, not exceeding 1 µg g^{-1}. By 168 h, both FosPEG formulations are almost absent from the spleen, whereas there appears to be a slight retention of Foscan at this time.

The slower distribution kinetics of FosPEG 8% are also demonstrated in the lung tissue (Fig 4.15), where FosPEG 8% remains consistently higher than Foscan (~6 fold) and FosPEG 2% (~2-3 fold) over 168 h, which are both cleared by this time, indicating they are not being unfavorably retained. This clearance pattern correlates very closely to the blood serum pharmacokinetics (Fig 4.12).

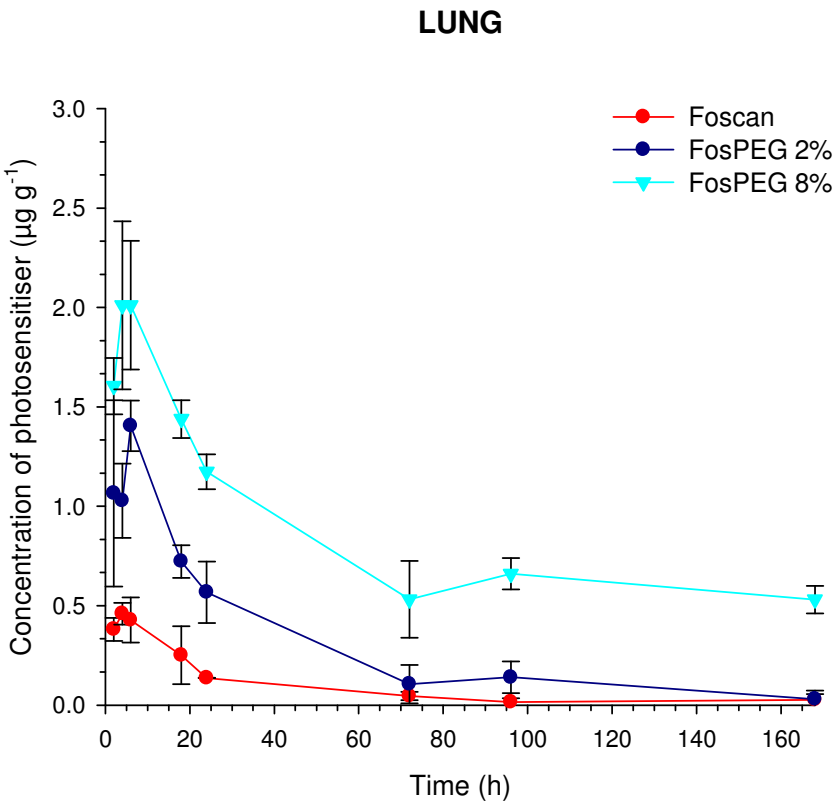

Figure 4.15. Concentration of m-THPC (µg g^{-1}) in the lung of the Wistar rat as a function of time following an intravenous injection of 0.3 mg kg^{-1} m-THPC in standard Foscan, FosPEG2% and FosPEG8% formulations. Data corrected for negative control tissue. Data points show the mean ± SD, $3 \leq n \leq 4$.

Foscan is found at the lowest concentration in the lungs over 168 h and at the earliest time points (t = 0-2 h) in comparison to liposomal m-THPC, measuring approximately 0.5 µg g^{-1}. This parallels its concentration in the serum at this time, ~0.5 µg mL^{-1}. Again, although FosPEG 2% and 8% appear to accumulate at greater concentrations in the lung tissue at t= 0-2 h, relative to blood serum concentrations at this time, they are taken up between 3-4 times *less* than Foscan from the central blood compartment. At ~6 h, all m-THPC formulations appear to peak in concentration before exponential decay occurs.

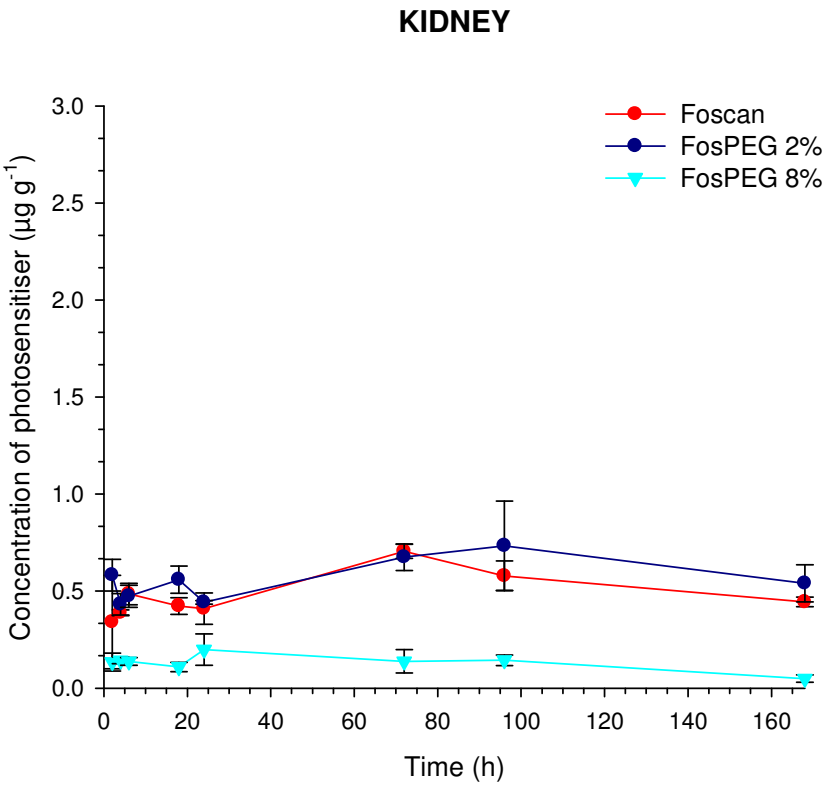

Figure 4.16. Concentration of m-THPC (µg g^{-1}) in the kidney of the Wistar rat as a function of time following an intravenous injection of 0.3 mg kg^{-1} m-THPC in standard Foscan, FosPEG2% and FosPEG8% formulations. Data corrected for negative control tissue. Data points show the mean ± SD, $3 \leq n \leq 4$.

In the kidneys (Fig 4.16) little variation in m-THPC uptake exists within the given time period for each individual formulation, which plateau from 2 – 168 h. However, the difference in m-THPC uptake between degrees of pegylation for each formulation, rather than m-THPC encapsulation alone, is significant. When delivered by FosPEG 8% the concentration of m-THPC remained at a consistently low level, typically < 0.2 µg g^{-1} versus ≤ 0.5 - 0.7 µg g^{-1} for Foscan and FosPEG 2%.

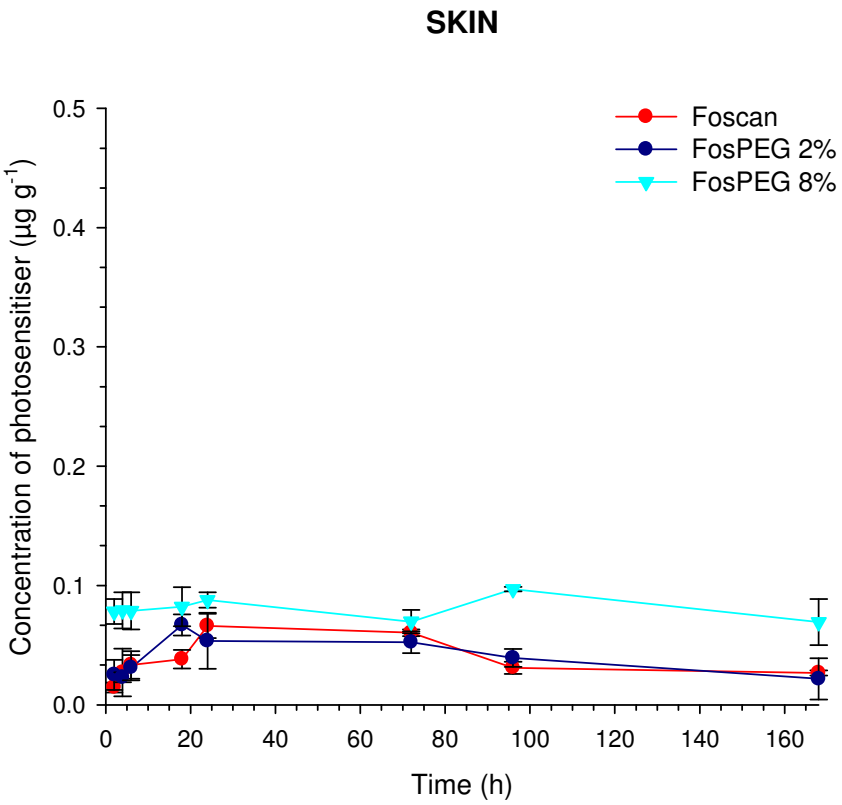

Figure 4.17. Concentration of m-THPC (µg g^{-1}) in the skin of the Wistar rat as a function of time following an intravenous injection of 0.3 mg kg^{-1} m-THPC in standard Foscan, FosPEG2% and FosPEG8% formulations. Data corrected for negative control tissue. Data points show the mean ± SD, $3 \leq n \leq 4$.

Skin tissue (Fig 4.17) displays the lowest concentrations of m-THPC in each formulation in comparison to all other tissues. Foscan and FosPEG 2% have highly similar kinetic profile patterns in the skin. The initial (≤ 5 mins) and final time points (72-168 h) indicate the concentration of Foscan and FosPEG 2% was approximately 0.02 µg g^{-1}, however, FosPEG8% showed continual elevated accumulation from 96 h, approximately 3-fold greater, at 0.07 µg g^{-1}.

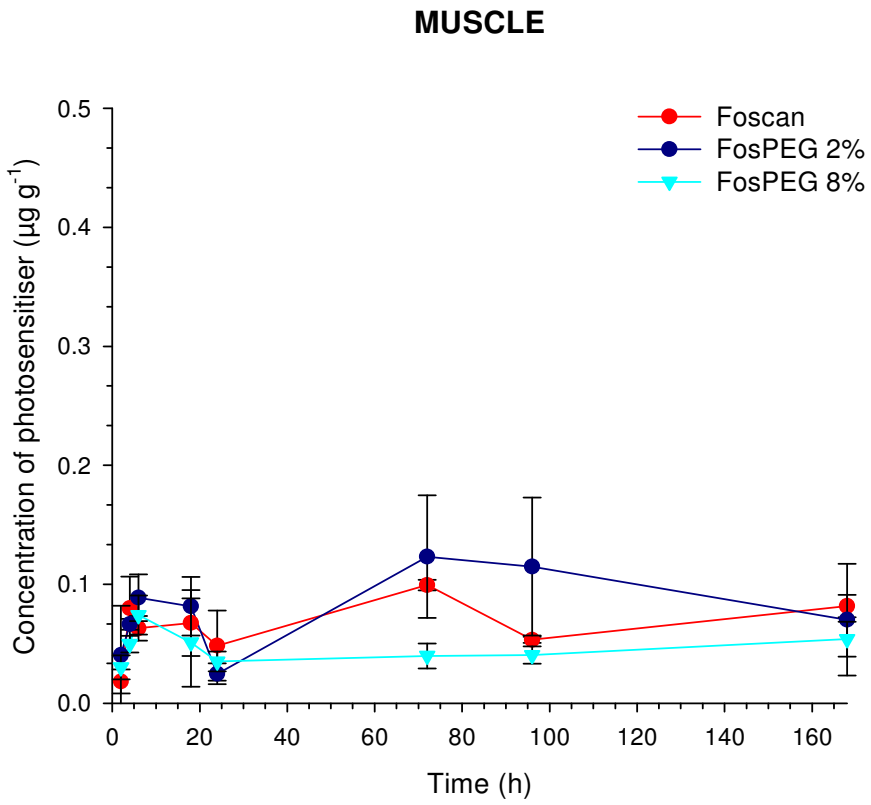

Figure 4.18. Concentration of m-THPC (µg g^{-1}) in the muscle of the Wistar rat as a function of time following an intravenous injection of 0.3 mg kg^{-1} m-THPC in standard Foscan, FosPEG2% and FosPEG8% formulations. Data corrected for negative control tissue. Data points show the mean ± SD, $3 \leq n \leq 4$.

In the muscle tissue (Fig 4.18), m-THPC uptake does not exceed 1.5 µg g^{-1} for all m-THPC formulations. There were no clear differences in the uptake of m-THPC between Foscan and FosPEG formulations by 168 h. Despite final concentrations of m-THPC being similar, FosPEG 8% appeared to clear more rapidly from muscle tissue between 24 and 168 h. Both muscle and skin tissues accumulate the least amount of m-THPC for all formulations compared to other tissues. Over the time course of this pharmacokinetic study, an elimination phase did not occur therefore m-THPC half-lives could not be calculated for muscle or skin.

Chemical extraction data of the colon indicated slower distribution kinetics for all m-THPC formulations with a gradual increase in the uptake of m-THPC (of approximately 0.25 µg g^{-1}) over 168 h, where it peaked. Although m-THPC in FosPEG 8% had a much higher uptake at the earliest time point (approximately 3-fold), there appeared to be no significant difference between each formulation for the remainder of the time series (*see* ***Appendix I – A.8 Chemical Extraction: Colon Accumulation***).

Tumour Accumulation of m-THPC (Foscan®, FosPEG 2% and 8%)

There is a significant increase in maximal m-THPC uptake in tumour tissue of the HL rat between 6 and 24 h with FosPEG 2% and 8%, in comparison to Foscan ($p \leq 0.001$) of approximately three-fold (~1.14 ± 0.98 vs. 0.33 μg g^{-1}) (Fig 2.10A). Although there is no significant difference in accumulation between the two FosPEG formulations over the majority of the time series, FosPEG 8% administration results in higher accumulation in the tumour tissue for up to 72 h post injection. At this time period it remains at more than four times the concentration obtained using Foscan (0.62 vs. 0.14 μg g^{-1}). By 24 h, all m-THPC formulations enter a linear, terminal phase of elimination from tumour tissue (Fig 4.19A).

Mean concentration ratios of tumour to skin tissue from the HL rat model were calculated for all m-THPC formulations (Fig 4.19B), as clinical m-THPC, Foscan, is known to cause prolonged skin photosensitivity in patients. The greatest difference in m-THPC uptake between the two tissue types was ~6 h. FosPEG 2% elicits a concentration ratio almost 5 times greater than that found with Foscan, whilst FosPEG 8% is slightly slower.

Blood serum pharmacokinetic data demonstrated there was an increase in m-THPC circulation time when incorporated into liposomal nanocarrier formulations in comparison to standard Foscan over 72 h. This corresponds to the pattern observed for m-THPC uptake in tumour tissue (Fig 4.19A). FosPEG formulations increase the concentration and therefore bioavailability of m-THPC in the blood greatly (≥4 fold), which simultaneously increases the concentration of m-THPC in tumour tissue (≥3 fold), due to encapsulation/pegylation, compared to Foscan. Although FosPEG formulations may not *preferentially* accumulate in tumour tissue from the blood (*see* ***Appendix I – Fig A.9 Concentration of m-THPC in blood plasma versus tumour from HL rat tissues: Foscan, FosPEG 2% and 8%)***, they improve the uptake between tumour and normal skin tissue (concentration ratios) in this fibrosarcoma model (≥3 fold).

Fig 4.19 indicates maximum tumour to skin m-THPC concentration ratios at 6 h, this presented an optimal drug light interval (DLI) at which to treat tumours with PDT. However, Fig 4.12 still shows high concentrations of m-THPC in the blood plasma by 6 h for all formulations, relative to m-THPC accumulation in tumour tissue (Fig 5A).

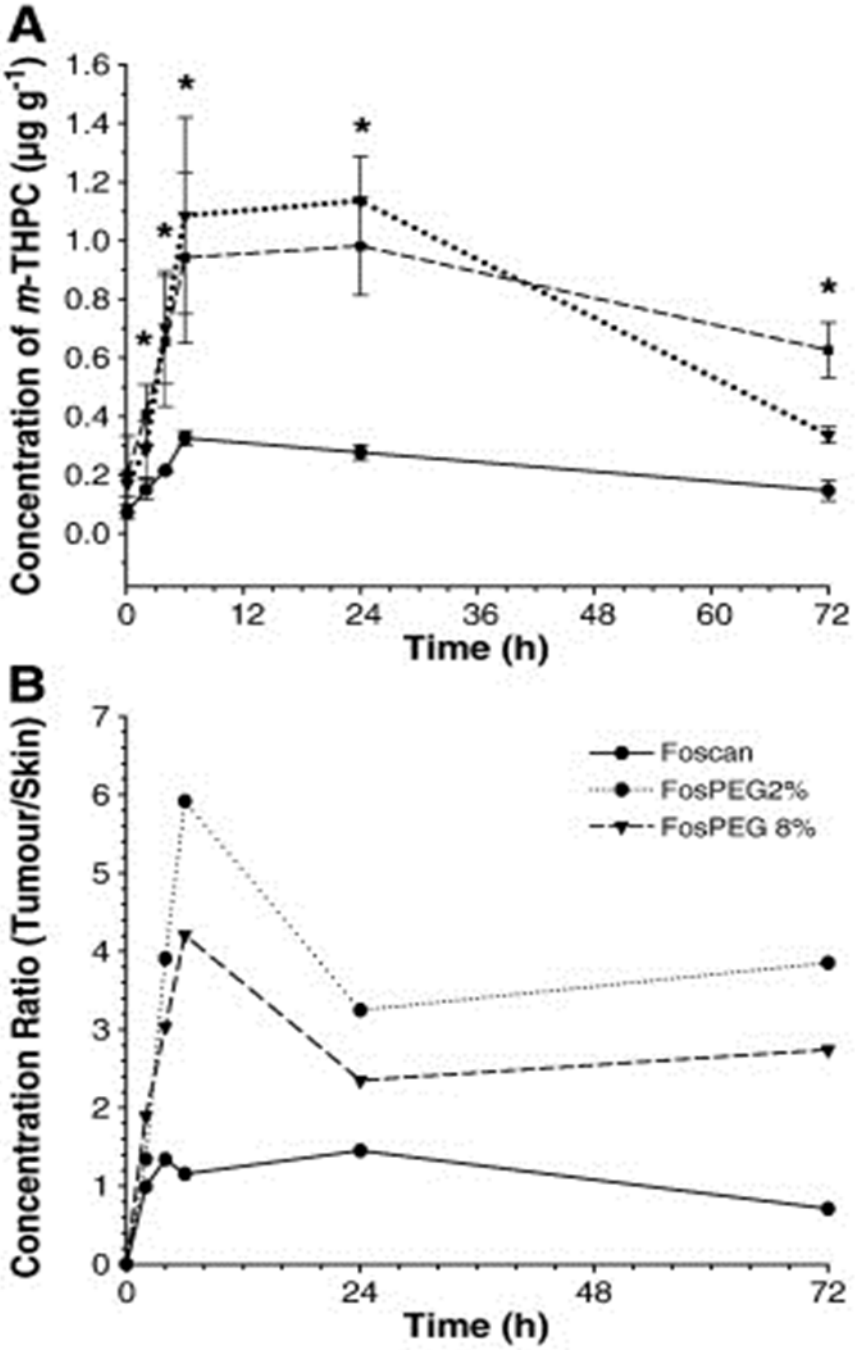

Figure 4.19. (A) Concentration of m-THPC in MC28 tumour tissue of female Hooded Lister rat as a function of time following an intravenous injection of 0.3 mg kg^{-1} m-THPC in standard Foscan, FosPEG 2% and FosPEG 8% formulations. (B) Mean concentration ratio of tumour to skin in female Hooded Lister rats over a time series following intravenous injection of 0.3 mg kg^{-1} m-THPC in Foscan, FosPEG2%, FosPEG 8% formulations. Data points show the mean ± SD, $n = 4$. *Taken from published work (Bovis, M.J. et al., 2011).*

Tissue	Foscan		FosPEG 2%		FosPEG 8%	
	Elimination Rate Constant ($x10^{-3}$ h^{-1})	Half-Life (h)	Elimination Rate Constant ($x10^{-3}$ h^{-1})	Half-Life (h)	Elimination Rate Constant ($x10^{-3}$ h^{-1})	Half-Life (h)
Serum	7.7	90.0	7.0	99.0	5.0	138.6
Tumour	13.2	52.5	8.5	81.5	9.4	73.7
Liver	6.8	101.9	35.8	19.4	8.9	77.9
Spleen	5.7	121.6	62.4	11.1	14.5	47.8
Kidney	4.5	154.0	2.8	247.6	11.7	59.2

Table 4.5. Elimination rate constants and half-lives of the terminal phase of elimination in selected tissues with each m-THPC formulation; Foscan, FosPEG 2% or FosPEG8%, after 0.3 mg kg^{-1} injected dose.

Compartments refer to the organs and tissues for which the rate of uptake and subsequent clearance of m-THPC are similar (Clark B et al. 1981). The elimination rates for all the different tissues are shown in Table 4.5 and were calculated from the log concentration versus time graphs (data not shown) using the terminal three data points (72, 96 and 168 h). These were similar in some tissues, indicating they could be part of one compartment. Through this method, tissues could essentially be grouped into three theoretical compartments taking into account their elimination rate constants and half-lives. Foscan had the fastest clearance from tumour tissue with a short half-life and high elimination rate constant (Table 4.5), therefore was placed in its own compartment (red). The blood serum and liver, however, had similar half-lives and elimination rate constants, therefore could be grouped into a second compartment (blue), much like the spleen and kidney, into a final third compartment (black). Compartments varied for each m-THPC formulation depending on their clearance, mean residence time, volume of distribution and half-life.

v. Tumour PDT response with m-THPC (Foscan, FosPEG 2% and 8%)

PDT studies were carried out in an MC28 tumour rat model to assess whether an increase in m-THPC uptake through the pegylated liposomal nanocarriers improved the efficacy of PDT treatment. H&E stained MC28 tumour sections were scanned with the Hamamatsu Nanozoomer to observe the extent of PDT damage with m-THPC, measured by the area of necrosis, using a 24 h drug: light interval (DLI), based on chemical extraction data. 0.3 mg kg^{-1} of m-THPC in Foscan (FS) and pegylated liposomal formulations (FosPEG 2% and FosPEG 8%) was injected intravenously into the tail vein of the rat. Control tissues

received light treatment with no drug. PDT was initially performed using clinical doses of m-THPC (0.3 mg kg^{-1}) and light was delivered at a total energy of either 2 J or 10 J at 100 mW interstitially to tumours. Subsequently m-THPC doses were lowered to 0.1 mg kg^{-1} and 0.05 mg kg^{-1}.

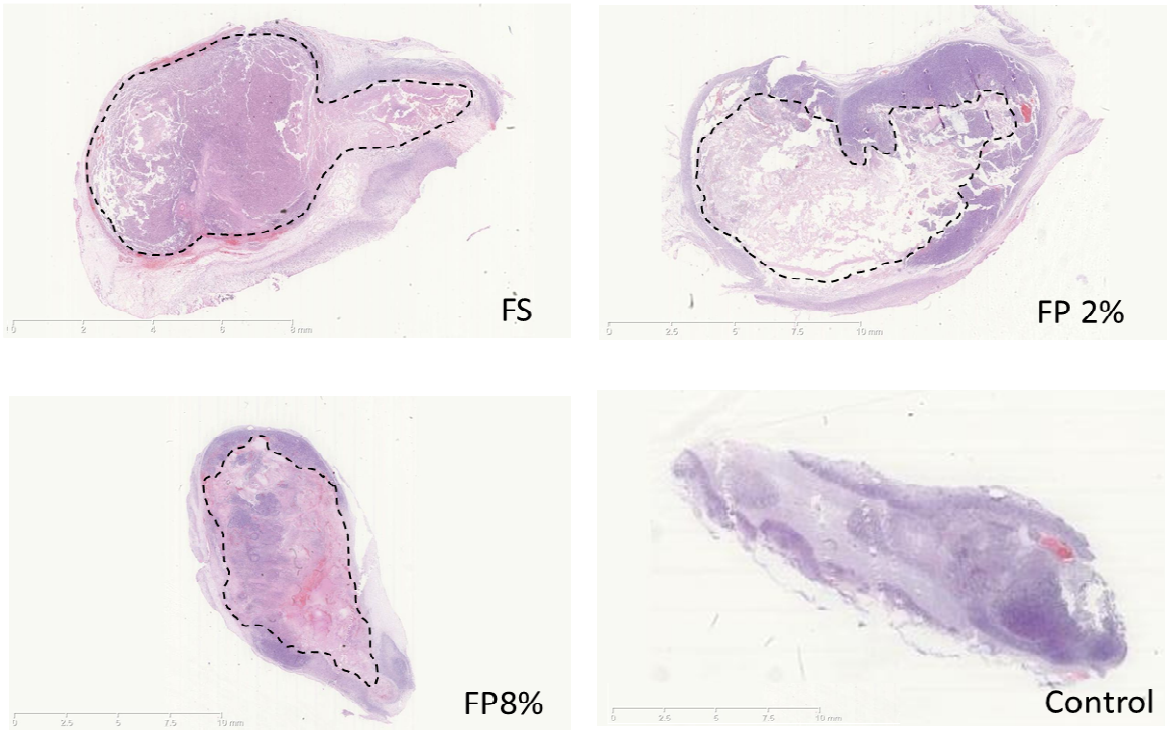

Figure 4.20. Histological analysis: H&E stained MC28 tumour sections scanned with the Hamamatsu Nanozoomer to observe the extent of PDT damage, measured by the area of necrosis (dotted perimeter), after 24 h DLI: 0.3 mg kg^{-1} of m-THPC in Foscan (FS) and pegylated liposomal formulations (FP 2% and FP 8%) was injected *i.v*. Negative control tissues received light and no drug (Control). *Permission for the use of histological images of PDT for liposomal m-THPC was granted courtesy of Dr Josephine Woodhams.*

H&E tumour sections of control MC28 tumour tissue (received light and no drug) were stained a deep purple colour, indicative of the presence of 'healthy' tumour cells from intact nuclei. The damage to tumour tissue at 24 h with PDT (10 J of light at 100 mW) with all 3 m-THPC formulations was very similar and more than 60 % of total tumour tissue surface area showed signs of necrosis (Fig 4.20). With Foscan, a large necrotic area (pink) induced by PDT damage was clearly visible. Tumour sections of FosPEG 2% displayed an undamaged tumour capsule periphery and a well-defined boundary between necrotic (pink) and'healthy' (purple) tumour tissue. Finally, with FosPEG 8%, the damage was much more irregular, occurring sporadically through, which may have been a consequence of the heterogeneous composition of the tumour tissue itself and the resulting m-THPC uptake. (Images shown are representative of multiple animals treated).

Although a high level of necrosis was observed with all m-THPC formulations, there did not appear to be an immediate or obvious variation in tumour damage between Foscan and pegylated liposomal m-THPC through qualitative histological examination of PDT. Hamamatsu Nanozoomer software was therefore employed to obtain quantitative results by calculating an estimated area of necrosis as a percentage of total tumour tissue (*see* ***Appendix I – A.15 Hamamatsu Nanozoomer: Calculating the Area of Necrosis***).

All formulations of m-THPC cause significant tumour necrosis, expressed as a percentage of the total tumour tissue (Fig. 4.21), in comparison to the control treatment group which received light without drug ($p \geq 0.001$). For each of the three variable treatment groups there is also a significant difference in percentage tumour necrosis between Foscan versus FosPEG formulations ($p \leq 0.001$). When exposed to 10 J of light following administration of 0.3 mg kg^{-1} of m-THPC, percentage tumour necrosis with FosPEG formulations is slightly lower than that with Foscan (Fig. 4.21). In contrast, with either low dose m-THPC (0.05 mg kg^{-1}) or low light energy (2 J), both FosPEG 2% and 8% produced a significantly greater percentage of tumour necrosis in response to PDT compared to Foscan, by either 10% or 20% ($p \geq 0.001$).

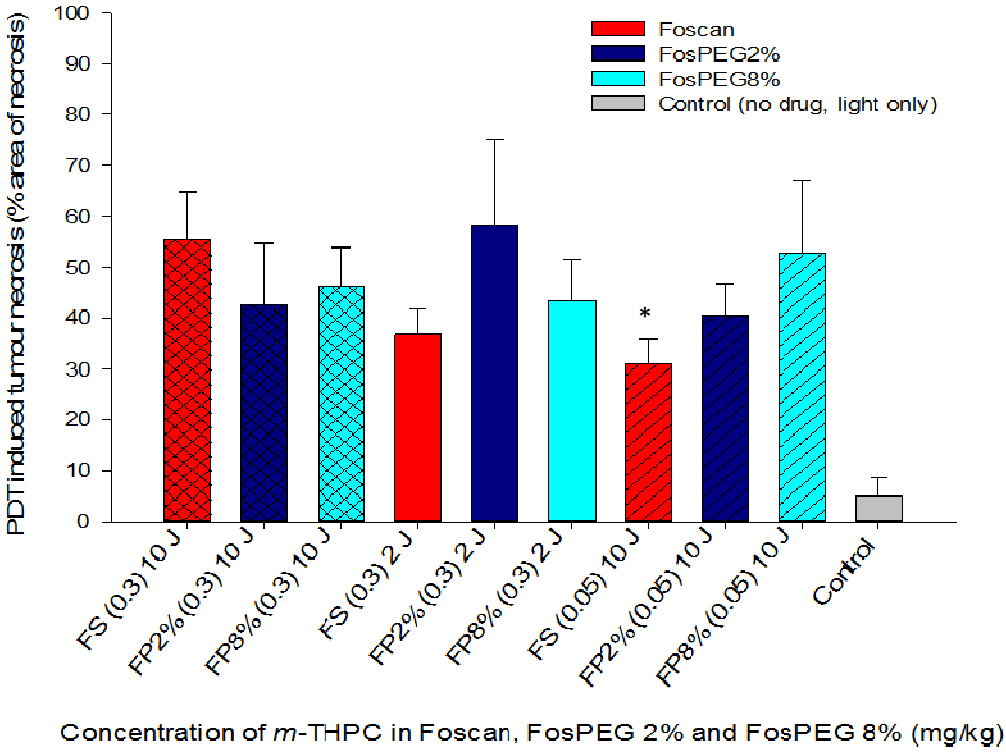

Fig. 4.21. The percentage area of PDT tumour necrosis following administration of either 2 J or 10 J of light to female Hooded Lister rats at a DLI of 24 h, after intravenous injection of 0.3 or 0.05 mg kg^{-1} m-THPC in ■ Foscan, ■ FosPEG2%, and ■ FosPEG 8% formulations. Control group received light treatment, 10 J, with no drug. Data points show the mean±SD, n=4.

PDT was performed to tumours also using a 0.1 mg kg^{-1} dose of m-THPC at the same DLI (24 h) using a light dose of 10 J. As chemical extraction data at 24 h indicated a three-fold increase in the uptake of pegylated liposomal m-THPC compared to Foscan, the administered dose was reduced by a factor of three, to one third of the original photosensitiser concentration (0.1 mg kg^{-1}). This was to deduce whether the higher accumulating m-THPC in pegylated liposomes produced the same PDT effect (percentage tumour necrosis) compared to Foscan. There was an increase in percentage tumour necrosis following PDT (10 J) with FosPEG formulations administered at 0.1 mg kg^{-1} compared to Foscan, however, overall, this was not significant when compared to necrosis exhibited by all m-THPC formulations at higher doses of 0.3 mg kg^{-1} m-THPC *(see **Appendix I –A.16 PDT to MC28 tumours using 0.1 mgkg^{-1} m-THPC dose**)*.

vi. Skin photosensitivity studies

Skin photosensitivity caused by m-THPC, following *i.v.* administration of either Foscan, FosPEG 2% and FosPEG 8% at clinical m-THPC doses of 0.3 and 0.1 mg kg^{-1}, were evaluated in female Wistar rats. These animals were exposed to either 0 (0 J), 5 (30 J), 15 (90 J) or 30 min (180 J) of 100 mW cm^{-2} of light (1 sun=solar equivalent spectrum) from a solar simulator source (Olympus CLV-S30) at drug-light intervals (DLIs) of either 96 or 168 h. Wistar rats were chosen as an appropriate *in vivo* model based on previous skin photosensitivity studies (Weersink, R. A. et al. 2005), due to the lack of skin pigmentation. Comparisons could also be drawn from quantitative m-THPC data collected through chemical extraction studies in Wistar rat normal tissues. Light power (100 mW) was kept consistent with PDT studies carried out here using Foscan and pegylated liposomal m-THPC. Longer DLIs were chosen as complete clearance of m-THPC was not observed for either m-THPC formulation (Foscan, FosPEG 2% and FosPEG 8%) by 96 h, therefore measuring any prolonged photosensitivity effects in the skin after this time were deemed appropriate for assessment.

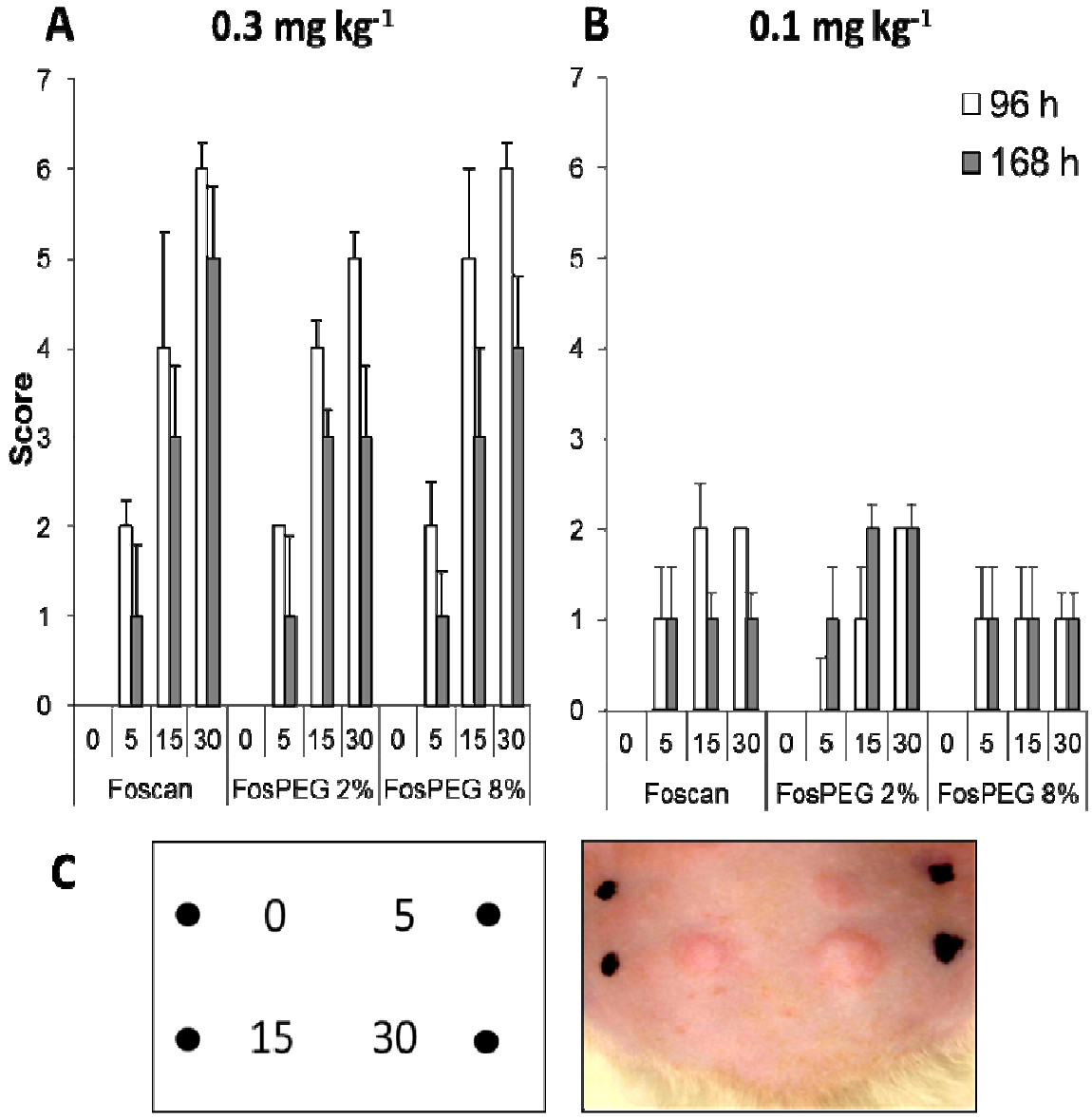

Fig. 4.22. (A) Wistar rats exposed to 0, 5, 15 or 30 min of 100 mW cm^{-2} (1 sun=solar equivalent spectrum) of light from a solar simulator source at drug-light intervals (DLI) of 96 and 168 h, following an intravenous injection of 0.3 mg kg^{-1} or (B) 0.1 mg kg^{-1} m-THPC in Foscan, FosPEG2% and FosPEG 8%. (C) Visual assessment of skin reactions carried out 24 h post-treatment and imaged areas scored by a double-blind grading model. Scores were averaged over each exposure time for each m-THPC formulation.

The results in Figure 4.22 A+B display a positive correlation between the length of light exposure (0 to 30 min) and observable photosensitive effects from graded skin analysis for both m-THPC doses, 0.3 and 0.1 mg kg^{-1}. Visually, for 0.3 mg kg^{-1} m-THPC doses, Foscan evoked greater cutaneous photosensitivity over time in comparison to milder effects observed with FosPEG 2%, which displays the lowest levels of skin photosensitivity at both DLIs at 30 min exposure (Fig 4.22A). FosPEG 8% demonstrates a slightly higher degree of skin photosensitivity at 96 h in comparison to both Foscan and

FosPEG 2%, as a result of greater skin damage observed between 15 and 30 min light exposure. This supports chemical extraction data of FosPEG 8% in skin tissue at this time (Fig. 4.17). However by 168 h, Foscan scored highest at a light exposure time of 30 min (Fig 4.22A) (*see* ***Appendix I – A.12 Skin Photosensitivity Studies: Raw skin scoring data 0.3 mg kg^{-1})***. At 0.1 mg kg^{-1} m-THPC doses, grading analysis shows an overall reduction in skin photosensitivity with each formulation of approximately 3-folds, which directly corresponds to the reduction in m-THPC dosage (Fig 4.22B). Foscan and FosPEG 2% show an increase in photosensitivity over 30 mins at a DLI of 96 h, however at the longer DLI, Foscan scores positively lower in sensitivity across all light exposure times whereas FosPEG 2% increases. FosPEG 8% appears to show the least amount of sensitivity at both DLIs over the 30 min exposure time (*see* ***Appendix I – A.13 Skin Photosensitivity Studies: Raw skin scoring data 0.1 mg kg^{-1})***. No blistering or necrosis (Score 8) of skin tissue was observed visually with any m-THPC formulation at the doses used in this study. Control tissue exposed to 0 min light was unaffected (Score 0), as were animals that only received light (no PS). Fig. 8 illustrates typical photosensitivity observed in histological rat skin sections from the same animal treatment groups at 0 min (control) and 30 min light exposure with 0.3 mg kg^{-1} m-THPC doses. Qualitative differences exist between m-THPC formulations, with Foscan eliciting extensive superficial damage to the epidermis at DLI of 96 h, illustrated by mass cell death, in comparison to FosPEG formulations which are slightly milder. At a DLI of 168 h, photoinduced damage is reduce with FosPEG 2%, showing no signs of sensitivity, whereas Foscan and FosPEG 8% demonstrate localised damage to regions of the epidermis and dermis respectively. No photosensitive effects to skin are detected at 0 min of light exposure (Fig. 4.23) and no damage was observed with those animals that were exposed to light but did not receive m-THPC (data not shown) (*see* ***Appendix I – A.14 Skin Photosensitivity Studies: control skin tissues).***

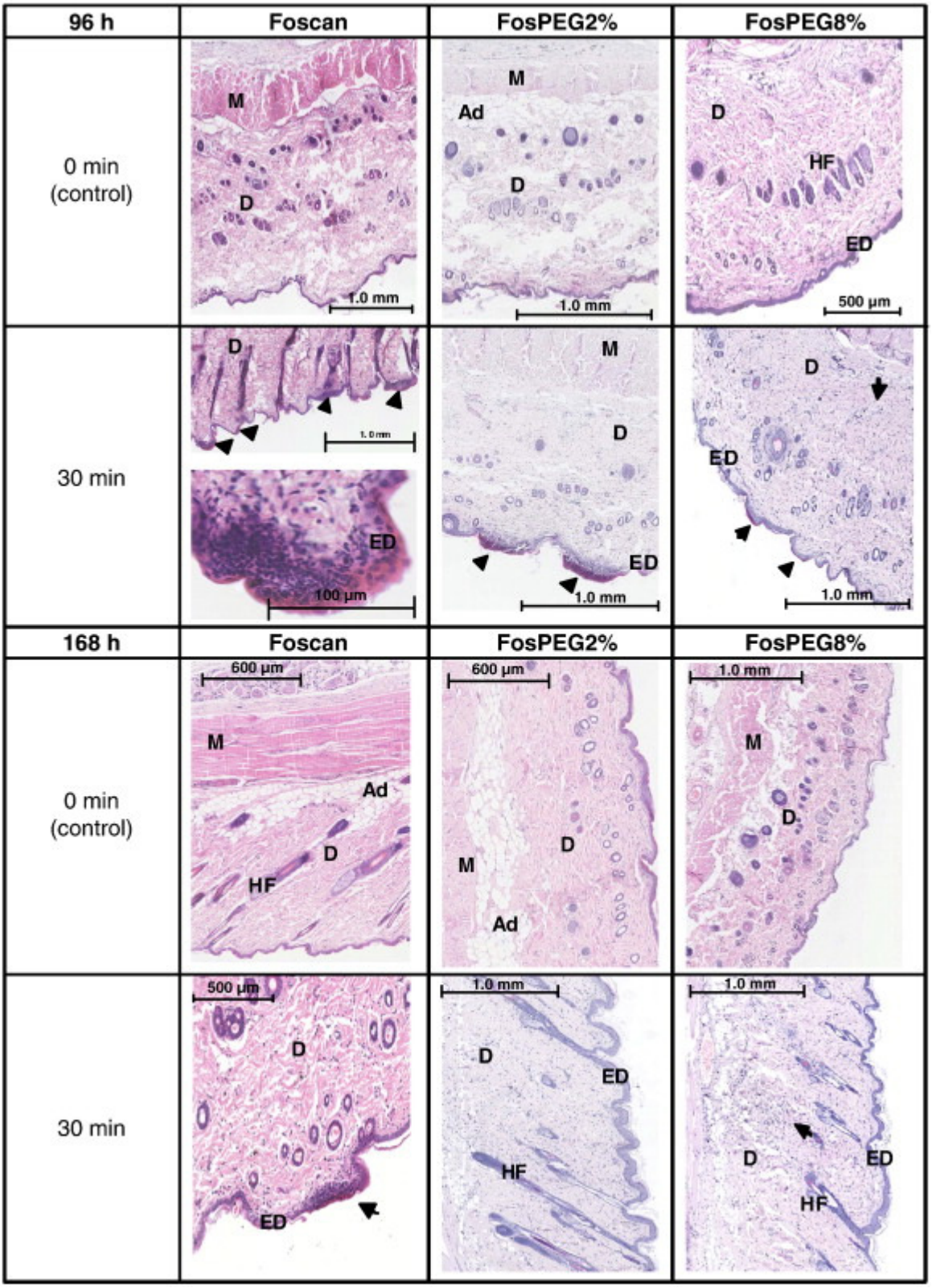

Fig.4.23. Histological sections of skin tissue removed from the animal 24 h after light treatment with 0.3 mg kg^{-1} m-THPC. Skin control samples at 0 min (no light) and treated samples at maximal exposure of 30 min were collected and cut through the centre of the treatment area. Adjacent halves of the skin tissue were sectioned (4 µm), stained with H&E and were observed with the Hamamatsu Nanozoomer. M—muscle, Ad—adipocytes, D—dermis, HF—hair follicle, ED—epidermis.

4.4 Discussion

The outcome of PDT treatment is dependent on a number of critical factors, each of which need to be optimised to improve its efficacy. The photosensitiser plays a fundamental role in this process as its potency (quantum yield of singlet oxygen production) and distribution determines the light dose, light wavelength (activation) and drug-light interval. m-THPC is currently approved for the palliative treatment of selected cancers with PDT (Brown, S. B. et al. 2004), however steps are being taken to reduce adverse skin photosensitivity through improving delivery of the PS to tumour tissues by its encapsulation into novel nano-vehicles.

Liposomes were chosen as a suitable model based on their biocompatibility and, following surface pegylation, have been reported to increase circulating m-THPC in feline and avian chorioallantoic membrane (CAM) models *in vivo* by reducing RES uptake (Buchholz, J. et al. 2005;Pegaz, B. et al. 2006). It is hypothesised that this subsequent improvement in m-THPC bioavailability increases the probability of uptake into tumour tissue. These studies aimed to correlate m-THPC pharmacokinetics of the standard clinical formulation, Foscan, and pegylated liposomal nanocarriers with PDT efficacy and skin photosensitivity in rat models. Through assessment of m-THPC uptake and its selective accumulation in tissues by different liposomal nanocarrier formulations *in vivo*, the maximal normal skin to tumour tissue ratio of m-THPC was deduced. This gave a strong indication as to the optimal treatment time and m-THPC dose in which to elicit the greatest tumour PDT response.

Photophysical studies: Liposomes

In this investigation, m-THPC was packaged into the fatty acid bilayer of unilamellar liposome shells (Torchilin, V. P. 2005). The distribution of m-THPC to the lipidic bilayer is influenced by its insolubility and hydrophobic properties. Pegylation of the liposome surface is further believed to inhibit the premature release of such hydrophobic compounds by minimising the adsorption of serum proteins, which can result in drug leaching (Satomi, T. et al. 2007). Varying, but defined, degrees of liposomal pegylation were used in this study to assess the effect of increased pegylation on m-THPC biodistribution. Two pegylated liposomal m-THPC formulations that displayed surface PEG (2000 M_w) polymer chains at concentrations of 2% mol (FosPEG 2%) and 8% mol (FosPEG 8%) were

investigated *in vivo* to compare the difference in accumulation and distribution of m-THPC in normal tissues and tumour tissue of rats, versus Foscan (Table 4.2). These liposomes were developed from Foslip formulations, which lack a stealth polymer coating (Fig 4.5), and have previously been tested in tumour-bearing murine models *in vivo* with some success (Garrier, J. et al. 2011;Lassalle, H. P. et al. 2009). Furthermore, veterinary studies in cats using other pegylated liposomal m-THPC formulations demonstrated improved distribution patterns in the plasma, tumour and skin, however, the degree of pegylation (2.5–5%) was not precisely defined (Buchholz, J. et al. 2005).

In this study, pegylations of 2% and 8% (molar equivalent) were chosen as the lower and upper limits since higher percentages of PEG are known to disrupt the integrity of the liposome membrane (Li, S. D. et al. 2008). The PEG chain length and degree of PEG surface coverage of the liposomes was dictated by the polydispersity index (PDI) and z-average measurements. It was established that longer PEG chains (*e.g.* 5000) with higher surface coverage (8% mol) were unstable and produced liposomes of inconsistent size, shape and mass distribution (high PDI) and as a result, despite their greater chain length, showed a reduction in mean particle diameter, likely due to the production of smaller subpopulations (data not shown). Similarly, shorter PEG lengths (eg. 750) with high surface coverage (8% mol) showed the greatest variation in particle size and m-THPC content following a 40 day storage period from the time of preparation, suggesting lower stability (data not shown).

Absorbance Properties

Spectroscopic changes provide a means of investigating sensitiser incorporation and distribution in liposomes. It has been reported that the corresponding absorption bands of porphyrins incorporated into liposomes undergo a red shift (approx. 10-20 nm) and their fluorescence intensities increase (Brault, D. et al. 1986) as a result of their hydrophobicity and subsequent local distribution within liposomes. These larger red shifts are thought to be attributed to the monomerisation of aggregates. m-THPC's hydrophobic chlorin structure suggests it would behaviour similarly, however, no significant red shift in absorption was observed following incorporation into pegylated liposomes (FosPEG) in either their loading buffer (histidine) (Fig 4.7) or 100% Solvable (solubiliser) solution (Fig 4.8). This indicates that m-THPC was predominantly confined to the lipidic bilayer as its

microenvironment did not change following interaction with DPPC/DPPG liposomes (Ricchelli, F. et al. 1986). Direct comparisons in aqueous media (*e.g.* PBS) with free m-THPC could not be tested to confirm this due to the poor solubility of m-THPC. However, absorbance measurements with Foscan (m-THPC) showed a detectable bathochromatic shift in the Soret band between different solvents (PEG system; λ = 419 nm, 100% Solvable; λ = 423 nm). These results correspond to the literature for the spectroscopic properties of m-THPC (Foscan) in Solvable (Kascakova, S. et al. 2008). Bathochromatic shifts in the Soret band, to longer light wavelengths, are usually indicative of conjugation of PS molecules. Like many photosensitisers, m-THPC is a highly hydrophobic molecule and has been described as forming almost non-fluorescent aggregates in aqueous environments, producing broadening of both bands (Soret and Q) due to stacking of its chlorin rings (J-aggregates) (Bonnett, R. et al. 2002). However, there was no detectable difference in half height bandwidths (~500 nm) between the PEG buffer and 100% Solvable to suggest the formation of dimers. As Solvable is an alkaline based solvent, known to realise m-THPC in its monomeric form, this was expected. No evidence of aggregate formation was detected through variations in absorption maxima, spectral peak broadening or deviations from Beer's law to account for this shift. Moreover, the shoulder observed on the Soret peak of m-THPC (Foscan) is indicative of highly conjugated systems and is common for these chromophores. This is often solvent dependent and as such disappeared upon incubation with 100% Solvable.

Fluorescence Properties

The fluorescence spectrum of increasing m-THPC concentrations (Fig 4.9) in 100% Solvable was the same for all m-THPC formulations. A slight shift from ~652 nm, when diluted in loading buffer (data not shown), to ~655 nm in 100% Solvable was observed. This has been attributed to the increase in the basicity of the environment with 100% Solvable (pH ~12.7) compared to the PEG solvent solution of Foscan (pH ~4.3) (Kascakova, S. et al. 2008). However, no significant changes in absorption and fluorescence intenisty of m-THPC were detected in 100% Solvable (Fig 4.8 & 4.9), which excludes possible chemical bleaching of m-THPC.

Recently, in a joint study with our laboratory, the photophysical properties of the same liposomes were investigated through fluorescence lifetime data studies (Compagnin, C. et

al. 2011). These studies revealed the period of time (ns) a photosensitiser remains in the activated, excited triplet state (*i.e.* the time in which the initial fluorescence intensity of the fluorophore decays). Fluorescence lifetime measurements of FosPEG formulations were carried out in aqueous histidine buffer and following incubation in DMSO (solvent). Data suggested m-THPC was aggregated when incorporated in pegylated liposomes (FosPEG 2% and 8%), since m-THPC fluorescence was strongly quenched and produced multi-exponential decays (histidine buffer) in comparison to monomeric m-THPC, which exhibited a longer mono-exponential lifetime of 9.6 ns in DMSO. This was thought to occur due to m-THPC dimerisation, in combination with energy-transfer between adjacent m-THPC monomers and weakly fluorescent aggregates within the liposomes, as a result of high m-THPC loading and close proximity of PS molecules in the lipid bilayer. Furthermore, the fluorescence intensity of m-THPC increased two-fold following dissolution of liposomes in DMSO in fluorescence spectra (Fig 4.10). This is in accordance with Reshetov *et al*., (Reshetov, V. et al. 2011), who observed lower fluorescence yields of m-THPC when incorporated into identical pegylated liposomes (FosPEG 2%) and in non-pegylated liposomes (Foslip) in human serum *in vitro*. Interestingly, this group observed slightly higher fluorescence intensities for FosPEG 8% in comparison to FosPEG 2% (ratio 1.25). Although m-THPC is water-insoluble and should reside within the liposomal membrane, it has been suggested there may be some partioning of m-THPC to the PEG layer of the liposomes, explaining the higher fluorescence efficiency of FosPEG 8%, as this formulation favours partioning of m-THPC (at 25°C), creating changes in its microenvironment (Compagnin, C. et al. 2011). These m-THPC molecules may exist as aggregates or monomers in the pegylated layer. Finally, despite no large bathochromic shifts being observed here in the absorbance spectra of FosPEG formulations between aqueous histidine buffer and Solvable (solvent) to account for these changes in m-THPC state, discrepancies may be attributed to differences in the water content between the two solvents used in each study (DMSO versus Solvable) and also high underlying background absorbance scatter from the liposomes. Regardless of the apparent aggregation of m-THPC within pegylated liposomes, Compagnin *et al*., demonstrated rapid degradation of liposomes following cellular uptake *in vitro* in human adenocarcinoma alveolar basal epithelial (A549) cells and release of m-THPC in its monomeric photoactive form inside the cell producing effective cell kill under illumination.

Liposome Stability

It is important to measure the stability of drug-loaded liposomes when in serum and when stored for prolonged periods. Serum proteins can exert an inhibitory effect with regards to therapeutic delivery, as they can bind to the particle surface and cause structural reorganisation, aggregation, drug leaching and/or dissociation of the delivery vehicle (Drummond, D. C. et al. 1999). Cationic liposomes have shown to strongly bind to blood components (Zelphati, O. et al. 1998) and increase uptake in the lungs. Redistribution of liposome-released photosensitiser by lipoproteins in circulation can in turn lead to tumour accumulation due to the elevated number of LDL-receptors expressed on tumour cells (Allison, B. A. et al. 1997) (Reddi, E. 1997), however, where selective delivery of a drug to a solid tumour is desired, there must be a substantial proportion of drug retained in the liposome while in circulation (Senior, J. H. 1987). This is not only to increase concentrations in tumour tissue but also to reduce adverse drug uptake in normal tissues.

Our collaborators (Scheglmann *et al.*, unpublished data) have shown liposomes used in studies here remain stable over 28 h in high concentrations (90%) of serum *(see **Appendix I –A.18**)*. When studying m-THPC transfer from different liposomes in the presence of serum proteins, almost 100% transfer of m-THPC from cationic pegylated liposomes (PEG-DSPE+DOTAP+DPPC) was observed in <45 mins in 5% FCS in comparison to pegylated (PEG-DSPE+DPPC+DPPG) and non-pegylated liposomes (DPPC+DPPG) alone (data not shown). Further collaborative studies demonstrated a greater transfer of m-THPC from FosPEG with increasing FCS (10%>50%>90%) over 2 h *(see **Appendix I –A.17**)* and *in vitro* studies showed a decrease in intracellular fluorescence with the same liposomes in A549 cells with increasing FBS (0%>3%>10%), suggesting possible release of m-THPC from pegylated liposomes (Compagnin, C. et al. 2011). These finding were corroborated *in vitro*, in human plasma, where a proportion of mTHPC was released much faster from pegylated liposomes compared to conventional liposomes (Foslip) (Reshetov, V. et al. 2011;Reshetov, V. et al. 2012), which may have been due to partioning of m-THPC into the PEG layer. However, the opposite was found to be true in later *in vivo* studies using the same liopsomal formulations in nude mice, demonstrating a 10% faster m-THPC release from Foslip in mouse plasma compared to FosPEG, with only half of *i.v.* injected liposomes intact after 24 h (Reshetov, V. et al. 2013). FosPEG formulations are composed of DPPC lipids, with a phase transition temperature of 41°C, therefore liposomes may

remain in their gel phase at lower temperatures (*in vivo*). Although, following incorporation of m-THPC into pegylated liposomes, their phase transition temperature is thought to decrease to 37°C, suggesting heavy leaching of m-THPC in the presence of serum proteins due to an increase in lipid fluidity *(see **Appendix I –A.17 & A.19**)*. Pegaz *et al*., (Pegaz, B. et al. 2006) observed slow leakage of m-THPC from FosPEG liposomes (lipid compositions of similar phase transition properties) in studies *in vivo* on a chick chorioallantoic membrane model in comparison to Visudyne (verteporfin in non-pegylated liposomes), thought to delay transfer to serum proteins. This has also been observed by collaborators with FosPEG formulations *in vitro* through FACS analysis, whereby the presence of ≥10% FBS significantly reduced m-THPC fluorescence intensity within human normal fibroblasts (CCD-34Lu) and A549 cells by almost 3-fold, compared to no serum (0%) (Compagnin, C. et al. 2011). This may explain the biphasic uptake of FosPEG, which was reported to be slower than that of free m-THPC, as the modality of cell internalisation may have been through the formation of serum protein complexes.

In vitro: liposomal m-THPC uptake

Confocal microscopy studies here indicated there was little difference between the intracellular uptake of m-THPC with either Foscan or FosPEG 2% into MC28 cells over 6 h, following prior incubation with 10% FCS (Fig 4.11), as both formulations demonstrated high levels of m-THPC fluorescence in the cytosol. These cell studies are in good agreement with the literature, which shows diffuse cellular distribution of m-THPC (Marchal, S. et al. 2007;Melnikova, V. O. et al. 1999a). Kiesslich *et al*., observed similar findings with Foslip, suggesting m-THPC attached to serum components to mediated cellular uptake (Kiesslich, T. et al. 2007). Although the addition of the PEG layer (FosPEG) should reduce serum interactions and enhance liposomal internalisation, transfer of m-THPC from liposomes to serum, as previously described, may facilitate internalisation. It has been demonstrated in other tumour cell lines that m-THPC accumulation becomes significantly greater with longer incubation periods, high m-THPC concentrations and increased cell surface area (Teiten, M. H. et al. 2001). The intracellular localisation of m-THPC was restricted to the cytoplasm for both formulations employed here, however, at the earliest incubation time (1 h) m-THPC appeared to accumulate in intracytoplasmic vesicles that resemble lysosomes in localisation and size. Using identical FosPEG formulations, Compagnin *et al*., showed, following liposomal internalisation, m-

THPC is promptly released and the major sites of localisation are the Golgi apparatus and endoplasmic reticulum (Compagnin, C. et al. 2011) at short (≤5 h at 37°C) and longer incubation periods (≥24 h at 37°C) at similar m-THPC concentrations (1.5 μM) in A549 cells. However, a 30-40% reduction in the cellular uptake of FosPEG was observed in comparison to m-THPC (Foscan), causing a corresponding reduction in photocytotoxicity but simultaneously reducing dark cytotoxicity. Lassalle *et al.*, demonstrated that Foscan and non-pegylated m-THPC liposomes (Foslip) enter HeLa cells via a similar mechanism and behave in a similar fashion once they have entered the cell, but at longer incubation times (≥24 h) may locate to different intracellular sites (Lassalle, H. P. et al. 2009). Compagnin *et al*., also showed FosPEG uptake occurred primarily through endocytosis due to complete inhibition of cellular uptake from 37°C to 4°C incubation temperature and a negative correlation between increasing concentrations of FBS and decreasing m-THPC fluorescence intensity. This was demonstrated in A549 cells following incubation of pegylated liposomes (FosPEG 8%) with 0%, 3% or 10% FBS; concluding the presence of FBS inhibits the uptake of m-THPC when delivered by FosPEG through either competition for m-THPC binding, interactions between liposomes and serum complexes or possible release of m-THPC to serum components before cellular internalisation (Compagnin, C. et al. 2011).

The intracellular localisation of a specific photosensitiser is believed to be dependent on its properties, which make an important contribution to the effectiveness of its photocytotoxic outcome due to the short half-life and reactive radius of singlet oxygen (Moan, J. et al. 1991). m-THPC self-quenching observed with FosPEG formulations could create fundamental drawbacks in the application of these nanocarriers in PDT, however, it has been hypothesised, upon liposomal degradation inside cells, m-THPC is released into the cytosol in its monomeric form. Hydrophobic drugs, such as m-THPC, and cationic compounds are known to trigger an overexpression of P-glycoprotein (P-gp) efflux protein pumps on the cell surface as a means to expel internal excessive of these drugs (Teiten, M. H. et al. 2001), which can lead to a multidrug resistance (MDR) phenotype. Despite its hydrophobicity, it was shown that m-THPC was not a transport substrate for the P-gp pump, as similar m-THPC localisation patterns and concentrations were found at short and long cell incubation periods (Compagnin, C. et al. 2011). Ball *et al*., also showed m-THPC is tightly sequestered upon entering cells and released very slowly regardless of the presence of serum components (Ball, D. J. et al. 1999). This is unlike first generation

porphyrin derived photosensitisers, such as Photofrin (anionic), and showed an impaired cellular uptake (Sharkey, S. M. et al. 1993).

In vivo: liposomal m-THPC uptake

To date, studies using m-THPC (Foscan) have been carried out in the clinic and in different *in vivo* models including murine, feline and avian CAM, demonstrating significant variations in uptake and distribution. In this investigation, pharmacokinetic studies with m-THPC in untargeted pegylated liposomal nanocarrier formulations, FosPEG 2% and FosPEG 8%, were carried out in reference to standard Foscan (m-THPC) formulation in rat models. Doses of 0.3 mg kg^{-1} (m-THPC drug equivalent) were employed for a time series analysis to quantify m-THPC distribution *in vivo* by measuring uptake in different tissues. A chemical extraction method was chosen, as other quantification methods, such as, radiolabeling (Jones, H. J. et al. 2003), chromatographic analysis (HPLC chromatography) (Cramers, P. et al. 2003;Morlet, L. et al. 1995) and optical absorption (Bellnier, D. A. et al. 1996;Henderson, B. W. et al. 1995) are more technically demanding, expensive and/or hazardous. A commercially available tissue solubiliser, Solvable™, was used to dissolve tissues and release m-THPC monomerically prior to fluorescence spectroscopic analysis. In formative studies, it was found that absorption and fluorescence spectroscopic properties of dissolved tissues changed with incubation time (Kascakova, S. et al. 2008), therefore all samples were corrected for background fluorescence of native tissues, having undergone the same experimental conditions, to obtain accurate m-THPC concentrations.

Pharmacokinetic analysis of liposomal m-THPC

Compartmental model

The serum clearance pharmacokinetics of the *in vivo* rat animal model presented here followed first-order elimination kinetics and best fit three exponential decays, based on compartmental grouping of m-THPC elimination from each tissue. This was similar to previous pharmacokinetic studies carried out with Foscan (Jones, H. J. et al. 2003) and a non-pegylated liposomal formulation, Foslip (Lassalle, H. P. et al. 2009), in other murine models. Studies with m-THPC (Foscan) *in vitro* in human plasma, demonstrated slow, steady-state distribution kinetics of m-THPC, owing to the hydrophobic nature of m-THPC causing high serum protein binding (*i.e.* LDL proteins) and prolonging the time at which patients could be treated (Triesscheijn, M. et al. 2007).

Each phase of decay represented a different route of elimination; as it takes different lengths of time for the drug to reach equilibrium in various tissues of the body, so will it affect its distribution. Initially, directly after an intravenous bolus injection of 0.3 mg kg^{-1} m-THPC into the tail vein, each formulation produced an instantaneous peak and a rapid linear distribution into a highly perfused central compartment (vasculature: blood plasma) (Veenhuizen, R. et al. 1997), representing the first phase of elimination. Following this, a less rapid distribution of drug uptake into a second compartment was observed, before a terminal elimination phase into a third, or deep tissue, compartment (Shargel, L. et al. 2005). The compartments refer to the organs and tissues for which the rate of uptake and subsequent clearance of m-THPC are similar (Clark B et al. 1981). Through this method, tissues could essentially be grouped into three theoretical compartments taking into account their elimination rate constants and half-lives (Table 4.5). Compartments varied for each m-THPC formulation depending on their clearance, volumes of distribution and half-lives. The accumulation and distribution of each m-THPC formulation to every organ was most probably due to their hydrophobicity, size, encapsulation and/or degree of pegylation, which determined the rate at which they moved from the blood into other tissues before being cleared by these organs, leading to expulsion from the body. The half-lives obtained for Foscan for each elimination phase (0.9, 3.3 and 90.0 h) (Table 2.2) are very close to the data of Jones *et al.*, (0.46, 6.91 and 82.5 h), carried out in LSBD1 fibrosarcomas implanted into BDIX rats with C-14 radiolabelled m-THPC (Jones, H. J. et al. 2003). Studies in felines using an earlier FosPEG formulation by Buchholz *et al*,. (Buchholz, J. et al. 2005) revealed equal peak plasma concentrations of Foscan (~ 0.45 μg mL^{-1}) at ≤ 5 min–2 h, as illustrated here (Fig 4.12), but found maximal plasma concentrations of FosPEG were only ~ 3.5 times higher than Foscan compared to >15-fold greater found here with FosPEG 8%. However, in the latter study few details were provided on liposome composition and the degree of pegylation.

Compartmental analysis (Table 4.4) demonstrated an initial volume of distribution of 407 mL kg^{-1} with Foscan, which is extremely high given the blood volume of a rat ~ 50–70 mL kg^{-1}. This indicates that the initial retention of Foscan in the blood is very low and it preferentially diffuses and accumulates out of the central compartment, where it is selectively retained in different tissues. This is perhaps as a result of Foscan being rapidly bound by serum proteins in the blood and taken up by phagocytosis. In contrast, FosPEG 2% and 8% have a low initial volume of distribution of 34.6 and 17.7 mL kg^{-1}

respectively. It is believed the PEG polymer coating sterically stabilises the liposomal particle, and prevents rapid uptake into macrophages at the earliest time points, thus increasing the longevity and accumulation of m-THPC in circulation, increasing its confinement to the vasculature. The extended m-THPC half-lives of FosPEG 2% (99.0 h) and FosPEG 8% (138.6 h), however, exhibit only moderate differences compared to Foscan (90.0 h) (Table 4.4). It is possible that by 96 h the liposomes have broken down *in vivo* so that only free m-THPC is being measured in the terminal phase of elimination (72-96 h), resulting in similar half-lives. However, evidence suggests the PEG coating may improve liposomes stability in serum and reduce drug release, as demonstrated using a similar pegylated liposomal composition (DPPC:DPPG, 9:1) (Crosasso, P. et al. 2000). A reduction in the release of a hydrophobic drug (paclitaxel) from pegylated liposomes was observed over 96 h when incubated at 37 °C in human serum (35% of initial encapsulated drug) compared to non-pegylated liposomes (72%). The same conclusion was reached by collaborators in *in vitro* studies using FosPEG, which demonstrated a reduction in m-THPC transfer to serum proteins (~2.1%) in 10% FCS compared to ~40% m-THPC release in 90% FCS when incubated for 2 h at 37°C *(see **Appendix I – A.17**)*.

Non-compartmental model

The non-compartmental approach was used as it compensates for individual data being collected from a number of animals, and is believed to give a more reliable measure of bioavailability, as it is directly proportional to the total amount of unchanged drug that reaches systemic circulation (Jones, H. J. et al. 2003). The advantage of this method is that no assumptions are made regarding specific tissue compartments therefore each m-THPC formulation can be analysed over the entire time series as a whole compartment. For Foscan versus pegylated liposomal m-THPC nanocarriers, FosPEG 2% and FosPEG 8%, a non-compartmental analysis gave m-THPC plasma clearance rates of 30, 6.4 and 3.2 mg kg^{-1} h^{-1} and $t_{1/2}$ lives of, 42.9 h, 50.2 h and 62.6 h. This decrease in m-THPC blood serum clearance rates and increase in $t_{1/2}$ values between formulations implies that with encapsulation and increasing pegylation, m-THPC remains in circulation for prolonged periods of time, due to a reduction in nanoparticle internalisation by macrophages (Opanasopit, P. et al. 2002). These macrophages are an essential component of the MPS and largely reside in the tissues of the liver (Kupffer cells), spleen (reticular cells) and bone marrow (Li, S. D. et al. 2008), however can also be found in a number of different organs,

such as, the lungs (alveolar cells), the blood (monocytes) and the kidneys (Kasravi, F. B. et al. 1995).

Non-compartmental analysis gave an average volume of distribution (V_d) of 1875.7 mL kg^{-1} for Foscan, 464.2 mL kg^{-1} for FosPEG 2% and 289.5 mL kg^{-1} for FosPEG 8%. This shows Foscan had a V_d six-fold greater than FosPEG 8%. Foslip studies gave a volume of distribution of 709 mL kg^{-1}, comparatively, in EMT6 xenografted nude mice (Lassalle, H. P. et al. 2009). This suggests m-THPC-loaded pegylated liposomes are more confined to the vasculature due to their much lower volume of distribution, which continues to decrease with further pegylation. This suggests, combined with mean residence times (MRT) of 61.9 h for Foscan versus 72.5 h for FosPEG 2% and 90.3 h for FosPEG 8%, that encapsulated m-THPC are less likely to be taken up into normal tissues to the same extent as Foscan within the same time frame. This, in turn, increases the probability of m-THPC being extravasated into tumour tissues through passive uptake from the blood when incorporated in pegylated liposomes. Foscan (m-THPC) is also a much smaller molecule than the 100 nm liposomes, therefore is able to diffuse out of normal blood vessels more easily, where it can distribute to other tissues. Other distribution factors include cardiac output/blood flow, permeability and perfusion of membranes, disease and plasma protein binding. Foscan's high V_d is more likely due to the latter, as m-THPC is a highly hydrophobic molecule, making it prone to rapid serum binding and the formation of m-THPC-serum complexes. This may subsequently lead to removal of m-THPC upon entering the blood stream, before redistribution to tissues for clearance, indicated by Foscan's reduced half-life and mean residence time in the plasma.

In these analyses, the volume of distribution (V_d) is not a physiological value but a theoretical volume that a drug needs to occupy in order to equal its concentration in the blood, based on a uniform distribution. Table 4.6 displays human blood volume concentrations (mL kg^{-1}) and total blood volume (L) based on an average 70 kg person. The total body water volume (L) is comprised of the extracellular volume (including blood serum and interstitial volume) and intracellular volumes (L) (Guzman, F. 2009). The same parameters are identified for a 200 g rat in Table 4.6 (Lee, H. B. et al. 1985).

This information, combined with calculated volumes of distribution from pharmacokinetic models can be used to interpret the distribution of a drug. For example, in a rat model (200

g), if the V_d for a drug is approximately equal to the total blood volume, 13 mL (65 mL kg^{-1}), it would suggest excessive binding to serum proteins and greater confinement to the central vascular compartment (Table 4.6). In the same model, a V_d between 13-43 mL (~65-215 mL kg^{-1}) indicates retention in the extracellular fluid, characteristic of hydrophilic drugs, and a V_d between 43-90 mL (~215-450 mL kg^{-1}), implies drug distribution to the interstitial volume. A V_d equal to the total body water volume or greater (>90 mL or >450 mL kg^{-1}), suggests diffusion to intracellular fluid or strong drug binding to tissues.

Parameter		**Human**	**Rat**
Total body weight (kg)		70	0.2
Blood Volume (mL kg^{-1})		~70	~65
Total blood volume (L)		~8	~0.013
55 % blood serum (L)		~5	~0.008
Total body water volume (L)		42 (100%)	~0.135
Extracellular volume (L)	Blood plasma	~4 (10 %)	~0.013
	Interstitial volume	~10 (23%)	~0.03
Intracellular volume (L)		~28 (66%)	~0.09

Table 4.6. Illustrates the relative size of various distribution volumes in average humans *(Guzman, F. 2009)* versus rats *(Lee, H. B. et al. 1985)*. Distribution volumes are related to certain parameters, such as, blood volume (mL kg^{-1}) and total body water volume (L), giving an indication of drug distribution following systemic administration.

In this investigation, Foscan has a V_d of ~1876 mL kg^{-1}. In a 200 g rat model this equates to ~375 mL, which supersedes the total body water volume and indicates strong m-THPC binding to tissues. V_d calculated for FosPEG 2% and FosPEG 8% give values of ~93 mL and ~58 mL respectively. The first indicates distribution to the intracellular volume and/or binding to tissues, whilst the latter suggests distribution to the interstitial volume. This is possibly due to the increasing hydrophilicity of the liposomes with increasing pegylation.

Liposomal m-THPC biodistribution in vivo: normal tissues

A large number of studies have documented the uptake of m-THPC (Foscan) at high concentrations into the RES using murine models; (Alian, W. et al. 1994;Cramers, P. et al. 2003;Jones, H. J. et al. 2003;Peng, Q. et al. 1995;Whelpton, R. et al. 1996) and although the PEG coating on the surface of the liposome reduces their rate of uptake into these tissues, it does not completely prevent it (Zamboni, W. C. 2005). The clearance of therapeutics from the blood is an important process for the removal of substances which could cause harmful side effects if retained in the body for long periods. However, rapid clearance of a drug may lead to its removal from circulation before adequate time has passed for it to elicit a therapeutic effect in target tissues. Fundamentally, it is crucial to establish a balance between clearance and adverse drug uptake into non-target tissues, however, this proves to be a difficult and on-going challenge.

Liver/Spleen

In this investigation, all formulations were found to show peak m-THPC levels at the earliest time points (Fig 4.13-15) in the liver, spleen and lungs. These tissues are highly vascularised and will receive a high blood flow from the total cardiac output and as a result, increase the probability of exposure to circulating therapeutics. These organs also constitute the RES and as such are involved in clearance pathways by acting as immunological filters of the blood (Yan, X. et al. 2005). The liver is known to contain ~20% of the total rat blood volume at any one time (~2.5 mL in 200 g rat) (Lee, H. B. et al. 1985), which may further contribute to these results. The liposomal encapsulation of m-THPC and PEG coating of the particle surface, led to significant differences in m-THPC uptake in the liver. Data from the liver show similar m-THPC concentrations at $t \leq 2$ h for both Foscan (~4 $\mu g\ g^{-1}$) and FosPEG 8% (~3.5 $\mu g\ g^{-1}$), m-THPC concentrations in the blood serum have to be taken into account in the same time frame. For example, Foscan is measured at ~0.5 $\mu g\ mL^{-1}$ in the blood at $t \leq 2$ h and FosPEG 8% at ~5.8 $\mu g\ mL^{-1}$ (Fig 4.12). This demonstrates that Foscan is almost immediately and extensively removed from the blood at the earliest time points, accumulating in the liver at a concentration 8 times greater than that of the blood serum (Fig 4.13). FosPEG 8%, however, shows little over half has been removed from the blood and distributed to the liver at this time. This pattern of m-THPC uptake corresponds to previous *in vivo* studies carried out in rats with Foscan (Jones, H. J. et al. 2003) and Foslip (Lassalle, H. P. et al. 2009) and in nude mice with

FosPEG (Reshetov, V. et al. 2013). This confirms a greater and prolonged accumulation of m-THPC in FosPEG formulations in the central blood compartment. The encapsulation of m-THPC and higher degrees of pegylation, may contribute to suppressed uptake into macrophages and organs of the RES (Alian, W. et al. 1994), such as the Kupffer cells of the liver, or stimulation of lymphocytes in the spleen (Bourdon, O. et al. 2002;Woodle, M. C. et al. 1992).

Lungs

Interestingly, the biodistribution of m-THPC formulations in the lung tissue (Fig. 4.15) correlated closely to the blood serum pharmacokinetics (Fig. 4.12), as lung uptake of m-THPC increased with liposomal pegylation. Following *i.v.* injection, the lungs are the first tissue to be perfused (Whelpton, R. et al. 1995). Combined with the high density of permeating blood vessels and the large surface area of endothelial cells it can be speculated that circulating, residual blood may still have been present in the extracted tissue, as it was not not possible to flush prior to removal, resulting in a similar pattern of m-THPC accumulation. Foscan results confirm this, as a 1:1 ratio of m-THPC in lung tissue: blood serum was observed. Complete removal of Foscan and FosPEG 2% from the lungs was observed by 168 h; indicating they were not being unfavorably retained, however a slower clearance rate was found for FosPEG8%, suggesting longer periods of time are required for their clearance. These slow distribution changes in the liver and lung could be the result of corresponding increased blood serum levels of FosPEG 8%, as nanocarriers are redistributed to different tissues of the RES through macrophage uptake (Xie, G. et al. 2010). Quantitative Foscan studies with lung tissue have been investigated *in vivo* (Peng, Q. et al. 1995;Svensson, J. et al. 2007;Whelpton, R. et al. 1995). Fielding *et al.*, have demonstrated localisation of m-THPC in the macrophages of lung tissue at 72 h (Fielding, D. I. et al. 1999). To date, no studies have focused on the cumulative deposition of m-THPC-loaded pegylated liposomes in normal lung tissue, but findings such as these offer exciting potential in treating diseased or cancerous lung tissue with PDT, as it is notoriously difficult to access. Other studies using comparable nanocarriers have indicated similar capabilities and applications. Schiffelers *et al*., used pegylated liposomes to deliver antibiotics *in vivo* to treat pneumonia in lung tissue of RP/AEur/RijHsd strain albino rats. It was found, the liposomes preferentially accumulated in infected lung compared to the contralateral non-infected lung and, as discovered here, a reduction in surface PEG density

resulted in a higher uptake by the RES and lower blood circulation time (Schiffelers, R. M. et al. 1999). Similarly, Zhang *et al*., used 100 nm pegylated nanostructured lipid carriers to improve the delivery of an anti-tumour agent which targets nuclear enzymes (HCPT), in nude mice bearing human A549 tumours. Biodistribution studies demonstrated an increase in HCPT circulation time, a reduction in RES uptake and superior tumour treatment efficacy in comparison to non-pegylated NPs and free HCPT (Zhang, X. et al. 2008). More recently, non-biodegradable polystyrene NPs were directly adsorbed onto the surface of red blood cells in Balb/C nude mice to improve NP accumulation in the lungs, whilst simultaneously reduce liver/spleen uptake.

Kidneys

Drugs and their metabolites are excreted primarily via the kidneys into urine, however, hydrophobic molecules, such as m-THPC, are thought to become rapidly bound by serum proteins upon entering the blood circulation, which contributes to their higher uptake and distribution to the RES, where they are transformated into hydrophilic liver metabolites (Li, S. D. et al. 2008). According to the literature, hydrophilic drugs (PEG) undergo less protein binding, therefore are eliminated quickly from the blood by renal filtration into the urine. In spite of the hydrophilic PEG coating of the liposomes, it is unlikely they are cleared significantly through the renal pathway due to their size. Accumulation of m-THPC may be on account of residing RES cells in the kidneys, as it is expected by 168 h that m-THPC may have leached from FosPEG formulations or they are likely to have been degraded. The kidneys receive 25% of the total cardiac output (Dawson, T. R. 2002) and also contain RES cells. Clearance of particles through the urinary system is more favorable with regards to toxicity as it reduces cumulative drug effects in the liver, and in the case of photosensitisers, prolonged cutaneous photosensitivity. Choi *et al*., have demonstrated a 13% retention of injected drug doses *in vivo* up to two years post *i.v.* administration for even the smallest nano-drug molecules (Choi, H. S. et al. 2007), indicating 100% maximum clearance for the majority of nanoparticles is unobtainable. Research carried out by Burns *et al*., (Burns, A. A. et al. 2009), showed very small nanoparticles of 3-6 nm could be successfully cleared from animals through renal excretion in the kidneys, while studies using quantum dots by Choi *et al*., suggests the cut-off size for renal clearance is 5.5 nm (Choi, H. S. et al. 2007). The liposomal nanocarriers used in our study were much larger than this (105-125 nm), suggesting ineffective clearance

through size dependent glomerular filtration. Although decreased drug excretion rates and long-term retention can lead to potential problems with associated toxicity in the liver from incomplete biodegradation of particles into biologically benign components (Choi, H. S. et al. 2007), an initial reduction in renal clearance of encapsulated m-THPC in NPs can result in an increase in blood circulation time and therefore increased probability of accumulation in target tissues. The uptake for all m-THPC formulations was much lower in the kidneys in comparison to the major organs of the RES (Fig. 4.16). FosPEG 8% accumulates at the lowest concentrations in the kidneys over 168 h ($\leq$ 0.1 μg g^{-1}) following intravenous injection and may be on account of its prolonged circulation time. Its clearance is in accordance with the pattern of excretion *via* the hepatobiliary pathway (Kumar, R. et al. 2010;Lassalle, H. P. et al. 2009) but cannot be confirmed, as metabolic experiments were not carried out in this investigation for urine or fecal collection. Bio-optical imaging by collaborators, however, indicated high levels of m-THPC fluorescence in fecal matter in *ex vivo* colon tissue with pegylated liposomes (Dr Wijnand Helfrich, NL – data not shown). Similar pharmacokinetic studies show corresponding results, with clearance closely related to uptake into the RES (Jones, H. J. et al. 2003;Kumar, R. et al. 2010;Lassalle, H. P. et al. 2009;Whelpton, R. et al. 1995) and excretion *via* the hepatobiliary mechanism (Kumar, R. et al. 2010), however, these studies used non-biodegradable nanocarrier systems.

Skin

It was essential to examine the uptake and retention of m-THPC in skin tissue due to its well documented prolonged cutaneous photosensitivity post-PDT and subsequent complications with patient management. Despite being highly vascularised, skin tissue has a low blood flow (5 mL/100 g tissue per min) relative to its percent of body weight (7 %) in comparison to the liver, which makes up 2% of total body weight and has a blood flow of 140-170 mL/100 g tissue per min in humans (Leiberman, D. P. et al. 1978;Shargel, L. et al. 2005). In addition, large levels of macrophages reside in the RES therefore redistribution of m-THPC to these organs may occur, unlike the skin, which explains the low m-THPC uptake at early time points in the skin (non-exponential) compared to the liver, lungs or spleen. The concentration of m-THPC in the skin tissue plateaus over 168 h (Fig 4.17) and may be accounted for by the same phenomena, as under normal steady state conditions only a small number of monocytes (precursors of macrophages) migrate to the skin (Vanfurth, R. et al. 1979). This reduced rate of phagocytosis suggests m-THPC may

not be efficiently cleared from the skin upon entering, it is essential to ensure m-THPC uptake into the skin is kept to a minimum. Skin tissue was found to accumulate the lowest concentrations of m-THPC (≤0.1 μg g^{-1}) here and when compared to previous studies (Jones, H. J. et al. 2003;Lassalle, H. P. et al. 2009;Whelpton, R. et al. 1996). Regrettably, Foscan and FosPEG 2% elicited similar kinetic profiles (Fig. 4.17) in the skin and slightly elevated concentrations of FosPEG 8% were observed. Like the skin, muscle is a peripheral tissue and elicited similar m-THPC kinetics. However, skin to tumour tissue ratios (~1.4 versus 6) (Fig. 4.19B), suggest pegylated liposomal m-THPC uptake may be sufficient to reduce DLIs and drug doses without detriment to PDT efficacy and patient treatment to overcome this problem. Reshetov *et al.,* also found improved tumour to skin ratios in nude mice with highly similar FosPEG formulations in comparison to Foslip (Reshetov, V. et al. 2013).

Other tissues

Drug uptake in brain tissue was not measured in these studies; however, successful treatment with liposomal therapeutics has been shown. Although there has been little documented on the uptake of m-THPC into neurons, preliminary studies in our group (unpublished) have shown no evidence of accumulation in these cells and preservation of nerve tissue during clinical PDT treatment. Based on the size of nanocarriers investigated here (~100 nm), it is highly unlikely they are able to cross the walls of non-sinusoidal non-fenestrated blood capillaries of blood-brain barrier (BBB), which have a physiologic upper limit pore size of <1 nm (Sarin, H. 2010). However, may be altered for targeted brain treatments, therefore any acute associated toxicity must not be ruled out.

Liposomal m-THPC biodistribution in vivo: tumour tissue

The pharmacokinetic data for tumour tissue (Fig. 4.19A) displayed a peak in m-THPC accumulation with all formulations between 6 and 24 h following the administration of clinical doses of m-THPC (0.3 mg kg^{-1}). This is in agreement with Foscan studies carried out by Jones *et al*., (Jones, H. J. et al. 2003), which show an m-THPC peak around 18–24 h in LSBD1 tumours in the BDIX rat along with Cramers *et al*., in H-MESO1 tumour-bearing mice after equal injected doses of m-THPC (Cramers, P. et al. 2003). More recently, Garrier *et al*., (Garrier, J. et al. 2010) found maximal Foscan uptake at 24 h in EMT6 tumour-bearing mouse models, comparable to Lassalle *et al*., (Lassalle, H. P. et al.

2009) who observed similar concentrations at time periods between 6 and 15 h with Foslip in the same model and m-THPC dose (0.3 mg kg^{-1}). Reshetov *et al*., found maximal tumour accumulation in nude mice over the same time periods following 0.15 mg kg^{-1} *i.v.* injection of either Foslip or FosPEG (~10% mol), but minimal differences in maximum m-THPC concentrations between formulations. It was speculated this may have been due to insufficient liposomal drug concentration in the plasma after 6 h (Reshetov, V. et al. 2013). By comparison, approximately 90% more m-THPC accumulated in tumour tissue using similar FosPEG formulations in studies presented here (Foslip ~0.1 μg g^{-1} vs. FosPEG ~1 μg g^{-1}). Furthermore, studies carried out in felines by Buchholz *et al.,* (Buchholz, J. et al. 2005) showed peak tumour-to-skin ratios at similar times (7 h) with m-THPC-loaded FosPEG (2.5% or 5%) versus Foscan, using lower administered dose of m-THPC (0.15 mg kg^{-1}). Despite differences in administered m-THPC doses, quantification techniques and tumour species/models, it is apparent there are distinct differences in the tumour pharmacokinetics of m-THPC when delivered by liposomes with or without the addition of an inert PEG polymer coating. This has been well documented since the introduction of Stealth® liposomes (Allen, T. M. et al. 1995;Papahadjopoulos, D. et al. 1991;van Vlerken, L. E. et al. 2007). The inherent accumulation of nanoparticles such as liposomes in tumour tissue can further be attributed to the EPR effect, since leaky tumour vasculature, characterised by rapid angiogenesis (Brannon-Peppas, L. et al. 2004), increases permeability of pegylated liposomes allowing them to extravasate into the surrounding tumour tissue where they are retained due to a dysfunctional lymphatic drainage system (Maeda, H. et al. 2000). Combined with prolonged periods in blood circulation, this is believed to aid their passive uptake into tumour tissue compared to normal tissue (Brown, J. M. et al. 2004). The dynamics are likely to be more complex, since m-THPC can also be slowly released from liposomes through binding to serum proteins in circulation prior to reaching their tumour tissue (D'Hallewin, M. A. et al. 2008;Lassalle, H. P. et al. 2009;Reshetov, V. et al. 2011). However, following cellular uptake, liposomes are degraded to release encapsulated photosensitiser in its monomeric and photoactive form (Lassalle, H. P. et al. 2009). Steric hindrance from bulky PEG groups at the nano-bio interface may explain why the relationship between increased uptake in tumour tissues of m-THPC incorporated into pegylated liposomal nanocarriers (2% mol) and increased pegylation of liposomes (8% mol) is non-linear and similarly why *in vitro* studies with some cell lines using these liposomes cause inefficient intracellular delivery (Li, S. D. et al.

2008). Differences in tumour uptake may also be a consequence of the heterogeneity of the tumour tissue between animals.

Summary: Biodistribution

The PEG polymer coating appears to offer the liposome a degree of protection from recognition by the host's immune system, increasing the longevity of m-THPC in the blood stream and its passive uptake into tumour tissue compared to Foscan *in vivo*. Low skin to tumour tissue ratios observed with FosPEG formulations could be advantageous for PDT.

PDT

PDT studies were carried out in subcutaneous rat tumour (MC28 fibrosarcoma) models following administration of either FosPEG formulation versus Foscan in order to assess differences in PDT treatment response. Drug: light intervals of 24 h were chosen based on the greatest uptake of m-THPC observed *in vivo* from pharmacokinetic data and optimal tumour: skin concentration ratios.

In PDT studies, tumour necrosis was measured as a percentage of whole tumour surface area from histological sections, as carried out previously (Garrier, J. et al. 2010). At m-THPC doses of 0.3mg kg^{-1} and exposure to 10 J of light, a high percentage of tumour necrosis was found for all formulations although no significant differences were evident, despite the greater m-THPC concentration in tumour tissue using the liposomal-m-THPC formulations (Fig. 4.19A). This may simply be due to the much larger light dose required to kill tissue at the tumour periphery, which may mask concentration differences, considering the complex dosimetry of interstitial light delivery (Berg, K. et al. 2011;Wilson, B. C. et al. 1997). A further factor is that the tumour periphery in sub-cutaneous models has been observed to be more resistant to PDT (Berg, K. et al. 2011). However, when either light energy or m-THPC doses were lowered to ≤20% of their original dose (2 J or 0.05 mg kg^{-1} m-THPC) a significant difference ($p \leq 0.001$) in percentage area tumour necrosis between Foscan versus FosPEG 2% and 8% was observed (Fig. 4.21) from ~30% necrosis to ≥40–50% necrosis. This implies not only that treatment times could be reduced, but also more importantly, that much lower doses of pegylated liposomal m-THPC may be administered in comparison to Foscan in order to elicit the same PDT effect witnessed at higher m-THPC doses. This pattern of PDT efficacy has

also been observed in the treatment of arthritic joints (Hansch, A. et al. 2008) with pegylated liposomal m-THPC and in spontaneous squamous cell carcinomas in felines (Buchholz, J. et al. 2007).

It is not feasible to discriminate clearly from these studies m-THPC damage to the vasculature and direct tumour cell kill. It is likely that damage to the tumour vasculature, due to the increased levels of the FosPEG formulations in the circulation, makes an important contribution. We note also that histological examination showed signs of haemorrhagic damage. Tumour cell damage may then arise primarily through the accumulative effect of blood vessel collapse and hypoxia, with a lesser extent of direct tumour cell damage (Cramers, P. et al. 2003;Veenhuizen, R. et al. 1997). A similar mechanism was proposed by Lassalle *et al*., using a Foslip formulation and more recent work by this group also attributed longer DLIs (≥15 h) and improved intratumoral localisation, throughout the tumour parenchyma and vasculature, to culminate in more effective PDT with FosPEG (Lassalle, H. P. et al. 2009;Reshetov, V. et al. 2013). Although both FosPEG formulations used here are effective, at this stage it is unclear as to which FosPEG formulation is optimum for tumour PDT and would be dependent upon the application owing to the complex dosimetry of different tissues.

PDT performed to tumours using an intermediate dose of m-THPC (0.1 mg kg^{-1}) at the same DLI (24 h) with a light dose of 10 J, showed an increase in the percentage tumour necrosis with FosPEG formulations (2% and 8%) compared to Foscan. However, statistical analysis revealed this was not significant between percentage PDT tumour necrosis induces with higher dose of 0.3 mg kg^{-1} m-THPC ***(see Appendix I –A.16 PDT to MC28 tumours using 0.1 mgkg^{-1} m-THPC dose)*** therefore a further reduction in drug dosage was employed (0.05 mg kg^{-1}).

Many reports have suggested that a PDT damage threshold could be a consequence of vasculature collapse, as PDT efficacy is dependent on the availability of oxygen in the tissues, delivered by a functional blood supply (Dougherty, T. J. et al. 1998). Therefore if significant vasculature damage occurs during treatment, the photochemical reaction cannot take place and treatment no longer becomes effective, as anoxic environments and hypoxic cells are protected from PDT damage (Henderson, B. W. et al. 1989a;Henderson, B. W. et al. 1989b). However, our study found when m-THPC drug doses were significantly

reduced (0.1 mg kg^{-1} or 0.05 mg kg^{-1}) and light parameters were fixed (10 J), an increase in percentage tumour tissue necrosis with PDT, at a DLI of 24 h, was observed with FosPEG formulations compared to Foscan. This suggests the extent of phototoxic damage elicited by m-THPC in FosPEG formulations was maintained at similar levels to those observed with higher m-THPC doses. One could argue, passive uptake of m-THPC into tumour tissues is more effective when m-THPC is delivered by nanocarriers (FosPEG), over standard formulation (Foscan), and therefore PDT response may also be attributed to PS extravasation and accumulation in tumour tissues rather than acting solely on the vasculature (Schacht, V. et al. 2006). Vascular-mediate effects have been heavily associated with m-THPC in many studies, which have been correlated with plasma drug levels at the time of irradiation, rather than tumour levels (Triesscheijn, M. et al. 2005). Veenhuizen *et al.,* (Veenhuizen, R. et al. 1997) and Cramers *et al.,* (Cramers, P. et al. 2003) showed PDT efficacy with Foscan paralleled m-THPC concentrations in the plasma. PDT damage here, however, shows an inverse relationship between m-THPC concentration and PDT response. For example, as *i.v.* injected m-THPC doses are reduced, an increase in PDT response is observed with FosPEG formulations compared to Foscan.

PDT efficacy is not only dependent on the bulk PS tumour concentration but also the spatial intratumoral localisation, therefore increasing specific tumour cell uptake following passive accumulation of NPs in tumour tissue is the focus for much research into future drug delivery strategies, targeting receptor-mediated uptake mechanisms overexpressed on many cancers. There is also evidence to suggest that PDT efficacy could potentially be improved further with FosPEG formulations if the light fluence rate was lowered to reduce oxygen consumption rates (Seshadri, M. et al. 2008) or PDT light delivery was fractionated to allow re-oxygenation of tissue (Pogue, B. W. et al. 1997), as destruction of blood vessels feeding rapid-proliferating tumour tissues may help aid in long-term tumour regression (Dougherty, T. J. et al. 1998).

Summary: PDT

In order to understand *in vivo* interactions of m-THPC and perhaps even its intracellular distribution, the PDT effect has to be correlated to photosensitiser levels and tumour localisation. Through encapsulation of m-THPC into pegylated liposomes the accumulation of photosensitiser in tumour tissues was improved and this was reflected in

PDT damage, whereby one sixth of the original administered dose resulted in maximal levels of tumour tissue necrosis, in comparison to standard formulation, Foscan.

Skin photosensitivity

The biodistribution of photosensitisers can lead to unfavourable uptake and retention in normal tissues, notably the skin. In the case of m-THPC, this uptake is likely due to its hydrophobicity and non-selectivity. Patients treated with PDT are advised to keep out of direct sunlight or strong indoor lighting in order to avoid common side-effects such as, skin blistering, sunburn, erythema and oedema. With Foscan (m-THPC) this prolonged cutaneous photosensitivity has been documented to last for up to several weeks post-treatment, complicating patient management (Wagnieres, G. et al. 1998).

Skin photosensitivity studies revealed extensive superficial damage to skin tissue with 0.3 mg kg^{-1} Foscan (*i.v.*) over the treatment area (5 mm^2) after 30 min of light exposure at 100 mW cm^{-2} (sun light equivalent) with a DLI of 96 h. This was illustrated through histological examination by the thickening of the epidermis due to mass cell death at this site and an infiltration of inflammatory cells (indicated by arrows) (Fig. 4.23), indicative of severe erythema. The histological effects of light exposure (30 min) were slightly milder when using FosPEG 2% and 8%, confirming damage to the epidermis at 96 h (Fig. 4.23). Visual assessment of skin effects at 96 h using FosPEG 8% (Fig. 4.22) correlated to chemical extraction results (Fig. 4.17), whereby elevated accumulation of FosPEG 8% in skin tissue was reflected in higher skin photodamage grading. However, disparities between histological data were thought to be due to differences in the cellular localisation of m-THPC within skin tissue, which primarily determined the site and outcome of photoinduced damage (Moor, A. C. 2000). Histologically there appeared to be less skin damage at a DLI of 168 h with all m-THPC formulations (Fig. 4.23). Foscan appeared to elicit the most severe symptoms, in accordance with visual assessment (Fig. 4.22); however damage was more sporadic and occurred in isolated areas of the epidermis. No further effects were observed with FosPEG 2%. The skin histology for FosPEG 8% showed an infiltration of mast cells and neutrophils into the dermis (Fig. 4.23); however in one animal, widespread damage to the epidermis was detected (data not shown). This correlated to m-THPC accumulation for FosPEG 8% at 168 h obtained through chemical extraction but the irregularity probably accounts for the increase in photosensitive grading

observed upon visual assessment. This was believed to be due to inter-animal variation, m-THPC localisation and small sampling size. All control skin samples including those that received no light (0 min exposure) and/or without m-THPC (data not shown) displayed no signs of cutaneous photosensitivity (Fig. 4.23). Recently, a reduction in skin photosensitivity has also been demonstrated using m-THPC encapsulation in micelles (Shieh, M. J. et al. 2010). At reduced m-THPC doses (0.1 mg kg^{-1}) grading analysis showed an overall reduction in skin photosensitivity with each formulation of approximately 3-fold, which directly corresponded to the reduction in m-THPC dosage (Fig 7B). Foscan and FosPEG 2% showed an increase in photosensitivity over 30 mins at a DLI of 96 h, however at the longer DLI, Foscan scored positively lower in sensitivity across all light exposure times. FosPEG 8% appeared to show the least amount of sensitivity at both DLIs over the 30 min exposure time, although cellular damage through histological examination was not carried out to confirm this.

Summary: Photosensitivity

Overall, there appeared to be a 2-3 fold reduction in skin photosensitivity over most light exposure times (0-30 mins) when the m-THPC dose was reduced but there did not seem to be a significant difference between FosPEGs and Foscan or DLIs.

4.5 Conclusions

Novel pegylated liposomal nanocarrier delivery systems (FosPEG) have been developed in this chapter to improve the uptake of a second generation photosensitiser, m-THPC, into tumour tissues. This was investigated by studying the biodistribution and accumulation of encapsulated m-THPC in comparison to standard formulation, Foscan, through *in vivo* pharmacokinetic analysis, which was then correlated with measurements of PDT efficacy and skin photosensitivity.

Our study has shown that improved tumour uptake of FosPEG formulations (FosPEG 2% and 8%) in comparison to Foscan. An increase in blood circulation half-life, combined with the influence of the tumour microenvironment (EPR effect), are believed to contribute to enhanced passive tumour uptake of m-THPC. Improved maximal tumour to skin ratios at$\leq$24 h with both FosPEG formulations indicate that significantly reduced administered doses of m-THPC could be employed over Foscan to produce the same PDT treatment efficacy. This could be improved further still with the attachment of targeting ligands to the liposome surface, capable of recognising tumour-associated receptors over-expressed on the surface of many cancers.

In a clinical setting, using lower administered m-THPC doses to achieve the same PDT anti-tumour response could reduce adverse prolonged skin photosensitivity, improve patient quality of life and significantly cut therapeutic costs.

5. Polymeric Nanoparticles

5.1 Introduction

Polymeric nanoparticles can be degraded into biocompatible, non-toxic products that can be cleared from the body. The polymer composition of the nanoparticle can help determine the rate of its degradation, mechanical strength, solubility and pore size. Polymeric nanoparticles can be prepared from a range of polymers that exist naturally including, collagen and complex sugars (chitosan, hyaluronan and saccharides) or fabricated synthetically (α-hydroxy acids, polyanhydrides and others).

PLGA poly(lactic-co-glycolic acid) is a synthetic, amorphous copolymer of two cyclic dimers, lactic acid (LA) and glycolic acid (GA), and is one of the most successfully developed biocompatible and biodegradable polymers owing to the production of endogenous metabolites (LA, GA), and their reabsorpability through natural pathways, following PLGA degradation (Danhier, F. et al. 2012). Lactic acid is converted into pyruvate and glycolate enters the tricarboxylic acid cycle (TCA or Kreb's cycle) and is eliminated from the body as carbon dioxide (CO_2) and water (Crotts, G. et al. 1998). Glycolic acid may be excreted via the same process or as an unchanged molecule via renal clearance (Crotts, G. et al. 1998). This minimal associated toxicity has rendered PLGA a promising biomaterial and has led to extensive research into its application in medicine, including micro- and nanoparticles, grafts, sutures, implants and prosthetic devices. As a result, PLGA has been approved by the US Food and Drug Administration (FDA) and European Medicine Agency (EMA) for various drug delivery systems since 1989 (Duncan, R. 2006).

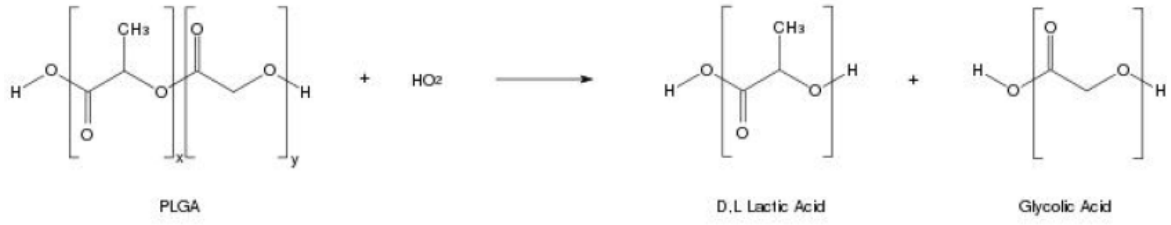

Figure 5.1. Lactic acid (LA) can undergo a condensation (dehydration) reaction with glycolic acid (GA) to form lactic-co-glycolic acid via ester linkages. Polymerisation of alternate repeating LA and GA units form the polymer, PLGA (*x* is the number of repeating lactic acid units and *y* the number of glycolide units). *Taken from (Makadia, H. K. et al. 2011).*

In aqueous environments, degradation of the PLGA copolymer matrix is the collective process of (i) bulk diffusion (from water penetration), (ii) surface diffusion, (iii) bulk erosion and (iv) surface erosion predominantly through the hydrolysis of ester bonds between monomer subunits. Furthermore, the biodegradation process autocatalyses due to the increasing number of carboxylic end groups available during degradation. The rate of polymer degradation is thought to be largely affected by pH, through the protonation/deprotonation of ester bonds in acidic/basic environments and additional enzymatic cleavage is believed to be a contributing factor *in vivo* due to differences in drug release rates in comparative *in vitro* studies (Alexis, F. et al. 2008). It has been shown by Makadia *et al*., that the degradation of PLGA is predominantly related to the composition of the polymer, specifically, the molar ratio of each monomer (LA:GA). It was found the higher the ratio of glycolide units, the faster the degradation rate of PLGA. This is due to the absence of hydrophobic methyl groups on glycolide units. This increases the hydrophilicity of PLGA molecules with a higher percentage GA. The presence of methyl groups on lactic acid monomer units means PLGA copolymers are able to absorb less water and therefore degrade more slowly (Makadia, H. K. et al. 2011). The molecular weight (Mw) of the polymer has also been shown to positively correlate with the mechanical properties of the material (higher Mw increases polymer strength) and therefore its physical breakdown (Kranz, H. et al. 2000). The degree of crystallinity within the polymer structure, which is directly related to its molecular weight, can also dictate its mechanical strength, rate of hydrolysis and subsequent degradation, with a reduction in crystallinity causing an increase in the rate of hydration/hydrolysis of PLGA (Makadia, H. K. et al. 2011). The degree of PLGA crystallinity is dependent on the poly lactic acid (PLA) enantiomer incorporated (*D* or *L*); as PLA exists in two forms due to the presence of an asymmetric α-carbon. P*L*LA occurs in a highly crystalline form whereas P*D*LA is

completely amorphous due to disordered polymer chains (Makadia, H. K. et al. 2011). Despite this, the physicochemical properties of optically active P*D*LA and P*L*LA are very similar. (PLGA is generally an acronym for poly D,L-lactic-co-glycolic acid where D- and L- lactic acid enantiomer forms are in equal ratio). Polymers of glycolic acid (PGA) are void of any methyl side groups, which ensure a highly crystalline structure; however, with a simultaneous increase in hydrophilicity, a higher ratio of GA monomers promotes a faster rate of PLGA degradation (Makadia, H. K. et al. 2011).

Nanoparticles made of polymers (poly(alkylcyanoacrylate) were first described in 1977 by Couvreur *et al*., but were precluded from clinical applications as drug carriers until the mid-1990s owing to their limited circulation half-life (Olivier, J. C. 2005). Several methods have since been proposed to increase the half-life of polymeric NPs in aqueous environments (Esmaeili, F. et al. 2008). Polymers end-capped with esters prevent the exposure of free carboxyl groups at the terminal ends of PLGA chains to reduce hydrolysis and polymer degradation. The addition of other biocompatible polymers, such as non-ionic polymers, Poloxamers (poly(oxypropylene/oxyethylene)), or hydrophilic PEG groups, prevents precipitation of the copolymer molecules (Makadia, H. K. et al. 2011). PLGA/PEG block copolymers have been processed as diblock molecules (PLGA-PEG) and are readily commercially available. The hydrophobic regions of PLGA (LA) form associative crosslinks and the hydrophilic PEG regions allow the copolymer molecules to stay in solution (Teply, B. A. et al. 2008). As with previously described nanoparticles, the layer of PEG can act as a protective barrier from rapid RES uptake, however, is also thought to reduce the encapsulation efficiency of certain drugs in PLGA NPs. The precise mechanism for this effect is unclear but is likely due to steric interference of drug-polymer interaction by the PEG chains (Makadia, H. K. et al. 2011). Complex and simple sugars, such as chitosan and trehalose, have also been studied for PLGA surface modification (Jain, A. K. et al. 2011). Each of these conjugated groups can reduce the electrostatic and hydrophobic interactions that enable opsonins to bind to the particle surface for clearance via the RES.

Drug encapsulation into polymeric nanoparticles can occur through a number of different techniques with varying encapsulation efficacies, largely dependent on the drug being incorporated. Inclusion of the drug can be made during the polymerisation process or by direct adsorption onto preformed nanoparticles. In the first instance, chemical reactions

may occur between drugs and polymer monomers, inhibiting their function (Guise, V. et al. 1990). If adsorbed directly onto the particle surface, drugs may be susceptible to serum protein competition of binding sites when in the blood or during subsequent surface modification steps, which may result in a reduction in nanoparticle stability and polymer degradation (Olivier, J. C. 2005). Alternatively a rapid, one-step nanoprecipitation method, first described by Fessi *et al*., (Fessi, H. et al. 1989), can be used to incorporate drugs, following their dispersion in solvent during nanoparticle synthesis, in an attempt to overcome some of these drawbacks (Bilati, U. et al. 2005). The method requires two miscible solvents; the first dissolves both the polymer and the drug (the solvent), whereas the second dissolves the polymer only (the non-solvent). The removal of the solvent from the polymer material in solution (desolvation) via the addition of the non-solvent causes nanoprecipitation. This process occurs rapidly upon diffusion of the polymer-containing solvent into the dispersing medium, causing immediate drug entrapment in polymer precipitates. Nanoprecipitation enables the production of small nanoparticles (100–300 nm) with narrow unimodal distribution from a wide range of preformed, commercially available polymers (Bilati, U. et al. 2005). Additionally, the procedure does not require toxic organic solvents, high temperatures or pH steps, which may modify drugs or denature proteins being incorporated. The nanoprecipitation method is more suitable for loading of hydrophobic, poorly soluble drugs into PLGA NPs, as opposed to water soluble drugs, due to the initial drug-polymer solvent dissolving phase, which promotes high encapsulation efficiency and prevents hydrophobic drug leakage (*see* ***Appendix I – B.1 Nanoprecipitation method: PLGA NPs***) (Barichello, J. M. et al. 1999;Fessi, H. et al. 1989;Govender, T. et al. 1999). 100% encapsulation of hydrophobic Paclitaxel into PLGA NPs was demonstrated by Fonseca *et al*., using this method (Fonseca, C. et al. 2002). Consequently, this method has been used to produce PLGA and PEG-PLGA particles incorporating m-THPC in these studies.

There is extensive research being carried out on the use of PLGA nanoparticles as drug delivery systems (targeted and untargeted) for use in various clinical applications, which is reflected in the literature (Table 5.1). Many examples described in Table 5.1 encapsulate various anti-cancer agents such as paclitaxel (Fonseca, C. et al. 2002), 9-nitrocamptothecin (Derakhshandeh, K. et al. 2007), cisplatin (Dhar, S. et al. 2008), doxorubicin (Park, J. W. 2002) etc. but a large proportion of PLGA NPs are also being developed for vaccinations and cerebral diseases (Danhier, F. et al. 2012). All of these examples are currently in the

experimental or pre-clinical stage. Despite improvements on polymeric NP stealth properties, issues associated with potential toxicity from dose dumping (initial drug burst), inconsistent drug release rates and *in vivo* drug-polymer interactions need to be evaluated (Makadia, H. K. et al. 2011).

Receptors	Ligands	Therapeutic compounds	Study design
Vaccination			
Targeted nanoparticles			
Toll-like receptors	MPLA	OVA	Preclinical (mice)
C-type lectins	Mannan	OVA	Preclinical (mice)
Siglec	Anti-Siglec-7 polyclonal antibody	–	*In vitro*
Claudins	CPE30	Influenza hemagglutinin	Preclinical (mice)
$\alpha_v\beta_3$ integrins	RGD/RGDp LDV/LDVp	OVA	Preclinical (mice)
STAT3	JSI-124	–	Preclinical
Cancer			
Untargeted nanopartides			
		Paclitaxel	Preclinical (mice)
		9-nitro-camptothecin	*In vitro*
		Rh-G-CSF	*In vitro*
		siRNA targeting MBD1	*In vitro*
		shRNA targeting AnxA2	Preclinical (mice)
Targeted nanoparticles			
ICAM-1	cLABL	Doxorubicin	*In vitro*
Folate receptor	Folate	Paclitaxel	Preclinical
Specific receptor of lymphatic metastatic tumors	LyP-1	–	Preclinical
Prostate specific receptor	PSMA	Cisplatin	Preclinical
$\alpha_v\beta_3$ integrins	RGD	Paclitaxel	Preclinical (mice)
Nucleolin	AS1411	Paclitaxel	*In vivo*
HER-2	rhuMAbHER2	PE38KDL	Preclinical (mice)
Inflammation			
Untargeted nanopartides			
		Diclofenac	*In vivo*
		Flubiprofen	Preclinical (rabbit)
		Rolipram	Preclinical
		Tacrolimus	Preclinical (rats)
		Betamethasone	Preclinical (rabbit)
		PS-341	Preclinical
Cerebral diseases			
Untargeted nanopartides			
		Superoxide dismutase	Preclinical (rats)
Targeted nanoparticles			
Transferrin receptor	Lactoferrin	Urocortin	Preclinical (rats)
Opioid receptor	Simil-opioid peptide (g7)	Loperamide	Preclinical
Opioid receptor	Simil-opioid peptide (g7)	Sialic acid	Preclinical
Specific brain receptor	Pep TGN	–	Preclinical
Regenerative medicine			
		GDNF	Preclinical (rats)
		VEGF	Preclinical (mice)
		FGF-2	Preclinical (mice)
		BMP-7/BMP-2	*In vitro*
Cardiovascular diseases			
Untargeted nanopartides			
		DNA	Preclinical (pig coronary arteri
Infections			
Untargeted nanopartides			
		Sparfloxacin	Preclinical (rabbits)
		Gentamycin	*In vivo*
Osteoporosis			
Untargeted nanopartides			
		Calcitonine	*In vivo*
Diabetes			
Untargeted nanopartides			
		Insulin	Preclinical

Table 5.1. PLGA-based nanoparticles currently being developed as drug delivery systems for various clinical applications. *Taken from (Danhier, F. et al. 2012).*

Drug release rates from polymeric nanoparticles are thought to be more complex than polymer degradation (Fig 5.2) and one can be independent from the other, as recent studies have found that the type of drug incorporated within the polymer delivery vehicle may also play a role in regulating release rates (Siegel, S. J. et al. 2006). Drug release from PLGA nanoparticles (NPs) may occur via drug diffusion through the polymer matrix and/or through erosion of the polymer material. This process is influenced by a combination of factors including (i) surface modification of NPs, (ii) method of NP preparation, (iii) particle size, (iv) molecular weight of encapsulated drug and (v) the ratio of lactide to glycolide (LA:GA) moieties (Makadia, H. K. et al. 2011). Drug release patterns over time can be variable; high-performance liquid chromatography (HPLC) studies with PLGA microspheres incorporating protein (BSA) have shown non-linear and dose-dependent release profiles (Yang, Y. Y. et al. 2001).

Drug release as a result of polymer degradation is believed to be an autocatalytic process, as the number of carboxylic end groups increases during hydrolytic biodegradation. Drug release from PLGA NP biodegradation exhibits a biphasic curve pattern:

(1) Initial burst of drug release (dose dumping) is related to drug compound, concentration and hydrophobicity. Drug is released as a function of solubility and penetration of water into polymer matrix. Random hydrolysis of PLGA chains significantly decreases polymer Mw, but no appreciable weight loss or production of soluble polymer monomers.

(2) In the second phase, drug is released progressively through further depletion of polymer. Water inside the matrix hydrolyses polymer into soluble oligo- or monomeric products, creating a passage for diffusion of drug and further exposure for polymer erosion. Drug type plays an important role in attracting the aqueous phase into the matrix.

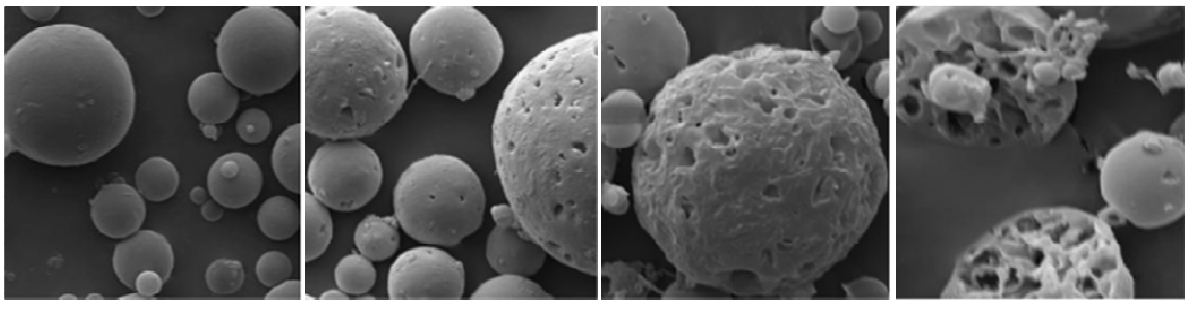

Figure 5.2. PLGA nanoparticle erosion over time; from left to right at 0 day, 1 week, 2 weeks and 5 weeks in PBS incubation media, pH 7.4. Particles prepared using the emulsification solvent evaporation method. Particle size increased from 150 to 345 nm during this period. *Taken from (Jain, A. K. et al. 2011).*

In vitro PLGA-nanoparticles are thought to enter cells either through fluid phase non-specific pinocytosis and/or through clathrin-mediated endocytosis (Vasir, J. K. et al. 2006). Vasir *et al*., have demonstrated rapid internalisation of PLGA NPs, which are able to escape endo-lysosomes due to transient and localised destabilisation of vesicular membranes, entering the cytoplasm within 10 min of incubation (Vasir, J. K. et al. 2006). As discussed in **Chapter 2**: Nanotechnology, NP surface charge plays an important role in their interaction with cells and subsequent intracellular uptake. Ionic interactions between positively charged particles and negatively charged cell membranes are believed to enhance non-phagocytic cellular uptake (Frohlich, E. 2012). Cationic nanoparticles have also shown an ability to escape from lysosomes and exhibit perinuclear localisation, whereas negatively or neutrally charged nanoparticles prefer to co-localise with lysosomes (Yue, Z. G. et al. 2011). However, non-specific uptake into macrophages (RES) *in vivo*, with untargeted pegylated positively charged NPs was higher compared to neutral particles on account of these properties (Yu, S. S. et al. 2012). PLGA nanoparticles used here have a slightly negative surface charge (ζ potential) which increases their colloidal stability due to dispersion by electrostatic repulsion (de Paula, C. S. et al. 2013) but particles with high anionicity also demonstrate greater non-specific uptake into macrophages (Raynal, I. et al. 2004;Yu, S. S. et al. 2012);. Surface modifications, such as pegylation or chitosan coating can alter particle surface charge to render particles less prone to opsonisation (Tahara, K. et al. 2009). However, macrophage uptake is believed to be more NP size-dependent, with studies carried out on a sub-100 nm pegylated polymeric NP range with different ζ potentials (between -9.0 mV and -3.5 mV), showing uptake was up to 42% more sensitive to particle size than charge (Yu, S. S. et al. 2012).

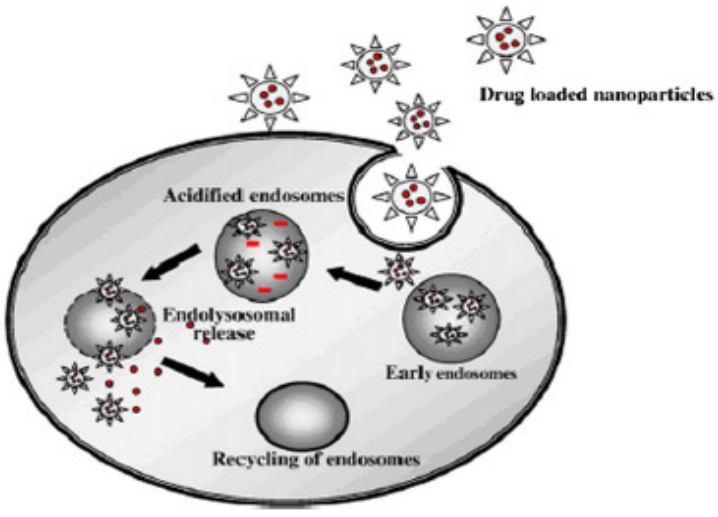

Figure 5.3. Schematic representation of intracellular uptake of PLGA nanoparticle (Acharya, S. et al. 2011).

Applications in PDT

Polymeric nanoparticles have been used with success for applications in PDT, incorporating various photosensitisers into different polymers and copolymers. Particles discussed here will largely focus on the utilisation of PLGA as the primary nanocomposite material (Table 5.2). Amphiphilic photosensitisers such as Hypericin and 5-aminolevulinic (ALA) have been encapsulated into the copolymer matrix of PLGA NPs. Recently, ALA PLGA NPs of ~65 nm diameter, with a PS encapsulation efficiency of 65%, have been studied *in vitro* in human skin squamous carcinoma cells (Shi, L. et al. 2013). This yielded positive results, with ALA uptake observed in the cell cytoplasm and more effective PDT to tumour cells (% cell survival) following 24 h incubation with loaded NPs than with free ALA alone at the same concentration (Shi, L. et al. 2013). Due to their insolubility in water, hydrophobic photosensitisers, such as AlClPc, ZnPc, ICG, Verteporfin, m-THPC, p-THPP have also been packaged into PLGA NPs for improved systemic administration (Table 5.2). Recently, Silva de Paula *et al*., observed a significant phototoxic effect of ≥80% cell kill in human fibroblasts at low laser light doses (3 J/cm^2) with AlClPc incorporated in nanocapsules comprised of either PLGA, PLA or PEG-PLA NPs (140-270 nm in diameter, ~60-90% encapsulation efficiency) compared to free AlClPc (de Paula, C. S. et al. 2013). PLA-PEG and PLGA NPs also showed the lowest AlClPc drug release *in vitro* compared to PLA. m-THPC-loaded PLGA NPs were found to completely eradicate dark toxicity effects of m-THPC *in vitro* in human colon carcinoma cells (HT29) (Low, K. et al. 2011) compared to free drug. In other studies performed with PLGA and PEG-PLGA NPs encapsulating m-THPC, a faster and greater release of m-THPC in 10% FBS was detected through ultracentrifugation with PEG-PLGA NPs but a significant reduction in m-THPC uptake into A549, MCF10A neoT and U937 cell lines was observed with pegylated NPs compared to PLGA NPs, demonstrating their stealth properties. Bioluminescence imaging *in vivo* (athymic nude-Foxn1 mice) of whole organs, with similar PLGA NPs as used in studies here, did not show any significant difference in m-THPC uptake in various tissues at 24 h post *i.v.* injection (0.3 mg kg^{-1} m-THPC) between pegylated and non-pegylated PLGA NPs, however, this was partially dependent on the optical properties of each tissue (Rojnik, M. et al. 2012).

Photosensitiser	NP polymer	Publication
5-aminolevulinic acid (ALA)	PLGA	Shi L, 2013
Chloro(29H,31H-phthalocyaninato)aluminium (AlClPc)	PLGA	Silva de Paula C, 2013
	PLA	
	PEG-PLA	
meta-tetra(hydroxyphenyl)chlorin (m-THPC)	PLGA	Rojnik, 2011
	PEG-PLGA	
Zinc (II) phthalocyanine (ZnPc)	PLGA	Fadel, 2009
Hypericin (Hy)	PLGA	Zeisser-Labouebe, 2006
	PLA	
Indocyanine green (ICG)	PLGA	Gomes A, 2006
Verteporfin (Visudyne)	PLGA	Konan-Kouakou, 2005
Bacteriochlorophyll-a (BChl-a)	PLGA	Gomes A, 2005
meso-tetra(hydroxyphenyl)porphyrin (p-THPP)	PLGA	Konan, 2003
	PLA	

Table 5.2. PLGA-based nanoparticles currently being developed for the delivery of photosensitisers for PDT. *Further details can be found in (Chatterjee, D. K. et al. 2008a).*

The aim of the present study was to investigate the *in vivo* biodistribution, accumulation and photodynamic efficacy of m-THPC when non-covalently incorporated into biodegradable polymeric nanoparticles in comparison to standard Foscan (m-THPC). Nanoparticles were synthesised and characterised by collaborators at the University of Ljubljana using a commercially available diblock copolymer, PEG-PLGA, and a non-pegylated PLGA copolymer. As with liposomal studies, m-THPC tissue accumulation was assessed in subcutaneous syngeneic fibrosarcoma (MC28) Hooded Lister rat models at selected time points. These results were correlated with PDT efficacy to tumours *in vivo* using identical time periods for selected drug to light intervals for PDT treatment. To our knowledge, these are the first *in vivo* PDT studies to be carried out incorporating m-THPC in PLGA NPs.

5.2 Materials & Methods

5.2.1 Chemicals and Photosensitisers

Poly(lactic-co-glycolic acid) (PLGA) and pegylated (PEG) PLGA NPs were prepared and supplied by Dr Kos' group at the University of Ljubljana using a modified nanoprecipitation method (Kocbek, P. et al. 2010) *(see **Appendix I – B.1 Nanoprecipitation method: PLGA NPs**)*. Brief preparation protocol as described by (Rojnik, M. et al. 2012): 45 mg of PLGA (Resomer RG 503H, Boehringer, Germany) and 5 mg of m-THPC (Biolitec AG, Germany) were dissolved in 1 ml acetone and the solution was slowly injected into 50 ml of 0.25% (w/v) poloxamer 188 (Lutrol F68, Sigma, UK) water solution with moderate magnetic stirring. The resulting NP dispersion was stirred for 15 min at RT and centrifuged at 15,000 rpm for 15 min to separate NPs from non-incorporated m-THPC and excess stabiliser. NPs were washed with 20 ml of distilled water, centrifuged at 15,000 rpm for 15 min, and dispersed in 10 ml of 5% (w/v) aqueous trehalose (Sigma, UK) solution. The NPs were freeze-dried at RT and 0.090 mbar for 24 h (Christ Beta 18–K, Germany) for storage and shipment. Pegylated NPs were prepared by the same procedure. A 1:1 weight ratio of PLGA (Resomer RG 503H) and PEG-PLGA (Resomer RGP d 50155) was used for preparation of pegylated NPs. NPs were characterised at the University of Ljubljana through photon correlation spectroscopy (PCS) using a Zetasizer Nano ZS (Malvern Instruments, Worcestershire, UK) to determine polydispersity index (PDI) and mean particle diameter (Table 5.3). Particle charge was quantified as ζ-potential by laser Doppler anemometry using a Zetasizer Nano ZS (Malvern). The total amount of m-THPC entrapped in NPs was measured by fluorescence spectroscopy after complete dissolution of the NPs in DMSO (Sigma, UK). m-THPC fluorescence was detected at λ_{exc} = 423 nm, λ_{em} = 652 nm.

Immediately prior to experiments, 1 mg of lyophilised PLGA and PEG-PLGA NPs supplied were re-suspended in 1 mL phosphate buffered saline (PBS) and transferred between a vortex and water bath ultrasonicator for 10 mins to obtain a homologous dispersion (avoid aggregation and sedimentation).

5.2.2 Absorbance spectra

The absorbance spectra of m-THPC in Foscan, PLGA and PEG-PLGA NPs were recorded using a Lambda 25-UV/Vis spectrophotometer (Perkin-Elmer, UK) as described in

Chapter 4: Liposomes. Samples were diluted in either PBS (saline) or solvent (dimethyl sulfoxide (DMSO), Sigma, UK) at equivalent m-THPC concentrations (10 μM) to ensure the characteristics of the absorbance spectrum of m-THPC had not been altered following encapsulation and release.

5.2.3 Fluorescence spectra

The fluorescence emission spectrum of noncovalently entrapped m-THPC in the copolymer matrix of PLGA and PEG-PLGA NPs (and that partially bound to the particle surface) was measured in stock solutions of PBS (pH 7.4) or DMSO (dissolution) at equivalent m-THPC concentrations. Additionally, fluorescence emission spectra of m-THPC formulations in Solvable were measured to construct calibration curves for pharmacokinetic studies (data not shown) as described in **Chapter 4**: Liposomes.

In a separate group of animals (no tumour) to those used in pharmacokinetic studies, *ex vivo* fluorescence emission spectra of m-THPC were taken from freshly excised rat liver tissue using a USB4000 Ocean Optics fibre-optic CCD spectrometer (Ocean Optics, U.K). Measurements were obtained from liver tissue removed immediately post-mortem at either 10 mins, 30 mins or 24 h (Table 5.2) following an intravenous tail vein injection of 0.3 mg kg^{-1} m-THPC for either Foscan, PLGA or PEG-PLGA NPs. Excitation was provided by a 405 nm blue emitting diode laser (Photonic Products, U.K.) and light was delivered via an optical fibre held in direct contact with the surface of the rat liver tissue. A second fibre was coupled to the spectrophotometer and a CCD capture transferred to a PC for fluorescence spectrum acquisition. Fluorescence measurements were recorded at three different sites in triplicate. Control groups did not receive an injection of m-THPC.

5.2.4 Confocal microscopy in vitro

For visualisation of m-THPC uptake and intracellular localisation following encapsulation in PLGA NPs, confocal microscopy was employed. 1 x 10^4 MC28 (rat fibrosarcoma) cells were prepared using identical incubation conditions and fluorodish seeding methods as described in **Chapter 4**: Liposomes. Cells were incubated for 4 h with either: 1 μM m-THPC (Foscan), 1 μM m-THPC in PLGA NPs or PEG-PLGA NPs (- FCS) or 1 μM m-THPC in PLGA NPs or PEG-PLGA (+ 10% FCS). Control cells were incubated without m-THPC. Following incubation, cells were washed twice with PBS before fresh media (minus serum and phenol red) was added.

5.2.5 Animals and tumour model

Female Hooded Lister (HL) rats (150–220 g) were used for all PLGA NP *in vivo* studies. The methylcholanthrene-induced fibrosarcoma cell line (MC28) was cultured and transplantaed into animals as described in **Chapter 4**: Liposomes. Following obtainment of sufficient tumour size between 7-10 days, m-THPC loaded PLGA or PEG-PLGA NPs were administered intravenously via a tail vein injection at a dose of 0.3 mg kg^{-1} m-THPC *(see **Appendix I – A.1 Dosage Calculations**)*. Animals were killed by cervical dislocation.

5.2.6 Biodistribution studies

Tissue samples selected for biodistribution studies were as described in **Chapter 4**: Liposomes. Immediately post-mortem tissues were removed under subdued lighting at 24 and 72 h from HL rats after intravenous administration of 0.3 mg kg^{-1} m-THPC in each PLGA NP formulation. m-THPC extraction from tissues and detection was acquired using the same equipment, under identical conditions, following the same methodologies and mathematical models as described in **Chapter 4**: Liposomes.

5.2.7 Confocal microscopy ex vivo

Confocal microscopy was used to obtained images of m-THPC localisation in fresh *ex vivo* liver tissue from HL rats (no tumour) following intravenous administration of 0.3 mg kg^{-1} m-THPC in either PLGA or PEG-PLGA NPS. Tissue samples were removed and observed immediately post-mortem using an inverted Olympus Fluoview 1000 confocal laser scanning microscope. Fluorescence confocal images were obtained using x60 magnification using an oil immersion objective (Olympus). Fluoview FV1000 (Olympus) and Image J software were used to analyse images. m-THPC fluorescence was detected between 640-80 nm following excitation with a blue 405 nm laser (m-THPC λ_{exc} = 423 nm, λ_{em} = 652 nm). Laser voltage, Gain and Offset were kept consistent throughout imaging.

5.2.8 Fluorescence lifetime studies

The fluorescence lifetimes of non-covalently entrapped m-THPC in PLGA and PEG-PLGA NPs were measured in stock solutions of PBS (pH 7.4) or following NP dissolution in DMSO at equivalent m-THPC concentrations (as described in ***5.2.3 Fluorescence Spectra***) in quartz cuvettes with a light path-length of 1 cm (Pye Unicam, UK). Control

solutions of m-THPC in DMSO only were run simultaneously but no lifetime data was recorded for m-THPC in PBS as m-THPC is insoluble in aqueous buffer.

Ex vivo fluorescence lifetime measurements of m-THPC were taken from freshly excised rat liver tissue (as described in ***5.2.3 Fluorescence Spectra***). Measurements were obtained from liver tissue removed immediately post-mortem at either 10 mins, 30 mins or 24 h (Table 5.2) following an intravenous tail vein injection of 0.3 mg kg^{-1} m-THPC in either Foscan, PLGA or PEG-PLGA NPs. Fluorescence lifetime data were obtained using time correlated single photon counting (TCSPC) (PC-mounted TimeHarp 100 board, Picoquant, Germany). The light source was a 405 nm pulsed laser diode (ELP-405, Edinburgh Instruments, UK) with a pulse duration of 90 picoseconds and a 5 MHz repetition rate. Samples were excited using a fibre-optically coupled picosecond 405 nm laser diode and fluorescence was detected using a fast multi-alkali photomultiplier (H5773-04, Hamamatsu Photonics K.K., U.K.) via a monochromator (M300, Bentham Instruments, U.K.) and longpass filter (OG510, Schott, U.K.). An Instrument Response Function (IRF) was also recorded to determine the temporal response of the detection system. For *ex vivo* samples a fibre probe was placed and fixed in direct contact with the surface of the tissue to deliver a uniform distribution of light (power density: 2 mW cm^{-2}). The fibre was cleaned with alcohol between measurements to remove traces of blood and tissue, which may have given rise to false positive readings. Approximately five measurements were taken for each sample and readings averaged. Results were analysed with Picoquant Fluofit Software (Picoquant, Germany) to obtain lifetimes.

Derivations of fluorescence lifetimes

The time-resolved fluorescence intensity decays *d(t)* were fitted to a sum of exponentials, as described in equation *5.1*.

$$d(t) = \sum_{i=1}^{n} \left[A_i \exp\left(-\frac{t - t_s}{\tau_i} \right) \right] \tag{5.1}$$

The definition of the fitting parameters is as follows:

A_i; Amplitude of the i^{th} component in counts (also as the pre-exponential factor). Therefore for the 50:50 mixture of two species, the values of *A* for each component would be 0.5.

τ_i: Lifetime of the i^{th} component

To obtain the time-integrated signal d(int), *i.e.* over the whole decay, for a bi-exponential fit (two fluorescence lifetimes) the equations *5.2* and *5.3* were used:

$$d(t) = A_1 \exp(-t/\tau_1) + A_2 \exp(-t/\tau_2) \quad (5.2)$$

$$d(int) = A_1\tau_1 + A_2\tau_2 \quad (5.3)$$

The integrated fluorescence is proportional to the weighted average of the lifetimes which is mathematically equivalent to the 'mean' lifetime. Fluorescence decays were analysed using proprietary fitting software (Fluofit, Picoquant GmbH).

5.2.9 Fluorescence microscopy (frozen tissue sections)

Animal tissues were removed post-mortem and snap frozen in liquid nitrogen under isopentane (VWR, UK) 24 h and 72 h post-intravenous injection with 0.3 mg kg^{-1} m-THPC in PLGA and PEG-PLGA NPs. 10 micron frozen sections of liver, spleen, lung, kidney and tumour tissue were cut using a cryostat and mounted on polylysine treated glass slides (VWR, UK). On average ten sections were taken per tissue sample from three animals. Sections were exposed to blue light for 10 secs using a 405 nm laser (3 mW) to excite m-THPC and detect fluorescence in tissues. CCD false coloured fluorescence microscopy images (512 pixels) were obtained with a PIXI 512 CCD camera (Princeton Instruments, USA) coupled to an inverted Olympus IMT-2 microscope (Olympus). This system was equipped with a dichroic mirror (505DCLP, Omega) and filters were set as follows: 660 nm DF33 bandpass filter, 595 nm long pass filter and 500 nm ACSP short pass filter. Sections were imaged at x10 magnification and analysed through WinSpec32 software (Roper Science Software). The image resolution was 512 x 512 pixels, corresponding to 557 x 557 microns.

5.2.10 Photodynamic therapy on MC28 tumours

Injected doses of 0.3 mg kg^{-1} of m-THPC in PLGA or PEG-PLGA NPS were administered to HL tumour animals prior to light delivery. Drug-light intervals of 24 h and 72 h were chosen based on pharmacokinetic data. Tumours were irradiated with red light using a 400 µm bare-cleaved tip optical fibre inserted approximately 1 mm into the tumour capsule via a small incision in the overlying skin and tumour capsule, to mimic interstitial clinical PDT with Foscan. A total of 10 J of light at 100 mW for 100 s was delivered from a 652 nm diode laser. Treatment with each m-THPC formulation was initiated when tumours had reached an optimal diameter of 10 mm. Each treatment group consisted of four animals. Animals were killed 24 h after treatment by cervical dislocation and whole tumours resected for histological analysis.

5.2.11 Histology and measuring necrosis (Hamamatsu Nanozoomer)

Treated tumour tissue samples were removed post-mortem and prepared by routine methods for histological analysis as described in **Chapter 4**: Liposomes. The damage was calculated from each tumour as a percentage of the whole tumour surface area. Six sections were averaged per tumour (3 from each tumour half). The mean percentage surface area of tumour necrosis was calculated through blind analysis per group of four identically treated animals and all data were represented as mean±SD.

5.2.12 Statistical analysis

Mean and standard deviation was calculated for each animal group (±SD, n=3–5). All data were represented as mean±SD. Statistical analysis was carried out using a two-tailed Student's t-test and a Mann–Whitney U test for PDT data. $p \leq 0.05$ was considered statistically significant, unless stated otherwise.

5.3 Results

5.3.1 Polymeric Nanocarriers

	PLGA NPs		*PEG-PLGA NPs*	
Size (nm)	179.0 ± 0.3	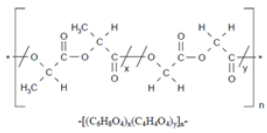	144.7 ± 2.0	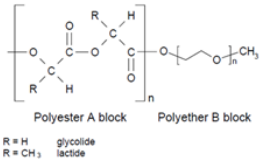
Charge	-5.5 ± 0.4		-2.5 ± 1.1	
PDI	0.27 ± 0.01	***PLGA**: Resomer RG® 503 H (Boehringer Ingelheim Ltd)*	0.13 ± 0.01	***PEG-PLGA**: Resomer RGP® d50155 (Boehringer Ingelheim Ltd)*
m-THPC (%, w/v)	6.90		6.70	

Table 5.3. Specifications of m-THPC loaded PLGA and pegylated PLGA NPs used in this investigation.

i. Absorption spectra

An absorbance spectrum of m-THPC in Foscan, PLGA and PEG-PLGA NPs was taken in PBS (dilution buffer), as when administered in animals (Fig 5.4) to deduce peak absorbance wavelengths.

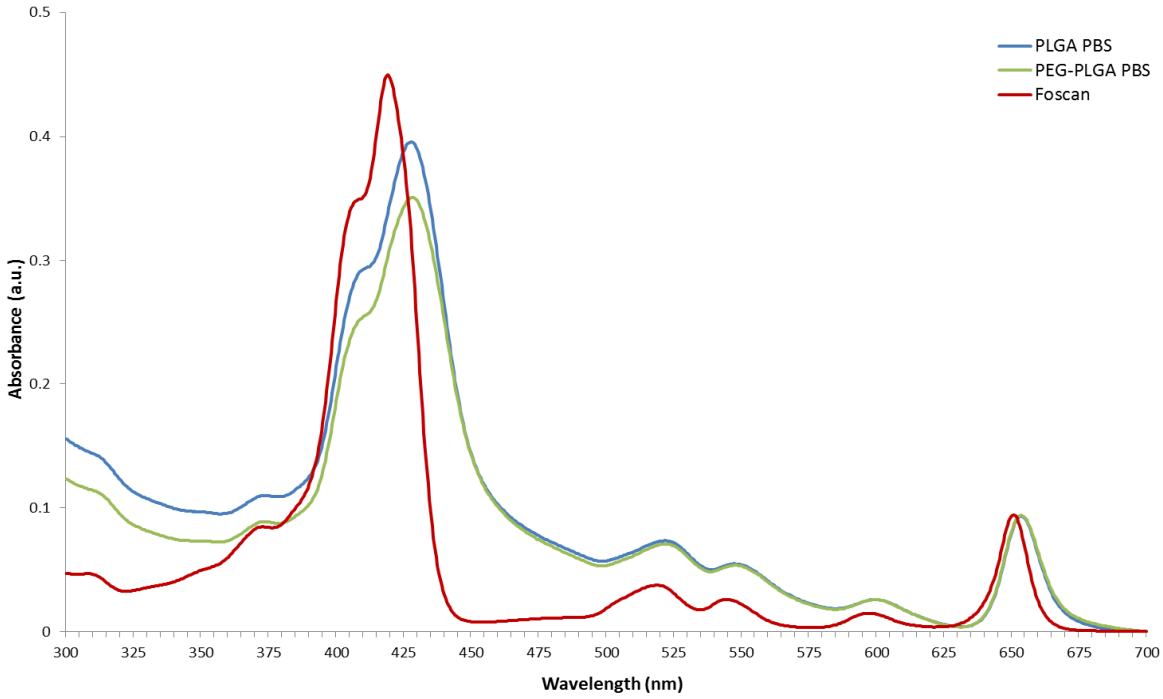

Figure 5.4. Absorbance spectra of m-THPC in Foscan and noncovalently incorporated in PLGA and pegylated PLGA nanoparticles in PBS. All solutions prepared at 10 µM m-THPC concentrations.

As described in the previous chapter (**Chpt 4**: Liposomes), Foscan demonstrated two strong absorbance peaks (Fig 5.4) with absorption maxima at ~ 423 nm (Soret band) and 652 nm (Q band), characteristic of m-THPC (Bonnett, R. et al. 1989b). When non-covalently incorporated in PLGA and PEG-PLGA polymer matrices, m-THPC demonstrated a slight peak broadening and small bathochromic shifts for both absorbance peaks; m-THPC λ_{exc} = 425 nm, λ_{em} = 654 nm, in comparison to Foscan. An absorbance spectrum could not be taken for pure m-THPC in PBS due to its hydrophobicity.

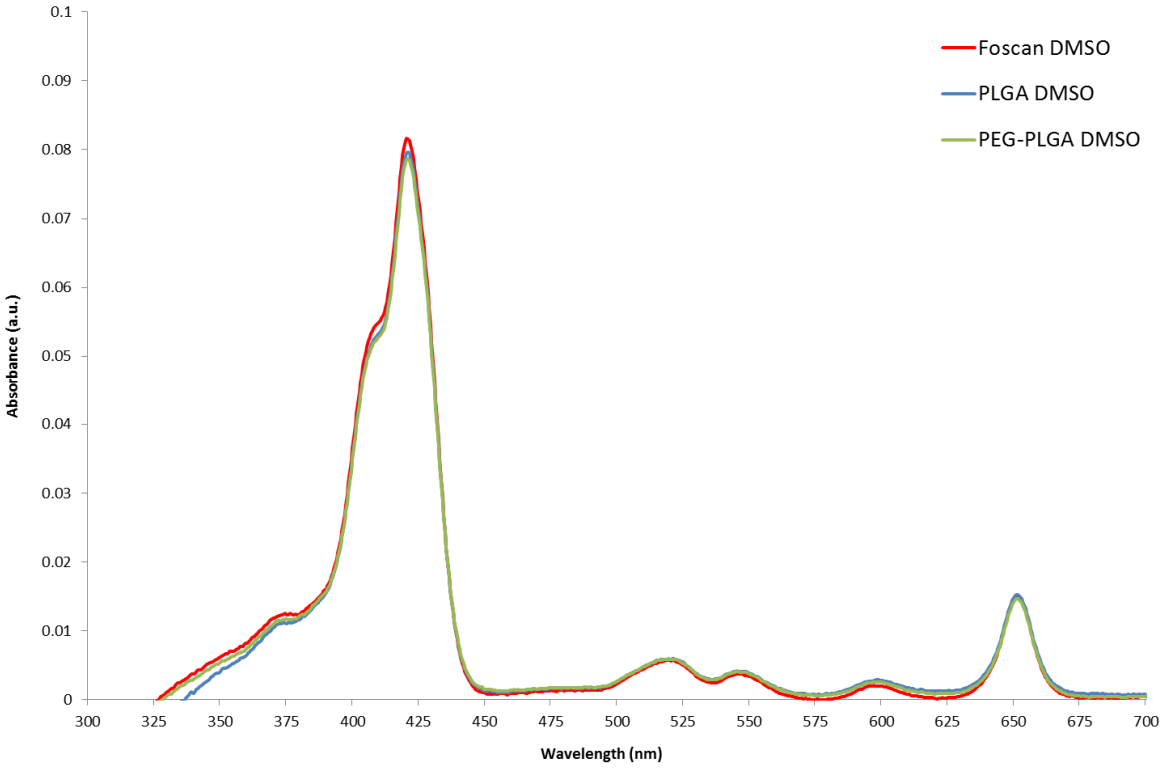

Figure 5.5. Absorbance spectra of m-THPC in Foscan and noncovalently incorporated in PLGA and pegylated PLGA nanoparticles in dimethyl sulfoxide (DMSO). All solutions prepared at 0.5 µM m-THPC concentrations.

Dimethyl sulfoxide (DMSO) is a solvent used for its ability to dissolve a wide range of analytes. DMSO disrupts PLGA polymer chains and causes NP collapse, releasing and solubilising m-THPC into its monomeric form. It was employed for absorbance spectra measurements and corresponding fluorescence spectra lifetime studies (Table 5.4) of m-THPC in Foscan, PLGA and PEG-PLGA NPs *(also see **Appendix I – B.2 Absorbance spectra of PLGA NPs in MeOD**)*. No spectral shift or peak broadening was detected for m-THPC in PLGA and PEG-PLGA NPs compared to Foscan in DMSO (Fig 5.5). Absorbance maxima for all m-THPC formulations in DMSO were recorded at 423 nm and

652 nm, respectively. There was an absence of light scattering between 300-400 nm compared to spectra taken in PBS, suggesting complete disruption of polymer NPs and m-THPC micelles (Foscan). Slight differences in absorbance maxima (Ab = εcl) may be due to experimental error in preparing solutions (c = concentration).

Absorbance measurements of m-THPC in PLGA and PEG-PLGA NPs in Solvable displayed similar spectra (data not shown), with a less pronounced shoulder on the Soret peak (~423 nm), as observed with m-THPC incorporated in liposomes (**Chpt 4**: Liposomes).

ii. Fluorescence spectra

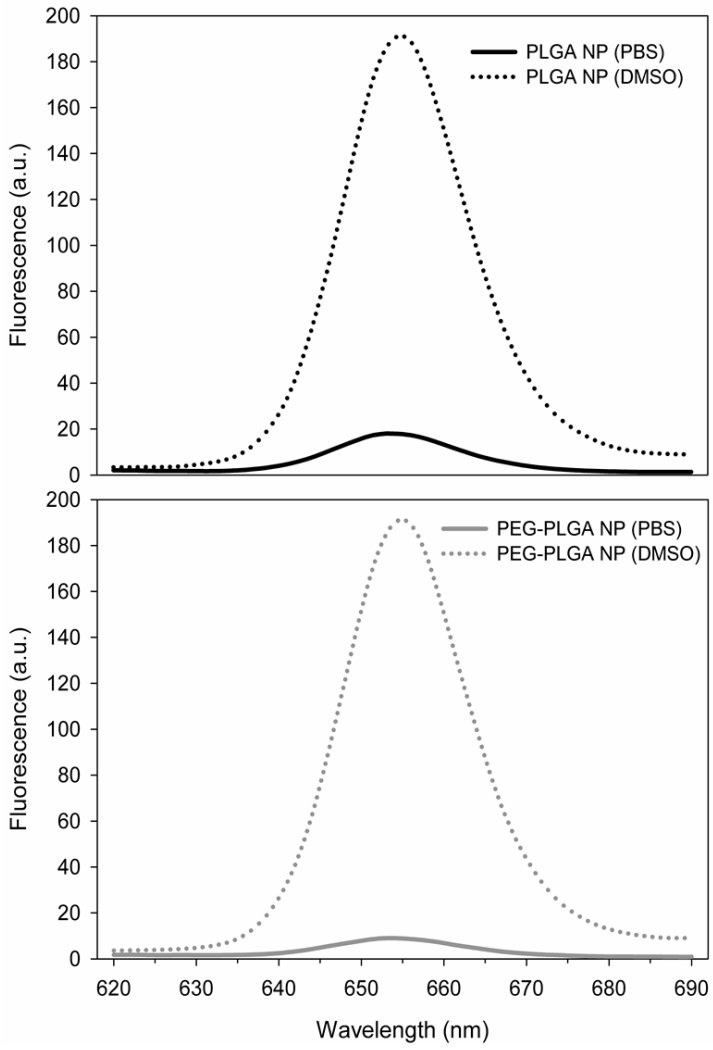

Figure 5.6. Fluorescence emission spectra of m-THPC in PLGA and pegylated PLGA NPs in loading buffer (PBS) or when dissolved in DMSO, using an excitation wavelength of 423 nm. Peak emission was recorded at 652 nm.

The fluorescence emission spectrum of m-THPC was recorded for PLGA and PEG-PLGA NPs in DMSO or loading buffer (PBS). Peak m-THPC fluorescence emission, using 423 nm light excitation, was recorded at 652 nm in PBS for PLGA and PEG-PLGA NPs but a small red-shift to 654 nm was observed for both NPs in DMSO. A large reduction in m-THPC fluorescence intensity was observed with PLGA and PEG-PLGA NPs in PBS loading buffer in comparison to DMSO (dissolution), by factors of 11 and 21, respectively (Fig 5.6). The Soret band (~423 nm) was also noticeably broader for NPs in DMSO (data not shown). m-THPC loading was similar for both NPs: 6.9% w/w PLGA and 6.7% w/w PEG-PLGA (Rojnik, M. et al. 2012).

Corresponding fluorescence lifetime data of m-THPC in Foscan, PLGA and PEG-PLGA NPs was taken in the same solutions (PBS and DMSO) and in *ex vivo* liver following intravenous injection of 0.3 mg kg^{-1} m-THPC in each formulation (Fig 5.10-12) at shorter (10-30 mins) and longer time (24 h) intervals (Table 5.4).

iii. Confocal microscopy in vitro

Confocal microscopy was used to image MC28 tumour cells following 4 h incubation with 1 μM m-THPC in Foscan, PLGA or PEG-PLGA NPs, either in the presence or absence of 10% FCS. Confocal images showed a strong uptake of m-THPC into the cytoplasm of healthy dividing tumour cells with Foscan (Fig 5.7 B), determined by a strong fluorescence intensity (white) and a dark nucleus. For both PLGA and PEG-PLGA NPs, m-THPC fluorescence is greater than the control group (without m-THPC), however, the presence of frequent bright white spots indicative of particle precipitation, aggregation and/or sedimentation can be observed in the absence of FCS (Fig 5.7 C & D) in comparison to the presence of 10% FCS (Fig 5.7 E & F). Control cells showed a low background level of autofluorescence (Fig 5.7 A).

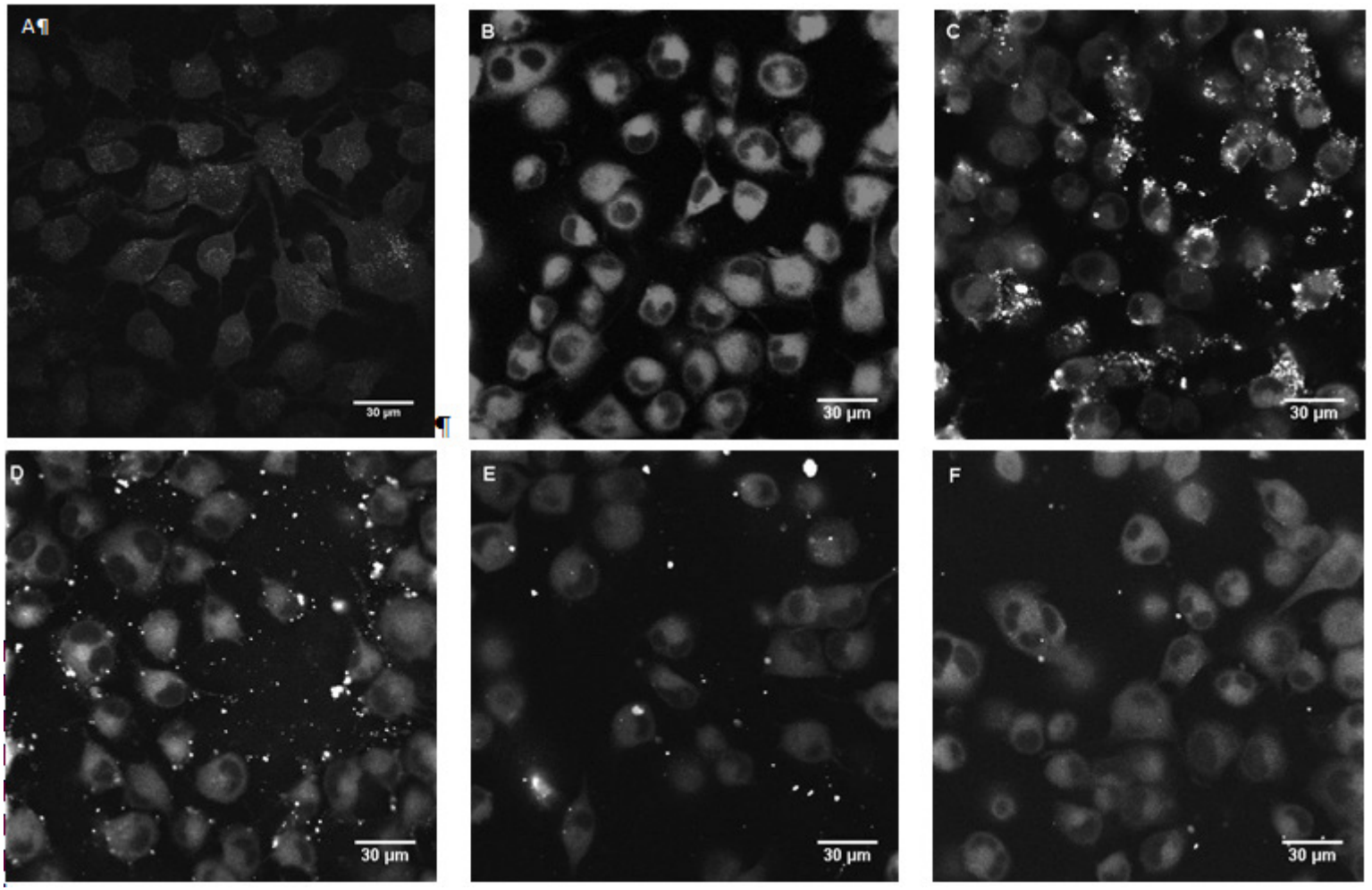

Figure 5.7. Confocal microscopy imaging: Qualitative uptake and localisation of m-THPC *in vitro* in MC28 cells of different formulations after 4 hours incubation. (**A**) Control MC28 cells (no m-THPC), (**B**) 1 µM Foscan (+) FCS, (**C**) 1 µM PLGA NPs (-) FCS, (**D**) 1 µM PEG-PLGA NPs (-) FCS, (**E**) 1 µM PLGA (+) 10% FCS, (**F**) 1 µM PEG-PLGA (+) 10% FCS.

iv. Biodistribution studies

Uptake and Distribution of Photosensitiser in Tissues

Biodistribution studies with m-THPC in non-pegylated PLGA or pegylated PLGA NPs were carried out with reference to standard Foscan formulation. Doses of 0.3 mg kg^{-1} (m-THPC drug equivalent) were administered in Hooded Lister rats implanted with subcutaneous tumours for analysis over selected time periods to measure levels of m-THPC in tissues using chemical extraction. Time intervals were chosen based on previous data from biodegradable pegylated nanocarrier systems (**Chpt 4**: Liposomes) in order to reduce animal numbers.

A range of organs were selected for quantitative analysis to compare the relative uptake of m-THPC to that of tumour tissue when delivered by PLGA NP formulations versus standard Foscan. At 24 h, m-THPC concentrations in the blood serum were more than four-fold lower when administered in Foscan (0.05 μg mL^{-1}) compared to its encapsulation in either PLGA or PEG-PLGA NPs (0.3-0.4 μg mL^{-1}) (Fig 5.8 A). By 72 h traces of m-THPC (Foscan) and in PLGA NPs are still detectable in the blood serum (Fig 5.8 B). The highest m-THPC concentrations were observed in the liver and spleen for all m-THPC formulations at 24 h. In both organs a much greater uptake of m-THPC in PLGA (~1.8 μg g^{-1}) and PEG-PLGA NPs (~1.5 μg g^{-1}) was observed in comparison to Foscan (~1.2 μg g^{-1}) but these concentrations were greatly reduced to levels below that of Foscan in the liver by 72 h. The m-THPC concentration for PLGA and PEG-PLGA NPs was almost 10 times greater (~1.5 μg g^{-1}) in the lung compared to Foscan (~0.15 μg g^{-1}) at 24 h, however, as observed in the liver and spleen, this was dramatically reduced by 72 h (≥0.25 μg g^{-1}). The biodistribution kinetics of m-THPC in the kidney showed some unexpected results. Foscan was observed at a higher concentration (~0.5 μg g^{-1}) than m-THPC-loaded NPs (~0.15 μg g^{-1}) in the kidneys which continues to increase by 72 h (~0.75 μg g^{-1}). Accumulation of m-THPC in skin tissue showed an increase in m-THPC accumulation with PLGA and PEG-PLGA NPs (~0.15 μg g^{-1}) in comparison to Foscan (~0.05 μg g^{-1}), which appears to be retained over 72 h. In tumour tissue an increase in m-THPC uptake was observed with both PLGA NPs (~0.8 μg g^{-1}) of more than two-fold in comparison to Foscan (~0.25 μg g^{-1}) at 24 h, however, this was not significant with PLGA NPs. By 72 h, m-THPC in PLGA NPs (~0.6 μg g^{-1}) remains significantly higher than Foscan (~0.15 μg g^{-1}), by approximately four-fold, whereas PEG-PLGA m-THPC concentrations are similar to that of Foscan *(also see **Appendix I – B.4 %ID/g of m-THPC in polymeric NPs in vivo**).*

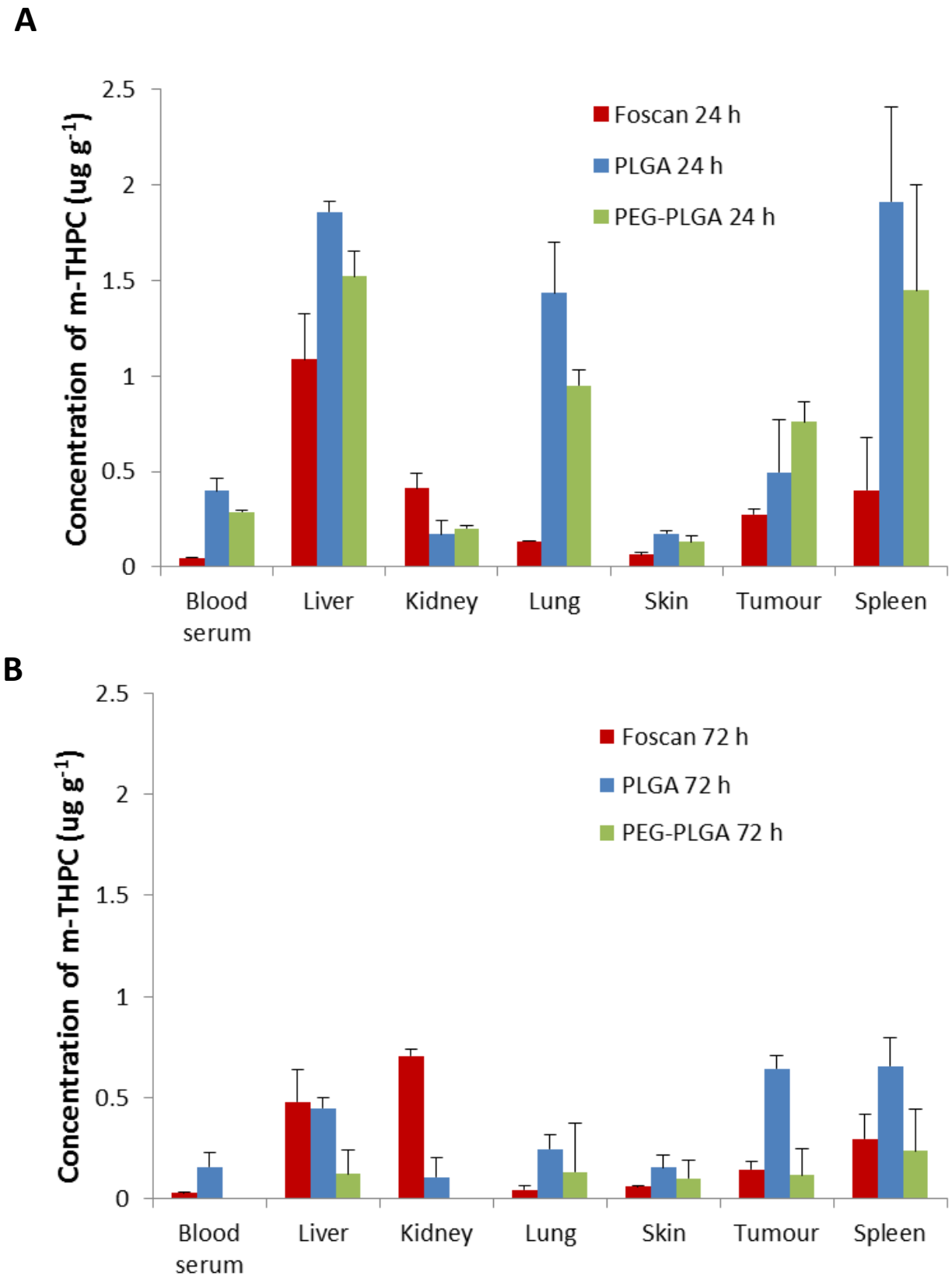

Fig 5.8. Concentration of m-THPC in selected tissues of the Hooded Lister rat following an intravenous injection of 0.3 mg kg^{-1} m-THPC in Foscan, PLGA and PEG-PLGA nanoparticles at (A) 24 h and (B) 72 h. Data points show the mean ± s.d., n = 4.

v. Confocal microscopy ex vivo

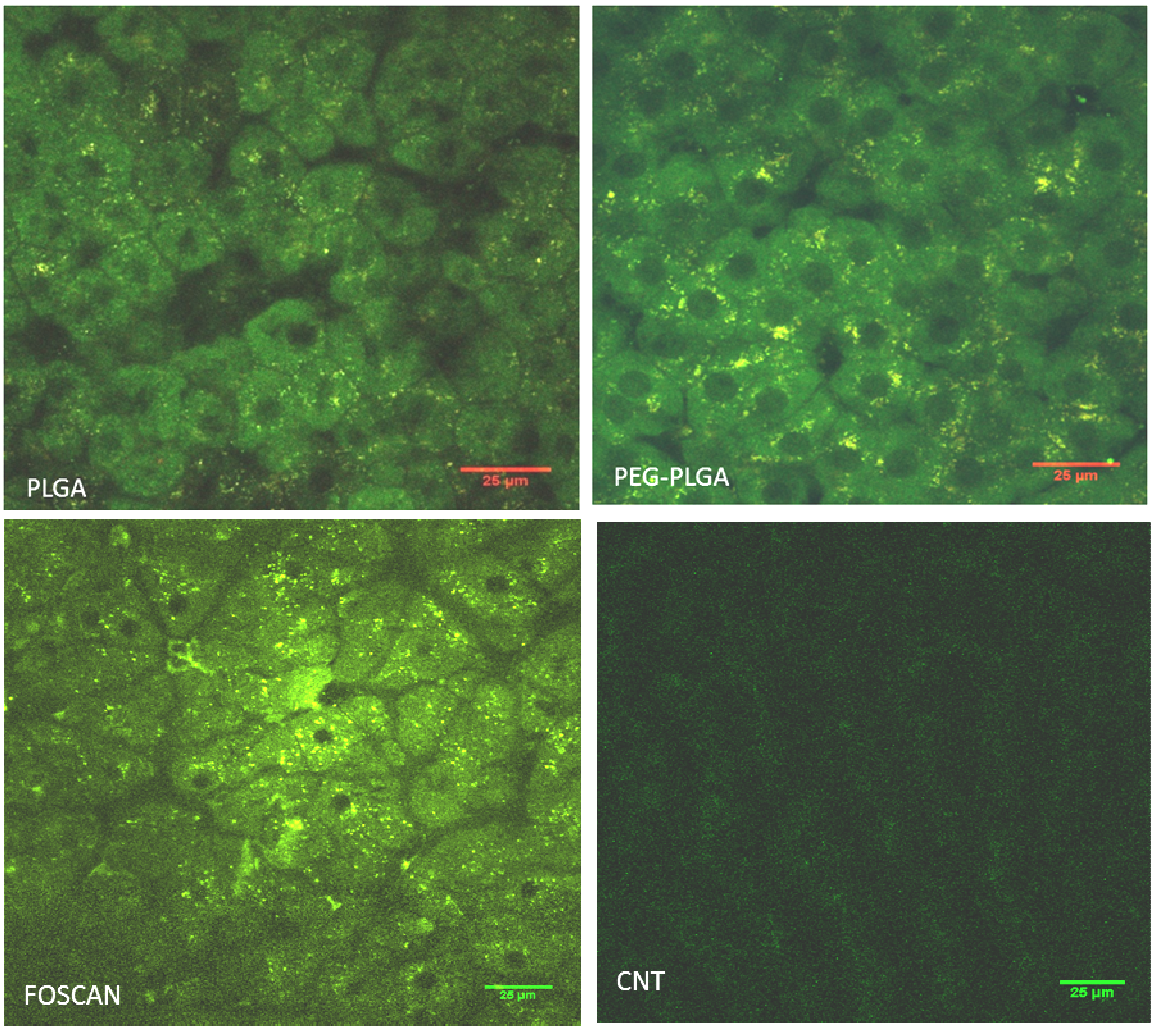

Fig 5.9. Confocal microscopy of m-THPC in *ex vivo* rat liver tissue at 24 h following an intravenous injection of 0.3 mg kg^{-1} m-THPC in Foscan (micellular), PLGA or PEG-PLGA NPs, CNT (control; without m-THPC).

Confocal microscopy images of *ex vivo* rat liver tissue following *i.v.* administration of 0.3 mg kg^{-1} m-THPC in either Foscan, PLGA or PEG-PLGA NPs (Fig 5.9) shows the presence of large hepatocytes (green autofluorescence) with a dark nucleus and yellow fluorescence, indicative of m-THPC fluorescence, at 24 h. This fluorescence appears in discrete bright yellow spots and may suggest localisation in the cytoplasm of hepatocytes in endo-lysosomal compartments. These images appear to show a greater distribution of Foscan in comparison to polymeric NPs at 24 h. Control images (without m-THPC) demonstrated a slight green autofluorescence from liver tissue.

vi. Fluorescence lifetime ex vivo studies

Following excitation, m-THPC decays back to a ground state (S_0) through a number of different (radiative and/or non-radiative) decay pathways, the rate of which can be measured from fluorescence lifetime. Fluorescence lifetime studies were carried out to investigate the decay rate of m-THPC fluorescence when non-covalently incorporated in PLGA and PEG-PLGA NPs in different solutions (PBS and DMSO) and in *ex vivo* rat liver tissue following intravenous injection of 0.3 mg kg^{-1} m-THPC equivalent (Table 5.4). As observed with fluorescence emission spectra of m-THPC encapsulated in PLGA and PEG-PLGA NPs (Fig 5.6), a large reduction in m-THPC fluorescence intensity was observed in PBS (loading buffer) in comparison to DMSO (dissolution), by factors of 11 and 21, respectively (Fig 5.6). This corresponded to fluorescence lifetime data (Table 5.4), which showed a significant change in fluorescence lifetimes ($\boldsymbol{\tau}$) between the two solvents. In DMSO, all m-THPC formulations demonstrated mono-exponential decays ($\mathbf{A_1}$) with identical lifetimes (~9.5 ns), however, in PBS, multi-exponential decays ($\mathbf{A_1 + A_2}$) with significantly shorter lifetimes were observed for both the polymeric NPs. Using bi-exponential fitting, the lifetimes of PEG-PLGA NPs in PBS were shorter (3.2 and 1.4 ns) than for PLGA NPs (6.2 and 2.3 ns). Lifetime data for m-THPC was collected in DMSO only due to its insolublity in PBS (Table 5.4).

Formulation	$\boldsymbol{\tau_1}$ **(ns)**	$\mathbf{A_1}$ **(%)**	$\boldsymbol{\tau_2}$ **(ns)**	$\mathbf{A_2}$ **(%)**
PLGA in PBS	6.2	67	2.3	32
PEG-PLGA in PBS	3.2	27	1.4	73
m-THPC in DMSO	9.6	100	-	-
PLGA in DMSO	9.5	100	-	-
PEG-PLGA in DMSO	9.5	100	-	-
PLGA LIVER 10 mins	6.1	43	1.0	57
PLGA LIVER 24 h	9.5	63	0.8	37
PEG-PLGA LIVER 10 mins	7.8	66	1.4	34
PEG-PLGA LIVER 24 h	8.4	100	-	-

Table 5.4. Fluorescence lifetimes ($\boldsymbol{\tau}$) of m-THPC in pegylated (PEG-PLGA) and non-pegylated (PLGA) NPs in PBS (loading buffer) and dimethyl sulfoxide (DMSO) solution, with pre-exponentional factors (**A**), and in *ex vivo* rat liver tissue following an intravenous injection of 0.3 mg kg^{-1} m-THPC equivalent at 10 or 30 mins and 24 h. *Results part-published in (Rojnik, M. et al. 2012).*

The fluorescence lifetimes of m-THPC (Table 5.4, Fig 5.10-12 A) and corresponding fluorescence emission spectra were also recorded on the outer surface of freshly excised *ex vivo* rat liver tissue following intravenous administration of 0.3 mg kg^{-1} m-THPC in PLGA (Fig 5.10 C) and PEG-PLGA NPs (Fig 5.11 C) at either 10 mins or 24 h. m-THPC in PLGA NPs exhibit multi-exponential decays at both time points in *ex vivo* liver (Table 5.4), but the fluorescence lifetime is longer at 24 h, paralleling that of m-THPC in DMSO (~9.5 ns) and similar to PLGA NPs in PBS at 10 mins (6.1 ns) following a bi-exponential fit (Fig 5.10 A + B). This longer fluorescence lifetime, consistent with less self-quenching, is also reflected in the fluorescence spectra, which shows a 2-fold increase of m-THPC fluorescence between 650-660 nm at 24 h versus 10 mins (Fig 5.10 C). In PEG-PLGA NPs, m-THPC shows a mono-exponential decay in liver at 24 h (Table 5.4) but a shorter fluorescence lifetime than PLGA NPs (~8.4 ns). A similar fluorescence lifetime is observed at 10 mins (~7.8 ns) (Fig 5.11 A + B).

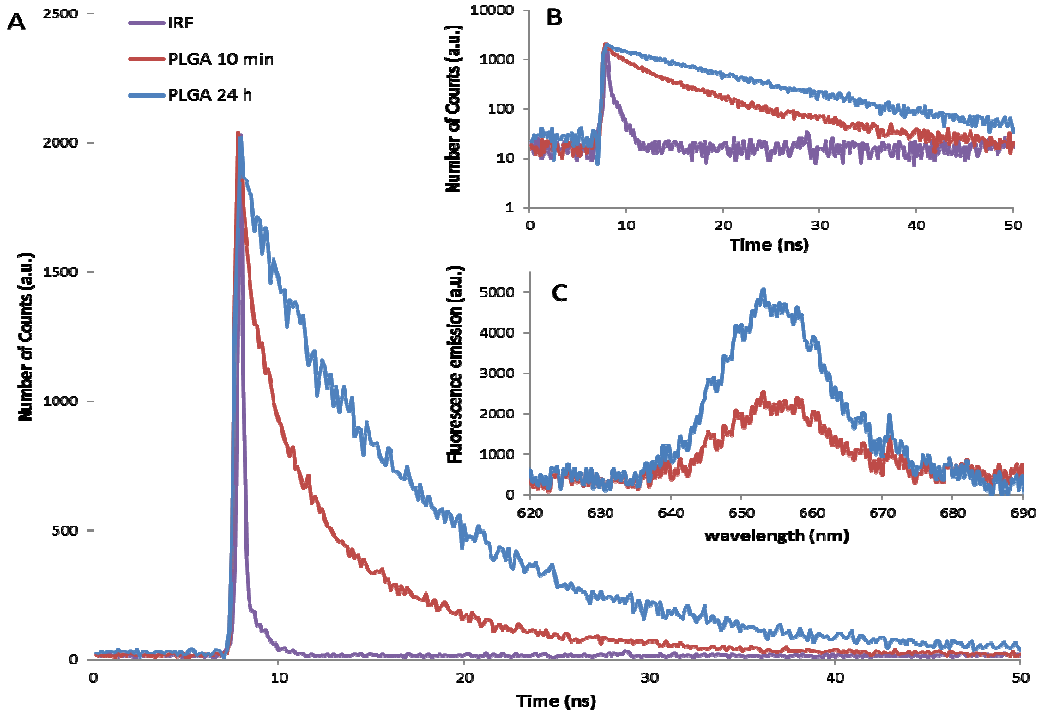

Fig 5.10. Fluorescence lifetime (**A**) linear scale (**B**) log scale of m-THPC in *ex vivo* rat liver tissue at 10 min and 24 h following an intravenous injection of 0.3 mg kg^{-1} m-THPC in PLGA nanoparticles (**C**) fluorescence emission spectra (620-690 nm) of m-THPC on the same *ex vivo* tissue.

Foscan demonstrated identical monoexponential decays in *ex vivo* liver tissue at both 30 mins and 24 h following intravenous injection of 0.3 mg kg^{-1} m-THPC (Fig 5.12 A + B). Fluorescence lifetimes of Foscan in liver tissue were the same as m-THPC in DMSO (~9.5 ns) (data not shown).

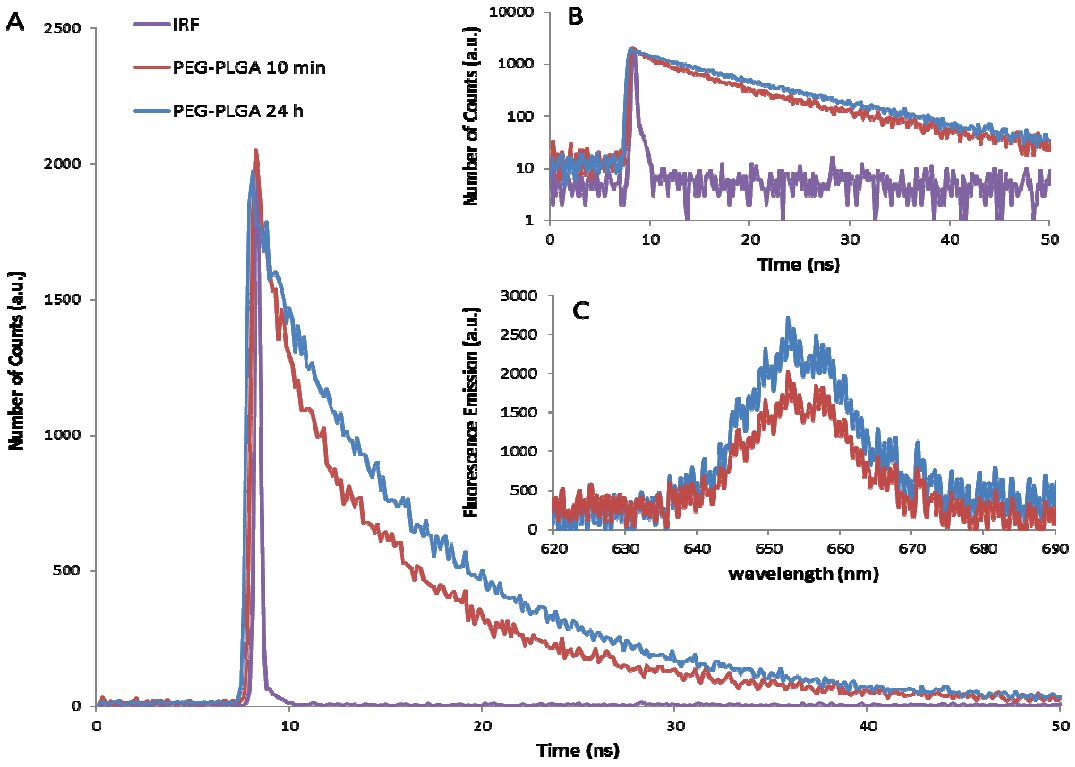

Fig 5.11. Fluorescence lifetime (**A**) linear scale (**B**) log scale of m-THPC in *ex vivo* rat liver tissue at 10 min and 24 h following an intravenous injection of 0.3 mg kg^{-1} m-THPC in PEG-PLGA nanoparticles (**C**) fluorescence emission spectra (620-690 nm) of m-THPC on the same *ex vivo* tissue.

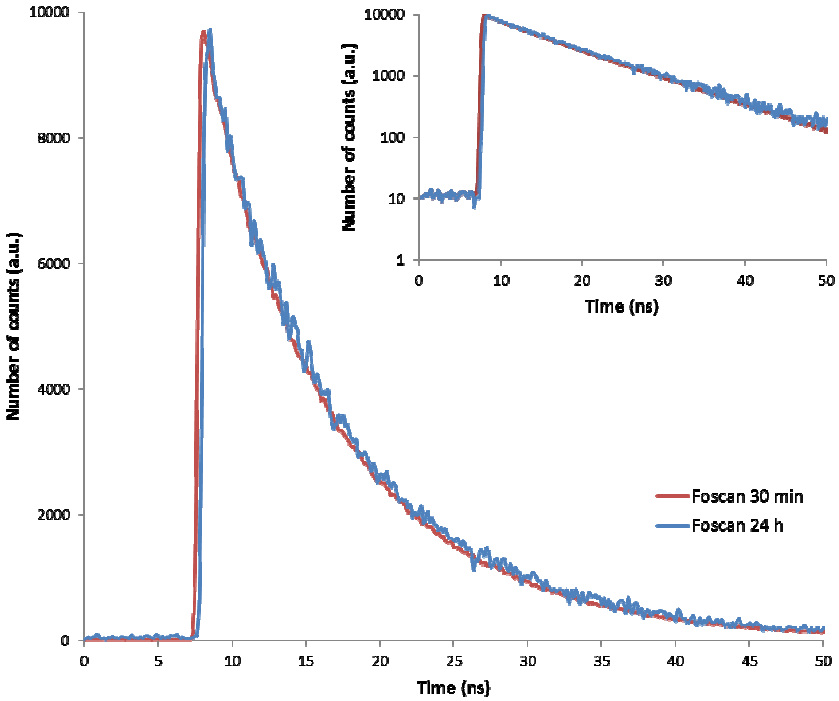

Fig 5.12. Fluorescence lifetime (**A**) linear scale (**B**) log scale of m-THPC in *ex vivo* rat liver tissue at 30 min and 24 h following an intravenous injection of 0.3 mg kg^{-1} m-THPC in Foscan.

vii. Fluorescence microscopy frozen sections

False colour fluorescence CCD images generally indicate higher m-THPC fluorescence intensity in all tissues at 24 h following intravenous administration of m-THPC-loaded PLGA NPs in comparison to PEG-PLGA NPs (Fig 5.13). Intense bright fluorescence spots, suggestive of high m-THPC uptake were observed in the greatest number in the liver, spleen and lungs for both nanoparticles at 24 h. m-THPC localisation in these organs was predominantly around blood vessels in the liver and distributed throughout spleen and lung tissue. Furthermore, PLGA NPs also showed m-THPC fluorescence in the kidneys compared to pegylated PLGA NPs, which appears to be focused around the glomeruli. The lowest fluorescence was observed in tumour tissue for both particles at this time.

At 72 h m-THPC fluorescence in liver tissue remains high with PLGA NPs and concentrated around blood vessels, however, is much lower with PEG-PLGA NPs (Fig 5.14). Foscan shows an even m-THPC fluorescence distribution throughout liver tissue between parenchyma cells, suggesting uptake in Kupffer cells. There is a reduction of intense bright m-THPC fluorescence spots with PLGA NPs at 72 h compared to 24 h in the spleen, however, uptake is greater for both polymeric NPs compared to Foscan. Lung tissue also shows bright m-THPC fluorescence spots with PEG-PLGA NPs but was more uniformly distributed throughout tissue and around blood vessels at a greater intensity with Foscan and PLGA NPs. Finally, in tumour tissue a higher fluorescence intensity was observed at 72 h for all m-THPC formulations in comparison to 24 h, but noticeably more with PLGA NPs, which corresponds to chemical extraction data at this time (Fig 5.8).

The histological structure of each tissue was determined by H&E staining of corresponding frozen tissue sections used for fluorescence microscopy (Fig 5.13). Lung tissue revealed a sponge-like appearance due to its composition of thin-walled alveoli, comprising a single layer of squamous epithelium between which lies a thin layer of connective tissue and capillaries. Hexagonal liver lobules formed of large hepatocytes (parenchymal cells) can be observed in liver with larger blood vessels clearly visible in tissue. H&E staining of spleen tissue demonstrates a clear boundary between white and red pulp structures. In the kidneys, red parenchymal tissue is punctuated by discrete bundles of cells, with nuclei stained purple, illustrating the presence of glomeruli and tumour tissue is typically heterogeneous (Fig 5.13).

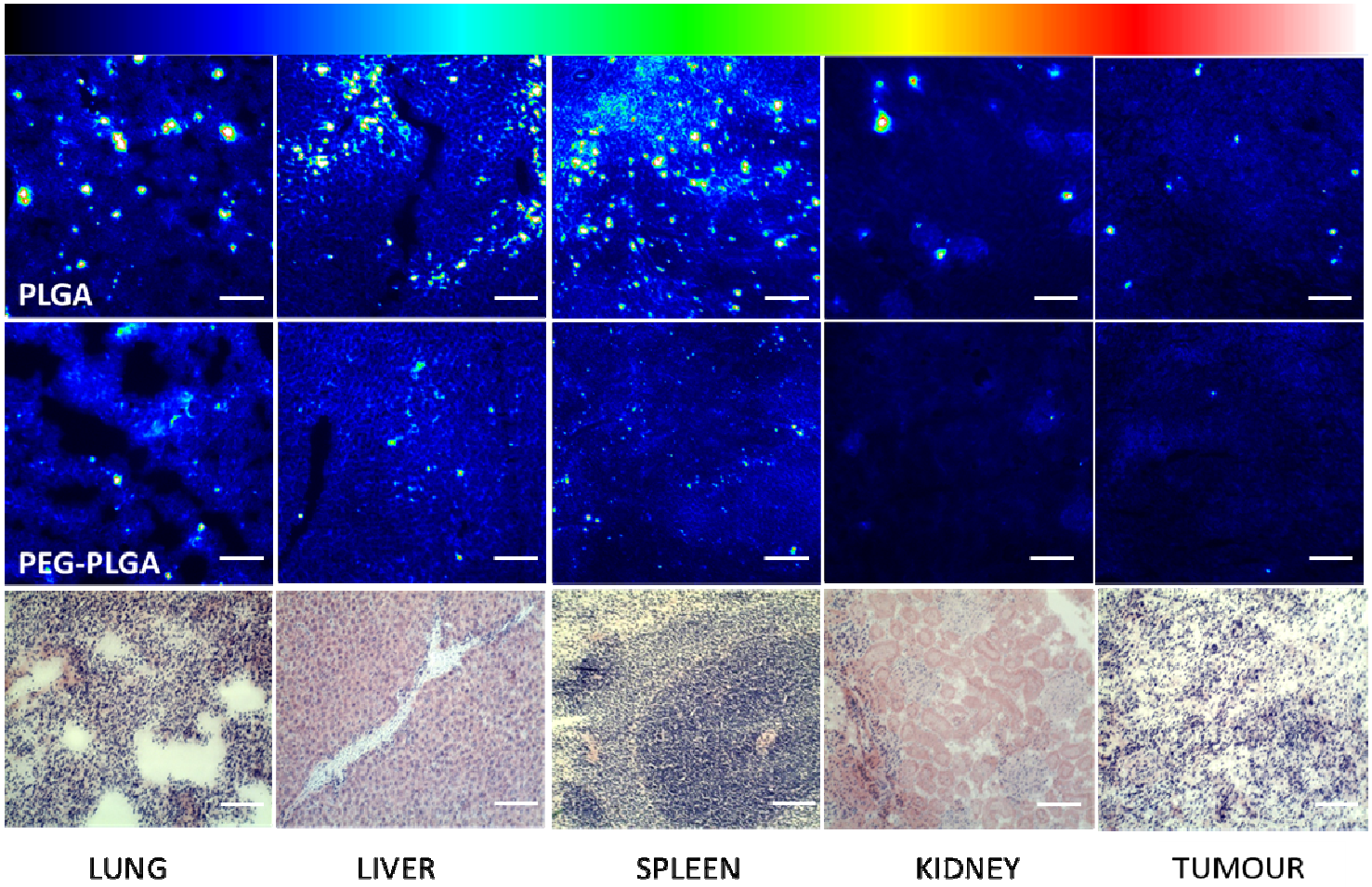

Fig 5.13. CCD false coloured fluorescence microscopy images of m-THPC in 10 micron thick tissue sections following an intravenous injection of 0.3 mg kg^{-1} m-THPC in either PLGA (top) and PEG-PLGA nanoparticles (middle) at 24 h. (Bottom) equivalent frozen tissue sections stained with H&E for histological analysis. 100 micron scale bar on each image and the fluorescence intensity scale, top, increases from black (background/no fluorescence) through to white (max. fluorescence).

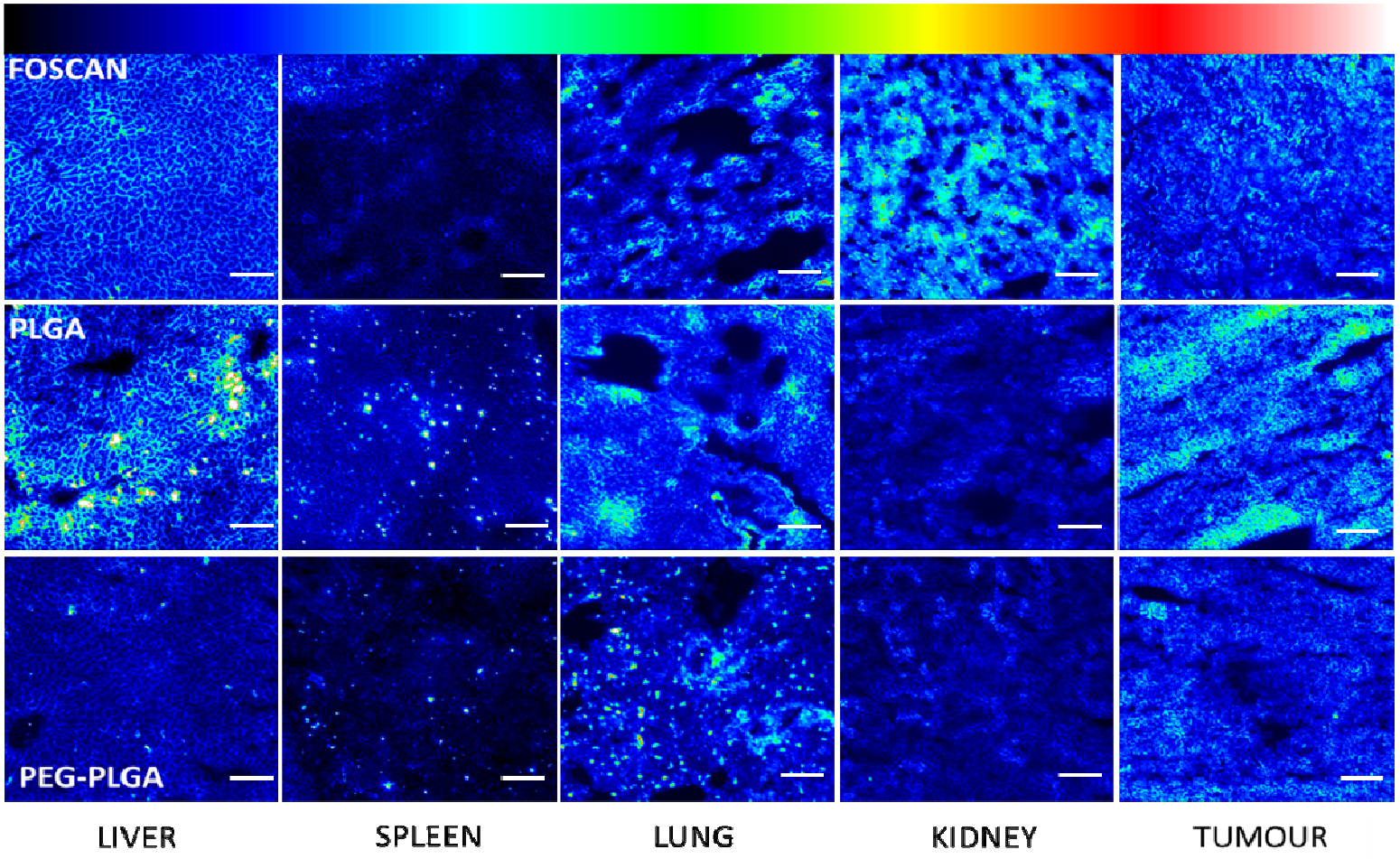

Fig 5.14. CCD false coloured fluorescence microscopy images of m-THPC in 10 micron thick tissue sections following an intravenous injection of 0.3 mg kg^{-1} m-THPC in either PLGA (top) and PEG-PLGA nanoparticles (middle) at 72 h. (Bottom) equivalent frozen tissue sections stained with H&E for histological analysis. 100 micron scale bar on each image and the fluorescence intensity scale, top, increases from black (background/no fluorescence) through to white (max. fluorescence).

viii. PDT

The second part of this investigation involved assessing the PDT efficacy to tumours *in vivo* with m-THPC-loaded PLGA and PEG-PLGA NPs in comparison to Foscan. In order to help establish optimal PDT parameters required for maximal tumour necrosis, two DLIs were chosen to perform PDT to subcutaneous MC28 fibrosarcomas in Hooded Lister rats.

H&E stained MC28 tumour sections were scanned with the Hamamatsu Nanozoomer following intravenous administration of 0.3 mg kg^{-1} m-THPC in either Foscan (FS), PLGA or PEG-PLGA NPs, prior to PDT treatment at 24 h (Fig 5.15) and 72 h with 10 J of light at 100 mW, in order to observe the extent of PDT damage, measured by the percentage area of necrosis. Control tissues received no drug or light.

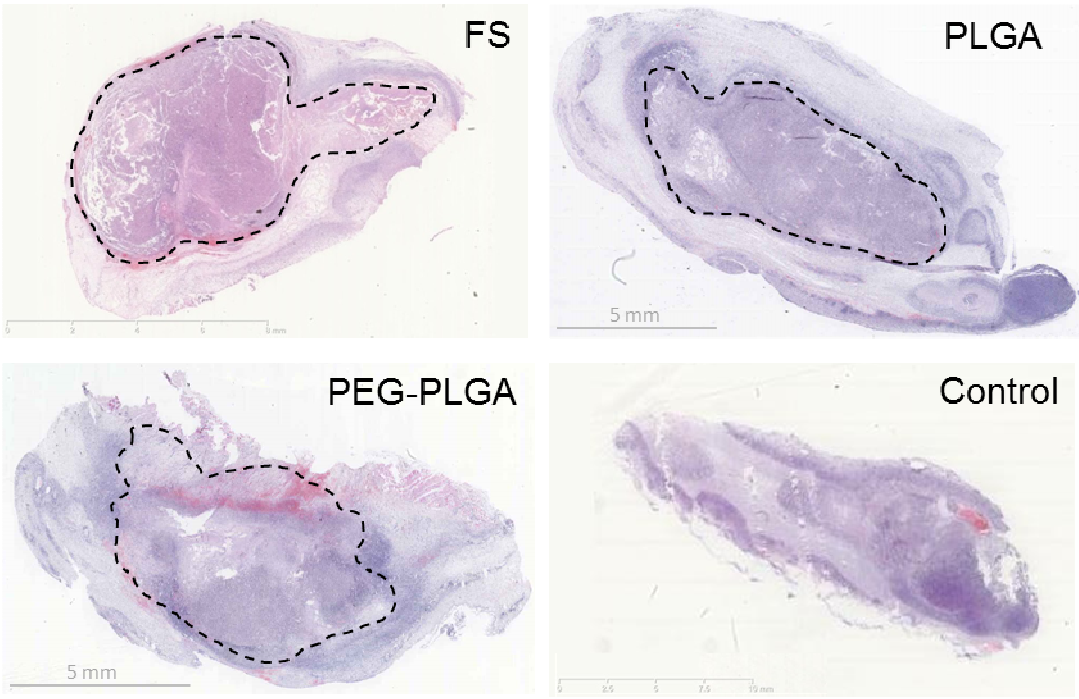

Figure 5.15. Examples of H&E stained MC28 tumour sections scanned with the Hamamatsu Nanozoomer to observe the extent of PDT damage with m-THPC, measured by the area of necrosis (dotted perimeter), after 24 h post *i.v.* injection of 0.3 mg kg^{-1} of m-THPC in Foscan (FS), PLGA or PEG-PLGA NPs. Negative control tissues received no drug or light (Control).

Control MC28 tumour tissue was typically heterogeneous in structure and stained dark purple with H&E, indicative of 'healthy' (non-necrotic) tumour cells. The PDT damage to tumour tissue at 24 h with Foscan appeared slightly greater than for m-THPC-loaded PLGA and PEG-PLGA NPs, with similar percentage necrosis exhibit between both formulations (Fig 5.15). Signs of necrosis, including haemorrhagic damage and condensed

cellular nuclei were observed with all m-THPC formulations, in addition to the presence of a more resistant tumour periphery.

When histologically analysed sections of MC28 tumour tissue were quantified to assess the percentage of MC28 tumour necrosis induced following PDT at 24 h and 72 h, there did not appear to be any significant difference between each m-THPC formulation (Foscan, PLGA or PEG-PLGA NPs) at either time point after a 0.3 mg kg^{-1} m-THPC (Fig 5.16). Results showed a greater percentage area of necrosis induced with PDT at 24 h following the administration of Foscan (55%) of approximately 5%, in comparison to PLGA (50%) and pegylated PLGA NPs (46%). At a 72 h drug light interval, PDT induced tumour necrosis appeared to fall by 13% with Foscan (42%) but the percentage area of necrosis remained identical for both PLGA formulations. Control tumour tissue, which received light treatment but no administration of m-THPC showed negligible levels of induced necrosis.

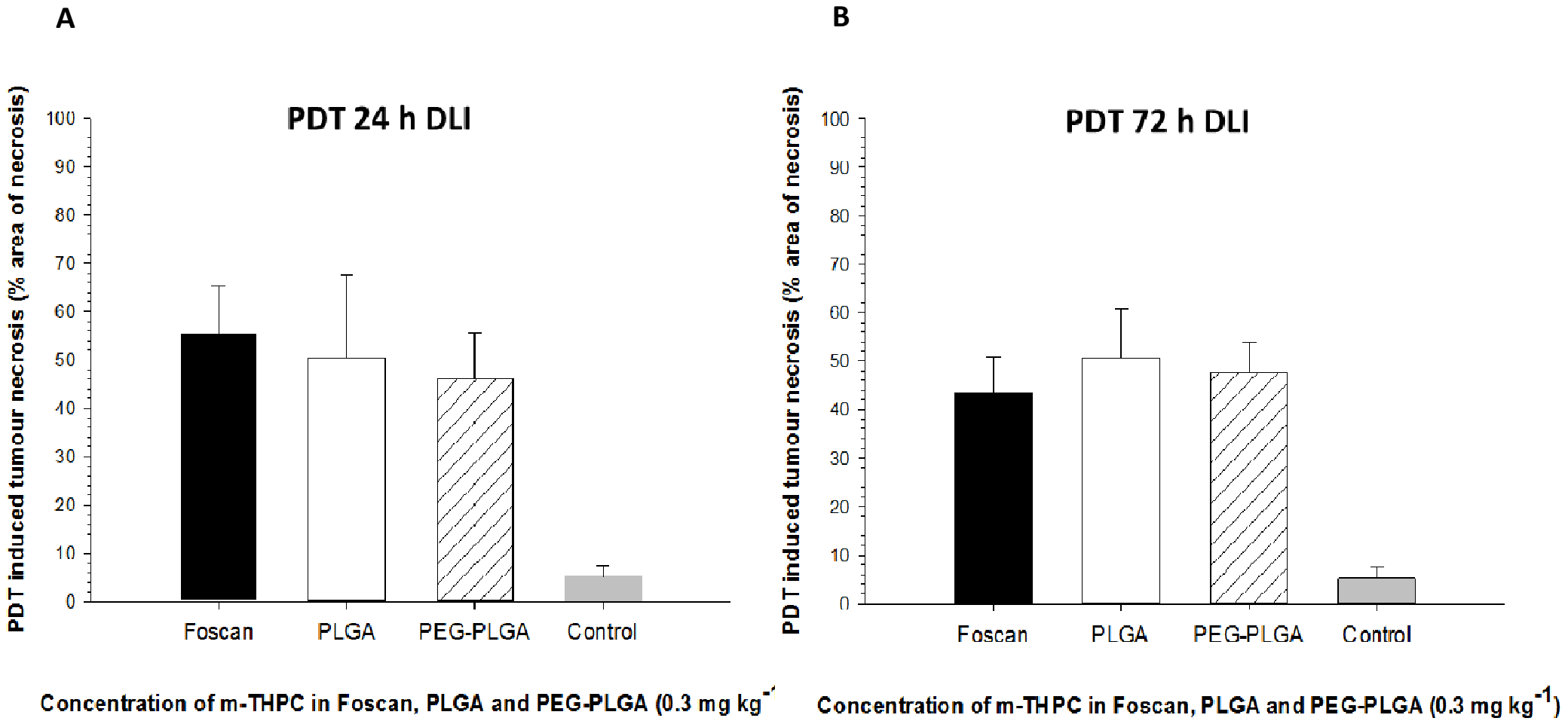

Figure 5.16. The percentage of MC28 tumour tissue necrosis (%) induced by PDT with 10 J of light at 100 mW following intravenous injection of 0.3 mg kg^{-1} of m-THPC in either Foscan, PLGA and pegylated PLGA NPs at drug:light intervals of (A) 24 h and (B) 72 h.

5.4 Discussion

The aim of this study was to investigate whether incorporation of m-THPC into an alternative biodegradable nano-vehicle system could facilitate its passive delivery into tumour tissue *in vivo* and improve PDT tumour efficacy. Pegylated and non-pegylated poly(lactide-co-glycolide) nanoparticles, PEG-PLGA and PLGA NPs, were used in these studies to encapsulate m-THPC and were prepared via a nanoprecipitation method (Rojnik, M. et al. 2012). Polymeric nanoparticles were supplied by the University of Ljubljana as freeze dried particles following their synthesis. To increase their long-term stability and improve their dispersion/reduce sedimentation upon resuspension in PBS (loading buffer), they were supplemented with trehalose (sugar) *(see **Appendix I – B.1 Nanoprecipitation method: PLGA NPs**)*. Characterisation studies *in vitro* and *in vivo* with these particles have previously been published (Rojnik, M. et al. 2012).

The particle diameter of polymeric particles used in these studies was 144.7±2.0 nm for PEG-PLGA NPs and 179.0±0.3 nm for PLGA NPs (Table 5.3). Interestingly, the addition of PEG groups decreased particle size and was thought to be due to the incorporation of more hydrophilic PEG chains in the hydrophobic PLGA polymer. Rojnik *et al*., reported covalently linked hydrophilic PEG blocks can change the physicochemical properties of PLGA polymers, enabling the formation of smaller particles (Rojnik, M. et al. 2012). Furthermore, the addition of trehalose as a stabilising agent was thought to contribute to an increase in nanoparticle diameter due to the attachment of bulky carbohydrates. The greater negative ζ-potential of PLGA NPs compared with PEG-PLGA NPs was attributed to the presence of a larger number of free carboxyl groups on the PLGA NP surface and a lack of uncharged PEG chains (Rojnik, M. et al. 2012). Both NP formulations, however, generally showed a low polydispersity index (PDI) and a low negative surface charge (≤-5.5 mV). A low surface charge of these NPs has indicated low stability, resulting in their aggregation/sedimentation from aqueous dispersions but a simultaneous reduction in macrophage uptake compared to highly anionic particles (≥-9 mV) (Yu, S. S. et al. 2012).

Loading efficiency

In colloidal systems, such as these, determining the precise drug content of NPs is challenging, however, ultracentrifugation can be employed to separate nanoparticles from non-encapsulated or non-adsorbed drug. This can help to determine the concentration of

drug remaining inside the polymeric NPs, as binding to serum proteins is only possible following drug release from the polymer matrix (Kumari, A. et al. 2010). While PLGA-based NPs often present high encapsulation efficiencies, drug loading has been described as generally poor, usually equating ~1% weight/weight (%, w/w) (Kumari, A. et al. 2010). This typically means that 1 mg of active drug is available per 100 mg of polymer in the nanoparticle. These terms have been described by Tripathi A *et al*., as the following (Tripathi, A. et al. 2010):

$$\textbf{Drug entrapment (\%, w/w)} = \frac{\textbf{(Mass of the total drug} - \textbf{Mass of free drug)} \times \textbf{100}}{\textbf{Mass of total drug}}$$

$$\textbf{Drug loading (\%, w/ w)} = \frac{\textbf{(Mass of the total drug} - \textbf{Mass of free drug)} \times \textbf{100}}{\textbf{Mass of total polymer}}$$

Equations 5.4. Equations describing drug encapsulation efficiency and drug loading efficiency in polymeric nanoparticles. *Taken from (Tripathi, A. et al. 2010).*

PEG-PLGA and PLGA NPs developed here had drug loadings of 6.7% and 6.9% (w/w), respectively (Table 5.3). In NP preparation, 50 mg of polymer and 5 mg of m-THPC were dissolved in acetone solution. The maximum m-THPC encapsulation efficiency achievable in this system is 9.1% (w/w): 5 mg of m-THPC/ (50 mg of polymer + 5 mg of m-THPC). The encapsulation efficiency of m-THPC in polymeric NPs, developed here, was ~75% (6.7-6.9%/9.1%). These values show that PEG chains did not drastically affect m-THPC loading through steric interference of drug-polymer interactions, as reported by Makadia *et al*., due to similar drug loadings for both NPs (Makadia, H. K. et al. 2011).

A 'high burst' drug release rate is also characteristic of polymeric nanoparticles, referred to as 'dose dumping'. This rapid initial release creates localised drug toxicity issues, whilst reducing the ability of therapeutics to reach target tissue or cells, leading to a loss of therapeutic efficacy. This has been attributed to the immediate release of a fraction of partially adsorbed drugs on the NP surface on account of their hydrophobicity and incompatibility with hydrophilic PEG chains (Kumari, A. et al. 2010). This has been observed by Compagnin *et al*., with m-THPC in pegylated liposomes (Compagnin, C. et al. 2011) and by Rojnik *et al*., with non-covalently entrapped m-THPC in PEG-PLGA NPs, similar to those used in studies here (Rojnik, M. et al. 2012). In the latter example, m-THPC demonstrated a faster release from PEG-PLGA NPs in 10% FBS compared to

PLGA NPs through ultracentrifugation. With PLGA NPs the rate of m-THPC release was believed to be directly proportional to the rate of polymer degradation but the mechanism of release for PEG-PLGA NPs followed a more biphasic pattern, with an initial burst release of 30% (w/w) m-THPC. Despite a more sustained released of m-THPC from PLGA NPs over 24 h in 10% FBS, ~68% m-THPC was still detectable at this time (24 h) in comparison to ~45% m-THPC in PEG-PLGA NPs as a result of the initial m-THPC burst release (Rojnik, M. et al. 2012) *(see **Appendix I – B.3 Rate of m-THPC release from polymeric NPs**)*.

Photophysical studies: polymeric NPs

Aggregates of porphyrin-based photosensitisers, such as m-THPC, are well known to possess inferior fluorescence properties with regards to shorter fluorescence lifetimes, lower triplet state yields, and thus poorer photodynamic efficiency than monomeric m-THPC (Bezdetnaya, L. et al. 1996). Fluorescence lifetime data (Table 5.4) and fluorescence emission spectra (Fig 5.6) indicated m-THPC fluorescence is strongly quenched when encapsulated in PEG-PLGA and PLGA NPs, in comparison to monomeric m-THPC. Monomerisation was achieved by disrupting polymeric NPs in DMSO to release m-THPC from particles and resulted in a significant increase in fluorescence intensity and lifetime in comparison to intact m-THPC-loaded particles suspended in their loading buffer (PBS). These results are consistent with the occurrence of fluorescence self-quenching due to the aggregation of m-THPC within NPs. The degree of quenching appeared to be greater for PEG-PLGA NPs versus PLGA NPs, despite comparable m-THPC loading (Table 5.3). This could be explained by the smaller size of PEG-PLGA NPs resulting in a higher local m-THPC concentration and a greater propensity for PS aggregation. Similar fluorescence quenching results have also been observed following the incorporation of m-THPC into liposomes. In liposomal studies, the fluorescence lifetime of encapsulated m-THPC was reduced to 1 ns from 20 ns (free m-THPC), which was attributed to aggregation (Lassalle, H. P. et al. 2009;Moan, J. et al. 1991;Vargas, A. et al. 2008). Absorbance spectra of the same PLGA and PEG-PLGA NPs demonstrated small spectral changes of m-THPC, including a slight peak broadening and small bathochromic shifts in PBS (Fig 5.4) compared to DMSO (Fig 5.5). This is likely due to the incorporation of m-THPC into polymer matrices and the formation of dimers, as Glanzmann *et al.*, reported broadening of both m-THPC bands due to dimerisation (such as

stacking of its chlorin rings) in aqueous environments (Glanzmann, T. et al. 1998). However, it should be noted, differences between monomeric and dimerised forms of m-THPC are less easy to interpret through this method. The most noticeable difference in absorbance spectra was between 300-400 nm (outside of m-THPC absorbance range), suggesting a reduction in NP light scattering from complete disruption of NP polymer chains when in a solvent.

Despite data indicating the presence of m-THPC forming aggregates when entrapped inside PLGA NPs, it has been shown these aggregates are able to dissociate to monomeric forms following their release from the NPs and transfer to plasma proteins when reaching tumour sites (Konan-Kouakou, Y. N. et al. 2005); (Hopkinson, H. J. et al. 1999); (Sasnouski, S. et al. 2007). This is preferable for ROS production and effective PDT (Triesscheijn, M. et al. 2007). The rate of m-THPC monomerisation is dependent on the rate of polymer degradation and release of m-THPC from the NP, affecting its availability and photo-activity (Rojnik, M. et al. 2012).

Fluorescence lifetime: ex vivo

The fluorescence lifetimes of m-THPC and corresponding fluorescence emission spectra were also recorded on the outer surface of freshly excised *ex vivo* rat liver tissue following intravenous administration of 0.3 mg kg^{-1} m-THPC in PLGA and PEG-PLGA NPs at either short (10 mins) or longer (24 h) time periods (Table 5.4, Fig 5.10-11 A). At shorter administration times, m-THPC in both PLGA NPs had multi-exponential decays, displaying sub-populations with much shorter fluorescence lifetimes that comprised a significant percentage (%). This suggests self-quenching of m-THPC through the formation of weak aggregates. At 24 h, m-THPC in PLGA NPs has a much greater population with longer fluorescence lifetimes, paralleling that of m-THPC in DMSO (~9.5 ns). In addition, m-THPC in PEG-PLGA NPs shows a mono-exponential decay in *ex vivo* liver by this time (Table 5.4). This demonstrates more monomerically active m-THPC, likely following the degradation and release of m-THPC from NPs at longer time points and its subsequent binding by serum proteins (Rojnik, M. et al. 2012). Foscan demonstrated identical monoexponential decays in *ex vivo* liver tissue at both 30 mins and 24 h following intravenous injection of 0.3 mg kg^{-1} m-THPC and fluorescence lifetimes were the same as m-THPC in DMSO. This suggests m-THPC in Foscan is present in its

monomeric active form in the liver due to the binding of serum proteins (Triesscheijn, M. et al. 2007).

In vitro: polymeric m-THPC uptake

Confocal microscopy was used to image MC28 tumour cells following 4 h incubation with 1 μM m-THPC in either Foscan, PLGA or PEG-PLGA NPs in the presence or absence of 10% FCS (Fig 5.7). Confocal images showed a strong uptake of m-THPC in the cytoplasm of tumour cells following incubation with micellular Foscan (+ 10% FCS). The association of m-THPC with various serum proteins has previously been shown in the literature to improve intracellular uptake of monomerised m-THPC (Hopkinson, H. J. et al. 1999); (Sasnouski, S. et al. 2007). Dissociation of m-THPC from polymeric NPs may occur before or after cellular uptake of particles, thus m-THPC released prior to NP internalisation may also contribute to intracellular fluorescence activity (Rojnik, M. et al. 2012). In this case, the observed fluorescence intensity of m-THPC was to a lesser degree with PLGA and PEG-PLGA NPs than free m-THPC (Foscan) in the cytoplasm. This would need to be confirmed with a Lysotracker *in vitro* to ensure this fluorescence is intracellular, however, a reduction in intracellular fluorescence may be attributed to the larger size of NPs being internalised (~150-180 nm), hindering m-THPC uptake efficiency through steric hinderance at the nanobio-interface, in comparison to Foscan over a 4 h period. According to Segat *et al*., PLGA NP size was said to increase further still, by almost two-fold, in the presence of 10% FCS due to protein binding (Segat, D. et al. 2011). Furthermore, m-THPC concentrations may decrease in continuously dividing cells (20 mins – 24 h cell cycle) reducing intracellular fluorescence (Compagnin, C. et al. 2009). In the absence of FCS, m-THPC uptake with both NPs demonstrated the presence of numerous bright white spots (Fig 5.7). This was thought to be indicative of particle precipitation, aggregation and/or sedimentation due to the lack of serum proteins available. Rojnik *et al*., supplemented PBS (loading buffer) with 10% FBS upon resuspension of freeze dried NPs prior to measurements in order to improve their dispersion and stabilisation. This appeared to be confirmed with confocal images (Fig 5.7).

Studies by collaborators showed intracellular localisation of m-THPC displayed similar distribution patterns throughout the cytoplasm of human-transformed breast cancer cells (MCF10A neoT) following incubation at 1, 3, 6 and 10 h (Rojnik, M. et al. 2012) with m-THPC-loaded PLGA or PEG-PLGA NPs. Red m-THPC fluorescence following cellular

incubation with both polymeric NPs was predominantly localised around the endoplasmic reticulum (ER) and Golgi apparatus, as demonstrated with m-THPC-loaded ORMOSIL NPs and liposomal-m-THPC with different (immortalised) cell lines *in vitro* (Compagnin, C. et al. 2009;Compagnin, C. et al. 2011). This localisation was believed to be due to m-THPC released from NPs prior to their internalisation. At longer incubation periods (10 h) an increase in the appearance of bright red spots was attributed to accumulation of m-THPC in lysosomal-endosomal compartments, as a result of intact NPs internalised via clathrin dependent endocytosis. The rate of PLGA degradation is expected to increase in acidic environments, such as the cytoplasmic vesicles of cells, due to acid-catalysed hydrolysis of ester bonds between LA and GA monomeric units, which may contribute to this observed fluorescence pattern (Alexis, F. et al. 2008).

Rojnik *et al*., also demonstrated a significant reduction of m-THPC uptake *in vitro* through flow cytometry (FACS) using A549 cells, MCF10A neoT cells and differentiated human promonocytic U937 cells (macrophages), with PEG-PLGA NPs compared to PLGA NPs (as used here) (Rojnik, M. et al. 2012). It was proposed that these results demonstrated the stealth-like properties of PEG-PLGA NPs, owing to the reduction of m-THPC fluorescence observed in all cells line, and particularly in phagocytotic cells (U937), compared to PLGA NPs. Furthermore, the faster initial release rate of m-THPC from pegylated PLGA NPs into the cell medium may have contributed to the loss in intracellular fluorescence observed through FACS. However, it should be noted, fluorescence measurements for m-THPC in these studies were recorded at wavelengths of λ_{exc} = 488 nm, λ_{em} = 670 nm, which is far from optimum for m-THPC (λ_{exc} = 423 nm, λ_{em} = 652 nm).

Ex vivo: polymeric m-THPC uptake

Confocal microscopy images of freshly excised *ex vivo* rat liver tissue were taken following 0.3 mg kg^{-1} intravenous administration of m-THPC in either PEG-PLGA or PLGA NPs (Fig 5.9) at 24 h in order to determine m-THPC distribution through fluorescence. m-THPC fluorescence appeared to be localised in the cytoplasm of large hepatocytes due to the presence of a dark nucleus. Fluorescence was detected as discrete bright yellow spots, suggesting uptake into lysosomal-endosomal compartments, which may affect the site and efficacy of photoactive damage. As previously discussed, this is likely to have been on account of their size, which has shown to strongly affect stealth properties and macrophage uptake *in vitro* (Yu, S. S. et al. 2012). Despite their larger size,

PLGA NPs (~150-180 nm), no detectable m-THPC uptake was observed in liver macorphages (Kupffer cells), which reside between hepatocytes, in comparison to smaller, non-biodegradable ORMOSIL NPs (~20-100 nm) discussed in **Chpt 6**: ORMOSIL. This could be due to the biodegradable nature of polymeric NPs. The fluorescence signal is generally weak in confocal images, with a yellow fluorescence observed for m-THPC, rather than red. This could also be on account of the strong green autofluorescence of liver tissue itself. The presence of m-THPC appears to be slightly greater with PEG-PLGAs compared to PLGA NPs in the liver at 24 h, however, these differences may be due to the confocal technique whereby fluorescence images depict a single plane of tissue (non-stacked). This produces a less powerful signal than fluorescence microscopy, which is cumulative for the depth of the tissue section.

Polymeric m-THPC biodistribution in vivo: normal tissue

m-THPC biodistribution was assessed by chemical extraction following complete dissolution of whole tissues and through fluorescence microscopy of frozen tissue sections at 24 h and 72 h following *i.v.* administration of 0.3 mg kg^{-1} m-THPC in either Foscan, PLGA and PEG-PLGA NPs. The average ~150 nm size of each NP aimed to target tumour tissue through passive accumulation via the EPR effect and promote NP internalisation into tumour cells (Maeda, H. et al. 2000). The addition of PEG polymer chains further aimed to prolong the blood circulation time of m-THPC-loaded NPs by preventing the adhesion of opsonins to the NP surface and discourage their removal through circulating macrophages (Whelpton, R. et al. 1996). Despite these predictions, chemical extraction results showed there was no detectable trace of m-THPC-loaded PEG-PLGA NPs in the blood serum by 72 h in comparison to PLGA NPs and Foscan (Fig 5.8). However, at both 24 and 72 h PLGA NPs demonstrated a greater retention in the blood serum, superseding that of Foscan by almost six-fold. This may have been due to the high initial burst release rate of m-THPC observed from PEG-PLGA NPs. Rojnik *et al*., indicated a difference of almost 23% drug loading between PLGA NPs at 24 h regardless of similar loading efficiencies (~6.7-6.9%) (Rojnik, M. et al. 2012).

Liver/spleen/lungs

The greatest uptake of Foscan (m-THPC) was observed in the liver and in both the liver and spleen for polymeric NPs at 24 h. This is concordant with previous studies presented in this investigation with biodegradable liposomal m-THPC (**Chpt 4**), which illustrates that

although the surface PEG coating can reduced the rate of NP/m-THPC uptake into these tissues, it does not completely prevent it (Zamboni, W. C. 2005). However, despite a much greater initial uptake of m-THPC-loaded polymeric NPs in the lungs and spleen at 24 h, m-THPC appears to be cleared from the lungs, liver and spleen at a much faster rate when non-covalently incorporated in polymeric NPs than Foscan. A significant reduction in m-THPC concentration of approximately three-fold was observed in these organs between 24-72 h, whereas Foscan remained at similar concentrations in the lung and spleen over this period (Fig 5.8). As demonstrated with m-THPC-loaded liposomes (**Chpt 4**), the biodistribution of m-THPC in the lungs correlated closely to that of the blood serum.

False coloured fluorescence CCD microscopy images corresponded to chemical extraction data, with the greatest m-THPC uptake observed in the liver, lung and spleen at 24 h (Fig 5.13). Intense bright fluorescence spots, suggestive of high m-THPC uptake were observed at the greatest number in these organs. Fluorescence was predominantly observed in the connective tissue, epithelium and capillaries of the lung and around the blood vessels in the liver and remained high over 72 h with PLGA NPs compared to PEG-PLGA NPs and Foscan (Fig 5.14). m-THPC accumulation is generally harder to determine in spleen tissue due to the difference in fluorescence properties of red and white pulp (splenic cords) (Bourdon, O. et al. 2002) but frozen sections appeared to show m-THPC fluorescence throughout the spleen, as concentrated bright spots, and uptake was greater for both m-THPC-loaded PLGA NPs compared to Foscan. High m-THPC uptake into these organs is likely due to the high number of macrophages that reside in these tissues (Li, S. D. et al. 2008), however, specific intracellular uptake could not be determined from these studies. The proinflammatory effects of these particles has been determined by Segat *et al*., who showed moderate capture of PLGA-NPs by different types of leukocytes and the effects of pegylation on monocytic uptake gradually diminish over long incubation times (Segat, D. et al. 2011).

Kidneys

Chemical extraction data for Foscan uptake in the kidneys reflected m-THPC fluorescence observed in frozen kidney tissue sections at 72 h (Fig 5.8). A greater concentration of Foscan was observed in the kidneys and a high level of m-THPC fluorescence was distributed around the glomeruli at this time, compared to PLGA and PEG-PLGA NPs. m-THPC's hydrophobicity promotes strong serum protein binding and its transformation into

hydrophilic liver metabolites (Li, S. D. et al. 2008). However, results indicate possible excretion or partial entrapment of Foscan via the kidneys by 72 h (Fig 5.14), which show the highest concentration of m-THPC in comparison to other tissues. It is unclear as to why Foscan concentrations in the kidney should increase over this time (24-72 h). Renal filtration cutoff size has been suggested at 5.5 nm (Choi, H. S. et al. 2007) but with bulky serum protein binding m-THPC molecules may become trapped. Furthermore, cell of the RES also reside in the kidneys therefore m-THPC maybe phagocytosed at this site. Polymeric NPs used in this study are much larger (~150 nm) and have shown to double in size in the presence of serum proteins (Segat, D. et al. 2011). On account of their size, it is more likely particles are cleared *via* the hepatobiliary (liver and bile) pathway, passing through the colon. Unfortunately no m-THPC biodistribution data for the intestine or colon was taken to confirm hepatobiliary excretion of NPs. By 72 h, biodegradable polymeric particles are also likely to have degraded significantly into biologically benign components and excreted from the body (Choi, H. S. et al. 2007). However, it was not possible to facilitate the collection of urine or fecal samples. Collaborators carrying out *in vivo* bioluminescence imaging studies to determine m-THPC biodistribution of m-THPC-loaded PLGA and PEG-PLGA NPs, following their intravenous administration (0.3 mg kg^{-1}) into mice, showed little difference between the delivery systems but a greater m-THPC uptake in the colon was observed with NPs compared to Foscan. Unlike here, however, this m-THPC distribution pattern was also reflected in the kidneys. Differences between results were attributed to differences in experimental technique, such as quantitative versus qualitative measurements of m-THPC and background autofluorescence of tissues from endogenous flavoproteins when imaging (Rojnik, M. et al. 2012).

Skin

Chemical extraction data indicated a greater uptake of m-THPC loaded polymeric NPs in the skin at both 24 and 72 h following intravenous administration in comparison to Foscan (Fig 5.8). These concentrations appeared to be retained over a 72 h period for all m-THPC formulations. This may indicate a slow terminal elimination rate from skin tissue that cannot be ascertained over this short time series. Alternatively, fluorescence measurements taken of extremely low m-THPC concentrations may reach the detection limit of this system.

Polymeric m-THPC uptake in vivo: tumour tissue

In tumour tissue an increase in m-THPC uptake was observed with both PLGA NPs of more than two-fold in comparison to Foscan at 24 h. By 72 h, m-THPC in PLGA NPs remains significantly higher than Foscan, by approximately four-fold, whereas PEG-PLGA m-THPC concentrations fall to similar levels as Foscan (Fig 5.8). This possible retention of PLGA NPs versus PEG-PLGA NPs at 72 h in the tumour may be on account of their ~30 nm size difference (Rojnik, M. et al. 2012;Segat, D. et al. 2011). Also m-THPC-loaded PLGA NP concentrations in this blood at this time also remain elevated but are undetectable for PEG-PLGA NPs. As previously discussed, it is thought an increased blood circulation time increases the probability of NPs reaching target tumour tissues to deliver m-THPC, where they are able to passively accumulate through the EPR effect *in vivo*. Their retention in the tumour parenchyma may also promote intracellular internalisation of either intact particles or released drug (Liu, D. et al. 1992;Nagayama, S. et al. 2007).

Quantitative chemical extraction measurements do not provide information on the distribution and retention of m-THPC throughout tumour tissue, only as a whole organ. Fluorescence microscopy was employed to image frozen tumour sections following administration of each m-THPC formulation. A greater fluorescence intensity was observed at 72 h (Fig 5.14) for all m-THPC formulations in comparison to 24 h (Fig 5.13) in tumour tissue, but noticeably more with PLGA NPs, which corresponded to chemical extraction data at this time. Unfortunately, in comparison to other selected tissues (liver, lung, spleen, kidney), tumour tissue demonstrated the lowest m-THPC fluorescence for all m-THPC formulations at these times. However, the heterogeneity of tumour tissue may create difficulty in interpreting m-THPC fluorescence.

PDT

A significant reduction in dark cytotoxicity was reported *in vitro* with the same pegylated and m-THPC-loaded PLGA NPs by collaborators, in comparison to Foscan in A549 cells (Rojnik, M. et al. 2012). Following irradiation with red light (600-700 nm), these cells demonstrated a similar phototoxic effect for both Foscan and PEG-PLGA NPs, despite a 50% reduction in intracellular m-THPC availability with pegylated PLGA NPs. It was concluded that m-THPC delivery via PEG-PLGA NPs resulted in complete conversion of particle aggregates into highly photoactive monomers, compensating for the reduction in

cellular uptake (Rojnik, M. et al. 2012). These results were in good agreement with other groups showing an enhanced photodynamic activity of meso-tetra(4-hydroxyphenyl)porphyrin and verteporfin incorporated in PLGA NPs compared to free PS (Konan-Kouakou, Y. N. et al. 2005); (Konan, Y. N. et al. 2003).

PDT studies were developed further here with the same PLGA NPs in MC28 subcutaneous rat tumours *in vivo* using 10 J of light at 100 mW following a dose of 0.3 mg kg^{-1} m-THPC equivalent. Unlike *in vitro* studies, despite an observed increase in m-THPC tumour uptake with both PLGA and PEG-PLGA NPs in comparison to Foscan at both 24 and 72 h through biodistribution studies (Fig 5.8) there was no significant difference detected in tumour PDT efficacy between each m-THPC formulation at the same selected drug:light intervals in this model (Fig 5.16). Low to negligible levels of necrosis observed in control animal tumours were attributed to the development of necrotic cores (hypoxia) from untreated, growing tumours or the small incision made to insert the laser fibre into the tumour capsule.

PDT results may have been due to limitations of this tumour model, as the maximum percentage area of necrosis capable of inducing was 50-60%. A resistance to PDT of the outer tumour capsule has been reported by other groups, which would have significantly reduced the total percentage of tumour necrosis (Berg, K. et al. 2011). It has been suggested by Desgrosellier *et al*., that invading fibroblasts, recognised as promoting the growth of fibrous tissue (desmoplasia) during tumour progression, deposit large amounts of collagen that might result in resistance to therapy in some tumours (Desgrosellier, J. S. et al. 2010). Alternatively, differences in the subcellular distribution of m-THPC when delivered by polymeric NPs versus Foscan at 24 or 72 h may affect photodynamic potential on account of differences in the route of entry and subsequent m-THPC localisation inside the cell. For example, Foscan has been shown to preferentially localise around the endoplasmic reticulum (ER) and Golgi apparatus (Compagnin, C. et al. 2009;Compagnin, C. et al. 2011) whereas Rojnik *et al*., demonstrated accumulation of m-THPC in lysosomal-endosomal compartments as a result of internalisation via clathrin dependent endocytosis with PLGA and PEG-PLGA NPs (Rojnik, M. et al. 2012). Despite these temporal differences, Rojnik and co-workers also showed intense m-THPC fluorescence in the same subcellular locations as Foscan (ER and Golgi) at shorter NP incubation periods, attributed to the high initial 'burst release rate' of m-THPC observed from polymeric NPs.

This may have accounted for the similarities observed in PDT efficacy between polymeric NPs and Foscan observed here at 24 h *in vivo*. Earlier DLIs (<24 h) were not selected for treatment due to concerns regarding initial rapid release of m-THPC from NPs potentially causing predominant vascular PDT damage *in vivo*. Furthermore, slow degradation rates of polymer NPs indicated by Jain *et al*., required longer DLIs to ensure total release of m-THPC from fully degraded NPs intracellularly following uptake (Jain, R. K. et al. 2010). At a longer DLI of 72 h, there was a trend or a slight increase in the percentage of PDT tumour necrosis induced with both PLGA and PEG-PLGA NPs in comparison to Foscan, however, it was not significant. This longer incubation period *in vivo* may have also favoured preferential m-THPC-NP uptake at the tumour site *i.e.* parenchyma (neoplastic cells) and/or stroma (non-malignant cells), compared to 24 h.

Although differences in PDT efficacy between m-THPC formulations were not significant, these findings create promise for the application of these polymeric nanoparticles as PDT agents, as they are able to exert the similar phototoxic effects to tumour tissue as Foscan. This shows that m-THPC is able to reach tumour tissue following it encapsulation in polymeric NPs and is released into its photoactive form for effective PDT. This is encouraging given these are the first *in vivo* PDT studies to be carried out with PLGA NPs to our knowledge.

5.5 Conclusion

The primary objective of the work described in this chapter was to investigate the uptake of m-THPC *in vivo* following intravenous administration of either non-pegylated or pegylated poly(lactic-co-glycolic acid) (PEG-PLGA) m-THPC-loaded NPs in comparison to standard Foscan. Non-covalent incorporation of m-THPC into polymeric NPs aimed to increase their longevity in the blood circulation by preventing rapid uptake into the RES to improve delivery of m-THPC to tumour tissue and enhance PDT efficacy. Quantitative chemical extraction and qualitative fluorescence microscopy were employed to demonstrate the biodistribution of m-THPC in selected tissues and fluorescence lifetime measurements were carried out on intact *ex vivo* tissue to determine the presence of m-THPC self-quenching. An increase in m-THPC uptake was observed in tumour tissue following its encapsulation in PLGA NPs over a 72 h period compared to Foscan; however, this was not reflected in PDT results. Despite observing no significant difference in PDT efficacy between m-THPC formulations these results create promise for the application of polymeric nanoparticles as PDT agents, as they demonstrated an equal level of phototoxicity to tumours *in vivo* as Foscan. This is encouraging given these are the first *in vivo* PDT studies to be carried out with PLGA NPs to our knowledge. Although limitations may exist in the *in vivo* tumour model adopted here, the selectivity of this delivery system, and hence PDT, could be further improved following the conjugation of active biological molecules to the NP surface that are capable of specifically recognising receptors over-expressed on tumour cells.

6. Organically Modified Silica Nanoparticles

6.1 Introduction

Untargeted ORMOSIL NPs

Human populations have long been exposed to non-biodegradable or partially biodegradable nano-sized components from a variety of sources including aerosols, dust, smoke, soot and pollen, which behave like foreign matter in the body. Non-biodegradable nanocarriers have been investigated for biomedical applications due to a number of advantageous characteristics; their usage extends to drug or gene delivery vehicles, imaging agents and diagnostic tools. However, problems associated with bioelimination and potential toxicity, as a result of their lack of degradation, have led to long-term health concerns. Presently, the degree to which they cause harmful side effects has yet to be fully understood or established and is perhaps considered a fundamental requisite for any *in vivo* study with these nanocarriers for translation into the clinic.

Many non-biodegradable nanocarriers have been synthesised from a diverse range of materials for applications in biomedicine and each carry their own unique properties; these include, metallic NPs, such as gold (Au) and silver (Ag), carbon nanotubes (CNs), quantum dots (QDs), ceramic and silica NPs, which have been touched upon in early chapters (**Chapter 2**: Nanotechnology). Here, we explore the use of silica as a non-biodegradable nanocarrier. Silica is an abundant natural compound existing in both crystalline and non-crystalline (amorphous) forms (Tavano, R. et al. 2010). The latter occurs naturally and can be synthesised commercially through polymerisation of silicates and other inorganic precursors under controlled conditions to produce silica NPs. Silica

NPs are used in a host of industrial practices, from food manufacturing to additives in chemical processes (Barik, T. K. et al. 2008). More recently they have received increased attention for their doping capabilities (with organic molecules) for use in therapeutic applications.

Owing to their robustness, multimodality and ease of manipulation, silica NPs offer distinct advantages over molecular agents. These include (i) synthesis of an extensive range of physical and chemical properties (size, shape, charge, porosity, monodispersity), (ii) morphological and chemical stability in extreme environments (pH and temperature), (iii) loading and protection of both hydrophilic and lipophilic agents, (iv) controlled release of molecules through their porous structure (v) tailored entrapment of monomeric molecules (vi) multi-loading of different agents (vii) better control over material characteristics (Chatterjee, D. K. et al. 2008a;Paszko, E. et al. 2011;Qian, J. et al. 2011;Shan, Y. et al. 2011). Furthermore, these NPs can be modified at their surface to improve functionality, such as the incorporation of PEG groups to improve biodistribution and the addition of targeted biomolecules for enhanced selectivity.

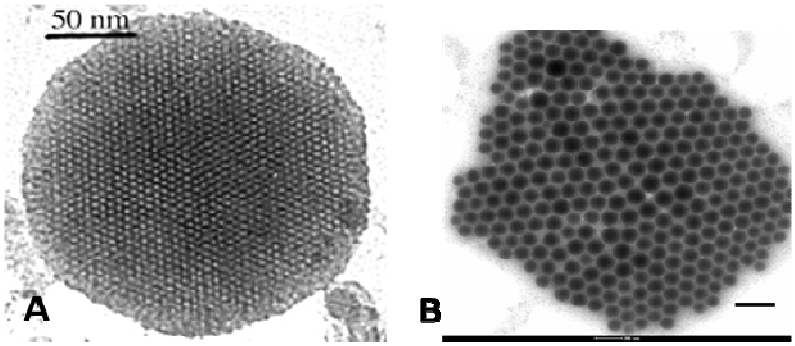

Figure 6.1. (**A**) mesoporous silica matrix (**B**) ~20 nm pegylated organically modified silica (ORMOSIL) nanoparticles. *Diagram provided by University of Padova, Italy (Selvestrel, F. et al. 2013).*

Organic/inorganic silica hybrid materials have been termed 'ormocers' (Schmidt H 1985), 'ceramers' (Wilkes, G. L. et al. 1985) and, more recently 'ORMOSILs'; ORganically MOdified SILica. A variety of alkylsilane and alkoxysilane precursors have been studied, which constitute the fundamental components of these hybrid materials, as they are amenable to surface modifications on account of their functional groups (Finnie, P. et al. 2000;Ulman, A. 1996). Inorganic and organic groups are connected to Si atoms through –O-Si-C≡ bonds forming a porous, cross-linked network or a wormhole-like silica matrix structure (Sharma, R. K. et al. 2004) (Fig 5.1A). The addition of these organic moieties to

the silica (ORMOSIL) increase its versatility, as different organic components can be selected during the production process to synthesise NPs with the desired physical and chemical characteristics.

The hydrolysis and polycondensation of organically modified alkoxysilanes, such as vinyl triethoxysilane (VTES) conjugated with PEGamine (biocompatible polymer), form spherical pegylated ORMOSIL NPs with improved physiochemical and stealth properties (Sharma, R. K. et al. 2004) (Fig 6.1B). Owing to the presence of lipophilic organic groups at their core, active hydrophobic molecules can be housed in the interior of ORMOSIL NPs, with the potential to form electrostatic complexes with surface ligands on their exterior (Diksha et al. 2012). Particle size can be controlled very precisely, achieving narrow size distributions, while still maintaining monodispersity (Dash, S. et al. 2008). The mechanical properties, such as hardness and elasticity, can also be tailored by varying the degree of alkylation of organosilane precursors (Dash, S. et al. 2008). Furthermore, these ORMOSIL materials are porous and have a tuneable pore size (Box 6.1); making them suitable for drug delivery.

Porosity of material	Pore size
Mesoporous	2 – 50 nm
Microporous	< 2 nm
Macroporous	> 50 nm

Box 6.0. (above) The porosity nomclamenture of a material as stipulated by the International Union of Pure & Applied Chemistry (IUPAC).

As a result, ORMOSIL NPs have been used to encapsulate a host of active molecules. Reetz *et al*., immobilised lipase in ORMOSIL of various compositions, observing an increase in enzyme activity (Reetz, M. T. et al. 1996). Delivery of plasmid DNA in ORMOSIL NPs as non-viral vectors was demonstrated by Kneuer *et al*., (Kneuer, C. et al. 2000). In the controlled delivery of hydrophobic chemotherapeutic agents, such as doxorubicin, Diksha *et al*., illustrated these anti-cancer drugs could be activated by external release factors *in vivo* (Diksha et al. 2012).

Toxicity

Silica, as a bulk material, is reported as being biologically inert, however as with many materials, its behaviour at the nanoscale level has not yet been established. Despite silica

NPs exhibiting ideal attributes for biomedical applications within *in vivo* environments; such as their monodispersity, lack of precipitation and enhanced biodistribution (Kumar, R. et al. 2010), their non-biodegradability causes concern for clinical translation, as these NPs cannot be broken down into biologically benign components. These concerns are largely due to the lack of understanding on clearance mechanisms and little available data on the potentially harmful long-term effects (>15 d) of silica NP accumulation in the body or successive accumulation from repeated doses. Studies illustrating a renal threshold of 5.5 nm (Choi, H. S. et al. 2007), suggests the route of clearance is size dependent and the only other major route of excretion for non-biodegradable NPs of a larger hydrodynamic diameter is the hepatobiliary pathway; via the liver, into bile and faeces. This is a much slower and inefficient process, increasing the exposure-time curve and the likelihood of toxicology from adverse side-effects and the creation of tissue abnormalities. In addition, despite dense PEG layers preventing capture and uptake in the liver (RES) to increase the blood circulation half-life and therapeutic bioavailability, it may also preclude NPs from elimination. Furthermore, it has been suggested that the retention of some NPs in the body could potentially affect other future medical tests (Choi, H. S. et al. 2007).

Applications in PDT

Important considerations must be taken into account for applications in PDT whereby the active photosensitiser molecule is retained in non-biodegradable nanocarriers. ORMOSIL NPs possess specific characteristics ideal for use in PDT (Table 6.1). Firstly, these NPs are transparent therefore allow the transmission of light through the particle surface for irradiation and activation of internalised photosensitiser. Secondly, the size, shape and porous structure of the ORMOSIL NP can be exquisitely controlled, allowing the diffusion of molecular oxygen into the silica matrix and release of singlet oxygen species out in order to elicit phototoxic damage. Thirdly, the hydrophobic photosensitiser (PS) may be incorporated monomerically within the silica shell without drastically altering its structure through chemical modification, thereby maintaining its spectrofluorimetric properties and singlet oxygen quantum yield. Lastly, the surface of these NPs can be functionalised with biomolecules to further enhance the uptake into cancer cells. Each of these parameters can be manipulated for optimised biodistribution and phototoxicity efficacy (Brevet, D. et al. 2009); (Zhang, C. et al. 2007).

Photosensitisers may be incorporated into ORMOSIL NPs through different mechanisms (Chatterjee, D. K. et al. 2008a). Physical entrapment of the photosensitiser, involves immobilisation through non-covalent interactions. The photosensitiser resides either within pores or the silica shell itself and has been achieved by numerous research groups using different photosensitisers. Primary examples included the physical incorporation of the photosensitiser, 2-(1-hexyloxyethyl)-2-devinyl pyropheophorbide (HPPH), a PS in Phase II clinical trials for oesophageal cancer, into ~30 nm ORMOSIL NPs by Roy *et al*., (Roy, I. et al. 2003). It was hypothesised that HPPH was encapsulated monomerically and the porosity of the silica matrix allowed for the diffusion of oxygen molecules based on the ability of the NPs to produce an effective singlet oxygen quantum yield. Photophysical studies with meta-tetra(hydroxyphenyl)chlorin (m-THPC) (**Chapter 1:** Introduction) in non-pegylated silica NPs of ~180 nm by Kopelman *et al*., in the same year showed there was no difference in the fluorescence spectra/intensity of embedded m-THPC and a positive effect on singlet oxygen production was observed in comparison to free m-THPC (Yan, F. et al. 2003). The same group encapsulated Methylene Blue (MB), an FDA approved photosensitiser, in ORMOSIL NPs of ~160 nm, which produced lower singlet oxygen yields that other NPs (Tang, W. et al. 2005). This was attributed to the microenvironment in the double shell ORMOSIL matrix. *In vitro* studies in human oesophageal squamous carcinoma (KYSE 510) with physically entrapped monomeric m-THPC in pegylated ORMOSIL NPs of ~30 nm showed low dark toxicity but a strong leaching effect (90% m-THPC) in the presence of serum proteins (3%) after 50 mins incubation (Compagnin, C. et al. 2009). It was also determined that there was no difference in the subcellular localisation of encapsulated m-THPC versus free m-THPC as a result, as serum-m-THPC complexes had formed at the NP surface prior to internalisation. However, the presence of surface PEG groups largely prevented this transfer to serum proteins. Investigations with the photosensitiser phthalocyanine Pc4 encapsulated in 25 nm ORMOSIL NPs (Zhao, B. et al. 2009) showed encapsulation increased the aqueous solubility/stability and delivery of the hydrophobic photosensitiser, whilst significantly enhancing the PDT efficacy of Pc4 (through Type II mechanisms) following 22.5 J cm^2 of light between 600 and 700 nm *in vitro* in both non-pigmented human melanoma (A375) and pigmented mouse melanoma (B16F10) cell lines in comparison to free photosensitiser. Various research groups have used the natural photosensitiser protoporphyrin IX, (PpIX) a precursor to haem synthesis, physically entrapped in ORMOSIL NPs *in vitro* in multiple cancer cell lines, including breast, colon,

lung, epidermoid and lymphoblastoid (Qian, J. et al. 2012;Shan, L. 2004;Simon, V. et al. 2010). These NPs ranged from ~10-60 nm and a high uptake was preferentially seen in some cancer cell lines over others, but all demonstrated greater cellular uptake than free PpIX alone. PDT with these NPs *in vitro* produced high levels of ROS causing large levels of cellular damage. The same PpIX silica NPs loaded with a tracer dye were used for optical imaging *in vivo* in tumour-bearing nude mice, implanted with either human colon, lung or glioblastoma multiforme tumours subcutaneously, to monitor and quantify their biodistribution in tissues. A high tumour uptake was demonstrated in relation to normal tissues but maximal accumulation was dependent on the tumour cell line implanted. High accumulation was also observed in the liver, spleen, lungs and lymph nodes of these animals following intravenous tail vein injection (Simon, V. et al. 2010). Studies in nude mice xenografted with subcutaneous-Hela tumours were used for *in vivo* near-infrared imaging and PDT studies following an intratumoral injection of MB entrapped in ORMOSIL NPs of ~105 nm. 12 hours post injection tumours were exposed to 5 min of continuous 635 nm light at 500 mW cm^{-2}. 10 days post-PDT signs of gradual tumour necrosis appeared (He, X. et al. 2009).

Problems associated with photosensitiser leaching and premature release of drug loads from NPs, particularly in the presence of serum proteins (Compagnin, C. et al. 2009), leading to loss of therapeutic bioavailability, reduced efficacy of treatment and side-effects, has prompted research into other means of incorporating molecules within ORMOSIL NPs. As PDT does not require release of the drug to elicit type I or type II phototoxic effects, covalent coupling of photosensitisers inside the silica matrix of ORMOSIL NPs has been proposed and performed in an attempt to overcome these drawbacks (Couleaud, P. et al. 2010). Initial concerns on the potential physiochemical changes covalent anchorage may induce to the photosensitiser, in terms of reducing its spectrofluorimetric properties, singlet oxygen yield, phototoxicity and ultimately PDT efficiency were soon alleviated, as discussed below.

Various photosensitisers have been covalently incorporated within silica NPs. Depending on the properties of the silica and/or the PS, covalent bonding can be achieved through spacers, linkers (Ohulchanskyy, T. Y. et al. 2007) or coupling (Rossi, L. M. et al. 2008). Covalent linking of PpIX in larger silica NPs of 110 nm for PDT studies was demonstrated by Mou *et al*., (Tu, H. L. et al. 2009). It was shown aggregation and self-quenching of PpIX could be avoided due to site-isolation of the PS in the porous structure of the NPs, as

there was no change in the absorption spectrum from free PpIX. Following this, *in vitro* studies found a linear relationship between cellular uptake and NP dosage. Further studies *in vitro* entrapping metalloporphyrins (Cheng, R. J. et al. 2003), porphyrin derivatives (Hocine, O. et al. 2010) , chlorins (Couleaud, P. et al. 2010) and merocyanine (Brevet, D. et al. 2009) in silica NPs have shown no influence of covalent incorporation of PS on singlet oxygen yield and spectroscopic properties, with some studies noting an increase in phototoxic activity with NP delivery in comparison to free PS (Zhao, B. et al. 2009). This is thought to be due to intracellular localisation, in particular, the strong association with lysosomes which localises the effect of generated ROS (Zhao, 2009).

Prasad *et al*., were the first to demonstrate the covalent incorporation of PS molecules within ORMOSIL NPs (pegylated) (Ohulchanskyy, T. Y. et al. 2007). Using a water microemulsion and the organosilane precursor VTES they were able to produce a monodispersed aqueous dispersion of ultralow size (~20 nm) ORMOSIL NPs with covalently linked PS (iodobenzylpyropheophorbide), whilst retaining the spectroscopic and functional capabilities of the PS. *In vitro* studies (colon-26 cells) with these NPs exhibited a phototoxic effect which was positively correlated to the increased loading of PS within the ORMOSIL NPs and their cellular uptake. 100% cell kill was observed following 24 h incubation with 0.5 μM of PS-ORMOSIL NPs and irradiation with 8 J cm^2 of light. Subsequently these ORMOSIL NPs have been studies *in vivo* for bioimaging, biodistribution, clearance and toxicity studies (Kumar, R. et al. 2010). Further investigations revealed the greatest uptake of the covalently incorporated fluorophore, DY776, in ~20 nm ORMOSIL NPs was observed in the liver, spleen and stomach of mice through PS fluorescence and microPET imaging every 24 h for up to 15 days following *i.v.* administration. The hepatobiliary excretion pathway was proposed as the predominant clearance route and no toxicity was identified through histological analysis of tissues. However, no further *in vivo* PDT studies were carried out with these ORMOSIL NPs. Many groups have now focused on using multi-modal silica NPs for different platforms. Silica NPs functionalised with bioactive molecules (*i.e.* transferrin, monoclonal Abs) and covalently incorporated fluorophores, have been reported for simultaneous imaging and therapy (Kumar, R. et al. 2008), in addition to NPs incorporating PpIX for PDT and undergoing two-photon irradiation for bioimaging (Qian, J. et al. 2012). Silica NPs with magnetic cores and PS embedded in their shells have been illustrated for MRI imaging in diagnostic applications and PDT by Lai *et al*., (Lai, C. W. et al. 2008).

Synthesis	Size	PS	C/E	λ_{absmax}	Φ_f	Φ_Δ	$^1O_2$ detection	Phototoxicity
ORMOSIL	180	*m*-THPC	E	410	—	$>\Phi_{\Delta PS}$	ADPA	—
ORMOSIL or Stöber	190/160	MB	E	650	—	—	ADPA	C6 (rat glioma)—positive PDT results (confocal microscopy)
Hollow ORMOSIL	130	Hypocrellin A	E	—	$>\Phi_{fPS}$	$>\Phi_{\Delta PS}$	EPR with TEMP	HeLa—phototoxicity
Hollow ORMOSIL-coated HA-NP	110	Hypocrellin A (HA)	E	490	$>\Phi_{fPS}$	$>\Phi_{\Delta PS}$	ADPA	HeLa—phototoxicity
AOT/1-butanol/H_2O ORMOSIL	30	HPPH	E	420	—	—	ADPA, *hν*	Growth inhibition 90% (UCl-107), 100% (HeLa)
AOT/1-butanol/H_2O ORMOSIL	25	PPIX	E	405	—	—	DPBF	Destruction of HeLa cells structures
AOT/1-butanol/H_2O ORMOSIL	30	*m*-THPC	E	420	—	—	—	100% loss of KYSE 510 cells viability
Tween 80/1-butanol/H_2O ORMOSIL	25–30	Pc4	E	674	—	—	ABMD ESR withTEMP	Phototoxicity on A375 and B16F10 cells
Tween 80/1-butanol/H_2O ORMOSIL	10;25;60	PPIX	E	—	—	—	APF ROS detection kit	HT-29, HCT 116, A431, LLBC37, MDA-MB-231, MCF7—phototoxicity
AOT/1-butanol/H_2O ORMOSIL	25.7 INP, 24.5 VNP	HPPH	E	420	$\Phi_{fINP} < \Phi_{fVNP}$	$\Phi_{\Delta INP} = 1.7 \times \Phi_{\Delta VNP}$	*hν*	Phototoxicity of INP > VNP (RIF-1 tumor)
W/O ORMOSIL	105	MB	E	—	$6 \times \Phi_{fPS}$	0.049	DPBF	HeLa cells—growth inhibition 90% *in vivo* (balb/c nude mice)
Stöber coated Fe_3O_4	30	MB	E	590	—	$0.03 < \Phi_{\Delta PS} = 0.5$	DPBF, *hν*	—
W/cottonseed O ORMOSIL coated Fe_3O_4	20–30	Purpurin-18	E	668	—	$<\Phi_{\Delta PS}$	RNO	—
AOT/1-butanol/H_2O ORMOSIL coated Fe_3O_4	20–30	PHPP	E	409	—	—	RNO	40% SW480 cell viability lost
Fe_3O_4 -loaded MSN	60–120	ZnPc	E	670	—	—	—	—
Silica-coated Fe_3O_4	30–50	HPPH	E	420	—	—	RNO	—
Mesoporous silica coated $NaYF_4$	35 × 60	ZnPc	E		—	—	ABDA	—
Stöber-coated PUNP	60 to 120	Merocyanin	E	420	—	—	ADPA	Phototoxicity on MCF7/AZ cells
W/O SiO_2	60	Two-photon sensitizer	E	370		0.51	*hν*	Two-photon toxicity on macrophage
AOT/1-butanol/H_2O ORMOSIL	30	HPPH–BDSA	E	420–400	0.17	—	—	Two-photon toxicity on HeLa Cells
Grafting on Silica	10 + C60	C_{60}	C	—	—	—	—	—
Stöber	77 ± 12	PPIX	C	400		0.9	DPBF, *hν*	—
Tween 80/1-butanol /H_2OORMOSIL	20	Iodobenzylpyropheophorbide	C	410	—	—	ADPA, *hν*	Colon-26—phototoxicity (confocal microscopy)
O/W MSN	110	PPIX	C	408	—	$=\Phi_{\Delta PS}$	DPBF, *hν*	Growth inhibition 100% (HeLa cells)
O/W MSN	—	PdTPP	C	400	—	—	DPBF, *hν*	Changes in MDA-MB-231 cell morphology (TEM)—phototoxicity
O/W MSN	160	Anionic porphyrin	C	418		0.57	*hν*	Phototoxicity on MDA-MB-231 cells
O/W MSN coated W/O ORMOSIL	57 core–shell, 37 silica	HP	C	400	—	$>\Phi_{\Delta PS}$	ABDM	HO-8910PM (only imaging)
W/O ORMOSIL-coated Fe_3O_4	55	Ir(III) complex	C	350	0.62	—	—	Phototoxicity on Hela cells

[a] Size: diameter in nm; PS: photosensitizer; C/E: C covalently coupled, E encapsulated; λ_{absmax}: maximum absorption wavelength; Φ_f: fluorescence quantum yield; Φ_Δ: singlet oxygen formation quantum yield for the NP; $\Phi_{\Delta PS}$: singlet oxygen formation quantum yield for the free PS; $^1O_2$: detection of $^1O_2$ with a chemical probe; *hν*: $^1O_2$ detection by direct luminescence at 1270 nm. MB: methylene blue; HPPH: 2-devinyl-2-(1-hexyloxyethyl)pyropheophorbide; PHPP: 2,7,12,18-tetramethyl-3,8-di(1-propoxyethyl)-13,17-bis-(3-hydroxypropyl)porphyrin; PPIX: protoporphyrin IX; PdTPP: palladium tetraphenyl porphyrin; HP: hematoporphyrin; ADBA: 9,10-anthracenedipropionic acid; DPBF: 1,3-diphenylisobenzofuran; RNO: *N,N*-dimethyl-4-nitrosoaniline with imidazole as a chemical trap; ABDM: 9,10-anthracenecliybis(methylene)dimalonic acid; ESR spin trapping technique with TEMP (2,2,6,6-tetraethyl-4-piperridone) as a spin-trapping agent.

Table 6.1. Summary of silica-based NPs for PDT applications. *Taken from (Couleaud, P. et al. 2010).*

m-THPC is a hydrophobic molecule, which aggregates in aqueous environments, hampering its phototoxic activity. Researchers have shown there was no difference in the fluorescence spectra of covalently embedded m-THPC in photophysical studies with m-THPC physically entrapped (non-covalent) in silica NPs. Additionally, a positive effect on singlet oxygen production was observed in comparison to free m-THPC (Yan, F. et al. 2003). However, following its physical entrapment in ORMOSIL NPs (Fig 5.2 A), m-THPC showed a strong tendency to transfer to serum proteins on the NP surface and as a result was heavily leached from ORMOSIL NPs *in vitro* (Compagnin, C. et al. 2009). Although this was largely prevented by the addition of PEG groups on the NP surface, its premature leakage is likely to lead to loss of bioavailability, reduced phototoxicity at the target site of action and a lowered therapeutic index on account of greater administered doses required to exert phototoxic effects *in vivo*.

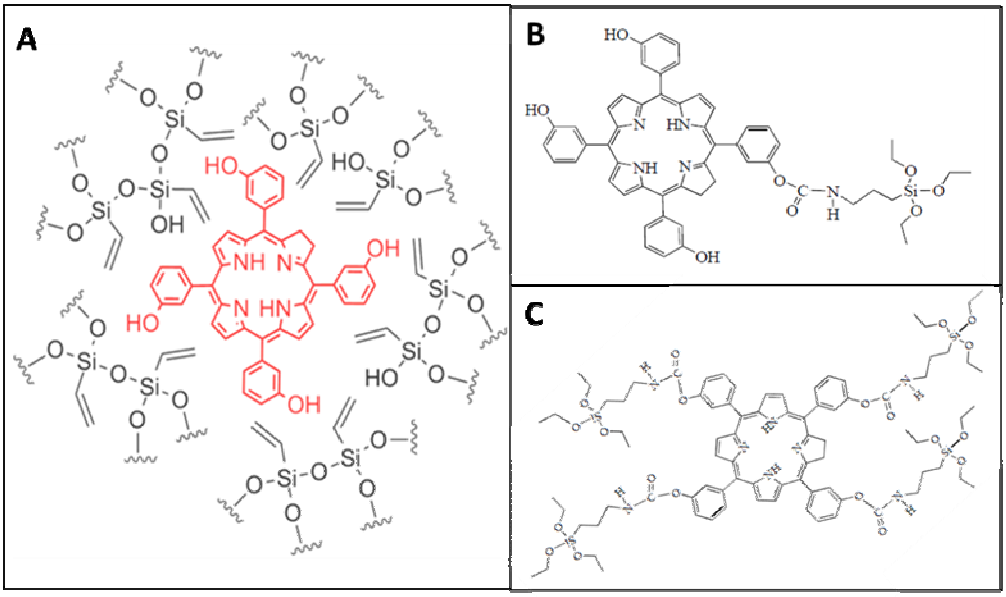

Figure 6.2. Schematic diagram (A) non-covalently incorporated m-THPC (red) and ORMOSIL groups (black) (B) Covalent monosilane m-THPC (C) Covalent tetrasilane m-THPC. *Diagram provided by University of Padova, Italy (Selvestrel, F. et al. 2013).*

Covalent incorporation of m-THPC into microporous (<2 nm) organically modified silica nanoparticles (ORMOSIL NPs) was therefore proposed here (Table 6.4) in order to prevent premature m-THPC leakage and facilitate its delivery into target cancerous tissues following systemic intravenous injection *in vivo*. Mono-silane (Fig 6.2 B) or tetra-silane (Fig 6.2 C) linkers were used to covalently anchor m-THPC within small (≤20 nm) or large (≥90 nm) ORMOSIL NPs. Photophysical studies by collaborators who provided

untargeted ORMOSIL NPs used here (Dr F Mancin *et al.*,) showed the silica matrix did not significantly deactivate singlet oxygen production from covalently embedded m-THPC (Selvestrel, F. et al. 2013). This suggests key ROS molecules are able to diffuse out of the NP to elicit phototoxic damage. The outer surface of the NP was modified with densely packed PEG chains (e.g. PEG2000) to increase stability and prevent rapid clearance by the RES (Fig 6.3).

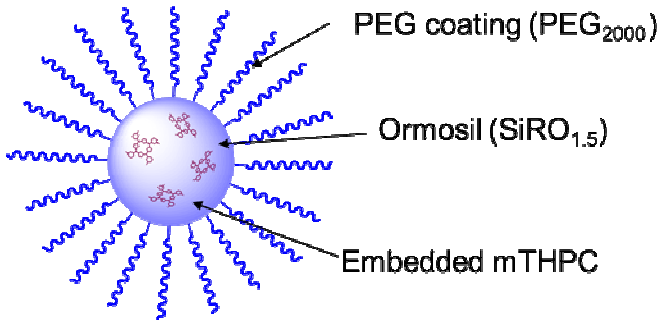

Figure 6.3. m-THPC loaded pegylated organically modified silica nanoparticles. *Diagram provided by University of Padova, Italy (Selvestrel, F. et al. 2013).*

Targeted cRGD-ORMOSIL NPs

The selectivity of drug molecule uptake into specific tissues has long been an outstanding issue in the treatment of disease and the focus of much research. In the field of oncology, addressing this issue is imperative in aiming to reduce drug-associated side effects and improving therapeutic efficacy (therapeutic index), in the monitoring, diagnosis and treatment of cancer, whilst simultaneously reducing cost. Through the encapsulation of therapeutics and imaging agents, nanotechnology has provided a promising platform in which to improve cancer targeting applications by increasing the half-life of circulating molecules for passive uptake into tumours (EPR effect). The opportunity to enhance uptake further through the surface engineering of nanocarriers, to preferentially seek tumour cells and minimise cytotoxicity to normal tissues, has been pursued over many years. Various ligands, whose complementary receptors are over-expressed on the surface of cancer cells, have been targeted in order to exploit the active uptake mechanism into malignant cells. These include transferrin, lectoferrin, lectin, folate, human growth factor (EGF, VEGF, TGF-β) receptors and scavenger, nuclear and integrin receptors (Mehra, N. K. et al. 2013). Despite encouraging progress in the targeted delivery of therapeutics and positive treatment outcomes at preferential tissue sites, the development of safe, effective

and stable targeted therapeutics remains a challenging necessity. ORMOSIL NPs were developed further for targeted studies in an attempt to further enchance tumour uptake and PDT efficacy by conjugating the cyclic RGD (Arg-Gly-Asp) peptide to the NP surface (Table 6.4), which has a known affinity for the integrin $\alpha_V\beta_3$ receptor overexpressed on a number of cancers.

Integrin targeting

The integrin are a family of cell adhesion receptors that span the lipid bilayer of cells and present themselves as heterodimeric glycoproteins on the cell surface. They mediate adhesion to the extracellular matrix (ECM) and immunoglobulin (Ig) superfamily molecules, whilst promoting intracellular signalling. Their repertoire consists of at least 24 distinct integrin heterodimers formed by the combination of 18 α-subunits and 8 β-subunits (Desgrosellier, J. S. et al. 2010). Specific integrin heterodimers preferentially bind to distinct ECM proteins and a given integrin expressed on a cell dictates the extent to which that cell will adhere to and migrate on different matrices. This mechanism is essential for normal cellular progression and tissue growth, but in the case of tumour proliferation, provides the necessary means for invasion and migration of cancer cells (Box 6.1).

Box 6.1. The role of integrins in tumours

i. Family of adhesion receptors involved in cell migration, invasion, proliferation and survival of solid tumours

ii. Integrins found on a host of other tumour-associated cells i.e. vascular endothelium, fibroblasts and platelets

iii. Integrins directly bind components of the extracellular matrix (ECM) providing the traction required for cell motility and invasion

iv. Integrins can profoundly influence the malignant potential (growth and metastasis) of a tumour

v. Integrins are involved in angiogenesis

vi. Promote intracellular signalling and crosstalk between tumour/host cells; activating cytokines, growth factors and oncogenes

Many solid tumours originate from epithelial cells and the integrins expressed by these epithelial cells are retained by tumours. As a consequence, integrins are expressed on a wide variety of cancers to different degrees and have been attributed to disease progression

(Table 6.2) (Desgrosellier, J. S. et al. 2010). Integrins $\alpha_v\beta_3$, $\alpha_5\beta_1$ and $\alpha_v\beta_6$, are typically expressed at low or undetectable levels in most adult epithelia but can be highly up regulated in some tumours. Conversely, some integrin expression, such as $\alpha_2\beta_1$, can be down-regulated in tumour cells to increase tumour dissemination (Kren, A. et al. 2007). These properties can be exploited for the purposes of cancer therapy and in recent years have led to great progression towards the use of integrins as therapeutic targets and imaging biomarkers.

Integrins have the ability to either enhance cell survival or induce apoptosis (e.g. p53 inactivation) in order to maintain the integrity of tissues and prevent cells surviving in an improper environment. This is achieved by drawing upon external environmental factors and through constant interaction with the ECM. Furthermore, the activation of complex signal transduction cascades controlling cellular fate are dependent on integrin ligation, as ligated integrins relay survival signals and unligated integrins are able to promote apoptosis (Desgrosellier, J. S. et al. 2010).

Tumour type	Integrins expressed	Associated phenotypes
Melanoma	**αvβ3** and α5β1	Vertical growth phase and lymph node metastasis
Breast	α6β4 and **αvβ3**	Increased tumour size and grade and decreased survival (α6β4) Increased bone metastasis (αvβ3)
Prostate	**αvβ3**	Increased bone metastasis
Pancreatic	**αvβ3**	Lymph node metastasis
Ovarian	α4β1 and **αvβ3**	Increased peritoneal metastasis (α4β1) Tumour proliferation (αvβ3)
Cervical	**αvβ3** and αvβ6	Decreased patient survival
Glioblastoma	**αvβ3** and αvβ5	Both are expressed at the tumour–normal tissue margin and have a possible role in invasion

Table 6.2. Selection of integrins involved in certain cancers. *Adapted from (Desgrosellier, J. S. et al. 2010).*

α_v integrins were first identified on the basis of their ability to recognise the RGD (Arg-Gly-Asp) peptide sequence (Pytela, R. et al. 1985) (Fig 6.4). Integrin $\alpha_V\beta_3$ consists of two components, integrin alpha V and integrin beta 3 (endothelial cells: CD61), and has shown to augment tumour progression. Integrin $\alpha_V\beta_3$ is able to regulate cell survival through crosstalk with fibroblast growth factor receptor (FGFR) via specific integrin-growth factor receptor pairing, which prevents cellular apoptosis through the intrinsic apoptotic pathway (Petitclerc, E. et al. 1999). Targeting of this integrin with antagonists can help to promote

endothelial cell death. In conjunction with integrin $\alpha_V\beta_5$ (crosstalk with vascular endothelial growth factor receptor 2, VEGFR2), integrin $\alpha_V\beta_3$ has been targeted with cyclic RGD pentapeptide, Cilengitide® (Merck KGaA), in Phase II clinical trials and has shown effectiveness in blocking tumour progression in the treatment of glioblastoma patients with few reported side effects (Mas-Moruno, C. et al. 2010).

This cyclic RGD peptide (cRGD) demonstrated 100 to 1000 times increased activity over linear reference peptides and initial positive clinical findings led to the first Phase III clinical trial being conducted with an integrin antagonist. However, in 2013 the trial suffered setbacks following disappointing late-stage results (500+ patients), as no significant increase in the overall survival of patients was found in comparison to the current standard chemo-radiotherapy regimen (i.e. temozolomide and radiotherapy). This highlights the clinical importance of continued research into the role integrins and integrin antagonists play as tumour inhibitors.

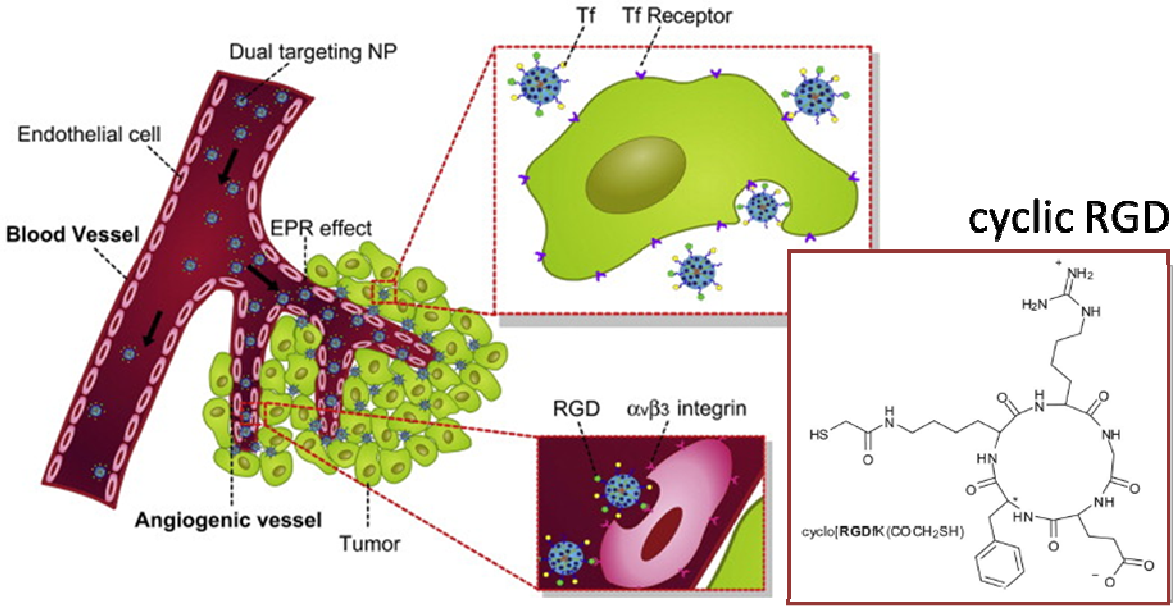

Fig 6.4. Targeted NPs used to deliver therapeutics to tumour tissues with greater efficacy following surface conjugation with RGD (Arg-Gly-Asp). Inset: cyclic RGD peptide. *Adapted from (Xu, J. et al. 2012).*

$\alpha_V\beta_3$ integrin: Applications in PDT

Other early phase clinical trials with integrin antagonists (RGD peptide and monoclonal antibodies, mAbs) and preclinical studies have been comprehensively reviewed by (Avraamides, C. J. et al. 2008) and (Desgrosellier, J. S. et al. 2010), respectively. RGD studies reviewed here will focus on integrin-targeted therapies for the delivery of

photosensitisers for applications in PDT (Table 6.3). Photosensitiser (PS)–peptide conjugates have been developed as a targeting strategy against human umbilical vein endothelial cells (HUVEC) overexpressing $\alpha_v\beta_3$ integrin by conjugating a linear or cyclic RGD peptide (cRGD) to 5-(4-carboxyphenyl)-10,15,20-triphenylchlorin (porphyrin) (Frochot, C. et al. 2007). The cellular uptake and phototoxicity of porphyrin was greatly enhanced following its conjugation to the RGD peptide in the HUVEC cell line, in comparison to free PS. The internalisation of either PS conjugate (linear or cyclic RGD motif) was approximately 80 – 100 greater than porphyrin alone after 24 h. Furthermore, despite a two-fold reduction in the quantum singlet oxygen yield produced by the RGD-porphyrin conjugates, a greater phototoxicity against HUVEC cells was observed with the conjugated versus unconjugated porphyrin. Some non-specific internalisation was detected towards the non-expressing $\alpha_v\beta_3$ integrin cell line, EMT-6, which was attributed to possible conjugate aggregation in the media, however, demonstrated no toxicity to cells (Frochot, C. et al. 2007). An enhanced cellular accumulation was observed in a human cervical cancer cell line (SiHa) with similar cyclic RGD peptides conjugated to the PS, Protoporphyrin IX (PpIX); precursor to the haem biosynthesis pathway. Pharmacokinetic analysis of PpIX-cRGD *in vivo* showed accumulation in the liver but significant retention of PpIX in tumour tissue, with 2-fold higher tumour: normal tissue ratios than the free PS following its administration into a CaNT mammary tumour mouse model (Conway, C. L. et al. 2008). Unfortunately, this was not reflected in the overall *in vivo* PDT data, at dose-light intervals of 0 and 6 h, as no significant difference between tumour PDT efficacy was observed with conjugated-PpIX versus free PpIX. This was thought to be due to differences in the target environment or in the subcellular localisation of the compounds.

Few studies have been carried out using RGD-targeted NPs incorporating photosensitisers for PDT applications *in vitro*. Concerns with NP-ligand include the potential for denaturation of RGD peptide and other proteins *i.e.* mAbs, when bound to the NP surface. This can affect binding of the ligand to its receptor, increase non-specific interactions, promote the production of protein-NP aggregates or stimulate inflammation. Selvestrel *et al.*, has recently investigated cyclic RGD targeted to PEG-ORMOSIL NPs via a commercially available MBS (*m*-Maleimidobenzoyl-*N*-hydroxysuccinimide ester) crosslinker. These RGD-NPs showed a higher uptake when incubated with HUVEC cells (overexpress integrin $\alpha_v\beta_3$ receptor) in comparison to identically prepared NPs conjugated with a control peptide, RAD, whereby the central glycine amino acid was substituted with

alanine to prevent integrin recognition and to eliminate the possibility of non-specific interactions. Furthermore, cellular uptake increased with increasing NP surface coating of RGD peptide, from 15 to 30% (Selvestrel, F. et al. 2013). In PDT studies with RGD-NPs, a significant reduction in cell viability was found following irradiation of cells, demonstrating their ability to induce a phototoxic effect with covalently embedded m-THPC. However, no difference in cell kill was observed between RGD and control RAD-conjugated NPs. Wang *et al*., encapsulated lipophilic ZnPc molecules in the hydrophobic layers of polymeric lipid micelles, which contained upconversion nanocrystals ($NaYF_4$) at the central core. The surface of these pegylated micelles was targeted with RGD and transmembrane peptide Tat and demonstrated a 60% reduction in MCF-7 ($\alpha_V\beta_3$–positive) cell viability with targeted micelles versus untargeted controls following PDT (Wang, H. et al. 2014).

To our knowledge, no studies have yet been conducted with RGD-targeted agents *in vivo* for use in PDT but many studies have demonstrated the efficacy and biodistribution of RGD-targeted NPs loaded with chemotherapeutics *in vivo*, in particular liposomal doxorubicin (Chen, Z. et al. 2012;Kim, J. W. et al. 2004;Schiffelers, R. M. et al. 2003;Xiong, X. B. et al. 2005c;Zhang, Y. F. et al. 2010). Doxorubicin-loaded pegylated liposomes targeted with RGD showed a higher uptake and cytotoxicity *in vitro* in human A375 melanoma cells in comparison to free drug or untargeted liposomes and *in vivo*, biodistribution and therapeutic efficacy showed more effective tumour regression in B16 tumour-bearing mice with RGD-targeted liposomes (Xiong, X. B. et al. 2005c). In the same *in vivo* model, Zhang *et al*., demonstrated similar tumour regression following co-encapsulation of doxorubicin with a vascular disrupting agent in RGD-modified liposomes (Zhang, Y. F. et al. 2010). These results show promise for PS uptake with RGD-targeted nanoparticles proposed here.

Despite multiple studies demonstrating the suitability of RGD as a targeting moiety for cancer treatment, it is important to consider the crucial, yet contradictory role integrins play in both tumour progression and the host's cellular response to cancer. For example, in addition to certain tumours, integrins are expressed on a vast number of endogenous cells, including endothelial cells, fibroblasts, pericytes, bone marrow-derived cells, inflammatory cells and platelets, which are involved in numerous host functions, such as angiogenesis

and desmoplasia, whilst also comprising a significant proportion of the immune system (Fig 6.5).

Typically these integrins are expressed to a lower degree on mature vessels and although their presence on many of these cells types creates a greater application for potential therapeutic targets, it also raises concerns regarding uptake of RGD-targeted nanosystems into cells of the host's immune system *in vivo* and associated toxicity. Abundant similarities exist between inflammation and the progression of cancer. For example, at a tissue level, in both cases, a common phenomenon is the increased infiltration of leukocytes, such as neutrophils, macrophages and lymphocytes at the disease site (Maeda, H. et al. 2000) and pro-tumorigenic integrin, $\alpha_v\beta_3$, is also expressed by platelets, dendritic cells and monocytes (precursor macrophages) (Fig 6.5). As such, research groups have used targeted RGD-liposomes for drug delivery to monocytes and macrophages (Kelly, C. et al. 2011).

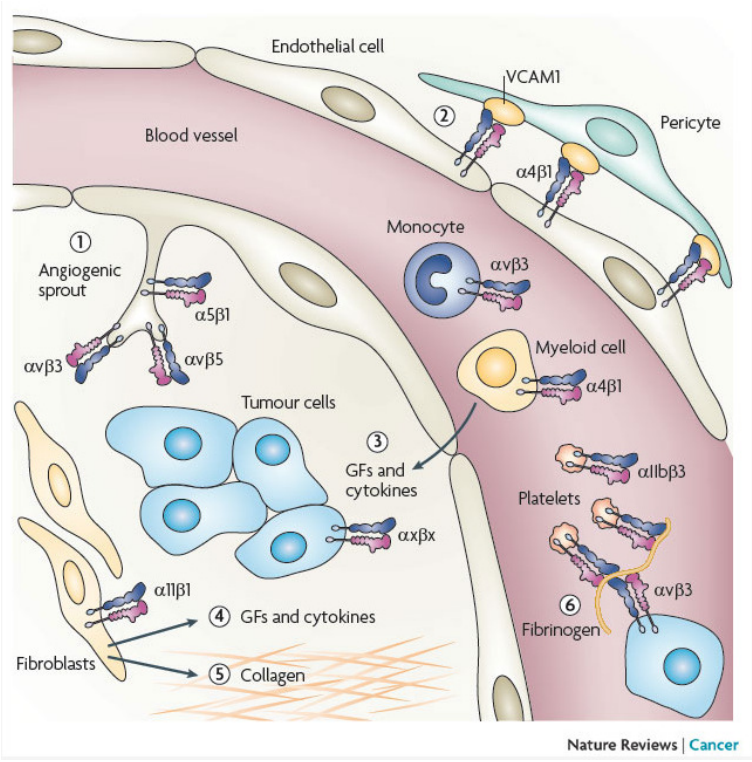

Fig 6.5. Role of integrins in the host response to cancer: (1) Integrins regulate the migration, proliferation and survival of endothelial cells for angiogenesis. (2) Integrins promote interaction between cells for the stabilisation of newly formed blood vessels (neovasculature). (3) Monocytes ($\alpha_v\beta_3$) may enhance disease progression by secreting cytokines and growth factors (GFs) to initiate angiogenesis and tumour cell migration. The growth of fibrous or connective tissue (desmoplasia) and (5) deposition of collagen involved in tumour progression requires the secretion of further GFs and cytokines from fibroblast infiltration (4). (6) Platelets have also been found to play an important role in possibly aiding metastatic dissemination by interacting with tumour cells through a fibrinogen bridge. *Taken from (Desgrosellier, J. S. et al. 2010).*

The recruitment of macrophages by integrin $\alpha_v\beta_3$ is important for tumour suppression (Taverna, D. et al. 2004), however, could conceivably lead to unfavourable uptake or stimulation of phagocytic cells through binding of RGD-targeted therapeutics, causing high accumulation or clearance through the liver, where resident macrophages reside under steady state conditions (also in the lungs). Conversely, several studies have shown that integrins have an essential role in the homing of myeloid cells and mononuclear phagocytes (*e.g.* monocytes, macrophages, dendritic cells) to tumours, which are also intrinsically implicated in innate immunity, primarily phagocytosis, and play a pivotal role in inflammation. Moreover, metastasis can be greatly facilitated by the recruitment of these cells to the disease site, leading to potential redistribution of phagocytosed RGD-targeted therapeutics from circulating monocytes under inflammatory conditions and result in an increase uptake in tumour tissue (Ferjancic, S. et al. 2013). Tumour tissue also contains its own associated macrophages (TAMs), which play a complex role in tumorigenesis, as they are involved in mechanism to both prevent (M1 macrophages) and promote (M2 macrophages) tumour activities. It was demonstrated through chemical extraction and FACS analysis that the PS Photofrin was taken up at greater levels into TAMs than into parenchymal 'tumour cells' derived from mice bearing squamous cell carcinoma (SCCVII) tumours following its administration (Korbelik, M. et al. 1991).

Further to this, the applicability of the integrin $\alpha_v\beta_3$ as an RGD-targeting moiety for cancer therapeutics is demonstrated via its role in tumour angiogenesis, whereby an increase in integrin expression on tumour-associated blood vessels is observed unlike well-established quiescent endothelium (Brooks, P. C. et al. 1994b). On account of the blood supply tumours demand to rapidly proliferate, vessels are structurally and biologically distinct from mature vessels. Leaky tumour vessels with enlarged fenestrae compromise blood flow and vascular drug delivery, whilst promoting fibrosis and tumour cell intravasation (Avraamides, C. J. et al. 2008). It is likely that an increased expression of integrin $\alpha_v\beta_3$, along with $\alpha_v\beta_5$, allows angiogenic endothelial cells to interact with the ECM and bind provisional matrix proteins (*i.e.* vitronectin, fibrinogen and fibronectin) which have been deposited in the tumour microenvironment and provide traction for invading endothelial cells. Angiogenesis at the primary tumour site, not only provides a necessary blood supply for sustained progression but also grants access to metastatic tumour cells to travel to distant sites, providing a strong rationale for targeting this integrin.

Photosensitiser	Nano-carrier	Targeting moiety	Tumour model	Reference
ZnPc	Pegylated lipid micelles	RGD Tat	Human breast cancer (MCF-7) cells	(Wang, H. et al. 2014)
m-THPC	Pegylated ORMOSIL NPs	cRGD	Human umbilical vein endothelial (HUVEC) cells	(Selvestrel, F. et al. 2013)
PpIX (5-ALA)	conjugate	cRGD	Subcut mouse mammary tumour (CaNT) and human cervical cells (SiHa)	(Conway, C. L. et al. 2008)
Porphyrin	conjugate	cRGD RGD (linear)	Human umbilical vein endothelial (HUVEC) cells and mouse mammary cells (EMT-6)	(Frochot, C. et al. 2007)
Cy 5.5	conjugate	cRGD	Human melanoma (HT21), breast cancer (MCF-7) and fibrosarcoma (HT-1080) cells	(von, W. A. et al. 2007)

Table 6.3. Preclinical targeting studies of photosensitisers conjugated to RGD or encapsulated in targeted RGD nanocarriers for applications in PDT. cRGD, cyclic arg-gly-asp peptide: PpIX, protoporphyrin IX; m-THPC, meta-tetra(hydroxyphenyl)chlorin; NPs, nanoparticles; ZnPc, Zinc phthalocyanine; Tat, peptide derived from the transactivator of transcription of HIV; ORMOSIL, organically modified silica.

The utilisation of NPs to deliver therapeutics in the treatment of cancer and other diseases is becoming increasingly relevant. Despite advancements in the field, poor overall delivery to the tumour microenvironment and internalisation to the tumour cell cytosol remains the greatest challenge towards achieving clinical translation. Ligands can be conjugated to the surface of NPs with the aim of improving selective accumulation into cancer cells by exploiting the active uptake mechanism involved in intracellular internalisation, targeting complementary receptors over-expressed on the extracellular membrane of certain malignant cells. The aim of studies presented in this chapter was to investigate the *in vivo* biodistribution and PDT efficacy of m-THPC when incorporated in non-biodegradable untargeted- and targeted-ORMOSIL NPs. To our knowledge, these are the first *in vivo* studies to have been carried out using m-THPC covalently incorporated within ORMOSIL NPs, of varying size, for anti-tumour PDT efficacy studies. Furthermore, few *in vivo* studies have been conducted involving targeted NPs for applications in PDT.

Silica NPs	size (nm)	m-THPC (μM)	m-THPC loading (%)	silane bonding	silica conc (mg mL^{-1})	total silica (mg kg^{-1})
IR194	19	421	2.34	mono	16.7	4.34
IR253	16	555	2.36	mono	21.8	3.47
IR254	17	505	2.16	mono	21.7	3.82
IR322	16	499	2.08	mono	22.3	3.92
IR347	20	431	1.72	mono	23.3	4.72
GG91UF*	100	470	2	**tetra**	~	~
SF142UF	95	267	1.2	mono	~	~
SF232UF	90	321	1.23	mono	17.7	4.87
SF288*	110	270	1.6	**tetra**	11.4	3.72
SF311	90	187	1.87	mono	9.3	4.39
cRGD* (Arg-Gly-Asp)	75	248	-	**tetra**	9.9	4.56
cRAD*(Arg-Ala-Asp)	75	504	-	**tetra**	20.2	3.03

Table 6.4. Specifications of ORMOSIL NP preparations used in these investigations (developed at University of Padova, Italy); IR ≤20 nm, SF/GG ≥ 90-100 nm. Targeted cRGD-ORMOSIL NPs (receptor: αvβ3 integrin) and corresponding inactive targeted cRAD-ORMOSIL NPs. ***** indicates tetrasilane m-THPC binding

6.2 Materials & Methods

6.2.1 Chemicals and Photosensitisers

Microporous (<2 nm) organically modified silica (ORMOSIL) nanoparticles (NPs) were synthesised, characterised and supplied by Dr Fabrizio Mancin at the University of Padova (Italy). Particles were prepared using a variation of the well-established Stöber procedure (Stober, W. et al. 1968) via reverse microemulsion (oil-in-water) to produce smaller NPs (<150 nm). In a one-pot synthesis method; ammonia-catalysed polymerisation of alkoxysilane precursors, vinyltriethoxysilane (VTES), occurred in the hydrophobic core of micelles in water (instead of ethanol) in the presence of surfactants (AOT in *n*-butanol, Tween, Brij 35) to control the growth of the nanoparticles (Selvestrel, F. et al. 2013). The addition of trialkoxysilane modified PEG ensured covalent grafting of PEG onto the NP surface at high densities (80-85 %) based on weight (*see* ***Appendix I – C.1 Synthesis of pegylated ORMOSIL NPs***). The reaction mixture was passed through a 0.22 µm membrane filter. The mean diameter of the ORMOSIL NPs was measured using transmission electron microscopy (TEM) (*see* ***Appendix I - C.6 Transmission electron microscopy images***). Dynamic light scattering (DLS) was used to measure the corresponding mean hydrodynamic diameter and zeta potential. The overall surface charge was slightly negative with a zeta potential value of ~ -5.2 mV (PBS, pH 7.4). The content of m-THPC was between 1-2 % (w/w). Particles were supplied in saline buffer. The specifications of individual batches of pegylated ORMOSIL NPs covalently incorporating m-THPC used in this investigation are detailed in Table 6.4. NPs were stored for up to 12 months (4°C) without any visible aggregation.

Targeted ORMOSIL NPs (PEG 2000: 30 %) and corresponding control ORMOSIL NPs (inactive targeted) were synthesised via the same process. m-THPC was covalently incorporated in the silica matrix of NPs via a tetrasilane linker. The cyclic-RGD peptide (Arg-Gly-Asp) ($\alpha_v\beta_3$ integrin receptor inhibitor) and inactive cyclic-RAD peptide (Arg-Ala-Asp) were conjugated to the NP surface to produce: m-THPC-loaded SF532 cRGD-targeted ORMOSIL NPs and SF532 cRAD-untargeted ORMOSIL NPs (Table 6.4).

6.2.2 Absorbance spectra

The absorbance spectra of m-THPC in each ORMOSIL NP batch were recorded using a Lambda 25-UV/Vis spectrophotometer (Perkin-Elmer, UK) between 300 – 700 nm light

wavelengths at 1 nm intervals in either storage buffer (saline) or solvent (ethanol/methanol) to ensure the characteristics of the absorbance spectrum of m-THPC had not been altered following covalent encapsulation. Spectra were obtained at a scanning speed of 480 nm min^{-1} and recorded through UV Winlab software®. The absorbance spectra of pure m-THPC, monosilane m-THPC, tetrasilane m-THPC, unloaded (no m-THPC) ORMOSIL NPs, SF532 cRGD-targeted, SF532 cRAD-untargeted ORMOSIL NP spectra were also recorded. In a separate group, absorbance of m-THPC in ORMOSIL NPs was measured following dilution and incubated in Solvable™ to replicate tissue chemical extraction conditions and assess any potential shifts in maximum absorbance peaks (λ_{max}). Optimal wavelengths at the highest sensitivity (to minimise deviations from Beer's Law, $A = \varepsilon\ l\ c$) were set to obtain measurements (m-THPC λ_{exc} = 423 nm, λ_{em} = 652 nm). Absorbance measurements of each solution were taken in quartz cuvettes with a light path-length of 1 cm (Pye Unicam, UK). Cuvettes were rinsed before each reading. Spectra were normalised with background absorbance values of the corresponding diluent.

6.2.3 Confocal microscopy in vitro

For visualisation of untartgeted *m*-THPC-ORMOSIL NP uptake and intracellular localisation confocal microscopy was adopted. 1 x 10^4 MC28 cells were prepared using identical incubation conditions and fluorodish seeding methods as described in **Chapter 4**: Liposomes. Cells were incubated for 4 h with 1 μM *m*-THPC (Foscan) or *m*-THPC ORMOSIL NPs; (i) ~20 nm (monosilane m-THPC) and (ii) ~100 nm (tetrasilane m-THPC). Control cells, without m-THPC, were incubated with 0.5 μM 4', 6-diemidino- 2-phenylindole (DAPI) (Sigma, UK) for 10 minutes prior to imaging to identify the presence of live cells. Following incubation, cells were washed twice with PBS before fresh media (minus serum and phenol red) was added *(see **Appendix I – C.4 Preparing Fluorodishes: ORMOSIL NPs**).* Cells were observed using an inverted Olympus Fluoview 1000 confocal laser scanning microscope. Fluorescence confocal images were obtained at x20 magnification and analysed with Fluoview FV1000 (Olympus)/Image J software. m-THPC fluorescence was detected using a 405 nm laser and a set of detection filters with 400 nm excitation and 640-80 nm emission. Laser voltage, Gain and Offset were kept consistent throughout imaging.

As a proof of concept for targeted ORMOSIL NP studies, a cRGD-FITC conjugate was provided by the University of Padova (Italy) to identify the expression of $\alpha_v\beta_3$ integrin on selected human cell lines, A549, MC28 and MCF-7, chosen based on previously published literature. The conjugate was administered to cells at a concentration of 50 nM. Targeted-NPs were added to cells at a concentration of 2 μM (m-THPC equivalent) and cells were cultured under standard conditions.

6.2.4 Animals and tumour model

Female HL rats (150–220 g) were used for all *in vivo* tissue pharmacokinetic studies and toxicology studies to reduce animal numbers. The methylcholanthrene-induced fibrosarcoma cell line (MC28), syngeneic and transplantable to Hooded Lister (HL) rats was cultured under identical conditions as described in **Chapter 4**: Liposomes. Animals were inoculated subcutaneously in the lower flank with approximately 1–2 × 10^6 MC28 cells in 0.1 mL injection volume. Tumours were monitored continuously and reached an optimal size of approximately 10 mm^3 after 7–10 days (as described in **Chapter 4**: Liposomes). Following obtainment of sufficient tumour size between days 7-10, ORMOSIL NPs were administered intravenously via a tail vein injection. Administered m-THPC doses were based on availability of compounds; untargeted ORMOSIL NPs (0.3 mg kg^{-1} m-THPC), targeted cRGD-ORMOSIL or inactive targeted cRAD-ORMOSIL (0.1 mg kg^{-1} m-THPC). Animals used for time points beyond 72 h were not inoculated with tumour cells on account of the maximal tumour growth threshold being exceeded beyond this time. At a specified time point between 2 and 672 h, animals were killed by cervical dislocation.

6.2.5 Pharmacokinetic study

Tissue samples selected for pharmacokinetic analysis included skin (right abdominal wall), liver, spleen, kidneys, lung, blood serum and tumour, taken from three animals at each time point. Immediately post-mortem tissues were removed under subdued lighting at 2, 6, 24, 72, (tumours) and a further 168 h, 2 weeks (336 h) and 28 days (672 h) from HL rats after intravenous administration of each untargeted-ORMOSIL NPs (0.3 mg kg^{-1} m-THPC) or at 24 h for targeted-ORMSOSIL NPs (0.1 mg kg^{-1} m-THPC). A lower injected dose of m-THPC was chosen for targeted studies based on the % m-THPC loading of NPs and the quantity of compound provided. Blood samples (~3 mL) were centrifuged to separate the serum at 2000 rpm (~300 g RCF) for 10 min for pharmacokinetic analysis and

for toxicological analysis (liver/renal function assays). Negative control animals at 0 h were run simultaneously. Samples were stored in the dark at −80 °C post-mortem. m-THPC extraction from tissues and detection was acquired using the same equipment, under identical conditions, following the same methodologies and mathematical models as described in **Chapter 4**: Liposomes. Solvable™ was capable of completely decomposing ORMOSIL NPs upon incubation (*see* ***Appendix I - C.6 Transmission Electron Microscopy (TEM) Images***).

6.2.6 Confocal microscopy ex vivo

Confocal microscopy was used to obtained images of the localisation of m-THPC in fresh *ex vivo* liver tissue following intravenous administration to HL rats of either 1 mg kg^{-1} Foscan or 0.3 mg kg^{-1} of monosilane m-THPC covalently bound in either ~20 nm or ~90 nm ORMOSIL NPS. Tissue samples were removed and observed immediately post-mortem using an inverted Olympus Fluoview 1000 confocal laser scanning microscope. Fluorescence confocal images were obtained using different combinations of magnification and objective lens; those imaged at x60 used an oil immersion objective (Olympus). Fluoview FV1000 (Olympus) and Image J software were used to analyse images. m-THPC fluorescence was detected using a 405 nm laser and a set of detection filters with 400 nm excitation and 640-80 nm emission. Laser voltage, Gain and Offset were kept consistent throughout imaging.

6.2.7 Fluorescence microscopy (frozen tissue sections)

Animal tissues were removed post-mortem and snap frozen in liquid nitrogen under isopentane (VWR, UK) 24 h post-intravenous injection with 0.3 mg kg^{-1} m-THPC of ~90 nm ORMOSIL NPs or 0.1 mg kg^{-1} m-THPC in targeted ORMOSIL NPS; with m-THPC covalently bound by either monosilane or tetrasilane linkers. For untargeted ORMOISL NP studies, 10 micron frozen sections of liver and tumour tissue were cut using a cryostat and mounted on glass slide coverslips (VWR, UK). For targeted ORMOSIL NP studies liver, spleen, lung, kidney and tumour tissue were cut and mounted on poly-lysine treated glass slides (VWR, UK). On average five sections were taken per tissue sample from three animals. Sections exposed to blue light for 10 secs using a 405 nm laser (3 mW) to excite m-THPC and visualise the extent of dye uptake and diffusion in tissues. CCD false coloured fluorescence microscopy images (512 pixels) were obtained with a PIXI 512 CCD camera (Princeton Instruments, USA) coupled to an inverted Olympus IMT-2

microscope (Olympus). This system was equipped with a dichroic mirror (505DCLP, Omega) and filters were set as follows: 660 nm DF33 colour bandpass filter, 595 nm long pass filter and 500 nm ACSP short pass filter. Sections were imaged using different combinations of magnification and objective lens and analysed through WinSpec32 software (Roper Science Software). Corresponding confocal images of frozen liver and tumour sections with untargeted ORMOSIL NPs were also imaged as described above, ***6.2.6 Confocal Microscopy ex vivo***. The image resolution was 512 x 512 pixels, corresponding to 557 x 557 microns.

6.2.8 Toxicology: Biochemical analysis

For quantitative plasma enzyme measurements of aspartate transaminase (AST) and alkaline phosphatase (ALP) to assess liver/renal function, blood samples were collected from HL rats immediately following cervical dislocation at each time intervals; 2, 6, 24, 72, 168 h, 2 weeks and 28 day, after intravenous administration of m-THPC in ORMOSIL NPs at a dose of 0.3 mg kg^{-1}. Blood samples were left to stand at RT for 20 mins then centrifuged at 5000 rpm for 10 mins. Separated plasma was assayed to determine plasma enzyme activities using a Roche/Hitachi 912/917/MODULAR analyser (ACN 413, Cobas) at The Royal Free Hospital, UCL (London) with reagent kits provided by the manufacturer (AST: α-ketoglutarate, malate dehydrogenase, L-aspartate, NADH; ALT: α-ketoglutarate, lactate dehydrogenase, L-alanine, NADH) (*see* ***Appendix I – C.7 Toxicology: liver/renal enzyme function test***).

6.2.9 Toxicology: Histological analysis

Major organs, including the liver, spleen, lungs and kidneys, were removed post-mortem from three animals at 2 weeks post intravenous administration of ~20 nm and ~100 nm m-THPC-ORMOSIL NPs. Selected portions of each organ were harvested and immersed in 4% neutral formalin buffer (4% w/v formaldehyde in phosphate buffered saline) for a minimum of 24 h at 20 °C. Samples were processed by routine histological methods. Tissues were embedded face down in paraffin wax blocks. Four-micrometre sections were cut and mounted on Vectabond (Vecta laboratories, UK) treated glass slides. Three sections were taken from each of the tissue samples. Slides were stained with Harris haematoxylin and eosin. Whole slides were scanned with the Hamamatsu Nanozoomer (Hamamatsu Photonics UK Ltd) and Hamamatsu virtual microscopy imaging software was used to observe any abnormalities in tissues indicative of toxicity at various

magnifications. Tissue histology was assessed by a pathologist 'blinded' to the treatment groups and liver/renal biochemistry data.

6.2.10 Photodynamic therapy on MC28 tumours

Injected doses of 0.3 mg kg^{-1} m-THPC for untargeted-ORMOSIL NP studies and 0.1 mg kg^{-1} m-THPC for targeted-ORMOSIL NP studies were administered to tumour animals prior to light delivery. A drug-light interval of 24 h were chosen based on pharmacokinetic data and a second DLI of 6 h was investigated for untargeted ORMOSIL NPs. Tumours were irradiated with red light using a 400 µm bare-cleaved tip optical fibre inserted approximately 1 mm into the tumour capsule via a small incision in the overlying skin and tumour capsule, to mimic interstitial clinical PDT with Foscan. A total of 10 J of light at 100 mW for 100 s was delivered from a 652 nm diode laser. Treatment with each m-THPC formulation was initiated when tumours had reached an optimal diameter of 10 mm. Each treatment group consisted of four animals. Animals were killed 24 h after treatment by cervical dislocation and whole tumours resected for histological analysis.

6.2.11 Histology and measuring necrosis (Hamamatsu nanozoomer)

Treated tumour tissue samples were removed post-mortem and prepared by routine methods for histological analysis as described in **Chapter 4**: Liposomes. The damage was calculated from each tumour as a percentage of the whole tumour surface area. Six sections were averaged per tumour (3 from each tumour half). The mean surface area of tumour necrosis was calculated through blind analysis per group of four identically treated animals and all data were represented as mean±SD.

6.2.12 Statistical analysis

Mean and standard deviation was calculated for each animal group (±SD, n=3–5). All data were represented as mean±SD. Statistical analysis was carried out using a two-tailed Student's t-test and a Mann–Whitney t-test for PDT data. $p \leq 0.05$ was considered statistically significant, unless stated otherwise.

6.3 Results

Untargeted ORMOSIL NPs

Characterisation studies carried out at the University of Padova using dynamic light scattering (DLS) indicated unimodal distribution and maximum percentage intensity of ~20 nm and ~100 nm (data not shown). It was reported TEM images (*see* ***Appendix I C.6 - TEM images***) correlated well with DLS results, showing a narrow size distribution and a spherical morphology (Compagnin, C. et al. 2011). In addition, the overall surface charge was found to be slightly negative, with a zeta potential value of ~ -5.2 mV, which can be attributed to the presence of PEG groups on the ORMOSIL NP surface and small traces of remnant surfactant from particle synthesis (Kumar, R. et al. 2010).

i. Absorption spectra

An absorbance spectrum of m-THPC and each pegylated ORMOSIL NP batch was taken in either, (i) saline buffer (data not shown), (ii) methanol or (iii) Solvable™. The first was to deduce absorbance maxima for NPs administered for *in vivo* studies (data not shown).

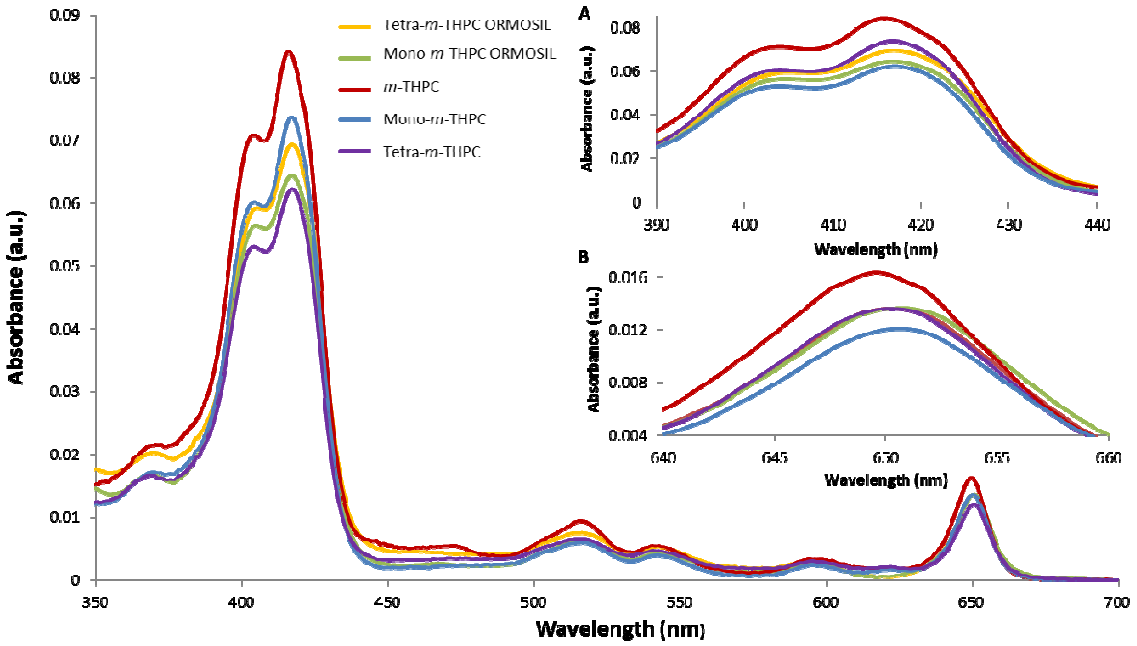

Figure 6.6. Absorbance spectra of m-THPC, monosilane or tetrasilane m-THPC derivatives and m-THPC monosilane or tetrasilane derivatives bound inside large (≥90 nm) ORMOSIL NPs diluted in MeOH. All solutions were prepared at 0.5 µM m-THPC equivalent.

Secondly, comparisons of free m-THPC, mono- or tetrasilane m-THPC and mono- or tetrasilane-mTHPC covalently bound in pegylated ORMOSIL NPs were carried out in methanol (MeOH), as m-THPC is highly hydrophobic, to ensure the spectroscopic properties of modified m-THPC and covalently encapsulated m-THPC had not been altered (Fig 6.6). Spectra indicated absorbance peaks characteristic of m-THPC (λ = 423 nm and 652 nm), which correspond to the literature (Kascakova, S. et al. 2008); (Bonnett, R. et al. 1999). There was no evidence of spectral broadening or dramatic shifts in absorbance maxima between m-THPC formulations, suggesting the same photoactive species of m-THPC were present. However, there was a small increase in absorbance intensity for both Soret and Q peaks with free versus modified or covalently encapsulated m-THPC but this may also be attributed to difference in solution concentrations (experimental error) (Fig 6.6 A and B). The shoulder observed on the Soret band for each m-THPC formulation is indicative of highly conjugated systems and is common for chlorin-compounds.

An absorbance spectrum of each m-THPC-loaded and unloaded ORMOSIL nanoparticle formulation was taken before *in vivo* studies to deduce peak absorbance wavelengths (Fig 6.7).

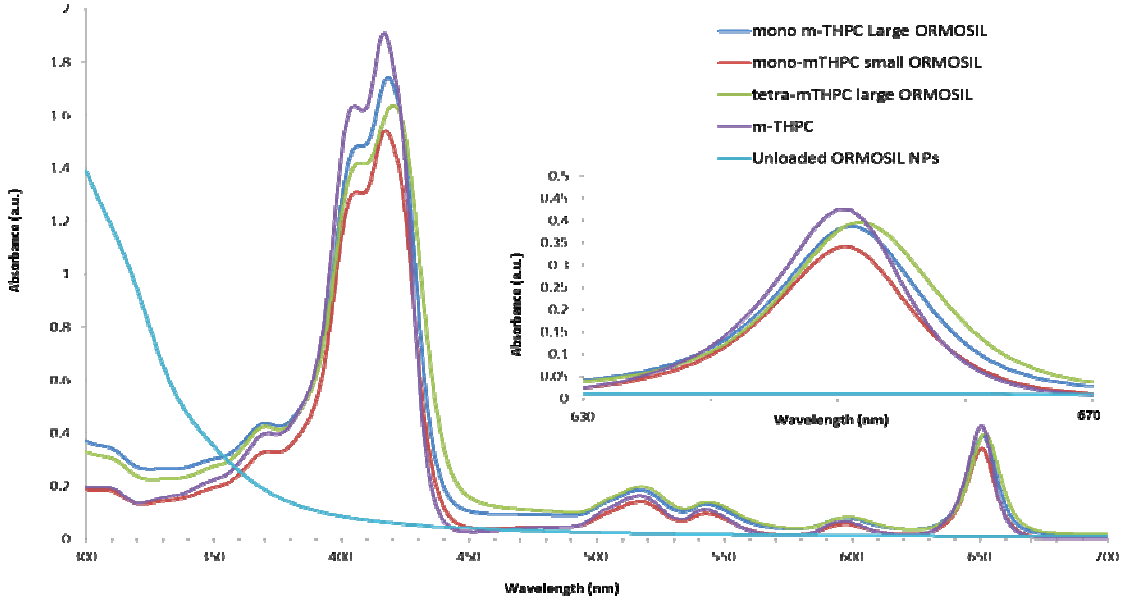

Figure 6.7. Absorbance spectra of m-THPC, unloaded ORMOSIL NPs (no m-THPC) and m-THPC monosilane or tetrasilane derivatives bound inside large (≥90 nm) or small (≤20 nm) ORMOSIL NPs diluted in MeOH. All solutions were prepared at 10 µM m-THPC equivalent.

Absorbance spectra of m-THPC loaded silica NPs in methanol (Fig 6.7) was in good agreement with the literature (Compagnin, C. et al. 2009). As with free m-THPC and liposomal encapsulated m-THPC (**Chapter 4**: Liposomes), the spectra showed two absorbance maxima peaks at ~ 420 nm (Soret band) and ~ 652 nm (Q band), suggesting the presence of monomerically active m-THPC (non-aggregated). Unloaded particles have an exaggerated light scattering (~300 nm) due to the higher concentration of particles per mL, as accurate concentrations could not be calculated without a fluorophore (Fig 6.7).

All ORMOSIL NPs were additionally incubated in Solvable™ for 2 h at 50°C to replicate conditions during chemical extraction (Fig 6.8) and ensure the preservation of spectroscopic m-THPC characteristics. There was no difference between absorbance spectra of ORMOSIL NPs taken in methanol (Fig 6.7) versus Solvable™ (Fig 6.8), with the exception of the loss of the shoulder on the Soret peak (~ 400 nm), which increased the peak intensity slightly. As the m-THPC chromophore is highly conjugated and solvent dependent this may be anticipated. However, this could indicate degradation of ORMOSIL NPs in Solvable (confirmed by TEM images, *see* ***Appendix I B.C - TEM images***) and release of m-THPC into its monomeric formation. Moreover, all ORMOSIL NPs diluted in saline buffer, as when administered to animals (data not shown), did not indicate any reduction in m-THPC absorbance intensity (652 nm). Around wavelengths of 300 – 350 nm, the absorbance spectra of m-THPC loaded particles showed light scattering of the ORMOSIL NPs increased with larger nanoparticle diameter size.

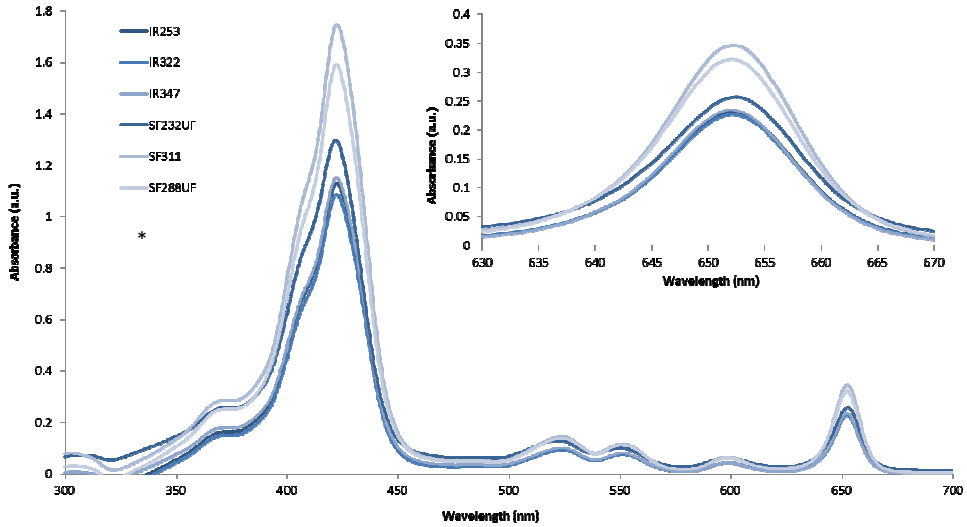

Figure 6.8. Absorbance spectra of m-THPC loaded ORMOSIL NPs (mono or tetra) in Solvable. All solutions were prepared at 10 µM. ORMOSIL NP batches beginning with IR: ~20 nm (mono-mTHPC), SF: ~100 nm (mono-mTHPC), * indicates ~100 n m ORMOSIL NPs with tetra-mTHPC.

ii. Confocal microscopy in vitro

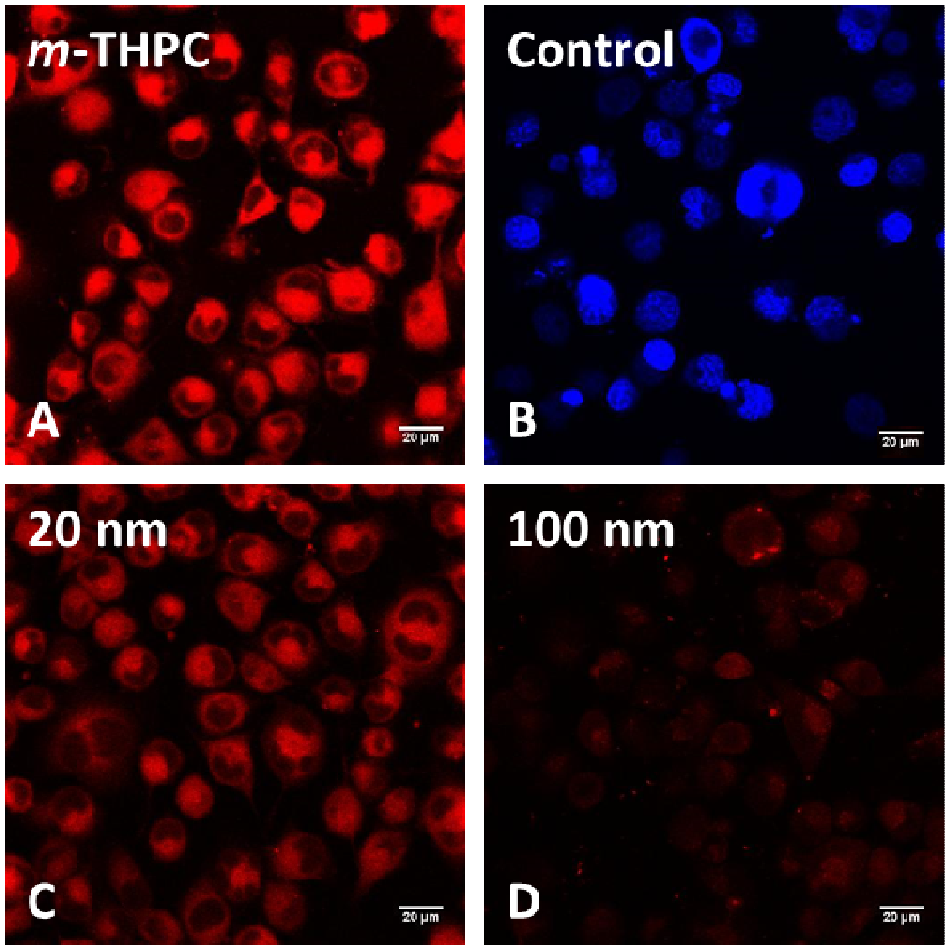

Figure 6.9. Confocal microscopy images of MC28 tumour cells following 4 h incubation with (A) free m-THPC, (B) Control, no m-THPC, + 0.5 µM DAPI (C) small ORMOSIL NPs of ~20 nm with mono-m-THPC (D) or large ORMOSIL NPs of ~100 nm with tetra-m-THPC. All m-THPC concentrations were administered at 1 µM.

In vitro studies were carried out with preliminary batches of pegylated ORMOSIL NPs whereby MC28 tumour cells were incubated for 4 h with either ~20 nm ORMOSIL NPs, incorporating covalently bound mono-mTHPC (Fig 6.9 C), or ~100 nm ORMOSIL NPs with tetrasilane-bound mTHPC (Fig 6.7 D). Confocal images indicated a higher uptake of smaller NPs (~20 nm) in comparison to larger NPs (~100 nm) due to the increase in observed red fluorescence. Free m-THPC (Fig 6.9 A) gave the most intense fluorescence signal and indicated uniform distribution throughout the cytoplasm of cells. This pattern of distribution was also demonstrated with the smaller NPs, with the nucleus defined as an enclosed black region. Control cells (without m-THPC) were incubated with DAPI (blue), a nuclear fluorescent stain which binds strongly to A-T rich regions of nuclear DNA, used to detect live cells (Fig 6.9 B) in the absence of red fluorescence.

iii. Pharmacokinetics of m-THPC (Foscan versus pegylated ORMSOIL NPs)

Pharmacokinetics studies were carried out in a selection of normal tissues and tumour tissue with pegylated ORMOSIL NPs, covalently incorporating m-THPC, to investigate their uptake and biodistribution *in vivo*. As with previously described with liposomal m-THPC formulations this was carried out through chemical extraction of m-THPC from tissues and spectrofluorimetric analysis using identical drug doses (0.3 mg kg^{-1} m-THPC equivalent).

Based on the limited supply of primary ORMOSIL NP batches (Table 6.5), initially only one time point was selected for preliminary biodistribution studies, rather than an entire time series. A 24 h time interval was chosen established from pharmacokinetic data of pegylated liposomal m-THPC in tumour tissue, which exhibited the greatest uptake of m-THPC. Both data sets of pegylated liposomal m-THPC and m-THPC in pegylated ORMOSIL NPs have been displayed for direct comparisons in tissue uptake at 24 h (Fig 6.10). It is important to consider differences in their biodegradation capabilities.

Sample	**IR194**	**SF142UF**	**GG91UF***
Size (nm)	19	95	100
m-THPC (µM)	421	267	470
Loading (%)	2.34	1.5	2.0
PEG length	2000	2000	2000
Silane bonding	mono	mono	tetra*

Table 6.5. Specifications of ORMOSIL NP preparations used for preliminary pharmacokinetics studies.

Preliminary data on the uptake of m-THPC in selected tissue of the HL rat at 24 h following administration of m-THPC at 0.3 mg kg^{-1} in either Foscan, FosPEG 2%, FosPEG 8%, and pegylated ORMOSIL NPs of ~20 nm or ~100 nm covalently incorporating either monosilane or tetrasilane bound m-THPC is illustrated in Figure 6.10 (*see* ***Appendix I - C.2 Quantitative ORMOSIL concentrations at 24 h in vivo***). Injected dose of m-THPC in ORMOSIL NPs showed little difference in the accumulation of m-THPC in the blood plasma between NP batches at 24 h (avg. ~1.5 µg g^{-1}), however, this was almost than three-fold the m-THPC concentration observed with pegylated liposomal nanocarriers (~0.5 µg

g^{-1}) and more than fifteen times that observed with Foscan (~0.05 µg g^{-1}) (Fig 6.10). No radical differences were identified between pegylated biodegradable liposomes (~1 µg g^{-1}) and pegylated non-biodegradable ORMOSIL NPs in the liver (~1.5 µg g^{-1}) versus Foscan (~1 µg g^{-1}) at 24 h (Fig 6.8), displaying only a small increase in m-THPC accumulation with ORMOSIL NPs. The same can be said for marginal differences in m-THPC accumulation in the kidney and skin following delivery by various pegylated nanocarriers in comparison to Foscan. The most evident difference in normal tissues is m-THPC concentrations in the lungs, with small (~20 nm) pegylated ORMOSIL NPs (~2 µg g^{-1}) drastically outweighing that of Foscan (~0.1 µg g^{-1}), larger ORMOSIL NPs (~0.7 µg g^{-1}) and pegylated liposomes (~1 µg g^{-1}). It should also be noted that m-THPC accumulation in the spleen (data not shown) when delivered by pegylated ORMOSIL NPs, regardless size, far surpassed m-THPC accumulation in any other organ or m-THPC formulation (*see* ***Appendix I - C.3 ORMOSIL NPs in the spleen at 24 h***).

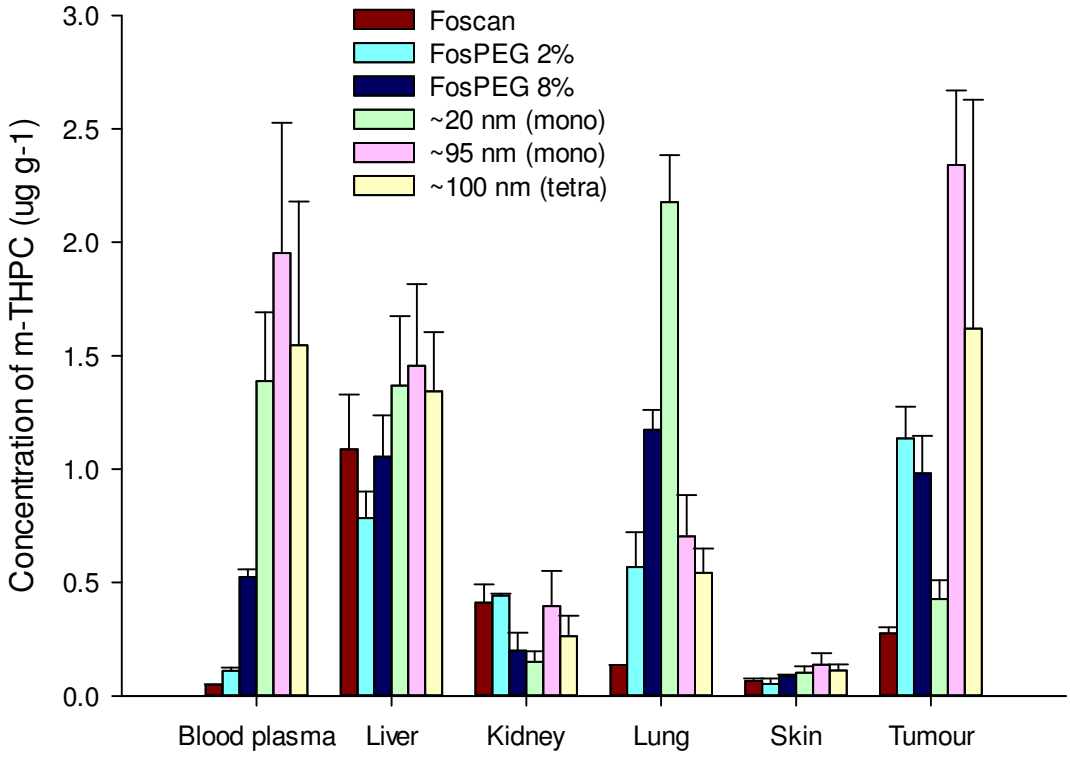

Figure 6.10. Concentration of m-THPC in tissues following intravenous administration of 0.3 mg kg^{-1} m-THPC covalently bound in non-biodegradable pegylated ORMOSIL nanoparticles; ■ ~20 nm (mono-m-THPC), ■ ~95 nm (mono-m-THPC), ■ ~100 nm (tetra-m-THPC), in comparison to biodegradable pegylated liposomal nanocarriers (■ FosPEG 2%, ■ FosPEG 8%) and standard m-THPC formulation (■ Foscan) at 24 h. Data points show the mean ± s.d., n=4.

In tumour tissue, results with preliminary NP batches appears to show an increase in the uptake of m-THPC when incorporated in large (~100 nm) pegylated ORMOSIL NPs (~2 $\mu g\ g^{-1}$), regardless of covalent encapsulation, in comparison this is almost fourfold > small (~20 nm) pegylated ORMOSIL NPs (~0.4 $\mu g\ g^{-1}$), twofold > pegylated liposomal nanocarriers (~1 $\mu g\ g^{-1}$) and threefold > Foscan (~0.3 $\mu g\ g^{-1}$) (Fig 6.10).

Sample	**IR253**	**IR254**	**SF232UF**
Size (nm)	16	17	90
m-THPC (μM)	555	505	321
Loading (%)	2.36	2.16	1.23
PEG length	2000	2000	2000
Silane bonding	mono	mono	mono

Table 6.6. Specifications of ORMOSIL NP preparations used for pharmacokinetic and toxicology studies. *****In these studies where batches IR253 & IR254 have been employed, samples will be referred to as 20 nm (mono) NPs. Similarly, larger NPs (SF232UF) will be referred to as 90 nm (mono) NPs for simplicity.

Subsequent ORMOSIL nanoparticle composites were redeveloped by our collaborators (Table 6.6) and pharmacokinetic studies were extended to assess accumulation and retention of non-biodegradable nanocarriers at longer time periods (28 days). Foscan data was acquired from studies in Wistar rats (**Chapter 4**: Liposomes) and is included as point of reference. Additionally, Foscan data from 168 h ≥ 672 h displayed here is based on predicted concentrations calculated using the rate constants of the terminal phase of elimination (72 h ≥ 168 h) from liposome studies (*also see* ***Appendix I - C.9 %ID/g of m-THPC in ORMOSIL NPs in different tissues in vivo***).

Figure 6.11 shows the plasma clearance after a single *i.v.* injection of 0.3 mg kg^{-1} m-THPC in Foscan, 20 nm or 90 nm pegylated ORMOSIL NPs (with covalently bound monosilane m-THPC) into the normal HL rat model between ≤5 min and 672 h. Foscan was observed at the lowest concentrations and was cleared most rapidly from the blood serum relative to pegylated ORMOSIL NPs (Fig 6.11). The greatest m-THPC concentration was observed with 20 nm ORMOSIL NPs at t=0 (~1 µg g^{-1}), with 90 nm NPs and Foscan at equal m-THPC concentrations ~0.5 µg g^{-1}. Concentrations of m-THPC remained similar between pegylated ORMOSIL NPs, despite differences in size, and remained consistently higher than Foscan over 672 h, however neither were significant.

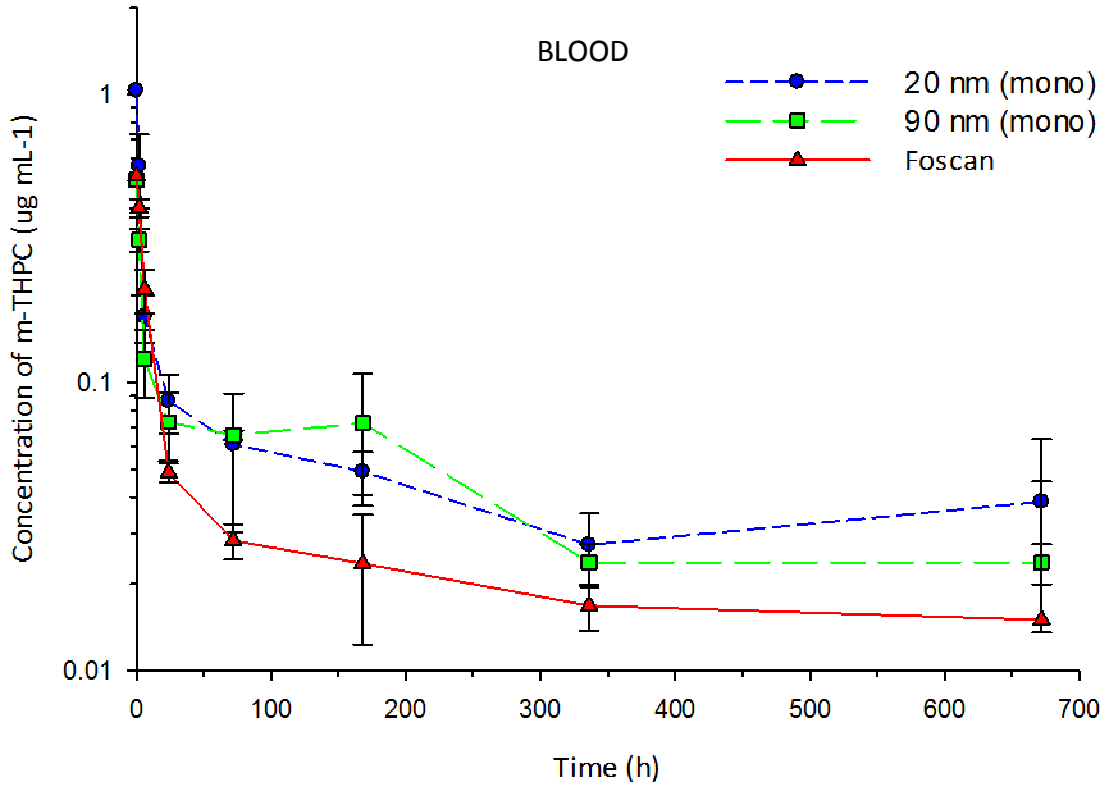

Figure 6.11. Semi-log plot of mean m-THPC concentration in blood serum after intravenous administration of 0.3 mg kg^{-1} m-THPC in either ■ Foscan or pegylated ORMOSIL nanoparticles ■ ~20 nm (mono-m-THPC) and ■ ~90 nm (mono-m-THPC) into female HL rats. Foscan blood data taken from Wistar rats is included as a reference. Data points show the mean ± SD, n = 3.

Following intravenous injection, m-THPC plasma concentrations peaked at the earliest time point for each formulation and appeared to decline exponentially. However, m-THPC clearance from plasma fitted multiple exponential decays; therefore data were analysed using both a compartmental (Clark B et al. 1981) and non-compartmental approach (Yamaoka, K. et al. 1978), as described in **Chapter 4**: liposomes.

Pharmacokinetic parameter	**Foscan**	**~20 nm ORMOSIL**	**~90 nm ORMOSIL**
Three compartmental model			
Initial dosage (D_o, mg kg^{-1})	0.3	0.3	0.3
Initial concentration (C_o, μg mL^{-1}, t=0)	0.7	1.03	1.55
Initial volume of distribution (V_d, mL kg^{-1})	407.4	290.7	194.1
V_d of first compartment (mL kg^{-1})	1373.9	528.4	300
V_d of second compartment (mL kg^{-1})	640.1	752.0	654.3
V_d of third compartment (mL kg^{-1})	6086.2	4596.6	3455.4
$t_{1/2}$ of first compartment (h^{-1})	0.9	1.1	0.4
$t_{1/2}$ of second compartment (h^{-1})	3.3	8.0	1.6
$t_{1/2}$ of third compartment (h^{-1})	90.0	577.6	301.4
Non-compartmental model			
Plasma clearance (C_l, mg kg^{-1} h^{-1})	30.0	0.002	0.007
Mean residence time (MRT, h^{-1})	61.9	2674.8	158
Volume of distribution (V_d, mL kg^{-1})	1875.7	5008	1131
Half-life ($t_{1/2}$, h^{-1})	42.9	1854	109.5
Elimination rate constant (K_{el}, h^{-1})	0.016	0.0001	0.006

Table 6.7. Plasma pharmacokinetic parameters of m-THPC after an *i.v.* injected dose of 0.3 m kg^{-1} m-THPC in either ~20 nm or ~90 nm pegylated ORMOSIL NPs incorporating covalently bound monosilane m-THPC in female HL rats, calculated using the exponential equations of the three compartment model ($A e^{-\alpha t}+Be^{-\beta t}+Ce^{-\gamma t}$), and the non-compartmental method. Foscan blood data taken from Wistar rats is included as a reference.

Using a compartmental approach (Table 4.4), the data best fit a tri-exponential decay curve, described by the equation $C = A e^{-\alpha t} + Be^{-\beta t} + Ce^{-\gamma t}$ (whereby C = concentration, A, B, C = y-intercepts (at t = 0), and α, β, γ = elimination rate constants), which describes the

rate of drug flow into and out of the central compartment and gave three compartmental half-lives ($t_{1/2}$) and elimination rate constants for 20 nm and 90 nm ORMOSIL NPs covalently incorporating monosilane bound m-THPC (Table 6.7). Foscan blood data taken from Wistar rats is included as a reference.

The non-compartment model (Table 6.6) gives half-lives of 1854 h for 20 nm ORMOSIL NPs and 109.5 h for 90 nm ORMOSIL NPs, with elimination rate constants of 0.0001 h^{-1} and 0.006 h^{-1}, respectively. The compartmental model estimates the initial volume of distribution (V_d) from the central compartment as 5008 mL kg^{-1} for 20 nm ORMOSIL NPs and 1131 mL kg^{-1} for 90 nm ORMOSIL NPs.

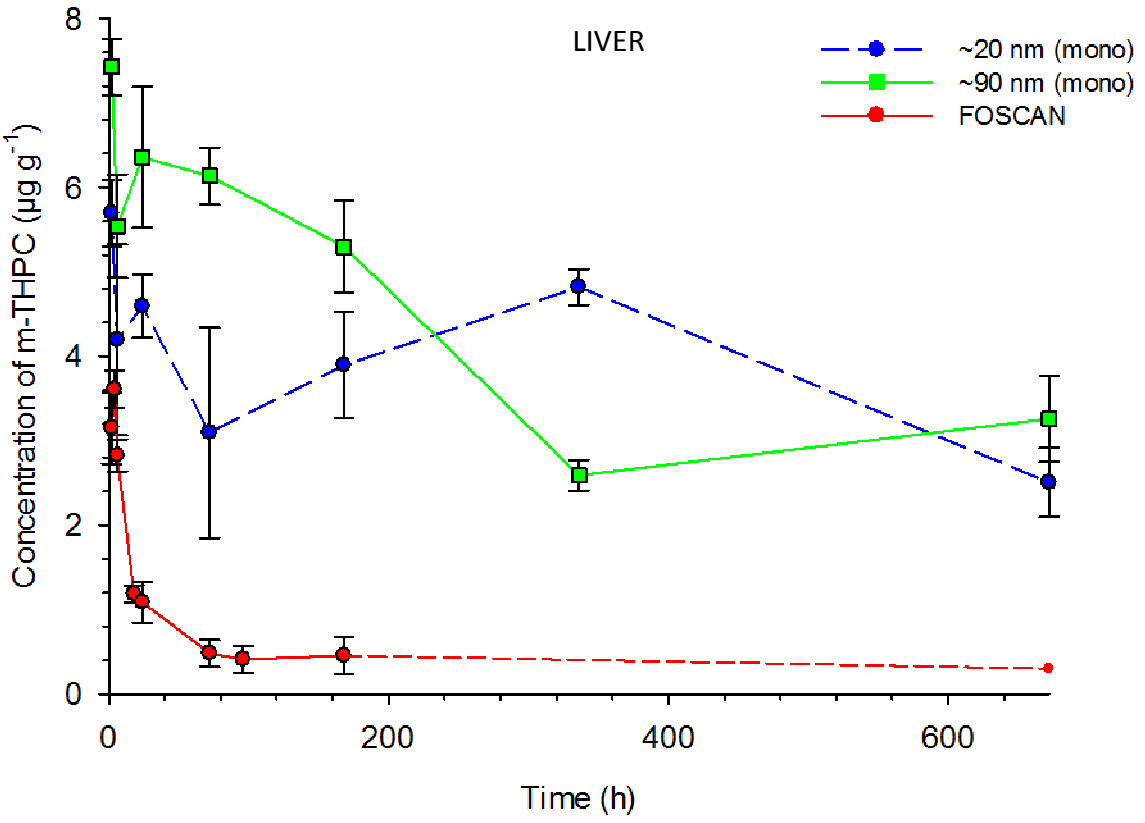

Figure 6.12. Concentration of m-THPC (µg g^{-1}) in the liver of the HL rat as a function of time following an intravenous injection of 0.3 mg kg^{-1} m-THPC in standard ■ Foscan, or pegylated ORMOSIL nanoparticles ■ ~20 nm (mono-m-THPC) and ■ ~90 nm (mono-m-THPC). Foscan liver data taken from Wistar rats is included as a reference. Data corrected for negative control tissue. Data points show the mean ± SD, n = 3.

Liver data (Fig 6.12) initially show a greater uptake of m-THPC when covalently bound in large (90 nm) pegylated ORMOSIL NPs (~7 µg g^{-1}) at the earliest time points compared to small (20 nm) pegylated ORMOSIL NPs (~6 µg g^{-1}), both of which are considerably

greater than concentrations of Foscan at this time (~4 µg g^{-1}). Pegylated ORMOSIL NPs remained at ~3 µg g^{-1} in the liver for the duration of the investigation (≥28 days). In comparison, this is the maximal m-THPC concentration observed with pegylated liposomal nanocarriers before they and Foscan were almost cleared from the liver ≤168 h.

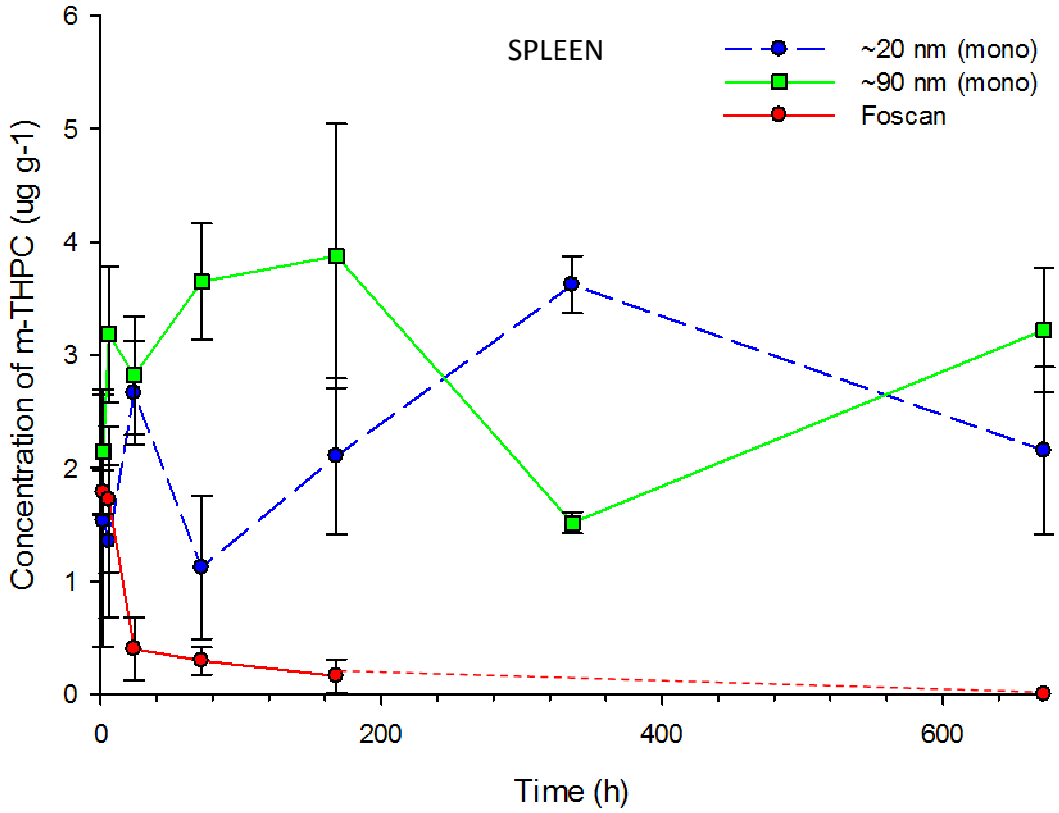

Figure 6.13. Concentration of m-THPC (µg g^{-1}) in the spleen of the HL rat as a function of time following an intravenous injection of 0.3 mg kg^{-1} m-THPC in standard ■ Foscan, or pegylated ORMOSIL nanoparticles ■ ~20 nm (mono-m-THPC) and ■ ~90 nm (mono-m-THPC). Foscan spleen data taken from Wistar rats is included as a reference. Data corrected for negative control tissue. Data points show the mean ± SD, n = 3.

In the spleen m-THPC in ORMOSIL NPs shows a highly similar pattern of uptake to that of the liver over 672 h, but at slightly lower m-THPC concentrations (Fig 6.13). Unlike the exponential decay of m-THPC observed with FosPEG formulations, a terminal elimination phase does not appear to be obtained with ORMOSIL NPs in the liver or spleen over 28 days. Although m-THPC in ORMOSIL NPs generally shows a negative pattern of decline ≥168 h from the liver and spleen, as seen with liposomal formulations, the concentrations of m-THPC at the same time points in comparison are far greater with ORMOSIL NPs.

In contrast to preliminary biodistribution data at 24 h with initial batches of ORMOSIL NPs (Fig 6.10), m-THPC accumulation in the lungs with either 20 nm or 90 nm ORMOSIL NPs is much lower, with a maximum m-THPC concentration of ≤0.8 µg g^{-1} observed at the earliest time points (Fig 6.14). These observed m-THPC concentrations are also much lower than those obtained with pegylated liposomal nanocarriers in the lung over 168 h and do not particularly correlate to the blood plasma pharmacokinetics of ORMOSIL NPs. Over 28 days a favorable decrease in m-THPC accumulation is observed with both small and large ORMOSIL NPs (~0.2 µg g^{-1}).

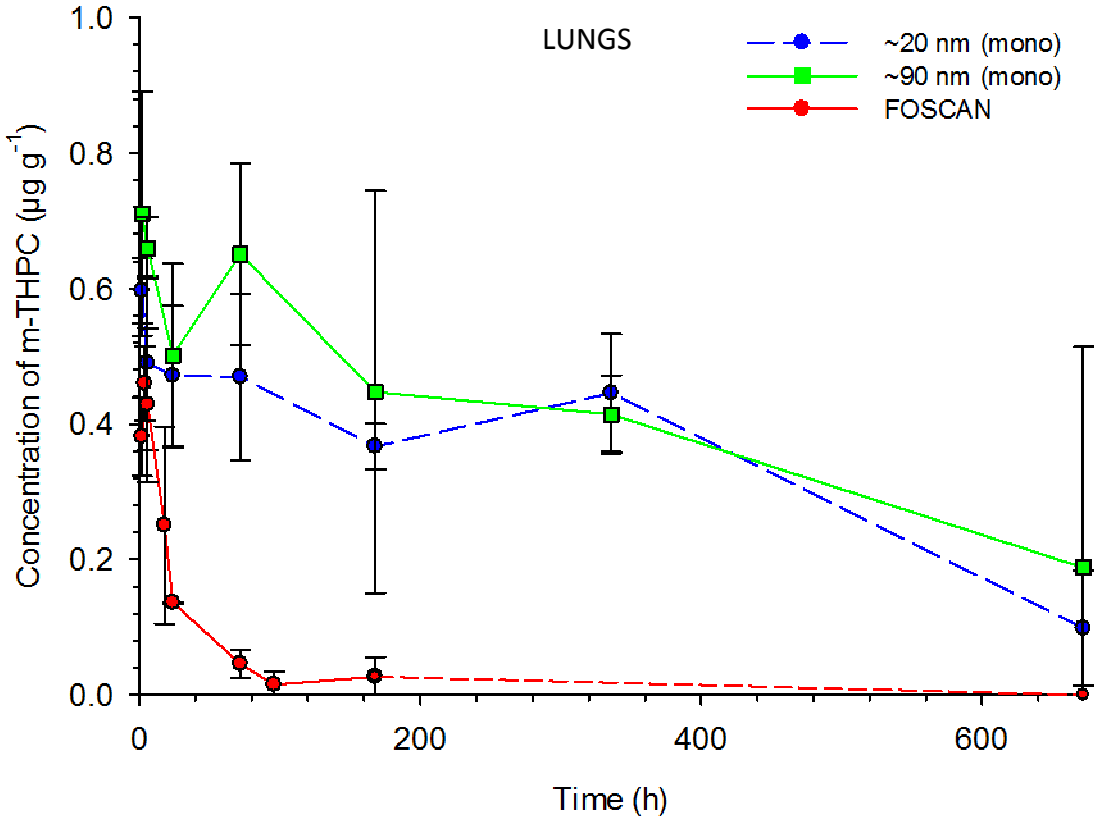

Figure 6.14. Concentration of m-THPC (µg g^{-1}) in the lungs of the HL rat as a function of time following an intravenous injection of 0.3 mg kg^{-1} m-THPC in standard ■ Foscan, or pegylated ORMOSIL nanoparticles ■ ~20 nm (mono-m-THPC) and ■ ~90 nm (mono-m-THPC). Foscan lung data taken from Wistar rats is included as a reference. Data corrected for negative control tissue. Data points show the mean ± SD, n = 3.

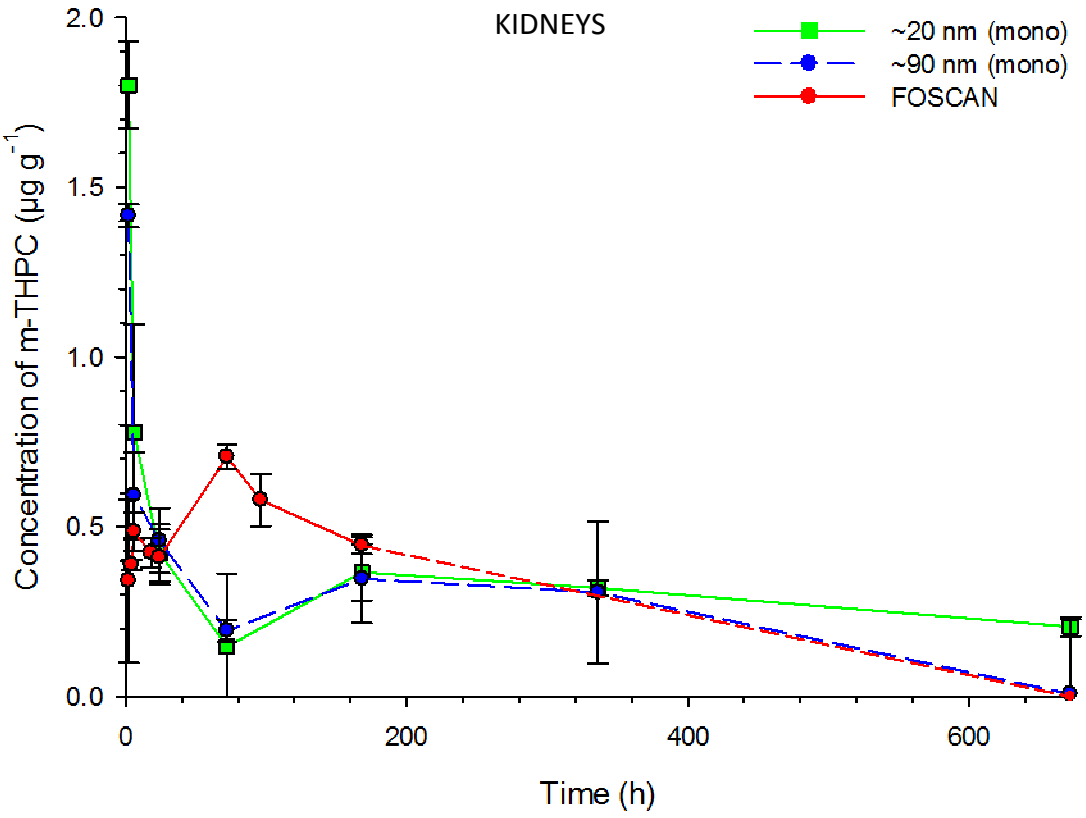

Figure 6.15. Concentration of m-THPC (µg g^{-1}) in the kidneys of the HL rat as a function of time following an intravenous injection of 0.3 mg kg^{-1} m-THPC in standard ■ Foscan, or pegylated ORMOSIL nanoparticles ■ ~20 nm (mono-m-THPC) and ■ ~90 nm (mono-m-THPC). Foscan kidney data taken from Wistar rats is included as a reference. Data corrected for negative control tissue. Data points show the mean ± SD, n = 3.

In the kidneys (Fig 6.15), as with liposomal m-THPC, no significant variation exists in m-THPC uptake between Foscan or either size pegylated ORMOSIL NP over 672 h. All m-THPC formulations appear to plateau from between 168 - 336 h, before a decline to baseline is observed with 20 nm ORMOSIL NPs and Foscan.

Figure 6.16 A + B show a direct comparison of m-THPC uptake in selected tissues at 24 h culminating all pegylated ORMOSIL NP batches of either small (~20 nm) or large (~90 nm) particles covalently incorporating monosilane m-THPC or tetrasilane m-THPC*. Generally, the greatest uptake of 20 nm pegylated ORMOSIL NPs (mono-m-THPC) is observed in the liver at 24 h. With 90 nm pegylated ORMOSIL NPs there appears to be no significant difference on the accumulation of NPs according to the covalent incorporation of m-THPC and the greatest m-THPC uptake appears to be in the liver. However, compared to 20 nm ORMOSIL NPs, the greatest m-THPC accumulation also extends to the blood plasma and tumour tissue when delivered by 90 nm ORMOSIL NPs at 24 h.

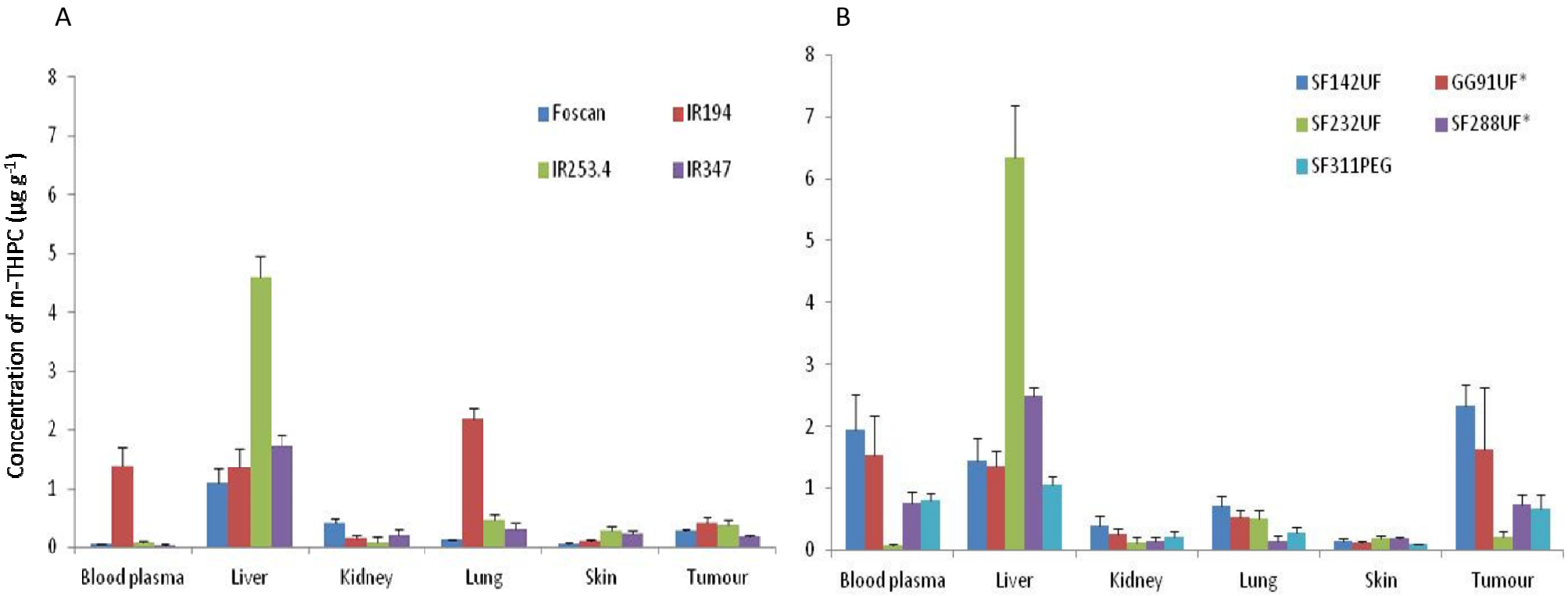

Figure 6.16. Direct comparison of small versus large pegylated ORMOSIL NPs on m-THPC accumulation (µg g^{-1}) in all tissues of the HL rat at 24 h following an intravenous injection of 0.3 mg kg^{-1} m-THPC covalently bound (monosilane) in pegylated ORMOSIL nanoparticles of either (**A**) ~20 nm or (**B**) ~90 nm. *m-THPC is covalently bound by tetrasilane linkers. Data corrected for negative control tissue. Data points show the mean ± SD, n = 3.

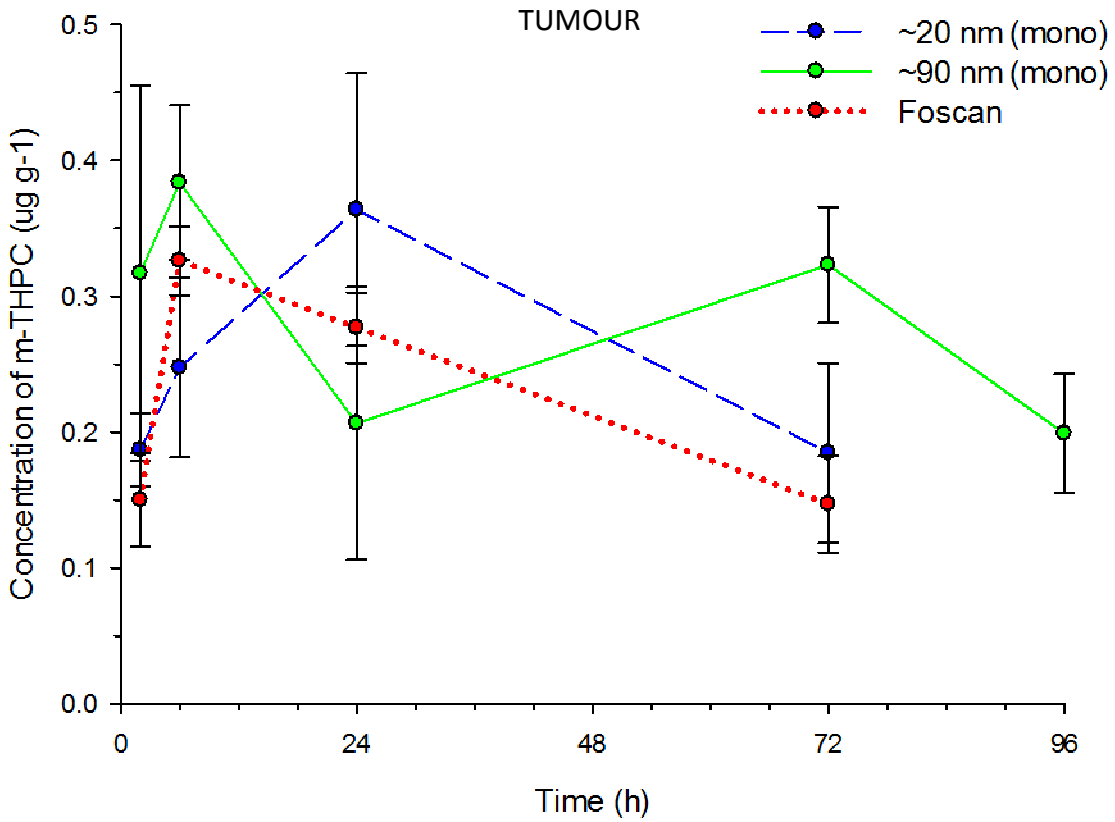

Figure 6.17. Concentration of m-THPC (μg g^{-1}) in tumour tissue of the HL rat as a function of time following an intravenous injection of 0.3 mg kg^{-1} m-THPC in standard ■ Foscan or pegylated ORMOSIL nanoparticles ■ ~20 nm (mono-m-THPC) and ■ ~90 nm (mono-m-THPC). Foscan tumour data taken from HL rats is included as a reference. Data corrected for negative control tissue. Data points show the mean ± SD, n = 3.

Contrary to Fig 6.17 and preliminary biodistribution studies at 24 h with initial batches of pegylated ORMOSIL NPs, there appears to be no significant difference in m-THPC uptake between 20 nm and 90 nm ORMOSIL NPs (covalently incorporating monosilane m-THPC) used for these tumour studies at any time interval over a 96 h period (Fig 6.17). There also appears to be no significant difference in m-THPC tumour uptake when comparing Foscan to ORMOSIL NPs over a 72 h period.

iv. Confocal microscopy ex vivo

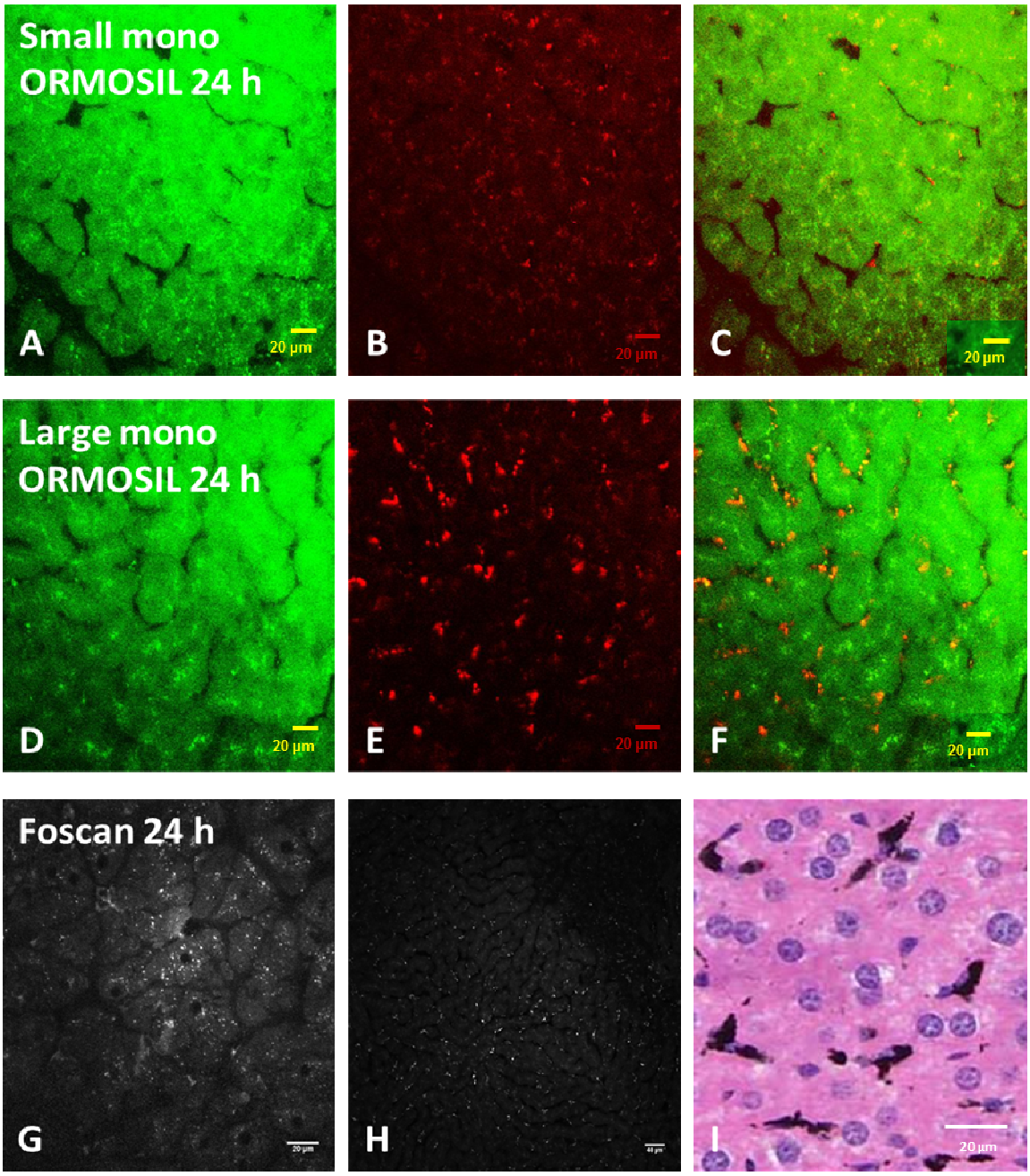

Figure 6.18. Confocal microscopy images of *ex vivo* rat liver tissue at 24 h following *i.v.* administration of 0.3 mg kg^{-1} m-THPC in (A-C) small (20 nm) ORMOSIL NPs (mono-m-THPC) or (D-F) large (90 nm) ORMOSIL NPs (mono-m-THPC). Images on the left indicate liver auto-fluorescence (green), central images show m-THPC fluorescence (red) and images on the right after merging of the two channels (green and red) to determine m-THPC localisation in liver tissue. (G-H) Different magnifications of *ex vivo* rat liver tissue at 24 h following *i.v.* administration of 1 mg kg^{-1} m-THPC in Foscan. Bright white spots are indicative of m-THPC fluorescence (I) India ink uptake into the Kupffer cells residing in the sinusoids of the liver (*taken from (Bowen, R. 2002).*

Qualitative confocal microscopy images of *ex vivo* liver tissue (green) show the localisation of m-THPC fluorescence (red) in the Kupffer cells (macrophages), residing in

the sinusoids of the liver (Fig 6.18) following intravenous injection of 0.3 mg kg^{-1} m-THPC in either 20 nm (Fig 6.18 C) or 90 nm (Fig 6.18 F) pegylated ORMOSIL NPs and removal of tissue at 24 h. The localisation of m-THPC in Kupffer cells is confirmed by Bowen *et al*., who demonstrated phagocytised India ink particles in fixed macrophage cells of the liver (black stained cells in Fig 6.18 I) forming part of the RES (Bowen, R. 2002). Confocal images (grey) of *ex vivo* liver tissue acquired following intravenous injection of 1 mg kg^{-1} m-THPC in Foscan and removal of tissue at 24 h (Fig 6.18 G & H) show m-THPC fluorescence as bright white spots, which appear to be intracellularly localised in liver hepatocytes rather than liver macrophages.

v. Fluorescence microscopy frozen tissue

10 micron frozen sections of liver tissue were imaged using fluorescence microscopy (Fig 6.19). Tissues were removed and snap frozen in liquid nitrogen under isopentane from rats 24 h following intravenous injection with 0.3 mg kg^{-1} m-THPC in Foscan (Fig 6.19 E-F) or 90 nm pegylated ORMOSIL NPs incorporating either covalently bound monosilane (Fig 6.19 A-B) or tetrasilane m-THPC (Fig 6.17 C-D). Qualitative CCD false coloured fluorescent images of m-THPC localisation were obtained at different magnifications (x10 or x60). The greatest m-THPC fluorescence (white) was observed with 90 nm pegylated ORMOSIL NPs in the liver at 24 h in comparison to Foscan. This is consistent with chemical extraction data of liver tissue.

Localisation of m-THPC fluorescence in ORMOSIL NPs observed with fluorescence microscopy was in accordance with corresponding confocal images of *ex vivo* liver tissue (Fig 6.18), suggesting the greatest m-THPC fluorescence is located in the sinusoids between the liver hepatocytes where the macrophages (Kupffer cells) reside at 24 h. Furthermore, confocal images of the same frozen liver sections used in fluorescence microscopy were obtained following excitation of m-THPC and red m-THPC fluorescence was also detected in the sinusoids of frozen liver tissue sections (Fig 6.20).

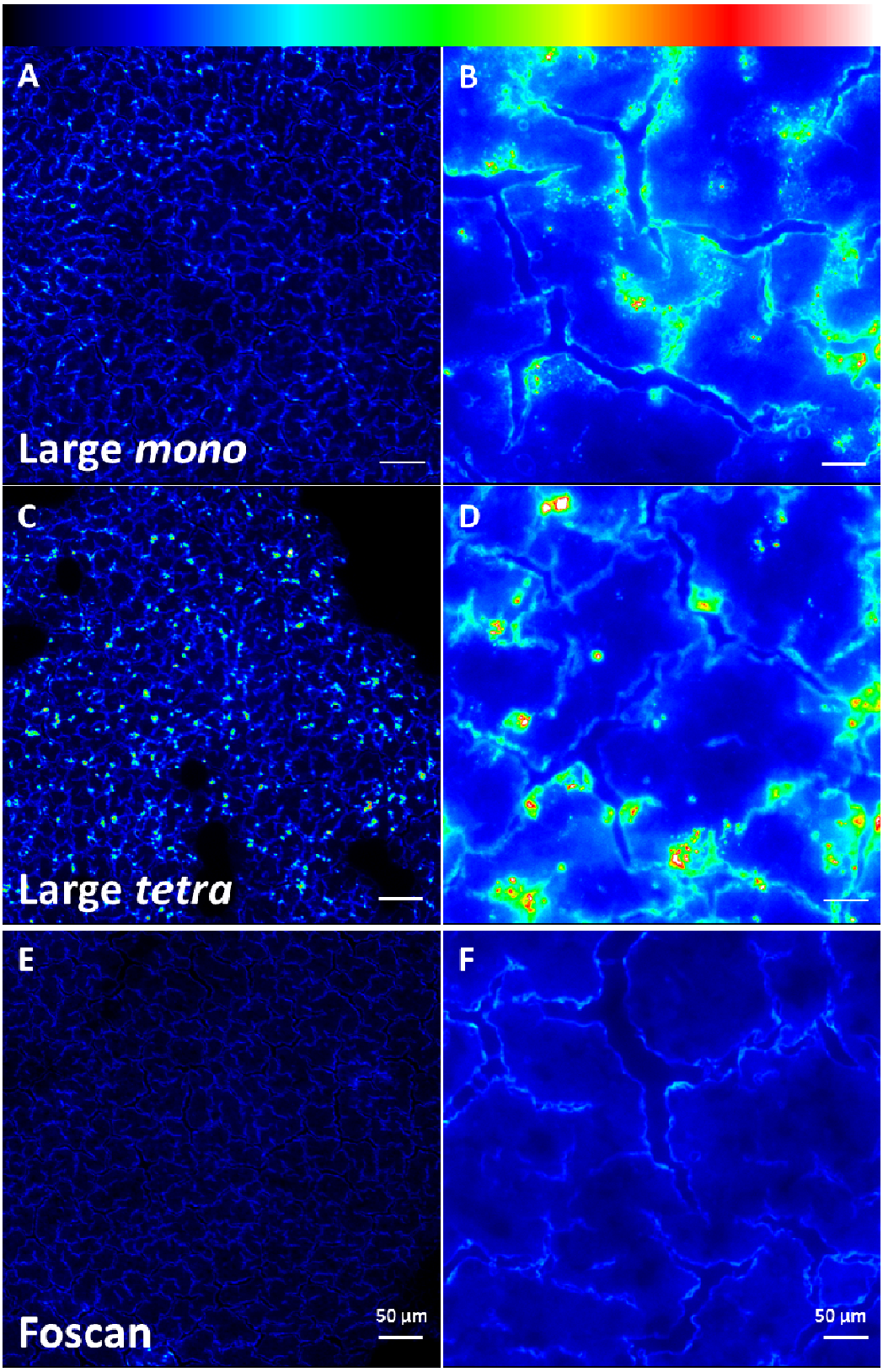

Figure 6.19. Fluorescence microscopy: qualitative uptake and localisation of m-THPC in 10 micron frozen liver sections at 24 h following intravenous administration of 0.3 mg kg^{-1} m-THPC in Foscan and covalently bound (*mono* or *tetrasilane*) in large ORMOSIL NPs (~100 nm). (**A**) Large (*mono*) x10 (**B**) Large (*mono*) x60 (**C**) Large (*tetra*) x10 (**D**) Large (*tetra*) x60 (**E**) Foscan x10 and (**F**) Foscan x60. 50 micron scale bar on each image and the fluorescence intensity scale, top, increases from black (background/no fluorescence) through to white (max. fluorescence).

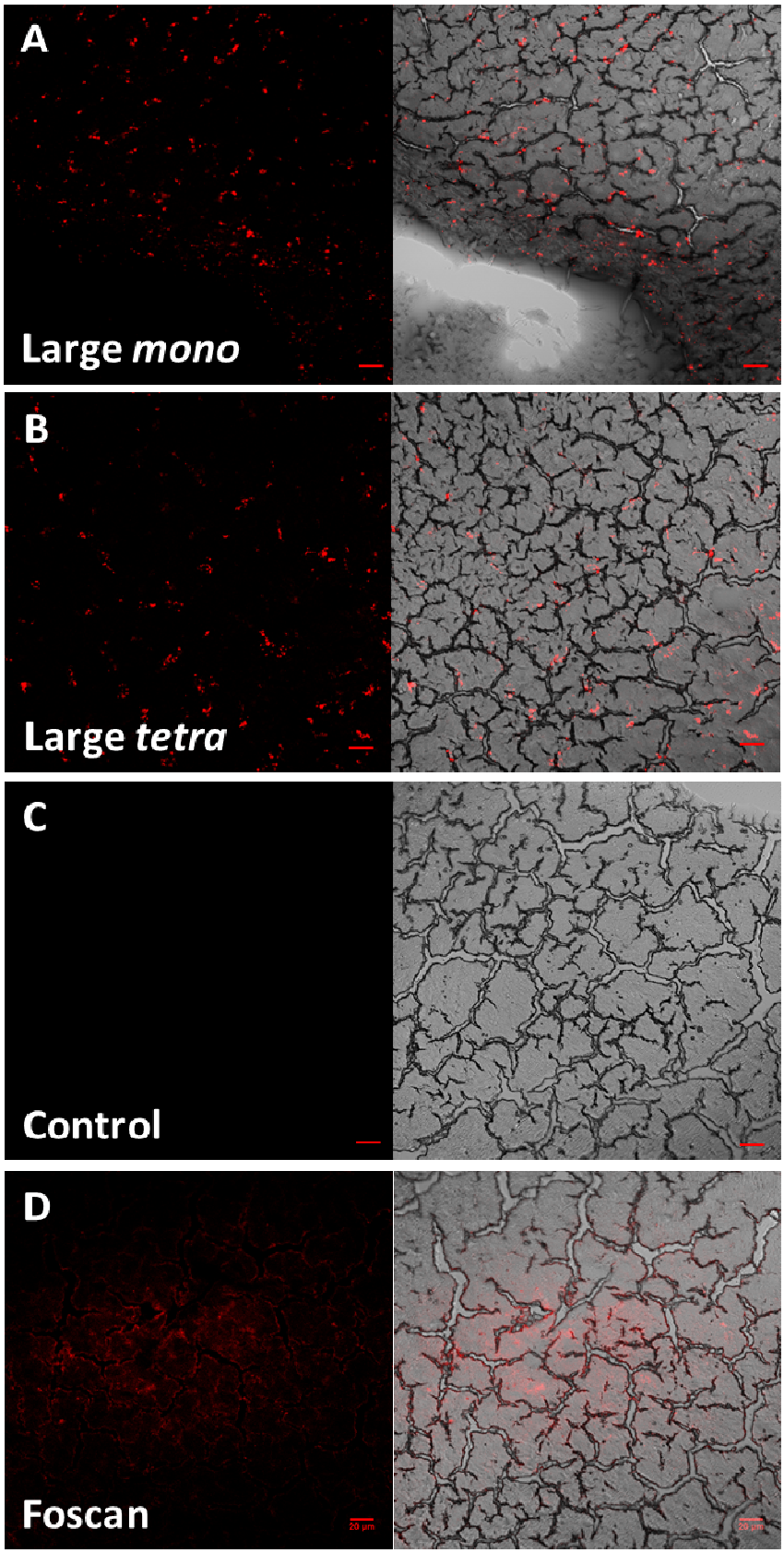

Figure 6.20. Confocal microscopy: qualitative uptake and localisation of m-THPC (red) in 10 micron frozen liver sections (grey) at 24 h following intravenous administration of 0.3 mg kg^{-1} m-THPC in Foscan and covalently bound (*mono* or *tetrasilane*) in large ORMOSIL NPs (~90 nm) at x20. (**A**) Large (*mono*) (**B**) Large (*tetra*) (**C**) Control (no m-THPC) (**D**) Foscan.

The same fluorescence microscopy and confocal microscopy techniques were employed to image 10 micron frozen sections of tumour tissue, obtained from rats under the same removal conditions. 0.3 mg kg^{-1} m-THPC was administered intravenously in either small 20 nm (monosilane m-THPC) or large 90 nm (mono- or tetrasilane m-THPC) pegylated ORMOSIL NPs. False coloured CCD fluorescent images of frozen tumour tissue sections (Fig 6.21) demonstrated the greatest m-THPC fluorescence intensity (white) was observed with 90 nm ORMOSIL NPs at 24 h in comparison to 20 nm ORMSIL NPs. This is consistent with chemical extraction data of tumour tissue.

Confocal microscopy images of frozen tumour tissue sections confirmed the greatest m-THPC red fluorescence signal was observed with 90 nm ORMOSIL NPs at 24 h in comparison to 20 nm ORMSIL NPs (Fig 6.22). The covalent incorporation of m-THPC into larger ORMOSIL NPs (mono- or tetrasilane) appeared to have no influence on observed red fluorescence intensity. Images of 20 nm ORMOSIL NPs looked extremely similar to images obtained with control tumour tissue which received no m-THPC and showed no red fluorescence signal following excitation of tissue.

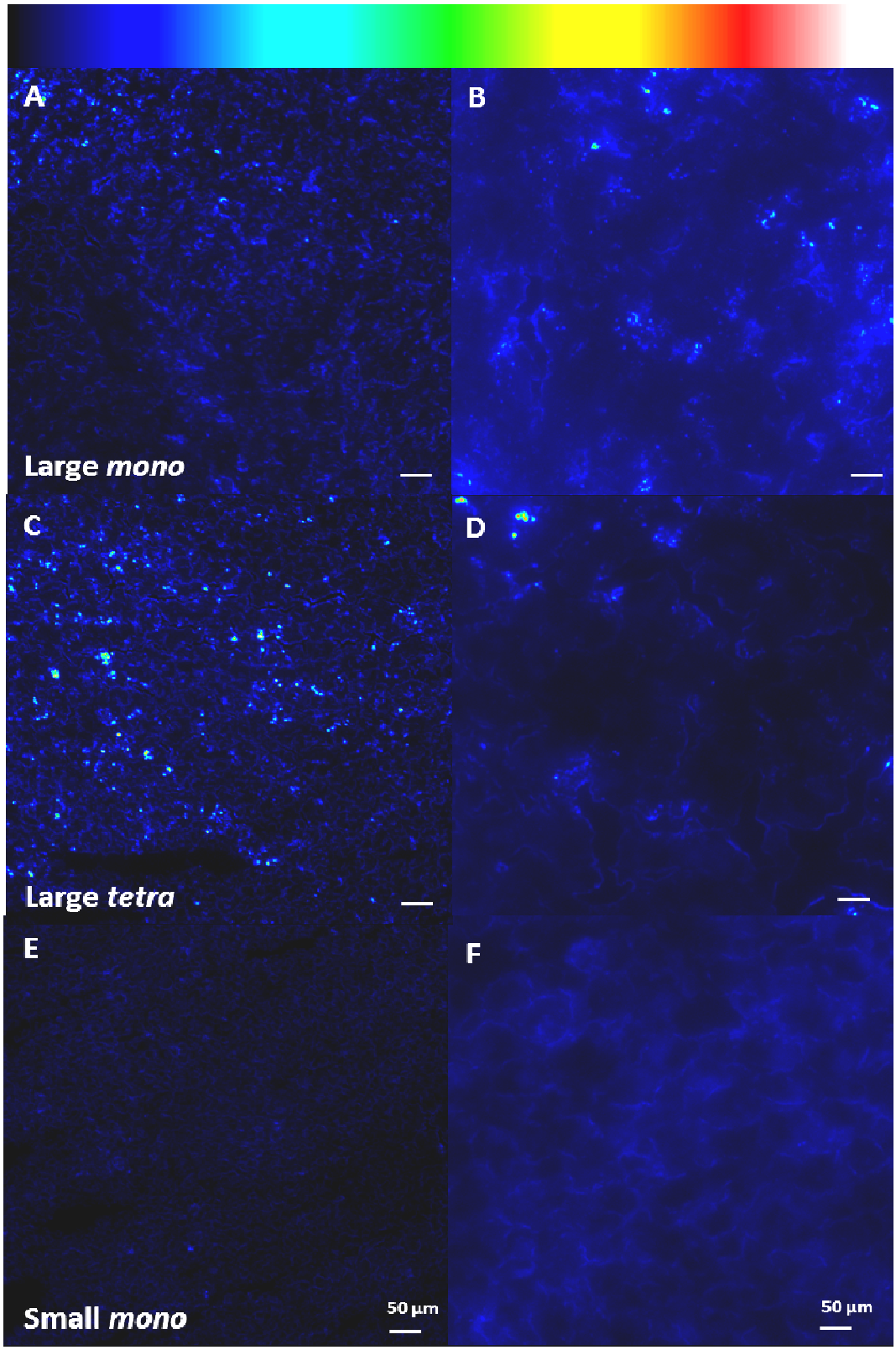

Figure 6.21. Fluorescence microscopy: qualitative uptake and localisation of m-THPC in 10 micron frozen tumour sections at 24 h following intravenous administration of 0.3 mg kg^{-1} m-THPC covalently bound (*mono* or *tetrasilane*) in small (~20 nm) or large (~90 nm) ORMOSIL NPs. (**A**) Large (*mono*) x10 (**B**) Large (*mono*) x60 (**C**) Large (*tetra*) x10 (**D**) Large (*tetra*) x60 (**E**) Small (*mono*) x10 and (**F**) Small (*mono*) x60. 50 micron scale bar on each image and the fluorescence intensity scale, top, increases from black (background/no fluorescence) through to white (max. fluorescence).

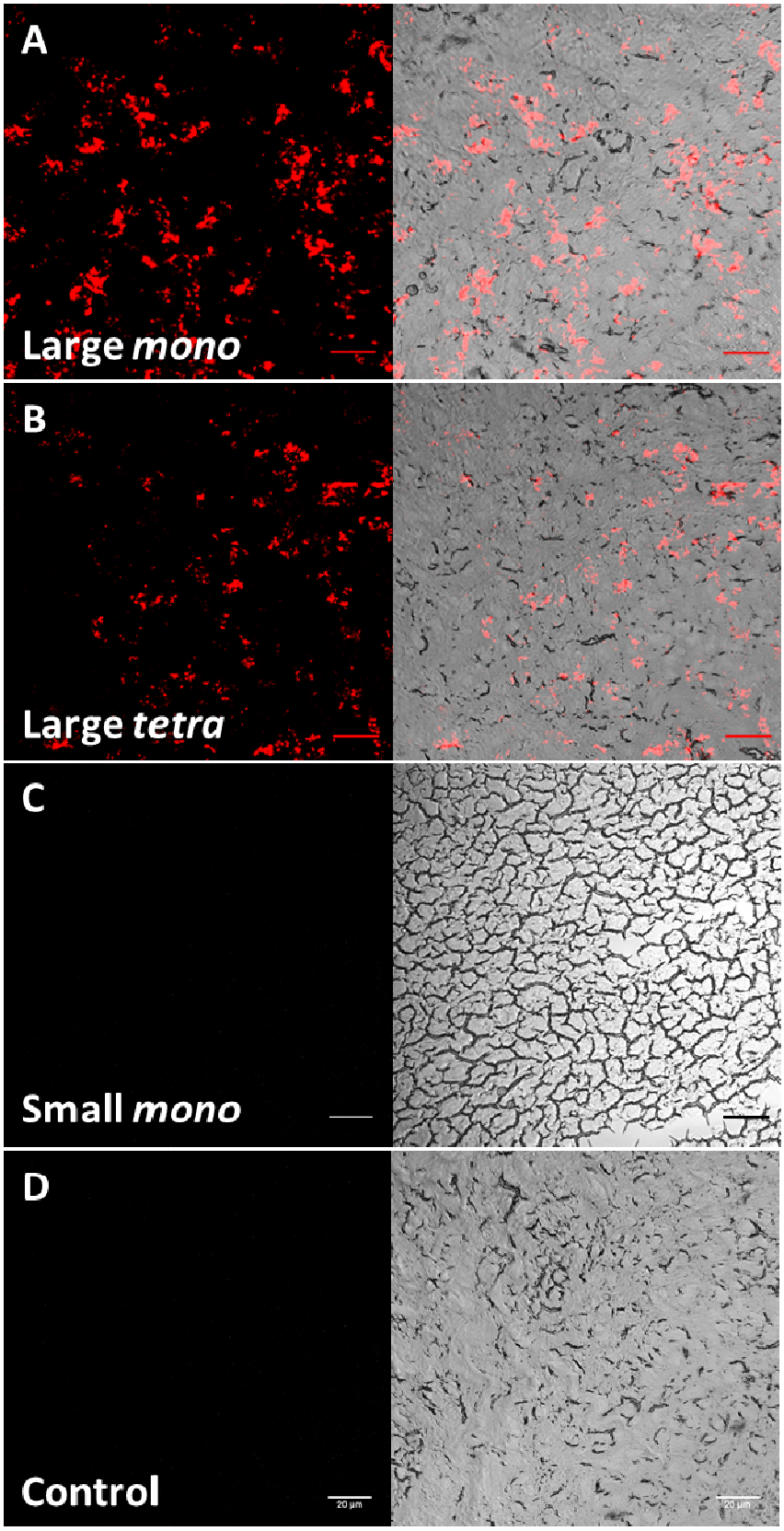

Figure 6.22. Confocal microscopy: qualitative uptake and localisation of m-THPC (red) in 10 micron frozen tumour sections (grey) at 24 h following intravenous administration of 0.3 mg kg^{-1} m-THPC in Foscan and covalently bound (*mono* or *tetrasilane*) in small (~20 nm) or large (~90 nm) ORMOSIL NPs at x20. (**A**) Large (*mono*) (**B**) Large (*tetra*) (**C**) Small (*mono*) (**D**) Control (no m-THPC).

vi. Toxicology

Biochemical blood tests to assess liver/renal enzyme functions were carried out simultaneously on blood serum collected from animals used in pharmacokinetic studies over a series of time points ≥28 days (1 M).

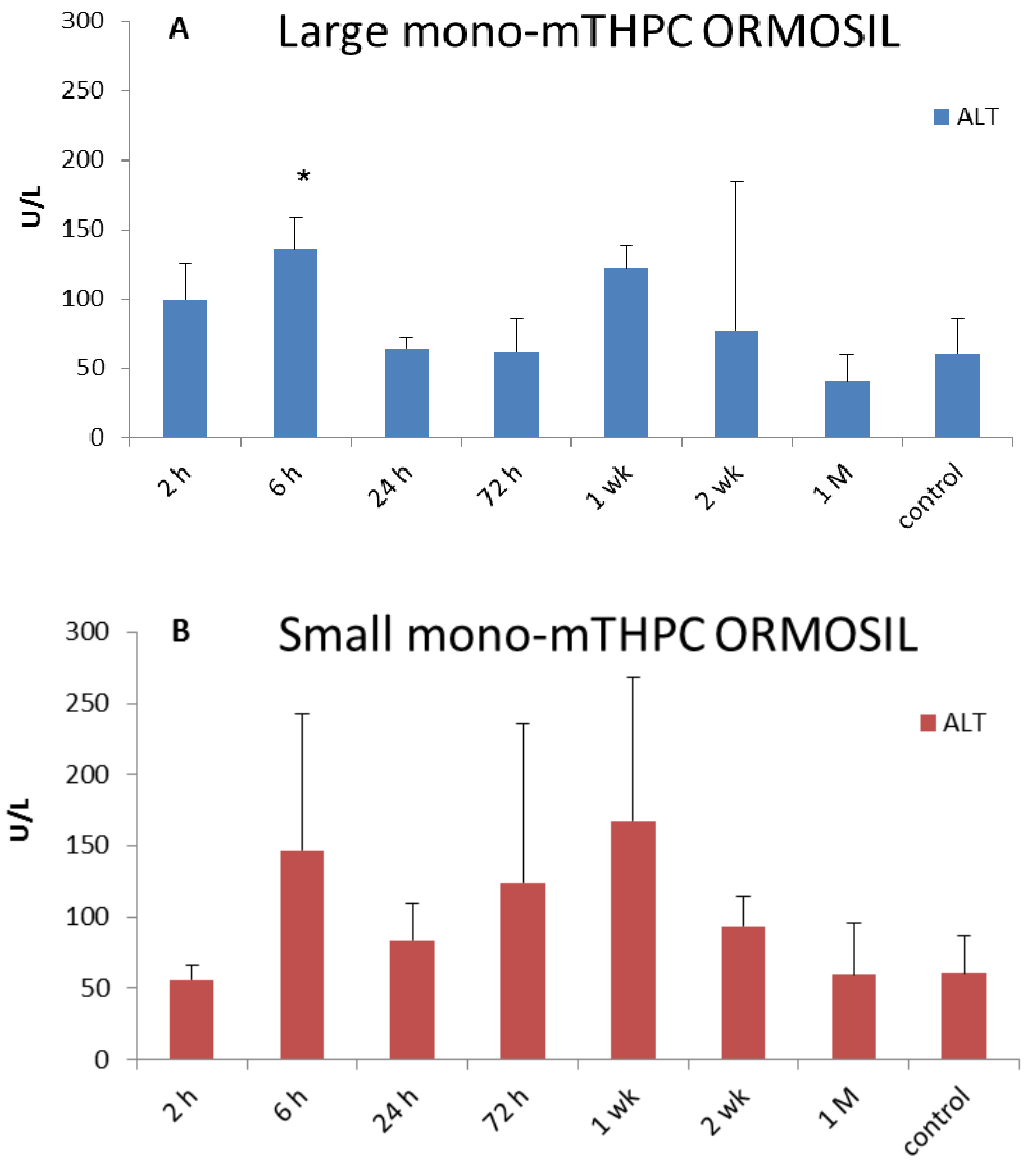

Figure 6.23. Liver/renal enzyme function assay performed on blood plasma to measure circulating concentrations of ALT following intravenous administration of 0.3 mg kg^{-1} m-THPC in either large (90 nm) or small (20 nm) pegylated ORMOSIL NPs covalently incorporating monosilane m-THPC into HL rats. Control animals received no m-THPC. Data points show the mean ± SD, n = 3.

Alanine Transaminase (ALT) is an enzyme which catalyses the two parts of the alanine cycle and its increased secretion into the blood circulation is commonly used as an indicator to diagnose hepatocellular injury or liver inflammation. Fig 6.23 A & B show no significant difference between levels of ALT in the blood serum of animals that were

intravenously administered 0.3 mg kg^{-1} m-THPC in either 20 nm (small) or 90 nm (large) pegylated ORMOSIL NPs with covalently incorporated monosilane m-THPC versus control animals, which received no m-THPC. Data were statistically analysed and this was true for animals at all time intervals, except at 6 h ($p \leq 0.05$), following administration of 90 nm pegylated ORMOSIL NPs. Overall results suggested no predominant signs of hepatocellular injury or liver toxicity were caused by the administration of pegylated ORMOSIL NPs *in vivo* over 28 days.

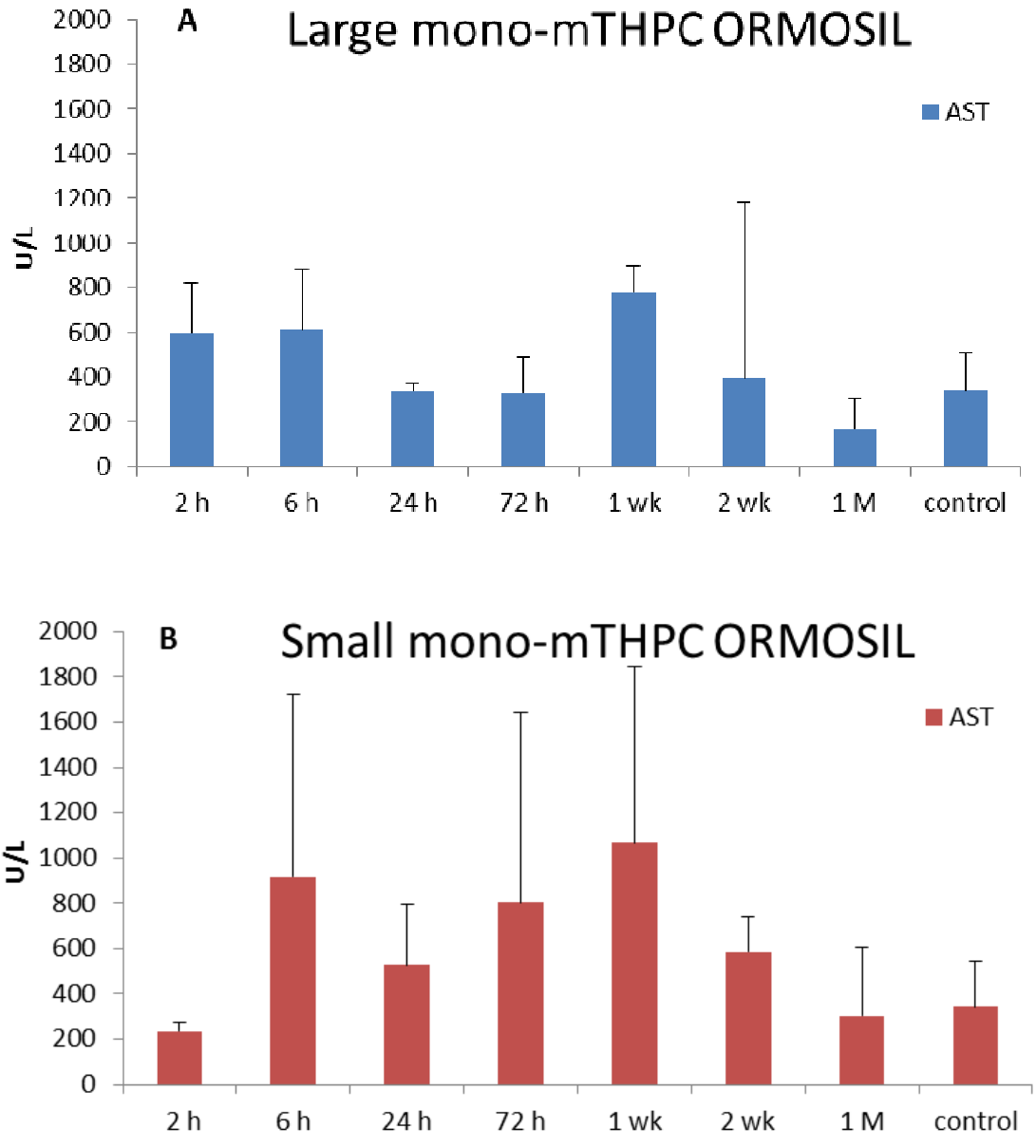

Figure 6.24. Liver/renal enzyme function assay performed on blood plasma to measure circulating concentrations of AST following intravenous administration of 0.3 mg kg^{-1} m-THPC in either large (90 nm) or small (20 nm) pegylated ORMOSIL NPs covalently incorporating monosilane m-THPC into HL rats. Control animals received no m-THPC. Data points show the mean ± SD, n = 3.

Aspartate Transaminase (AST) is an enzyme which catalyses the reversible transfer of an α-amino group between aspartate and glutamate and is essential in amino acid metabolism. Its increased secretion into the blood circulation is commonly used as an indicator to both diagnose liver injury and assess renal function (acute renal disease). Fig 6.24 A & B show no significant difference between levels of AST in the blood serum of animals that were intravenously administered 0.3 mg kg^{-1} m-THPC in either 20 nm (small) or 90 nm (large) pegylated ORMOSIL NPs with covalently incorporated monosilane m-THPC versus control animals, which received no m-THPC. Data were statistically analysed and this was true for animals at all time intervals. Overall results suggested no predominant signs of liver toxicity or renal impairment were caused by the administration of pegylated ORMOSIL NPs *in vivo* over 28 days.

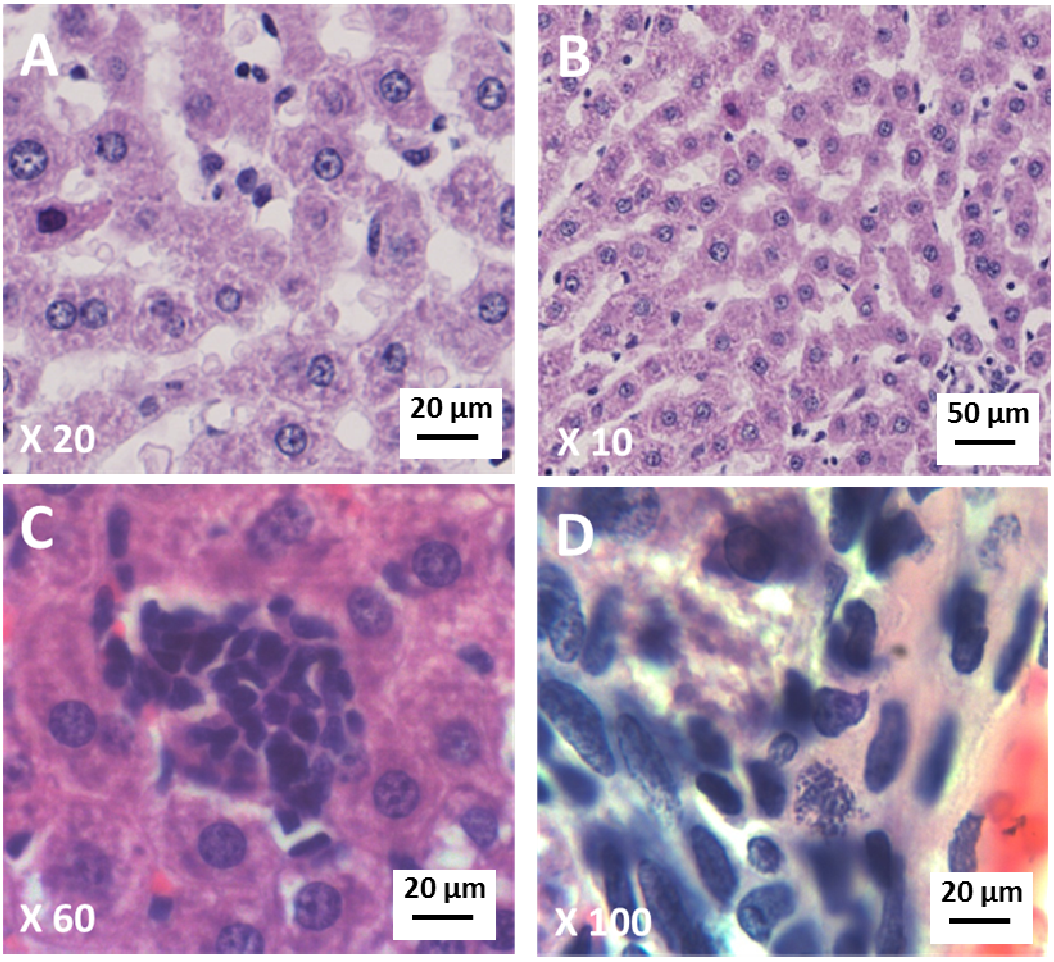

Figure 6.25. H&E stained 4 micron sections of rat liver following intravenous administration of 0.3 mg kg^{-1} *mono*-m-THPC in ORMOSIL NPs or no injection (control). (**A**) Control liver x20 (**B**) Control liver x10 (**C**) m-THPC in small ORMOSIL NPs (~20 nm) following 2 weeks administration (x60) (**D**) m-THPC in large ORMOSIL NPs (~90 nm) following 2 weeks administration (x100).

Liver tissue acquired from the same HL rats used in pharmacokinetic studies was fixed and stained. H&E sections showed evidence of mild inflammation following intravenous injection of 0.3 mg kg^{-1} m-THPC in 20 nm pegylated ORMOSIL NPs (mono-mTHPC) at 2 weeks (Fig 6.25 C). This was indicated by the presence of dense cell bodies (granulomas) observed in selected regions of the liver compared to control liver tissue (no ORMOSIL NPs). Liver sections imaged following intravenous injection of 0.3 mg kg^{-1} m-THPC in 90 nm pegylated ORMOSIL NPs (mono-mTHPC) at 2 weeks (Fig 6.25 D) also showed evidence of mild inflammation due to the presence of granular bodies inside macrophages (D).

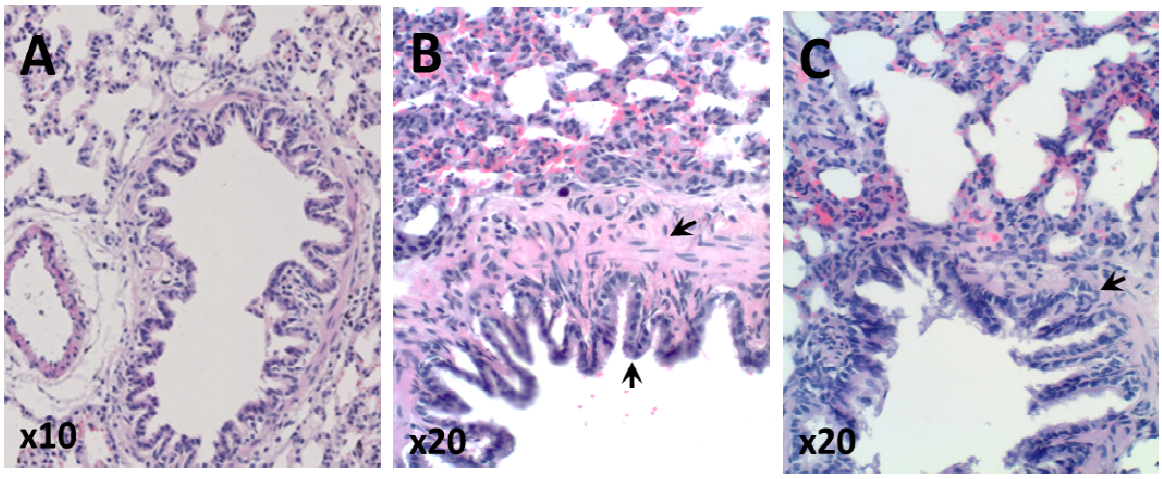

Figure 6.26. H&E stained 4 micron sections of rat lung following intravenous administration of 0.3 mg kg^{-1} *mono*-m-THPC in ORMOSIL NPs or no injection (control). (**A**) Control lung x10 (**B**) m-THPC in small ORMOSIL NPs (~20 nm) following 2 weeks administration (x20) (**C**) m-THPC in large ORMOSIL NPs (~90 nm) following 2 weeks administration (x20).

H&E lung tissue sections showed evidence of mild inflammation following intravenous injection of 0.3 mg kg^{-1} m-THPC in both 20 nm and 90 nm pegylated ORMOSIL NPs (mono-mTHPC) at 2 weeks (Fig 6.26) versus control lung tissue (no ORMOSIL NPs). This was indicated by the thickening and increase in cellularity of the epithelial lining of the alveoli with the presence of a large number of foamy macrophages (indicated by black arrows).

In kidney sections no apparent signs of toxicity were observed following intravenous administration of either 20 nm or 90 nm pegylated ORMOSIL NPs (mono-mTHPC) at 2 weeks (Fig 6.27), with perhaps only a slight increase in cell number with ORMOSIL NPs kidney sections in comparison to control kidney tissue (no ORMOSIL NPs).

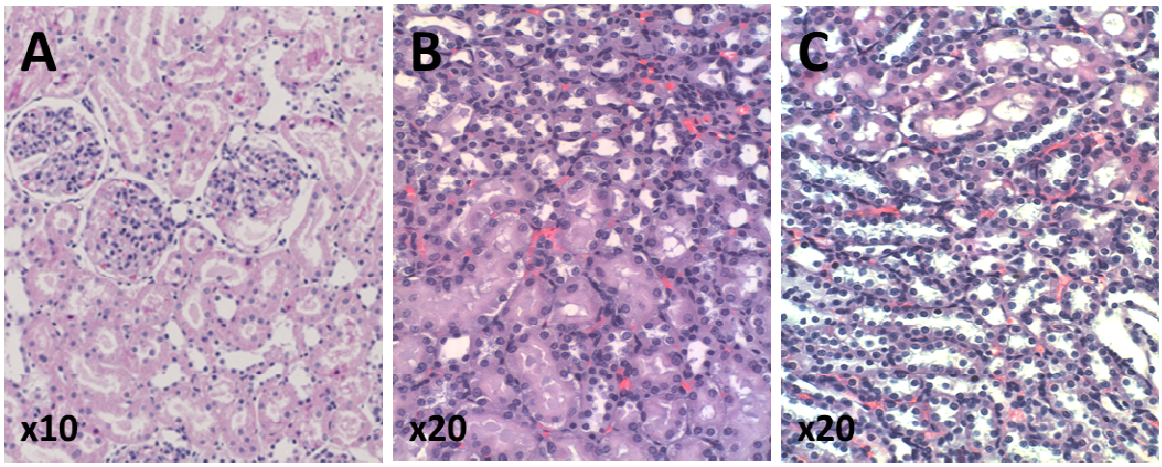

Figure 6.27. H&E stained 4 micron sections of rat kidney following intravenous administration of 0.3 mg kg^{-1} *mono*-m-THPC in ORMOSIL NPs or no injection (control). (**A**) Control kidney x10 (**B**) m-THPC in small ORMOSIL NPs (~20 nm) following 2 weeks administration (x20) (**C**) m-THPC in large ORMOSIL NPs (~90 nm) following 2 weeks administration (x20).

Spleen H&E sections (Fig 6.28) showed no significant difference in appearance of red or white pulp to suggest apparent signs of toxicity following intravenous administration of either 20 nm or 90 nm pegylated ORMOSIL NPs (mono-mTHPC) at 2 weeks versus control spleen tissue (no ORMOSIL NPs).

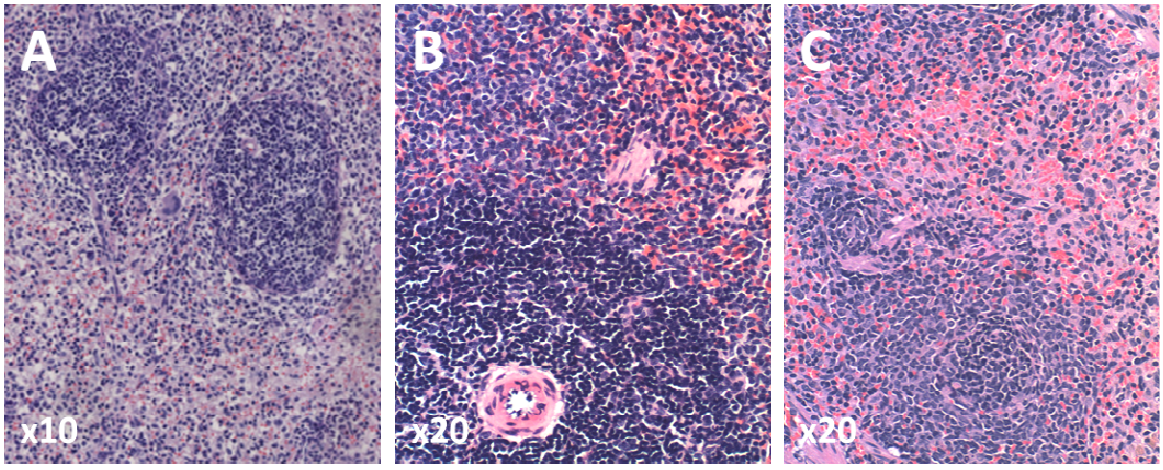

Figure 6.28. H&E stained 4 micron sections of rat spleen following intravenous administration of 0.3 mg kg^{-1} *mono*-m-THPC in ORMOSIL NPs or no injection (control). (**A**) Control spleen x10 (**B**) m-THPC in small ORMOSIL NPs (~20 nm) following 2 weeks administration (x20) (**C**) m-THPC in large ORMOSIL NPs (~90 nm) following 2 weeks administration (x20).

vii. PDT studies

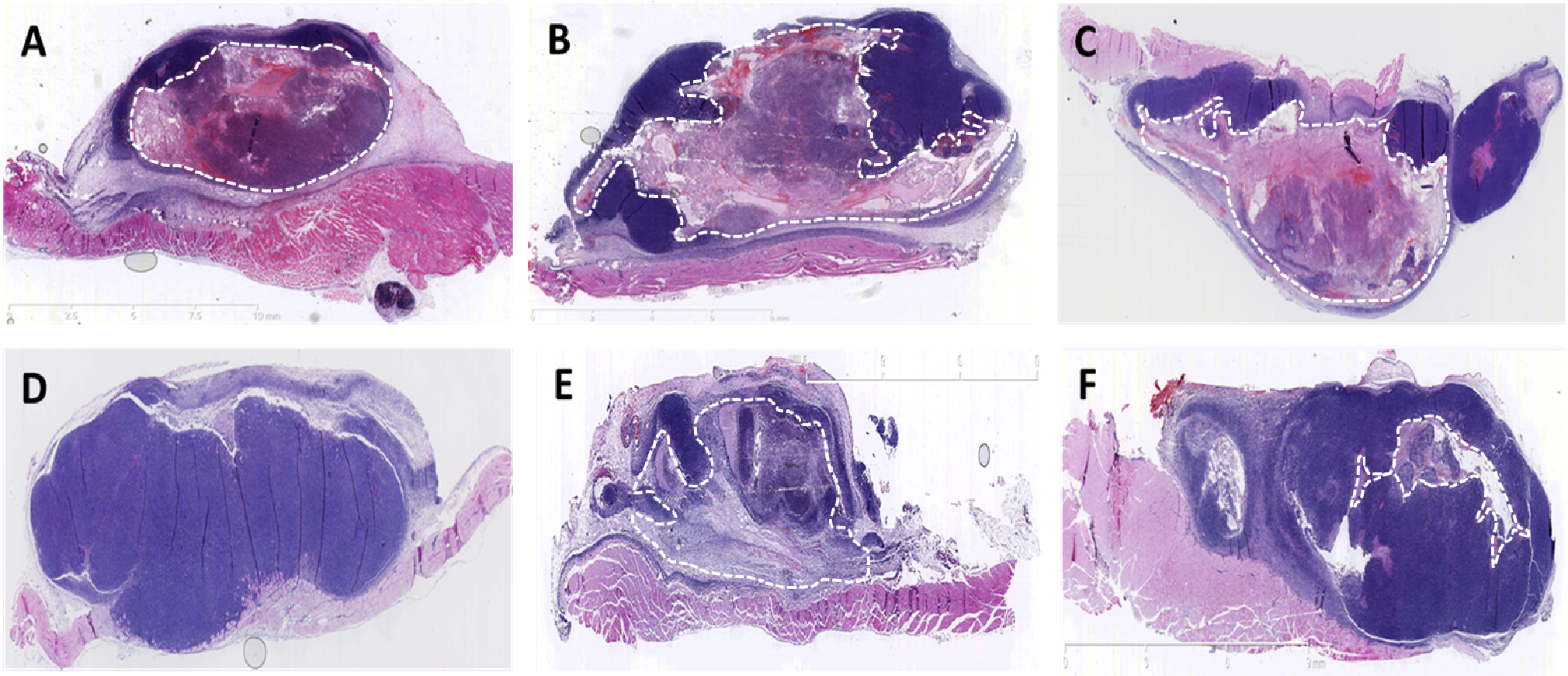

Figure 6.29. Typical H&E stained MC28 tumour sections scanned with the Hamamatsu Nanozoomer to observe the extent of PDT damage, measured by the area of necrosis (dotted perimeter), after 0.3 mg kg^{-1} of m-THPC was injected *i.v* (**A**) Foscan DLI: 6 h, and pegylated ORMOSIL NPs bound with monosilane m-THPC (**B**) ~20 nm, DLI: 6 h (**C**) ~90 nm, DLI: 6 h (**D**) Control (no m-THPC) (**E**) ~20 nm, DLI: 24 h (**F**) ~90 nm, DLI: 24 h. *Permission for the use of histological images of PDT was granted courtesy of Dr Josephine Woodhams.*

Sample	**IR322**	**SF311**	**SF288***
Size (nm)	16	90	110
m-THPC (µM)	499	187	270
Loading (%)	2.08	1.87	1.6
PEG length	2000	2000	2000
Silane bonding	mono	mono	tetra*

Table 6.8. Specifications of ORMOSIL NP preparations used for PDT studies.

Table 6.8 identifies pegylated ORMOSIL NPs used in PDT studies. PDT studies were carried out in the MC28 tumour rat model to deduce the efficacy of treatment with pegylated ORMOSIL NPs covalently incorporating m-THPC in comparison to Foscan. PDT damage was observed through H&E sections cut from treated tumour tissues (Fig 6.29) and the area of tumour necrosis (mm^2) was calculated. Tumour sections are indicative of typical PDT damage observed following intravenous administration of 0.3 mg kg^{-1} of either Foscan or pegylated ORMOSIL NPs with monosilane bound m-THPC in either 20 nm or 90 nm sized NPs at DLIs of either 6 or 24 h (Fig 6.29). These qualitative images were quantified and show maximal PDT tumour necrosis was observed with Foscan at both DLIs (50 mm^2) when tumours were irradiated with 10 J of light delivered at 100 mW (100 s) interstitially (Fig 6.30). 20 nm ORMOSIL NPs demonstrated equal PDT efficacy to Foscan at a DLI of 6 h (50 mm^2), however, this decreased twofold at a DLI of 24 h (Fig 6.29 B & E). Larger 90 nm ORMOSIL NPs follow the same pattern of PDT induced necrosis, with a decrease in observed damage at a DLI of 24 h compared to 6 h (Fig 6.29 C & F). Fig 6.30 additionally illustrates the PDT efficacy of large ORMOSIL NPs with tetrasilane bound m-THPC. Interestingly, these NPs showed an increase in PDT tumour damage (50 mm^2) to rival that of Foscan at the longer selected DLI (24 h) compared to the shorter DLI of 6 h (H&E sections not displayed in Fig 6.29). Control tissues that received either no drug or light showed no response to treatment (Fig 6.29 D).

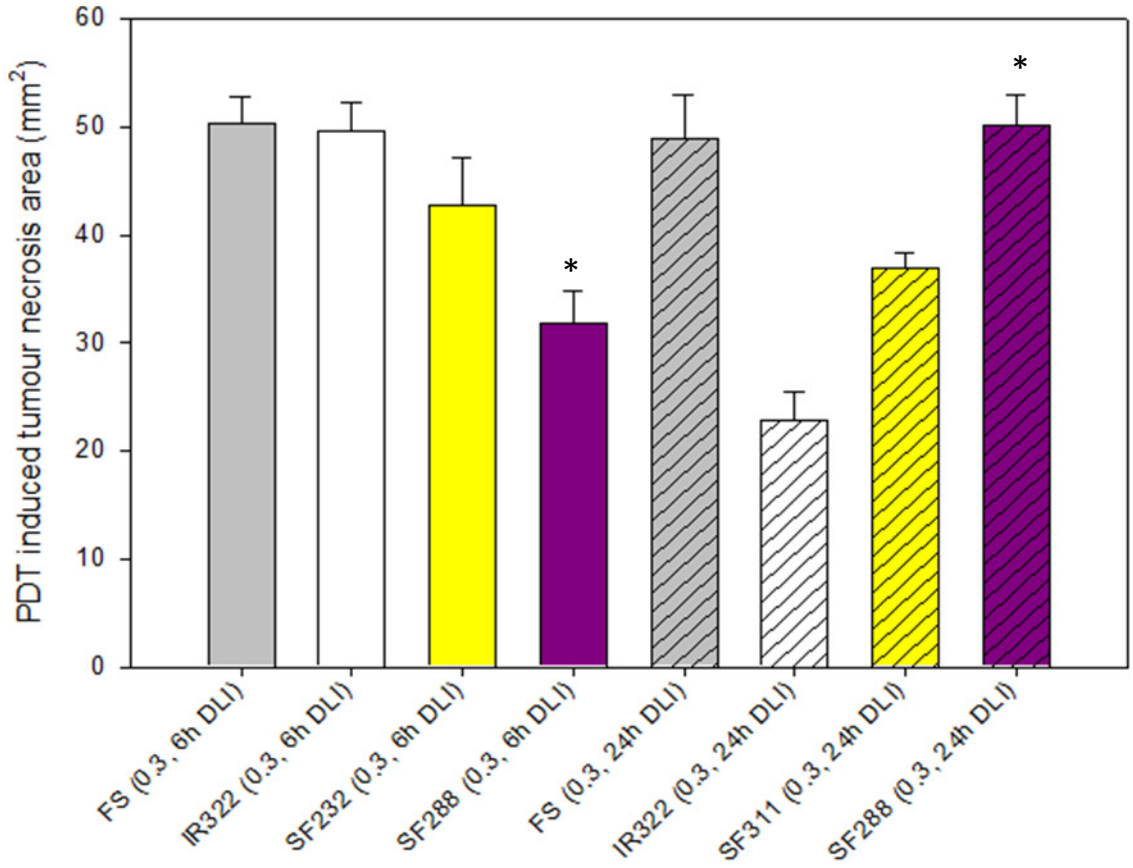

Figure 6.30. The area of PDT tumour necrosis (mm^2) following irradiation of tumours in female HL rats with 10 J of light at 100 mW at a DLI of either 6 h or 24 h, after intravenous injection of 0.3 mg kg^{-1} m-THPC in Foscan or pegylated ORMOSIL NPs; ≤20 nm, mono-m-THPC (IR322), ≥90 nm, mono-m-THPC (SF232/311), ≥90 nm, *tetra-m-THPC (SF288). Negative control tumour tissue (received either no drug or light treatment, data not shown). Data points show the mean±SD, n=4.

Targeted cRGD ORMOSIL NPs

i. Absorbance Spectra

m-THPC covalently linked (tetrasilane) in targeted cRGD- and inactive targeted cRAD-ORMOSIL NPs (Fig 6.31) demonstrated a slight peak broadening and small bathochromic shifts for both absorbance peaks (m-THPC λexc = 425 nm, λem = 654 nm), in comparison to Foscan. There was also a greater amount of light scattering between 300-400 nm likely due to the presence of silica, as observed in previous ORMOSIL spectra.

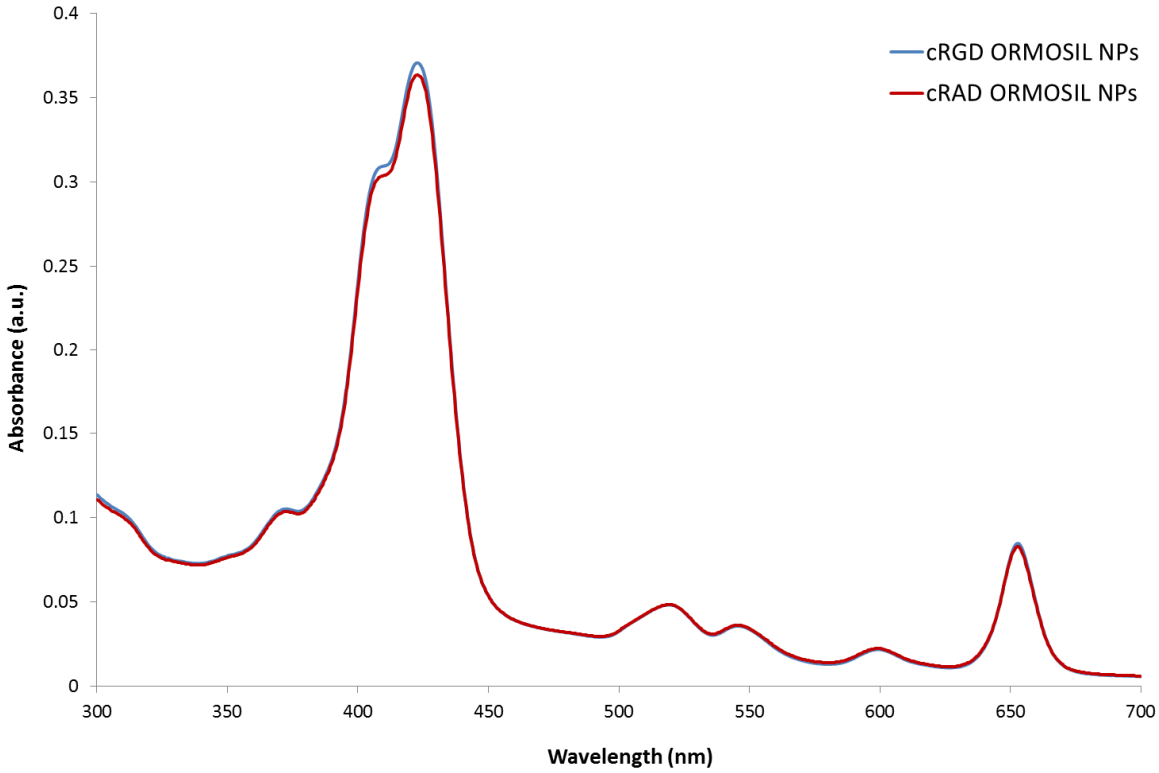

Figure 6.31. Absorbance spectra of m-THPC covalently incorporated (tetrasilane) in targeted cRGD-ORMOSIL NPs and inactive targeted cRAD-ORMOSIL NPs in PBS. All solutions prepared at 10 μM m-THPC concentrations.

ii. Confocal microscopy in vitro

Tumour cell lines were incubated with a cRGD-FITC conjugate to assess the presence of the $\alpha_v\beta_3$ integrin. This was identified through the expression of a positive green fluorescence FITC signal, indicative of conjugate binding to the $\alpha_v\beta_3$ integrin on the cell surface. A549 cells are recognised as positively expressing $\alpha_v\beta_3$ integrin, which has been demonstrated here following inbucation with cRGD-FITC conjugate for 4 h (Fig 6.32). Lower levels of green fluorescence were observed with MCF-7 cells (Fig 6.33), in accordance with the literature. A positive FITC fluorescence was detected with the domestic MC28 cells (Fig 6.33), under the same conditions, suggestive of $\alpha_v\beta_3$ integrin expression.

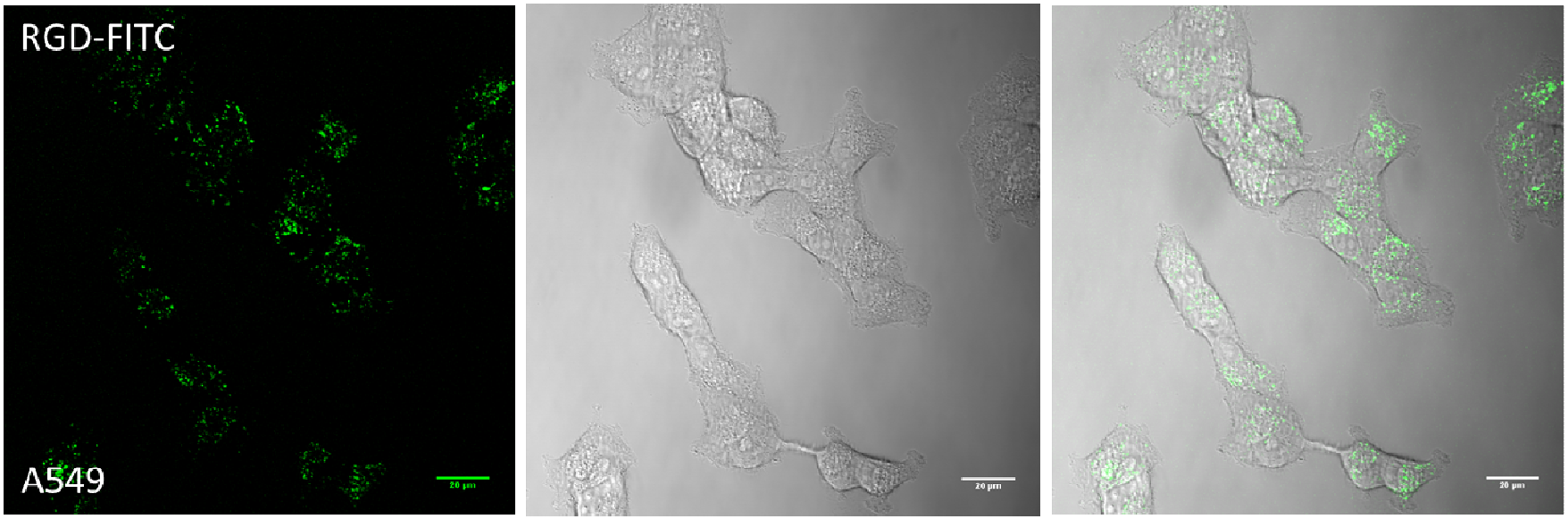

Fig 6.32. Confocal microscopy images *in vitro* following incubation with 50 nM cRGD-FITC conjugate for 4 h in human A549 adenocarcinoma alveolar basal epithelial cells to determine αvβ3 integrin expression.

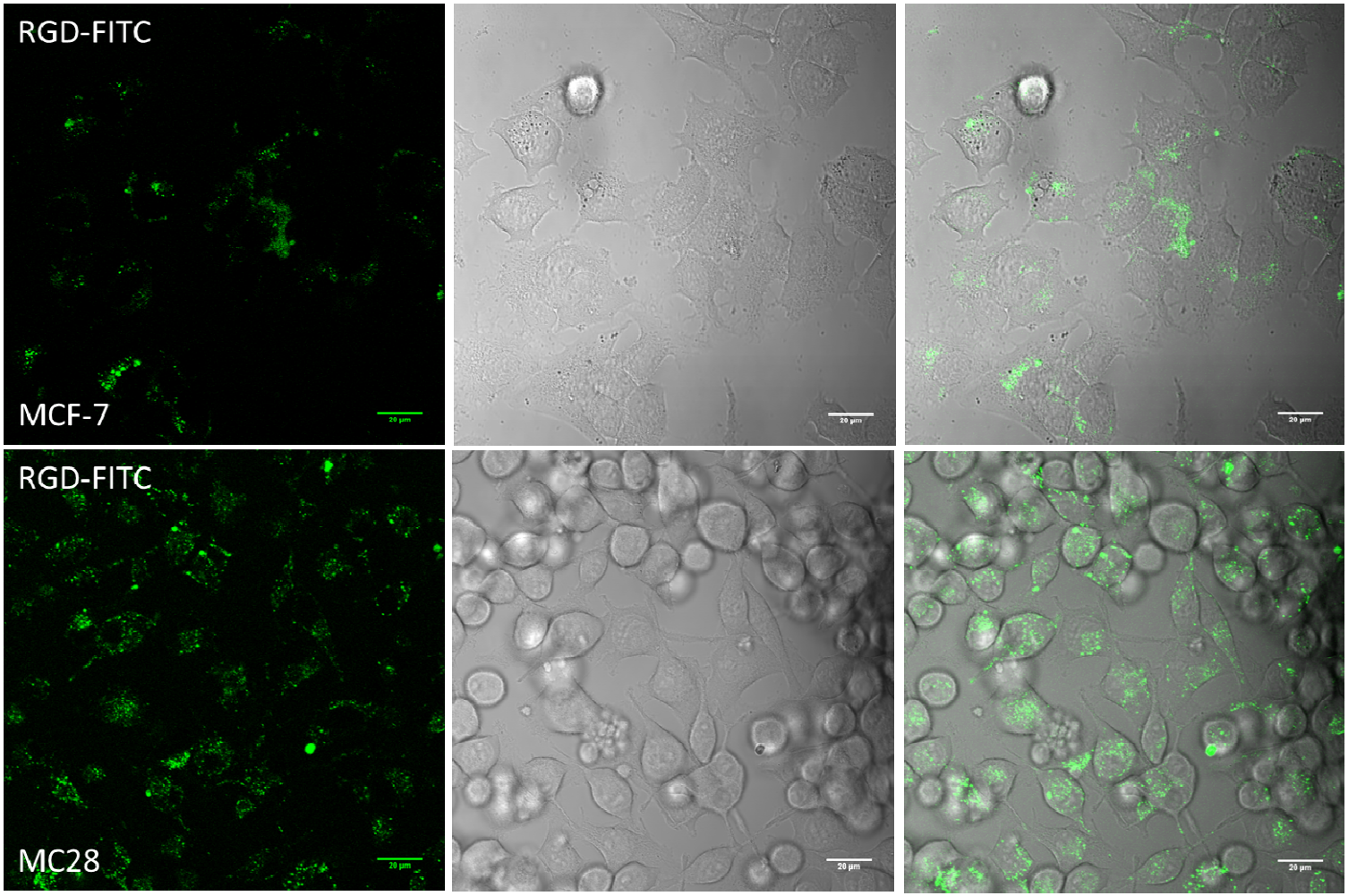

Fig 6.33. Confocal microscopy images *in vitro* following incubation with 50 nM cRGD-FITC conjugate for 4 h in either human MCF-7 breast adenocarcinoma cells or rat MC28 fibrosarcoma cells to determine αvβ3 integrin expression.

iii. Biodistribution studies in vivo

Targeted uptake studies with targeted cRGD-ORMOSIL NPs were not carried out *in vitro* here due to more extensive work having been previously published by collaborators. Due to the strong cRGD-FITC fluorescence signal observed with MC28 cells, these cells were taken forward for *in vivo* studies.

Biodistribution studies with m-THPC covalently incorporated in targeted cRGD-ORMOSIL NPs and inactive targeted cRAD-ORMOSIL NPs were carried out in selected tissues. Doses of 0.1 mg kg^{-1} (m-THPC drug equivalent) were administered in Hooded Lister rats implanted with MC28 subcutaneous tumours for analysis at 24 h to measure levels of m-THPC in tissues using chemical extraction. These studies focused on one time interval to compare data with studies on untargeted non-biodegradable pegylated ORMOSIL NPs, previously described in this chapter.

A range of organs were selected for quantitative analysis to compare the relative uptake of m-THPC to that of tumour tissue when delivered by cRGD- and cRAD-ORMOSIL NPs. At 24 h, a trend for m-THPC concentrations in the blood serum were observed as approximately two-fold greater when administered in cRAD- ORMOSIL NPs (~0.2 μg mL^{-1}) compared to cRGD-ORMOSIL NPs (~0.1 μg mL^{-1}), however, this was not significant (Fig 6.34). The highest m-THPC concentrations were observed in the liver (~0.7 μg g^{-1}) and spleen (~1.4 μg g^{-1}) for both ORMOSIL NPs at 24 h, where m-THPC uptake was almost identical. m-THPC uptake in the kidneys, lung and skin were observed at the lowest concentrations at this time, with almost negligible m-THPC concentrations detected for each NP (≤0.05 μg g^{-1}). m-THPC accumulation in tumour tissue appeared to parallel that of the blood serum, with similar concentrations of m-THPC for both NPs, but a greater uptake of cRAD-ORMOSIL NPs observed in comparison to cRGD-NPs, which is significant at this time (Fig 6.34).

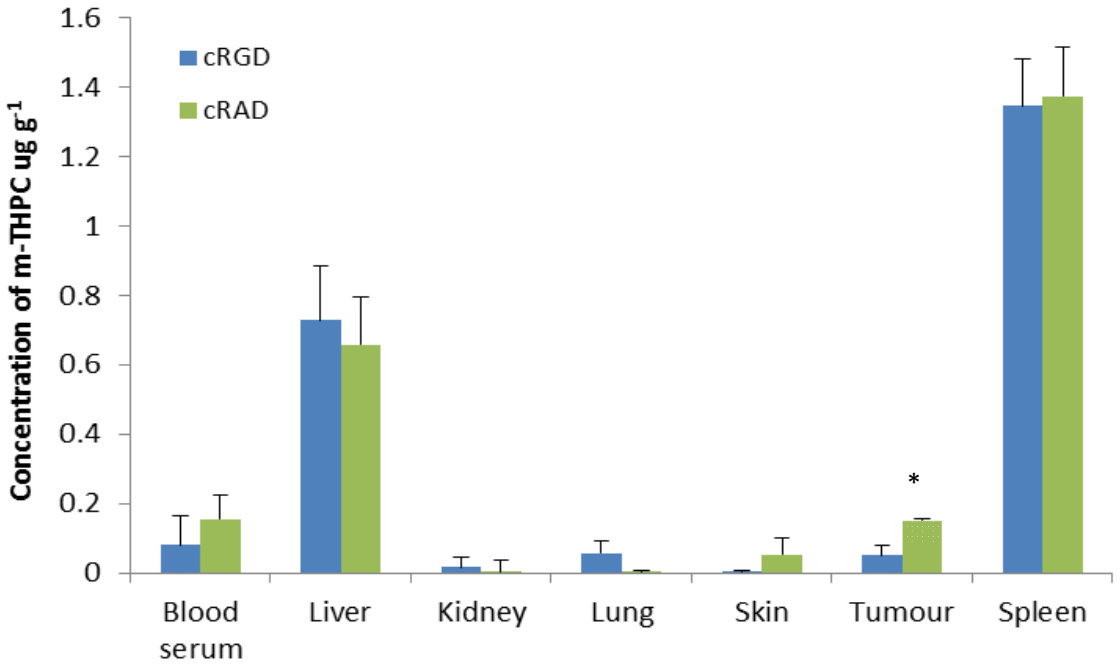

Fig 6.34. Concentration of m-THPC (μg g^{-1}) in selected tissues of the Hooded Lister rat following an intravenous injection of 0.1 mg kg^{-1} m-THPC in targeted cRGD-ORMOSIL NPs (blue) or inactive targeted cRAD-ORMOSIL NPs (green) ~75 nm at 24 h. Data points show the mean ± s.d., n = 4.

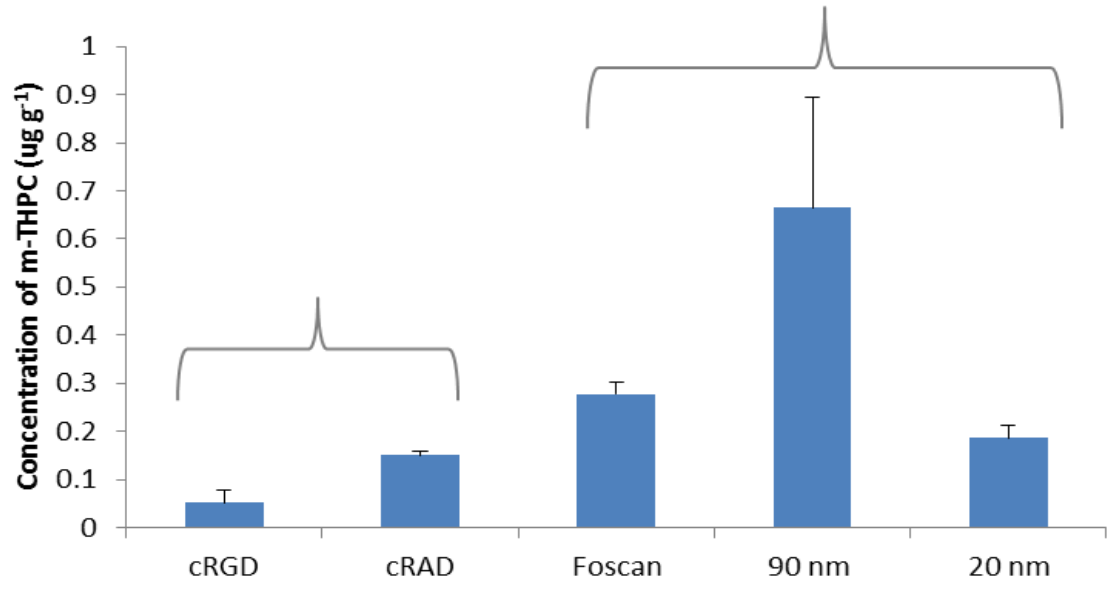

Fig 6.35. Comparing the concentration of m-THPC (μg g^{-1}) in tumour tissue of the Hooded Lister rat following an intravenous injection of either 0.1 mg kg^{-1} m-THPC in targeted cRGD-ORMOSIL NPs or inactive targeted cRAD-ORMOSIL NPs (75 nm) versus 0.3 mg kg^{-1} m-THPC in Foscan or 90 nm and 20 nm untargeted pegylated ORMOSIL NPs at 24 h. Data points show the mean ± s.d., n = 4.

Figure 6.35 demonstrates a primitive comparison between previously discussed untargeted pegylated ORMOSIL NPs, both large (90 nm) and small (20 nm), administered at a higher m-THPC dose (0.3 mg kg^{-1}) versus targeted cRGD- ORMOSIL NPs (75 nm) administered at a lower m-THPC dose (0.1 mg kg^{-1}). m-THPC was covalently bound inside ORMOSIL NPs by a tetrasilane linker in all formulations represented in Fig 6.35. Despite the difference in m-THPC doses, small (20 nm) untargeted pegylated ORMOSIL NPs and inactive targeted cRAD-ORMOSIL NPs (75 nm) appear to accumulate at similar concentrations in MC28 tumour tissue of the HL rat. cRGD- ORMOSIL NPs demonstrate the lowest uptake in the tumour at 24 h.

iv. Fluorescence microscopy

Fluorescence microscopy of frozen tissue sections taken from the same animals (MC28 HL rats) as used in chemical extraction studies (0.1 mg kg^{-1} m-THPC intravenous injection in cRGD- and cRAD-ORMOSIL NPs at 24 h), shown in Figure 6.36, demonstrated the presence of intense bright fluorescence spots in false coloured CCD images, which were distributed throughout the liver (Fig 6.36). This was indicative of high m-THPC uptake when covalently (tetrasilane) incorporated in both cRGD- and cRAD-ORMOSIL NPs at 24 h. The same high m-THPC fluorescence was also observed for both NP groups in the spleen, with m-THPC localisation predominantly in the red pulp of spleen tissue (bulk) compared to the clearly visible outline of the darker white pulp. Lung tissue generally showed low levels of m-THPC fluorescence but the incidence of bright white spots, suggestive of m-THPC fluorescence, was greater following administration of cRAD- versus cRGD-ORMOSIL NPs. Furthermore, images also revealed high m-THPC fluorescence within the kidneys for both particles at this time but the lowest observed fluorescence in tumour tissue.

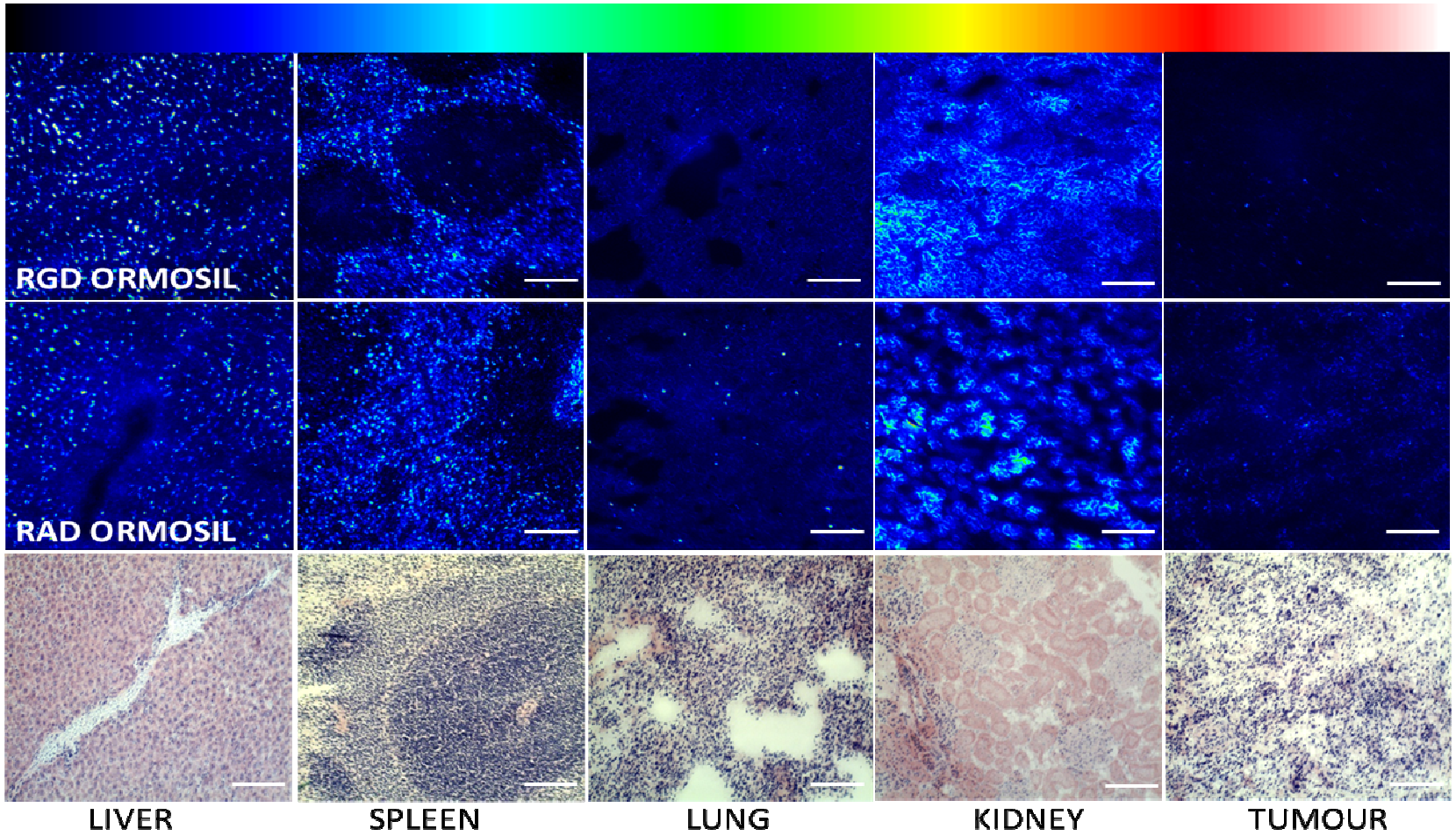

Fig 6.36. Typical examples of false coloured fluorescence microscopy CCD images of m-THPC in 10 micron frozen tissue sections following an intravenous injection of 0.1 mg kg^{-1} m-THPC in either pegylated RGD targeted (top) or pegylated RAD untargeted ORMOSIL NPs (middle) (75 nm) at 24 h. (Bottom) equivalent frozen tissue sections stained with H&E. 100 micron scale bar on each image and the fluorescence intensity scale, top, increases from black (background/no fluorescence) through to white (max. fluorescence).

v. PDT studies

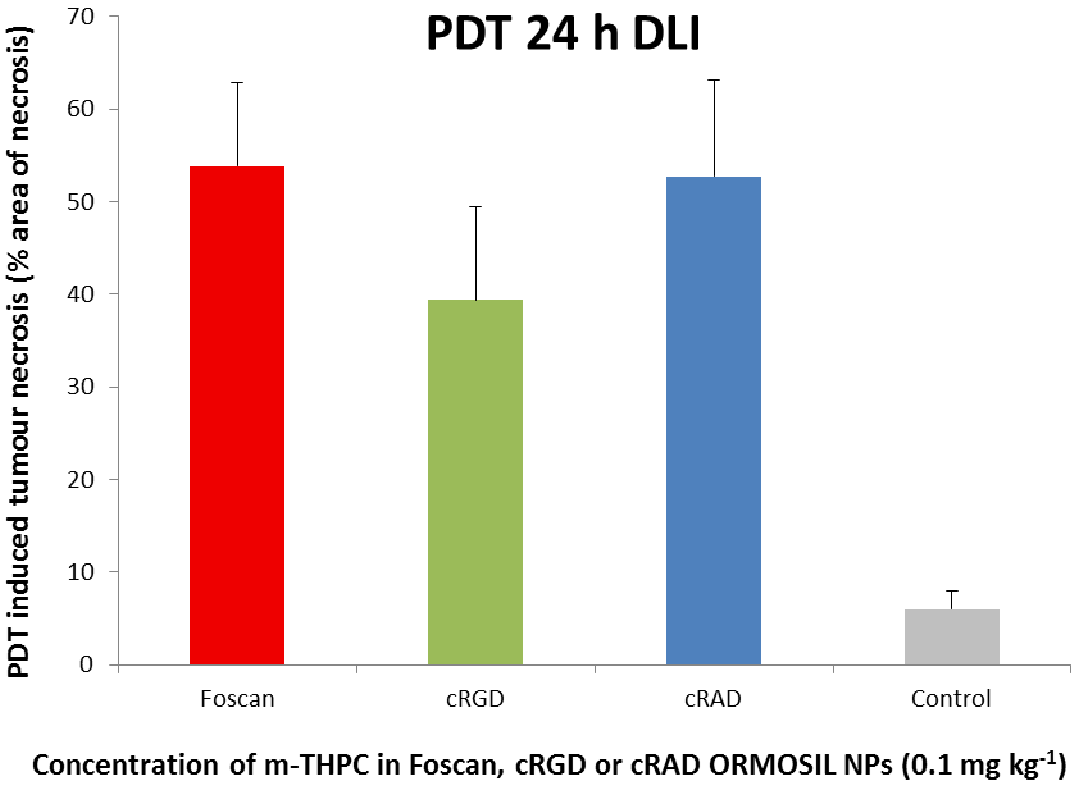

Figure 6.37. The percentage of MC28 tumour tissue necrosis (%) in the HL rat induced by PDT with 10 J of light at 100 mW following intravenous injection of 0.1 mg kg^{-1} of m-THPC in either Foscan, targeted cRGD-ORMOSIL NPs and inactive targeted cRAD-ORMOSIL NPs at a drug:light interval of 24 h.

When examined histologically, the percentage area of tumour necrosis (from the total tumour tissue section) induced by PDT at a drug light interval of 24 h showed there was no significant difference between Foscan, cRGD or cRAD- ORMOSIL NPs following their intravenous administration at a dose of 0.1 mg kg^{-1} m-THPC equivalent (Fig 6.37). Results showed there was a trend towards a greater percentage area of tumour necrosis induced with Foscan (53%) and cRAD-ORMOSIL NPs (52%), which were almost 15% higher than tumour necrosis induced with cRGD-ORMOSIL NPs (39%), however, this was not significant. There was a significant difference in PDT tumour necrosis following administration of m-THPC formulations versus the control group, which received light treatment but no m-THPC ($p \leq 0.001$).

6.4 Discussion

In recent years the use of non-biodegradable NPs, such as silica NPs, offer many advantageous properties in fulfilling requirements for applications in PDT and are explored in this chapter. On account of their rigid, porous structures, they are able to covalently anchor, rather than physically entrap (non-covalent) photosensitisers, without affecting their photophysical and spectroscopic capabilities (Selvestrel, F. et al. 2013). As the PS does not need to be released in order to elicit phototoxic effects, this circumvents the problems of premature drug leakage, increases PS bioavailability at the site of action and reduces exposure to normal tissues. Additionally, composite materials can be modified (PEG attachment) to avoid rapid capture by the RES (*i.e.* ORMOSIL), and increase either passive tumour uptake via the EPR effect or active tumour uptake through the conjugation of surface biomolecules to further improve tumour selectivity. However, issues associated with the retention and long-term toxicity of non-biodegradable NPs must be considered upon *in vivo* investigation and are explored here. The central aim of these studies was to deduce m-THPC biodistribution when covalently incorporated inside non-biodegradable ORMOSIL NPs, versus Foscan, and assess PDT efficacy for the first time *in vivo* with these NPs. Furthermore, the latter section of this chapter explored the potential of targeting ORMOSIL NPs with cRGD peptide to enhance these properties further.

Untargeted ORMOSIL NPs

Photophysical studies

The absorbance spectra of pegylated ORMOSIL NPs was used to deduce spectroscopic characteristics of m-THPC versus covalently encapsulated m-THPC (derivatives). There was little observed difference between free forms of m-THPC and monosilane or tetrasilane bound forms of m-THPC in methanol or Solvable. This is perhaps expected as the addition of the silane linker is peripheral to the porphyrin ring of m-THPC and the covalent linkage of other photosensitisers into ORMOSILs has been demonstrated by other groups without detrimental effect to their photochemical properties due to the low polarity of the organosilica matrix (Ohulchanskyy, T. Y. et al. 2007;Selvestrel, F. et al. 2013). Moreover, all ORMOSIL NPs diluted in saline buffer, as when administered to animals (data not shown), did not indicate any reduction in m-THPC absorbance intensity (652 nm) or suggest the presence of hydrophobic aggregates, confirming that the covalently bound m-THPC was indeed encapsulated within the particles as monomers.

In vitro

m-THPC release from ORMOSIL NPs

Release rates of physically entrapped m-THPC (non-covalent) from non-pegylated and pegylated ORMOSIL NPs were carried out by collaborators at the University of Padova (*see* ***Appendix I – Fig C.5 Rate of m-THPC release from ORMOSIL NPs***). These studies indicated >90% release of m-THPC following incubation with non-pegylated ORMOSIL NPs in 3% FBS compared to ~20% release of m-THPC from pegylated ORMOSIL NPs under the same conditions. This increased to ~30% release of m-THPC in the presence of 10% FBS and >60% release with 50% FBS and was confirmed by *in vitro* studies in human oesophageal squamous carcinoma cells (KYSE 510), which showed cellular uptake of physically entrapped m-THPC in ~30 nm ORMOSIL NPs was mediated by transfer to serum proteins, promoting premature release of m-THPC from NPs to the media (Compagnin, C. et al. 2009). As a result, there was little difference exhibited in the cellular uptake of free m-THPC or when delivered by the NPs. This phenomenon was significantly reduced using pegylated NPs, where a much smaller (<20%) and slower release of mTHPC from the nanoparticles was observed with cell culture medium containing 3% FBS.

No such serum release-rate experiments were replicated with covalently incorporated m-THPC in ORMOSIL NPs in studies here, however, confocal images obtained through *in vitro* studies with MC28 tumour cells, indicated a higher uptake of m-THPC with smaller NPs (~20 nm) in comparison to large NPs (~100 nm) following a 4 h incubation period (Fig 6.9). The smaller size of the NPs may be more favourable in promoting intracellular internalisation, as larger NPs may be more inhibited from entering the cell due to steric hindrance at the cell membrane on account of their size. It is believed m-THPC fluorescence is directly associated with NP uptake in these studies due to the covalent anchorage of m-THPC within ORMOSIL NPs, therefore differences in NP size may be a greater contributing factor in the total m-THPC cell uptake. However, no m-THPC release rate experiments (+ FBS) have been carried out to date with these NPs to confirm this. Differences in covalent m-THPC incorporation within each of the NPs for *in vitro* experiments, *i.e.* monosilane bound m-THPC in 20 nm NPs versus tetrasilane bound in 100 nm NPs, may also have contributed to the decrease in observed intracellular fluorescence with the larger NPs (Fig 6.9). There was little difference indicated between the absorbance

spectra of mono- versus tetrasilane m-THPC (free or bound in ORMOSIL NPs) in MeOH (Fig 6.6), however, *in vitro* conditions, including incubation with cell media containing 10% FCS, may have affected their fluorescence properties. It is unlikely FCS directly interacts with the PS to cause aggregation and fluorescence quenching as serum proteins are too bulky to enter through silica NP pores. Furthermore, any decrease in fluorescence is unlikely to be due to the formation of hydrophobic aggregates as tetrasilane bound m-THPC molecules cannot migrate towards each other in aqueous environments on account of strong covalent bonding within the NP (Fig 6.2C). Any reduction in fluorescence signal was thought to be attributed to unanticipated perturbation in photophysical properties, such as the lack of mobility and restricted rotation of tetrasilane m-THPC due to its anchorage at four points to the silica matrix. As porphyrins are planar molecules, which rotate to preferentially maintain this planarity, any forced distortion is likely to induce a reduction in fluorescence lifetime as a result of flexing dye molecules, causing quenching. The excessive rigidity of tetrasilane m-THPC to the ORMOSIL framework in highly similar NPs was described by collaborators in the presence of water and was thought to potentially lead to a reduction in singlet oxygen yield in aqueous environments (Selvestrel, F. et al. 2013). This would not apply to the same degree with monosilane bound m-THPC, as its single bond to the silica matrix allows for a much greater range of movement. The greater red fluorescence signals observed in cells with 20 nm ORMOSIL NPs, bound with monosilane m-THPC, are in accordance with previous studies carried out in our laboratory (MacKenzie *et al*., 2011 – data not published), where no spectroscopic changes were observed with monosilane bound m-THPC in ORMOSIL NPs in the presence of FCS.

m-THPC uptake and localisation

Confocal images presented here also offered information on the intracellular localisation of m-THPC, as the fluorescence for each nanocarrier was not detected in the nucleus but uniformly dispersed in the cytoplasm (Fig 6.9). This was also observed upon incubation of free m-THPC (Foscan) with MC28 tumour cells but the intracellular fluorescence was more intense. This pattern of uptake is in good accordance with the literature (Marchal, S. et al. 2007;Melnikova, V. O. et al. 1999a). Compagnin *et al*., have shown red m-THPC fluorescence distributed throughout the cytoplasm of when using similar (non-pegylated) ORMOSIL NPs but also suggested localisation at the RER and Golgi. However, this was proceeding leaching of m-THPC from NPs mediated by serum proteins and as such was

attributed to the localisation of free intracellular m-THPC (Compagnin, C. et al. 2009). More recently, the same group investigated the cellular uptake of free m-THPC versus pegylated ORMOSIL NPs loaded with tetra-silane bound m-THPC following 24 h incubation with lung cancer cells (A549) and normal lung cells (CCD-34Lu) for 24 h 3% FCS. Using a FACS analysis, a much lower uptake of m-THPC embedded in NPs was taken up by both cell lines (~5%) in comparison to measurements of free m-THPC (Selvestrel, F. et al. 2013). In this investigation, red fluorescence can be attributed to bound m-THPC within ORMOSIL NPs

Preliminary pharmacokinetics at 24 h

Initial batches of small ORMOSIL NPs of ~20 nm indicated m-THPC remained at approximately 1.5 μg g^{-1} in the blood serum at 24 h, which was much greater than that of previous investigated biodegradable pegylated liposomal formulations (Fig 6.10). However, despite this high circulating m-THPC concentration with non-biodegradable NPs, much lower levels of m-THPC accumulated in corresponding tumour tissue at this time. Conversely, 90 nm ORMOSIL NPs were also retained in the blood at similar high concentrations at 24 h and delivered m-THPC at much higher concentrations to tumour tissue. This is thought to be attributed to passive targeting of large NPs in solid tumours. No radical differences in m-THPC uptake of tissues were identified between FosPEG and ORMOSIL NPs, which is perhaps surprising given the expected differences in their tissue retention and routes of elimination from the body as a result of their level of biodegradability. It is probable by 24 h liposomal nanocarriers may have degraded therefore liver accumulation at this time solely indicates released m-THPC rather than liposomally entrapped m-THPC. Released m-THPC may be potentially bound by serum complexes and transported to the liver to produce similar levels of m-THPC accumulation as ORMOSIL NPs. 20 nm ORMOSIL NPs displayed high m-THPC accumulation in lung tissue at 24 h (~ 2.2 μg g^{-1}); which was more than threefold greater than 90 nm silica NPs (~ 0.6 μg g^{-1}), between 2-3 times greater than FosPEG formulations (~ 0.5 – 1.0 μg g^{-1}) and almost fifteen times that of Foscan (~ 0.15 μg g^{-1}). Unlike FosPEG data in the lung (**Chapter 4**: Liposomes), this did not mimic the concentration of m-THPC in the blood plasma at this time. Increased uptake in the lungs has been identified in a number of biodistribution studies with various NPs, such as other ORMOSIL NPs (Kumar, R. et al. 2010), quantum dots (Choi, H. S. et al. 2007) and silica NPs (Yu, T. et al. 2012b). Lung

accumulation in these studies was believed to be the result of passive entrapment in the pulmonary arteries due to the large surface area of lung tissue, its abundant blood supply and specialised anatomical structures, and dependency of size and charge on uptake. Greater retention was observed with larger (>34 nm) and/or positively charged NPs in mice (Choi, H. S. et al. 2010). It is unclear in the present investigation why initial batches of smaller ORMOSIL NPs are preferentially retained in the lungs over larger ORMOSIL NPs. All ORMOSIL NPs used in this investigation were reported as slightly negatively charged (-5.2 mV). It has recently been reported that accumulation of NPs in the lungs may be preferential in the treatment of cancer, as this area is notoriously difficult to access (Anselmo, A. C. et al. 2013).

Pharmacokinetic analysis

The plasma clearance pharmacokinetics of m-THPC in redeveloped ORMOSIL NPs of 20 nm and 90 nm in the HL rat model best fit a three exponential decay and were analsysed by methods described in ; **Chapter 4**: Liposomes.

Compartmental approach

Compartmental analysis gave a biological half-life ($t_{1/2}$ third compartment) of 577 h and 301 h for 20 nm and >90 nm ORMOSIL NPs, respectively, following intravenous administration of 0.3 mg kg^{-1} mTHPC (Table 6.6) compared to 90 h for Foscan (Foscan data from **Chapter 4**: Liposomes). To our knowledge no other *in vivo* studies investigating the biodistribution of ORMOSIL NPs have reported on pharmacokinetic parameters for direct comparisons but biological half-lives calculated for other PEG-modified non-biodegradable silica NPs have shown much lower half-lives, *i.e.* $t_{1/2}$ 80 mins for RuBYP doped NPs of ~45 nm in mice (He, X. et al. 2008). These differences could be a result of various silica precursors, NP sizes, dye incorporation methods and animal models used. The increase in $t_{1/2}$ deduced for 20 nm ORMOSIL NPs compared to 90 nm NPs is surprising given extensive evidence on the faster clearance and elimination of smaller sized NPs from *in vivo* models (Choi J et al. 2011). However, both 20 nm and 90 nm ORMOSIL NPs are equally likely to be cleared by longer excretion pathways on account of their non-bioderadability. The compartmental model estimated the initial V_d from the central compartment as 5008 mL kg^{-1} for 20 nm ORMOSIL NPs and 1131 mL kg^{-1} for 90 nm ORMOSIL NPs. These values strongly indicate that m-THPC covalently

bound in non-biodegradable ORMOSIL NPs is selectively retained in different tissues at early time points, as the volumes of distribution are so much greater than the blood volume of a rat (50 – 70 mL kg^{-1}) (Jones, H. J. et al. 2003). Moreover, 20 nm ORMOSIL NPs (20 nm) have a higher volume of distribution (V_d) indicating a greater uniform migration out of the vascular compartment into deep tissues, likely due to their smaller size. Foscan has a much higher volume of distribution than both ORMOSIL NPs in first and third compartments, probably due to the fact it is a smaller molecule and is rapidly bound by serum proteins (Triesscheijn, M. et al. 2007). Interestingly, all m-THPC formulations have a similar volume of distribution for the second compartment (V_d), which is representative of the first phase of migration out of the central blood compartment into tissues.

Non-compartmental approach

Non-compartmental analysis gave plasma m-THPC clearance rates of 0.002 and 0.007 mg kg^{-1} h^{-1} and $t_{1/2}$ lives of, 1854 h (~77 days) and 109 h (~5 days) for 20 nm and 90 nm ORMOSIL NPs, respectively. The large dissimilarity in $t_{1/2}$ values of m-THPC between 90 nm NPs and 20 nm NPs implies that with increasing NP size, m-THPC remains in circulation for shorter periods. This is perhaps because larger NPs are not taken up as effectively into cells therefore are eliminated more efficiently (as demonstrated with *in vitro* studies).

m-THPC biodistribution and uptake in vivo: normal tissues

Liver

Foscan was observed at the lowest concentrations in the blood serum, relative to pegylated ORMOSIL NPs (20 nm & 90 nm), which was comparable to biodegradable pegylated liposomal m-THPC. Xie *et al*. reported a greater uptake of 20 nm silica NPs versus 80 nm in the major organs of the RES; liver, spleen and lungs in mice (Xie, G. et al. 2010). Accumulation of m-THPC incorporated in ORMOSIL NPs was observed at the earliest time points (≤6 h) in the liver and spleen, regardless of size, and was much greater than that of biodegradable pegylated liposomal nanocarriers and Foscan, than in all other organs over 28 days. Furthermore, unlike the exponential decay observed with FosPEG formulations, a terminal elimination phase does not appear to be obtained with m-THPC in ORMOSIL NPs in the liver or spleen over this period. Qualitative confocal microscopy images of *ex vivo* liver tissue (Fig 6.18) and frozen sections of liver tissue (Fig 6.19-21) in

this investigation showed m-THPC localised in the Kupffer cells (macrophages) of the liver, following administration of 0.3 mg kg^{-1} m-THPC in 20 nm and 90 nm pegylated ORMOSIL NPs at 24 h, whereas Foscan was internalised and appeared as bright white spots, indicative of accumulation in lysosomes in the cytoplasm (Fig 6.16). Both techniques also demonstrated a slightly higher accumulation of m-THPC in 90 nm NPs compared to 20 nm NPs in these organs, suggesting their size and case material are important contributing factors.

Lungs

ORMOSIL NPs used in this investigation are known to interact with serum proteins (Compagnin, C. et al. 2009). Other studies have indicated the binding of serum proteins can lead to strong RES uptake and increase the hydrodynamic diameter of NPs, which is more likely to cause obstruction in vessels, partially explaining any increase in NP accumulation in lung tissue (Yu, T. et al. 2012b). It was also demonstrated that nanocarriers were able to redistribute to different tissues of the RES through macrophage uptake and smaller silica NPs can aggregate, causing transient embolisms in lung capillaries in mice *in vivo* which are endocytosed by macrophages (Xie, G. et al. 2010;Zhang, J. S. et al. 2005). Surprisingly, a lower maximal uptake of m-THPC in ORMOSIL NPs was observed in the lungs over 28 days compared to liposomal m-THPC formulations (Fig 6.14). However, ORMOSIL NP accumulation was still greater in the lungs than in most other organs over the full time series (Fig 6.18). This data is in contrast with Prasad *et al.,* who showed 20 nm ORMOSIL NPs accumulated at less than 5% of similar injected doses in the lungs of mice using an NIR fluorophore DY776 and radiolabelled ^{124}I, with the majority of particles (75%) accumulating in the liver and spleen at 24 h. This difference is potentially due to the conjugation of ^{124}I on to the outer surface of the ORMOSIL NPs, which the authors claimed may have altered the surface properties. Furthermore, the amide linker used to attach the ^{124}I was susceptible to enzymatic cleavage *in vivo*, reducing its half-life and therefore the accuracy of scintillation counting, whereas m-THPC was covalently incorporated in the current investigation. Other reports with mesoporous silica NPs (~120 nm) have also shown a preferential accumulation in lung tissue compared to nonporous silica NPs in immune-competent CD-1 mice following intravenous injection. However, redistribution of transient NPs from this organ was observed by 72 h without significant internalisation (Yu, T. et al. 2012a). Lung data (Fig 6.14) presented in this chapter showed redeveloped batches of pegylated ORMOSIL NPs

accumulated to a much lesser degree than initial batches at 24 h (Fig 6.10). Furthermore, unlike liposomal NPs, ORMOSIL NP data did not particularly correlate to the blood plasma pharmacokinetics. A sharp decline in m-THPC concentration was observed with both ORMOSIL NPs in lung tissue by 28 days, which suggests redistribution or clearance at this time (Fig 6.14).

Kidneys

Recently, silica NPs (~150 nm) have been reported as being capable of dissolving *in vivo* in rat models as 36% of injected doses were eliminated through the urine within four days; however, information from these studies was limited with no details on methods used to quantify silica NP concentration (Borak, B. et al. 2012). ORMOSIL NPs used in these studies were much larger than suggested renal thresholds (20≥100 nm), indicating ineffective clearance through glomerular filtration as it is size dependent. The kidneys showed a much lower uptake of m-THPC in 20 nm and 90 nm ORMOSIL NPs in comparison to the liver at the same time intervals. Decreased excretion rates or extended exposure can lead to associated toxicity from the accumulation of non-biodegradable NPs. It is more likely ORMOSIL NPs were excreted *via* the hepatobiliary (liver and bile) pathway, passing through the colon (Kumar, R. et al. 2010). However, this cannot be confirmed, as metabolic studies were carried out in these investigations.

m-THPC uptake in vivo: tumour tissue

Initial batches of pegylated ORMOSIL NPs showed a much higher uptake of m-THPC in 90 nm particles into tumour tissue at 24 h than 20 nm particles or Foscan, which corresponded to the blood serum pharmacokinetics of m-THPC with each formulation (Fig 6.11). Moderately elevated levels of tumour accumulation via passive targeting have been demonstrated previously using PpIX loaded silica NPs of ~45 nm in tumour-bearing mice (Simon, V. et al. 2010). The use of larger NPs appears to be more effective in optimally exploiting this natural EPR phenomenon (Maruyama et al., 1999), but there remains a balance between ideal particle size for clearance and for tumour retention.

Pharmacokinetic data of redeveloped ORMOSIL NPs revealed a much longer biological half-life for smaller (20 nm) ORMOSIL NPs than larger NPs (90 nm) but showed little significant difference in m-THPC accumulation in tumour tissue over 96 h with 90 nm

versus 20 nm pegylated ORMOSIL NPs in comparison to Foscan (Fig 6.17), but larger NPs levels were consistently higher. These observations were thought to be related to particle size and results were confirmed by confocal (Fig 6.22) and fluorescence microscopy (6.21) carried out at 24 h post inoculation. A much greater uptake of larger (90 nm) ORMOSIL NPs was observed, regardless of covalent m-THPC linkage within particles (mono or tetra), compared to 20 nm ORMOSIL NPs and controls (no m-THPC). m-THPC fluorescence was uniform in distribution throughout heterogeneous tumour tissue.

Toxicology

Many studies have reported on the biological inertness and non-antigenicity of silica-based materials, along with their ability to resist microbial attack (Jain, T. K. et al. 1998;Kumar, R. et al. 2010). However, even an inert material in bulk may be active at the nanoscopic level (Nel, A. et al. 2006). The size and surface chemistry of silica NPs, as with other NPs, has been widely reported as having a significant influence on their toxicity, as a result of different physiological lipoproteins binding to the NP surface upon systemic administration and dictating NP clearance from the body (Choi, H. S. et al. 2007;Decuzzi, P. et al. 2010;Greish, K. et al. 2012). The medical hazards associated with intravenously injected NPs are related to the release of proinflammatory cytokines and ROS upon administration, which may trigger systemic hypersensitivity reactions or intravascular coagulation, due to recognition by the immune system receptors (Oberdorster, G. 2010). This is most pertinent in the case of non-biodegradable nanoparticles. Studies investigating the proinflammatory effects *in vitro* on blood leukocytes (human) with bare and pegylated ORMOSIL NPs, as used in these investigations, have demonstrated that the latter, if captured, are predominantly bound by circulating monocytes, following little interaction with other leukocytes (Segat, D. et al. 2011). ORMOSIL NP size was a significant contributing factor in monocyte selectivity, with smaller ORMOSIL NPs (20 nm) appearing to have a higher monocyte association than larger NPs (≥100 nm). High density surface pegylation of ORMOSIL NPs helped to inhibit these effects and strongly decreased monocytic uptake and the activation of blood coagulation cascades upon incubation compared to bare ORMOSIL NPs (~85%). As monocytes may release significant amounts of proinflammatory cytokines/chemokines into the blood when suitably stimulated, causing dangerous conditions such as generalised shock, this reduction in NP monocytic uptake

from pegylation is certainly advantageous (Segat, D. et al. 2011). Furthermore, other studies using the similar pegylated ORMOSIL NPs showed they were poorly endocytosed by macrophages and demonstrated a reduced procoagulant activity in comparison to non-pegylated ORMOSIL NPs (Tavano, R. et al. 2010). This suggests prevention of rapid phagocytosis by the mononuclear phagocytic system (MPS, or RES) and the potential of pegylated ORMOSIL NPs as valuable drug delivery vehicles.

Route of administration

The route of administration can also play a fundamental role in NP toxicity. The biokinetics of NPs in the body differs depending on the portal of entry, particularly between intravenous administration of NPs versus NPs entering the blood circulation via translocation from either the respiratory tract, GI-tract or skin (Oberdorster, G. 2010). The interaction of NPs with different media following administration by various routes results in different biological secondary coatings. Subsequently, their entry into the blood circulation will occur at different doses, dose rates and blood oxygenation states, all of which affect NP biodistribution to secondary target organs. For example, many naturally occurring (*i.e.* pollen, dust) or man-made (*i.e*. fuel emissions, soot) foreign agents enter humans via the respiratory system undetected but when delivered systemically, these NPs may translocate to the central nervous system (CNS) causing more severe damage by oxidative stress (Medina, C. et al. 2007). Although there have been no reports published on the uptake of m-THPC specifically into nerve cells when administered intravenously, this may not necessary be true for silica NPs. Lung tissue is commonly the pro-target, particularly for nano-sized particles due to their increased surface area (Medina, C. et al. 2007). In the gastro-intestinal (GI) tract; the smaller the particle diameter, the faster they can diffuse through the GI secretion to reach the colonic enterocytes (Szentkuti, L. 1997). However, there is a caveat between particle size and intracellular uptake or clearance. If not renally filtered (cut-off suggested as 5.5 nm by (Choi, H. S. et al. 2007)) NPs may be excreted via the hepatobiliary pathway, which increases their exposure to the GI tract. Like the lungs, the GI-tract is highly accessible to stimuli that can induce an inflammatory response. These include inflammatory bowel disease (IBD), ulcerative colitis and the chronic inflammatory condition, Crohn's disease (CD). Non-biodegradable NPs may additionally be reabsorbed by the gut wall depending on their size and permeability increasing the area under the drug exposure curve over time. However, to date, there have

been no *in vivo* studies published on the effects of nanoparticles directly on the GI tract (Medina, C. et al. 2007).

Undesirable, prolonged retention of non-biodegradable NPs can cause potential problems, as eventually substances that cannot be broken down into biologically benign components accumulate in the liver (Choi, H. S. et al. 2007), which can lead to liver injury, including mononuclear inflammatory infiltrate at the portal area and hepatocyte necrosis at the portal triads (Xie, G. et al. 2010). It has been speculated that the greater the mass of the NP absorbed, the greater the toxic effect (Sahu, M. et al. 2010). In the case of m-THPC delivery with ORMOSIL NPs, the injected concentration of silica, in addition to the injected concentration of m-THPC, was calculated for each NP batch based on an animal weighing ~200 g (Table 6.4). All quantitative data was obtained through the detection of m-THPC and its accumulation in tissues, not direct ORMOSIL concentrations. Firstly, as these NPs are non-biodegradable, it can be assumed they remain fully intact for their duration *in vivo*. Secondly, as m-THPC is covalently bound in its monomeric form through silane linkers (mono- or tetra-silane) to the ORMOSIL matrix, assuming all its spectrofluorimetric properties are retained (*i.e.* minimal quenching or photobleaching), a rough estimation of the concentration of silica can be calculated based on the percentage loading of m-THPC in each batch of NPs (Table 6.4). Upon comparison of maximum silica concentrations injected for each ORMOSIL NP batch, there appeared to be no significant correlation with chemical extraction (Fig 6.11-6.17) and toxicology data obtained (Fig 6.23-6.29).

Liver function assay: AST/ALP

Qualitatively ORMOSIL NPs alone cannot be visualised *in vitro* or in *ex vivo* tissue on account of their size, transparency and lack of fluorescence to assess the effects and localisation of silica itself. Toxicology studies therefore focused on detecting abnormalities in *ex vivo* rat blood samples following the administration of m-THPC doped ORMOSIL NPs, using biochemical markers. This included liver/renal function assays to establish changes in the concentrations of liver and renal enzyme secreted into the blood circulation as markers of organ damage. Aspartate Transaminase (AST) is an enzyme which catalyses the reversible transfer of an α-amino group between aspartate and glutamate. Its increased secretion into the blood circulation is commonly used as an indicator to diagnose liver injury and assess renal function (acute renal disease). Results

suggested no significant difference ($p<0.05$) in the levels of AST in the blood (U/L) over 28 days following the administration of 20 or 90 nm pegylated ORMOSIL NPs (Fig 6.24). This may have been due to large variations in animal groups at selected time intervals as a result of the quality of blood samples. Unsurprisingly the pattern of liver enzyme secretion was similar for both enzymes, as the two are synonymously linked in amino acid metabolism. Alanine Transaminase (ALT) catalyses the two parts of the alanine cycle and its increased secretion into the blood circulation is commonly used as an indicator to diagnose hepatocellular injury or liver inflammation (*see* ***Appendix I - C.7 Toxicology: liver/renal enzyme function test***). Results showed a significant increase in ALT blood levels at 6 h ($p<0.05$) following administration of 90 nm ORMOSIL NPs (Fig 6.23) compared to control samples (no m-THPC NP injection), which was consistent with peak accumulations observed in the liver through chemical extraction data at this time (Fig 6.12). Overall results suggested no predominant signs of hepatocellular injury, liver toxicity or renal impairment were caused by the administration of either small or large pegylated ORMOSIL NPs *in vivo* over 28 days, as data were not significant ($p<0.05$) for all other time intervals up to this period. It should be noted that large variations (s.d.) in data may account for this, likely due to small animal numbers per group (n=3), and both enzymes generally showed an increase in blood concentration at 6 h, 1 week and 2 weeks.

Histological analysis

Owing to the longevity of non-biodegradable particles and their suspected accumulation from inconclusive biochemical assays, tissue sections from organs involved in major clearance pathways (RES), which typically house large numbers of residing macrophages, were additionally prepared for histological analysis to identify any signs of toxicity, such as, the infiltration of pro-inflammatory cells, pulmonary toxicity or tissue damage (necrosis). Liver, spleen, lung and kidney tissues were removed at two weeks post intravenous injection of 0.3 mg kg^{-1} m-THPC in either 20 nm or 90 nm pegylated ORMOSIL NPs (mono-mTHPC). A two week time interval was chosen based on previously published *in vivo* studies using ORMOSIL NPs, which showed clearance of NPs by 15 days through histological assessment without any overt signs of toxicity or tissue damage (Kumar, R. et al. 2010). Control tissues were collected from animals which received no m-THPC injection and were housed under the same conditions.

The most predominant toxicological effects were observed in histological sections of the liver and lungs, where signs of an acute proinflammatory response were observed two weeks post ORMOSIL NP administration (Fig 6.25-26). This correlates with *in vivo* biodistribution studies of normal tissues which showed the highest accumulation of ORMOSIL NPs, regardless of size, was in these organs. Histopathology of the liver by Ivanov *et al.,* revealed the presence of granulomas, small collections of macrophages, following systemic administration of silica NPs in rats, but demonstrated no significance difference in liver biochemical markers in the blood (Ivanov, S. et al. 2012); these findings were replicated here (Fig 6.25 C). This may be due to the sensitivity of the technique, poor quality blood samples or differences in physiology. The presence of granulomas in the liver, whose migration and cell number are triggered by the perceived presence of foreign bodies, which they are unable to eliminate, is applicable to the anticipated *in vivo* behaviour of non-biodegradable silica NPs. For examples, macrophages may be able to recognise and phagocytise NPs but are unable to degrade them due to their chemical stability. This can lead to potential long-term retention in tissues and has also been reported by Xie *et al*., over 30 days, who observed a greater uptake of 20 nm silica NPs (TeOS) versus 80 nm in the major organs of the RES; liver, spleen and lung, compared to control samples. They noted the presence of both silica NPs in phagolysosomes within the macrophages of the liver and spleen at 7 days using TEM, with a higher cellular uptake of smaller NPs on account of their larger surface area in mice (Xie, G. et al. 2010). Histological sections of the same organs at the same time interval showed a mononuclear inflammatory infiltrate and hepatocyte necrosis at the portal triads of the liver which was observed ≥30 days.

In the lungs, histopathology at two weeks following intravenous administration of both 20 nm and 90 nm pegylated ORMOSIL NPs showed a thickening and increase in the cellularity of the epithelial lining of the alveoli with the presence of a large number of foamy macrophages (Fig 6.26) in comparison to control tissue (no NP administration). This histology is believed to be similar to that of bronchitis, where an inflammation of the mucous membrane is observed. Brown *et al*., (Brown, D. M. et al. 2001) demonstrated a significantly greater influx of neutrophils into rat lung tissue following direct administration of smaller non-biodegradable polystyrene nanoparticles (64-nm) compared to larger polystyrene particles (202- and 535-nm) into the trachea. This size-dependent phenomenon was also reflected in other parameters of lung inflammation, including an

increase in protein and lactate dehydrogenase production and an increase in proinflammatory gene expression (IL-8). This was attributed to the increase in their surface area, however, it should be noted that these effects were observed following instillation, not systemic intravenous injection, of NPs and polystyrene particles used were not fully characterised (surface charge, chemical surface modifications).

Future toxicology studies

With advancements in nanotechnology, one of the key concerns with regards to the administration of non-biodegradable NPs is their penetration across the blood-brain barrier (BBB). Although the BBB is highly restrictive in nature, it is important to consider potential adverse implications (Krol, S. 2012;Oberdorster, G. 2010). More extensive toxicity studies on brain tissue were not carried out here due to time and resource constraints, however, future studies would need to strongly consider this possibility and note important changes in brain tissue pathology from either PS or non-biodegradable NPs, if indeed they occur. It should also be taken into consideration that removal of tissue sections for histological analysis here were not standardised between animals, including the perfusion of lung tissue prior to fixation and sectioning of tissues. Furthermore, specialised, expert veterinary histopathologists were not at our disposal for full histological examination of animal tissues. Future toxicology studies would need to entail a much broader range of tests including; (i) escalated and/or repeated drug doses to obtain the maximum tolerated dose (MTD), (ii) immunological markers for proinflammatory factors as these particles are non-biodegradable, (iii) more extensive biochemical assays of quality controlled live animal blood serum collection, (iv) brain tissue histology, (v) localisation studies and (vi) changes in gene expression from increased immunological infiltration (RT-PCR).

PDT

There have been PDT studies conducted *in vitro* with ORMOSIL NPs by Roy *et al*., (Roy, I. et al. 2003) and Ohulchanskyy *et al*., (Ohulchanskyy, T. Y. et al. 2007) carried out with HPPH doped NPs in human epithelial ovarian carcinoma (UCI-107) cells and colon cells (CT26), respectively, with success. Qian *et al.*, investigated the cytotoxic effects of encapsulated PpIX in mesoporous silica NPs on HeLa cells and the use of ORMOSIL NPs doped with IR-820 for brain and sentinel lymph node mapping applications in mice (Qian,

J. et al. 2009). Very few studies, to our knowledge, have focused on *in vivo* work with ORMOSIL NPs for applications in PDT. Prasad *et al.*, carryed out extensive studies in mice to assess biodistribution, toxicity and clearance of ORMOSIL NPs following animal imaging (Kumar, R. et al. 2010). This chapter demonstrates the first PDT studies to be carried out *in vivo* using ORMOSIL NPs. The extent of PDT necrosis was assessed in subcutaneous rat tumours following intravenous administration of ORMOSIL NPs (20 nm and 90 nm) covalently incorporating (mono or tetrasilane) m-THPC.

m-THPC is able to maintain its phototoxic ability and efficiently produce ROS at lower pH, such as those that occur in the microenvironment of tumours (Kascakova, S. et al. 2008). In addition, silica NPs are highly resistant to acidic degradation and their documented sub-cellular localisation in acidic lysosomes, importantly, should not affect ROS production but can influence cell death pathways induced by PDT; apoptotic or necrotic (Guo, W. et al. 1999). Unlike biodegradable liposomes, which release m-THPC once inside the cell, silica NPs remain intact, with m-THPC chemically linked within the particle. Absorbance spectra indicate m-THPC is largely in its monomeric form inside silica NPs (Fig 6.4) and other characterisation methods show its incorporation into ORMOSIL NPs does not affect its ability to produce singlet oxygen (Selvestrel, F. et al. 2013). The size of the NP is thought to contribute to its photodynamic efficacy due to size-dependent interactions of particles, in terms of their biodistribution and cellular uptake. Chatterjee *et al.,* (Chatterjee, D. K. et al. 2008a) reported preferable sub-50 nm silica NP size for effective phototoxic treatment, which was additionally supported by studies using 30 nm silica-based NPs *in vitro* in cellular uptake studies in tumour cell lines by Roy *et al.,* (Roy, I. et al. 2003).

Maximal PDT tumour necrosis (50 mm^2) was observed with Foscan at both DLIs (6 or 24 h) (Fig 6.28) and with different sized m-THPC loaded ORMOSIL. This confirmed activated m-THPC was not perturbed following its incorporation into particles through chemical covalent linkage (mono- or tetrasilane) to the NP matrix (monomeric formation). However, PDT with NPs did appear to be specifically dependent on (i) covalent linkage within NPs, (ii) DLIs (6 and 24 h) and (iii) NP size. All of which appeared to be contributing factors in the outcome of PDT induced necrosis. 20 nm ORMOSIL NPs incorporating monosilane bound m-THPC demonstrated equal PDT efficacy to Foscan at a DLI of 6 h (50 mm^2) compared to 90 nm NPs (30-40 mm^2) (Fig 6.28). This was initially

attributed to their smaller radii and larger surface area, which allowed for a greater volume of distribution. However, this figure decreased two-fold at a DLI of 24 h (Fig 6.27 B & E), suggesting PDT necrosis may have been predominantly induced by effects on the vasculature st earlier DLIs (6 h) *i.e.* vessel collapse, due to higher concentrations in the blood at early time points (Schacht, V. et al. 2006). Interestingly, *in vitro* studies with collaborators showed a low cellular uptake in A549 cells following incubation with tetrasilane bound m-THPC in ORMOSIL NPs at 24 h compared to free m-THPC (Foscan), whereas *in vivo* biodistribution studies here, tumour uptake of ORMOSIL NPs was greater than Foscan at this time. This was reflected in PDT studies *in vivo*, whereby tetrasilane bound m-THPC in ORMOSIL NPs demonstrated equal PDT efficacy to Foscan at a DLI of 24 h (50 mm^2). Therefore despite their poor intracellular uptake into tumour cells, these particles were still able to elicit an effective PDT response through damage to the extracellular matrix, interstitial space or vasculature, or a combination of all three.

Larger 90 nm ORMOSIL NPs incorporating monosilane bound m-THPC followed a similar pattern of PDT induced necrosis, but with slightly lower levels of tumour damage in general and therefore a less pronounced decrease in PDT damage between DLIs of 6 and 24 h (Fig 6.27 C & F). Lower concentrations of 90 nm were observed in the blood compared to 20 nm at early time points (~6 h), which may account for this, if PDT damage is vascular-associated. In addition, a decrease in m-THPC uptake was observed for 90 nm ORMOSIL NPs between 6 and 24 h in tumour tissue, but larger NPs were retained to a greater degree in tumour tissue compared to smaller NPs at 24 h, both of which are reflected in PDT induce tumour damage (Fig 6.28).

Interestingly PDT efficacy for large ORMOSIL NPs with tetrasilane bound m-THPC showed an increase in PDT tumour damage (50 mm^2), to rival that of Foscan, at a longer selected DLI of 24 h compared to 6 h. As discussed with *in vitro* studies in MC28 cells earlier, any decrease in singlet oxygen yield is unlikely to be due to the formation of hydrophobic aggregates as tetrasilane bound m-THPC molecules cannot migrate towards each other to form dimers. However, excessive rigidity of the framework, in the case of tetrasilane m-THPC derivative, may cause a reduction in singlet oxygen yield in the aqueous environment *in vivo* compared to monosilane bound m-THPC, as reported by collaborators (Selvestrel, F. et al. 2013). This may be true for DLIs of 6h between both large sets of ORMOSIL NPs (mono- vs tetrasilane m-THPC) however; the increase in PDT

necrosis at 24 h with large ORMOSIL NPs incorporating tetrasilane bound m-THPC compared to all other NP formulations at this time remains unclear. It has been shown that covalently bound m-THPC can induce a greater PDT effect as it can produce highly localised ROS generation intracellularly compared to non-localised free m-THPC (Guo, H. et al. 2011). Unfortunately PDT studies with 20 nm ORMOSIL NPs incorporating tetrasilane bound m-THPC were not carried out in order to make direct comparisons on the effects of covalent m-THPC incorporation and to eliminate any size-related factors.

Targeted cRGD-ORMOSIL NPs

Encouraging results of tumour uptake from untargeted ORMOSIL NPs led us to speculate as to whether a further increase in m-THPC tumour uptake could be achieved through active targeting of nanocarrier formulations to cancerous tissues. The goal of untargeted stealth NPs (*i.e.* PEG coated) was to maximise the blood circulation half-life, as longer circulation periods increase the likelihood of passive tumour accumulation of NPs from greater exposure. However, there may be an over-reliance on the EPR effect as an explanation and methodology to deliver NPs into tumours, as this phenomenon may not be a universal property of all tumours. Second, no single NP size can access all areas of the tumour and accumulate in significant quantities. Large NPs do not appear to extravasate far beyond the blood vessel and small NPs are more likely to be able to travel deeper into tumour tissue but remain there only transiently (~24 h). Finally, PEG-modified NPs have been shown to partially activate the immune system and lose efficacy upon repeated administrations (Anselmo, A. C. et al. 2013). Although active-targeting NPs also rely on the EPR effect to access the intratumoral space, targeting moieties can also be used to by anchor the nanoparticles onto tumour cells, in addition to triggering intracellular uptake (Albanese, A. et al. 2012).

Differences in non-targeted cellular uptake studies are typically dependent on drug loading, drug leaching (+/- serum proteins) and the size and/or surface charge of the delivery agent being internalised. The same factors apply with targeted uptake studies; however, uptake is directed via specific receptor-mediate pathways. Once bound to the receptor, the targeted NP-receptor complex produces a localised decrease in Gibb's free energy, which causes the membrane to wrap around the NP, forming a closed endocytic-vesicle structure. Receptor-mediated endocytosis typically ensures sequestration of the active agent into

lysosomes, which are degraded over time, rather than direct delivery to the cytosol. Smaller spherical NPs (≤20 nm) have less ligand-to-receptor interactions than larger NPs (≥100 nm). A small ligand-coated NP may interact with only one or two cell receptors and must bind to receptors in close proximity to produce enough available energy (Gibb's) to drive membrane folding (Albanese, A. et al. 2012). Larger targeted-NPs can act as cross-linking agents to cluster receptors and induce uptake. The binding strength of multiple receptor-ligand complexes (avidity) is greater than the total sum of individual affinities. Conversely, low molecular weight drug-ligand conjugates may allow for more efficient uptake via receptor-mediated endocytosis due to their smaller size, whereas bulkier NPs may not be as effectively internalised by this route on account of steric hindrance at the surface due to the nature of their cargo. Thermodynamically, a large ligand-coated NP binding a large number of cell surface receptors may limit further uptake of additional NPs due to redistribution of receptors (via diffusion) and receptor recycling required to compensate for the local depletion (Albanese, A. et al. 2012). Despite this apparent drawback, it is important to note, a large number of drug molecules (*e.g.* ~20,000 per liposome) may be delivered to the site of interest with very few targeting ligands attached to a NP surface *i.e.* ≤10 per vesicle. This translates to >1000-fold delivery amplification factor when considering the drug: ligand ratio, in comparison to the 1:1 drug-to-ligand ratio of smaller drug-conjugates. For this reason, alongside advantageous stealth properties, targeted ORMOSIL NPs were explored in the latter section of this chapter with the aim of improving the specificity of m-THPC delivery into tumour tissue for PDT.

cRGD-ORMOSIL NPs

The $\alpha_v\beta_3$ integrin is overexpressed on tumour neovasculature in comparison to mature, quiescent endothelial cells. It has shown to be involved in tumour progression, angiogenesis and metastasis through expression on proliferating cells (mature osteoclasts, angiogenic endothelial cells and tumour cells). The specific targeting of $\alpha_v\beta_3$ integrin cell adhesion receptor with the most common integrin binding sequence, the cyclic Arg-Gly-Asp (cRGD) peptide, was investigated following its conjugation to the surface of ORMOSIL NPs. Cyclic peptides have been reported as stronger and more selective inhibitors of cell adhesion, compared to linear variants, due to the preservation of less exposed sites (Aumailley, M. et al. 1991). As a result, this motif has been widely reported for diagnostic and therapeutic purposes in cancer (Temming, K. et al. 2005).

For targeted studies presented here, collaborators conjugated cRGD-ORMOSIL NPs loaded with covalently bound m-THPC and assessed their uptake in human umbilical vein endothelial cells (HUVEC), which overexpress the $\alpha_v\beta_3$ integrin, in comparison to inactive targeted cRAD-ORMOSIL NPs that have an amino acid substitution (central glycine with alanine). Results showed an increase in targeted cRGD NPs uptake with respect to cRAD NPs, largely regardless of size (70 nm versus 40 nm) and percentage ligand coverage of the NP (15% vs. 30%) (Selvestrel, F. et al. 2013). Conversley, studies using cRGD targeted liposomes loaded with doxorubicin showed that they were cleared from the blood plasma faster than non-targeted liposomes in Sprague-Dawley rats (Chen, Z. et al. 2012) and polymeric NPs were excluded from targeted studies due to limited resources and the high m-THPC release observed from these NPs at early time periods in *in vitro* studies by collaborators (Rojnik, M. et al. 2012).

cRGD-ORMOSIL NPs: in vitro

Tumour cell lines were incubated with a cRGD-FITC conjugate to assess the presence of the $\alpha_v\beta_3$ integrin on domestic cell lines to assess their suitablility for *in vivo* studies following implantation of tumours. Confocal imaging of positive green fluorescence was indicative of conjugate binding to the $\alpha_v\beta_3$ integrin receptors and intracellular uptake. A549 and MCF-7 cells, reported to be positive for αvβ3 integrin demonstrated a strong green fluorescence following incubation with cRGD-FITC for 4 h (Fig 6.31), with fluorescence largely confined to bright spots in the cytoplasm, indicative of receptor-mediated endocytosis from lyso-endosome formation. The greatest qualitative FITC fluorescence appeared to be detected in rat MC28 fibrosarcoma cells (Fig 6.32). Although higher cell density observed in MC28 cell confocal images may distort results, these findings are supported by studies carried out *in vitro* on human fibrosarcoma (HT-1080) cells, which were described as overexpressing the $\alpha_v\beta_3$ integrin receptor (Garrigues, H. J. et al. 2008;von, W. A. et al. 2007). These cells were therefore deemed appropriate for *in vivo* studies with targeted cRGD- ORMOSIL NPs in syngeneic, fully immune competent animals.

cRGD-ORMOSIL NPs: in vivo

Hooded Lister rats implanted with MC28 subcutaneous tumours were employed for biodistribution studies of m-THPC loaded (tetrasilane) targeted cRGD- and inactive targeted cRAD-ORMOSIL NPs. Animals were intravenously injected with low m-THPC

doses of 0.1 mg kg^{-1} due to limited NP batch volumes. *In vivo* experiments with corresponding low dose Foscan were not repeated in order to keee animal numbers to a minimum. Selected tissues from treatment groups were removed at 24 h for quantitative analysis via chemical extraction of m-THPC. As described in previous chapters, the highest m-THPC concentrations were observed in the blood, liver and spleen (>90% ID/g; *see* ***Appendix I – C.10 %ID/g cRGD-ORMOSIL NPs***), however, there was no significant difference observed in tissue m-THPC concentrations (μg g^{-1}) between cRGD- or cRAD-ORMOSIL NPs (Fig 6.34). This corresponded with *in vivo* studies carried out by research groups Chen *et al.*, and Xiong *et al.*, who used cRGD-pegylated liposomes loaded with doxorubicin. Following intravenous injection, studies showed both targeted and non-targeted liposomes demonstrated long circulating properties in rat plasma but there was no significant difference in $t_{1/2}$ (~25 h) between formulations (Chen, Z. et al. 2012).

m-THPC uptake in the lungs and skin was observed at the lowest concentrations following tareged cRGD- or cRAD-ORMOSIL NP delivery. Despite the difference in administered doses (0.1 vs. 0.3 mg kg^{-1}) between targeted and former untargeted ORMOSIL NP studies discussed in this chapter, this was encouraging, as the latter previously demonstrated higher accumulation in the lungs and no difference in m-THPC concentrations in the skin compared to Foscan. Surprisingly, m-THPC accumulation in tumour tissue showed a significantly greater uptake of inactive targeted cRAD ORMOSIL NPs in comparison to cRGD NPs (Fig 7.18). Other groups that have used RGD-targeted therapies *in vivo* have found prolonged circulation times and increased tumour accumulation compared to free drug but have reported little difference in uptake between targeted and untargeted NPs. For example Xiong *et al.*, demonstrated no significant difference in biodistribution studies with RGD versus untargeted doxorubicin loaded liposomes in B16 tumour-bearing mice but managed to observe effective tumour regression (Xiong, X. B. et al. 2005b).

False coloured fluorescence images were obtained from frozen tissue sections and confirmed the highest m-THPC accumulation was in the liver and spleen. m-THPC fluorescence in the liver was not localised around blood vessels for either cRGD- or RAD-ORMOSIL NPs, suggesting NPs may have extravasated out into the surrounding tissue by 24 h. Both NPs also demonstrated a preference for the white pulp, rather than the red pulp (cords), in the spleen. The white pulp contains elevated levels of T cells, including monocytes that express the $\alpha_v\beta_3$ integrin, which may promote binding of targeted cRGD-

NPs (Swirski, F. K. et al. 2009). Extraordinarily high splenic uptake was also observed by Xiong *et al*., with RGD-targeted liposomes *in vivo* in mice in comparison to other organs (Xiong, X. B. et al. 2005a), however, this can also be said for cRAD- NPs and in previous untargeted ORMOSIL studies at 24 h (*see* ***Appendix I - C.3 ORMOSIL NPs & C.10 % ID/g targeted cRGD-ORMOSIL NPs***). A high fluorescence signal was detected with both NPs in the kidneys through fluorescence microscopy compared to other organs. This does not corroborate with quantitative chemical extraction studies; it is unlikely NPs are excreted renally through the kidneys due to their size (~75 nm) and the issue remains unclear at this time. Tumour fluorescence images demonstrated a higher uptake with cRAD-NPs, in comparison to targeted cRGD-NPs, which corresponded well with chemical extraction data of tumour tissue but unfortunately confirmed there was no improvement in tumour uptake of targeted NPs in comparison to uptake in other normal tissues and control NPs. Recruitment and redistribution of mononuclear phagocytes to cancer sites from the spleen, may improve m-THPC uptake, as tumour tissue areas are typically high in macrophage presence.

PDT with cRGD-ORMOSIL NPs

PDT was performed under the same light treatment parameters as described in untargeted ORMOSIL NP studies. The percentage area of PDT induced tumour necrosis at a drug light interval of 24 h showed there was no significant difference between Foscan, targeted cRGD or inactive targeted cRAD-ORMOSIL NPs following their intravenous administration at a dose of 0.1 mg kg^{-1} (m-THPC equivalent) (Fig 6.37). Contrary to cRGD NPs improving *in vivo* efficacy of PDT to tumours, results showed a trend towards a greater percentage area of tumour necrosis induced with cRAD-NPs and Foscan alone (>50% versus <40%); although this was not significant.

To our knowledge, there have been no studies conducted using targeted cRGD conjugates or NPs for *in vivo* PDT for direct or indirect comparisons. The RGD peptide targets the $\alpha_v\beta_3$ integrin receptors abundantly expressed on tumour neovasculature (Stromblad, S. et al. 1996), despite MC28 tumours being highly vascularised there did not appear to be any improvement in tumour uptake or PDT efficacy with cRGD-ORMOSIL NPs. Conversely, cRAD-ORMSOSIL NPs demonstrated a higher uptake in tumour tissue through quantitative chemical extraction studies, which was reflected in PDT data. Despite no

significant differences following cRGD targeting, these NPs are still able to elicit an effective PDT response, with tumour necrosis ≥50%. This is comparable to that of Foscan alone and PDT results following much higher doses of administered m-THPC (0.3 mg kg^{-1}) in previous chapters (**Chpts: 4 & 5**). There was a significant difference in PDT tumour necrosis following administration of m-THPC formulations versus the control group, which received light treatment but no m-THPC ($p \leq 0.001$).

PDT studies *in vitro* in HUVEC cells ($\alpha_v\beta_3$ integrin positive) following incubation with cRGD-targeted and inactive targeted cRAD ORMOSIL NPs (tetrasilane m-THPC) found no difference in photokill activity between dose-response curves for both NPs. This was attributed to the partial protection of cells by cRGD peptide from PDT-induced phototoxicity, such as an anti-oxidant and anti-apoptotic effect, not exhibited by cRAD peptide (Allen, C. M. et al. 2002;Selvestrel, F. et al. 2013). Selvestrel *et al.*, found photokill efficiency did not appear to correspond to NP uptake between cell lines. This was thought to be due to differences between each cell type in their ability to resist the cytotoxicity of generated ROS (Selvestrel, F. et al. 2013). Differences in PDT efficacy *in vitro* could also be due to differences in intracellular localisation of free m-THPC (Golgi/ER) and when delivered by targeted NPs (endosomes) and the efficiency of singlet oxygen ($^1O_2$) production at these sites (Compagnin, C. et al. 2011). In untargeted tetrasilane bound m-THPC loaded ORMOSIL NPs PDT studies *in vivo*, PDT induced tumour necrosis was greater than treatment with either monosilane bound m-THPC or Foscan, suggesting sufficient $^1O_2$ generation, however, the conjugation of additional surface targeting moieties could modify this behaviour.

The difficulty with assessing effective treatment outcome, regardless of the tumour model employed, is deciphering underlying mechanisms that contribute to cell death, which cannot always be determined through histological analysis alone. Whilst this may initially be regarded 'irrelevant' in the clinical, with tumour regression, patient survival and quality of life taking a higher precedence, it is important to distinguish between types of cell death; necrosis, apoptosis and autophagy. For example, apoptosis (programmed) and necrosis (premature) are irreversible form of cell death, whereas autophagy (self-engulf) can induce cell death or paradoxically maintain cell survival. If cells are able to recover, this creates problems in long-term tumour regression and patient prognosis, therefore understanding these pathways allows the development of therapeutic strategies that maximise irreversible

tumour cell death and/or anti-tumour immunity; sustaining cancer regression. Although this was not the focus of these investigations, differentiating between cellular fates to clearly establish the type of cell death induced following *in vivo* PDT studies would be interesting to investigate in future studies and potentially beneficial in treatment outcome.

Summary: cRGD-ORMOSIL NPs

RGD peptide is more hydrophilic (zwitterionic) therefore attraction by the PEG pseudophase was assumed less likely, with $\alpha_v\beta_3$ integrin cellular receptors purportedly remaining available for interaction, however, despite encouraging cellular uptake in *in vitro* studies, targeted cRGD ORMOSIL NPs used here, showed no overall improvement in tumour uptake, biodistribution or in PDT tumour damage *in vivo* in comparison to untargeted NPs. It is speculated that the addition of excess targeting ligands may paradoxically increase uptake and clearance by the RES due to the presence of more proteins "visible" on the NP surface than with PEG alone. Furthermore, positive results achieved with active targeting may be offset by a 'barrier effect' *in vivo* whereby the majority of NPs are not able to migrate beyond the first few layers of tumour cells due to adherence with their targeted receptors (Albanese, A. et al. 2012). Although active targeting of NPs appeared to increase internalisation into cancerous cells *in vitro*, it did not translate *in vivo*.

6.5 Conclusions

The primary objective of the work described in this chapter was to investigate differences in the biodistribution of m-THPC when delivered by ORMOSIL NPs (small and larger) and targeted cRGD-ORMOSIL NPs, compared to standard Foscan formulation, to demonstrate PDT efficacy for the first time *in vivo* in MC28 tumour-bearing rats.

Pharmacokinetic analysis gave data on their accumulation within different tissues of normal and tumour animal models. It was found that larger (90 nm) pegylated ORMOSIL NPs appeared to accumulate to a greater degree in tumour tissue compared to smaller NPs (20 nm) and Foscan, which was likely due to passive uptake and retention of larger NPs in malignant tissue through the EPR effect. Conversely, 20 nm particles had a surprisingly longer blood plasma half-life than 90 nm *in vivo*, which was thought to be attributed to their larger surface and higher volume of distribution in tissues. The greatest m-THPC uptake with ORMOSIL NPs was observed in the major organs of the RES, particularly the liver and spleen, regardless of NP size. Studies with cRGD-ORMOSIL NPs showed no further significant increase in active m-THPC tumour uptake over untargeted NPs.

Clearance of non-biodegradable NPs was most likely via the hepatobiliary excretion pathway on account of NP chemical stability and particle size, which was incompatible with renal filtration (>5 nm). Toxicity studies revealed little significant difference in biochemical blood markers for liver and renal enzymes over 28 days but potential signs of inflammation were observed in histological analysis of the lungs and liver at two weeks post NP administration, likely due to their increased uptake in these tissues.

PDT studies carried out in collaboration with biodistribution studies demonstrated an equal maximum level of tumour necrosis induced with 20 nm pegylated ORMOSIL NPs and Foscan at early DLI (6 h). This was attributed to potential effects on the vasculature as an increase in PDT tumour necrosis was observed at a longer DLI (24 h) with larger NPs (90 nm), which corresponded to their higher retention in tumour tissue at this time. These results are encouraging as some of the first PDT studies to be carried out *in vivo* investigating the treatment efficacy of ORMOSIL NPs. Unfortunately, results with targeted nanosystems using cRGD-ORMOSIL NPs did not produce any significant improvement in PDT efficacy and were largely inconclusive.

7. Conclusions and Future Work

This thesis is a study of photodynamic therapy (PDT) and aimed to determine whether encapsulation of the photosensitiser, m-THPC, into different nanocarriers altered its delivery to tumour tissue and improved PDT efficacy at the tumour site *in vivo*.

The biodistribution and accumulation of m-THPC was assessed *in vivo*. Primarily, m-THPC in its standard micellular clinical formulation, Foscan®, was compared to its incorporation into biodegradable phospholipid membranes (liposomes) each with varying degrees of pegylation, FosPEG 2% and FosPEG 8%. Intravenously administered, the pharmacokinetic parameters of each formulation were established through compartmental and non-compartmental analysis in a syngeneic, subcutaneous tumour rat model. It was discovered the longevity of m-THPC in the blood stream increased with liposomal encapsulation and further increased with higher surface pegylation. This was reflected in biodistribution data of tumour tissue, which demonstrated a three-fold increase in m-THPC uptake between Foscan and liposomal formulations at 24 h. Normal tissue damage was assessed through skin photosensitivity studies over 7 days and revealed minimal damage.

Incorporation of m-THPC into an alternative biodegradable, pegylated nanoparticles, comprised of biocompatible polymer subunits (PLGA), was also examined in the same *in vivo* model and demonstrated a similar increase in m-THPC uptake in tumour tissue in comparison to Foscan over 72 h.

Finally, organically modified silica (ORMOSIL) nanoparticles, with covalently bound m-THPC (mono- or tetra-silane), were assessed as a non-biodegradable nano-system. A higher uptake of larger ORMOSIL NPs was observed in malignant tissue in comparison to smaller ORMOSIL NPs and Foscan alone, attributed to the EPR effect. Toxicology studies in organs involved in major clearance pathways were carried out and showed little detectable toxicity over a 28 day period.

In PDT studies with these pegylated nanoparticles, the central methodology employed was post mortem histological analysis to determine the extent of tumour PDT necrosis. Effects of dose, light parameters and drug:light intervals on PDT efficacy were assessed. Liposomal formulations of m-THPC showed equal percentages of tumour necrosis following administration of m-THPC doses three-fold less than clinical doses of Foscan. Furthermore, this thesis explored, for the first time, the use of pegylated PLGA and ORMOSIL NPs, encapsulating m-THPC, as PDT agents *in vivo*. As such, these NPs showed encouraging results, with equal PDT efficacy exhibited as standard Foscan.

Encouraging results from these studies lead to the bioconjugation of active targeting ligands to pegylated groups on m-THPC-loaded nanoparticles in a bid to further enhance uptake and treatment efficacy at the tumour site. Optimal performing nanoparticles from untargeted studies were elected, in addition to their ability to effectively couple bioactive molecules, capable of recognising receptors overexpressed by malignant tissues, to their surface. Despite encouraging results observed *in vitro* by collaborators with these nanoparticles, *in vivo* studies conducted here with targeted cRGD- ORMOSIL NPs, were largely inconclusive with minimal differences in m-THPC tumour uptake and PDT efficacy detected.

The overall results have established that the selectivity of m-THPC *in vivo* can be improved upon encapsulation in pegylated nanoparticles. The major clinical advantage of this would be the potential to lower injected m-THPC doses to avoid adverse side-effects to normal tissues, reducing damage to adjacent tissue during treatment and problems with patient management from skin photosensitivity. This encapsulation and high drug delivery payload of administered m-THPC could afford a similar treatment efficacy whilst minimising these effects and reducing therapeutic costs.

Future work

Despite promising experimental data from laboratory studies demonstrated here following the incorporation of m-THPC into nanoparticles, the complexity of cancer as a disease requires time to establish the optimal PDT treatment parameters, which may vary significantly between tumour types. The efficacy of most cancer therapies is dependent on accessibility to their site of action, which is often intracellular or vascular; each bringing their own set of complexities. In PDT, tumour destruction can be achieved both by cell death and by photodestruction of the tumour vasculature. Due to the heterogeneity and adaptive resistance within a single tumour, combinational therapy or adjuvant therapy may be the best approach, as adopted by the clinic for many current cancer treatments. Understanding tumour cell kill mechanisms and examining vascular architecture within tumours may be fundamental in establishing effective PDT treatment in the future.

Appendix I

SECTION A: Liposomes

A.1 Dosage Calculations

Example:

For a dose of 0.3 mg kg^{-1} for a 200 g rat from a stock solution of drug at 0.3 mg mL^{-1} an injection volume of 0.2 mL would be administered:

$$\frac{0.3 \text{ mg kg}^{-1} \text{ x } 0.2 \text{ kg}}{0.3 \text{ mg mL}^{-1}} = 0.2 \text{ mL}$$

Injected dose per rat gives a total concentration of approx. 60 µg g^{-1} of m-THPC.

A.2 Cell Counts and Calculations

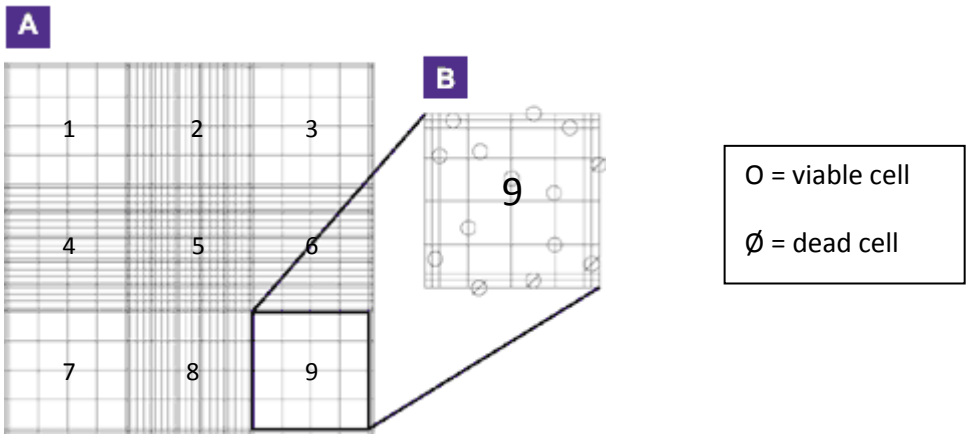

Figure A.2. Haemocytometer and cell counts. *Adapted from* www40.homepage.villanova.edu/.../pd2.htm.

Viable cells were counted that overlay the grid of the haemocytometer (A) in the centre and on the top and left hand borders of the sub squares; 1, 3, 5, 7 and 9, (B) on both sides.

Example: Average cell count ≈ $\frac{(56 + 48)}{2}$ = **52 cells**

10 µl taken from a 5 ml cell suspension and diluted 1:1 in trypan blue therefore;

Dilution factor = $\frac{(10\ \mu L + 10\ \mu L)}{10\ \mu L}$ = **2**

Volume of 1 square = 0.1 mm^3

10^{-4} cm ≈ 10^{-4} mL

Number of cells per ml: 52 cells x 2 x 10^4 = **1.04×10^6 cells mL^{-1}**

A.3 Preparing Fluorodishes: Foscan® and FosPEG2%

MC28 cells: Require a cell concentration of 1 x 10^4 cells/200 µL (fluorodish volume).

$\frac{1 \times 10^4 \text{ cells}}{1} \times \frac{1\ mL}{1.04 \times 10^6 \text{ cells}}$ = 9.6 µL of cell suspension

200 µL – 9.6 µL = 190.4 µL of supplemented DMEM media (- FCS).

Foscan® and FosPEG2% supplied in 100 µM stock solution; require final concentration of 1 µM:

Add 2 µL of 100 µM stock solution to 198 µL of media (comprised of 9.6 µL cell suspension and 188.4 µL supplemented media (-FCS)) = 1 µM.

A.4 Chemical Extraction: Raw Data Calculations

Example: Preparing stock solutions for standard curve:

M_w m-THPC = 680.24 g mol^{-1}

Foscan® provided at 4 mg mL^{-1} from Biolitec, Jena, Germany.

1. Calculate number of moles mL^{-1} in stock solution (Foscan).

$$\frac{0.004\ \text{g}}{1\ \text{mL}} \times \frac{1\ \text{mol}}{680.24\ \text{g}} = \frac{5.88 \times 10^{-6}\ \text{mol}}{\text{mL}} \text{ or } \mathbf{\frac{5.88\ \mu mol}{mL}}$$

2. Calculate number of moles needed to make 20 mL of a 10 µM solution.

$$\frac{10\ \mu\text{mol}}{1\ \text{L}} \times \frac{1\ \text{L}}{1000\ \text{mL}} \times 20\ \text{mL} = \mathbf{0.2\ \mu mol}$$

3. Calculate the amount of stock solution needed (volume) to make 20 mL of a 10 µM solution.

$$0.2\ \cancel{\mu mol} \times \frac{1\ mL}{5.88\ \cancel{\mu mol}} = 34.0 \times 10^{-3}\ mL \quad \text{or} \quad \mathbf{34\ \mu L}$$

Table A.4i. Preparation of Foscan® stock solution.

FosPEG2% and **FosPEG8%** provided at 1.5 mg mL^{-1} from Biolitec, Jena, Germany.

1. Calculate number of moles mL^{-1} in stock solution (FosPEG2% & 8%).

$$\frac{0.0015\ \cancel{g}}{1\ mL} \times \frac{1\ mol}{680.24\ \cancel{g}} = \frac{2.205 \times 10^{-6}\ mol}{mL} \quad \text{or} \quad \frac{\mathbf{5.88\ \mu mol}}{\mathbf{mL}}$$

2. Calculate number of moles needed to make 20 mL of a 10 µM solution.

$$\frac{10\ \mu mol}{1\ \cancel{L}} \times \frac{1\ \cancel{L}}{1000\ \cancel{mL}} \times 20\ \cancel{mL} = \mathbf{0.2\ \mu mol}$$

3. Calculate the amount of stock solution needed (volume) to make 20 mL of a 10 µM solution.

$$0.2\ \cancel{\mu mol} \times \frac{1\ mL}{2.205\ \cancel{\mu mol}} = 90.7 \times 10^{-3}\ mL \quad \text{or} \quad \mathbf{91\ \mu L}$$

Table A.4ii. Preparation of FosPEG 2% and FosPEG8% stock solution.

A serial dilution was carried out to prepare additional stock solutions of 1 µM and 0.1 µM, whereby 1 mL of a 10 µM m-THPC solution was pipetted into 9 mL of Solvable™ and so forth.

Construction of standard curves:

Stock solution (uM)	0	0.01	0.1	0.1	0.1	1	1	10	10
Standard mTHPC uM	**0**	**0.001**	**0.005**	**0.01**	**0.05**	**0.1**	**0.5**	**1**	**5**
mTHPC uM solution (ml)	0	0.3	0.15	0.3	1.5	0.3	1.5	0.3	1.5
Tissue 0.1g/2 ml solvable (ml)	1.5	1.5	1.5	1.5	1.5	1.5	1.5	1.5	1.5
Solvable (100%) (ml)	1.5	1.2	1.35	1.2	0	1.2	0	1.2	0
(if no tissue - solvable)	*3*	*2.7*	*2.85*	*2.7*	*1.5*	*2.7*	*1.5*	*2.7*	*1.5*

Table A.4iii. Construction of standard curves.

Converting µM concentrations into µg g^{-1}:

$$M_w \text{ m-THPC} = 680.24 \text{ g mol}^{-1}$$

$$1 \text{ mL} \approx 1 \text{ g}$$

$$1 \text{ mole} = 680.24 \text{ g}$$

$$1 \text{ µmole} = 680.24 \times 10^{-6} \text{ g } \textbf{OR } 680.24 \text{ µg}$$

$$1 \text{ µM (1 µmole L}^{-1}) = \frac{680.24 \text{ µg}}{1000 \text{ ml}}$$

$$1 \text{ µM} = 0.68024 \text{ µg mL}^{-1} \textbf{ OR } \text{µg g}^{-1}$$

Calculating the concentration (µg g^{-1}) of m-THPC in each tissue:

Example:

Standard curve of Foscan® for liver tissue, which was linear between 0 and 0.5 µM.

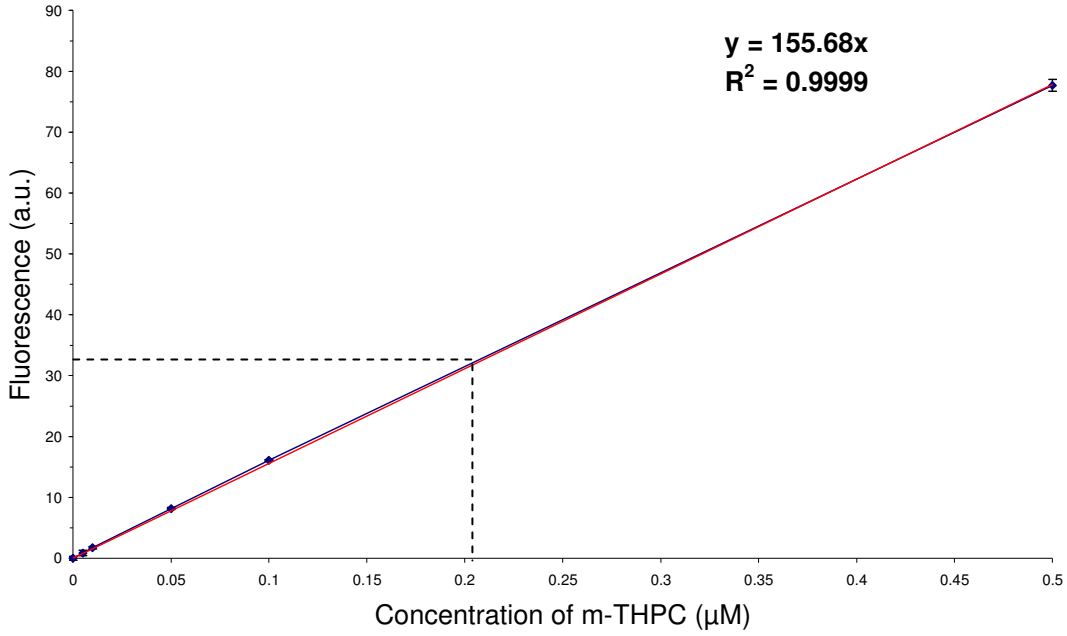

Figure A.4. Standard curve of known concentrations of m-THPC in control liver tissue.

Average fluorescence (a.u.) of liver at 2 h after 0.3 mg kg^{-1} Foscan® dose ≈ 48 a.u.

Minus averaged negative control values of liver = 48 - 14.36 a.u. = 33.64 a.u.

Therefore if y = 155.68x, x = 33.64/155.68 = 0.216 µM

If 1 µM = 0.68024 µg g^{-1}

Then 0.216 µM = 0.147 µg g^{-1}

However, the original tissue sample, 0.1 g wet weight, was diluted in 2 mL of Solvable™ therefore the original dilution factor (x 20) plus the displacement of liquid (~ 1) means the concentration is multiplied by 21:

Concentration of m-THPC (Foscan®) in the liver at 2h, 0.147 µg g^{-1} x 21 = **3.1 µg g^{-1}**

A.5 Pharmacokinetic Analysis: Compartmental Approach

The individual sets of plasma m-THPC concentrations for each liposomal formulation, Foscan®, FosPEG 2% and FosPEG 8%, were plotted on a semi-logarithmic scale (see Figs A.2, A.3, & A.4) for the compartmental analysis.

The plasma level decline did not follow a mono-exponential decay (see Section 2.3.1; Fig 2.3) and instead could fit to multi-exponentials; therefore the graph could be divided in to three phases. To calculate the parameters of the third compartment, the terminal points of the graph (72, 96 and 168 h) represented the log linear phase, and the gradient of this line could be used to determine the time constant γ (see Tables A.5, A.6, & A.7). This log/linear phase signifies the elimination of m-THPC from the second compartment in equilibrium now with the third compartment.

The t = 0 y-intercept C, represents the *apparent concentration* if the drug had been distributed instantaneously throughout all compartments. Intercept C could therefore be used to calculate the volume of distribution in the third compartment (V_d) *i.e.* dosage/y-intercept C (t=0).

The equation of the third compartment line (blue) could then be used to calculate the m-THPC concentration at different time points (0 – 168 h). To deduce the line of the second compartment (green), concentrations values which lay on third compartment line were deducted from real values of m-THPC concentration (Tables A.5, A.6, & A.7) obtained from original plasma data (see Section 2.3.1; Fig 2.3, and raw data; Table A.8). These values were plotted and the equation of this line (green) gave a new set of parameters (**β, B**) to deduce V_d in the second compartment. This process was repeated to obtain α, A, V_d in the first compartment. Time constant α is the constant that governs the distribution of m-THPC into the second compartment.

The biological half-life of m-THPC for each formulation was calculated using the time constants, α,β,γ, (Tables A.5, A.6, & A.7) which were substituted with one of the corresponding values for each of the decay phases:

$$t_{1/2} = \frac{\log_e 0.5}{\alpha} = \frac{0.693}{\alpha}$$

The sum of the exponential y-intercept values at t=0 (A, B and C) were used to calculate the initial concentration (C_o) of m-THPC in each formulation (Tables A.5, A.6, & A.7), in the blood plasma at time 0. This value was used to calculate the theoretical volume into which the drug was initially introduced, in the central compartment (initial V_d).

This compartmental analysis was completed for all liposomal nanocarrier formulations (Figs A.2, A.3, A.4 and Tables A.5, A.6, A.7).

Foscan®:

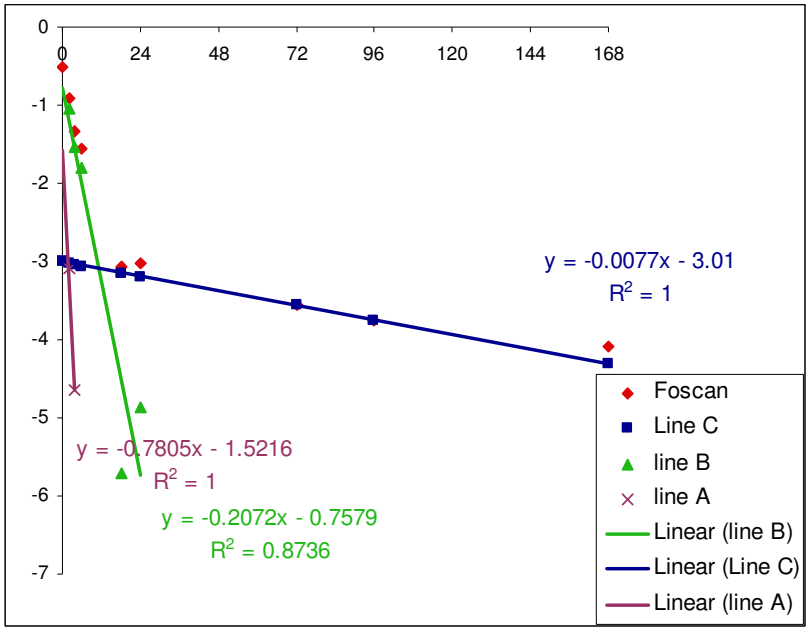

Figure A.5i. The decline of the m-THPC plasma concentrations after i.v. injection of 0.3 mg kg^{-1} in a Foscan formulation. Data plotted on a semi-logarithmic scale in three phases, representing the three compartments.

Time Constant			Y-intercept (t=0)			Y-intercept (t=0)			Half life			C_o (µg ml^{-1})
α	β	γ	ln(A)	ln(B)	ln(C)	A	B	C	A	B	C	
0.78	0.21	0.0077	-1.522	-0.7579	-3.01	0.218	0.469	0.049	0.9	3.3	90.0	**0.74**

Table A.5i. Time constants α, β, γ, logged y-intercept values from semi-log plot at t=0 ln(A), ln(B), ln(C), inversed log y-intercept values at t=0 A, B, C, calculated compartmental half-lives using each time constant and initial concentration, C_o (µg ml^{-1}), of m-THPC after 0.3 mg kg^{-1} i.v. administered dose in Foscan formulation.

FosPEG 2%:

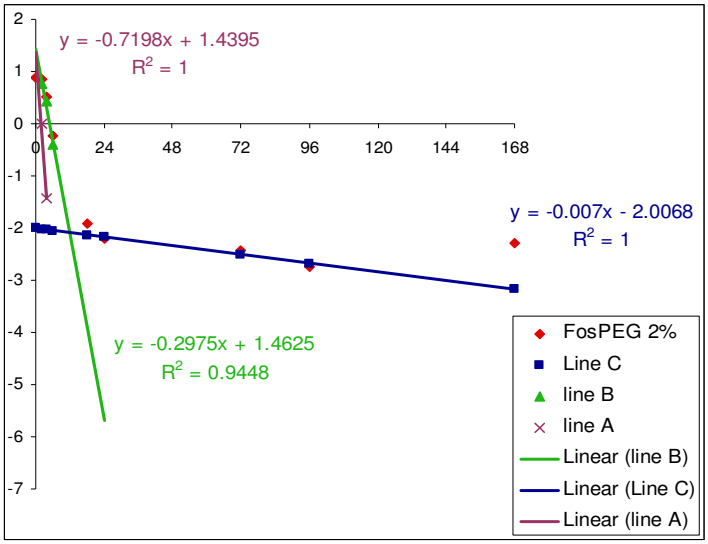

Figure A.5ii. The decline of the m-THPC plasma concentrations after i.v. injection of 0.3 mg kg^{-1} in a FosPEG 2% formulation. Data plotted on a semi-logarithmic scale in three phases, representing the three compartments.

Time Constant			Y-intercept (t=0)			Y-intercept (t=0)			Half life			C_o (ug ml^{-1})
A	b	c	ln(A)	ln(B)	ln(C)	A	B	C	A	B	C	
0.72	0.3	0.007	1.44	1.4625	-2.007	4.219	4.317	0.134	1.0	2.3	99.0	**8.67**

Table A.5ii. Time constants α, β, γ, logged y-intercept values from semi-log plot at t=0 ln(A), ln(B), ln(C), inversed log y-intercept values at t=0 A, B, C, calculated compartmental half-lives using each time constant and initial concentration, C_o (μg ml^{-1}), of m-THPC after 0.3 mg kg^{-1} i.v. administered dose in FosPEG 2% formulation.

FosPEG 8%:

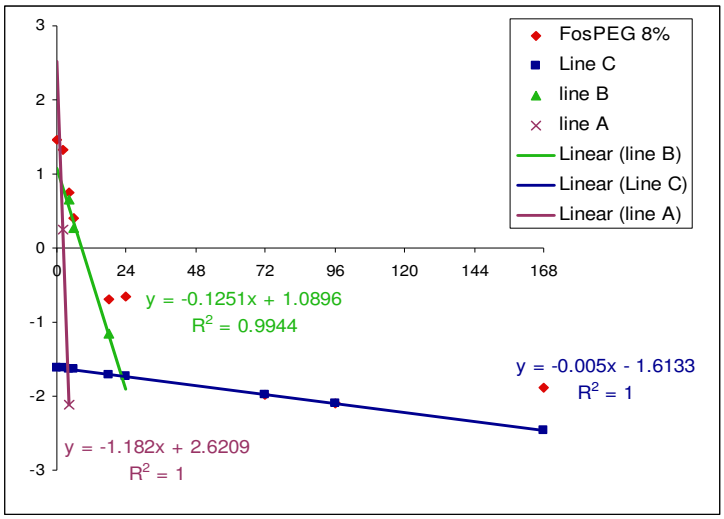

Figure A.5iii. The decline of the m-THPC plasma concentrations after i.v. injection of 0.3 mg kg^{-1} in a FosPEG 8% formulation. Data plotted on a semi-logarithmic scale in three phases, representing the three compartments.

Time Constant			Y-intercept (t=0)			Y-intercept (t=0)			Half life			C_o (ug ml^{-1})
A	b	c	ln(A)	ln(B)	ln(C)	A	B	C	A	B	C	
1.18	0.13	0.005	2.621	1.0896	-1.613	13.748	2.973	0.199	0.6	5.5	138.6	**16.92**

Table A.5iii. Time constants α, β, γ, logged y-intercept values from semi-log plot at t=0 ln(A), ln(B), ln(C), inversed log y-intercept values at t=0 A, B, C, calculated compartmental half-lives using each time constant and initial concentration, C_o (µg ml^{-1}), of m-THPC after 0.3 mg kg^{-1} i.v. administered dose in FosPEG 8% formulation.

FOSCAN										
time (hrs)	O	ln o	ln c	c	(o-c)	ln (o-c)	ln b	b	(c-b)	ln (o.b)
0			-3.010	0.049			-0.758	0.469		
0.083	0.5947	-0.51963	-3.011	0.049	0.545		-0.775	0.461		
2	0.4040	-0.90626	-3.025	0.049	0.355	-1.034	-1.172	0.310	0.046	-3.08258
4	0.2620	-1.33933	-3.041	0.048	0.214	-1.541	-1.587	0.205	0.010	-4.64353
6	0.2108	-1.557	-3.056	0.047	0.164	-1.810	-2.001	0.135		
18	0.0462	-3.07498	-3.149	0.043	0.003	-5.720	-4.488	0.011		
24	0.0486	-3.02351	-3.195	0.041	0.008	-4.872	-5.731	0.003		
72	0.0283	-3.56445	-3.564	0.028	0.000		-15.676	0.000		
96	0.0235	-3.74928	-3.749	0.024	0.000		-20.649	0.000		
168	0.0168	-4.08579	-4.304	0.014	0.003		-35.568	0.000		

Table A.5iv. Raw data from compartmental pharmacokinetic analysis for each formulation

FosPEG 2%									
time (hrs)	o	ln o	ln c	c	(o-c)	ln (o-c)	ln b	b	(c-b)
0			-2.007	0.134			1.463	4.317	
0.083	2.4159	0.882087	-2.007	0.134	2.282		1.438	4.211	
2	2.3237	0.843148	-2.021	0.133	2.191	0.784	0.868	2.381	-0.190
4	1.6810	0.519385	-2.035	0.131	1.550	0.438	0.273	1.313	0.237
6	0.7954	-0.22887	-2.049	0.129	0.667	-0.406	-0.323	0.724	
18	0.1468	-1.91861	-2.133	0.119	0.028		-3.893	0.020	
24	0.1102	-2.20504	-2.175	0.114	-0.003		-5.678	0.003	
72	0.0892	-2.41655	-2.511	0.081	0.008		-19.958	0.000	
96	0.0647	-2.73815	-2.679	0.069	-0.004		-27.098	0.000	
168	0.1025	-2.27797	-3.183	0.041	0.061		-48.518	0.000	
FosPEG 8%									
time (hrs)	o	ln o	ln c	c	(o-c)	ln (o-c)	ln b	b	(c-b)
0			-1.613	0.199			1.090	2.973	
0.083	4.3320	1.466033	-1.614	0.199	4.133		1.079	2.942	
2	3.8052	1.336363	-1.623	0.197	3.608		0.839	2.315	1.293
4	2.1194	0.751148	-1.633	0.195	1.924	0.654	0.589	1.803	0.122
6	1.4939	0.401398	-1.643	0.193	1.301	0.263	0.339	1.404	
18	0.4983	-0.69655	-1.703	0.182	0.316	-1.151	-1.162	0.313	
24	0.5249	-0.64446	-1.733	0.177	0.348		-1.913	0.148	
72	0.1390	-1.97323	-1.973	0.139	0.000		-7.918	0.000	
96	0.1233	-2.0932	-2.093	0.123	0.000		-10.920	0.000	
168	0.1519	-1.88429	-2.453	0.086	0.066		-19.927	0.000	

Table A.5iv. (continued) Raw data from compartmental pharmacokinetic analysis for each formulation.

A.6 Pharmacokinetic Analysis: Non-compartmental Approach

To calculate the pharmacokinetic parameters using the non-compartmental approach the following method was applied for each formulation; Foscan®, FosPEG 2% and FosPEG 8%:

1) The plasma concentration of m-THPC at time zero (C_o) was estimated by extrapolation of the log concentration versus time graph back to zero, using the slope of the line for the initial three time points (2, 4 and 6 h).

2) The slope of the log linear (elimination) phase was estimated between 72 & 168 h.

3) The area under the concentration versus time graph (AUC) was calculated from time zero (t =0) to the last time point (168 h) by the trapezoidal rule (A = ½ (a + b) *h*) (see figure below) and from 168 h to infinity (∞) the area was approximated as; Area = C(last)/k', where C(last) is the plasma concentration at the last time point (168 h) and k' is the elimination rate constant (gradient of slope between 72 – 168 h).

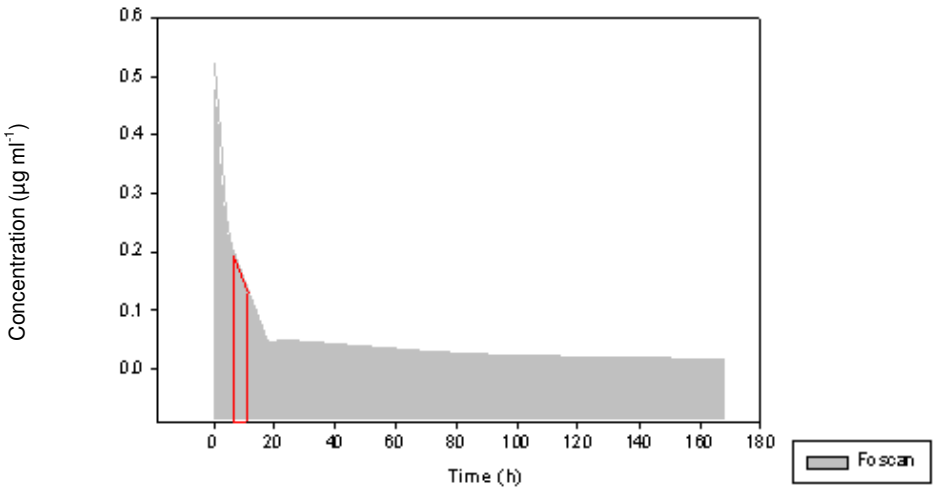

Figure A.6. Area under the curve graph for non-compartmental analysis.

4) The area under the moment curve (AUMC; (concentration x time) versus the time curve). The AUMC was calculated from time zero (t = 0) to 168 h by the trapezoidal rule and 168 h to infinity ∞ as Area = C(last)/(k')².

5) Plasma clearance: $C_L = \frac{DOSE}{AUC}$

6) Mean residence time: $MRT = \frac{AUMC}{AUC}$

7) Volume of distribution: $V_d = C_L \times MRT$

8) Half-life: $t_{1/2} = MRT \times \ln(2)$

9) Elimination rate constant: $K_{el} = \frac{1}{MRT}$

A.7 Time and Concentration of Maximal m-THPC Levels

	Foscan		FosPEG 2%		FosPEG 8%	
Tissue	**Peak (h)**	**Concentration (ug g^{-1})**	**Peak (h)**	**Concentration (µg g^{-1})**	**Peak (h)**	**Concentration (µg g^{-1})**
Plasma	< 5min	0.74 ± 0.15	< 5min	8.67 ± 0.24	< 5min	16.92 ± 1.35
Tumour	6	0.33 ± 0.025	24	1.13 ± 0.15	24	0.98 ± 0.17
Liver	4	3.61 ± 0.22	2	2.30 ± 0.27	2	3.03 ± 0.26
Spleen	4	2.38 ± 0.32	6	2.66 ± 0.74	4	1.15 ± 0.34
Lung	4	0.46 ± 0.05	6	1.40 ± 0.13	6	2.01 ± 0.32
Skin	24	0.07 ± 0.01	18	0.07 ± 0.01	96	0.1 ± 0.003

Table A.7. Time and concentration of maximal levels of m-THPC (µg g^{-1}) in selected tissues with each formulation; Foscan, FosPEG 2% or FosPEG8%, after 0.3 mg kg^{-1} injected dose (data represent mean ± s.d., n = 3).

A.8 Chemical Extraction: Colon Accumulation

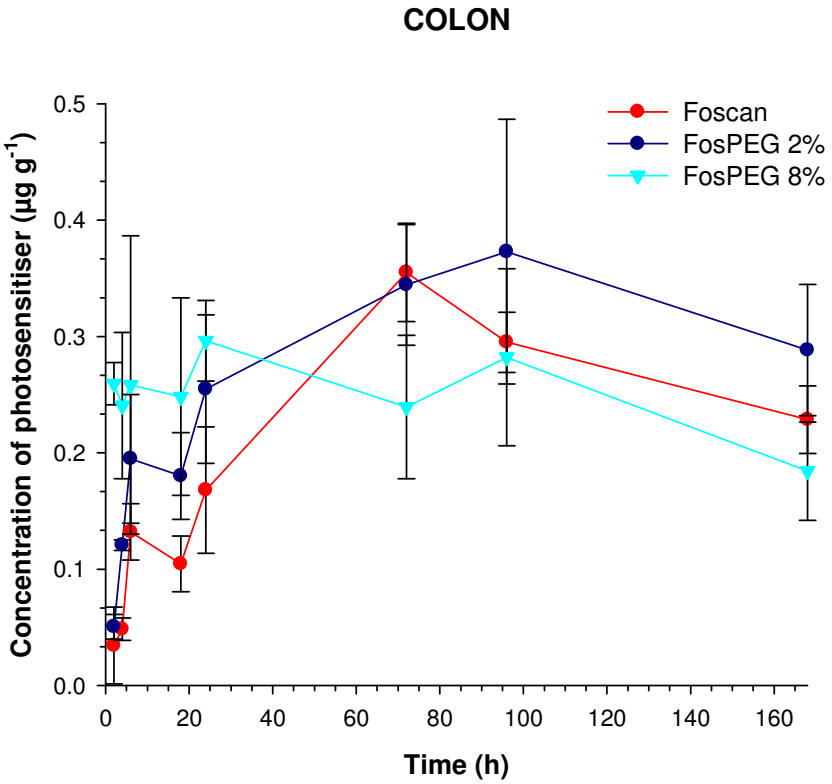

Figure A.8. Concentration of m-THPC (µg g^{-1}) in colon tissue of the Wistar rat at different time intervals after intravenous injection of either, Foscan, FosPEG2% or FosPEG8%, at 0.3 mg kg^{-1}. Data corrected for negative control tissue. (Data points show the mean ± s.d., n = 3).

A.9 Concentration of m-THPC in blood plasma versus tumour from HL rat tissues: Foscan, FosPEG 2% and 8%)

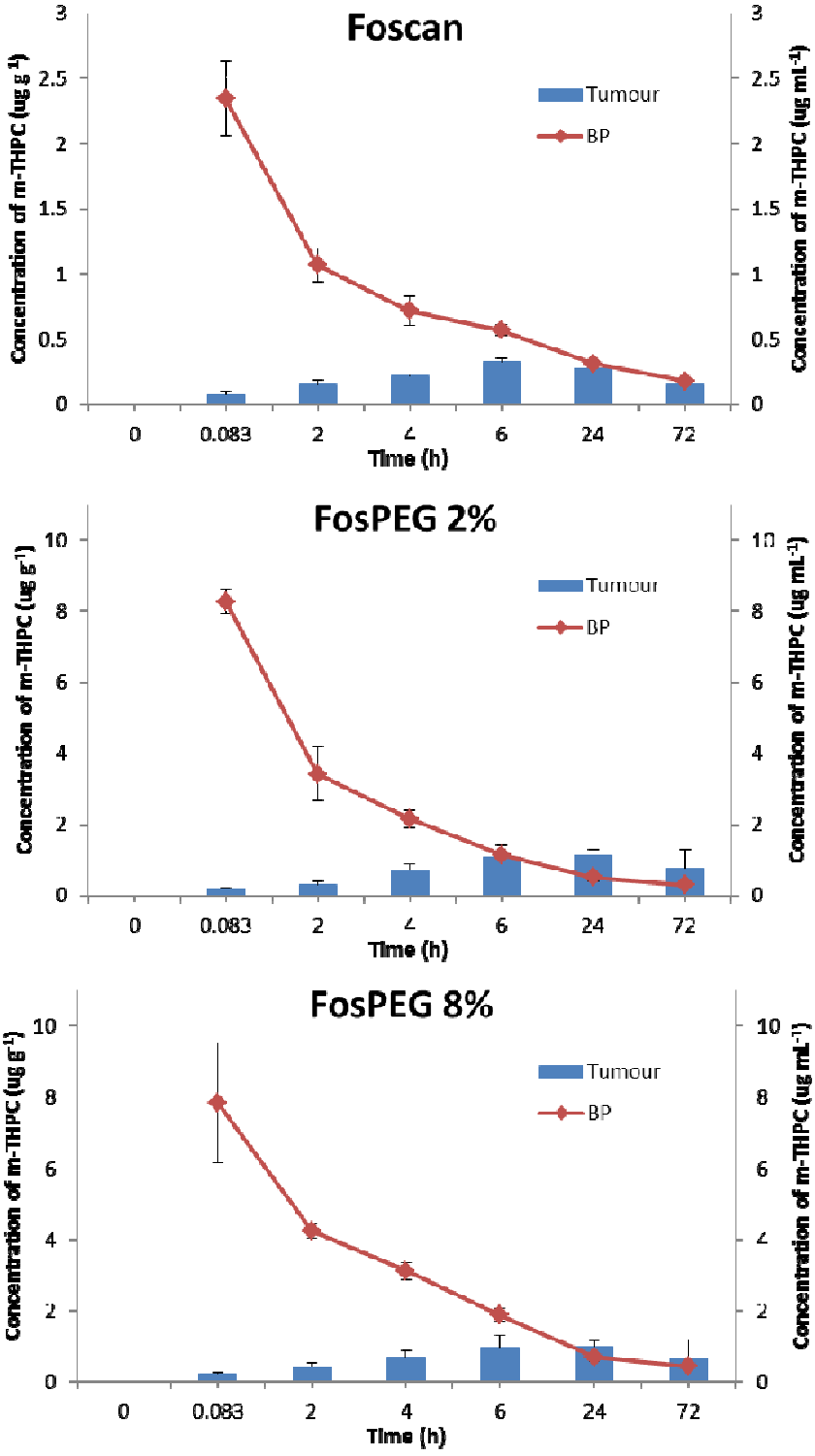

Figure A.9 Concentration of m-THPC in MC28 tumour tissue (μg g^{-1}) of female Hooded Lister rat versus m-THPC in blood plasma from HL rat (μg mL^{-1}) as a function of time (h) following an intravenous injection of 0.3 mg kg^{-1} m-THPC in standard Foscan, FosPEG 2% and FosPEG 8% formulations. Data points show the mean ± SD, $n = 4$.

A.10 Skin Photosensitivity Studies: Solar Simulator Spectra

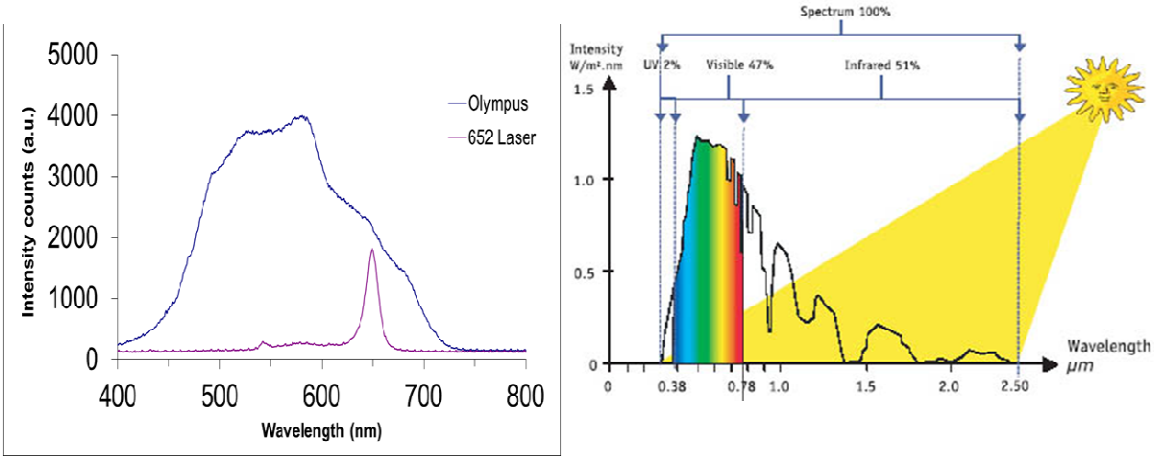

Figure A.10. Absorption spectrum of light from solar simulator (Olympus CLV-S30) and a 652 nm laser (left) in comparison to the spectrum of natural sunlight (right), *taken from nature photonics*.

A.11 Skin Photosensitivity Studies: Skin scoring model

Score	Observation
0	No observable effect
1	Mild erythema
2	Moderate erythema
3	Strong erythema
4	Slight oedema
5	Moderate oedema
6	Severe oedema
7	Blistering + oedema
8	Necrosis

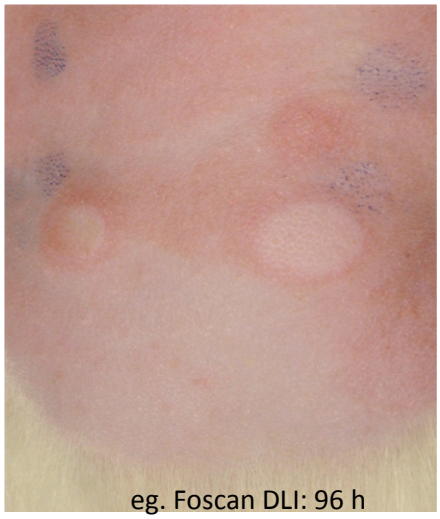

Figure A.11. Skin scoring system used for skin photosensitivity studies to visually assess skin damage following administration of 0.3 mg kg^{-1} or 0.1 mg kg^{-1} m-THPC in either Foscan, FosPEG2% and FosPEG 8% after exposure to either 0, 5, 15 or 30 mins of sunlight (equivalent) at DLIs of either 96 or 168 h. *Model taken from Weersink et al., 2005*

A.12 Skin Photosensitivity Studies: Raw skin scoring data 0.3 mg kg^{-1}

DLI	Exposure Time	m-THPC Formulation	Average Grade	Rank*	Description
96 h	0 min	Foscan	0.00	1	No observable effect
		FosPEG2%	0.00	1	No observable effect
		FosPEG8%	0.00	1	No observable effect
	5 min	Foscan	1.67	2	Moderate erythema
		FosPEG2%	1.50	1	Moderate erythema
		FosPEG8%	2.00	3	Moderate erythema
	15 min	Foscan	4.00	2	Slight oedema
		FosPEG2%	3.67	1	Slight oedema
		FosPEG8%	4.67	3	Moderate oedema
	30 min	Foscan	5.67	2	Severe oedema
		FosPEG2%	5.17	1	Moderate oedema
		FosPEG8%	5.67	2	Severe oedema
168 h	0 min	Foscan	0.00	1	No observable effect
		FosPEG2%	0.00	1	No observable effect
		FosPEG8%	0.00	1	No observable effect
	5 min	Foscan	1.17	3	Mild erythema
		FosPEG2%	1.00	1	Mild erythema
		FosPEG8%	1.00	1	Mild erythema
	15 min	Foscan	2.83	2	Strong erythema
		FosPEG2%	2.67	1	Strong erythema
		FosPEG8%	3.00	3	Strong erythema
	30 min	Foscan	4.83	3	Moderate oedema
		FosPEG2%	3.33	1	Strong erythema
		FosPEG8%	4.17	2	Slight oedema

** based on the average grade; where 1 is the least affected and 3 is most affected.*

Table A.12. Skin scoring results following administration of 0.3 mg kg^{-1} m-THPC in either Foscan, FosPEG2% and FosPEG 8% after exposure to either 0, 5, 15 or 30 mins of sunlight (equivalent) at DLIs of either 96 or 168 h. *Model taken from Weersink et al., 2005.*

A.13 Skin Photosensitivity Studies: Raw skin scoring data 0.1 mgkg^{-1}

DLI	Exposure Time	m-THPC Formulation	Average Grade	Rank*	Description
96 h	0 min	Foscan	0.00	1	No observable effect
		FosPEG2%	0.00	1	No observable effect
		FosPEG8%	0.00	1	No observable effect
	5 min	Foscan	0.67	2	Mild erythema
		FosPEG2%	0.30	1	Mild erythema
		FosPEG8%	0.67	2	Mild erythema
	15 min	Foscan	1.50	3	Moderate erythema
		FosPEG2%	1.33	1	Mild erythema
		FosPEG8%	1.33	1	Mild erythema
	30 min	Foscan	1.50	2	Moderate erythema
		FosPEG2%	1.50	2	Moderate erythema
		FosPEG8%	1.33	1	Mild erythema
168 h	0 min	Foscan	0.00	1	No observable effect
		FosPEG2%	0.00	1	No observable effect
		FosPEG8%	0.00	1	No observable effect
	5 min	Foscan	0.67	1	Mild erythema
		FosPEG2%	0.67	1	Mild erythema
		FosPEG8%	0.67	1	Mild erythema
	15 min	Foscan	1.33	1	Mild erythema
		FosPEG2%	1.83	3	Moderate erythema
		FosPEG8%	1.33	1	Mild erythema
	30 min	Foscan	1.17	1	Mild erythema
		FosPEG2%	1.67	3	Moderate erythema
		FosPEG8%	1.33	2	Mild erythema

** based on the average grade; where 1 is the least affected and 3 is most affected.*

Table A.13. Skin scoring results following administration of 0.3 mg kg^{-1} m-THPC in either Foscan, FosPEG2% and FosPEG 8% after exposure to either 0, 5, 15 or 30 mins of sunlight (equivalent) at DLIs of either 96 or 168 h. *Model taken from Weersink et al., 2005*.

A.14 Skin Photosensitivity Studies: control skin tissues

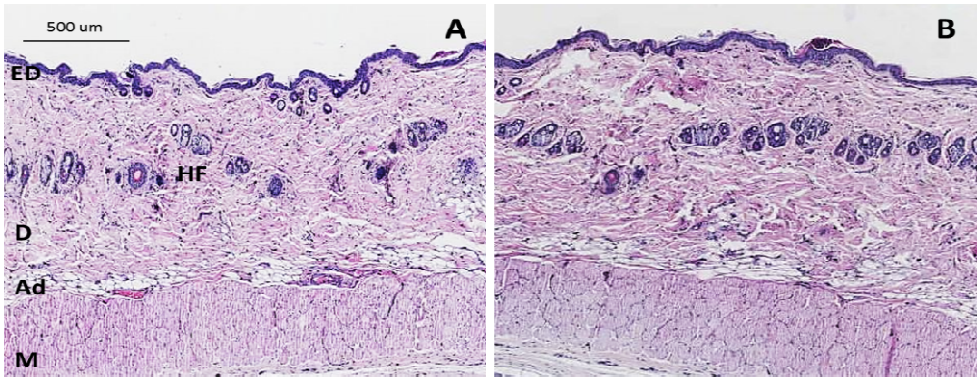

Fig.A. 14. . Histological sections of skin tissue removed from the animal 24 h after light treatment. (A) Skin control samples at 0 min (no light) and (B) control samples at 30 mins light exposure (no m-THPC), were collected and cut through the centre of the treatment area. Adjacent halves of the skin tissue were sectioned (4 μm) and stained with H&E. Images were observed with the Hamamatsu Nanozoomer. M—muscle, Ad—adipocytes, D—dermis, HF—hair follicle, ED—epidermis.

A.15 PDT - Hamamatsu Nanozoomer: Calculating the Area of Necrosis

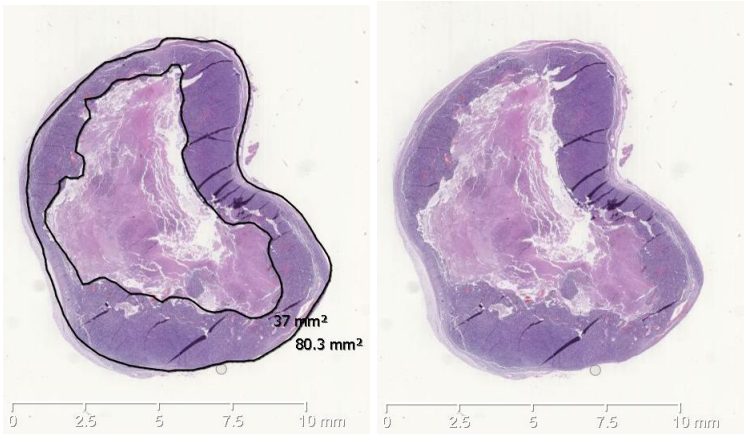

Figure A.15i. Hamamatsu Nanozoomer software was used to measure a crude surface area of necrosis as a percentage of total tissue from PDT tumour tissue damage after 24 h post i.v. injection of m-THPC at 0.3 µg g^{-1} and 0.1 µg g^{-1} in Foscan, FosPEG2% and FosPEG8%.

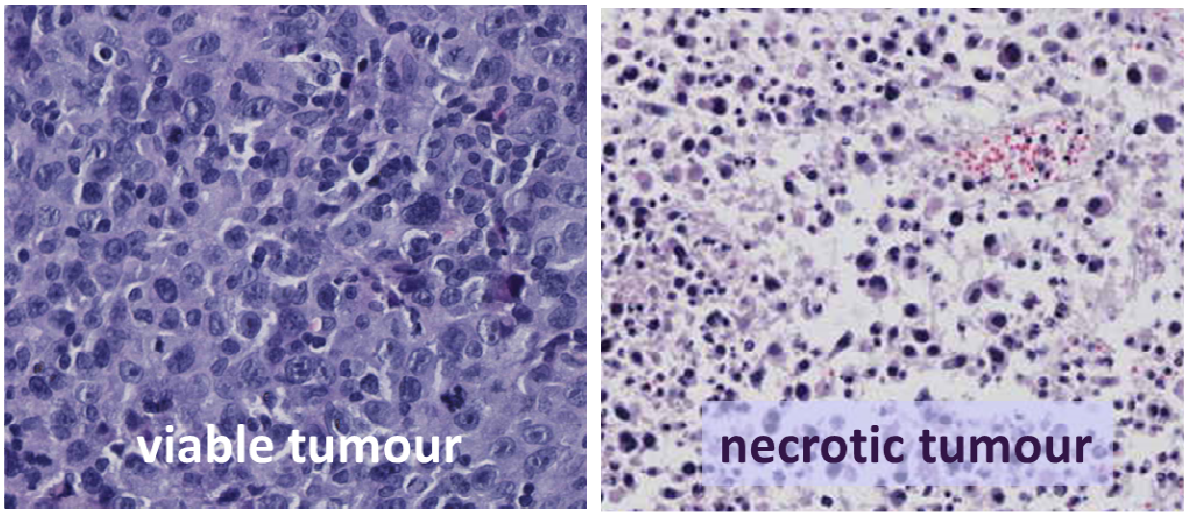

Figure A.15ii. Hamamatsu Nanozoomer software was used to differentiate between healthy tumour tissue and non-viable necrotic tumour tissue. Classic structure changes indicative of necrosis were observed in cells of tumour tissue *i.e.* loss of cell membrane integrity, nuclear changes (pyknosis- small, densely basophilic, round, homogenous nucleus) and colour change from swelling/lysis of cells.

A.16 PDT to MC28 tumours using 0.1 mgkg^{-1} m-THPC dose

PDT was performed to tumours using 0.1 mg kg^{-1} dose of m-THPC at a DLI of 24 h, however, no significant difference in percentage tumour necrosis was observed between 0.3 mg kg^{-1} m-THPC and these reduced doses with a 10J light dose.

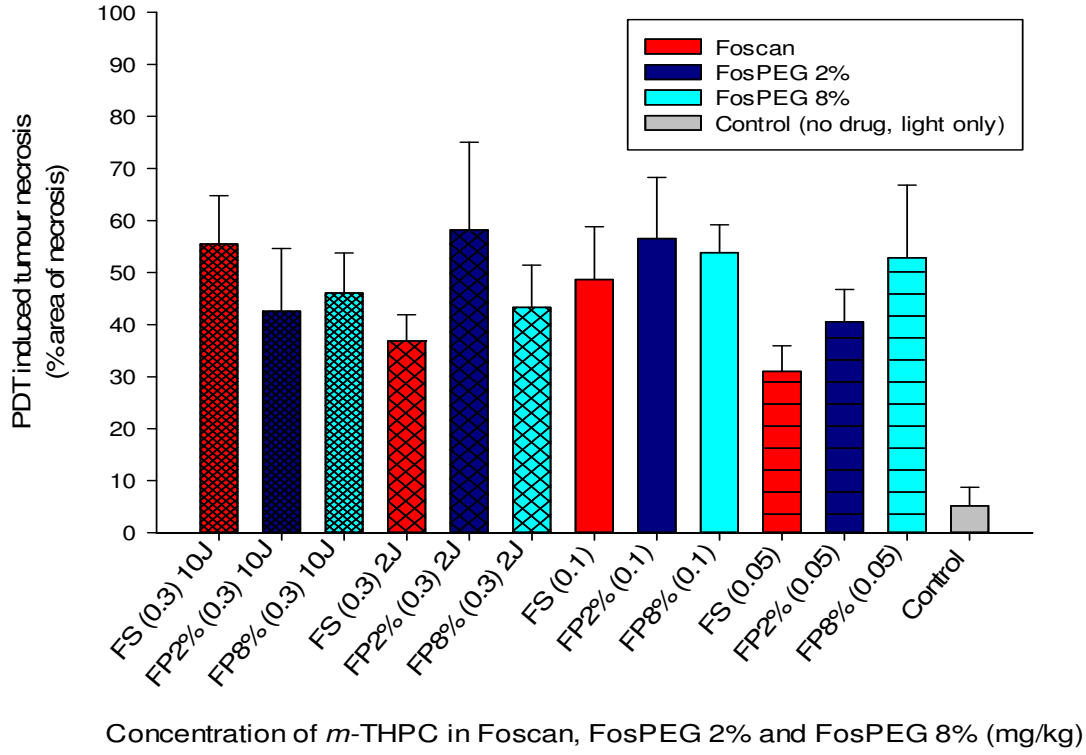

Figure A.16. The percentage area of PDT tumour necrosis following administration of either 2 J or 10 J of light to female Hooded Lister rats at a DLI of 24 h, after intravenous injection of either 0.3, 0.1 or 0.05 mg kg^{-1} m-THPC in ■ Foscan, ■ FosPEG2%, and ■ FosPEG 8% formulations. Control tumour tissue (received either no drug or light treatment). Data points show the mean±SD, n=4.

A.17 Release of m-THPC from Liposomes

Pegylated liposomes (FosPEG) were incubated in (A) 10%, (B) 50% or (C) 90% serum (FCS) to assess (i) electrical repulsion and/or interaction between lipids and plasma proteins and (ii) the effect on m-THPC release rate/transfer to plasma proteins from liposomes. The fluorescence of mTHPC was investigated photometrically by collaborators using Fluostar (unpublished data). The highest transfer of mTHPC to serum proteins was observed from FosPEG in 90% FCS following 2h incubation periods at 37°C.

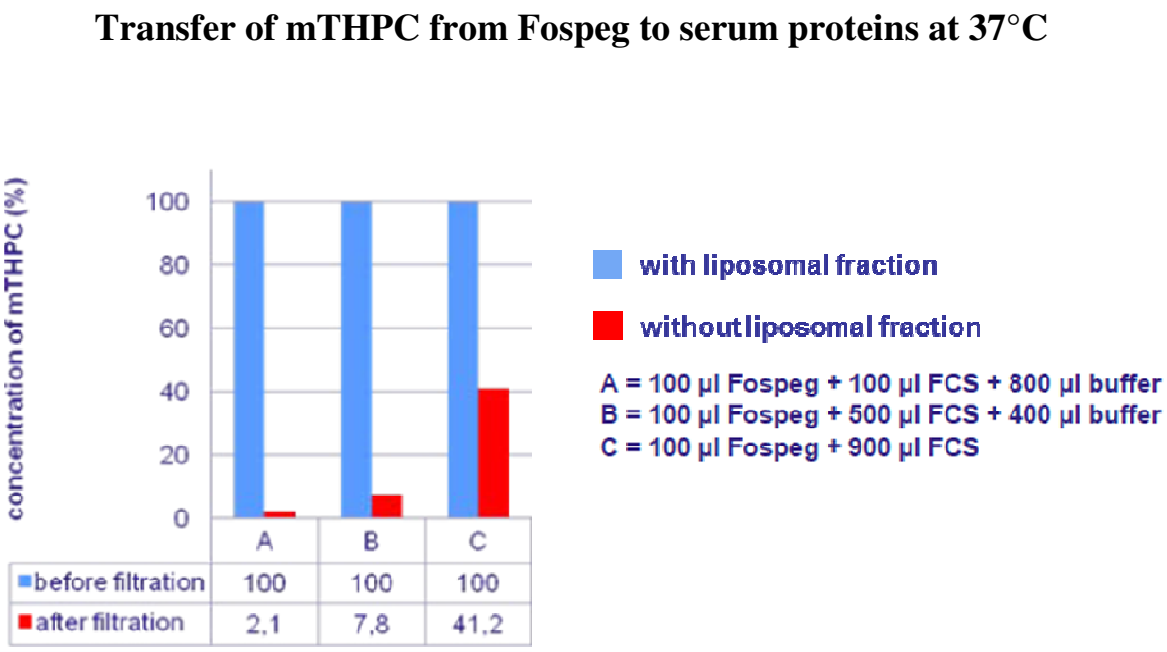

Figure A.17. Concentration of mTHPC (%) in FosPEG mixtures before or after 20 nm pore filtration at RT (with or without liposomal fraction) following 2 h incubation at 37°C with increasing concentrations of FCS (A:10%, B:50% or C:90%); measured photometrically. *Data courtesy of Dr Scheglmann, Biolitec, Jena, Germany.*

A.18 Stability of m-THPC from Liposomes

To investigate the stability of pegylated liposomes the size and PDI were measured following incubation in 90% FCS at 37°C. Negligible changes in particle size (z-average) and polydispersity (PDI) were observed over 28 h.

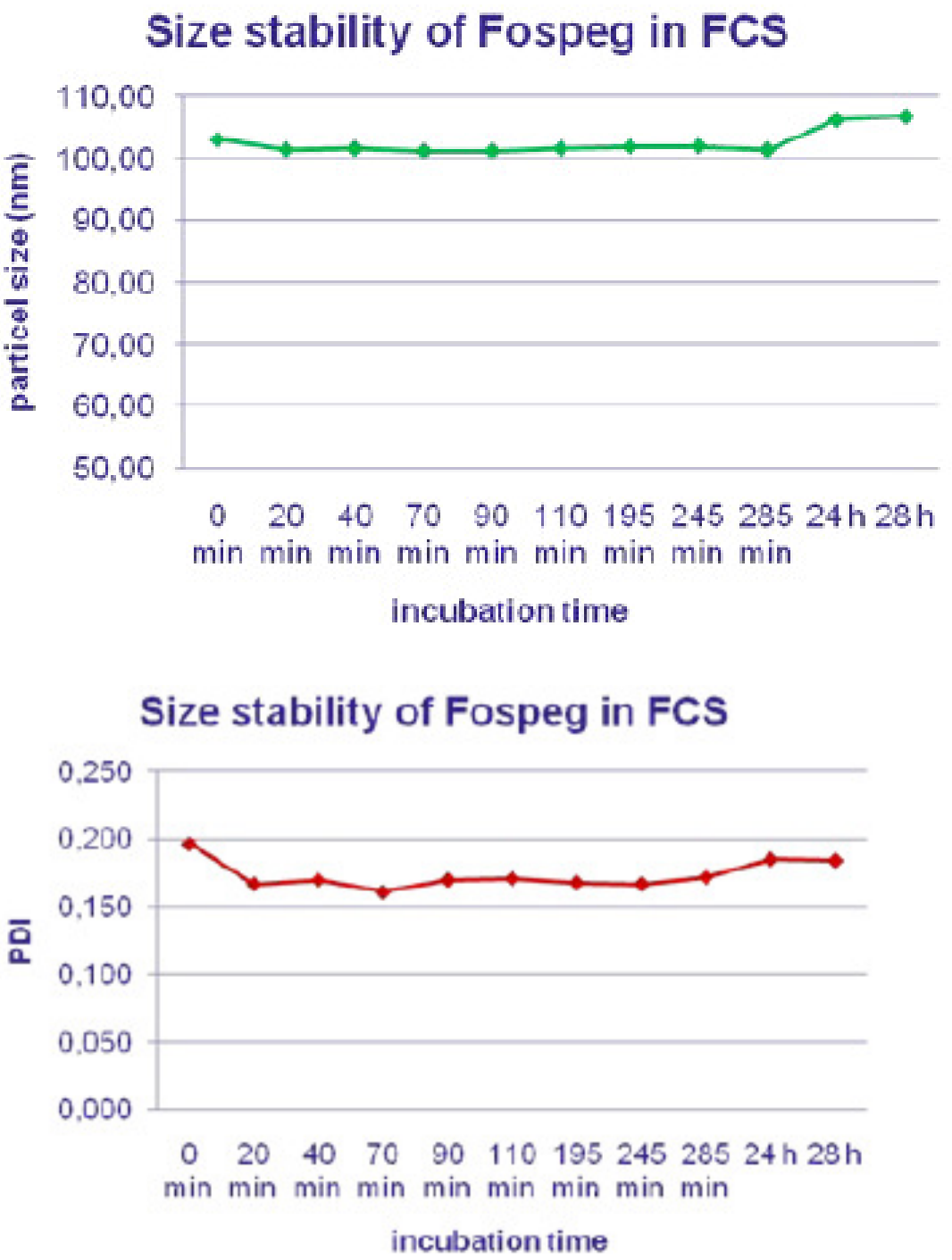

Figure A.18. The stability of pegylated liposomes was measured by changes in particle size (z-average) and polydispersity indices (PDI). *Data courtesy of Dr Scheglmann, Biolitec, Jena, Germany.*

A.19 Phase transition temperature of liposomes

The phase transition behaviour of pegylated liposomes (DSPE-PEG+ DPPC+DPPG) with or without m-THPC was investigated through differential scanning calorimetry (DSC). Unloaded liposomes appear to a phase-transition temperature of 41°C, whereas m-THPC loaded liposomes have a phase transition temperature around 37°C. At lower temperatures lipids are in a gel phase (<37°C), above this temperature lipids are in a fluid phase (>40°C).

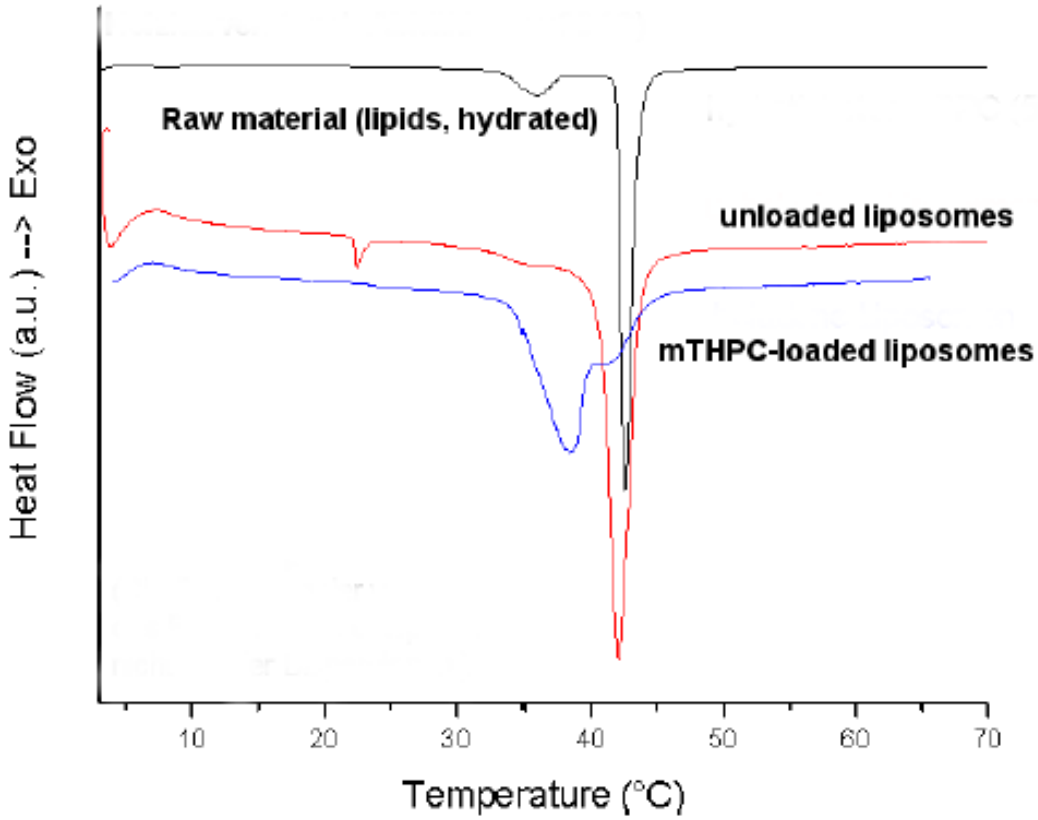

Figure A.19. The phase transition temperature of pegylated liposomes (DSPE-PEG+ DPPC+DPPG) with or without m-THPC. *Data courtesy of Dr Scheglmann, Biolitec, Jena, Germany.*

A.20 Equation: percentage injected dose g^{-1}

$$\%ID/g = \frac{\text{m-THPC in organ (µg)}}{\text{Injected dose to rat (µg)/ weight of organ (g)}} * 100$$

i.e. Foscan in the liver at 2 h ~3.14 µg g^{-1}

m-THPC in organ ~3.14 µg

Injected dose to rat: stock solution (mg kg^{-1}) x average weight of rat (kg)

0.3 mg kg^{-1} x 0.2 kg = 60 µg

Average weight of the liver ~ 11 g

Therefore, Foscan in the liver at 2 h = 57% ID% g^{-1}

A.21 % Injected dose/g of liposomal m-THPC in different tissues *in vivo*

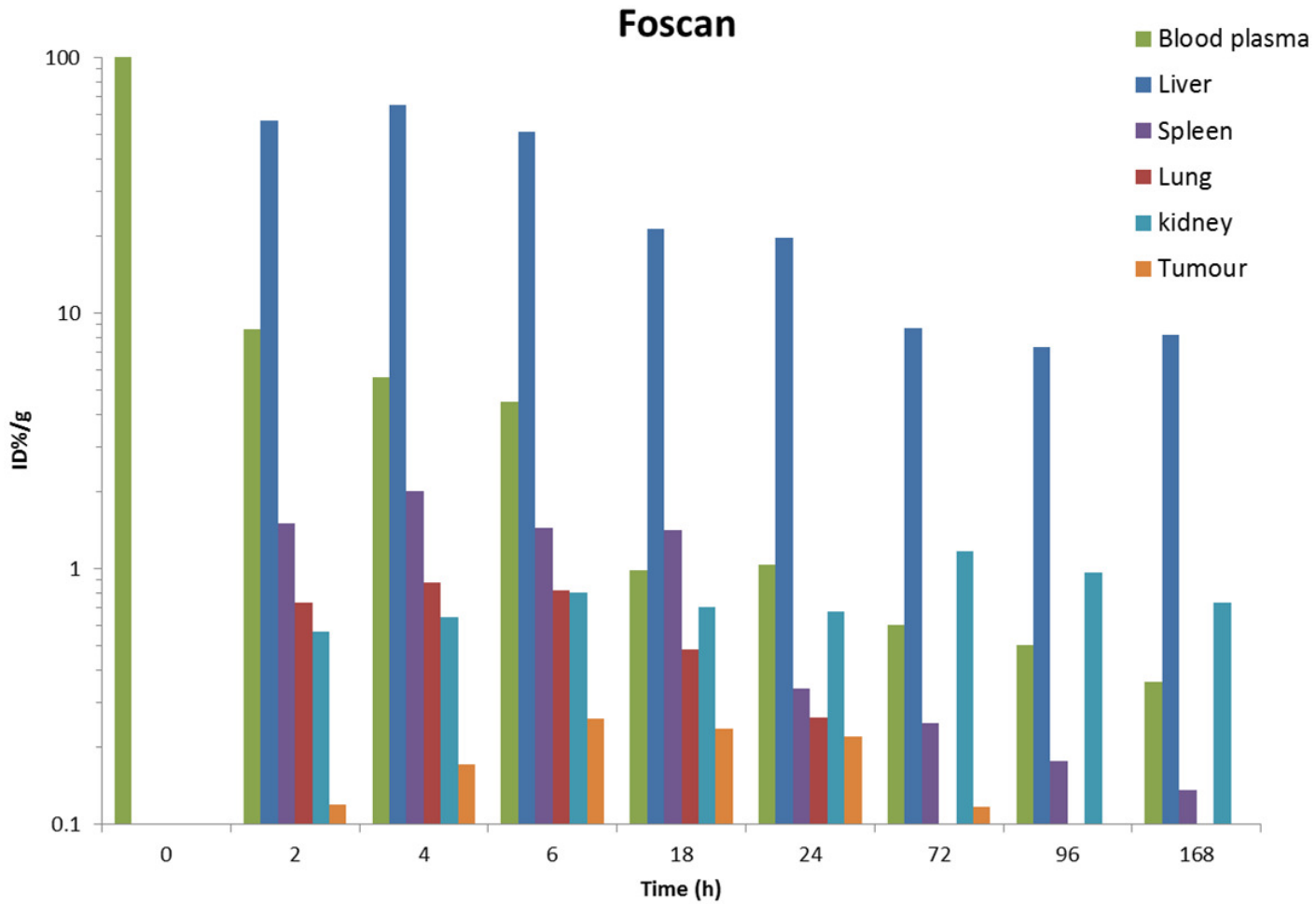

Figure A.21i. Semi-log plot of the percentage injected dose of m-THPC (%ID/g) in different tissues of a rat model as a function of time following an intravenous injection of 0.3 mg kg^{-1} m-THPC in standard Foscan. Data calculated from the mean m-THPC concentration (µg g^{-1}) in each organ, hence no S.D.

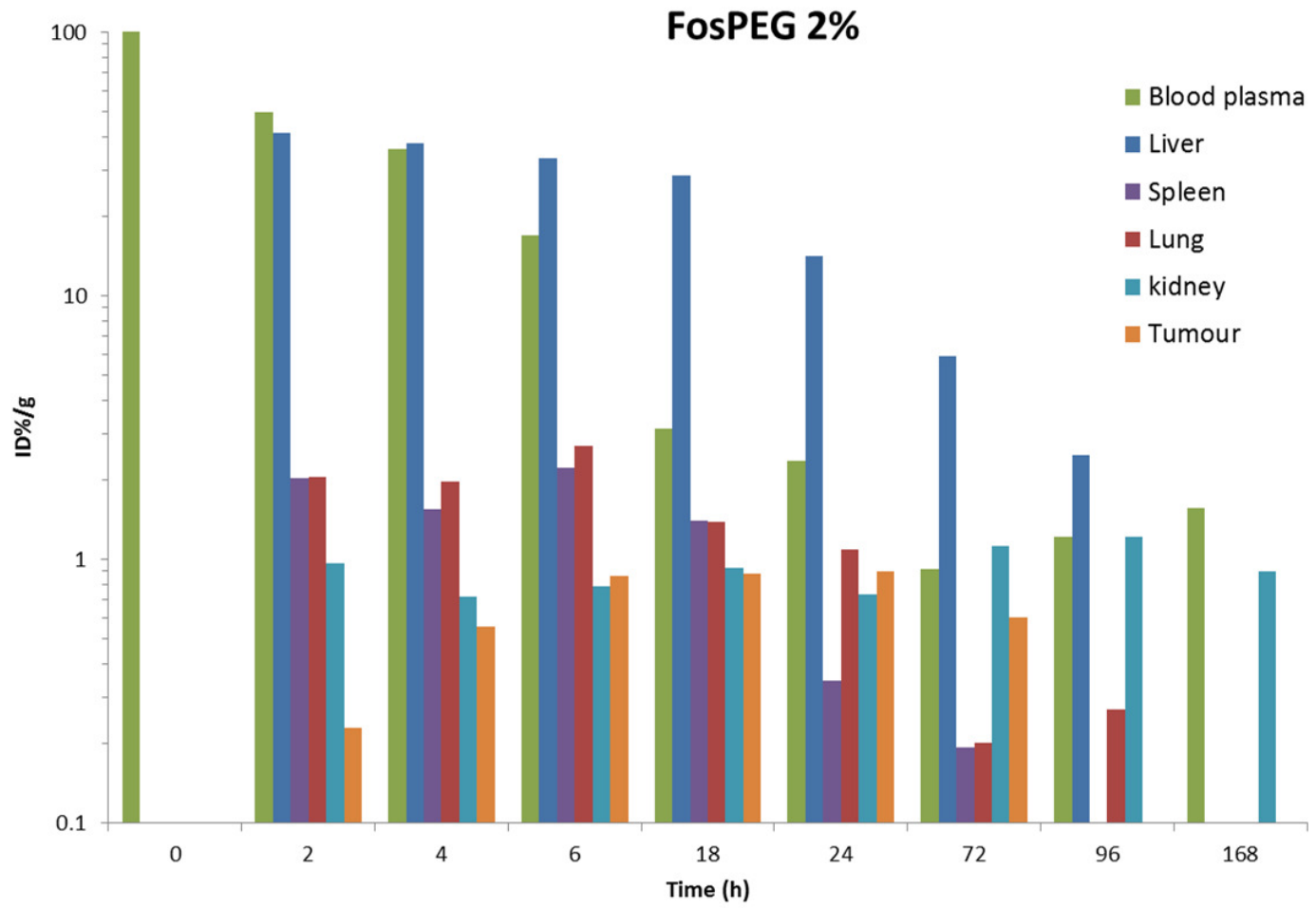

Figure A.21ii. Semi-log plot of the percentage injected dose of m-THPC (%ID/g) in different tissues of a rat model as a function of time following an intravenous injection of 0.3 mg kg^{-1} liposomal m-THPC in FosPEG 2%. Data calculated from the mean m-THPC concentration (µg g^{-1}) in each organ, hence no S.D.

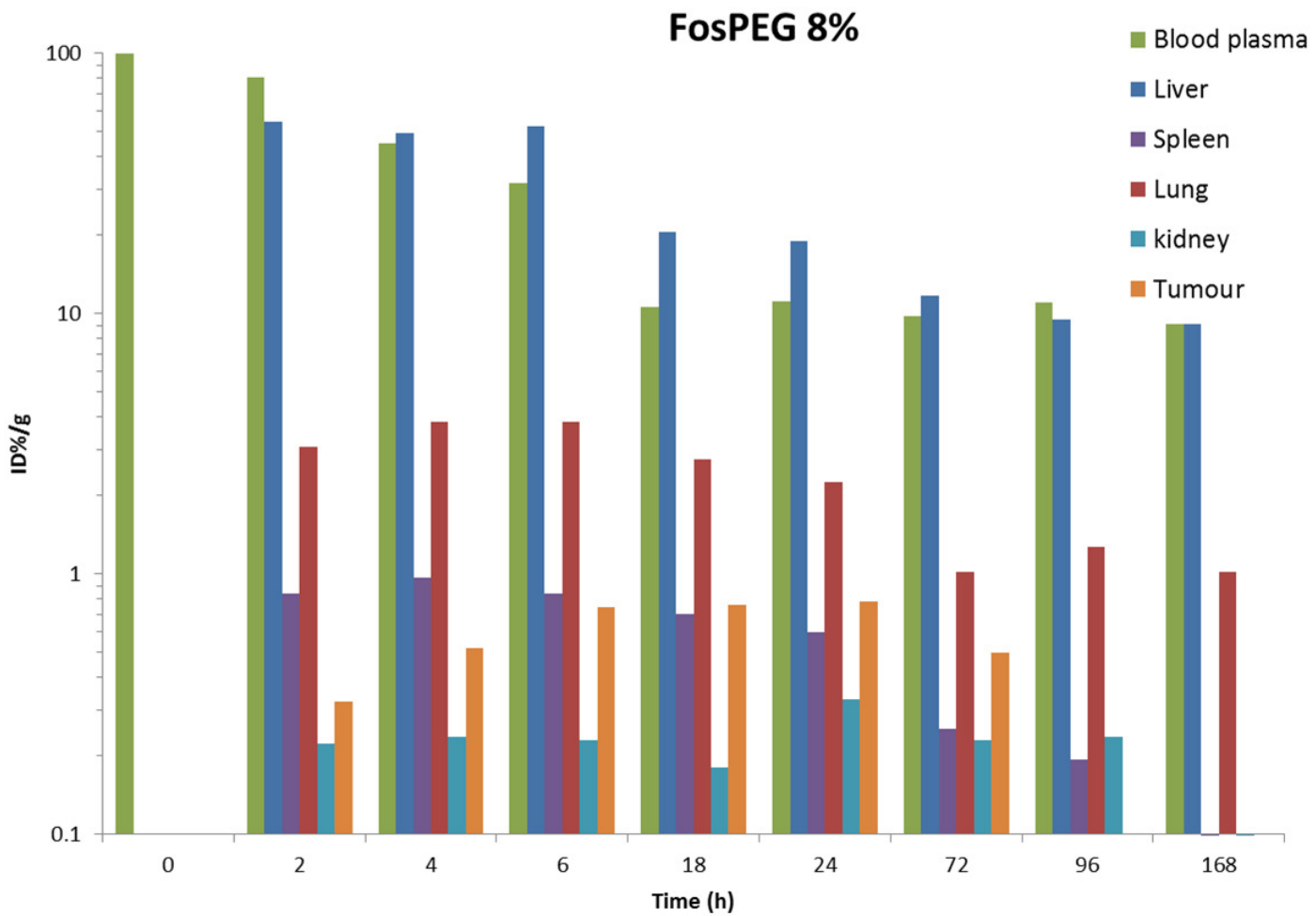

Figure A.20iii. Semi-log plot of the percentage injected dose of m-THPC (%ID/g) in different tissues of a rat model as a function of time following an intravenous injection of 0.3 mg kg^{-1} liposomal m-THPC in FosPEG 8%. Data calculated from the mean m-THPC concentration (µg g^{-1}) in each organ, hence no S.D.

SECTION B: Polymeric Nanoparticles

B.1 Nanoprecipitation Method for synthesis PLGA and PEG-PLGA NPs

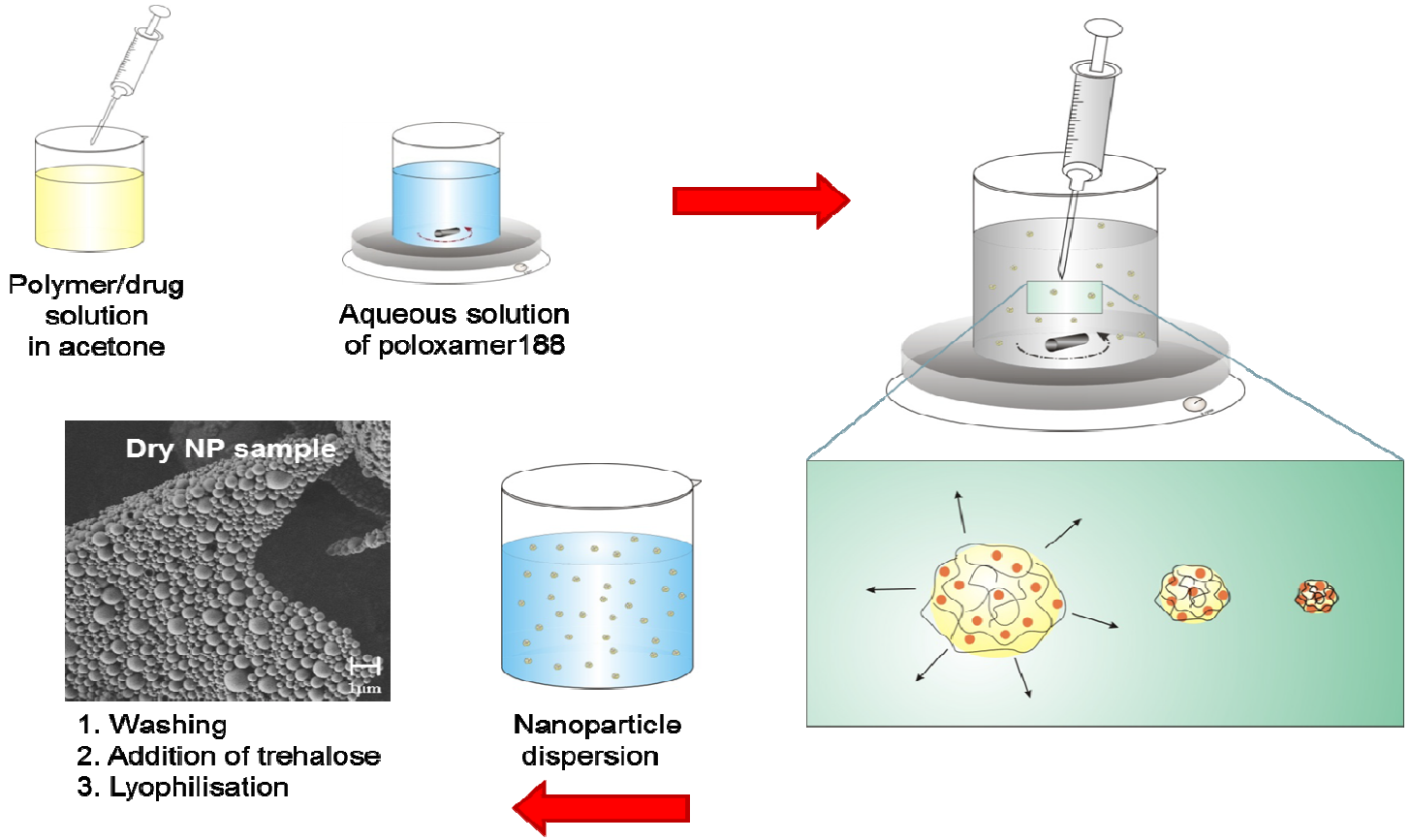

Fig B.1. Polymer and drug are dissolved in acetone and added to an aqueous solution containing Poloxamer 188 (surface modifier and stabiliser). The acetone is evaporated at appropriate temperatures and reduced pressures leaving behind the polymer encapsulated nanoparticles with drug. *Image taken from Dr Kos, University of Ljubljana.*

B.2 Absorbance spectra of PLGA and PEG-PLGA NPs in MeOD

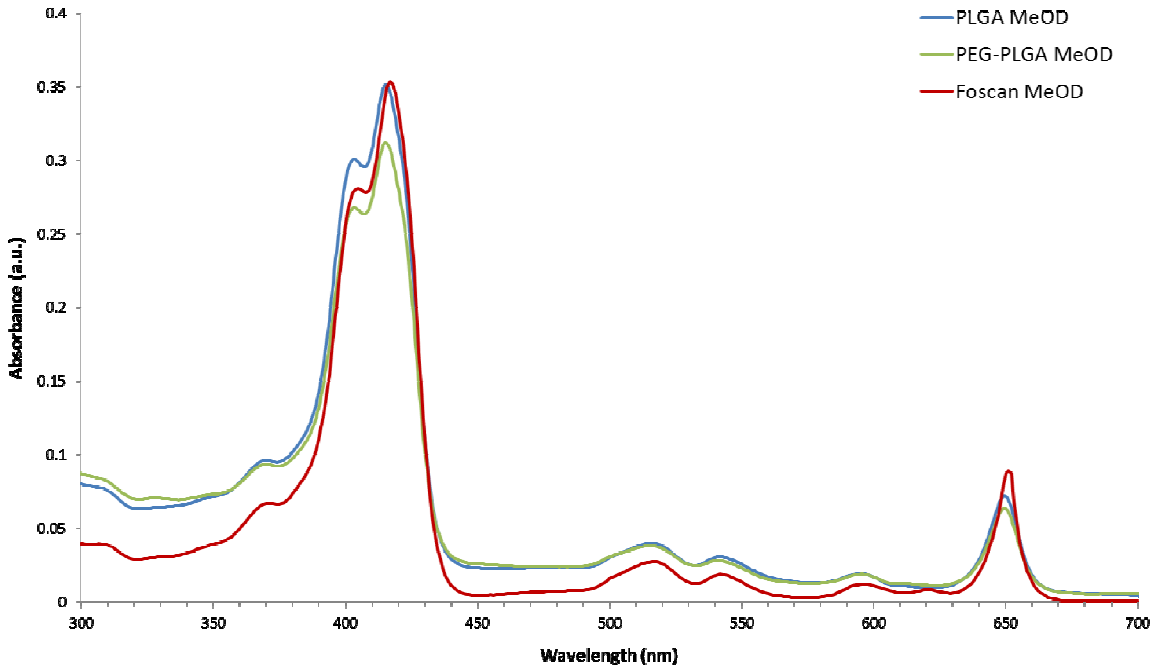

Figure B.2. Absorbance spectra of m-THPC in Foscan and noncovalently incorporated in PLGA and pegylated PLGA nanoparticles in deuterated methanol (MeOD). All solutions prepared at 10 µM m-THPC concentrations.

Deuterated methanol (MeOD or CH_3OD) is a solvent in which hydrogen atoms have been replaced with deuterium (heavy hydrogen) isotope, removing water from the solution and permitting complete solubilisation of m-THPC into its monomeric form, whilst prolonging the half-life of singlet oxygen. Absorbance spectra of m-THPC in Foscan, PLGA and PEG-PLGA NPs were performed in MeOD. No spectral shifts or peak broadening was detected for m-THPC in PLGA and PEG-PLGA NPs compared to Foscan in MeOD (Fig 5.5). Absorbance maxima for all m-THPC formulations in MeOD were recorded at 423 nm and 652 nm, respectively. Slight differences in absorbance maxima (Ab = εcl) may be due to experimental error in preparing solutions (c = concentration).

B.3 Rate of m-THPC release from polymeric NPs

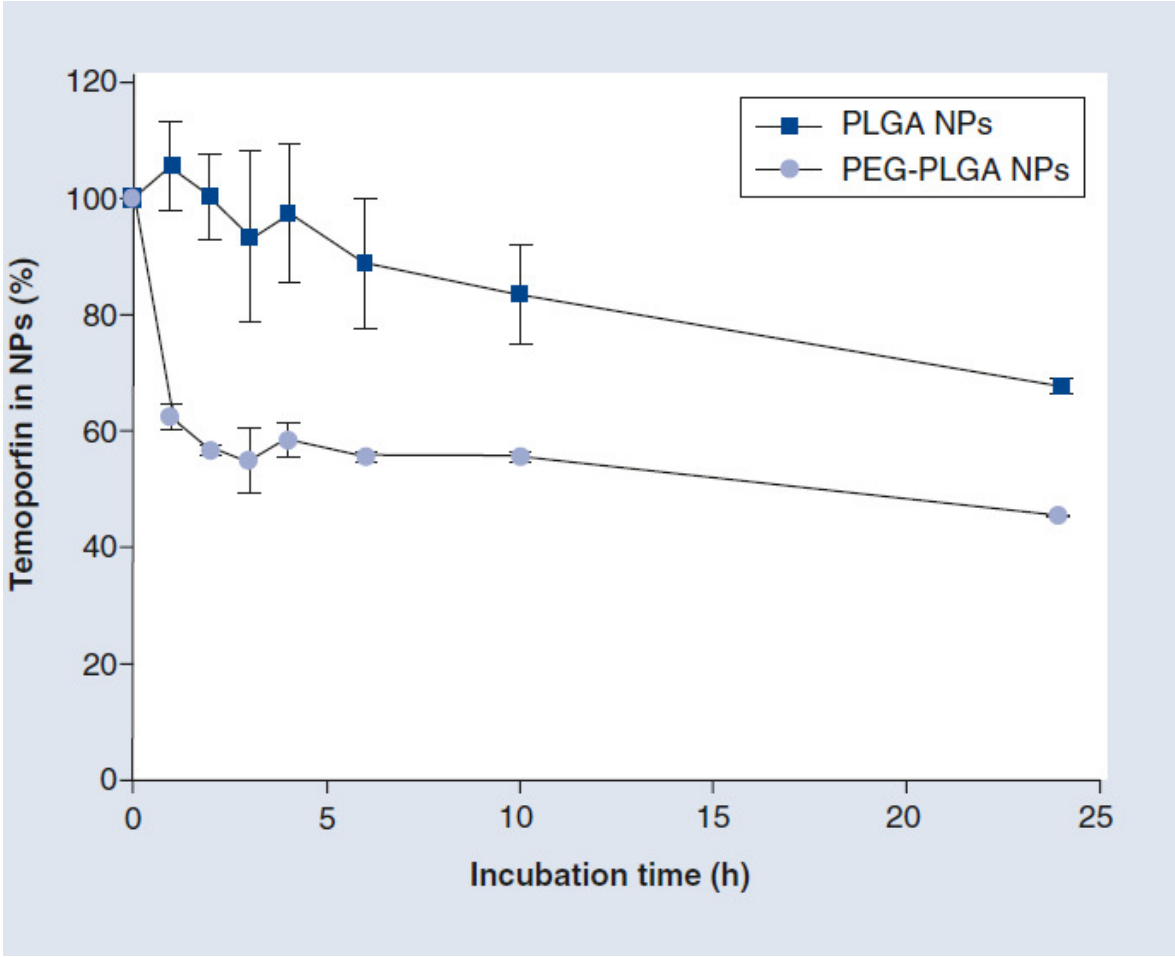

Figure B.3. The release rate of m-THPC (temoporfin) from pegylated (PEG-PLGA) and non-pegylated (PLGA) NPs over time (h) in phosphate-buffered saline (PBS) with 10% foetal bovine serum (FBS). m-THPC retained in NPs was measured following ultracentrifugation and dissolution of polymeric NPs in dimethyl sulfoxide (DMSO); established by collaborators *Rojnik et al., 2012*.

B.4 % Injected dose/g of m-THPC in polymeric NPs in different tissues *in vivo*

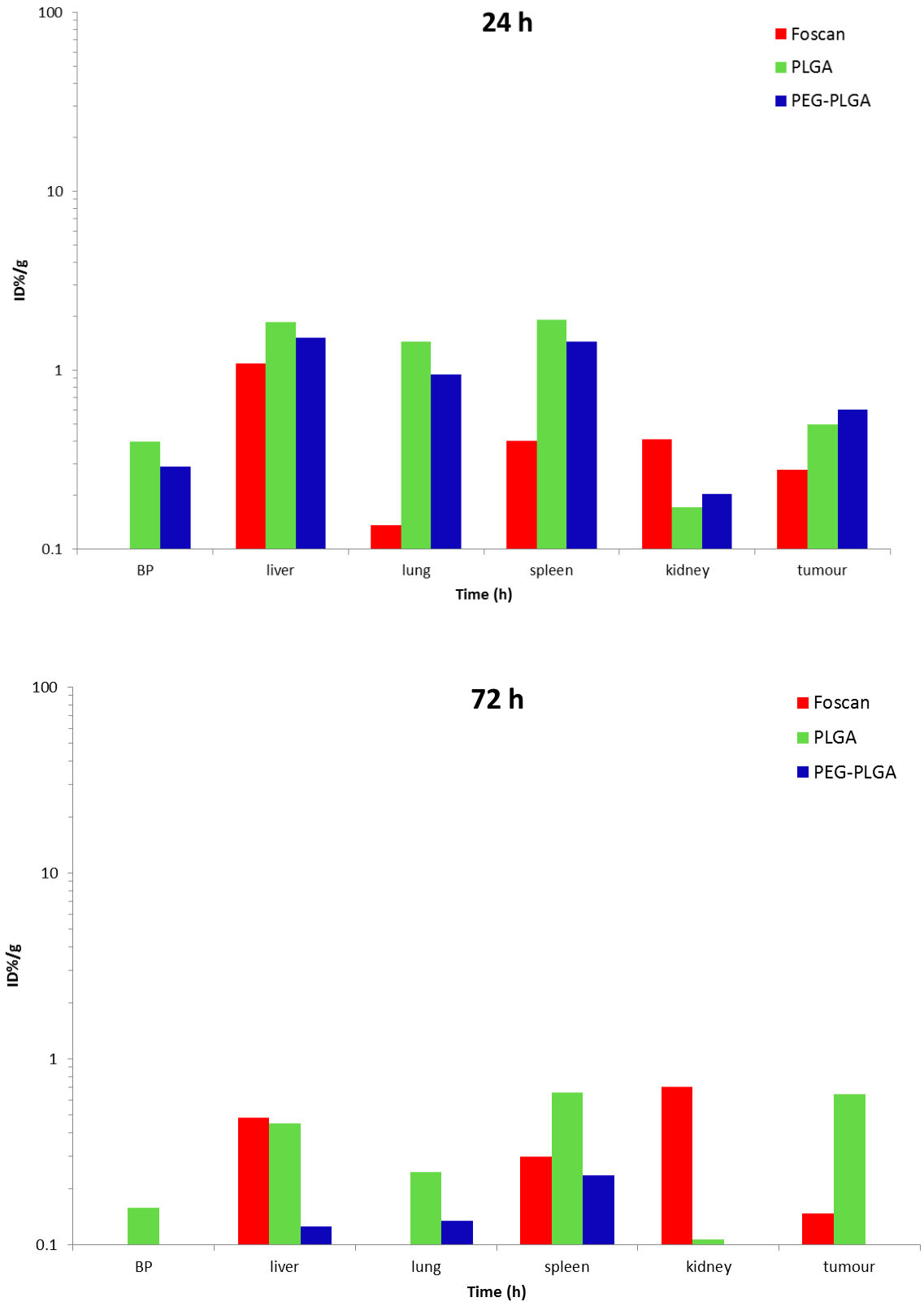

Figure C.4. Semi-log plot of the percentage injected dose of m-THPC (%ID/g) in different tissues of a rat model at 24 & 72 h following an intravenous injection of 0.3 mg kg^{-1} m-THPC in Foscan, PLGA or PEG-PLGA NPs. Data calculated from the mean m-THPC concentration (µg g^{-1}) in each organ, hence no S.D.

SECTION C: Organically Modified Silica Nanoparticles

C.1 Synthesis of pegylated ORMOSIL NPs

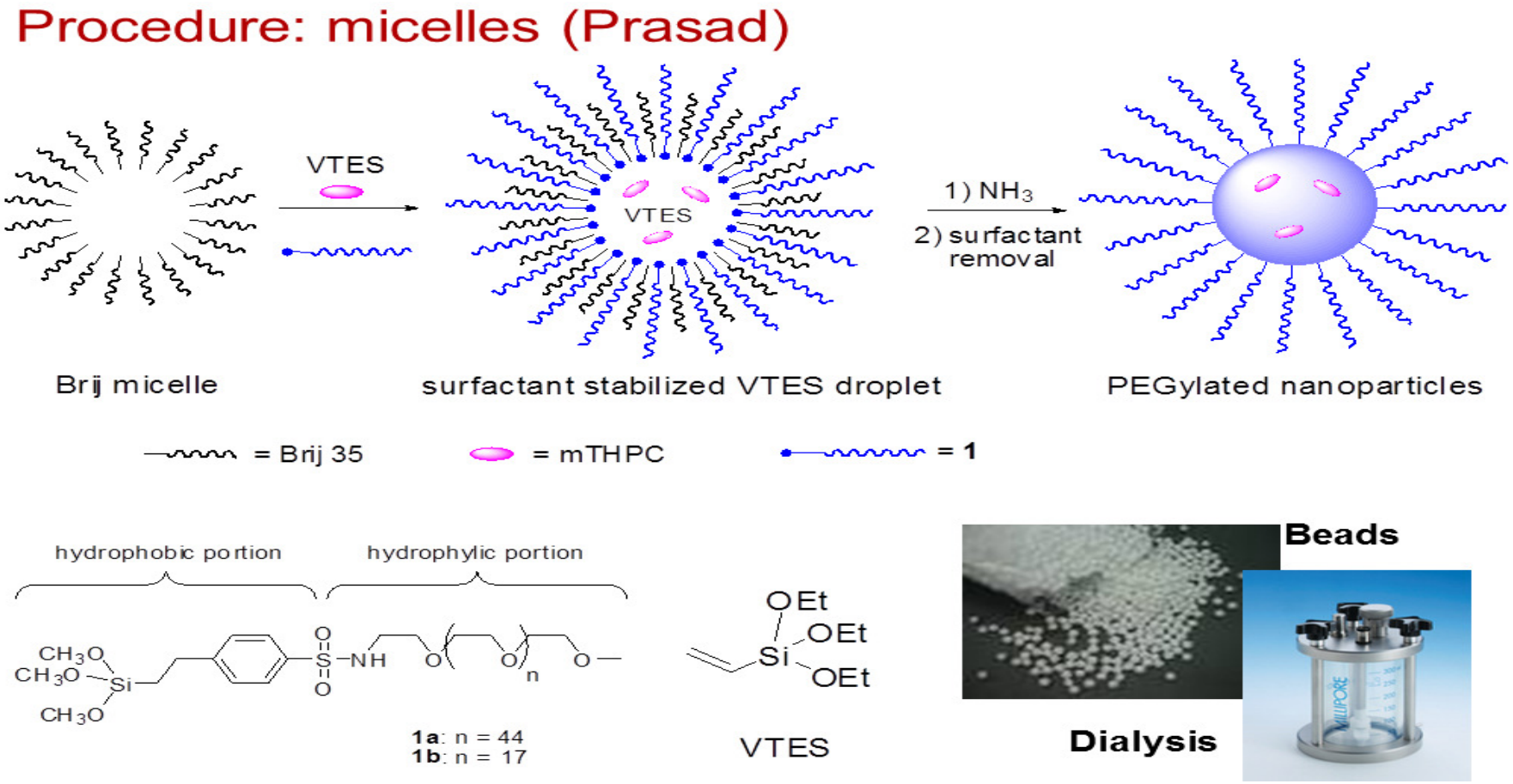

Figure C.1 Pegylated ORMOSIL NPs covalently incorporating m-THPC prepared by the condensation of VTES (*proposed by Prasad et al 2008*).

C.2 Quantitative ORMOSIL concentrations at 24 h *in vivo*

Sample	**IR194**	**SF142UF**	**GG91UF**
Size	19 nm	95 nm	100 nm
Fluorophore	mTHPC 421	mTHPC 267	mTHPC 470
Loading (%)	2.34	1.5	2
PEG length	2000	2000	2000
Binding to silica	Covalent	covalent	covalent
	Concentration (µg g^{-1}) of m-THPC at 24 h		
Blood plasma	1.39 ± 0.30	1.95 ± 0.58	1.55 ± 0.63
Liver	1.37 ± 0.31	1.46 ± 0.36	1.34 ± 0.23
Spleen	1.25 ± 0.34	8.40 ± 2.40	20.4 ± 6.50
Lung	2.18 ± 0.21	0.70 ± 0.18	0.54 ± 0.11
Kidney	0.15 ± 0.05	0.40 ± 0.16	0.26 ± 0.09
Skin	0.10 ± 0.03	0.14 ± 0.05	0.11 ± 0.03
Tumour	0.43 ± 0.08	2.34 ± 0.33	~

Table C.2. Specifications of silica nanoparticle preparations and their uptake into different tissues at 24 h after 0.3 mg kg^{-1} injected dose, measured by concentration (µg g^{-1}) of m-THPC. (Data points show the mean ± s.d., n = 4).

C.3 ORMOSIL NPs in the spleen at 24 h

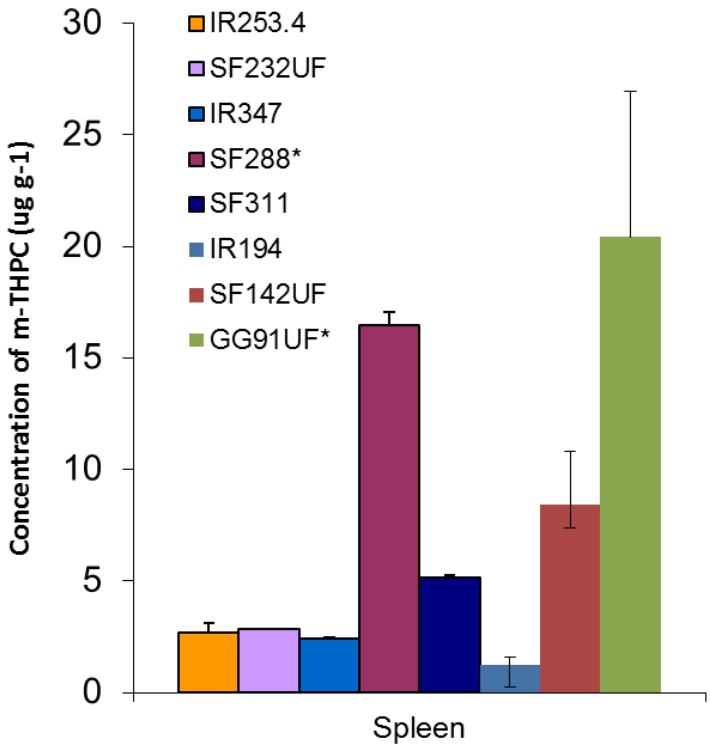

Figure C.3. Concentration of m-THPC (µg g^{-1}) in the spleen of the HL rat at 24 h following an intravenous injection of 0.3 mg kg^{-1} m-THPC in pegylated ORMOSIL nanoparticles ~20 nm (mono-m-THPC) or ~90 nm (mono- or tetra*-m-THPC). Data corrected for negative control tissue. Data points show the mean ± SD, n = 3.

C.4 Preparing Fluorodishes: ORMOSIL NPs

Example: eg. MC28 cells

MC28 cells: Require a cell concentration of 1 x 10^4 cells/200 µL (fluorodish volume)

Average cell count ≈ $\frac{(223 + 157)}{2}$ = **190 cells** (from a 5 mL suspension)

Number of cells per ml: 190 cells x 2 x 10^4 = **3.8 x 10^6 cells mL^{-1}**

1 Fluorodish: $\frac{1 \times 10^4 \text{ cells}}{1}$ x $\frac{1 \text{ mL}}{380 \times 10^4 \text{ cells}}$ = 2.6 µL of cell suspension

Require 7 fluorodishes: 200 µL x 7 = 1400 µL ≈ 2 mL

Total volume = 2 mL x (5 x 10^4) cells mL^{-1} = 1 x 10^5 cells

Seeding density = $\frac{1 \times 10^5 \text{ cells}}{38 \times 10^5 \text{ cells}}$ = 26.3 µL of original cell suspension

Total volume 2 mL - 26.3 µL = 1.974 mL of supplemented DMEM media.

C.5 Rate of m-THPC release from ORMOSIL NPs

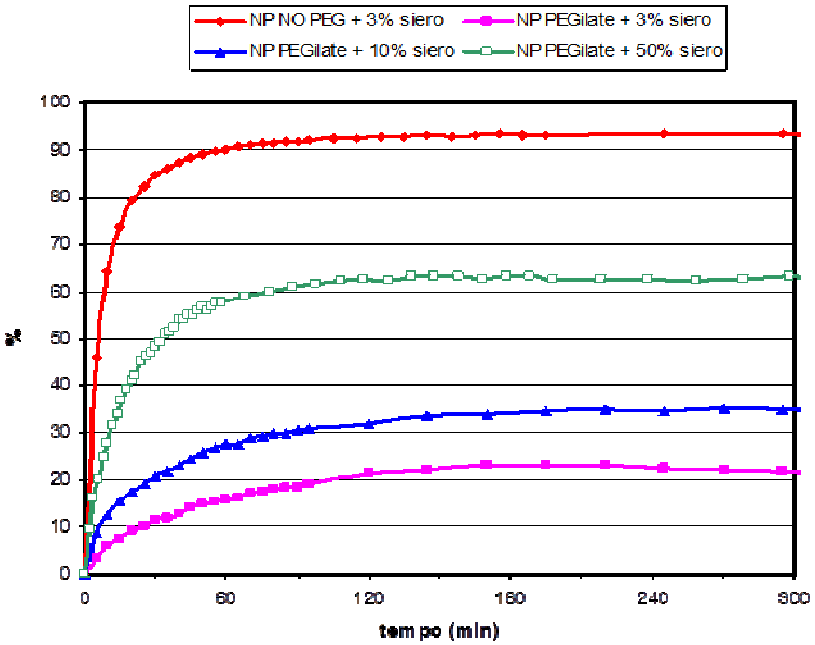

Figure C.5. Rate of m-THPC release (%) from pegylated (blue, green & pink) versus non-pegylated ORMOSIL NPs (red), following the physical entrapment (non-covalent) of m-THPC, in the presence of different percentages of FCS (%) over time (min); established by collaborators through FRET experiments (*Dr Mancin, Padova, Italy*).

C.6 Transmission Electron Microscopy (TEM) Images

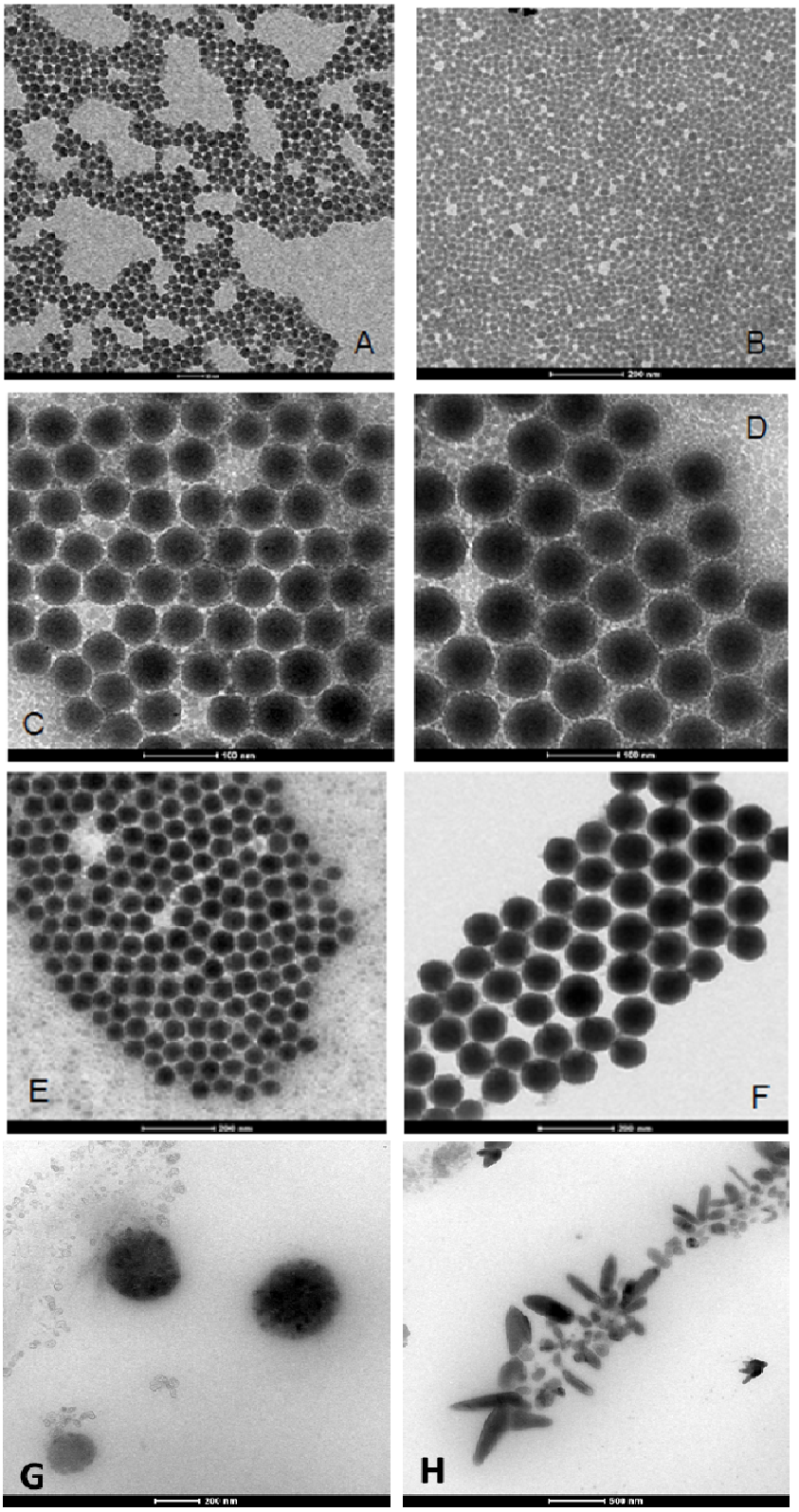

Figure C.6. ORMOSIL NPs were imaged using TEM to assess their size and dispersity by collaborators at the University of Padova under the direction of Dr F Mancin. Fully intact ORMOSIL NPs in saline (**A** & **B**) ≤20 nm, (**C** & **E**) 55 nm, (**D**) 70 nm and (**F**) 90 nm. Fully decomposed ORMOSIL structure in the presence of Solvable™, used in chemical extraction studies, to ensure all covalently bound m-THPC is released (**G** & **H**) indicate the presence of silica debris and salt crystals.

C.7 Toxicology: liver/renal enzyme function test

Liver enzymatic markers and reactions (Cobas®-Roche), Royal Free Hospital, UCL:

1. **ALT – alanine aminotransferase** (cytoplasm of hepatocytes):

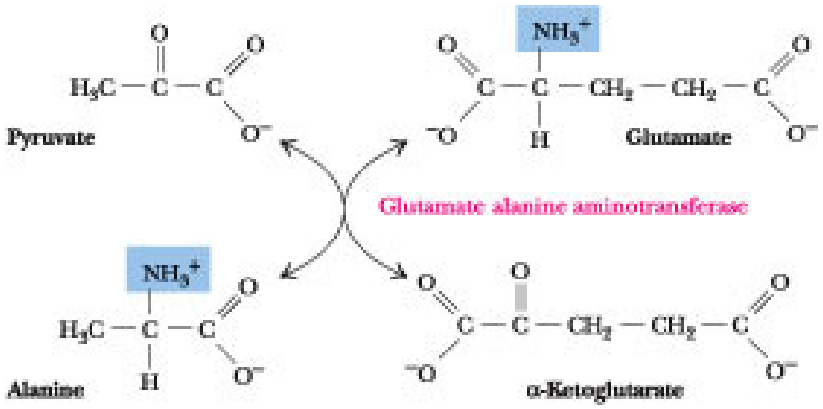

Pyruvate + NADH + H^+ ⇌ LDH ⇌ L-lactate + NAD^+

Rate of the NADH decrease α rate of formation of Pyruvate.

2. **AST – aspartate aminotransferase** (cytoplasm & mitochondria of hepatocytes):

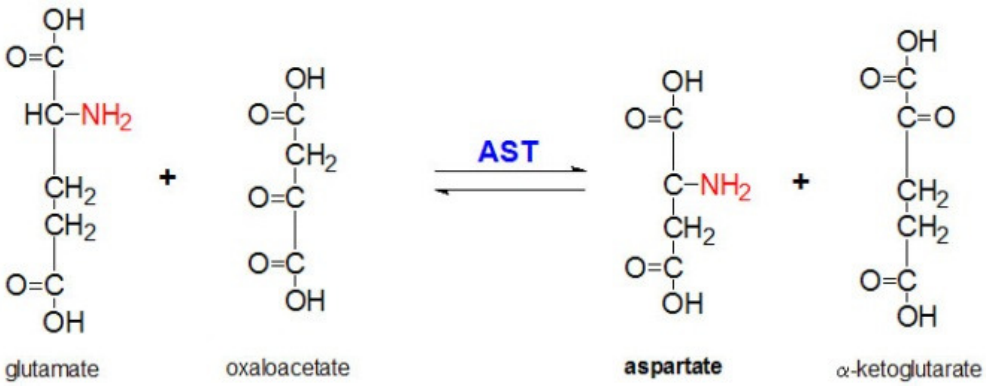

Oxaloacetate + NADH + H^+ ⇌ MDH ⇌ Malate + NAD^+

Rate of the NADH decrease α rate of formation of Oxaloacetate.

C.8 Calculations: concentration of silica injected

	IR194	IR253	IR254	IR322	IR347
Density of glass (g cm^{-3})	1.5	1.5	1.5	1.5	1.5
Diameter (nm)	19	16	17	16	20
Volume (nm^3)	3.59E-18	2.14E-18	2.57E-18	2.1449E-18	4.19E-18
Mass of np (g)	5.39E-18	3.22E-18	3.86E-18	3.2174E-18	6.28E-18
Mass of silica (mg mL^{-1})	16.7	21.8	21.7	22.3	23.3
Number of (nps mL^{-1})	3.1E+15	6.78E+15	5.62E+15	6.931E+15	3.66E+15
m-THPC conc NP (µM)	421	555	505	499	431
m-THPC conc injection stock (mg mL^{-1})	0.286	0.378	0.344	0.339	0.293
Injection volume for 0.3 mg kg^{-1} mTHPC (mL)	0.209	0.159	0.176	0.176	0.205
Number of nps for 0.3 mg kg^{-1} mTHPC (nps kg^{-1})	6.48E+14	1.08E+15	9.9E+14	1.2199E+15	7.5E+14
Amount of silica per rat (mg kg^{-1})	3.4903	3.4662	3.8192	3.9248	4.715
Surface area of each silica np (nm^2)	1134.262	804.352	908.038	804.352	1256.8

	GG91UF*	SF142UF	SF232UF	SF288*	SF311
Density of glass (g cm^{-3})	1.5	1.5	1.5	110	1.5
Diameter (nm)	110	95	90	55	45
Volume (nm^3)	6.97E-16	4.49E-16	3.82E-16	6.97E-16	3.82E-16
Mass of np (g)	1.05E-15	6.73E-16	5.73E-16	1.0455E-15	5.73E-16
Mass of silica (mg mL^{-1})	?	?	17.7	11.4	9.3
Number of (nps mL^{-1})	?	?	3.09E+13	1.0904E+13	1.62E+13
m-THPC conc NP (µM)	470	267	321	270	187
m-THPC conc injection stock (mg mL^{-1})	0.32	0.182	0.218	0.184	0.127
Injection volume for 0.3 mg kg^{-1} mTHPC (mL)	0.1875	0.33	0.275	0.326	0.472
Number of nps for 0.3 mg kg^{-1} mTHPC (nps kg^{-1})	?	?	8.5E+12	3.5547E+12	7.67E+12
Amount of silica per rat (mg kg^{-1})	?	?	4.8675	3.7164	4.3896
Surface area of each silica np (nm^2)	38018.2	28356.55	25450.2	38018.2	25450.2

C.9 % Injected dose/g of m-THPC in ORMOSIL NPs in different tissues *in vivo*

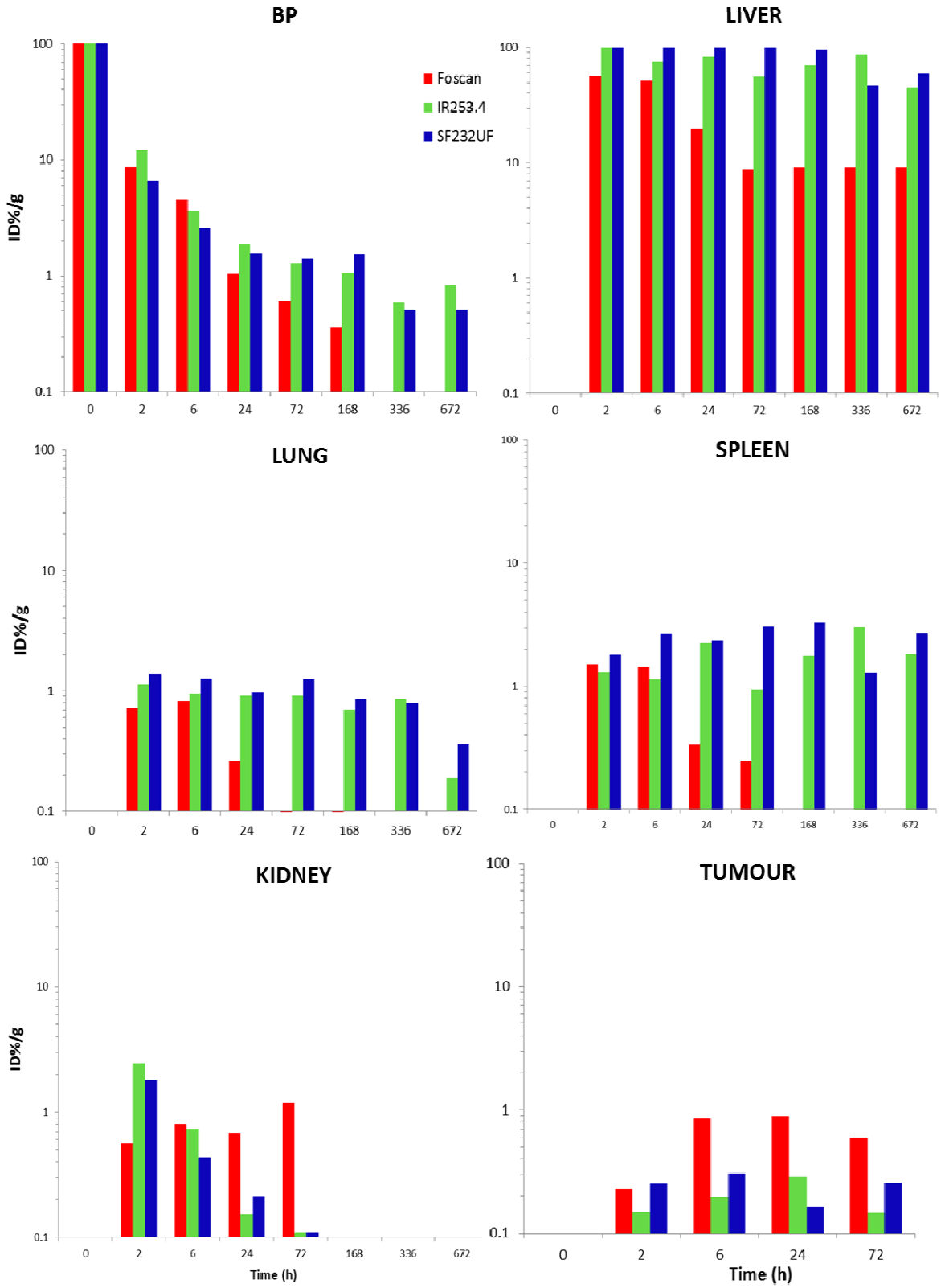

Figure C.9. Semi-log plot of the percentage injected dose of m-THPC (%ID/g) in different tissues of a rat model as a function of time following an intravenous injection of 0.3 mg kg^{-1} m-THPC in Foscan or small (IR253.4) or larger (SF232UF) ORMOSIL NPs. Data calculated from the mean m-THPC concentration (µg g^{-1}) in each organ, hence no S.D.

C.10 % ID/g of m-THPC in targeted cRGD ORMOSIL NPs in different tissues at 24 h *in vivo*

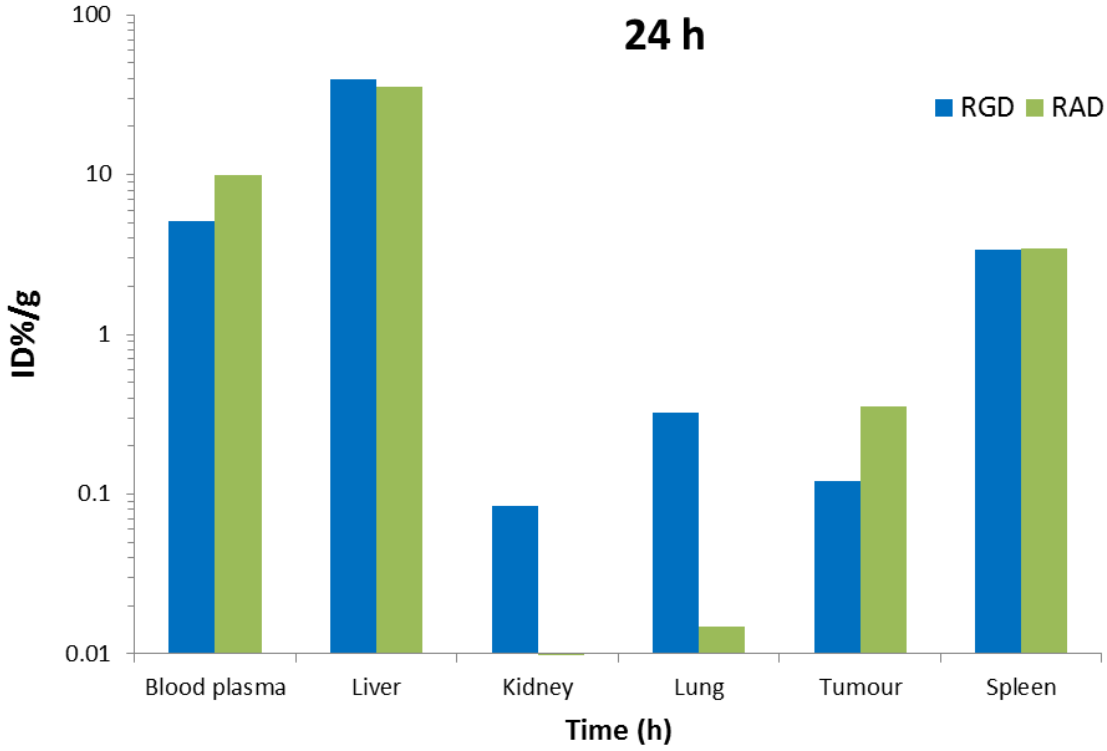

Figure C.10. Semi-log plot of the percentage injected dose of m-THPC (%ID/g) in different tissues of the HL rat at 24 following an intravenous injection of 0.1 mg kg^{-1} m-THPC in either targeted cRGD-ORMOSIL NPs or inactive targeted cRAD-ORMOSIL NPs. Data calculated from the mean m-THPC concentration (µg g^{-1}) in each organ, hence no S.D.

Appendix II

Published papers

MJ Bovis, JH Woodhams, M Loizidou, D Scheglmann, SG Bown, AJ MacRobert (2012). Improved in vivo delivery of m-THPC via pegylated liposomes for use in photodynamic therapy. Journal of Controlled Release 157 (2): 196-205. Impact factor 7.6.

M Rojnik, P Kocbek, F Moret, C Compagnin, L Celotti, MJ Bovis, JH Woodhams, AJ Macrobert, D Scheglman, W Helfrich, MJ Verkaik, E Papini, E Reddi, J Kos (2012). In vitro and in vivo characterization of temoporfin-loaded PEGylated PLGA nanoparticles for use in photodynamic therapy. Nanomedicine (5): 663-77. Impact factor 6.9.

MD Ball, IC Bonzani, MJ Bovis, A Williams, MM Stevens (2011). Human periosteum is a source of cells for orthopaedic tissue engineering: a pilot study. Clinical Orthopaedics and Related Research 469(11):3085-93. Impact factor 2.78.

Papers being prepared for submission

MJ Bovis, S Noimark, JH Woodhams, CWM Kay, J Weiner, W Peveler, A Correia, M Wilson, IP Parkin, AJ MacRobert. Photosensitised generation of singlet oxygen in silicone polymer substrates doped with methylene blue and nanogold for antimicrobial applications. (Manuscript in preparation).

MJ Bovis, JH Woodhams, M Rojnik, P Kocbek, R Fisher, J Kos, AJ Macrobert. Assessing the efficacy of photodynamic therapy in vivo using m-THPC loaded PLGA nanoparticles. (Manuscript in preparation).

JH Woodhams, MJ Bovis, IH Yim, E Reddi, F Mancin, F Selvestrel, I Rio-Echevarria, M Loizidou, SG Bown, AJ MacRobert. In vivo photodynamic activity of meta-tetra(hydroxyphenyl)chlorin entrapped in pegylated ORMOSIL nanoparticles. (Manuscript in preparation).

Conference Presentations

12th World Congress of the International Photodynamic Association (IPA), June 2009, Seattle, Washington, USA. MJ Bovis: Improved m-THPC delivery via novel pegylated liposomal nano-carriers.

13th Congress of the European Society for Photobiology in conjunction with the 2nd Conference of the European Platform for Photodynamic Medicine (EPPM), Sept 2009, Wroclaw, Poland. MJ Bovis: Pharmacokinetics of novel pegylated liposomal nano-carriers for improved m-THPC delivery.

8th International Symposium of European Platform of Photodynamic Medicine, Oct 2010, Brixen, Italy. MJ Bovis: Improving the delivery of m-THPC via liposomal nanocarriers.

14th Congress of the European Society of Photobiology, Sept 2011, Geneva, Switzerland. MJ Bovis: Using PEGylated PLGA nanoparticles to enhance the delivery of m-THPC for in vivo PDT.

36th Congress of the American Society of Photobiology, June 2012, Montreal, Canada. MJ Bovis: Investigating the Delivery of m-THPC incorporated in pegylated PLGA nanoparticles for in vivo PDT.

International Conference on Nanotechnology in Medicine, Nov 2012, London, UK. MJ Bovis: Investigating the Delivery of m-THPC incorporated in Pegylated PLGA Nanoparticles for in vivo PDT.

Society of Academic & Research Surgery, Jan 2013, London, UK. MJ Bovis: m-THPC delivery via pegylated PLGA nanoparticles for in vivo photodynamic therapy (PDT).

15th Congress of the European Society of Photobiology, Sept 2013, Liege, Belgium. MJ Bovis: Photosensitised generation of singlet oxygen in silicone polymer substrates doped with methylene blue for antimicrobial applications.

References

Abu-Yousif, A. O., Moor, A. C., Zheng, X., Savellano, M. D., Yu, W., Selbo, P. K., & Hasan, T. 2012. Epidermal growth factor receptor-targeted photosensitizer selectively inhibits EGFR signaling and induces targeted phototoxicity in ovarian cancer cells. ***Cancer Lett.***, 321(2): 120-127.

Acharya, S. & Sahoo, S. K. 2011. PLGA nanoparticles containing various anticancer agents and tumour delivery by EPR effect. ***Advanced Drug Delivery Reviews***, 63(3): 170-183.

Agnihotri, S. A., Mallikarjuna, N. N., & Aminabhavi, T. M. 2004. Recent advances on chitosan-based micro- and nanoparticles in drug delivery. ***J Control Release***, 100(1): 5-28.

Aicher, A., Miller, K., Reich, E., & Hautmann, R. 1994. Photodynamic therapy of human bladder carcinoma cells in vitro with pH-sensitive liposomes as carriers for 9-acetoxy-tetra-n-propylporphycene. ***Urol.Res.***, 22(1): 25-32.

Albanese, A., Sykes, E. A., & Chan, W. C. 2010. Rough around the edges: the inflammatory response of microglial cells to spiky nanoparticles. ***ACS Nano.***, 4(5): 2490-2493.

Albanese, A., Tang, P. S., & Chan, W. C. 2012. The effect of nanoparticle size, shape, and surface chemistry on biological systems. ***Annu.Rev.Biomed.Eng***, 14: 1-16.

Alexiades-Armenakas, M. 2006. Laser-mediated photodynamic therapy. ***Clin.Dermatol.***, 24(1): 16-25.

Alexis, F., Pridgen, E., Molnar, L. K., & Farokhzad, O. C. 2008. Factors affecting the clearance and biodistribution of polymeric nanoparticles. ***Mol.Pharm.***, 5(4): 505-515.

Alian, W., Anderssonengels, S., Svanberg, K., & Svanberg, S. 1994. Laser-Induced Fluorescence Studies of Meso-Tetra(Hydroxyphenyl)Chlorin in Malignant and Normal-Tissues in Rats. ***British Journal of Cancer***, 70(5): 880-885.

Allen, C. M., Sharman, W. M., La, M. C., van Lier, J. E., & Weber, J. M. 2002. Attenuation of photodynamically induced apoptosis by an RGD containing peptide. ***Photochem.Photobiol.Sci.***, 1(4): 246-254.

Allen, T. M., Hansen, C. B., & Demenezes, D. E. L. 1995. Pharmacokinetics of Long-Circulating Liposomes. ***Advanced Drug Delivery Reviews***, 16(2-3): 267-284.

Allison, B. A., Crespo, M. T., Jain, A. K., Richter, A. M., Hsiang, Y. N., & Levy, J. G. 1997. Delivery of benzoporphyrin derivative, a photosensitizer, into atherosclerotic plaque of Watanabe heritable hyperlipidemic rabbits and balloon-injured New Zealand rabbits. ***Photochem.Photobiol.***, 65(5): 877-883.

Allison, R. R., Sibata, C., & Gay, H. 2009. PDT for cancers of the head and neck. ***Photodiagnosis and Photodynamic Therapy***, 6(1): 1-2.

Angeli, N. G., Lagorio, M. G., San Roman, E. A., & Dicelio, L. E. 2000. Meso-substituted cationic porphyrins of biological interest. Photophysical and physicochemical properties in solution and bound to liposomes. ***Photochem.Photobiol.***, 72(1): 49-56.

Anselmo, A. C., Gupta, V., Zern, B. J., Pan, D., Zakrewsky, M., Muzykantov, V., & Mitragotri, S. 2013. Delivering Nanoparticles to Lungs while Avoiding Liver and Spleen through Adsorption on Red Blood Cells. ***ACS Nano.***, 7(12): 11129-11137.

Arteaga, C. L. 2003. ErbB-targeted therapeutic approaches in human cancer. ***Experimental Cell Research***, 284(1): 122-130.

Arvizo, R. R., Miranda, O. R., Thompson, M. A., Pabelick, C. M., Bhattacharya, R., Robertson, J. D., Rotello, V. M., Prakash, Y. S., & Mukherjee, P. 2010. Effect of nanoparticle surface charge at the plasma membrane and beyond. ***Nano.Lett.***, 10(7): 2543-2548.

Ashraf, S., Loizidou, M., Crowe, R., Turmaine, M., Taylor, I., & Burnstock, G. 1997. Blood vessels in liver metastases from both sarcoma and carcinoma lack perivascular innervation and smooth muscle cells. ***Clinical & Experimental Metastasis***, 15(5): 484-498.

Auler, H. & Banzer, G. 1942. Untersuchungen über die Rolle der Porphyrine bei geschwulstkranken Mensch en und Tieren. ***Z Krebsforsch***, 53(65): 68.

Aumailley, M., Gurrath, M., Muller, G., Calvete, J., Timpl, R., & Kessler, H. 1991. Arg-Gly-Asp Constrained Within Cyclic Pentapeptides - Strong and Selective Inhibitors of Cell-Adhesion to Vitronectin and Laminin Fragment-P1. ***Febs Letters***, 291(1): 50-54.

Avraamides, C. J., Garmy-Susini, B., & Varner, J. A. 2008. Integrins in angiogenesis and lymphangiogenesis. ***Nat.Rev.Cancer***, 8(8): 604-617.

Baas, P., Saarnak, A. E., Oppelaar, H., Neering, H., & Stewart, F. A. 2001. Photodynamic therapy with meta-tetrahydroxyphenylchlorin for basal cell carcinoma: a phase I/II study. ***Br.J Dermatol.***, 145(1): 75-78.

Bae, B. C. & Na, K. 2010. Self-quenching polysaccharide-based nanogels of pullulan/folate-photosensitizer conjugates for photodynamic therapy. ***Biomaterials***, 31(24): 6325-6335.

Ball, D. J., Vernon, D. I., & Brown, S. B. 1999. The high photoactivity of m-THPC in photodynamic therapy. Unusually strong retention of m-THPC by RIF-1 cells in culture. ***Photochemistry and Photobiology***, 69(3): 360-363.

Barichello, J. M., Morishita, M., Takayama, K., & Nagai, T. 1999. Encapsulation of hydrophilic and lipophilic drugs in PLGA nanoparticles by the nanoprecipitation method. ***Drug Dev.Ind.Pharm.***, 25(4): 471-476.

Barik, T. K., Sahu, B., & Swain, V. 2008. Nanosilica-from medicine to pest control. ***Parasitol.Res.***, 103(2): 253-258.

Basal, E., Eghbali-Fatourechi, G. Z., Kalli, K. R., Hartmann, L. C., Goodman, K. M., Goode, E. L., Kamen, B. A., Low, P. S., & Knutson, K. L. 2009. Functional folate receptor alpha is elevated in the blood of ovarian cancer patients. ***PLoS.One.***, 4(7): e6292.

Basu, M. K. & Lala, S. 2004. Macrophage specific drug delivery in experimental leishmaniasis. ***Curr.Mol.Med.***, 4(6): 681-689.

Battah, S., Balaratnam, S., Casas, A., O'Neill, S., Edwards, C., Batlle, A., Dobbin, P., & MacRobert, A. J. 2007. Macromolecular delivery of 5-aminolaevulinic acid for photodynamic therapy using dendrimer conjugates. ***Molecular Cancer Therapeutics***, 6(3): 876-885.

Bawarski, W. E., Chidlowsky, E., Bharali, D. J., & Mousa, S. A. 2008. Emerging nanopharmaceuticals. ***Nanomedicine.***, 4(4): 273-282.

Bechet, D., Couleaud, P., Frochot, C., Viriot, M. L., Guillemin, F., & Barberi-Heyob, M. 2008. Nanoparticles as vehicles for delivery of photodynamic therapy agents. ***Trends in Biotechnology***, 26(11): 612-621.

Bellnier, D. A. & Dougherty, T. J. 1996. A preliminary pharmacokinetic study of intravenous Photofrin in patients. ***J Clin.Laser Med.Surg.***, 14(5): 311-314.

Berg, K., Nordstrand, S., Selbo, P. K., Tran, D. T., Angell-Petersen, E., & Hogset, A. 2011. Disulfonated tetraphenyl chlorin (TPCS2a), a novel photosensitizer developed for clinical utilization of photochemical internalization. ***Photochem.Photobiol.Sci.***, 10(10): 1637-1651.

Betz, C. S., Rauschning, W., Stranadko, E. P., Riabov, M. V., Albrecht, V., Nifantiev, N. E., & Hopper, C. 2008. Optimization of treatment parameters for Foscan-PDT of basal cell carcinomas. ***Lasers Surg.Med.***, 40(5): 300-311.

Bezdetnaya, L., Zeghari, N., Belitchenko, I., BarberiHeyob, M., Merlin, J. L., Potapenko, A., & Guillemin, F. 1996. Spectroscopic and biological testing of photobleaching of porphyrins in solutions. ***Photochemistry and Photobiology***, 64(2): 382-386.

Bhawalkar, J. D., Kumar, N. D., Zhao, C. F., & Prasad, P. N. 1997. Two-photon photodynamic therapy. ***J.Clin.Laser Med.Surg.***, 15(5): 201-204.

Bhuvaneswari, R., Gan, Y. Y., Soo, K. C., & Olivo, M. 2009. Targeting EGFR with photodynamic therapy in combination with Erbitux enhances in vivo bladder tumor response. ***Molecular Cancer***, 8.

Bhuvaneswari, R., Yuen, G. Y., Chee, S. K., & Olivo, M. 2011. Antiangiogenesis Agents Avastin and Erbitux Enhance the Efficacy of Photodynamic Therapy in a Murine Bladder Tumor Model. ***Lasers in Surgery and Medicine***, 43(7): 651-662.

Bienert, G. P., Schjoerring, J. K., & Jahn, T. P. 2006. Membrane transport of hydrogen peroxide. ***Biochim.Biophys.Acta***, 1758(8): 994-1003.

Bilati, U., Allemann, E., & Doelker, E. 2005. Development of a nanoprecipitation method intended for the entrapment of hydrophilic drugs into nanoparticles. ***European Journal of Pharmaceutical Sciences***, 24(1): 67-75.

Birrenbach, G. & Speiser, P. P. 1976. Polymerized micelles and their use as adjuvants in immunology. ***J Pharm.Sci.***, 65(12): 1763-1766.

Blank, S. V., Chang, R., & Muggia, F. 2005. Epidermal growth factor receptor inhibitors for the treatment of epithelial ovarian cancer. ***Oncology (Williston.Park)***, 19(4): 553-559.

Blant, S. A., Glanzmann, T. M., Ballini, J. P., Wagnieres, G., van den, B. H., & Monnier, P. 2002. Uptake and localisation of mTHPC (Foscan) and its 14C-labelled form in normal and tumour tissues of the hamster squamous cell carcinoma model: a comparative study. ***Br.J.Cancer***, 87(12): 1470-1478.

Blume, G. & Cevc, G. 1993. Molecular mechanism of the lipid vesicle longevity in vivo. ***Biochim.Biophys.Acta***, 1146(2): 157-168.

Bonnett, R. & Berenbaum, M. 1989a. Porphyrins as photosensitizers. ***Ciba Found.Symp.***, 146: 40-53.

Bonnett, R., Charlesworth, P., Djelal, B. D., Foley, S., McGarvey, D. J., & Truscott, T. G. 1999. Photophysical properties of 5,10,15,20-tetrakis(m-hydroxyphenyl)porphyrin-(m-THPP), 5,10,15,20-tetrakis(m-hydroxyphenyl)chlorin (m-THPC) and 5,10,15,20-tetrakis(m-hydroxyphenyl)bacteriochlorin (m-THPBC): a comparative study. ***Journal of the Chemical Society-Perkin Transactions 2***,(2): 325-328.

Bonnett, R. & Martinez, G. 2002. Photobleaching of compounds of the 5,10,15,20-Tetrakis(m-hydroxyphenyl)porphyrin Series (m-THPP, m-THPC, and m-THPBC). ***Org.Lett.***, 4(12): 2013-2016.

Bonnett, R., White, R. D., Winfield, U. J., & Berenbaum, M. C. 1989b. Hydroporphyrins of the meso-tetra(hydroxyphenyl)porphyrin series as tumour photosensitizers. ***Biochem.J.***, 261(1): 277-280.

Borak, B., Biernat, P., Prescha, A., Baszczuk, A., & Pluta, J. 2012. In vivo study on the biodistribution of silica particles in the bodies of rats. ***Adv.Clin.Exp.Med.***, 21(1): 13-18.

Borovkov, V. V., Anikin, M., Wasa, K., & Sakata, Y. 1996. Structurally Controlled Porphyrin - Aggregation Process in Phospholipid Membranes. ***Photochem.Photobiol.***, 63: 477-482.

Bosi, S., Da, R. T., Spalluto, G., & Prato, M. 2003. Fullerene derivatives: an attractive tool for biological applications. ***Eur.J.Med.Chem.***, 38(11-12): 913-923.

Bourdon, O., Laville, I., Carrez, D., Croisy, A., Fedel, P., Kasselouri, A., Prognon, P., Legrand, P., & Blais, J. 2002. Biodistribution of meta-tetra(hydroxyphenyl)chlorin incorporated into surface-modified nanocapsules in tumor-bearing mice. ***Photochem.Photobiol.Sci.***, 1(9): 709-714.

Bowen, R. The Hepatic Phagocytic System. 5-8-2002.

Bown, S. G. 1990. Photodynamic Therapy to Scientists and Clinician - One World Or 2. ***Journal of Photochemistry and Photobiology B-Biology***, 6(1-2): 1-12.

Bown, S. G., Rogowska, A. Z., Whitelaw, D. E., Lees, W. R., Lovat, L. B., Ripley, P., Jones, L., Wyld, P., Gillams, A., & Hatfield, A. W. 2002. Photodynamic therapy for cancer of the pancreas. ***Gut***, 50(4): 549-557.

Boyle, P. &. L. B. World Cancer Report. 2008. World Health Organisation, IRAC.

Boyle, R. W. & Dolphin, D. 1996. Structure and biodistribution relationships of photodynamic sensitizers. ***Photochemistry and Photobiology***, 64(3): 469-485.

Braichotte, D., Savary, J. F., Glanzmann, T., Monnier, P., Wagnieres, G., & vandenBergh, H. 1996. Optimizing light dosimetry in photodynamic therapy of the bronchi by fluorescence spectroscopy. ***Lasers in Medical Science***, 11(4): 247-254.

Brannon-Peppas, L. & Blanchette, J. O. 2004. Nanoparticle and targeted systems for cancer therapy. ***Advanced Drug Delivery Reviews***, 56(11): 1649-1659.

Brault, D., Vever-Bizet, C., & Le, D. T. 1986. Spectrofluorimetric study of porphyrin incorporation into membrane models--evidence for pH effects. ***Biochim.Biophys.Acta***, 857(2): 238-250.

Braun, K., Wiessler, M., Pipkorn, R., Ehemann, V., Bauerle, T., Fleischhacker, H., Muller, G., Lorenz, P., & Waldeck, W. 2010. A cyclic-RGD-BioShuttle functionalized with TMZ by DAR(inv) "Click Chemistry" targeted to alpha(v)beta(3) integrin for therapy. ***International Journal of Medical Sciences***, 7(6): 326-339.

Bressler, N. M. & Bressler, S. B. 2000. Photodynamic therapy with verteporfin (Visudyne): impact on ophthalmology and visual sciences. ***Invest Ophthalmol.Vis.Sci.***, 41(3): 624-628.

Brevet, D., Gary-Bobo, M., Raehm, L., Richeter, S., Hocine, O., Amro, K., Loock, B., Couleaud, P., Frochot, C., Morere, A., Maillard, P., Garcia, M., & Durand, J. O. 2009. Mannose-targeted mesoporous silica nanoparticles for photodynamic therapy. ***Chem.Commun (Camb.)***,(12): 1475-1477.

Brooks, P. C., Clark, R. A., & Cheresh, D. A. 1994a. Requirement of vascular integrin alpha v beta 3 for angiogenesis. ***Science***, 264(5158): 569-571.

Brooks, P. C., Montgomery, A. M., Rosenfeld, M., Reisfeld, R. A., Hu, T., Klier, G., & Cheresh, D. A. 1994b. Integrin alpha v beta 3 antagonists promote tumor regression by inducing apoptosis of angiogenic blood vessels. ***Cell***, 79(7): 1157-1164.

Brown, D. M., Wilson, M. R., MacNee, W., Stone, V., & Donaldson, K. 2001. Size-dependent proinflammatory effects of ultrafine polystyrene particles: a role for surface area and oxidative stress in the enhanced activity of ultrafines. ***Toxicol.Appl.Pharmacol.***, 175(3): 191-199.

Brown, J. M. & Wilson, W. R. 2004. Exploiting tumour hypoxia in cancer treatment. ***Nat.Rev.Cancer***, 4(6): 437-447.

Brown, S. B., Brown, E. A., & Walker, I. 2004. The present and future role of photodynamic therapy in cancer treatment. ***Lancet Oncology***, 5(8): 497-508.

Buchholz, J., Kaser-Hotz, B., Khan, T., Bleyl, C. R., Melzer, K., Schwendener, R. A., Roos, M., & Walt, H. 2005. Optimizind photodynamic therapy: In vivo pharmacokinetics of liposomal meta-(tetrahydroxyphenyl)chlorin in feline squamous cell carcinoma. ***Clinical Cancer Research***, 11(20): 7538-7544.

Buchholz, J., Wergin, M., Walt, H., Grafe, S., Bley, C. R., & Kaser-Hotz, B. 2007. Photodynamic therapy of feline cutaneous squamous cell carcinoma using a newly developed liposomal photosensitizer: preliminary results concerning drug safety and efficacy. ***J Vet.Intern.Med.***, 21(4): 770-775.

Burns, A. A., Vider, J., Ow, H., Herz, E., Penate-Medina, O., Baumgart, M., Larson, S. M., Wiesner, U., & Bradbury, M. 2009. Fluorescent silica nanoparticles with efficient urinary excretion for nanomedicine. ***Nano Lett.***, 9(1): 442-448.

Calvo, P., Remunan-Lopez, C., Vila-Jato, J. L., & Alonso, M. J. 1997. Chitosan and chitosan/ethylene oxide-propylene oxide block copolymer nanoparticles as novel carriers for proteins and vaccines. ***Pharm.Res.***, 14(10): 1431-1436.

Calzavara-Pinton, P. G., Venturini, M., & Sala, R. 2007. Photodynamic therapy: update 2006. Part 1: Photochemistry and photobiology. ***J Eur.Acad.Dermatol.Venereol.***, 21(3): 293-302.

Cancer Research UK. Cancer Research UK. 2014.

Carpenter, G. & Cohen, S. 1990. Epidermal growth factor. ***J Biol.Chem.***, 265(14): 7709-7712.

Castano, A. P., Demidova, T. N., & Hamblin, M. R. 2005. Mechanisms in photodynamic therapy: part two--cellular signaling, cell metabolism and modes of cell death. ***Photodiagnosis and Photodynamic Therapy***, 2(1): 1-23.

Cedervall, T., Lynch, I., Lindman, S., Berggard, T., Thulin, E., Nilsson, H., Dawson, K. A., & Linse, S. 2007. Understanding the nanoparticle-protein corona using methods to quantify exchange rates and affinities of proteins for nanoparticles. ***Proc.Natl.Acad.Sci.U.S.A***, 104(7): 2050-2055.

Cengel, K. A., Hahn, S. M., & Glatstein, E. 2005. C225 and PDT combination therapy for ovarian cancer: the play's the thing. ***J Natl.Cancer Inst.***, 97(20): 1488-1489.

Chang, H. I. & Yeh, M. K. 2012. Clinical development of liposome-based drugs: formulation, characterization, and therapeutic efficacy. ***Int.J Nanomedicine.***, 7: 49-60.

Chatterjee, D. K., Fong, L. S., & Zhang, Y. 2008a. Nanoparticles in photodynamic therapy: an emerging paradigm. ***Adv.Drug Deliv.Rev.***, 60(15): 1627-1637.

Chatterjee, D. K. & Yong, Z. 2008b. Upconverting nanoparticles as nanotransducers for photodynamic therapy in cancer cells. ***Nanomedicine***, 3(1): 73-82.

Chemical, B. &. M. E. C. Carbon Nanotube Composites. 2008.

Chen, B., Pogue, B. W., & Hasan, T. 2005. Liposomal delivery of photosensitising agents. ***Expert.Opin.Drug Deliv***, 2(3): 477-487.

Chen, H., Ahn, R., Van den, B. J., Thompson, D. H., & O'Halloran, T. V. 2009. Folate-mediated intracellular drug delivery increases the anticancer efficacy of nanoparticulate formulation of arsenic trioxide. ***Mol Cancer Ther.***, 8(7): 1955-1963.

Chen, J. Y., Mak, N. K., Yow, C. M. N., Fung, M. C., Chiu, L. C., Leung, W. N., & Cheung, N. H. 2000. The binding characteristics and intracellular localization of temoporfin (mTHPC) in myeloid leukemia cells: Phototoxicity and mitochondrial damage. ***Photochemistry and Photobiology***, 72(4): 541-547.

Chen, K. 2010. *Photophysical characterization and optimization of novel polymer based photosensitizer carrier systems for PDT*.

Chen, W. & Zhang, J. 2006. Using nanoparticles to enable simultaneous radiation and photodynamic therapies for cancer treatment. ***J Nanosci.Nanotechnol.***, 6(4): 1159-1166.

Chen, Z., Deng, J., Zhao, Y., & Tao, T. 2012. Cyclic RGD peptide-modified liposomal drug delivery system: enhanced cellular uptake in vitro and improved pharmacokinetics in rats. ***Int.J Nanomedicine***, 7: 3803-3811.

Chen, Z. L., Sun, Y., Huang, P., Yang, X. X., & Zhou, X. P. 2009. Studies on Preparation of Photosensitizer Loaded Magnetic Silica Nanoparticles and Their Anti-Tumor Effects for Targeting Photodynamic Therapy. ***Nanoscale.Res.Lett.***, 4(5): 400-408.

Cheng, L., Wang, C., & Liu, Z. 2013. Upconversion nanoparticles and their composite nanostructures for biomedical imaging and cancer therapy. ***Nanoscale.***, 5(1): 23-37.

Cheng, R. J., Chen, P. Y., Lovell, T., Liu, T., Noodleman, L., & Case, D. A. 2003. Symmetry and bonding in metalloporphyrins. A modern implementation for the bonding analyses of five- and six-coordinate high-spin iron(III)-porphyrin complexes through density functional calculation and NMR spectroscopy. ***J Am.Chem.Soc***, 125(22): 6774-6783.

Cheng, Y., Meyers, J. D., Agnes, R. S., Doane, T. L., Kenney, M. E., Broome, A. M., Burda, C., & Basilion, J. P. 2011a. Addressing Brain Tumors with Targeted Gold Nanoparticles: A New Gold Standard for Hydrophobic Drug Delivery? ***Small***.

Cheng, Y., Meyers, J. D., Broome, A. M., Kenney, M. E., Basilion, J. P., & Burda, C. 2011b. Deep penetration of a PDT drug into tumors by noncovalent drug-gold nanoparticle conjugates. ***J.Am.Chem.Soc.***, 133(8): 2583-2591.

Cheng, Y., Samia, A. C., Li, J., Kenney, M. E., Resnick, A., & Burda, C. 2010. Delivery and efficacy of a cancer drug as a function of the bond to the gold nanoparticle surface. ***Langmuir***, 26(4): 2248-2255.

Cherian, A. K., Rana, A. C., & Jain, S. K. 2000. Self-assembled carbohydrate-stabilized ceramic nanoparticles for the parenteral delivery of insulin. ***Drug Dev.Ind.Pharm.***, 26(4): 459-463.

Choi J & Wang NS 2011. Nanoparticles in Biomedical Applications and Their Safety Concerns. In Reza Fazel-Rezai (Ed.), *Biomedical Engineering - From Theory to Applications*.

Choi, H. S., Ashitate, Y., Lee, J. H., Kim, S. H., Matsui, A., Insin, N., Bawendi, M. G., Semmler-Behnke, M., Frangioni, J. V., & Tsuda, A. 2010. Rapid translocation of nanoparticles from the lung airspaces to the body. ***Nature Biotechnology***, 28(12): 1300-U113.

Choi, H. S., Liu, W., Misra, P., Tanaka, E., Zimmer, J. P., Itty, I. B., Bawendi, M. G., & Frangioni, J. V. 2007. Renal clearance of quantum dots. ***Nat.Biotechnol.***, 25(10): 1165-1170.

Clark B & Smith DA 1981. *An Introduction to Pharmacokinetics*. Blackwell Scientific Publications.

Compagnin, C., Bau, L., Mognato, M., Celotti, L., Miotto, G., Arduini, M., Moret, F., Fede, C., Selvestrel, F., Rio, E., I, Mancin, F., & Reddi, E. 2009. The cellular uptake of meta-tetra(hydroxyphenyl)chlorin entrapped in organically modified silica nanoparticles is mediated by serum proteins. ***Nanotechnology.***, 20(34): 345101.

Compagnin, C., Moret, F., Celotti, L., Miotto, G., Woodhams, J. H., MacRobert, A. J., Scheglmann, D., Iratni, S., & Reddi, E. 2011. Meta-tetra(hydroxyphenyl)chlorin-loaded liposomes sterically

stabilised with poly(ethylene glycol) of different length and density: characterisation, in vitro cellular uptake and phototoxicity. ***Photochem.Photobiol.Sci.***, 10(11): 1751-1759.

Conway, C. L., Walker, I., Bell, A., Roberts, D. J., Brown, S. B., & Vernon, D. I. 2008. In vivo and in vitro characterisation of a protoporphyrin IX-cyclic RGD peptide conjugate for use in photodynamic therapy. ***Photochem.Photobiol.Sci.***, 7(3): 290-298.

Copper, M. P., Tan, I. B., Oppelaar, H., Ruevekamp, M. C., & Stewart, F. A. 2003. Meta-tetra(hydroxyphenyl)chlorin photodynamic therapy in early-stage squamous cell carcinoma of the head and neck. ***Arch.Otolaryngol.Head Neck Surg.***, 129(7): 709-711.

Couleaud, P., Morosini, V., Frochot, C., Richeter, S., Raehm, L., & Durand, J. O. 2010. Silica-based nanoparticles for photodynamic therapy applications. ***Nanoscale.***, 2(7): 1083-1095.

Couvreur, P., Kante, B., Grislain, L., Roland, M., & Speiser, P. 1982. Toxicity of polyalkylcyanoacrylate nanoparticles II: Doxorubicin-loaded nanoparticles. ***J.Pharm.Sci.***, 71(7): 790-792.

Couvreur, P. & Vauthier, C. 2006. Nanotechnology: intelligent design to treat complex disease. ***Pharm.Res.***, 23(7): 1417-1450.

Cramers, P., Ruevekamp, M., Oppelaar, H., Dalesio, O., Baas, P., & Stewart, F. A. 2003. Foscan (R) uptake and tissue distribution in relation to photodynamic efficacy. ***British Journal of Cancer***, 88(2): 283-290.

Crosasso, P., Ceruti, M., Brusa, P., Arpicco, S., Dosio, F., & Cattel, L. 2000. Preparation, characterization and properties of sterically stabilized paclitaxel-containing liposomes. ***J Control Release***, 63(1-2): 19-30.

Crotts, G. & Park, T. G. 1998. Protein delivery from poly(lactic-co-glycolic acid) biodegradable microspheres: release kinetics and stability issues. ***Journal of Microencapsulation***, 15(6): 699-713.

D'Hallewin, M. A., Kochetkov, D., Viry-Babel, Y., Leroux, A., Werkmeister, E., Dumas, D., Grafe, S., Zorin, V., Guillemin, F., & Bezdetnaya, L. 2008. Photodynamic therapy with intratumoral administration of Lipid-Based mTHPC in a model of breast cancer recurrence. ***Lasers Surg.Med.***, 40(8): 543-549.

Dadashzadeh, S., Vali, A. M., & Rezaie, M. 2008. The effect of PEG coating on in vitro cytotoxicity and in vivo disposition of topotecan loaded liposomes in rats. ***Int.J Pharm.***, 353(1-2): 251-259.

Damen, J., Regts, J., & Scherphof, G. 1981. Transfer and exchange of phospholipid between small unilamellar liposomes and rat plasma high density lipoproteins. Dependence on cholesterol content and phospholipid composition. ***Biochim.Biophys.Acta***, 665(3): 538-545.

Danhier, F., Ansorena, E., Silva, J. M., Coco, R., Le Breton, A., & Preat, V. 2012. PLGA-based nanoparticles: An overview of biomedical applications. ***Journal of Controlled Release***, 161(2): 505-522.

Dash, S., Mishra, S., Patel, S., & Mishra, B. K. 2008. Organically modified silica: synthesis and applications due to its surface interaction with organic molecules. ***Adv.Colloid Interface Sci.***, 140(2): 77-94.

Dawson, T. R. 2002. *Pharmacology: Second Edition*. World Publishing Company.

de Nonancourt-Didion, M., Gueant, J. L., Adjalla, C., Chery, C., Hatier, R., & Namour, F. 2001. Overexpression of folate binding protein alpha is one of the mechanism explaining the adaptation of HT29 cells to high concentration of methotrexate. ***Cancer Lett.***, 171(2): 139-145.

de Paula, C. S., Tedesco, A. C., Primo, F. L., Vilela, J. M., Andrade, M. S., & Mosqueira, V. C. 2013. Chloroaluminium phthalocyanine polymeric nanoparticles as photosensitisers: photophysical and physicochemical characterisation, release and phototoxicity in vitro. ***Eur.J Pharm.Sci.***, 49(3): 371-381.

De Rosa, F. S. & Bentley, M. V. L. B. 2000. Photodynamic therapy of skin cancers: Sensitizers, clinical studies and future directives. ***Pharmaceutical Research***, 17(12): 1447-1455.

Decuzzi, P., Godin, B., Tanaka, T., Lee, S. Y., Chiappini, C., Liu, X., & Ferrari, M. 2010. Size and shape effects in the biodistribution of intravascularly injected particles. ***J Control Release***, 141(3): 320-327.

Derakhshandeh, K., Erfan, M., & Dadashzadeh, S. 2007. Encapsulation of 9-nitrocamptothecin, a novel anticancer drug, in biodegradable nanoparticles: Factorial design, characterization and release kinetics. ***European Journal of Pharmaceutics and Biopharmaceutics***, 66(1): 34-41.

Deribe, Y. L., Pawson, T., & Dikic, I. 2010. Post-translational modifications in signal integration. ***Nat.Struct.Mol.Biol.***, 17(6): 666-672.

Derycke, A. S. & de Witte, P. A. 2004. Liposomes for photodynamic therapy. ***Advanced Drug Delivery Reviews***, 56(1): 17-30.

Desai, J. P., Pillarisetti, A., & Brooks, A. D. 2007. Engineering approaches to biomanipulation. ***Annu.Rev.Biomed.Eng***, 9: 35-53.

Desgrosellier, J. S. & Cheresh, D. A. 2010. Integrins in cancer: biological implications and therapeutic opportunities. ***Nature Reviews Cancer***, 10(1): 9-22.

Dhar, S., Gu, F. X., Langer, R., Farokhzad, O. C., & Lippard, S. J. 2008. Targeted delivery of cisplatin to prostate cancer cells by aptamer functionalized Pt(IV) prodrug-PLGA-PEG nanoparticles. ***Proceedings of the National Academy of Sciences of the United States of America***, 105(45): 17356-17361.

Diamond, I., Jaenicke, R., Wilson, C. B., Mcdonagh, A. F., Nielsen, S., & Granelli, S. G. 1972. Photodynamic Therapy of Malignant Tumors. ***Lancet***, 2(7788): 1175-&.

Diksha & Roy, I. 2012. Synthesis, surface modification, characterization, and biomedical in vitro applications of organically modified silica (ORMOSIL) nanoparticles. ***Methods Mol.Biol.***, 906: 365-379.

Ding, H., Sumer, B. D., Kessinger, C. W., Dong, Y., Huang, G., Boothman, D. A., & Gao, J. 2011. Nanoscopic micelle delivery improves the photophysical properties and efficacy of photodynamic therapy of protoporphyrin IX. ***J Control Release***, 151(3): 271-277.

Doane, T. L. & Burda, C. 2012. The unique role of nanoparticles in nanomedicine: imaging, drug delivery and therapy. ***Chem.Soc.Rev.***, 41(7): 2885-2911.

Dolmans, D. E., Fukumura, D., & Jain, R. K. 2003. Photodynamic therapy for cancer. ***Nature Reviews Cancer***, 3(5): 380-387.

Dos, S. N., Allen, C., Doppen, A. M., Anantha, M., Cox, K. A., Gallagher, R. C., Karlsson, G., Edwards, K., Kenner, G., Samuels, L., Webb, M. S., & Bally, M. B. 2007. Influence of poly(ethylene glycol) grafting density and polymer length on liposomes: relating plasma circulation lifetimes to protein binding. ***Biochim.Biophys.Acta***, 1768(6): 1367-1377.

Dougherty, T. J., Gomer, C. J., Henderson, B. W., Jori, G., Kessel, D., Korbelik, M., Moan, J., & Peng, Q. 1998. Photodynamic therapy. ***Journal of the National Cancer Institute***, 90(12): 889-905.

Dougherty, T. J., Gomer, C. J., & Weishaupt, K. R. 1976. Energetics and efficiency of photoinactivation of murine tumor cells containing hematoporphyrin. ***Cancer Res.***, 36(7 PT 1): 2330-2333.

Dougherty, T. J., Grindey, G. B., Fiel, R., Weishaupt, K. R., & Boyle, D. G. 1975. Photoradiation therapy. II. Cure of animal tumors with hematoporphyrin and light. ***J.Natl.Cancer Inst.***, 55(1): 115-121.

Dreborg, S. & Akerblom, E. B. 1990. Immunotherapy with monomethoxypolyethylene glycol modified allergens. ***Crit Rev.Ther.Drug Carrier Syst.***, 6(4): 315-365.

Drummond, D. C., Meyer, O., Hong, K., Kirpotin, D. B., & Papahadjopoulos, D. 1999. Optimizing liposomes for delivery of chemotherapeutic agents to solid tumors. ***Pharmacol.Rev.***, 51(4): 691-743.

Duncan, R. 2006. Polymer conjugates as anticancer nanomedicines. ***Nature Reviews Cancer***, 6(9): 688-701.

El-Samaligy, M. S. & Rohdewald, P. 1983. Reconstituted collagen nanoparticles, a novel drug carrier delivery system. ***J.Pharm.Pharmacol.***, 35(8): 537-539.

Elnakat, H. & Ratnam, M. 2004. Distribution, functionality and gene regulation of folate receptor isoforms: implications in targeted therapy. ***Adv.Drug Deliv Rev.***, 56(8): 1067-1084.

Erbas, S., Gorgulu, A., Kocakusakogullari, M., & Akkaya, E. U. 2009. Non-covalent functionalized SWNTs as delivery agents for novel Bodipy-based potential PDT sensitizers. ***Chem.Commun.(Camb.)***,(33): 4956-4958.

Esmaeili, F., Ghahremani, M. H., Esmaeili, B., Khoshayand, M. R., Atyabi, F., & Dinarvand, R. 2008. PLGA nanoparticles of different surface properties: Preparation and evaluation of their body distribution. ***International Journal of Pharmaceutics***, 349(1-2): 249-255.

Fadel, M., Kassab, K., & Youssef, T. 2010. Photodynamic efficacy of hypericin targeted by two delivery techniques to hepatocellular carcinoma cells. ***Lasers Med.Sci.***, 25(5): 675-683.

Fan, Z., Senapati, D., Khan, S. A., Singh, A. K., Hamme, A., Yust, B., Sardar, D., & Ray, P. C. 2013. Popcorn-shaped magnetic core-plasmonic shell multifunctional nanoparticles for the targeted magnetic separation and enrichment, label-free SERS imaging, and photothermal destruction of multidrug-resistant bacteria. ***Chemistry.***, 19(8): 2839-2847.

Farokhzad, O. C. 2008. Nanotechnology for drug delivery: the perfect partnership. ***Expert.Opin.Drug Deliv.***, 5(9): 927-929.

Farokhzad, O. C. & Langer, R. 2006. Nanomedicine: developing smarter therapeutic and diagnostic modalities. ***Adv.Drug Deliv.Rev.***, 58(14): 1456-1459.

Farokhzad, O. C. & Langer, R. 2009. Impact of nanotechnology on drug delivery. ***ACS Nano.***, 3(1): 16-20.

Ferjancic, S., Gil-Bernabe, A. M., Hill, S. A., Allen, P. D., Richardson, P., Sparey, T., Savory, E., McGuffog, J., & Muschel, R. J. 2013. VCAM-1 and VAP-1 recruit myeloid cells that promote pulmonary metastasis in mice. ***Blood***, 121(16): 3289-3297.

Ferlay J, Shin HR, Bray F, Forman D, Mathers C, & Parkin DM. GLOBOCAN 2008 v2.0, Cancer Incidence and Mortality Worldwide: IARC CancerBase No. 10 [Internet]. 2008. Lyon, France: International Agency for Research on Cancer; 2010. Available from: http://globocan.iarc.fr.

Fessi, H., Puisieux, F., Devissaguet, J. P., Ammoury, N., & Benita, S. 1989. Nanocapsule Formation by Interfacial Polymer Deposition Following Solvent Displacement. ***International Journal of Pharmaceutics***, 55(1): R1-R4.

Fielding, D. I., Buonaccorsi, G. A., MacRobert, A. J., Hanby, A. M., Hetzel, M. R., & Bown, S. G. 1999. Fine-needle interstitial photodynamic therapy of the lung parenchyma: photosensitizer distribution and morphologic effects of treatment. ***Chest***, 115(2): 502-510.

Finnie, P. & Homma, Y. 2000. Stability-instability transitions in silicon crystal growth. ***Phys.Rev.Lett.***, 85(15): 3237-3240.

Foged, C., Brodin, B., Frokjaer, S., & Sundblad, A. 2005. Particle size and surface charge affect particle uptake by human dendritic cells in an in vitro model. ***International Journal of Pharmaceutics***, 298(2): 315-322.

Fonseca, C., Simoes, S., & Gaspar, R. 2002. Paclitaxel-loaded PLGA nanoparticles: preparation, physicochemical characterization and in vitro anti-tumoral activity. ***Journal of Controlled Release***, 83(2): 273-286.

Foote, C. S. 1991. Definition of type I and type II photosensitized oxidation. ***Photochem.Photobiol.***, 54(5): 659.

Fraikin, J. L., Teesalu, T., McKenney, C. M., Ruoslahti, E., & Cleland, A. N. 2011. A high-throughput label-free nanoparticle analyser. ***Nat.Nanotechnol.***, 6(5): 308-313.

Frederiksen, L., Anton, K., van, H. P., Keller, H. R., & Leuenberger, H. 1997. Preparation of liposomes encapsulating water-soluble compounds using supercritical carbon dioxide. ***J Pharm.Sci.***, 86(8): 921-928.

Freitas, I. 1985. Role of hypoxia in photodynamic therapy of tumors. ***Tumori***, 71(3): 251-259.

Frochot, C., Di, S. B., Vanderesse, R., Belgy, M. J., Dodeller, M., Guillemin, F., Viriot, M. L., & Barberi-Heyob, M. 2007. Interest of RGD-containing linear or cyclic peptide targeted tetraphenylchlorin as novel photosensitizers for selective photodynamic activity. ***Bioorg.Chem.***, 35(3): 205-220.

Frohlich, E. 2012. The role of surface charge in cellular uptake and cytotoxicity of medical nanoparticles. ***Int.J Nanomedicine***, 7: 5577-5591.

Funato, K., Yoda, R., & Kiwada, H. 1992. Contribution of complement system on destabilization of liposomes composed of hydrogenated egg phosphatidylcholine in rat fresh plasma. ***Biochim.Biophys.Acta***, 1103(2): 198-204.

Gaber, M. H., Hong, K., Huang, S. K., & Papahadjopoulos, D. 1995. Thermosensitive sterically stabilized liposomes: formulation and in vitro studies on mechanism of doxorubicin release by bovine serum and human plasma. ***Pharm.Res.***, 12(10): 1407-1416.

Gamaleia, N. F., Shishko, E. D., Dolinsky, G. A., Shcherbakov, A. B., Usatenko, A. V., & Kholin, V. V. 2010. Photodynamic activity of hematoporphyrin conjugates with gold nanoparticles: experiments in vitro. ***Exp.Oncol.***, 32(1): 44-47.

Garcia-Diaz, M., Nonell, S., Villanueva, A., Stockert, J. C., Canete, M., Casado, A., Mora, M., & Sagrista, M. L. 2011. Do folate-receptor targeted liposomal photosensitizers enhance photodynamic therapy selectivity? ***Biochim.Biophys.Acta***, 1808(4): 1063-1071.

Garin-Chesa, P., Campbell, I., Saigo, P. E., Lewis, J. L., Jr., Old, L. J., & Rettig, W. J. 1993. Trophoblast and ovarian cancer antigen LK26. Sensitivity and specificity in immunopathology and molecular identification as a folate-binding protein. ***Am.J Pathol.***, 142(2): 557-567.

Garrier, J., Bezdetnaya, L., Barlier, C., Grafe, S., Guillemin, F., & D'Hallewin, M. A. 2011. Foslip (R)-based photodynamic therapy as a means to improve wound healing. ***Photodiagnosis and Photodynamic Therapy***, 8(4): 321-327.

Garrier, J., Bressenot, A., Grafe, S., Marchal, S., Mitra, S., Foster, T. H., Guillemin, F., & Bezdetnaya, L. 2010. Compartmental targeting for mTHPC-based photodynamic treatment in vivo: Correlation of efficiency, pharmacokinetics, and regional distribution of apoptosis. ***Int.J.Radiat.Oncol.Biol.Phys.***, 78(2): 563-571.

Garrigues, H. J., Rubinchikova, Y. E., DiPersio, C. M., & Rose, T. M. 2008. Integrin alpha(V)beta(3) binds to the RGD motif of glycoprotein B of Kaposi's sarcoma-associated herpesvirus and functions as an RGD-dependent entry receptor. ***Journal of Virology***, 82(3): 1570-1580.

Gary-Bobo, M., Mir, Y., Rouxel, C., Brevet, D., Basile, I., Maynadier, M., Vaillant, O., Mongin, O., Blanchard-Desce, M., Morere, A., Garcia, M., Durand, J. O., & Raehm, L. 2011. Mannose-functionalized mesoporous silica nanoparticles for efficient two-photon photodynamic therapy of solid tumors. ***Angew.Chem.Int.Ed Engl.***, 50(48): 11425-11429.

Gbadamosi, J. K., Hunter, A. C., & Moghimi, S. M. 2002. PEGylation of microspheres generates a heterogeneous population of particles with differential surface characteristics and biological performance. ***FEBS Lett.***, 532(3): 338-344.

Generalov, R., Kavaliauskiene, S., Westrom, S., Chen, W., Kristensen, S., & Juzenas, P. 2011. Entrapment in phospholipid vesicles quenches photoactivity of quantum dots. ***Int.J.Nanomedicine.***, 6: 1875-1888.

Gillies, E. R. & Frechet, J. M. 2005. Dendrimers and dendritic polymers in drug delivery. ***Drug Discov.Today***, 10(1): 35-43.

Glanzmann, T., Hadjur, C., Zellweger, M., Grosiean, P., Forrer, M., Ballini, J. P., Monnier, P., van den, B. H., Lim, C. K., & Wagnieres, G. 1998. Pharmacokinetics of tetra(m-hydroxyphenyl)chlorin in human plasma and individualized light dosimetry in photodynamic therapy. ***Photochem.Photobiol.***, 67(5): 596-602.

Gottfried, V., Peled, D., Winkelman, J. W., & Kimel, S. 1988. Photosensitizers in organized media: singlet oxygen production and spectral properties. ***Photochem.Photobiol.***, 48(2): 157-163.

Govender, T., Stolnik, S., Garnett, M. C., Illum, L., & Davis, S. S. 1999. PLGA nanoparticles prepared by nanoprecipitation: drug loading and release studies of a water soluble drug. ***J Control Release***, 57(2): 171-185.

Gratton, S. E., Ropp, P. A., Pohlhaus, P. D., Luft, J. C., Madden, V. J., Napier, M. E., & Desimone, J. M. 2008. The effect of particle design on cellular internalization pathways. ***Proc.Natl.Acad.Sci.U.S.A***, 105(33): 11613-11618.

Gravier, J., Schneider, R., Frochot, C., Bastogne, T., Schmitt, F., Didelon, J., Guillemin, F., & Barberi-Heyob, M. 2008. Improvement of meta-tetra(hydroxyphenyl)chlorin-like photosensitizer selectivity with folate-based targeted delivery. synthesis and in vivo delivery studies. ***J.Med.Chem.***, 51(13): 3867-3877.

Greish, K., Thiagarajan, G., Herd, H., Price, R., Bauer, H., Hubbard, D., Burckle, A., Sadekar, S., Yu, T., Anwar, A., Ray, A., & Ghandehari, H. 2012. Size and surface charge significantly influence the toxicity of silica and dendritic nanoparticles. ***Nanotoxicology***, 6(7): 713-723.

Gu, F., Langer, R., & Farokhzad, O. C. 2009. Formulation/preparation of functionalized nanoparticles for in vivo targeted drug delivery. ***Methods Mol.Biol.***, 544: 589-598.

Guise, V., Drouin, J. Y., Benoit, J., Mahuteau, J., Dumont, P., & Couvreur, P. 1990. Vidarabine-loaded nanoparticles: a physicochemical study. ***Pharm.Res.***, 7(7): 736-741.

Guo, H., Qian, H., Sun, S., Sun, D., Yin, H., Cai, X., Liu, Z., Wu, J., Jiang, T., & Liu, X. 2011. Hollow mesoporous silica nanoparticles for intracellular delivery of fluorescent dye. ***Chem.Cent.J***, 5(1): 1.

Guo, W. & Lee, R. L. 1999. Receptor-targeted gene delivery via folate-conjugated polyethylenimine. ***AAPS.PharmSci.***, 1(4): E19.

Gupta, A. K. & Gupta, M. 2005. Synthesis and surface engineering of iron oxide nanoparticles for biomedical applications. ***Biomaterials***, 26(18): 3995-4021.

Guzman, F. Pharmacokinetics video and PowerPoint: volume of distribution and factors that affect it. 22-1-2009.

Haase, M. & Schafer, H. 2011. Upconverting nanoparticles. ***Angew.Chem.Int.Ed Engl.***, 50(26): 5808-5829.

Han, D., Zhu, G., Wu, C., Zhu, Z., Chen, T., Zhang, X., & Tan, W. 2013. Engineering a cell-surface aptamer circuit for targeted and amplified photodynamic cancer therapy. ***ACS Nano.***, 7(3): 2312-2319.

Hansch, A., Frey, O., Gajda, M., Susanna, G., Boettcher, J., Brauer, R., & Kaiser, W. A. 2008. Photodynamic treatment as a novel approach in the therapy of arthritic joints. ***Lasers Surg.Med.***, 40(4): 265-272.

Harada, M., Woodhams, J., MacRobert, A. J., Feneley, M. R., Kato, H., & Bown, S. G. 2005. The vascular response to photodynamic therapy with ATX-S10Na(II) in the normal rat colon. ***J Photochem.Photobiol.B***, 79(3): 223-230.

Harris, A. L., Nicholson, S., Sainsbury, R., Wright, C., & Farndon, J. 1992. Epidermal growth factor receptor and other oncogenes as prognostic markers. ***J Natl.Cancer Inst.Monogr***,(11): 181-187.

Hatz, S., Lambert, J. D., & Ogilby, P. R. 2007. Measuring the lifetime of singlet oxygen in a single cell: addressing the issue of cell viability. ***Photochem.Photobiol.Sci.***, 6(10): 1106-1116.

He, J., Larkin, H. E., Li, Y. S., Rihter, D., Zaidi, S. I., Rodgers, M. A., Mukhtar, H., Kenney, M. E., & Oleinick, N. L. 1997. The synthesis, photophysical and photobiological properties and in vitro structure-activity relationships of a set of silicon phthalocyanine PDT photosensitizers. ***Photochem.Photobiol.***, 65(3): 581-586.

He, X., Nie, H., Wang, K., Tan, W., Wu, X., & Zhang, P. 2008. In vivo study of biodistribution and urinary excretion of surface-modified silica nanoparticles. ***Anal.Chem.***, 80(24): 9597-9603.

He, X., Wu, X., Wang, K., Shi, B., & Hai, L. 2009. Methylene blue-encapsulated phosphonate-terminated silica nanoparticles for simultaneous in vivo imaging and photodynamic therapy. ***Biomaterials***, 30(29): 5601-5609.

Helm, C. A., Israelachvili, J. N., & McGuiggan, P. M. 1992. Role of hydrophobic forces in bilayer adhesion and fusion. ***Biochemistry***, 31(6): 1794-1805.

Henderson, B. W. & Bellnier, D. A. 1989a. Tissue Localization of Photosensitizers and the Mechanism of Photodynamic Tissue Destruction. ***Ciba Foundation Symposia***, 146: 112-130.

Henderson, B. W. & Fingar, V. H. 1989b. Oxygen Limitation of Direct Tumor-Cell Kill During Photodynamic Treatment of A Murine Tumor-Model. ***Photochemistry and Photobiology***, 49(3): 299-304.

Henderson, B. W., Vaughan, L., Bellnier, D. A., van, L. H., Johnson, P. G., & Oseroff, A. R. 1995. Photosensitization of murine tumor, vasculature and skin by 5-aminolevulinic acid-induced porphyrin. ***Photochem.Photobiol.***, 62(4): 780-789.

Hilgenbrink, A. R. & Low, P. S. 2005. Folate receptor-mediated drug targeting: from therapeutics to diagnostics. ***J Pharm.Sci.***, 94(10): 2135-2146.

Hirsch, L. R., Gobin, A. M., Lowery, A. R., Tam, F., Drezek, R. A., Halas, N. J., & West, J. L. 2006. Metal nanoshells. ***Ann.Biomed.Eng***, 34(1): 15-22.

Hocine, O., Gary-Bobo, M., Brevet, D., Maynadier, M., Fontanel, S., Raehm, L., Richeter, S., Loock, B., Couleaud, P., Frochot, C., Charnay, C., Derrien, G., Smaihi, M., Sahmoune, A., Morere, A., Maillard, P., Garcia, M., & Durand, J. O. 2010. Silicalites and Mesoporous Silica Nanoparticles for photodynamic therapy. ***Int.J Pharm.***, 402(1-2): 221-230.

Hoedemakers, R. M., Vossebeld, P. J., Daemen, T., & Scherphof, G. L. 1993. Functional characteristics of the rat liver macrophage population after a single intravenous injection of liposome-encapsulated muramyl peptides. ***J.Immunother.Emphasis.Tumor Immunol.***, 13(4): 252-260.

Hofheinz, R. D., Gnad-Vogt, S. U., Beyer, U., & Hochhaus, A. 2005. Liposomal encapsulated anti-cancer drugs. ***Anticancer Drugs***, 16(7): 691-707.

Hong RL 2004. Liposomal anti-cancer drug researches the myth of long circulation. ***J Chinese Oncol Soc***, 20: 10-21.

Hopkinson, H. J., Vernon, D. I., & Brown, S. B. 1999. Identification and partial characterization of an unusual distribution of the photosensitizer meta-tetrahydroxyphenyl chlorin (temoporfin) in human plasma. ***Photochem.Photobiol.***, 69(4): 482-488.

Hopper, C. 2000. Photodynamic therapy: a clinical reality in the treatment of cancer. ***Lancet Oncol.***, 1: 212-219.

Hopper, C., Suhr, M., Jones, L., Nakanishi, H., Jaeger, R., & Brookes, J. 2000. Interstitial photodynamic therapy in head and neck cancer. ***British Journal of Cancer***, 83: 48.

Hrkach, J. S., Peracchia, M. T., Domb, A., Lotan, N., & Langer, R. 1997. Nanotechnology for biomaterials engineering: Structural characterization of amphiphilic polymeric nanoparticles by H-1 NMR spectroscopy. ***Biomaterials***, 18(1): 27-30.

Huang YY, Sharma SK, Dai T, Hoon C, Yaroslavsky A, Garcia-Diaz M, Chang J, Chiang LY, & Hamblin, M. R. Can nanotechnology potentiate photodynamic therapy? Nanotechnology Reviews 1[2], 111-146. 1-12-2012.

Huang, P., Lin, J., Yang, D., Zhang, C., Li, Z., & Cui, D. 2011a. Photosensitizer-loaded dendrimer-modified multi-walled carbon nanotubes for photodynamic therapy. ***J.Control Release***, 152 Suppl 1: e33-e34.

Huang, P., Xu, C., Lin, J., Wang, C., Wang, X., Zhang, C., Zhou, X., Guo, S., & Cui, D. 2011b. Folic Acid-conjugated Graphene Oxide loaded with Photosensitizers for Targeting Photodynamic Therapy. ***Theranostics.***, 1: 240-250.

Hunter, C. A. & Sanders, J. K. M. 1990. The porphyrin handbook. ***J.Am.Chem.Soc***, 112(14): 5525.

Ichikawa, K., Hikita, T., Maeda, N., Takeuchi, Y., Namba, Y., & Oku, N. 2004. PEGylation of liposome decreases the susceptibility of liposomal drug in cancer photodynamic therapy. ***Biol.Pharm.Bull.***, 27(3): 443-444.

Idris, N. M., Gnanasammandhan, M. K., Zhang, J., Ho, P. C., Mahendran, R., & Zhang, Y. 2012. In vivo photodynamic therapy using upconversion nanoparticles as remote-controlled nanotransducers. ***Nat.Med.***, 18(10): 1580-1585.

Immordino, M. L., Brusa, P., Arpicco, S., Stella, B., Dosio, F., & Cattel, L. 2003. Preparation, characterization, cytotoxicity and pharmacokinetics of liposomes containing docetaxel. ***J.Control Release***, 91(3): 417-429.

Immordino, M. L., Dosio, F., & Cattel, L. 2006. Stealth liposomes: review of the basic science, rationale, and clinical applications, existing and potential. ***Int.J.Nanomedicine.***, 1(3): 297-315.

Ivanov, S., Zhuravsky, S., Yukina, G., Tomson, V., Korolev, D., & Galagudza, M. 2012. In Vivo Toxicity of Intravenously Administered Silica and Silicon Nanoparticles. ***Materials***, 5(10): 1873-1889.

Jablonski, A. 1933. Efficiency of Anti-Stokes Fluorescence in Dyes. ***Nature***, 131: 839-840.

Jain, A. K., Das, M., Swarnakar, N. K., & Jain, S. 2011. Engineered PLGA Nanoparticles: An Emerging Delivery Tool in Cancer Therapeutics. ***Critical Reviews in Therapeutic Drug Carrier Systems***, 28(1): 1-45.

Jain, R. K. 1994. Barriers to drug delivery in solid tumors. ***Sci.Am.***, 271(1): 58-65.

Jain, R. K. & Stylianopoulos, T. 2010. Delivering nanomedicine to solid tumors. ***Nat.Rev.Clin.Oncol.***, 7(11): 653-664.

Jain, T. K., Roy, I., De, T. K., & Maitra, A. 1998. Nanometer silica particles encapsulating active compounds: A novel ceramic drug carrier. ***Journal of the American Chemical Society***, 120(43): 11092-11095.

Jiang, W., Kim, B. Y., Rutka, J. T., & Chan, W. C. 2008. Nanoparticle-mediated cellular response is size-dependent. ***Nat.Nanotechnol.***, 3(3): 145-150.

Jin, H., Heller, D. A., Sharma, R., & Strano, M. S. 2009. Size-dependent cellular uptake and expulsion of single-walled carbon nanotubes: single particle tracking and a generic uptake model for nanoparticles. ***ACS Nano.***, 3(1): 149-158.

Jones, H. J., Vernon, D. I., & Brown, S. B. 2003. Photodynamic therapy effect of m-THPC (Foscan (R)) in vivo: correlation with pharmacokinetics. ***British Journal of Cancer***, 89(2): 398-404.

Jori, G. 1989. Invivo Transport and Pharmacokinetic Behavior of Tumor Photosensitizers. ***Ciba Foundation Symposia***, 146: 78-94.

Jori, G. 1996. Tumour photosensitizers: approaches to enhance the selectivity and efficiency of photodynamic therapy. ***J Photochem.Photobiol.B***, 36(2): 87-93.

Jori, G., Beltramini, M., Reddi, E., Salvato, B., Pagnan, A., Ziron, L., Tomio, L., & Tsanov, T. 1984. Evidence for A Major Role of Plasma-Lipoproteins As Hematoporphyrin Carriers Invivo. ***Cancer Letters***, 24(3): 291-297.

Jori, G. & Reddi, E. 1993. The role of lipoproteins in the delivery of tumour-targeting photosensitizers. ***Int.J Biochem.***, 25(10): 1369-1375.

Juarranz, A., Jaen, P., Sanz-Rodriguez, F., Cuevas, J., & Gonzalez, S. 2008. Photodynamic therapy of cancer. Basic principles and applications. ***Clin.Transl.Oncol.***, 10(3): 148-154.

Juzenas, P., Chen, W., Sun, Y. P., Coelho, M. A., Generalov, R., Generalova, N., & Christensen, I. L. 2008. Quantum dots and nanoparticles for photodynamic and radiation therapies of cancer. ***Adv.Drug Deliv.Rev.***, 60(15): 1600-1614.

Kamen, B. A. & Capdevila, A. 1986. Receptor-Mediated Folate Accumulation Is Regulated by the Cellular Folate Content. ***Proceedings of the National Academy of Sciences of the United States of America***, 83(16): 5983-5987.

Kamen, B. A. & Smith, A. K. 2012. Farletuzumab, an anti-folate receptor alpha antibody, does not block binding of folate or anti-folates to receptor nor does it alter the potency of anti-folates in vitro. ***Cancer Chemother.Pharmacol.***, 70(1): 113-120.

Kamen, B. A., Wang, M. T., Streckfuss, A. J., Peryea, X., & Anderson, R. G. 1988. Delivery of folates to the cytoplasm of MA104 cells is mediated by a surface membrane receptor that recycles. ***J Biol.Chem.***, 263(27): 13602-13609.

Kameyama, N., Matsuda, S., Itano, O., Ito, A., Konno, T., Arai, T., Ishihara, K., Ueda, M., & Kitagawa, Y. 2011. Photodynamic therapy using an anti-EGF receptor antibody complexed with verteporfin nanoparticles: a proof of concept study. ***Cancer Biother.Radiopharm.***, 26(6): 697-704.

Kascakova, S., Kruijt, B., de Bruijn, H. S., van der Ploeg-van den Heuvel, Robinson, D. J., Sterenborg, H. J., & Amelink, A. 2008. Ex vivo quantification of mTHPC concentration in tissue: influence of chemical extraction on the optical properties. ***J.Photochem.Photobiol.B***, 91(2-3): 99-107.

Kasravi, F. B., Wang, X. D., Guo, W. D., Andersson, R., Norgren, L., Jeppsson, B., & Bengmark, S. 1995. Reticuloendothelial system function in acute liver injury induced by D-galactosamine. ***Journal of Hepatology***, 23(6): 727-733.

Kato, K., Chin, K., Yoshikawa, T., Yamaguchi, K., Tsuji, Y., Esaki, T., Sakai, K., Kimura, M., Hamaguchi, T., Shimada, Y., Matsumura, Y., & Ikeda, R. 2012. Phase II study of NK105, a paclitaxel-incorporating micellar nanoparticle, for previously treated advanced or recurrent gastric cancer. ***Invest New Drugs***, 30(4): 1621-1627.

Kawasaki, E. S. & Player, A. 2005. Nanotechnology, nanomedicine, and the development of new, effective therapies for cancer. ***Nanomedicine.***, 1(2): 101-109.

Kelly, C., Jefferies, C., & Cryan, S. A. 2011. Targeted liposomal drug delivery to monocytes and macrophages. ***J Drug Deliv.***, 2011: 727241.

Kelly, J. F., Snell, M. E., & Berenbaum, M. C. 1975. Photodynamic destruction of human bladder carcinoma. ***Br.J.Cancer***, 31(2): 237-244.

Kessel, D. 1993. Sites of Photodamage by the Iminium Salt of A Copper Octaethylbenzochlorin. ***Photochemistry and Photobiology***, 58(4): 623-626.

Kiesslich, T., Berlanda, J., Plaetzer, K., Krammer, B., & Berr, F. 2007. Comparative characterization of the efficiency and cellular pharmacokinetics of Foscan- and Foslip-based photodynamic treatment in human biliary tract cancer cell lines. ***Photochem.Photobiol.Sci.***, 6(6): 619-627.

Kim, B., Han, G., Toley, B. J., Kim, C. K., Rotello, V. M., & Forbes, N. S. 2010. Tuning payload delivery in tumour cylindroids using gold nanoparticles. ***Nat.Nanotechnol.***, 5(6): 465-472.

Kim, J. W. & Lee, H. S. 2004. Tumor targeting by doxorubicin-RGD-4C peptide conjugate in an orthotopic mouse hepatoma model. ***Int.J Mol.Med.***, 14(4): 529-535.

Kim, T., Lee, C. H., Joo, S. W., & Lee, K. 2008. Kinetics of gold nanoparticle aggregation: experiments and modeling. ***J Colloid Interface Sci.***, 318(2): 238-243.

Klibanov, A. L., Maruyama, K., Beckerleg, A. M., Torchilin, V. P., & Huang, L. 1991. Activity of amphipathic poly(ethylene glycol) 5000 to prolong the circulation time of liposomes depends on the liposome size and is unfavorable for immunoliposome binding to target. ***Biochim.Biophys.Acta***, 1062(2): 142-148.

Klibanov, A. L., Maruyama, K., Torchilin, V. P., & Huang, L. 1990. Amphipathic polyethyleneglycols effectively prolong the circulation time of liposomes. ***FEBS Lett.***, 268(1): 235-237.

Kneuer, C., Sameti, M., Bakowsky, U., Schiestel, T., Schirra, H., Schmidt, H., & Lehr, C. M. 2000. A nonviral DNA delivery system based on surface modified silica-nanoparticles can efficiently transfect cells in vitro. ***Bioconjug.Chem.***, 11(6): 926-932.

Knight, S. F., Kundu, K., Joseph, G., Dikalov, S., Weiss, D., Murthy, N., & Taylor, W. R. 2012. Folate receptor-targeted antioxidant therapy ameliorates renal ischemia-reperfusion injury. ***J Am.Soc.Nephrol.***, 23(5): 793-800.

Kocbek, P., Teskac, K., Brozic, P., Rizner, T. L., Gobec, S., & Kristl, J. 2010. Effect of Free and in Poly(epsilon-caprolactone) Nanoparticles Incorporated New Type 1 17 beta-Hydroxysteroid Dehydrogenase Inhibitors on Cancer Cells. ***Current Nanoscience***, 6(1): 69-76.

Konan, Y. N., Berton, M., Gurny, R., & Allemann, E. 2003. Enhanced photodynamic activity of meso-tetra(4-hydroxyphenyl)porphyrin by incorporation into sub-200 nm nanoparticles. ***Eur.J Pharm.Sci.***, 18(3-4): 241-249.

Konan-Kouakou, Y. N., Boch, R., Gurny, R., & Allemann, E. 2005. In vitro and in vivo activities of verteporfin-loaded nanoparticles. ***J.Control Release***, 103(1): 83-91.

Korbelik, M. & Dougherty, G. J. 1999. Photodynamic therapy-mediated immune response against subcutaneous mouse tumors. ***Cancer Research***, 59(8): 1941-1946.

Korbelik, M. & Krosl, G. 1994a. Cellular-Levels of Photosensitizers in Tumors - the Role of Proximity to the Blood-Supply. ***British Journal of Cancer***, 70(4): 604-610.

Korbelik, M. & Krosl, G. 1994b. Enhanced Macrophage Cytotoxicity Against Tumor-Cells Treated with Photodynamic Therapy. ***Photochemistry and Photobiology***, 60(5): 497-502.

Korbelik, M., Krosl, G., Olive, P. L., & Chaplin, D. J. 1991. Distribution of Photofrin between tumour cells and tumour associated macrophages. ***Br.J Cancer***, 64(3): 508-512.

Kozlowska, M. K., Jurgens, B. F., Schacht, C. S., Gross, J., & de Loos, T. W. 2009. Phase behavior of hyperbranched polymer systems: experiments and application of the perturbed-chain polar SAFT equation of state. ***J.Phys.Chem.B***, 113(4): 1022-1029.

Krall, J. A., Beyer, E. M., & MacBeath, G. 2011. High- and low-affinity epidermal growth factor receptor-ligand interactions activate distinct signaling pathways. ***PLoS One***, 6(1): e15945.

Kranz, H., Ubrich, N., Maincent, P., & Bodmeier, R. 2000. Physicomechanical properties of biodegradable poly(D,L-lactide) and poly(D,L-lactide-co-glycolide) films in the dry and wet states. ***Journal of Pharmaceutical Sciences***, 89(12): 1558-1566.

Kratz, F. 2008. Albumin as a drug carrier: design of prodrugs, drug conjugates and nanoparticles. ***J.Control Release***, 132(3): 171-183.

Kren, A., Baeriswyl, V., Lehembre, F., Wunderlin, C., Strittmatter, K., Antoniadis, H., Fassler, R., Cavallaro, U., & Christofori, G. 2007. Increased tumor cell dissemination and cellular senescence in the absence of beta1-integrin function. ***EMBO J***, 26(12): 2832-2842.

Krol, S. 2012. Challenges in drug delivery to the brain: nature is against us. ***J Control Release***, 164(2): 145-155.

Kübler, A. C. 2005. Photodynamic therapy. ***Medical Laser Application***, 20(1): 37-45.

Kudinova, N. V. & Berezov, T. T. 2009. [Photodynamic therapy: search for ideal photosensitizer]. ***Biomed.Khim.***, 55(5): 558-569.

Kumar, R., Roy, I., Ohulchanskky, T. Y., Vathy, L. A., Bergey, E. J., Sajjad, M., & Prasad, P. N. 2010. In vivo biodistribution and clearance studies using multimodal organically modified silica nanoparticles. ***ACS Nano***, 4(2): 699-708.

Kumar, R., Roy, I., Ohulchanskyy, T. Y., Goswami, L. N., Bonoiu, A. C., Bergey, E. J., Tramposch, K. M., Maitra, A., & Prasad, P. N. 2008. Covalently dye-linked, surface-controlled, and bioconjugated organically modified silica nanoparticles as targeted probes for optical imaging. ***ACS Nano.***, 2(3): 449-456.

Kumari, A., Yadav, S. K., Pakade, Y. B., Singh, B., & Yadav, S. C. 2010. Development of biodegradable nanoparticles for delivery of quercetin. ***Colloids Surf.B Biointerfaces***, 80(2): 184-192.

Kunz, M. & Ibrahim, S. M. 2003. Molecular responses to hypoxia in tumor cells. ***Mol.Cancer***, 2: 23.

Kuwai, T., Nakamura, T., Sasaki, T., Kitadai, Y., Kim, J. S., Langley, R. R., Fan, D., Wang, X., Do, K. A., Kim, S. J., & Fidler, I. J. 2008. Targeting the EGFR, VEGFR, and PDGFR on colon cancer cells and stromal cells is required for therapy. ***Clin.Exp.Metastasis***, 25(4): 477-489.

Lai, C. W., Wang, Y. H., Lai, C. H., Yang, M. J., Chen, C. Y., Chou, P. T., Chan, C. S., Chi, Y., Chen, Y. C., & Hsiao, J. K. 2008. Iridium-complex-functionalized Fe3O4/SiO2 core/shell nanoparticles: a facile three-in-one system in magnetic resonance imaging, luminescence imaging, and photodynamic therapy. ***Small***, 4(2): 218-224.

Lassalle, H. P., Dumas, D., Grafe, S., D'Hallewin, M. A., Guillemin, F., & Bezdetnaya, L. 2009. Correlation between in vivo pharmacokinetics, intratumoral distribution and photodynamic efficiency of liposomal mTHPC. ***J.Control Release***, 134(2): 118-124.

Leamon, C. P. 2008. Folate-targeted drug strategies for the treatment of cancer. ***Curr.Opin.Investig.Drugs***, 9(12): 1277-1286.

Leamon, C. P. & Jackman, A. L. 2008a. Exploitation of the folate receptor in the management of cancer and inflammatory disease. ***Vitam.Horm.***, 79: 203-233.

Leamon, C. P., Reddy, J. A., Dorton, R., Bloomfield, A., Emsweller, K., Parker, N., & Westrick, E. 2008b. Impact of high and low folate diets on tissue folate receptor levels and antitumor responses toward folate-drug conjugates. ***J Pharmacol.Exp.Ther.***, 327(3): 918-925.

Ledoux-Lebards 1902. ***C.Annales De L'Institut Pasteur***, 16: 593.

Lee, H. B. & Blaufox, M. D. 1985. Blood volume in the rat. ***J.Nucl.Med.***, 26(1): 72-76.

Lee, R. J. & Low, P. S. 1994. Delivery of liposomes into cultured KB cells via folate receptor-mediated endocytosis. ***J.Biol.Chem.***, 269(5): 3198-3204.

Lee, R. J. & Low, P. S. 1995. Folate-mediated tumor cell targeting of liposome-entrapped doxorubicin in vitro. ***Biochim.Biophys.Acta***, 1233(2): 134-144.

Leiberman, D. P., Mathie, R. T., Harper, A. M., & Blumgart, L. H. 1978. An isotope clearance method for measurement of liver blood flow during portasystemic shunt in man. ***Br.J.Surg.***, 65(8): 578-580.

Leung, K. 2004. Folate-polyethylene glycol-ultrasmall superparamagnetic iron oxide nanoparticles..

Levy, J. G. 1994. Photosensitizers in photodynamic therapy. ***Semin.Oncol.***, 21(6 Suppl 15): 4-10.

Li, S. D. & Huang, L. 2008. Pharmacokinetics and biodistribution of nanoparticles. ***Mol Pharm.***, 5(4): 496-504.

Lin, C. W., Shulok, J. R., Wong, Y. K., Schanbacher, C. F., Cincotta, L., & Foley, J. W. 1991. Photosensitization, uptake, and retention of phenoxazine Nile blue derivatives in human bladder carcinoma cells. ***Cancer Res.***, 51(4): 1109-1116.

Liu, D., Mori, A., & Huang, L. 1992. Role of liposome size and RES blockade in controlling biodistribution and tumor uptake of GM1-containing liposomes. ***Biochim.Biophys.Acta***, 1104(1): 95-101.

Liu, Y. Y., Miyoshi, H., & Nakamura, M. 2007. Nanomedicine for drug delivery and imaging: A promising avenue for cancer therapy and diagnosis using targeted functional nanoparticles. ***International Journal of Cancer***, 120(12): 2527-2537.

Lovell, J. F., Jin, C. S., Huynh, E., Jin, H., Kim, C., Rubinstein, J. L., Chan, W. C., Cao, W., Wang, L. V., & Zheng, G. 2011. Porphysome nanovesicles generated by porphyrin bilayers for use as multimodal biophotonic contrast agents. ***Nat.Mater.***, 10(4): 324-332.

Low, K., Knobloch, T., Wagner, S., Wiehe, A., Engel, A., Langer, K., & von, B. H. 2011. Comparison of intracellular accumulation and cytotoxicity of free mTHPC and mTHPC-loaded PLGA nanoparticles in human colon carcinoma cells. ***Nanotechnology***, 22(24): 245102.

Lu, Y. & Low, P. S. 2002. Folate-mediated delivery of macromolecular anticancer therapeutic agents. ***Adv.Drug Deliv.Rev.***, 54(5): 675-693.

Lu, Y., Xu, L. C., Parker, N., Westrick, E., Reddy, J. A., Vetzel, M., Low, P. S., & Leamon, C. P. 2006. Preclinical pharmacokinetics, tissue distribution, and antitumor activity of a folate-hapten conjugate-targeted immunotherapy in hapten-immunized mice. ***Mol.Cancer Ther.***, 5(12): 3258-3267.

Luz R, Iost R, & Crespilho 2013. Nanomaterials for Biosensors and Implantable Biodevices. *Nanobioelectrochemistry from Implantable Biosensors to Green Power Generation*: 27-48. Springer-Verlag Berlin Heidelberg.

Lynch, I., Salvati, A., & Dawson, K. A. 2009. Protein-nanoparticle interactions: What does the cell see? ***Nat.Nanotechnol.***, 4(9): 546-547.

Maeda, H., Wu, J., Sawa, T., Matsumura, Y., & Hori, K. 2000. Tumor vascular permeability and the EPR effect in macromolecular therapeutics: a review. ***J.Control Release***, 65(1-2): 271-284.

Makadia, H. K. & Siegel, S. J. 2011. Poly Lactic-co-Glycolic Acid (PLGA) as Biodegradable Controlled Drug Delivery Carrier. ***Polymers***, 3(3): 1377-1397.

Malam, Y., Loizidou, M., & Seifalian, A. M. 2009. Liposomes and nanoparticles: nanosized vehicles for drug delivery in cancer. ***Trends Pharmacol.Sci.***, 30(11): 592-599.

Marchal, S., Francois, A., Dumas, D., Guillemin, F., & Bezdetnaya, L. 2007. Relationship between subcellular localisation of Foscan (R) and caspase activation in photosensitised MCF-7 cells. ***British Journal of Cancer***, 96(6): 944-951.

Mas-Moruno, C., Rechenmacher, F., & Kessler, H. 2010. Cilengitide: the first anti-angiogenic small molecule drug candidate design, synthesis and clinical evaluation. ***Anticancer Agents Med.Chem.***, 10(10): 753-768.

Master, A., Livingston, M., & Sen, G. A. 2013. Photodynamic nanomedicine in the treatment of solid tumors: Perspectives and challenges. ***J.Control Release***, 168(1): 88-102.

Matherly, L. H. & Goldman, D. I. 2003. Membrane transport of folates. ***Vitam.Horm.***, 66: 403-456.

Matsumura, Y., Hamaguchi, T., Ura, T., Muro, K., Yamada, Y., Shimada, Y., Shirao, K., Okusaka, T., Ueno, H., Ikeda, M., & Watanabe, N. 2004. Phase I clinical trial and pharmacokinetic evaluation of NK911, a micelle-encapsulated doxorubicin. ***Br.J.Cancer***, 91(10): 1775-1781.

Medina, C., Santos-Martinez, M. J., Radomski, A., Corrigan, O. I., & Radomski, M. W. 2007. Nanoparticles: pharmacological and toxicological significance. ***Br.J Pharmacol.***, 150(5): 552-558.

Mehra, N. K., Mishra, V., & Jain, N. K. 2013. Receptor-based targeting of therapeutics. ***Ther.Deliv.***, 4(3): 369-394.

Melnikova, V. O., Bezdetnaya, L. N., Bour, C., Festor, E., Gramain, M. P., Merlin, J. L., Potapenko, A. Y., & Guillemin, F. 1999a. Subcellular localization of meta-tetra(hydroxyphenyl) chlorin in human tumor cells subjected to photodynamic treatment. ***Journal of Photochemistry and Photobiology B-Biology***, 49(2-3): 96-103.

Melnikova, V. O., Bezdetnaya, L. N., Potapenko, A. Y., & Guillemin, F. 1999b. Photodynamic properties of meta-tetra(hydroxyphenyl)chlorin in human tumor cells. ***Radiation Research***, 152(4): 428-435.

Mendelsohn, J. 2002. Targeting the epidermal growth factor receptor for cancer therapy. ***J Clin.Oncol.***, 20(18 Suppl): 1S-13S.

Messmann, H., Mlkvy, P., Buonaccorsi, G., Davies, C. L., Macrobert, A., & Bown, S. G. 1995. Enhancement of Photodynamic Therapy with 5-Aminolevulinic Acid-Induced Porphyrin Photosensitization in Normal Rat Colon by Threshold and Light Fractionation Studies. ***British Journal of Cancer***, 72(3): 589-594.

Metselaar, J. M., Mastrobattista, E., & Storm, G. 2002. Liposomes for intravenous drug targeting: design and applications. ***Mini.Rev.Med.Chem.***, 2(4): 319-329.

Meyer-Betz, F. 1913. Untersuchungen uber die biologische photodynamische Wirkung des Hematoporphyrins und anderer Derivative des Blut unde Galenafarbstoffs. ***Deutsch Arch Klin***,(112): 476-503.

Minchinton, A. I. & Tannock, I. F. 2006. Drug penetration in solid tumours. ***Nat.Rev.Cancer***, 6(8): 583-592.

Misawa, J., Moriwaki, S., Takigawa, M., Moriwaki, S., Kohno, E., Hirano, T., & Tokura, Y. 2005. The role of low-density lipoprotein receptors in sensitivity to killing by Photofrin-mediated photodynamic therapy in cultured human tumor cell lines. ***Journal of Dermatological Science***, 40(1): 59-61.

Mlkvy, P., Messmann, H., Regula, J., Conio, M., Pauer, M., Millson, C. E., MacRobert, A. J., & Bown, S. G. 1995. Sensitization and Photodynamic Therapy (Pdt) of Gastrointestinal Tumors with 5-Aminolevulinic Acid (Ala) Induced Protoporphyrin-Ix (Ppix) - A Pilot-Study. ***Neoplasma***, 42(3): 109-113.

Moan, J. & Berg, K. 1991. The photodegradation of porphyrins in cells can be used to estimate the lifetime of singlet oxygen. ***Photochem.Photobiol.***, 53(4): 549-553.

Moan, J. & Berg, K. 1992. Photochemotherapy of cancer: experimental research. ***Photochem.Photobiol.***, 55(6): 931-948.

Modjtahedi, H., Styles, J., & Dean, C. 1993. The growth-response of human tumor-cell lines expressing the EGF receptor to treatment with EGF and or mabs that block ligand-binding. ***Int.J Oncol.***, 3(2): 237-243.

Moor, A. C. 2000. Signaling pathways in cell death and survival after photodynamic therapy. ***J.Photochem.Photobiol.B***, 57(1): 1-13.

Moore, C. M., Nathan, T. R., Lees, W. R., Mosse, C. A., Freeman, A., Emberton, M., & Bown, S. G. 2006. Photodynamic therapy using meso tetra hydroxy phenyl chlorin (mTHPC) in early prostate cancer. ***Lasers in Surgery and Medicine***, 38(5): 356-363.

Moreira, J. N., Gaspar, R., & Allen, T. M. 2001. Targeting Stealth liposomes in a murine model of human small cell lung cancer. ***Biochim.Biophys.Acta***, 1515(2): 167-176.

Moret, F., Scheglmann, D., & Reddi, E. 2013. Folate-targeted PEGylated liposomes improve the selectivity of PDT with meta-tetra(hydroxyphenyl)chlorin (m-THPC). ***Photochem.Photobiol.Sci.***, 12(5): 823-834.

Moriwaki, S. I., Misawa, J., Yoshinari, Y., Yamada, I., Takigawa, M., & Tokura, Y. 2001. Analysis of photosensitivity in Japanese cancer-bearing patients receiving photodynamic therapy with porfimer sodium (Photofrin (TM)). ***Photodermatology Photoimmunology & Photomedicine***, 17(5): 241-243.

Morlet, L., Vonarx-Coinsmann, V., Lenz, P., Foultier, M. T., de Brito, L. X., Stewart, C., & Patrice, T. 1995. Correlation between meta(tetrahydroxyphenyl)chlorin (m-THPC) biodistribution and photodynamic effects in mice. ***J Photochem.Photobiol.B***, 28(1): 25-32.

Morosini, V., Bastogne, T., Frochot, C., Schneider, R., Francois, A., Guillemin, F., & Barberi-Heyob, M. 2011. Quantum dot-folic acid conjugates as potential photosensitizers in photodynamic therapy of cancer. ***Photochem.Photobiol.Sci.***, 10(5): 842-851.

Morse, Blood, E. Stump, Brooker, B.Owl, Hepburn, Jay. Pee, 2015. Dream team may you live on; Paradise procrastination, parties and poor workmanship. ***J STI.Positive.Sci.***, 10(4): 2011-2013.

Murphy, P., Alexander, P., Kirkham, N., Fleming, J., & Taylor, I. 1986. Pattern of Spread of Bloodborne Tumor. ***British Journal of Surgery***, 73(10): 829-834.

Muzykantov, V. R., Radhakrishnan, R., & Eckmann, D. M. 2012. Dynamic factors controlling targeting nanocarriers to vascular endothelium. ***Curr.Drug Metab***, 13(1): 70-81.

Nagayama, S., Ogawara, K., Fukuoka, Y., Higaki, K., & Kimura, T. 2007. Time-dependent changes in opsonin amount associated on nanoparticles alter their hepatic uptake characteristics. ***Int.J Pharm.***, 342(1-2): 215-221.

Nandiyanto, A. B. D., Kim, S. G., Iskandar, F., & Okuyama, K. 2009. Synthesis of spherical mesoporous silica nanoparticles with nanometer-size controllable pores and outer diameters. ***Microporous and Mesoporous Materials***, 120(3): 447-453.

Nathan, T. R., Whitelaw, D. E., Chang, S. C., Lees, W. R., Ripley, P. M., Payne, H., Jones, L., Parkinson, M. C., Emberton, M., Gillams, A. R., Mundy, A. R., & Bown, S. G. 2002. Photodynamic therapy for prostate cancer recurrence after radiotherapy: A phase I study. ***Journal of Urology***, 168(4): 1427-1432.

Needham, D., McIntosh, T. J., & Lasic, D. D. 1992. Repulsive interactions and mechanical stability of polymer-grafted lipid membranes. ***Biochim.Biophys.Acta***, 1108(1): 40-48.

Nel, A., Xia, T., Madler, L., & Li, N. 2006. Toxic potential of materials at the nanolevel. ***Science***, 311(5761): 622-627.

Nishiyama, N., Morimoto, Y., Jang, W. D., & Kataoka, K. 2009a. Design and development of dendrimer photosensitizer-incorporated polymeric micelles for enhanced photodynamic therapy. ***Adv.Drug Deliv.Rev.***, 61(4): 327-338.

Nishiyama, N., Nakagishi, Y., Morimoto, Y., Lai, P. S., Miyazaki, K., Urano, K., Horie, S., Kumagai, M., Fukushima, S., Cheng, Y., Jang, W. D., Kikuchi, M., & Kataoka, K. 2009b. Enhanced photodynamic cancer treatment by supramolecular nanocarriers charged with dendrimer phthalocyanine. ***J.Control Release***, 133(3): 245-251.

Nyati, M. K., Morgan, M. A., Feng, F. Y., & Lawrence, T. S. 2006. Integration of EGFR inhibitors with radiochemotherapy. ***Nat.Rev.Cancer***, 6(11): 876-885.

Nyst, H. J., Tan, I. B., Stewart, F. A., & Balm, A. J. M. 2009. Is photodynamic therapy a good alternative to surgery and radiotherapy in the treatment of head and neck cancer? ***Photodiagnosis and Photodynamic Therapy***, 6(1): 3-11.

O'Brien, M. E., Wigler, N., Inbar, M., Rosso, R., Grischke, E., Santoro, A., Catane, R., Kieback, D. G., Tomczak, P., Ackland, S. P., Orlandi, F., Mellars, L., Alland, L., & Tendler, C. 2004. Reduced cardiotoxicity and comparable efficacy in a phase III trial of pegylated liposomal doxorubicin HCl (CAELYX/Doxil) versus conventional doxorubicin for first-line treatment of metastatic breast cancer. ***Ann.Oncol***, 15(3): 440-449.

O'Shannessy, D. J., Somers, E. B., Albone, E., Cheng, X., Park, Y. C., Tomkowicz, B. E., Hamuro, Y., Kohl, T. O., Forsyth, T. M., Smale, R., Fu, Y. S., & Nicolaides, N. C. 2011. Characterization of the human folate receptor alpha via novel antibody-based probes. ***Oncotarget.***, 2(12): 1227-1243.

Oberdorster, G. 2010. Safety assessment for nanotechnology and nanomedicine: concepts of nanotoxicology. ***J Intern.Med.***, 267(1): 89-105.

Ogilby, P. R. 2010. Singlet oxygen: there is still something new under the sun, and it is better than ever. ***Photochem.Photobiol.Sci.***, 9(12): 1543-1560.

Ohulchanskyy, T. Y., Roy, I., Goswami, L. N., Chen, Y., Bergey, E. J., Pandey, R. K., Oseroff, A. R., & Prasad, P. N. 2007. Organically modified silica nanoparticles with covalently incorporated photosensitizer for photodynamic therapy of cancer. ***Nano.Lett.***, 7(9): 2835-2842.

Oku, N. & Namba, Y. 1994. Long-circulating liposomes. ***Crit Rev.Ther.Drug Carrier Syst.***, 11(4): 231-270.

Oku, N., Saito, N., Namba, Y., Tsukada, H., Dolphin, D., & Okada, S. 1997. Application of long-circulating liposomes to cancer photodynamic therapy. ***Biological & Pharmaceutical Bulletin***, 20(6): 670-673.

Oleinick, N. L. & Evans, H. H. 1998. The photobiology of photodynamic therapy: Cellular targets and mechanisms. ***Radiation Research***, 150(5): S146-S156.

Olivier, J. C. 2005. Drug transport to brain with targeted nanoparticles. ***NeuroRx.***, 2(1): 108-119.

Opanasopit, P., Nishikawa, M., & Hashida, M. 2002. Factors affecting drug and gene delivery: Effects of interaction with blood components. ***Critical Reviews in Therapeutic Drug Carrier Systems***, 19(3): 191-233.

Pagona, G. & Tagmatarchis, N. 2006. Carbon nanotubes: materials for medicinal chemistry and biotechnological applications. ***Curr.Med.Chem.***, 13(15): 1789-1798.

Palumbo, G. 2007. Photodynamic therapy and cancer: a brief sightseeing tour. ***Expert.Opin.Drug Deliv.***, 4(2): 131-148.

Papahadjopoulos, D., Allen, T. M., Gabizon, A., Mayhew, E., Matthay, K., Huang, S. K., Lee, K. D., Woodle, M. C., Lasic, D. D., Redemann, C., & . 1991. Sterically stabilized liposomes: improvements in pharmacokinetics and antitumor therapeutic efficacy. ***Proc.Natl.Acad.Sci.U.S.A***, 88(24): 11460-11464.

Park, J. W. 2002. Liposome-based drug delivery in breast cancer treatment. ***Breast Cancer Res.***, 4(3): 95-99.

Parker, N., Turk, M. J., Westrick, E., Lewis, J. D., Low, P. S., & Leamon, C. P. 2005. Folate receptor expression in carcinomas and normal tissues determined by a quantitative radioligand binding assay. ***Anal.Biochem.***, 338(2): 284-293.

Paszko, E., Ehrhardt, C., Senge, M. O., Kelleher, D. P., & Reynolds, J. V. 2011. Nanodrug applications in photodynamic therapy. ***Photodiagnosis.Photodyn.Ther.***, 8(1): 14-29.

Patel, D. D. & Goldberg, R. M. 2006. Cetuximab-associated infusion reactions: pathology and management. ***Oncology (Williston.Park)***, 20(11): 1373-1382.

Patel, H. M. 1992. Serum opsonins and liposomes: their interaction and opsonophagocytosis. ***Crit Rev.Ther.Drug Carrier Syst.***, 9(1): 39-90.

Paulos, C. M., Reddy, J. A., Leamon, C. P., Turk, M. J., & Low, P. S. 2004. Ligand Binding and Kinetics of Folate Receptor Recycling in Vivo: Impact on Receptor-Mediated Drug Delivery. ***Molecular Pharmacology***, 66(6): 1406-1414.

Peer, D., Karp, J. M., Hong, S., Farokhzad, O. C., Margalit, R., & Langer, R. 2007. Nanocarriers as an emerging platform for cancer therapy. ***Nat.Nanotechnol.***, 2(12): 751-760.

Pegaz, B., Debefve, E., Ballini, J. P., Wagnieres, G., Spaniol, S., Albrecht, V., Scheglmann, D. V., Nifantiev, N. E., van den, B. H., & Konan-Kouakou, Y. N. 2006. Photothrombic activity of m-THPC-loaded liposomal formulations: pre-clinical assessment on chick chorioallantoic membrane model. ***Eur.J.Pharm.Sci.***, 28(1-2): 134-140.

Peng, Q., Moan, J. H., Ma, L. W., & Nesland, J. M. 1995. Uptake, Localization, and Photodynamic Effect of Meso-Tetra(Hydroxyphenyl)Porphine and Its Corresponding Chlorin in Normal and Tumor-Tissues of Mice Bearing Mammary-Carcinoma. ***Cancer Research***, 55(12): 2620-2626.

Peng, Z. & Yang, H. 2009. Synthesis and oxygen reduction electrocatalytic property of Pt-on-Pd bimetallic heteronanostructures. ***J Am.Chem.Soc.***, 131(22): 7542-7543.

Perry, J. L., Reuter, K. G., Kai, M. P., Herlihy, K. P., Jones, S. W., Luft, J. C., Napier, M., Bear, J. E., & Desimone, J. M. 2012. PEGylated PRINT nanoparticles: the impact of PEG density on protein binding, macrophage association, biodistribution, and pharmacokinetics. ***Nano Lett.***, 12(10): 5304-5310.

Petitclerc, E., Stromblad, S., von Schalscha, T. L., Mitjans, F., Piulats, J., Montgomery, A. M., Cheresh, D. A., & Brooks, P. C. 1999. Integrin alpha(v)beta3 promotes M21 melanoma growth in human skin by regulating tumor cell survival. ***Cancer Res.***, 59(11): 2724-2730.

Pharmainfo.net. 2014.

Pietryga, J. M., Schaller, R. D., Werder, D., Stewart, M. H., Klimov, V. I., & Hollingsworth, J. A. 2004. Pushing the band gap envelope: mid-infrared emitting colloidal PbSe quantum dots. ***J Am.Chem.Soc.***, 126(38): 11752-11753.

Plaetzer, K., Krammer, B., Berlanda, J., Berr, F., & Kiesslich, T. 2009. Photophysics and photochemistry of photodynamic therapy: fundamental aspects. ***Lasers Med.Sci.***, 24(2): 259-268.

Pogue, B. W. & Hasan, T. 1997. A theoretical study of light fractionation and dose-rate effects in photodynamic therapy. ***Radiat.Res.***, 147(5): 551-559.

Popovic, E. A., Kaye, A. H., & Hill, J. S. 1996. Photodynamic therapy of brain tumors. ***J.Clin.Laser Med.Surg.***, 14(5): 251-261.

Powell GM & Davidson RL 1980. *Handbook of Water-Soluble Gums: Chapter 18 Polyethylene Glycol*. McGraw-Hill, New York.

Pytela, R., Pierschbacher, M. D., & Ruoslahti, E. 1985. A 125/115-kDa cell surface receptor specific for vitronectin interacts with the arginine-glycine-aspartic acid adhesion sequence derived from fibronectin. ***Proc.Natl.Acad.Sci.U.S A***, 82(17): 5766-5770.

Qian, J., Dai, H. C., Pan, X. H., & Liu, S. Q. 2011. Simultaneous detection of dual proteins using quantum dots coated silica nanoparticles as labels. ***Biosensors & Bioelectronics***, 28(1): 314-319.

Qian, J., Gharibi, A., & He, S. 2009. Colloidal mesoporous silica nanoparticles with protoporphyrin IX encapsulated for photodynamic therapy. ***J Biomed.Opt.***, 14(1): 014012.

Qian, J., Wang, D., Cai, F., Zhan, Q., Wang, Y., & He, S. 2012. Photosensitizer encapsulated organically modified silica nanoparticles for direct two-photon photodynamic therapy and in vivo functional imaging. ***Biomaterials***, 33(19): 4851-4860.

Qualls, M. M. & Thompson, D. H. 2001. Chloroaluminum phthalocyanine tetrasulfonate delivered via acid-labile diplasmenylcholine-folate liposomes: intracellular localization and synergistic phototoxicity. ***Int.J Cancer***, 93(3): 384-392.

Quesnelle, K. M. & Grandis, J. R. 2011. Dual Kinase Inhibition of EGFR and HER2 Overcomes Resistance to Cetuximab in a Novel In Vivo Model of Acquired Cetuximab Resistance. ***Clinical Cancer Research***, 17(18): 5935-5944.

Raab, O. 1900. Uber die Wirkung fluoreszierender Stoffe auf Infusorien. ***Zeitung Biologie***,(39): 524-526.

Rapozzi, V., Miculan, M., & Xodo, L. E. 2009. Evidence that photoactivated pheophorbide a causes in human cancer cells a photodynamic effect involving lipid peroxidation. ***Cancer Biology & Therapy***, 8(14): 1318-1327.

Raynal, I., Prigent, P., Peyramaure, S., Najid, A., Rebuzzi, C., & Corot, C. 2004. Macrophage endocytosis of superparamagnetic iron oxide nanoparticles - Mechanisms and comparison of Ferumoxides and Ferumoxtran-10. ***Investigative Radiology***, 39(1): 56-63.

Real, F. X., Rettig, W. J., Chesa, P. G., Melamed, M. R., Old, L. J., & Mendelsohn, J. 1986. Expression of epidermal growth factor receptor in human cultured cells and tissues: relationship to cell lineage and stage of differentiation. ***Cancer Res.***, 46(9): 4726-4731.

Reddi, E. 1997. Role of delivery vehicles for photosensitizers in the photodynamic therapy of tumours. ***J Photochem.Photobiol.B***, 37(3): 189-195.

Redmond, R. W., Land, E. J., & Truscott, T. G. 1985. Aggregation effects on the photophysical properties of porphyrins in relation to mechanisms involved in photodynamic therapy. ***Adv.Exp.Med.Biol.***, 193: 293-302.

Reetz, M. T., Zonta, A., & Simpelkamp, J. 1996. Efficient immobilization of lipases by entrapment in hydrophobic sol-gel materials. ***Biotechnol.Bioeng.***, 49(5): 527-534.

Renno, R. Z. & Miller, J. W. 2001. Photosensitizer delivery for photodynamic therapy of choroidal neovascularization. ***Adv.Drug Deliv.Rev.***, 52(1): 63-78.

Reshetov, V., Kachatkou, D., Shmigol, T., Zorin, V., D'Hallewin, M. A., Guillemin, F., & Bezdetnaya, L. 2011. Redistribution of meta-tetra(hydroxyphenyl)chlorin (m-THPC) from conventional and PEGylated liposomes to biological substrates. ***Photochem.Photobiol.Sci.***.

Reshetov, V., Lassalle, H. P., Francois, A., Dumas, D., Hupont, S., Grafe, S., Filipe, V., Jiskoot, W., Guillemin, F., Zorin, V., & Bezdetnaya, L. 2013. Photodynamic therapy with conventional and PEGylated liposomal formulations of mTHPC (temoporfin): comparison of treatment efficacy and distribution characteristics in vivo. ***Int.J Nanomedicine.***, 8: 3817-3831.

Reshetov, V., Zorin, V., Siupa, A., D'Hallewin, M. A., Guillemin, F., & Bezdetnaya, L. 2012. Interaction of liposomal formulations of meta-tetra(hydroxyphenyl)chlorin (temoporfin) with serum proteins: protein binding and liposome destruction. ***Photochem.Photobiol.***, 88(5): 1256-1264.

Ribo, J. M., Crusats, J., Farrera, A. J., & Valero, M. L. 1994. Aggregation in water solutions of tetrasodium diprotonated meso-tetrakis(4-sulfonatophenyl)porphine. ***J.Chem.Soc.Chem.Commun***, 681-682.

Ricchelli, F. 1995. Photophysical properties of porphyrins in biological membranes. ***J Photochem.Photobiol.B***, 29(2-3): 109-118.

Ricchelli, F., Gobbo, S., Moreno, G., Salet, C., Brancaleon, L., & Mazzini, A. 1998. Photophysical properties of porphyrin planar aggregates in liposomes. ***Eur.J Biochem.***, 253(3): 760-765.

Ricchelli, F. & Jori, G. 1986. Distribution of Porphyrins in the Various Compartments of Unilamellar Liposomes of Dipalmitoyl-Phosphatidylcholine As Probed by Fluorescence Spectroscopy. ***Photochemistry and Photobiology***, 44(2): 151-157.

Ricci-Junior, E. & Marchetti, J. M. 2006. Zinc(II) phthalocyanine loaded PLGA nanoparticles for photodynamic therapy use. ***Int.J Pharm.***, 310(1-2): 187-195.

Richter, A. M., Waterfield, E., Jain, A. K., Canaan, A. J., Allison, B. A., & Levy, J. G. 1993. Liposomal delivery of a photosensitizer, benzoporphyrin derivative monoacid ring A (BPD), to tumor tissue in a mouse tumor model. ***Photochem.Photobiol.***, 57(6): 1000-1006.

Ris, H. B., Altermatt, H. J., Inderbitzi, R., Hess, R., Nachbur, B., Stewart, J. C., Wang, Q., Lim, C. K., Bonnett, R., Berenbaum, M. C., & . 1991. Photodynamic therapy with chlorins for diffuse malignant mesothelioma: initial clinical results. ***Br.J Cancer***, 64(6): 1116-1120.

Robertson, C. A., Evans, D. H., & Abrahamse, H. 2009. Photodynamic therapy (PDT): a short review on cellular mechanisms and cancer research applications for PDT. ***J.Photochem.Photobiol.B***, 96(1): 1-8.

Rocha-Lima, C. M., Soares, H. P., Raez, L. E., & Singal, R. 2007. EGFR targeting of solid tumors. ***Cancer Control***, 14(3): 295-304.

Rojnik, M., Kocbek, P., Moret, F., Compagnin, C., Celotti, L., Bovis, M. J., Woodhams, J. H., MacRobert, A. J., Scheglmann, D., Helfrich, W., Verkaik, M. J., Papini, E., Reddi, E., & Kos, J. 2012. In vitro and in vivo characterization of temoporfin-loaded PEGylated PLGA nanoparticles for use in photodynamic therapy. ***Nanomedicine.(Lond)***, 7(5): 663-677.

Rosenholm, J. M., Mamaeva, V., Sahlgren, C., & Linden, M. 2012. Nanoparticles in targeted cancer therapy: mesoporous silica nanoparticles entering preclinical development stage. ***Nanomedicine.(Lond)***, 7(1): 111-120.

Rossi, L. M., Silva, P. R., Vono, L. L., Fernandes, A. U., Tada, D. B., & Baptista, M. S. 2008. Protoporphyrin IX nanoparticle carrier: preparation, optical properties, and singlet oxygen generation. ***Langmuir***, 24(21): 12534-12538.

Rovers, J. P., de Jode, M. L., Rezzoug, H., & Grahn, M. F. 2000. In vivo photodynamic characteristics of the near-infrared photosensitizer 5,10,15,20-tetrakis(M-hydroxyphenyl) bacteriochlorin. ***Photochem.Photobiol.***, 72(3): 358-364.

Roy, I., Ohulchanskyy, T. Y., Pudavar, H. E., Bergey, E. J., Oseroff, A. R., Morgan, J., Dougherty, T. J., & Prasad, P. N. 2003. Ceramic-based nanoparticles entrapping water-insoluble photosensitizing anticancer drugs: a novel drug-carrier system for photodynamic therapy. ***J.Am.Chem.Soc.***, 125(26): 7860-7865.

Saba, N. F., Wang, X., Muller, S., Tighiouart, M., Cho, K., Nie, S. M., Chen, Z., & Shin, D. M. 2009. Examining Expression of Folate Receptor in Squamous Cell Carcinoma of the Head and Neck As A

Target for A Novel Nanotherapeutic Drug. ***Head and Neck-Journal for the Sciences and Specialties of the Head and Neck***, 31(4): 475-481.

Sabharanjak, S. & Mayor, S. 2004. Folate receptor endocytosis and trafficking. ***Adv.Drug Deliv.Rev.***, 56(8): 1099-1109.

Sahu, M. & Biswas, P. 2010. Size distributions of aerosols in an indoor environment with engineered nanoparticle synthesis reactors operating under different scenarios. ***Journal of Nanoparticle Research***, 12(3): 1055-1064.

Sarin, H. 2010. Overcoming the challenges in the effective delivery of chemotherapies to CNS solid tumors. ***Ther.Deliv.***, 1(2): 289-305.

Sasnouski, S., Pic, E., Dumas, D., Zorin, V., D'Hallewin, M. A., Guillemin, F., & Bezdetnaya, L. 2007. Influence of incubation time and sensitizer localization on meta-tetra(hydroxyphenyl)chlorin (mTHPC)-induced photoinactivation of cells. ***Radiat.Res.***, 168(2): 209-217.

Satomi, T., Nagasaki, Y., Kobayashi, H., Tateishi, T., Kataoka, K., & Otsuka, H. 2007. Physicochemical characterization of densely packed poly(ethylene glycol) layer for minimizing nonspecific protein adsorption. ***Journal of Nanoscience and Nanotechnology***, 7(7): 2394-2399.

Savellano, M. D. & Hasan, T. 2003. Targeting cells that overexpress the epidermal growth factor receptor with polyethylene glycolated BPD verteporfin photosensitizer immunoconjugates. ***Photochem.Photobiol.***, 77(4): 431-439.

Schacht, V., Szeimies, R. M., & Abels, C. 2006. Photodynamic therapy with 5-aminolevulinic acid induces distinct microcirculatory effects following systemic or topical application. ***Photochemical & Photobiological Sciences***, 5(5): 452-458.

Schiffelers, R. M., Bakker-Woudenberg, I. A., Snijders, S. V., & Storm, G. 1999. Localization of sterically stabilized liposomes in Klebsiella pneumoniae-infected rat lung tissue: influence of liposome characteristics. ***Biochim.Biophys.Acta***, 1421(2): 329-339.

Schiffelers, R. M., Koning, G. A., ten Hagen, T. L., Fens, M. H., Schraa, A. J., Janssen, A. P., Kok, R. J., Molema, G., & Storm, G. 2003. Anti-tumor efficacy of tumor vasculature-targeted liposomal doxorubicin. ***J Control Release***, 91(1-2): 115-122.

Schmidt H 1985. *Preparation, application and potential of ORMOCERs*.

Schneider, R., Schmitt, F., Frochot, C., Fort, Y., Lourette, N., Guillemin, F., Muller, J. F., & Barberi-Heyob, M. 2005. Design, synthesis, and biological evaluation of folic acid targeted tetraphenylporphyrin as novel photosensitizers for selective photodynamic therapy. ***Bioorg.Med.Chem.***, 13(8): 2799-2808.

Schroeder, J. E., Shweky, I., Shmeeda, H., Banin, U., & Gabizon, A. 2007. Folate-mediated tumor cell uptake of quantum dots entrapped in lipid nanoparticles. ***J Control Release***, 124(1-2): 28-34.

Schuitmaker, J. J., Bass, P., vanLeengoed, H. L. L. M., vanderMeulen, F. W., Star, W. M., & vanZandwijk, N. 1996. Photodynamic therapy: A promising new modality for the treatment of cancer. ***Journal of Photochemistry and Photobiology B-Biology***, 34(1): 3-12.

Segat, D., Tavano, R., Donini, M., Selvestrel, F., Rio-Echevarria, I., Rojnik, M., Kocbek, P., Kos, J., Iratni, S., Sheglmann, D., Mancin, F., Dusi, S., & Papini, E. 2011. Proinflammatory effects of bare and PEGylated ORMOSIL-. ***Nanomedicine (Lond)***, 6(6): 1027-1046.

Selvestrel, F., Moret, F., Segat, D., Woodhams, J. H., Fracasso, G., Echevarria, I. M., Bau, L., Rastrelli, F., Compagnin, C., Reddi, E., Fedeli, C., Papini, E., Tavano, R., MacKenzie, A., Bovis, M., Yaghini, E., MacRobert, A. J., Zanini, S., Boscaini, A., Colombatti, M., & Mancin, F. 2013. Targeted delivery of photosensitizers: efficacy and selectivity issues revealed by multifunctional ORMOSIL nanovectors in cellular systems. ***Nanoscale.***, 5(13): 6106-6116.

Sengupta, S. & Kulkarni, A. 2013. Design principles for clinical efficacy of cancer nanomedicine: a look into the basics. ***ACS Nano***, 7(4): 2878-2882.

Senior, J. & Gregoriadis, G. 1982. Stability of small unilamellar liposomes in serum and clearance from the circulation: the effect of the phospholipid and cholesterol components. ***Life Sci.***, 30(24): 2123-2136.

Senior, J. H. 1987. Fate and behavior of liposomes in vivo: a review of controlling factors. ***Crit Rev.Ther.Drug Carrier Syst.***, 3(2): 123-193.

Seshadri, M., Bellnier, D. A., Vaughan, L. A., Spernyak, J. A., Mazurchuk, R., Foster, T. H., & Henderson, B. W. 2008. Light delivery over extended time periods enhances the effectiveness of photodynamic therapy. ***Clin.Cancer Res.***, 14(9): 2796-2805.

Shan, L. 2004. Protoporphyrin IX and IR-820 fluorophore-encapsulated organically modified silica nanoparticles..

Shan, Y., Xu, J. J., & Chen, H. Y. 2011. Enhanced electrochemiluminescence quenching of CdS:Mn nanocrystals by CdTe QDs-doped silica nanoparticles for ultrasensitive detection of thrombin. ***Nanoscale.***, 3(7): 2916-2923.

Shargel, L., Wu-Pong, S., & Yu, A. B. C. 2005. *Applied Biopharmaceutics & Pharmacokinetics*. McGraw-Hill.

Sharkey, S. M., Wilson, B. C., Moorehead, R., & Singh, G. 1993. Mitochondrial alterations in photodynamic therapy-resistant cells. ***Cancer Res.***, 53(20): 4994-4999.

Sharma, H. S., Hussain, S., Schlager, J., Ali, S. F., & Sharma, A. 2010. Influence of nanoparticles on blood-brain barrier permeability and brain edema formation in rats. ***Acta Neurochir.Suppl***, 106: 359-364.

Sharma, R. K., Das, S., & Maitra, A. 2004. Surface modified ormosil nanoparticles. ***J Colloid Interface Sci.***, 277(2): 342-346.

Sharman, W. M., Allen, C. M., & van Lier, J. E. 1999. Photodynamic therapeutics: basic principles and clinical applications. ***Drug Discov.Today***, 4(11): 507-517.

Sharman, W. M., Allen, C. M., & van Lier, J. E. 2000. Role of activated oxygen species in photodynamic therapy. ***Methods Enzymol.***, 319: 376-400.

Shi, L., Wang, X., Zhao, F., Luan, H., Tu, Q., Huang, Z., Wang, H., & Wang, H. 2013. In vitro evaluation of 5-aminolevulinic acid (ALA) loaded PLGA nanoparticles. ***Int.J Nanomedicine***, 8: 2669-2676.

Shieh, M. J., Peng, C. L., Chiang, W. L., Wang, C. H., Hsu, C. Y., Wang, S. J., & Lai, P. S. 2010. Reduced skin photosensitivity with meta-tetra(hydroxyphenyl)chlorin-loaded micelles based on a poly(2-ethyl-2-oxazoline)-b-poly(d,l-lactide) diblock copolymer in vivo. ***Mol Pharm.***, 7(4): 1244-1253.

Shiraki, T., Dawn, A., Le, T. N., Tsuchiya, Y., Tamaru, S., & Shinkai, S. 2011. Heat and light dual switching of a single-walled carbon nanotube/thermo-responsive helical polysaccharide complex: a new responsive system applicable to photodynamic therapy. ***Chem.Commun.(Camb.)***, 47(25): 7065-7067.

Shoyab, M., De Larco, J. E., & Todaro, G. J. 1979. Biologically active phorbol esters specifically alter affinity of epidermal growth factor membrane receptors. ***Nature***, 279(5712): 387-391.

Siboni, G., Weitman, H., Freeman, D., Mazur, Y., Malik, Z., & Ehrenberg, B. 2002. The correlation between hydrophilicity of hypericins and helianthrone: internalization mechanisms, subcellular distribution and photodynamic action in colon carcinoma cells. ***Photochemical & Photobiological Sciences***, 1(7): 483-491.

Siegel, S. J., Kahn, J. B., Metzger, K., Winey, K. I., Werner, K., & Dan, N. 2006. Effect of drug type on the degradation rate of PLGA matrices. ***European Journal of Pharmaceutics and Biopharmaceutics***, 64(3): 287-293.

Simon, V., Devaux, C., Darmon, A., Donnet, T., Thienot, E., Germain, M., Honnorat, J., Duval, A., Pottier, A., Borghi, E., Levy, L., & Marill, J. 2010. Pp IX silica nanoparticles demonstrate differential interactions with in vitro tumor cell lines and in vivo mouse models of human cancers. ***Photochem.Photobiol.***, 86(1): 213-222.

Slepushkin, V. A., Simoes, S., Dazin, P., Newman, M. S., Guo, L. S., Pedroso de Lima, M. C., & Duzgunes, N. 1997. Sterically stabilized pH-sensitive liposomes. Intracellular delivery of aqueous contents and prolonged circulation in vivo. ***J.Biol.Chem.***, 272(4): 2382-2388.

Soergel, P., Loning, M., Staboulidou, I., Schippert, C., & Hillemanns, P. 2008. Photodynamic diagnosis and therapy in gynecology. ***J.Environ.Pathol.Toxicol.Oncol.***, 27(4): 307-320.

Souza, C. S., Neves, A. B. S., Felicio, L. A. B., Ferreira, J., Kurachi, C., & Bagnato, V. S. 2007. Optimized photodynamic therapy with systemic photosensitizer following debulking technique for nonmelanoma skin cancers. ***Dermatologic Surgery***, 33(2): 194-198.

Spikes, J. D. 1985. The historical development of ideas on applications of photosensitized reactions in health sciences. ***Primary Photoprocesses in Biology and Medicine***, 209-227.

Stefflova, K., Li, H., Chen, J., & Zheng, G. 2007. Peptide-based pharmacomodulation of a cancer-targeted optical imaging and photodynamic therapy agent. ***Bioconjug.Chem.***, 18(2): 379-388.

Stevens, P. J., Sekido, M., & Lee, R. J. 2004. Synthesis and evaluation of a hematoporphyrin derivative in a folate receptor-targeted solid-lipid nanoparticle formulation. ***Anticancer Res.***, 24(1): 161-165.

Stober, W., Fink, A., & Bohn, E. J. 1968. Controlled Growth of Monodisperse Silica Spheres in the Micron Size Range. ***Colloid Interface Science***, 26(62).

Stromblad, S. & Cheresh, D. A. 1996. Integrins, angiogenesis and vascular cell survival. ***Chemistry & Biology***, 3(11): 881-885.

Study Group 1999. Photodynamic therapy of subfoveal choroidal neovascularization in age-related macular degeneration with verteporfin: one-year results of 2 randomized clinical trials--TAP report. Treatment of age-related macular degeneration with photodynamic therapy (TAP) Study Group. ***Arch.Ophthalmol.***, 117(10): 1329-1345.

Stylianopoulos, T., Poh, M. Z., Insin, N., Bawendi, M. G., Fukumura, D., Munn, L. L., & Jain, R. K. 2010. Diffusion of particles in the extracellular matrix: the effect of repulsive electrostatic interactions. ***Biophys.J.***, 99(5): 1342-1349.

Sun, X., Xing, L., Ling, C. C., & Li, G. C. 2010. The effect of mild temperature hyperthermia on tumour hypoxia and blood perfusion: relevance for radiotherapy, vascular targeting and imaging. ***Int.J.Hyperthermia***, 26(3): 224-231.

Svensson, J., Johansson, A., Grafe, S., Gitter, B., Trebst, T., Bendsoe, N., ndersson-Engels, S., & Svanberg, K. 2007. Tumor selectivity at short times following systemic administration of a liposomal temoporfin formulation in a murine tumor model. ***Photochem.Photobiol.***, 83(5): 1211-1219.

Swirski, F. K., Nahrendorf, M., Etzrodt, M., Wildgruber, M., Cortez-Retamozo, V., Panizzi, P., Figueiredo, J. L., Kohler, R. H., Chudnovskiy, A., Waterman, P., Aikawa, E., Mempel, T. R., Libby, P., Weissleder, R., & Pittet, M. J. 2009. Identification of Splenic Reservoir Monocytes and Their Deployment to Inflammatory Sites. ***Science***, 325(5940): 612-616.

Symon, Z., Peyser, A., Tzemach, D., Lyass, O., Sucher, E., Shezen, E., & Gabizon, A. 1999. Selective delivery of doxorubicin to patients with breast carcinoma metastases by stealth liposomes. ***Cancer***, 86(1): 72-78.

Syu, W. J., Yu, H. P., Hsu, C. Y., Rajan, Y. C., Hsu, Y. H., Chang, Y. C., Hsieh, W. Y., Wang, C. H., & Lai, P. S. 2012. Improved photodynamic cancer treatment by folate-conjugated polymeric micelles in a KB xenografted animal model. ***Small***, 8(13): 2060-2069.

Szeimies, R. M., Lorenzen, T., Karrer, S., Abels, C., & Plettenberg, A. 2001. [Photochemotherapy of cutaneous AIDS-associated Kaposi sarcoma with indocyanine green and laser light]. ***Hautarzt***, 52(4): 322-326.

Szentkuti, L. 1997. Light microscopical observations on luminally administered dyes, dextrans, nanospheres and microspheres in the pre-epithelial mucus gel layer of the rat distal colon. ***Journal of Controlled Release***, 46(3): 233-242.

Tahara, K., Sakai, T., Yamamoto, H., Takeuchi, H., Hirashima, N., & Kawashima, Y. 2009. Improved cellular uptake of chitosan-modi fled PLGA nanospheres by A549 cells. ***International Journal of Pharmaceutics***, 382(1-2): 198-204.

Takeuchi, H., Kojima, H., Yamamoto, H., & Kawashima, Y. 2001. Passive targeting of doxorubicin with polymer coated liposomes in tumor bearing rats. ***Biol.Pharm.Bull.***, 24(7): 795-799.

Talekar, M., Kendall, J., Denny, W., & Garg, S. 2011. Targeting of nanoparticles in cancer: drug delivery and diagnostics. ***Anticancer Drugs***, 22(10): 949-962.

Tallury, P., Payton, K., & Santra, S. 2008. Silica-based multimodal/multifunctional nanoparticles for bioimaging and biosensing applications. ***Nanomed.***, 3(4): 579-592.

Tang, K. S., Hashmi, S. M., & Shapiro, E. M. 2013. The effect of cryoprotection on the use of PLGA encapsulated iron oxide nanoparticles for magnetic cell labeling. ***Nanotechnology***, 24(12).

Tang, W., Xu, H., Kopelman, R., & Philbert, M. A. 2005. Photodynamic characterization and in vitro application of methylene blue-containing nanoparticle platforms. ***Photochem.Photobiol.***, 81(2): 242-249.

Tappeiner, H. v. & A.Jodlbauer 1904. Uber die Wirkung der photodynamischen (fluorescierenden) Stoffe auf Protozoen und Enzyme. ***Dtsch.Arch.Klin.Med.***, 80: 427-487.

Tavano, R., Segat, D., Reddi, E., Kos, J., Rojnik, M., Kocbek, P., Iratni, S., Scheglmann, D., Colucci, M., Echevarria, I. M., Selvestrel, F., Mancin, F., & Papini, E. 2010. Procoagulant properties of bare and highly PEGylated vinyl-modified silica nanoparticles. ***Nanomedicine.(Lond)***, 5(6): 881-896.

Taverna, D., Moher, H., Crowley, D., Borsig, L., Varki, A., & Hynes, R. O. 2004. Increased primary tumor growth in mice null for beta3- or beta3/beta5-integrins or selectins. ***Proc.Natl.Acad.Sci.U.S A***, 101(3): 763-768.

Teiten, M. H., Bezdetnaya, L., Merlin, J. L., Bour-Dill, C., Pauly, M. E., Dicato, M., & Guillemin, F. 2001. Effect of meta-tetra(hydroxyphenyl)chlorin (mTHPC)-mediated photodynamic therapy on sensitive and multidrug-resistant human breast cancer cells. ***Journal of Photochemistry and Photobiology B-Biology***, 62(3): 146-152.

Temming, K., Schiffelers, R. M., Molema, G., & Kok, R. J. 2005. RGD-based strategies for selective delivery of therapeutics and imaging agents to the tumour vasculature. ***Drug Resistance Updates***, 8(6): 381-402.

Teng, L., Xie, J., Teng, L., & Lee, R. J. 2012. Clinical translation of folate receptor-targeted therapeutics. ***Expert Opin.Drug Deliv.***, 9(8): 901-908.

Teply, B. A., Tong, R., Jeong, S. Y., Luther, G., Sherifi, I., Yim, C. H., Khademhosseini, A., Farokhzad, O. C., Langer, R. S., & Cheng, J. 2008. The use of charge-coupled polymeric microparticles and micromagnets for modulating the bioavailability of orally delivered macromolecules. ***Biomaterials***, 29(9): 1216-1223.

Thorek, D. L. & Tsourkas, A. 2008. Size, charge and concentration dependent uptake of iron oxide particles by non-phagocytic cells. ***Biomaterials***, 29(26): 3583-3590.

Tian, B., Wang, C., Zhang, S., Feng, L., & Liu, Z. 2011. Photothermally enhanced photodynamic therapy delivered by nano-graphene oxide. ***ACS Nano.***, 5(9): 7000-7009.

Toffoli, G., Cernigoi, C., Russo, A., Gallo, A., Bagnoli, M., & Boiocchi, M. 1997. Overexpression of folate binding protein in ovarian cancers. ***International Journal of Cancer***, 74(2): 193-198.

Tong, R., Chiang, H. H., & Kohane, D. S. 2013. Photoswitchable nanoparticles for in vivo cancer chemotherapy. ***Proc.Natl.Acad.Sci.U.S.A***, 110(47): 19048-19053.

Torchilin, V. P. 2005. Recent advances with liposomes as pharmaceutical carriers. ***Nature Reviews Drug Discovery***, 4(2): 145-160.

Triesscheijn, M., Ruevekamp, M., Aalders, M., Baas, P., & Stewart, F. A. 2005. Outcome of mTHPC mediated photodynamic therapy is primarily determined by the vascular response. ***Photochem.Photobiol.***, 81(5): 1161-1167.

Triesscheijn, M., Ruevekamp, M., Out, R., Van Berkel, T. J., Schellens, J., Baas, P., & Stewart, F. A. 2007. The pharmacokinetic behavior of the photosensitizer meso-tetra-hydroxyphenyl-chlorin in mice and men. ***Cancer Chemother.Pharmacol.***, 60(1): 113-122.

Tripathi, A., Gupta, R., & Saraf, S. A. 2010. PLGA Nanoparticles of Anti Tubercular Drug: Drug Loading and Release Studies of a Water In-Soluble Drug. ***Internation Journal of PharmTech Research***, 2(3): 2116-2123.

Tsutsui, H., MacRobert, A. J., Curnow, A., Rogowska, A., Buonaccorsi, G., Kato, H., & Bown, S. G. 2002. Optimisation of illumination for photodynamic therapy with mTHPC on normal colon and a transplantable tumour in rats. ***Lasers in Medical Science***, 17(2): 101-109.

Tu, H. L., Lin, Y. S., Lin, H. Y., Hung, Y., Lo, L. W., Chen, Y. F., & Mou, C. Y. 2009. In vitro Studies of Functionalized Mesoporous Silica Nanoparticles for Photodynamic Therapy. ***Advanced Materials***, 21(2): 172-+.

Turek, J. J., Leamon, C. P., & Low, P. S. 1993. Endocytosis of folate-protein conjugates: ultrastructural localization in KB cells. ***J.Cell Sci.***, 106 (Pt 1): 423-430.

Ulman, A. 1996. Formation and Structure of Self-Assembled Monolayers. ***Chem.Rev.***, 96(4): 1533-1554.

van Vlerken, L. E., Vyas, T. K., & Amiji, M. M. 2007. Poly(ethylene glycol)-modified nanocarriers for tumor-targeted and intracellular delivery. ***Pharm.Res***, 24(8): 1405-1414.

Vanfurth, R. & Hamminga, L. 1979. Mononuclear Phagocytes and Skin Diseases. ***Archives of Dermatological Research***, 265(3): 331-336.

Vangeel, I. P. J., Oppelaar, H., Oussoren, Y. G., Vandervalk, M. A., & Stewart, F. A. 1995. Photosensitizing Efficacy of Mthpc-Pdt Compared to Photofrin-Pdt in the Rif1 Mouse-Tumor and Normal Skin. ***International Journal of Cancer***, 60(3): 388-394.

Vargas, A., Eid, M., Fanchaouy, M., Gurny, R., & Delie, F. 2008. In vivo photodynamic activity of photosensitizer-loaded nanoparticles: Formulation properties, administration parameters and biological issues involved in PDT outcome. ***European Journal of Pharmaceutics and Biopharmaceutics***, 69(1): 43-53.

Vasir, J. K. & Labhasetwar, V. 2006. Polymeric nanoparticles for gene delivery. ***Expert Opinion on Drug Delivery***, 3(3): 325-344.

Veenhuizen, R., Oppelaar, H., Ruevekamp, M., Schellens, J., Dalesio, O., & Stewart, F. 1997. Does tumour uptake of Foscan determine PDT efficacy? ***Int.J.Cancer***, 73(2): 236-239.

Vemuri, S. & Rhodes, C. T. 1995. Preparation and characterization of liposomes as therapeutic delivery systems: a review. ***Pharm.Acta Helv.***, 70(2): 95-111.

Verma, S., Watt, G. M., Mal, Z., & Hasan, T. 2007. Strategies for enhanced photodynamic therapy effects. ***Photochemistry and Photobiology***, 83(5): 996-1005.

von, W. A., Holtke, C., Zuhlsdorf, M., Heindel, W., Schafers, M., & Bremer, C. 2007. In vivo imaging of integrin alpha v beta 3 expression using fluorescence-mediated tomography. ***Eur.J Nucl.Med.Mol.Imaging***, 34(5): 745-754.

Vrouenraets, M. B., Visser, G. W., Stigter, M., Oppelaar, H., Snow, G. B., & van Dongen, G. A. 2002. Comparison of aluminium (III) phthalocyanine tetrasulfonate- and meta-tetrahydroxyphenylchlorin-monoclonal antibody conjugates for their efficacy in photodynamic therapy in vitro. ***Int.J Cancer***, 98(5): 793-798.

Wagner V, Husing B, & Gaisser S. Nanomedicine: Drivers for development and possible impacts. Bock AK. 1-10-2006.

Wagnieres, G., Hadjur, C., Grosjean, P., Braichotte, D., Savary, J. F., Monnier, P., & van den Bergh, H. 1998. Clinical evaluation of the cutaneous phototoxicity of 5,10,15,20-tetra(m-hydroxyphenyl)chlorin. ***Photochem.Photobiol.***, 68(3): 382-387.

Wald, G. 1959. Life and Light. ***Scientific American***, 201(4): 92-&.

Wang, H., Wang, S., Liu, Z., Dong, C., Yang, J., Gong, X., & Chang, J. 2014. Upconverting crystal/dextran-g-DOPE with high fluorescence stability for simultaneous photodynamic therapy and cell imaging. ***Nanotechnology***, 25(15): 155103.

Wang, J. B. & Liu, L. X. 2007. Use of photodynamic therapy in malignant lesions of stomach, bile duct, pancreas, colon and rectum. ***Hepato-Gastroenterology***, 54(75): 718-724.

Wang, K. K., Lutzke, L., Borkenhagen, L., Westra, W., Song, M. W. K., Prasad, G., & Buttar, N. S. 2008. Photodynamic therapy for Barrett's esophagus: does light still have a role? ***Endoscopy***, 40(12): 1021-1025.

Wang, X. H., Zhang, W. M., Xu, Z. Y., Luo, Y. F., Mitchell, D., & Moss, R. W. 2009. Sonodynamic and Photodynamic Therapy in Advanced Breast Carcinoma:A Report of 3 Cases. ***Integrative Cancer Therapies***, 8(3): 283-287.

Wani, N. A., Hamid, A., & Kaur, J. 2008. Folate status in various pathophysiological conditions. ***IUBMB.Life***, 60(12): 834-842.

Weersink, R. A., Forbes, J., Bisland, S., Trachtenberg, J., Elhilali, M., Brun, P. H., & Wilson, B. C. 2005. Assessment of cutaneous photosensitivity of TOOKAD (WST09) in preclinical animal models and in patients. ***Photochem.Photobiol.***, 81(1): 106-113.

Weitman, S. D., Lark, R. H., Coney, L. R., Fort, D. W., Frasca, V., Zurawski, V. R., Jr., & Kamen, B. A. 1992. Distribution of the folate receptor GP38 in normal and malignant cell lines and tissues. ***Cancer Research***, 52(12): 3396-3401.

Weng, J. & Ren, J. 2006. Luminescent quantum dots: a very attractive and promising tool in biomedicine. ***Curr.Med.Chem.***, 13(8): 897-909.

Whelpton, R., Michael-Titus, A. T., Basra, S. S., & Grahn, M. 1995. Distribution of temoporfin, a new photosensitizer for the photodynamic therapy of cancer, in a murine tumor model. ***Photochem.Photobiol.***, 61(4): 397-401.

Whelpton, R., MichaelTitus, A. T., Jamdar, R. P., Abdillahi, K., & Grahn, M. F. 1996. Distribution and excretion of radiolabeled temoporfin in a murine tumor model. ***Photochemistry and Photobiology***, 63(6): 885-891.

Wilkes, G. L., Orler, B., & Huang, H. 1985. "Ceramers": hybrid materials incorporating polymeric/oligomeric species into inorganic glasses utilizing a sol-gel approach. ***Polymer Preprints (American Chemical Society, Division of Polymer Chemistry)***, 26(2): 300.

Wilson, B. C., Patterson, M. S., & Lilge, L. 1997. Implicit and explicit dosimetry in photodynamic therapy: a New paradigm. ***Lasers Med.Sci.***, 12(3): 182-199.

Wong, C., Stylianopoulos, T., Cui, J., Martin, J., Chauhan, V. P., Jiang, W., Popovic, Z., Jain, R. K., Bawendi, M. G., & Fukumura, D. 2011. Multistage nanoparticle delivery system for deep penetration into tumor tissue. ***Proc.Natl.Acad.Sci.U.S.A***, 108(6): 2426-2431.

Woodhams, J. H., Kunz, L., Bown, S. G., & MacRobert, A. J. 2003. Monitoring the effect of PDT on in vivo oxygen saturation and microvascular circulation. ***Oxygen Transport to Tissue Xxv***, 540: 235-244.

Woodhams, J. H., MacRobert, A. J., Novelli, M., & Bown, S. G. 2006. Photodynamic therapy with WST09 (Tookad): Quantitative studies in normal colon and transplanted tumours. ***International Journal of Cancer***, 118(2): 477-482.

Woodle, M. C. & Lasic, D. D. 1992. Sterically stabilized liposomes. ***Biochim.Biophys.Acta***, 1113(2): 171-199.

Xie, G., Sun, J., Zhong, G., Shi, L., & Zhang, D. 2010. Biodistribution and toxicity of intravenously administered silica nanoparticles in mice. ***Arch.Toxicol.***, 84(3): 183-190.

Xiong, X. B., Huang, Y., Lu, W. L., Zhang, H., Zhang, X., & Zhang, Q. 2005a. Enhanced intracellular uptake of sterically stabilized liposomal Doxorubicin in vitro resulting in improved antitumor activity in vivo. ***Pharm.Res.***, 22(6): 933-939.

Xiong, X. B., Huang, Y., Lu, W. L., Zhang, X., Zhang, H., Nagai, T., & Zhang, Q. 2005b. Enhanced intracellular delivery and improved antitumor efficacy of doxorubicin by sterically stabilized liposomes modified with a synthetic RGD mimetic. ***J Control Release***, 107(2): 262-275.

Xiong, X. B., Huang, Y., Lu, W. L., Zhang, X., Zhang, H., Nagai, T., & Zhang, Q. 2005c. Intracellular delivery of doxorubicin with RGD-modified sterically stabilized liposomes for an improved antitumor efficacy: in vitro and in vivo. ***J Pharm.Sci.***, 94(8): 1782-1793.

Xu, J., Zhao, J. H., Liu, Y., Feng, N. P., & Zhang, Y. T. 2012. RGD-modified poly(D,L-lactic acid) nanoparticles enhance tumor targeting of oridonin. ***Int.J Nanomedicine***, 7: 211-219.

Xu, L., Wempe, M. F., & Anchordoquy, T. J. 2011. The effect of cholesterol domains on PEGylated liposomal gene delivery in vitro. ***Ther.Deliv.***, 2(4): 451-460.

Yaghini, E. 2011. *Biological and Spectroscopic Studies of Fluorescent Nanoparticles*.

Yaghini, E., Giuntini, F., Eggleston, I. M., Suhling, K., Seifalian, A. M., & MacRobert, A. J. 2014. Fluorescence lifetime imaging and FRET-induced intracellular redistribution of Tat-conjugated quantum dot nanoparticles through interaction with a phthalocyanine photosensitiser. ***Small***, 10(4): 782-792.

Yamaoka, K., Nakagawa, T., & Uno, T. 1978. Statistical moments in pharmacokinetics. ***J.Pharmacokinet.Biopharm.***, 6(6): 547-558.

Yan, F. & Kopelman, R. 2003. The embedding of meta-tetra(hydroxyphenyl)-chlorin into silica nanoparticle platforms for photodynamic therapy and their singlet oxygen production and pH-dependent optical properties. ***Photochem.Photobiol.***, 78(6): 587-591.

Yan, X., Scherphof, G. L., & Kamps, J. A. 2005. Liposome opsonization. ***J.Liposome Res***, 15(1-2): 109-139.

Yang, K. & Liu, Z. 2012. In vivo biodistribution, pharmacokinetics, and toxicology of carbon nanotubes. ***Curr.Drug Metab***, 13(8): 1057-1067.

Yang, S. J., Lin, C. F., Kuo, M. L., & Tan, C. T. 2013. Photodynamic detection of oral cancers with high-performance chitosan-based nanoparticles. ***Biomacromolecules***, 14(9): 3183-3191.

Yang, S. J., Lin, F. H., Tsai, K. C., Wei, M. F., Tsai, H. M., Wong, J. M., & Shieh, M. J. 2010. Folic acid-conjugated chitosan nanoparticles enhanced protoporphyrin IX accumulation in colorectal cancer cells. ***Bioconjug.Chem.***, 21(4): 679-689.

Yang, Y. Y., Wan, J. P., Chung, T. S., Pallathadka, P. K., Ng, S., & Heller, J. 2001. POE-PEG-POE triblock copolymeric microspheres containing protein - I. Preparation and characterization. ***Journal of Controlled Release***, 75(1-2): 115-128.

Yano, S., Kondo, K., Yamaguchi, M., Richmond, G., Hutchison, M., Wakeling, A., Averbuch, S., & Wadsworth, P. 2003. Distribution and function of EGFR in human tissue and the effect of EGFR tyrosine kinase inhibition. ***Anticancer Research***, 23(5A): 3639-3650.

Yokoyama, M. & Okano, T. 1998. [Targeting of anti-cancer drugs with nano-sized carrier system]. ***Nihon Rinsho***, 56(12): 3227-3234.

Yotsumoto, F., Sanui, A., Fukami, T., Shirota, K., Horiuchi, S., Tsujioka, H., Yoshizato, T., Kuroki, M., & Miyamoto, S. 2009. Efficacy of ligand-based targeting for the EGF system in cancer. ***Anticancer Res.***, 29(11): 4879-4885.

Yu, S. S., Lau, C. M., Thomas, S. N., Jerome, W. G., Maron, D. J., Dickerson, J. H., Hubbell, J. A., & Giorgio, T. D. 2012. Size- and charge-dependent non-specific uptake of PEGylated nanoparticles by macrophages. ***Int.J Nanomedicine***, 7: 799-813.

Yu, T., Greish, K., Mcgill, L. D., Ray, A., & Ghandehari, H. 2012a. Influence of Geometry, Porosity, and Surface Characteristics of Silica Nanoparticles on Acute Toxicity: Their Vasculature Effect and Tolerance Threshold. ***ACS Nano***, 6(3): 2289-2301.

Yu, T., Hubbard, D., Ray, A., & Ghandehari, H. 2012b. In vivo biodistribution and pharmacokinetics of silica nanoparticles as a function of geometry, porosity and surface characteristics. ***Journal of Controlled Release***, 163(1): 46-54.

Yuan, F., Dellian, M., Fukumura, D., Leunig, M., Berk, D. A., Torchilin, V. P., & Jain, R. K. 1995. Vascular permeability in a human tumor xenograft: molecular size dependence and cutoff size. ***Cancer Res.***, 55(17): 3752-3756.

Yuan, F., Leunig, M., Huang, S. K., Berk, D. A., Papahadjopoulos, D., & Jain, R. K. 1994. Microvascular permeability and interstitial penetration of sterically stabilized (stealth) liposomes in a human tumor xenograft. ***Cancer Res.***, 54(13): 3352-3356.

Yue, Z. G., Wei, W., Lv, P. P., Yue, H., Wang, L. Y., Su, Z. G., & Ma, G. H. 2011. Surface Charge Affects Cellular Uptake and Intracellular Trafficking of Chitosan-Based Nanoparticles. ***Biomacromolecules***, 12(7): 2440-2446.

Zamboni, W. C. 2005. Liposomal, nanoparticle, and conjugated formulations of anticancer agents. ***Clin.Cancer Res***, 11(23): 8230-8234.

Zaruba, K., Kralova, J., Rezanka, P., Pouckova, P., Veverkova, L., & Kral, V. 2010. Modified porphyrin-brucine conjugated to gold nanoparticles and their application in photodynamic therapy. ***Org.Biomol.Chem.***, 8(14): 3202-3206.

Zelphati, O., Uyechi, L. S., Barron, L. G., & Szoka, F. C., Jr. 1998. Effect of serum components on the physico-chemical properties of cationic lipid/oligonucleotide complexes and on their interactions with cells. ***Biochim.Biophys.Acta***, 1390(2): 119-133.

Zguris, J. & Pishko, M. V. 2006. Nitric oxide sensitive fluorescent poly(ethylene glycol) hydrogel microstructures. ***Sensors and Actuators B-Chemical***, 115(1): 503-509.

Zhang, C., Wangler, B., Morgenstern, B., Zentgraf, H., Eisenhut, M., Untenecker, H., Kruger, R., Huss, R., Seliger, C., Semmler, W., & Kiessling, F. 2007. Silica- and alkoxysilane-coated ultrasmall superparamagnetic iron oxide particles: a promising tool to label cells for magnetic resonance imaging. ***Langmuir***, 23(3): 1427-1434.

Zhang, J. S., Liu, F., & Huang, L. 2005. Implications of pharmacokinetic behavior of lipoplex for its inflammatory toxicity. ***Adv.Drug Deliv.Rev.***, 57(5): 689-698.

Zhang, L., Gu, F. X., Chan, J. M., Wang, A. Z., Langer, R. S., & Farokhzad, O. C. 2008. Nanoparticles in medicine: therapeutic applications and developments. ***Clin.Pharmacol.Ther.***, 83(5): 761-769.

Zhang, L., Xia, J., Zhao, Q., Liu, L., & Zhang, Z. 2010. Functional graphene oxide as a nanocarrier for controlled loading and targeted delivery of mixed anticancer drugs. ***Small***, 6(4): 537-544.

Zhang, X., Gan, Y., Gan, L., Nie, S., & Pan, W. 2008. PEGylated nanostructured lipid carriers loaded with 10-hydroxycamptothecin: an efficient carrier with enhanced anti-tumour effects against lung cancer. ***J.Pharm.Pharmacol***, 60(8): 1077-1087.

Zhang, Y. F., Wang, J. C., Bian, D. Y., Zhang, X., & Zhang, Q. 2010. Targeted delivery of RGD-modified liposomes encapsulating both combretastatin A-4 and doxorubicin for tumor therapy: in vitro and in vivo studies. ***Eur.J Pharm.Biopharm.***, 74(3): 467-473.

Zhao, B., Yin, J. J., Bilski, P. J., Chignell, C. F., Roberts, J. E., & He, Y. Y. 2009. Enhanced photodynamic efficacy towards melanoma cells by encapsulation of Pc4 in silica nanoparticles. ***Toxicol.Appl.Pharmacol.***, 241(2): 163-172.

Zheng, G., Chen, J., Li, H., & Glickson, J. D. 2005. Rerouting lipoprotein nanoparticles to selected alternate receptors for the targeted delivery of cancer diagnostic and therapeutic agents. ***Proc.Natl.Acad.Sci.U.S A***, 102(49): 17757-17762.

Zhou, L., Ning, Y. W., Wei, S. H., Feng, Y. Y., Zhou, J. H., Yu, B. Y., & Shen, J. 2010. A nanoencapsulated hypocrellin A prepared by an improved microemulsion method for photodynamic treatment. ***J.Mater.Sci.Mater.Med.***, 21(7): 2095-2101.

Zhu, Z., Tang, Z., Phillips, J. A., Yang, R., Wang, H., & Tan, W. 2008. Regulation of singlet oxygen generation using single-walled carbon nanotubes. ***J.Am.Chem.Soc.***, 130(33): 10856-10857.

Zimmermann, M., Zouhair, A., Azria, D., & Ozsahin, M. 2006. The epidermal growth factor receptor (EGFR) in head and neck cancer: its role and treatment implications. ***Radiat.Oncol.***, 1: 11.